Layer-by-Layer Nanoparticles for Cytokine Delivery

by

Ivan S. Pires

B.S. Chemical Engineering, The Ohio State University (2019)

SUBMITTED TO THE DEPARTMENT OF CHEMICAL ENGINEERING IN PARTIAL FULFILLMENT OF THE REQUIREMENTS FOR THE DEGREE OF

DOCTOR OF PHILOSOPHY IN CHEMICAL ENGINEERING

AT THE

MASSACHUSETTS INSTITUTE OF TECHNOLOGY

SEPTEMBER 2024

Signature of Author _____
Ivan S. Pires
Department of Chemical Engineering
July 23, 2024

Certified by _____
Paula T. Hammond
Vice Provost for Faculty and Institute Professor in Chemical Engineering
Thesis Supervisor

Certified by _____
Darrell J. Irvine
Professor of Biological Engineering and Materials Science and Engineering
Thesis Supervisor

Accepted by _____
Hadley D. Sikes
Willard Henry Dow Professor of Chemical Engineering
Graduate Officer

Layer-by-Layer Nanoparticles for Cytokine Delivery

by

Ivan S. Pires

Submitted to the Department of Chemical Engineering
on July 23, 2024, in Partial Fulfillment of the
Requirements for the Degree of Doctor of Philosophy in
Chemical Engineering

ABSTRACT

In the past decade, cancer immunotherapy has been a promising therapeutic strategy for cancer treatment. However, immunotherapy has failed to improve responses in certain cancers such as ovarian cancer (OC). The action of cytokines in the tumor microenvironment (TME) is key to regulating immune responses, but dose-limiting toxicities limit the application of cytokines in cancer therapy. One promising approach to improve treatment with cytokines are nanoparticles (NPs) which, when modulated via layer-by-layer (LbL) assembly, can provide many of the desirable characteristics of cytokine-delivery vehicles including tumor cell targeting, subcellular localization, and improved pharmacokinetics.

In this thesis, we address some aspects of NPs that have limited their clinical utility including manufacturing, control over self-assembly, and mechanistic understanding of their interactions in biological environments The focus here was on using liposomal LbL-NPs coated with a bilayer of poly-L-arginine (PLR) and poly-L-glutamate (PLE). The coating of NPs with PLR/PLE enables targeting towards cancer cell surfaces which allows for extended extracellular presentation of cargos. This ability is used for targeted delivery of a potent immunostimulant – interleukin-12 (IL-12) to disseminated tumors in metastatic OC. Aspects on the manufacturing of other lipid-based nanocarriers such as discoidal assemblies and immune stimulating complexes (ISCOMs) are also explored.

We show that employing a bottom-up approach to produce lipid-based NPs from mixed micelles allows for greater control over NP self-assembly. With this procedure, we generated immune stimulating complexes (ISCOMs) co-loaded with monophosphoryl-lipid-A (MPLA) via a scalable approach for clinical-scale manufacturing of the adjuvant termed Saponin MPLA NanoParticles (SMNP). Moreover, we discover that this approach allows for precise control over liposome size from 50 nm to 1 μm with minimal polydispersity. Lastly, by exploiting the lipid headgroup charge repulsion, we find that multivalent charged lipids yield discoidal lipid nanoparticles through this approach. Unlike previous attempts to generate lipid-based discs, this new class of NPs termed charge-stabilized nanodiscs (CND) do not require disc-stabilizing agents such as proteins or polymers. CNDs are shown to be promising drug delivery vehicles, especially when coated with PLR/PLE via the LbL technique where they have greater tumor accumulation than LbL-coated liposomes.

On the use of LbL-NP for cytokine delivery via PLR/PLE coated NPs, we found that covalent conjugation of IL-12 to the liposomal core of LbL-NPs greatly improves targeting and retention of IL-12 in peritoneally-disseminated OC tumors, enabling immunological and therapeutic effects not observed with free cytokine treatment. Mechanistic investigations revealed that these LbL-NPs rapidly accumulated in tumor nodules upon intraperitoneal (i.p.) administration, wherein shedding of the LbL coating allowed for gradual release of IL-12-lipid

conjugates via lipid extraction by serum proteins present in interstitial fluid. Upon a single dose of IL-12 conjugated to LbL-NPs using an intraperitoneally disseminated OV2944 highly-metastatic (HM-1) mouse model, we observed a dramatic increase in T cell levels within the ascites and the tumor nodules dispersed within the i.p. space which was not observed with either free cytokine or unlayered IL-12-NPs. When evaluated for its effectiveness in this highly aggressive model, two doses could significantly enhance survival compared to even five times (5x) the amount of free cytokine. Remarkably, while the model was non-responsive to checkpoint inhibitor (CPI) therapy with anti-PD1 and anti-CTLA4, when combined with LbL-IL-12-NPs, we achieved complete responses with robust immune memory induction. The mice were able to rapidly clear rechallenges with fresh cancer cells in the i.p. space.Towards the clinical translation of LbL-IL-12-NPs, we demonstrate that LbL assembly is readily performed via microfluidic mixing technology amenable for clinical-scale manufacturing. We also find that we can titrate the polymer amount used to omit time-consuming purification steps. We also find that the LbL film conformation is key to maintaining therapeutic efficacy as thicker films hinder IL-12 delivery. Lastly, we uncover that the binding target of PLE on the surface of cancer cells is SLC1A5, a glutamine amino acid transporter.

Thesis supervisor: Paula T. Hammond
Title: Vice Provost for Faculty and Institute Professor in Chemical Engineering

Thesis supervisor: Darrell J. Irvine
Title: Professor of Biological Engineering and Materials Science and Engineering

Members of Thesis Committee

Paula T. Hammond, Ph.D.
Vice Provost for Faculty and Institute Professor in Chemical Engineering
Massachusetts Institute of Technology
Thesis Supervisor

Darrell J. Irvine, Ph.D.
Professor of Biological Engineering and Materials Science and Engineering
Massachusetts Institute of Technology
Thesis Supervisor

K. Dane Wittrup, Ph.D.
Carbon P. Dubbs Professor in Chemical Engineering and Biological Engineering
Massachusetts Institute of Technology

Kevin Elias, MD.
Director of Gynecologic Oncology Laboratory
Assistant Professor in Obstetrics, Gynecology and Reproductive Biology
Brigham and Women's Hospital, Harvard Medical School

To my loving parents,
Ivanete Susin and Alexandre Vaz Pires,

Acknowledgments

It would not have been possible for me to complete this doctoral program without the guidance, help, and support of so many people. I would like to extend my sincere gratitude to the following:

First and foremost, to my thesis advisors: Prof. Paula Hammond and Prof. Darrell Irvine. Since first meeting Paula at the Lowrie Awards Banquet at OSU, I can only describe her as inspirational. I am very grateful for having the opportunity to join the Hammond Lab and have you as a mentor to guide me in the world of drug delivery. Your kindness, patience, and immensely positive attitude are qualities that make you undoubtedly a mentor that anyone could want. While I had not met Darrell until my first semester at MIT, I very quickly understood why he has been successful at developing a multitude of innovative technologies for immunomodulation. Darrel remained deeply connected to the many unique projects ongoing in the lab. The level of detail and immunological insights are truly remarkable. It has been a privilege to meet you and have the opportunity to discuss research ideas and learn from you. I feel incredibly lucky to have been co-mentored by two amazing scientists. The freedom you have both provided me during the PhD program is invaluable, allowing me to pursue research directions that even I was not sure of the direct outcomes, but that seemed interesting to dive deeper. Diving deep is indeed one of the many items I really learned from my time in the labs where we had the resources to ask key questions that allowed us to develop a better understanding of how to design biomaterials. Moreover, both have attracted amazing and talented scientists to fill their labs giving me a highly supportive and resourceful environment to not only conduct research, but also develop meaningful connections.

To my undergraduate mentor: Prof. Andre F. Palmer – I am indebted to you so quickly and openly accepting me into your research lab. The opportunity and mentorship you provided has been the foundation of my passion for research. The openness and proximity between you and lab members was key to motivating me to believe we could achieve more.

To my thesis committee: Prof. Dane Wittrup and Dr. Kevin Elias. Our discussion and your insights have been key to influencing the direction of the work. Whether it was providing a connection for an experiment or a clinical insight into how a treatment could benefit patients, our meetings guided me to effective and meaningful solutions.

To my research collaborators and lab mates at The Ohio State University: Starting with the mentors who showed me the ropes to research including Donald Belcher and Richard Hickey. The lab mates all of whom made research a fun experience including Chintan Savla and Quintin T. O'Boyle. And collaborators who enabled the work to propel forward including Dr. Pedro Cabrales, Dr. Paul Buehler, and Dr. David Irwin.

For colleagues who were vital to the work at MIT: Dr. Gil Covarrubias who was always willing to help with new ideas and many last-minute experiments. Your companionship on the many long experiments and optimism in the face of uncertainty were critical to my success. Dr. Apoorv Shanker who made long days in the lab an opportunity to have fun with long conversations ranging from meaningful to obscure. Victoria Gomerdinger who helped with planning, organizing, and executing many experiments. To Dr. Antonio Barberio who showed me how to make my first nanoparticle and Dr. Sean Smith who showed me how to perform my first pilot experiments.

To the undergraduate students Ezra Gordon, Jack Suggs, Isabella Carlo, and Gonzalo Ezparza who in addition to helping with many key experiments, were critical to starting various side projects. I have been very fortunate to have had such an amazing team to work with and to turn research in the lab significantly more worthwhile.

To the many lab mates I had the pleasure to work with and interact on the day-to-day. In the Hammond Lab: Mae, Andrew, Eva, Justin, Namita, Sasan, Steph, Adam, Sheryl, Colin, Elad, Brandon, Natalie, Rami, Simone, Joelle, Celestine, Maylin, Yanpu, Tamara, Maggie, Nick, Pooria, Joon, Michael, Kimberly, Rachel, Eduardo, Alex, Zhi Kai, Chau. In the Irvine Lab: Kristen, Sachin, Bingxu, Yash, Alex, Anna, Jason, Luciano, Maureen, Riyam, Bill, Ashley, B.J., Elana, Kewen, Jonathan, Namit, Parisa, Mariane, Laura, Aggi, Kasia, Heikyung, Ozgun, Aereas, Coralie, Kaiyuan, Leyuan, Eric, Murillo, Jason, Ryan, Parastoo, Justin, Shengwei, Tanaka, Maurice.

To the amazing administrative staff Liz Galoyan, Valerie Corapi, Mark Miller and Xiuyun Hou.

To the technical support at shared facilities at MIT: Dr. DongSoo Yun and Dr. Abigail Lytton-Jean at the nanotechnology materials core, Jeff Wyckoff at the microscopy facility, Dr. Glenn Paradis and Michael Tramontanis at the flow cytometry core, Dr. Virginia Spanoudaki at the animal Imaging and preclinical testing core.

To the sources of my financial support: the first-year support from the Department of Chemical Engineering at MIT, the Marble Center for Nanomedicine, Howard Hughes Medical Institute, and the National Cancer Institute.

Finally, my heartfelt thanks to my family and close friends for their support and companionship. Especially my brother Alex Pires who has been a constant source of support. And, to my parents, Ivanete Susin and Alexandre Vaz Pires – for your sacrifices and deep commitment towards raising me. I am fortunate for the family I have.

With my sincerest gratitude to you all,

Ivan S. Pires
July 23, 2024
Massachusetts Institute of Technology

Biographical Note

Ivan S. Pires

EDUCATION

Massachusetts Institute of Technology Sept.2019 – present
Ph.D, Chemical Engineering expected July.2024

The Ohio State University Sept.2015 – May.2019
B.S, Chemical Engineering

RESEARCH EXPERIENCE

Graduate Research Assistant
Advisor: Paula T. Hammond, co-advised with Darrell J. Irvine, Massachusetts Institute of Technology
- Layer-by-Layer Nanoparticles for Cancer Immunotherapy Jan.2020 – present

Undergraduate Research Assistant, Pelotonia Fellow
Advisor: Prof. Andre F. Palmer, The Ohio State University
- Engineering therapeutics to detoxify hemoglobin, heme, and iron May.2016 – Aug.2019

TEACHING EXPERIENCE

Graduate Student Teaching Assistant (Chemical Engineering Projects Lab) Jan.2019 – May.2019
Dept. Chemical Engineering, Massachusetts Institute of Technology

ACADEMIC AWARDS

- Scripps Consortium for HIV/AIDS Vaccine Development (CHAVD) 2023 Young Investigator Award
- National Cancer Institute (NCI) F99/K00 Fellowship
- OSU Board of Trustees Student Recognition Award for outstanding leadership and dedicated service.
- OSU Undergraduate Pelotonia Fellowship.
- American Institute of Chemists Foundation Outstanding Undergraduate Student Award being awarded membership into the organization
- OSU William G. Lowrie Dept. of Chemical and Biomol. Eng. Undergraduate Patents/Publishing Award in 2018
- OSU William G. Lowrie Dept. of Chem. and Biomol. Eng. Outstanding Undergraduate Award for Research Excellence in 2017.
- North Carolina State 2018 Future Leaders in Chemical Engineering Award Symposium – one of fifteen chemical engineering students selected nationally
- OSU Office of Undergraduate Research Summer Research Fellowship.
- OSU Office of Undergraduate Research & Creative Inquiry Advanced Undergraduate Research Award
- OSU International Undergraduate Scholarship for Academic Excellence.
- OSU Honors Undergraduate Research Distinction Scholarship.
- OSU Minority Engineering Program Academic Achievement Award.
- OSU College of Engineering Dean's List.

PUBLICATIONS

As first or co-first author (*equal contribution)

1. **Pires, I. S.**, Berthiaume, F. & Palmer, A. F. Engineering Therapeutics to Detoxify Hemoglobin, Heme, and Iron. *Annu Rev Biomed Eng* 25, 1–21 (2023).

2. **Pires, I. S.**, Ni, K., Melo, M. B., Li, N., Ben-Akiva, E., Maiorino, L., Dye, J., Rodrigues, K. A., Yun, D., Kim, B., Hosn, R. R., Hammond, P. T. & Irvine, D. J. Controlled lipid self-assembly for

scalable manufacturing of next-generation immune stimulating complexes. *Chemical Engineering Journal* 464, 142664 (2023).

3. Munoz, C. J.*, **Pires, I. S.***, Jani, V., Gopal, S., Palmer, A. F. & Cabrales, P. Apohemoglobin-haptoglobin complex alleviates iron toxicity in mice with β-thalassemia via scavenging of cell-free hemoglobin and heme. *Biomedicine & Pharmacotherapy* 156, 113911 (2022).

4. **Pires, I. S.**, Hammond, P. T. & Irvine, D. J. Engineering Strategies for Immunomodulatory Cytokine Therapies: Challenges and Clinical Progress. *Adv Ther (Weinh)* 4, 2100035 (2021).

5. **Pires, I. S.**, Govender, K., Munoz, C. J., Williams, A. T., O'Boyle, Q. T., Savla, C., Cabrales, P. & Palmer, A. F. Purification and analysis of a protein cocktail capable of scavenging cell-free hemoglobin, heme, and iron. *Transfusion (Paris)* 61, 1894–1907 (2021).

6. **Pires, I. S.** & Palmer, A. F. Selective protein purification via tangential flow filtration – Exploiting protein-protein complexes to enable size-based separations. *J Memb Sci* 618, 118712 (2021).

7. **Pires, I. S.** & Palmer, A. F. Tangential flow filtration of haptoglobin. *Biotechnol Prog* 36, (2020).

8. **Pires, I. S.**, O'Boyle, Q. T., Munoz, C. J., Savla, C., Cabrales, P. & Palmer, A. F. Enhanced Photodynamic Therapy Using the Apohemoglobin-Haptoglobin Complex as a Carrier of Aluminum Phthalocyanine. *ACS Appl Bio Mater* 3, 4495–4506 (2020).

9. Munoz, C. J.*, **Pires, I. S.***, Baek, J. H., Buehler, P. W., Palmer, A. F. & Cabrales, P. Apohemoglobin-haptoglobin complex attenuates the pathobiology of circulating acellular hemoglobin and heme. *American Journal of Physiology-Heart and Circulatory Physiology* 318, H1296–H1307 (2020).

10. **Pires, I. S.***, Savla, C.* & Palmer, A. F. Poly(ethylene glycol) Surface-Conjugated Apohemoglobin as a Synthetic Heme Scavenger. *Biomacromolecules* 21, 2155–2164 (2020).

11. **Pires, I. S.**, Belcher, D. A., Hickey, R., Miller, C., Badu-Tawiah, A. K., Baek, J. H., Buehler, P. W. & Palmer, A. F. Novel manufacturing method for producing apohemoglobin and its biophysical properties. *Biotechnol Bioeng* 117, 125–145 (2020). Front Cover and Gaden Award Winner.

12. **Pires, I. S.***, Belcher, D. A.* & Palmer, A. F. Quantification of Active Apohemoglobin Heme-Binding Sites via Dicyanohemin Incorporation. *Biochemistry* 56, 5245–5259 (2017).

Other publications

1. Reddy, S. V., Kumar S., Patel D., Manjunath G.,Kungumaraj H. J., Lugo J., **Pires I. S.**, O'Boyle Q., Mao Y., Palmer A. F., Berthiaume F.. Human Plasma Protein Cocktail Decreases Burn Wound Expansion and Bacterial Growth. *Journal of Biological Regulators and Homeostatic Agents*. 38(5): 3815-3827 (2024) doi:10.23812/j.biol.regul.homeost.agents.20243805.301

2. Munoz, C.J., Lucas, D., Martinez, J., Ricario, M., O'Boyle, Q.T., **Pires, I.S.**, Palmer, A.F. and Cabrales, P., Toxic side-effects of diaspirin cross-linked human hemoglobin are attenuated by the apohemoglobin-haptoglobin complex. *Biomedicine & Pharmacotherapy*, 174, p.116569 (2024)

3. Liu, B.*, Carlson, R. J.*, **Pires, I. S.^**, Gentili, M.^, Feng, E., Hellier, Q., Schwartz, M. A., Blainey, P. C., Irvine, D. J. & Hacohen, N. Human STING is a proton channel. *Science* (1979) 381, 508–514 (2023).

4. Ma, L., Hostetler, A., Morgan, D. M., Maiorino, L., Sulkaj, I., Whittaker, C. A., Neeser, A., **Pires, I. S.**, Yousefpour, P., Gregory, J., Qureshi, K., Dye, J., Abraham, W., Suh, H., Li, N., Love, J. C. & Irvine, D. J. Vaccine-boosted CAR T crosstalk with host immunity to reject tumors with antigen heterogeneity. *Cell* 186, 3148-3165.e20 (2023).
5. He, Y., Hong, C., Huang, S., Kaskow, J. A., Covarrubias, G., **Pires, I. S**., Sacane, J. C., Hammond, P. T. & Belcher, A. M. STING Protein-Based In Situ Vaccine Synergizes CD4 + T, CD8 + T, and NK Cells for Tumor Eradication. *Adv Healthc Mater* (2023). doi:10.1002/adhm.202300688 – Back Cover

6. Barberio, A. E., Smith, S. G., **Pires, I. S.**, Iyer, S., Reinhardt, F., Melo, M. B., Suh, H., Weinberg, R. A., Irvine, D. J. & Hammond, P. T. Layer-by-layer interleukin-12 nanoparticles drive a safe and effective response in ovarian tumors. *Bioeng Transl Med* (2022). doi:10.1002/btm2.10453

7. Kong, S., Moharil, P., Handly-Santana, A., Boehnke, N., Panayiotou, R., Gomerdinger, V., Covarrubias, G., **Pires, I. S.**, Zervantonakis, I., Brugge, J. & Hammond, P. T. Synergistic combination therapy delivered via layer-by-layer nanoparticles induces solid tumor regression of ovarian cancer. *Bioeng Transl Med* 8, (2023).

8. Gu, X., Bolden-Rush, C., Cuddington, C. T., Belcher, D. A., Savla, C., **Pires, I. S.** & Palmer, A. F. Comprehensive characterization of tense and relaxed quaternary state glutaraldehyde polymerized bovine hemoglobin as a function of cross-link density. *Biotechnol Bioeng* 117, 2362–2376 (2020).

9. Krzyszczyk, P., Kang, H. J., Kumar, S., Meng, Y., O'Reggio, M. D., Patel, K., **Pires, I. S.**, Yarmush, M. L., Schloss, R. S., Palmer, A. F. & Berthiaume, F. Anti-inflammatory effects of haptoglobin on LPS -stimulated macrophages: Role of HMGB1 signaling and implications in chronic wound healing. *Wound Repair and Regeneration* 28, 493–505 (2020).

10. Belcher, D. A., Munoz, C., **Pires, I. S**., Williams, A. T., Cabrales, P. & Palmer, A. F. Apohemoglobin-haptoglobin complexes attenuate the hypertensive response to low-molecular-weight polymerized hemoglobin. *Blood Adv* 4, 2739–2750 (2020).

11. Belcher, D. A., Cuddington, C. T., Martindale, E. L., **Pires, I. S.** & Palmer, A. F. Controlled Polymerization and Ultrafiltration Increase the Consistency of Polymerized Hemoglobin for Use as an Oxygen Carrier. *Bioconjug Chem* 31, 605–621 (2020).

12. Hugelshofer, M., Buzzi, R. M., Schaer, C. A., Richter, H., Akeret, K., Anagnostakou, V., Mahmoudi, L., Vaccani, R., Vallelian, F., Deuel, J. W., Kronen, P. W., Kulcsar, Z., Regli, L., Baek, J. H., **Pires, I. S.**, Palmer, A. F., Dennler, M., Humar, R., Buehler, P. W., Kircher, P. R., Keller, E. & Schaer, D. J. Haptoglobin administration into the subarachnoid space prevents hemoglobin-induced cerebral vasospasm. *Journal of Clinical Investigation* 129, 5219–5235 (2019).

Table of Contents

List of Figures and Tables

Figure 1.6. Schematic of an alginate-based polymeric matrix designed for in situ gelation to enable prolonged and dual release of IL-2 and CpG as well as harbor and attract immune cells. Reproduced with permission. [205] Copyright 2009, Elsevier.

Figure 1.7. Bioresponsive polymeric microparticles for anti-inflammatory cytokine delivery to osteoarthritis. Reproduced with permission.[231] Copyright 2019, Wiley Periodicals, Inc.

Figure 1.8. Synthesis and bioactivity of liposomes surface conjugated with anti-CD137 antibody or IL2-Fc fusion protein. **(A)** schematic for synthesis of liposomes. **(B)** Flow cytometry of $CD4^+$ and $CD8^+$ T cells incubated with fluorescently-labeled liposomes (solid), unconjugated liposomes (dashed), or no liposomes (grey area). **(C)** In vitro T cell proliferation normalized to unstimulated cells. **(D)** IFN-γ production by polyclonal T cells. Reproduced with permission.[240] Copyright 2013, American Association for Cancer Research.

Figure 1.9. Cancer-cell targeting liposomal layer-by-layer nanoparticle containing surface conjugated IL-12. (A) Diagram for assembly of nanoparticle. (B) Cancer cell association and subsequent targeted immune activation. Adapted with permission.[241] Copyright 2020, American Chemical Society.

Figure 1.10. Schematic for synthesis of liposomal nanogel encapsulating a TGF-β inhibitor and IL-2 and its effects when intratumorally administered to a subcutaneous mouse metastatic melanoma model. **(a)** Components and final liposomal nanogel assembly. **(b)** Plot of tumor area versus time (day 0 was day of tumor inoculation). Red arrows indicate treatment. **(c)** Tumor masses after 7 days of treatment. **(d)** Survival plot of animals in **(b)**. Complete tumor regression and survival was obtained in 40% of the group after 60 days (data not shown). Adapted with permission.[247] Copyright 2012, Nature Publishing Group.

Table 1.1 Clinically approved recombinant cytokine therapies for *in vivo* immunomodulation.

Table 1.2. Current cytokine therapy clinical trials (parenthesis indicates number of trials still ongoing) and indications of active clinical trials (excluding approved indications).

Table 1.3. Immunocytokines in clinical trials.

Figure 2.1: Critical micelle concentration (CMC) of detergent controls self-assembly of ISCOMs. (A) Schematic illustrating strategy of micelle dilution for ISCOM assembly. (B) DLS volume-based size distribution of MEGA-10 detergent at various concentrations in the presence or absence of ISCOM components. (C) DLS intensity-weighted size measurements (Z-avg) and polydispersity index (PDI) of 5 mg/mL ISCOMs rapidly diluted from an initial 7.5% (w/v) MEGA-10 to the indicated final concentrations of surfactant (arrows indicate change in size after incubation sample overnight at room temperature).

Figure 2.2: Analytical modeling predicts that dilution of surfactants to CMC prior to TFF does not significantly affect filtration performance. (A) Schematic depicting the close-association model of micelle-monomer equilibrium. (B) Simplified schematic TFF system used to derive mass balance equations. (C) Concentration over time from TFF model using a 10 kDa membrane to remove detergent monomers from a mixture with 7.5% MEGA-10 and 5 mg/mL saponin. (D) Concentration over time from TFF model using a 100 kDa membrane to first concentrate a mixture with 0.15% MEGA-10 and 0.1 mg/mL saponin to 5 mg/mL saponin then purify mixture from detergent monomers.

Figure 2.3: Comparison of Quil-A ISCOMs and SMNP generated via dialysis or dTFF. (A) Schematic for process to generate ISCOMs via dialysis, standard dTFF or low detergent dTFF. (B) DLS intensity-based distribution of final particles. (C) DLS number-based distribution of final particles. (D) DLS Z-avg, number average (#-avg) and PDI of final particles. (E) Representative Zeta Potential distribution of SMNP particles generated via dialysis of dTFF with average and standard deviation provided of three measurements. (F) TEM micrograph of ISCOMs or SMNPs generated via dialysis, dTFF or LD-dTFF. White arrowheads indicate worm-like species.

Figure 2.4: Quil-A SMNP generated via dialysis or dTFF have indistinguishable biological adjuvant activity in vivo. (A) Timeline of immunizations with SMNP and HIV Env trimer antigen N332-GT2. (B) ELISA analysis of serum IgG response at week 4 for mice immunized with 2 μg

of N332-GT2 trimer and 5 μg of SMNP from the different preparations. (C) Serum titers of IgG measured from curves in (B).

Figure 2.5: Slow dilution of QS-21 SMNP components in surfactant enables well-defined ISCOM self-assembly. (A) DLS Z-avg size measurements and PDI of 5 mg/mL of QS-21 SMNPs in 7.5% MEGA-10 at various dilutions. (B) Diagram illustrating slow dilution at room temperature to generate SMNP. (C) DLS Z-avg, number-avg and PDI for QS-21 SMNP samples slowly diluted continuously then processed via TFF (dTFF) compared to QS-21 SMNP generated via dialysis. (D) Representative zeta potential distribution of QS-21 SMNP generated via dTFF or dialysis with average zeta potential of three measurements displayed. (E) TEM micrographs of samples QS-21 SMNPs generated via dialysis (left) or via dTFF (right). Scale bars indicate 200 nm.

Figure 2.6: QS-21 SMNP is bioactive and stable when stored at -20 °C without use of cryoprotectants. (A) Representative DLS intensity-based and number-based distribution of QS-21 SMNP particles stored at 4 °C or frozen at -20 °C or -80 °C then thawed at room temperature. (B) DLS Z-avg, and number-avg for QS-21 SMNP samples stored at 4 °C or frozen at -20 °C or -80 °C then thawed at room temperature. (C) ELISA analysis of serum IgG response at week 6 for mice immunized with 2 μg of N332-GT2 trimer and 5 μg of SMNP stored at 4 °C or frozen at -20 °C or -80 °C then thawed at room temperature. (D) Serum titer from ELISA curves in (C). TEM micrographs of QS-21 SMNP stored at 4 °C (E) or frozen at -20 °C (F) or -80 °C (G) then thawed at room temperature. Scale bars indicate 200 nm.

Figure 2.7: Room temperature QS-21 SMNPs synthesis is facilitated through staggered dilution. (A) Diagram for staggered room temperature (RT) dilution where the sample is repeatedly partially diluted then let sit until fully equilibrated (equilibration times and dilution factors at for each step shown in **Supplementary Table A2**). (B) DLS Z-avg, PDI and number-avg for room temperature QS-21 SMNP samples synthesized via staggered dilution compared to FPLC purified SMNPs from dialysis synthesis. (C) TEM micrographs of QS-21 SMNP generated at room temperature through the staggered dilution protocol. (D) Summary of serum IgG titers at week 2 and week 4 from mice immunized with 2 μg of N332-GT2 trimer and 5 μg of SMNP using the staggered dilution room temperature protocol (E) IFN-γ ELISpot of splenocytes harvested two weeks after immunization and stimulated with a pool of N332-GT2 trimer peptides.

Table 2.1: Mass ratio of QS-21 SMNPs components relative to saponin. Values indicate average of three independent batches and standard deviation.

Figure 3.1. Detergent concentration during nanoparticle formation dictates equilibrium size of nanoparticles. **(A)** Schematic of liposome assembly from mixed micelle dilution. **(B)** Particle size determined by DLS of samples diluted with PBS to various final concentrations of MEGA-10 starting from an initial mixture of 10 mg/mL of 6:3:1 molar mixture of DSPC:cholesterol:POPG in 10% MEGA-10. **(C)** Particle size evolution over time determined by DLS for mixed micelles diluted to 0.1% and 0.01% MEGA-10. **(D)** Polydispersity index (PDI) kinetics for mixed micelles diluted to 0.1% and 0.01% MEGA-10.

Figure 3.2. Purified lipid nanoparticles maintain size and monodispersity. **(A)** DLS intensity and number distribution for liposomes generated by diluting a lipid mix (of 10 mg/mL of 6:3:1 molar mixture of DSPC:cholesterol:POPG in 10% MEGA-10) to 0.1%, 0.02% and 0.004% of detergent. **(B)** Size and PDI of samples from **(A)**. **(C)** Zeta potential of samples from **(A)** - the variation in measured zeta potentials can be explained by the approximation of the Henry's function as a constant in our instrument given that for a given zeta potential, increased particle size increases electrophoretic mobility.[29] Representative cryoTEM images of samples from samples generated at **(D)** 0.004%, **(E)** 0.02%, **(F)** and 0.1% – internal shading on large liposomes are due to particle protrusion from ice.[30] **(G)** Histograms of particles measured on cryoTEM micrographs from samples in **(A)** – parenthesis indicates the total number of particles quantified and PDI based on the measured particle sizes from cryoTEM. **(H)** Box and whiskers plot of size distribution from **(G)**.

Figure 3.3. Solution ionic strength and lipid composition regulates the self-assembly from lipid/detergent micelles into liposomes. **(A)** Particle size (Z-avg) and PDI after lipid/detergent micelle dilution (10 mg/mL of 6:3:1 molar mixture of DSPC:cholesterol:POPG in 10% MEGA-10) with 10 mM HEPES and overnight incubation. **(B)** Z-avg and PDI of neutral lipid/detergent micelles (10 mg/mL of 7:3 molar mixture of DSPC:cholesterol in 10% MEGA-10) diluted with either PBS or 10 mM HEPES. **(C)** Z-avg and PDI of anionic lipid/detergent micelles charged with

DSPG either containing or lacking cholesterol (10 mg/mL of either 6:3:1 or 9:1 molar mixture of DSPC:cholesterol:DPSG or DSPC:DSPG in 10% MEGA-10) diluted with PBS. **(D)** Z-avg and PDI of cholesterol-free unsaturated (unsat) mixed micelles (9:1 DSPC:POPG) and saturated (sat) mixed micelles (9:1 DSPC:DSPG) diluted with PBS to various final MEGA-10 concentration and allowed to incubate overnight at room temperature.

Figure 3.4. FRET of diluted mixed micelles reveals intermediates with high rates of lipid exchange. **(A)** Schematic for dilution of FRET micelles. **(B)** Schematic for separately diluting donor-only or acceptor-only micelles and then mixing the diluted samples (sepFRET). **(C)** Normalized FRET efficiency of FRET micelles and sepFRET micelles right after mixing donor and acceptor (0 hr). **(D)** Time course of normalized FRET efficiency since mixing donor and acceptor micelles at 0.0125% MEGA-10 for FRET micelles and sepFRET micelles. **(E)** Time course of normalized FRET efficiency since mixing donor and acceptor micelles at 0.1% MEGA-10 for FRET micelles and sepFRET micelles. **(F)** Normalized FRET efficiency of FRET micelles and sepFRET micelles two days after mixing donor and acceptor (48 hrs).

Figure 3.5. Cryo-TEM micrographs of particles incubated in 0.1% MEGA-10 reveal formation of large disc assemblies and coexistence of micelles with fully assembled bilayer vesicles. **(A-D)** Cryo-TEM micrograph of 10 mg/mL 6:3:1 DSPC:Chol:POPG sample in 10% MEGA-10 rapidly diluted to 0.1% MEGA-10 with 10 mM HEPES 150 mM NaCl and frozen 5 minutes, 2 hours, 5 hours and 24 hours after dilution, respectively. **(E)** Schematic for the two proposed main driving mechanism of particle coalescence and growth upon mixed micelle dilution.

Figure 3.6. Controlled assembly of liposomes reveals a linear size-dependence effect on NP uptake in macrophages *in vitro*. **(A)** Intensity weighted size (Z-avg) and PDI of liposomes generated for this experiment. **(B)** NP uptake on RAW264.7 macrophage cells after 4 or 24 hours of incubation with NPs. Dashed lines indicate 95% confidence interval of linear fit.

Figure 4.1. **Charge-stabilized nanodiscs (CND) with monovalent lipids are unstable in physiological ionic strength media. (A)** Schematic process for dilution of mixed micelles to generate discoidal lipid assemblies or liposomes. **(B)** Lipid/detergent micelles (10 mg/mL of 6:3:1

molar mixture of DSPC:cholesterol:POPG in 10% MEGA-10) in 10 mM HEPES buffer with different concentration of NaCl were diluted to indicated final MEGA-10 concentrations and particle sizes (hydrodynamic Z-avg) were assessed by DLS. (**C, D**) CryoTEM micrographs of purified samples from dilution of lipid/detergent micelles using **(C)** 200 mM NaCl and **(D)** 0 mM NaCl. **(E)** Intensity-weighted diameter (Z-avg) of PBS-diluted lipid/detergent micelles containing 10 mg/mL of lipids in 10% MEGA-10 composed of either 5:3:2, 4:3:3, or 3:3:4 molar ratios of DSPC:cholesterol:POPG. **(F)** Representative cryoTEM micrograph of a 3:3:4 molar composition (DSPC:cholesterol:POPG) of mixed micelles allowed to equilibrate at 0.05% MEGA-10 overnight then purified via TFF to remove MEGA-10.

Figure 4.2. **Charge density of anionic lipid DOPE-glutaryl enables synthesis of CNDs stable at physiological ionic strength buffers. (A)** Chemical structure of POPG and DOPE-glutaryl. **(B)** DLS size (Z-avg, and #-avg) and polydispersity index (PDI) of particles assembled from varying compositions of DPSC, cholesterol, and DOPE-glutaryl diluted in PBS to 0.1% MEGA-10 concentrations (all samples contained 30 mol% cholesterol and the mol% indicated of DOPE-glutaryl with the remainder being DSPC). **(C)** DLS count rate with or without polarized light filters. **(D)** Zeta potential of CNDs composed with 10 mol% DOPE-glutaryl compared to extrusion-based liposomes with 10 mol% POPG (both samples contained 30% cholesterol and 60% DSPC). **(E)** Representative negative stain TEM (NS-TEM) micrograph of purified CNDs from (C). **(F)** Proposed structure of CNDs composed of DOPE-glutaryl, DSPC, and cholesterol.

Figure 4.3. **CNDs show greater tumor accumulation than liposomes in solid tumors. (A)** DLS Z-avg, #-avg, and PDI of purified CNDs composed with 10 mol% DOPE-glutaryl compared to extrusion-based liposomes with 10 mol% POPG (both samples contained 30% cholesterol and 60% DSPC). **(B)** In vivo study timeline in which mice were inoculated subcutaneously with 10^6 MC38 cells and then dosed intravenously on day 7 with 1 nmol of cyanine-5 labeled NPs (1 mol%). **(C)** Tumor radiant efficiency measured in vivo via IVIS. **(D)** Area under the curve (AUC) or data from (H). **(E)** Serum fluorescence of CNDs and liposome dosed animals at 4 and 16 hours after dosing. **(F)** Recovered radiant efficiency from tumor, liver and spleen 24 hours after dosing mice with either CNDs or liposomes. Error bars represent SEM (n = 3 for C-D and n = 4 for E-F). Statistical comparisons in C, E and F were performed using two-way analysis of variance

(ANOVA), with Tukey's multiple-comparisons test and an unpaired two-tailed t-test was performed for D. Asterisks denote p-values: ****p < 0.0001, ***p < 0.001, **p < 0.01, *p < 0.05.

Figure 4.4. **Deposition of polyelectrolyte layers composed of PLR and PLE onto CNDs enables improved association of CNDs with ovarian cancer cells *in vitro*. (A)** Schematic of LbL technique to generate LbL-liposomes and LbL-CNDs. **(B)** Size and PDI of CND and liposomes before and after LbL modification. **(C)** In vitro measurement of total HM-1-associated NP fluorescence relative to liposomes using a plate reader after 4 or 24 hours of incubation. **(D)** Confocal images of HM-1 cells after 4 hrs of incubation with NPs. Error bars represent SEM. Statistical comparisons in C was performed using two-way analysis of variance (ANOVA), with Tukey's multiple-comparisons. Asterisks denote p-values: ****p < 0.0001, ***p < 0.001, **p < 0.01, *p < 0.05.

Figure 4.5. LbL-CNDs NPs efficiently target metastatic ovarian cancer in vivo. (A) In vivo timeline for treatment of fluorescently-labeled NPs i.p. in ovarian cancer model. Mice were inoculated with 10^6 HM-1-luc cells i.p. and dosed with NPs 14 days later. **(B)** Total radiant efficiency of NP fluorescence from peritoneum. **(C)** AUC of peritoneal fluorescence readings from B. **(D)** *Ex vivo* weight normalized NP fluorescence in liver, spleen, UGT, and omentum. **(E)** Spearman's correlation coefficient between weight-normalized NP fluorescence and weight-normalized BLI readings. Error bars (s.e.m.) derived from parameter estimates for each group. **(F)** Slope of linear fit between weight-normalized NP fluorescence and weight-normalized BLI readings. Error bars (s.e.m.) represent variation between each animal in respective treatment groups (n = 4 mice/group). Statistical comparisons in B and D were performed using two-way analysis of variance (ANOVA) one-way ANOVA was used in C and F with Tukey's multiple-comparisons test. Spearman's correlation significance for E was performed based on a t-test analysis with the null hypothesis of no (r=0) correlation. Asterisks denote p-values: ****p < 0.0001, ***p < 0.001, **p < 0.01, *p < 0.05.

Figure 5.1. LbL NPs undergo dynamic reorganization on contact with physiologic fluids. a, Schematic for assembly of LbL- NPs with either Mal or Ni linker chemistries for conjugation of IL-12 onto NPs. **b,** Quantification of total PLE and PLR retained with LbL-NPs upon incubation

in cell-free ascites fluid at 37 °C (* indicates fluorophore tagged polymer) (mean ± s.e.m.). **c,** Quantification of total IL-12 available for monoclonal antibody binding from Mal NPs either in diH_2O or 10% FBS media (mean ± s.e.m.). **d,** Quantification of total IL-12 released from LbL-NPs upon incubation in cell-free ascites fluid at 37 °C (mean ± s.e.m.). **e,** Representative flow cytometry fluorescence histogram of HM-1 cells incubated with unlayered (UL) or PLE-coated LbL-NPs for 4 hours *in vitro*. **f,** Quantification of median fluorescence intensity (MFI) of treated HM-1 cells from e (mean ± s.d.). **g-h,** Representative confocal images of HM-1 cells incubated with UL (**g**) or LbL NPs (**h**) for 4 hours – UL images adjusted relative to LbL to visualize internalized NPs (blue, Hoechst 33342 nuclear stain; green , wheat germ agglutinin (WGA) cell surface stain; cyan, nanoparticles). Data are representative of at least two independent experiments. Statistical comparisons in **c** and **f** were performed using two and one-way analysis of variance (ANOVA), respectively, with Tukey's multiple-comparisons test.

Figure 5.2. LbL coating enables targeting of tumor tissue *in vivo* and enhanced i.p. retention of NPs and IL-12. **a-c,** B6C3F1 mice (*n*=8/group for 0-24 hrs and n=3/group for 24-96 hrs) inoculated with 10^6 HM-1-luc tumor cells on day 0 were administered fluorescently-tagged NPs carrying 20 μg IL-12 (or an equivalent dose of free IL-12) on day 14. Shown are whole-animal imaging NP fluorescence **(a)** and IL-12 fluorescence **(b, c)** from the i.p. space collected over time post dosing (mean ± s.e.m.). **d-e,** B6C3F1 mice (n=4/group) inoculated with 10^6 HM-1-luc tumor cells on day 0 were administered 100 μg fluorescently-tagged LbL-NPs or UL-NPs (devoid of IL-12) on day 14. UGT and omentum tissue were harvested at 1, 2, 4, 12 and 24 hrs after dosing and imaged ex-vivo via IVIS. Shown are weight-normalized tissue NP fluorescence in **d** UGT and **e** omentum (mean ± s.e.m.). **f-h,** B6C3F1 mice (*n*=4/group) were treated as **a-c**. Four hours after dosing, animals were sacrificed, and tissues were analyzed ex-vivo via IVIS. Shown are weight-normalized tissue NP fluorescence (mean ± s.e.m., **f**), Pearson's correlation coefficient for groups with significant ($p<0.05$) correlation between weight-normalized tissue NP fluorescence and BLI 4 hours after dosing **(g),** and representative omentum and UGT tissue IVIS BLI and NP fluorescence images for LbL NPs and UL NPs **(h)**. Correlation significance performed based on a t-test analysis with the null hypothesis of no (r=0) correlation. Group statistical comparisons in **f** were performed using a two-way ANOVA with Tukey's multiple-comparisons test.

Figure 5.3. Mal-LbL NPs efficiently target and deliver IL-12 to ovarian cancer tumor nodules. A-e, B6C3F1 mice (n=4-5/group) inoculated with 10^6 HM-1-luc tumor cells on day 0 were administered fluorescently-tagged NPs carrying 20 µg IL-12 on day 14. Four hours or one day after dosing, animals were sacrificed, and tissues were analyzed ex-vivo via IVIS. Shown are Pearson's correlation coefficient for groups with significant ($p<0.05$) correlation between weight-normalized tissue NP fluorescence and IL-12 fluorescence 4 hours after dosing **(a)**, weight-normalized tissue IL-12 fluorescence one day after dosing in UGT and omentum (mean ± s.e.m., **b**), Pearson's correlation coefficient for groups with significant ($p<0.05$) correlation between weight-normalized tissue IL-12 fluorescence and BLI one day after dosing **(c)**, representative omentum and UGT tissue IVIS BLI and IL-12 fluorescence images for Mal-UL and Mal-LbL **(d)**, and pixel-by-pixel Spearman's correlation coefficient between IL-12 fluorescence and BLI one day after dosing from IVIS images. **E-f,** B6C3F1 mice were treated as in **a**. One day after dosing, Mal-LbL NP animals were sacrificed, and the omentum containing tumor nodules was frozen in optimal cutting temperature (OCT) compound then frozen sectioned and stained for confocal microscopy analysis. Shown are representative confocal microscopy images of tumor nodules in omental tissue at low **(f)** and high magnification **(g)**. Green arrows indicate areas with high NP signal relative to IL-12 whereas yellow arrowheads indicate areas with high IL-12 relative to NP. Correlation significance was performed based on a t-test analysis with the null hypothesis of no ($r=0$) correlation. Group statistical comparisons were performed using two-way ANOVA for **b** and one-way ANOVA for **e** with Tukey's multiple-comparisons test.

Figure 5.4. IL-12 delivered by Mal-LbL NPs exhibits potent anti-tumor activity and enhances T cell infiltration of tumors. a-d, B6C3F1 mice (n = 10/group) inoculated with 10^6 HM-1-luc tumor cells on day 0 were treated on days 7 and 14 with 20 µg of IL-12 as a free cytokine or conjugated to NPs. Shown are the experimental timeline **(a),** in vivo IVIS whole-animal i.p. BLI readings (mean ± s.e.m., **b)**, and overall survival **(c)**. On day 30, peripheral blood mononuclear cells (PBMCs) of surviving and naïve mice (n = 5) were analyzed via IFN-γ ELISpot restimulated with HM-1-luc tumor cells. Shown are quantitation of spots detected (mean ± s.e.m., **d**). **e-k**, B6C3F1 mice inoculated with 10^6 HM-1 tumor cells on day 0 were treated on days 10 with 20 µg of IL-12 as a free cytokine or conjugated to Mal NPs (UL and LbL). Two days after dosing ascites (n = 6/group) and i.p. tumor nodules (primarily omentum tissue, n = 4/group) were harvested and

processed for flow cytometry analysis. Show are timeline for experiment (**e**), representative flow plots of T cell ($CD45^+CD3^+$) in ascites fluid (**f**), quantitation of T cells in ascites fluid (**g**), quantitation of $CD8^+$ to $CD4^+$ T cell ratio in ascites fluid (**h**), representative flow plots of T cell ($CD45^+CD3^+$) in tumor nodules (**i**), quantitation of T cells in tumor nodules (**j**), quantitation of $CD8^+$ to $CD4^+$ T cell ratio in tumor nodules (**k**). *P* values were determined by the log-rank (Mantel–Cox) test **(c)** and one-way ANOVA followed by Tukey's multiple comparison test (**d, g, h, j, k**).

Figure 5.5. Efficacy of Mal-LbL NPs is dependent on lipid exchange properties which alter lipid distribution inside tumor nodules. a, Schematic of proposed mechanism of tumor targeted IL-12 lipid-conjugate dissemination from Mal-LbL NPs. **b-c**, B6C3F1 mice were inoculated with 10^6 HM-1-luc tumor cells on day 0 were administered fluorescently-tagged Mal-LbL of SAT-LbL NPs carrying 20 μg IL-12 on day 14. One day after dosing, animals were sacrificed, and the omentum containing tumor nodules was frozen in optimal cutting temperature (OCT) compound then frozen sectioned and stained for confocal microscopy analysis. Shown are representative high-magnification confocal images of omental tumor nodules from Mal-LbL (**b**) and SAT-LbL (**c**). **d-f**, B6C3F1 mice (n = 7/group) inoculated with 10^6 HM-1-luc tumor cells on day 0 were treated on days 7 with NP vehicle control (unloaded-LbL), 20 μg of IL-12 as a free cytokine or conjugated to Mal-LbL or SAT-LbL. Shown are the experimental timeline **(d),** in vivo IVIS whole-animal i.p. BLI readings **(**mean ± s.e.m., **e)**, and overall survival **(f)**. Statistical comparisons between survival curves were performed using a log-rank (Mantel–Cox) test.

Figure 5.6. Combination of immune checkpoint inhibitors with two dose treatment of Mal-LbL eradicates metastatic ovarian cancer. a-e, B6C3F1 mice (n = 10/group) inoculated with 10^6 HM-1-luc tumor cells on day 0 were treated on days 7 and 14 with 20 μg of IL-12 as a free cytokine or conjugated to Mal-LbL or Ni-LbL. Mice were also treated with 250 μg of anti-PD1 and 100 μg of anti-CTLA4 i.p. on days 8 and 15. Shown are the experimental timeline **(a),** *in vivo* IVIS whole-animal i.p. BLI readings **(**mean ± s.e.m., **b)**, and overall survival **(c)**. On day 150, surviving mice were rechallenged with either $3x10^5$ (**d**) or 10^6 (**e**) HM-1-luc tumor cells i.p. Shown are in vivo IVIS whole-animal i.p. BLI readings post rechallenge **(**mean ± s.e.m) and the

percentage of mice per group that survived rechallenge. Statistical comparisons between survival curves were performed using a log-rank (Mantel–Cox) test.

Figure 6.1. Characterization of nanoparticle surface charge conversion upon polyelectrolyte deposition. (a) Schematic for small-scale deposition of PLR onto IL-12 loaded NPs, intensity-weighted particle size (Z-avg), number-averaged (#-avg) size, polydispersity index (PDI), and zeta potential of the resulting polymer-nanoparticle mixtures at increasing PLR weight equivalents to bare anionic IL-12-NP. **(b)** Schematic for small-scale deposition of PLE onto PLR-IL-12 loaded NPs, Z-avg, #-avg, PDI, and zeta potential of the resulting polymer-nanoparticle mixtures from increasing weight equivalent PLE to PLR-coated IL-12 NPs. **(c)** Schematic representing the different possible resulting assemblies upon increasing polymer weight equivalents.

Figure 6.2. Excess polymers prevent NP aggregation during layering via optimized bath sonication protocol. (a) Z-avg size, PDI and zeta potential of IL-12 NPs during LbL assembly. **(b)** Polymer-to-NP wt. eq. retained with the NPs after TFF purification. **(c)** Z-avg size, PDI and zeta potential of the resulting PLR-IL-12-NPs generated via different layering strategies. **(d)** Z-avg size, PDI and zeta potential of the resulting PLR/PLE-IL-12-NPs generated via different layering strategies on TFF purified PLR-IL-12-NPs.

Figure 6.3. Microfluidic fluid mixing chips enable homogeneous LbL-NP assembly without the need of purification steps. (a) Schematic for polymer deposition onto NPs via microfluidics chip. **(b)** Z-avg size and PDI, of NPs layered with POP PLR using a microfluidics chip with increasing channel fluid flow rates (both polymer and NP channels had equal flow rates). Shaded regions indicate target NP measurements from optimal layering conditions for the current NP formulation. **(c)** Zeta potential measurements of particle mixtures from **b**. **(d)** Schematic for LbL-NP assembly using titrated polymer-to-NP wt. eq. without the need of purification steps. **(e)** Z-avg size, PDI, and zeta potential of the resulting PLR-IL-12-NPs generated using titrated PLR-to-NP wt.eq. via MCF compared to target NP measurements. **(f)** Z-avg size, PDI, and zeta potential of the resulting PLE/PLR-IL-12-NPs generated using titrated PLR-to-NP wt.eq. then titrated PLE-to-NP wt. eq. via MCF compared to target NP measurements. **(g)** Fraction of fluorescently labeled PLE polymer associated with NPs after optimized TFF-based layering before and after TFF

purification compared to titrated polymer layering using MCF. **(h)** Negative stain transmission electron microscopy (TEM) of unlayered (UL) IL-12 NPs or PLE/PLR-IL-12-NPs assembled via either the optimized TFF-based protocol or the titrated polymer-to-NP wt. eq. MCF protocol.

Figure 6.4. MCF-LbL-NPs maintain the desired *in vitro* characteristics of PLE/PLR LbL-NPs. (a) Fluorescence ratio of NPs associated with HM-1 cells relative to NPs remaining in the supernatant at 4 and 24 hours after dosing. **(b)** Representative confocal microscopy of HM-1 cells dosed with UL NPs for 24 hours. **(c)** Representative confocal microscopy of HM-1 cells dosed with TFF-based LbL-NPs for 24 hours. **(d)** Representative confocal microscopy of HM-1 cells dosed with MCF-based LbL-NPs for 24 hours.

Figure 6.5. MCF-LbL-NPs maintain the bioactivity of IL-12 *in vitro* and its *in vivo* effectiveness in a metastatic mice model of ovarian cancer. (a) HEK-Blue IL-12 reporter cell line response curves for free IL-12 or IL-12 loaded onto LbL-NPs generated via either TFF-based or MCF-based LbL assembly. **(b)** Calculated EC_{50} of curves in **(a)**. **(c)** In vivo treatment scheme of metastatic ovarian cancer. **(d)** Whole animal bioluminescence reading via IVIS of luciferase expressing tumors cells from mice treated as in **(c)**. **(e)** Survival curves of mice treated as in **(c)**.

Figure 7.1. Assembly of LbL film under mild ionic strength generates thicker layers, but reduces IL-12 bioavailability and limits lipid release. (a) Schematic of LbL film conformation on IL-12 LbL-NPs due to assembly in higher ionic strength buffer. Negative stain TEM of IL-12 LbL-NPs assembled either in DI (b) or hNa (c). Scale bars represent 100 nm. (d) Assessment of LbL-NP film stability through exposure of NPs to increasing concentrations of sodium chloride (NaCl). (e) Fluorescently labeled NPs were dosed to HM-1 cells *in vitro*. Four hours after dosing, cells were washed and the NP fluorescence associated with cells was measured on a fluorescence plate reader. Shown are the normalized fluorescence readings relative to an unlayered negatively charged liposome. (f-g) Fluorescently labeled NPs were dosed to HM-1 cells in vitro. Four hours after dosing, cells were washed, fixed, and then stained with wheat germ agglutinin (cell membrane stain) and Hoechst 33342 (nucleus stain), and then visualized via confocal microscopy. Shown are representative confocal microscopy images of HM-1 cells incubated for 4 hours with LbL-NP assembled in DI (f) or hNa (g). (h) Quantification of lipid release from LbL-hNa relative to LbL-

DI after 24 hours incubation in serum-containing media. (i-k) B6C3F1 mice (n = 7/group) inoculated with 10^6 HM-1-luc tumor cells on day 0 were treated on days 7 with 20 μg of IL-12 conjugated to LbL-NPs assembled in either DI or hNa. Shown are the experimental timeline **(i),** in vivo IVIS whole-animal i.p. BLI readings **(**mean ± s.e.m., **j)**, and overall survival **(k)**. Statistical comparisons between survival curves were performed using a log-rank (Mantel–Cox) test.

Figure 7.2. High MW polyelectrolytes stabilize LbL-NP but maintain IL-12 bioactivity and lipid release properties (a) Schematic IL-12 LbL-NPs with films composed of low or high molecular weight (MW) polymers. (b) Dynamic light scattering size and polydispersity measurements of LbL-NPs composed of low or high molecular weight (MW) polymers. (c) Apparent surface zeta potential measurements of LbL-NPs composed of low or high molecular weight (MW) polymers. (d) Assessment of LbL film and NP stability via a salt stress test. (e) Release of PLE from LbL-NPs in 10% serum. (f) HEK-Blue IL-12 response. (g) Relative lipid release in 10% serum from LbL-NPs assembled in deionized water with low molecular weight polymers or high molecular weight.

Figure 7.3. High MW polyelectrolytes increase cancer cell binding and increased PLE MW augments efficiency of the surface presentation of LbL-NPs. (a-d) Fluorescently labeled NPs were dosed to HM-1 cells *in vitro*. Four hours after dosing, cells were washed, and stained with anti-IL-12 monoclonal antibody. After IL-12 Ab binding, cells were again washed and the NP and IL-12 fluorescence associated with cells was measured on a fluorescence plate reader. Shown are the normalized fluorescence readings relative to an unlayered negatively charged liposome (a), schematic for staining extracellular presented IL-12 NPs (b), the ratio of IL-12 to NP fluorescence of UL and $PLR_{50}PLE_{100}$ NPs normalized to $PLR_{50}PLE_{100}$, and the ratio of IL-12 to NP fluorescence for the library of polyelectrolyte MWs normalized to $PLR_{50}PLE_{100}$. (e-f) Fluorescently labeled NPs were dosed to HM-1 cells *in vitro*. Four hours after dosing, cells were washed, suspended, stained with an anti-IL-12 monoclonal antibody, re-washed and fixed. Shown are representative flow plots of IL-12 fluorescence and NP fluorescence of HM-1 cells dosed with 15 μg/mL of $PLR_{50}PLE_{100}$ (LMW) or $PLR_{700}PLE_{800}$ (HMW) (e), and quantitation of extracellular IL-12 median fluorescence intensity (MFI) of HM-1 cells dosed with LMW and HMW LbL-NPs across various NP concentrations (f).

Figure 7.4. HMW polyelectrolyte LbL films increase the half-life of IL-12 on cancer cell membranes. (a-b) Fluorescently labeled NPs were dosed to HM-1 cells *in vitro*. Four hours after dosing, cells were washed, and fresh cell culture media was added. After 0, 24 or 48 hrs after removing unbound NPs, cells were stained with anti-IL-12 monoclonal antibody, washed, and total IL-12 fluorescence associated with cells was evaluated on a fluorescence plate reader to determine an IL-12 fluorescence half-life. Shown are the derived IL-12 half-life for the panel of PLR and PLE MW films (a) and the decay curves comparing the LWM ($PLR_{50}PLE_{100}$) to the HMW ($PLR_{700}PLE_{800}$) film. (c) Fluorescently labeled NPs were dosed to HM-1 cells in vitro. Two days (48 hrs) after dosing, cells were washed, fixed, and then stained with wheat germ agglutinin (cell membrane stain), Hoechst 33342 (nucleus stain), and anti-IL-12 antibody. Cells were then visualized via confocal microscopy. Shown are representative confocal microscopy images of HM-1 cells treated with LMW or HMW LbL-NPs.

Figure 7.5. HMW polyelectrolyte LbL films increase cancerous tissue NP targeting and increase total IL-12 presentation. (a-h) B6C3F1 mice (*n*=4-5/group) inoculated with 10^6 HM-1-mCherrry-luc tumor cells on day 0 were administered fluorescently-tagged NPs carrying 20 μg IL-12 (or an equivalent dose of free IL-12) on day 14. Four hours after dosing, animals were sacrificed, ascites was collected and processed for flow cytometry whereas tissues were analyzed ex-vivo via IVIS. Shown are the median fluorescence intensity (MFI) of NP signal in cancer cells ($CD45^-mCherry^+$, mean ± s.d., a) and immune cells ($CD45^+$, mean ± s.d., b), the percentage of immune cells and cancer cells that were NP-positive (mean ± s.d., c), representative flow cytometry plot of NP and extracellular IL-12 fluorescence of tumor cells (d), the percentage of immune cells and cancer cells that were IL-12-positive (mean ± s.d., e), the weight-normalized tissue NP fluorescence (mean ± s.e.m., **f**), Pearson's correlation coefficient between weight-normalized tissue NP fluorescence and BLI 4 hours after dosing (g), and the significance of the correlation estimates (h).

Figure 7.6. HMW polyelectrolytes increase LbL-NP treatment efficacy in a metastatic model of ovarian cancer B6C3F1 mice (*n* = 10/group) inoculated with 10^6 HM-1-luc tumor cells on day 0 were treated on days 7 and 14 with 20 μg of IL-12 as a free cytokine or conjugated to LbL-NPs.

Shown are the experimental timeline **(a),** *in vivo* IVIS whole-animal i.p. BLI readings **(**mean ± s.e.m., **b)**, and overall survival **(c)**.

Figure 8.1. Solution conditions during LbL assembly control film thickness. (a) Diagram of LbL assembly either in deionized water (DI) or in the presence of a mild ionic strength solution (salt). (b) Particle hydrodynamic size (Z-avg) and polydispersity index (PDI) during LbL assembly. (c) Zeta potential of particles during LbL assembly. (d) Negative stain transmission electron microscopy of unlayered (UL), DI-LbL, or salt-LbL NPs.

Figure 8.2. Stable peptide loading onto DI-LbL and salt-LbL NPs depends on film conformation and peptide charge. (a) Schematic of peptides used in adsorption studies. (b) Diagram of peptide adsorption under DI conditions onto DI-LbL NPs. (c) Hydrodynamic size and zeta potential of DI-LbL NPs after peptide adsorption. (d) Diagram of peptide adsorption under salt conditions onto salt-LbL NPs. (e) Hydrodynamic size and zeta potential of salt-LbL NPs after peptide adsorption.

Figure 8.3. The generation of chemical crosslinks on LbL-NPs yields greater film stability. (a) Diagram of salt stress test. (b) Z-avg size of DI-LbL and salt-LbL at various concentrations of NaCl during the salt stress test. (c) Salt stress test of DI-LbL with various peptide loadings. (d) Diagram of crosslinking polymers on the surface of LbL-NPs. (e) Salt stress curves from various scLbL-NPs assembled in either DI or salt conditions with varying amounts of peptides adsorbed on the surface.

Figure 8.4. Increased film stability of scLbL-NP inhibit IL-12 recognition from the NP surface. (a) Schematic for IL-12-NPs, LbL-NPs, and IL-12-scLbL-NPs. Salt stability stress test in DI assembled (b) and salt-assembled (c) IL-12 scLbL-NPs. HEK-Blue IL-12 response curves from DI-assembled (d) and salt-assembled (e) IL-12 scLbL-NPs. (f) Calculated IL-12 EC_{50} form UL NPs compared to DI and salt-assembled LbL-NPs. (g) Calculated IL-12 EC_{50} from all scLbL-NPs tested.

Figure 8.5. Exposure of IL-12 scLbL-NPs to MMP-9 recovers IL-12 bioactivity. (a) Diagram of MMP-9 effect on IL-12 scLbL-NPs. (b) HEK-Blue IL-12 curves of DI-scLbL-NP incubated with or without MMP-9 enzyme. (e) HEK-Blue IL-12 curves of salt-scLbL-NP incubated with or without MMP-9 enzyme. (d) The change in EC_{50} of DI-assembled IL-12 scLbL-NPs incubated with or without MMP-9. (f) The change in EC_{50} of salt-assembled IL-12 scLbL-NPs incubated with or without MMP-9.

Figure 9.1. LbL film enables high-affinity binding to cancer cells. (a) Diagram of different surface modifications with PLE. (b) Fluorescently labeled NPs were dosed to HM-1 cells *in vitro*. Four hours after dosing, cells were washed and NP fluorescence associated with cells was measured on a fluorescence plate reader. Shown are the normalized fluorescence readings relative to an unlayered negatively charged liposome. (c) PLE labeled with a fluorescence tag was dosed to HM-1 cells either in the LbL-film on an NP (PLE100 was used to assemble film on NP) or as free polymers at a degree of polymerization of 100 or 800. Cells were washed and suspended to read via flow cytometry for the percentage of PLE+ cells. Shown are the results of the experiment with varying PLE concentrations. Curve represents dose-response fit. PLE-NP concentration indicates the number of PLE-coated NPs. (d) Relationship between estimated number of glutamate (E) residues per particle and the derived EC_{50} from the experiment in (c) and EC_{50} of NP+ cells dosed with PLE-coated carboxylate-modified polystyrene (PS) NPs of varying diameters (40 nm, 100 nm, and 200 nm). (e-f) Data from NanoPrism was used to rank cell lines based on their uptake of NPs, the median gene expression of the top 100 cell lines was compared to the median expression of the bottom 100 cell lines to derive the fold chance in gene expression for each formulation that was then used to perform gene-set enrichment analysis (GSEA) against the hallmark gene sets. Shown are the volcano plot for liposomal PLE-NP and UL-NP with the top 20 Hallmark gene sets hits (e), GSEA enrichment plot of liposomal PLE-NP against the epithelial-to-mesenchymal transition (EMT) Hallmark gene set. (g-h) The fold change in gene expression for PLE, HA, and PAA LbL coated NPs made with either liposomal or polylactic-co-glycolic acid (PLGA) cores were normalized to their unlayered cores to derive gene expression signatures that corresponded to high LbL-film binding, but low binding towards the unlayered cores. Upregulated genes were compared to find genes specific towards PLE-coated NPs of either liposomal or PLGA cores. Shown are venn diagram of genes upregulated on cells high for LbL-NP binding relative to

UL-NPs for the indicated NP formulations (g) and calculated Z-score of extracellular cell membrane genes shared between PLE_LIPO and PLE_PLGA NPs (h).

Figure 9.2. Association of PLE-coated NPs is blocked with glutamine transport inhibitors. (a-c) HM-1 cells were plated in 96 wells at a density of 50k cells/well and left to adhere overnight. Cells were then treated with varying concentrations of amino acid transport inhibitors for 15 minutes before NP dosing at 50 μg/mL (a) or 25 μg/mL (b-c) per well. Four (a) or two (b-c) hours after NP dosing, wells were washed twice with PBS and total NP fluorescence associated with cells and remaining in supernatant was measured in a fluorescence plate reader to determine total NP uptake. Shown are the normalized NP uptake of PLE-coated NPs relative to UL at different inhibitor concentrations of GPNA, TFB-TBOA and V9302 (a), the normalized NP uptake of various outer layer LbL-coated NPs relative to UL at different inhibitor concentrations of GPNA (b), and the normalized NP utpake of various outer layer LbL-coated NPs relative to UL at different inhibitor concentrations of V9302 (c). Arrows indicate IC_{50} for inhibitors derived from literature. (d-i) HM-1 cells were plated in 96 well plates at 50 k cells/well and left to adhere overnight. Cells were then treated with 100 μM of V9302 for 15 minutes prior to NP dosing at varying concentrations. Two hours after NP treatment, cells were washed with PBS, and suspended for flow cytometry analysis of NP uptake. Shown are representative NP fluorescence histograms of HM-1 cells dosed with 30 μg/mL of PLE-NPs (d), UL-NPs (e), or HA-NPs (f) with or without 100 μM of V9302 compared to untreated cells, and the percentage of NP-positive cells in PLE-NP treated (g), UL-treated (h), or HA-NP treated (i) HM-1s with or without 100 μM of V9302 across a range of NP concentrations.

Figure 9.3. Modulation of SLC1A5 availability regulates PLE-NP binding. (a-d) HM-1 cells were plated in 96 well plates at 50 k cells/well and left to adhere overnight. Cells were then treated with antibodies (Abs) against either CD44 or two extracellular epitopes of SLC1A5 for 1 hr. After Ab treatment, cells were dosed with 10 μg/mL of NPs for 15 minutes, washed with PBS, and suspended for flow cytometry analysis of NP uptake. Shown are representative histogram plots of NP fluorescence for cells treated with PLE-NPs (a), UL-NPs (b), and HA-NPs (c) in the presence of anti-SLC1A5 antibody or control treatments, and the percentage of NP+ cells with or without Abs for PLE, UL and HA NPs. (e-i) HM-1 cells were plated in 96 well plates at 5 k cells/well and

left to adhere overnight. The next day, cells were treated with either anti-SLC1A5 siRNA or scramble siRNA at 200 nM for 96 hrs. Cells were then washed with fresh complete media and dosed with 10 μg/mL of NPs for 30 min. After NP incubation, cells were washed with PBS, and suspended for flow cytometry analysis of NP uptake. Shown are representative flow cytometry of total anti-SLC1A5 Ab staining in cells treated with either scramble of anti-SLC1A5 siRNA (e), quantitation of median fluorescence intensity (MFI) of total anti-SLC1A5 staining (f), representative flow cytometry histograms of NP fluorescence of HM-1 cells with partial SLC1A5 knockdown for PLE-NP (g) and HA-NP (h) treatments, and the percentage of NP positive cells with partial SLC1A5 RNA knockdown treated with PLE-NP or HA-NP (i).

Figure 9.4. PLE-NPs colocalize with SLC1A5 transporters on the cell surface. (a-c) HM-1 cells were plated in 8-well glass chamber slides at 10 k cells/well and left to adhere overnight. Cells were dosed with 1.5 μg/mL of NPs for 2 hrs. After NP treatment, cells were washed with PBS, fixed with PFA, and then rapidly permeabilized with saponin. Cells were then treated with primary antibodies for 3 hours followed by secondary antibody for 30 minutes. Shown are high magnification images of HM-1 cells treated with UL-NPs stained against SLC1A5 and HM-1 cells treated with PLE-NPs stained against either SLC1A5 or GLUT-1 transporters (a), correlation analysis between NP signal and cell membrane transporter stain (b), and correlation analysis between varied NP formulations and SLC1A5 staining (c). (d) HM-1 cells were plated in 96-well plates at 50 k cells/well and allowed to adhere overnight. Cells were then dosed with varying concentration of PLE-IL12 NPs. Four hours after dosing, cells were processed for flow cytometry. Shown are the percentage of NP-positive cells for each concentration of NP dosed. (e) The same process as (a-c) was followed but various concentrations of LbL-NPs were tested. Shown are the correlation between NP signal and SLC1A5 stain. (f) The same protocol of (d) was followed but prior to cell fixing, cells were incubated with anti-IL-12 antibody for 1 hr at 4 °C and washed. Shown is the extracellular IL-12 presentation efficiency (ratio between extracellular IL-12 stain to total NP uptake at 24 hrs compared to the same ratio at 4 hrs after dosing). (g-h) HM-1 cells were plated in 8-well glass chamber slides at 10 k cells/well and left to adhere overnight. Cells were dosed with 1 μg/mL of NPs for 4 hrs. After NP treatment, cells were washed with PBS, fixed with PFA, and then stained with Hoechst 33342 and wheat germ agglutinin (WGA) and visualized on

a confocal microscope. Shown are representative HM-1 cells dosed with 20 nm PLE-PS particles (g) and the quantification of the fraction of NP pixels colocalized with cell membrane pixels (h).

Figure 9.5. AlphaFold artificial intelligence model predicts PLE binding to SLC1A5 and its expression correlated with PLE-NP association. (a) Representative AlphaFold 3 model structure of SLC1A5 and PLE and the calculated chain-pair ipTM scores between SLC1A5 with PLQ, PLE and PLF. (b) Representative AlphaFold 3 model structure of SLC38A2 and PLE and the calculated chain-pair ipTM scores between SLC38A2 with PLQ and PLE. (c) SLC1A5 expression from human samples from normal, tumor, or metastatic tissue (data from TMNplot) showing increased SLC1A5 expression in cancerous and metastatic tissues. (d) Analysis of PLE-NP Z-scores from NP screen against various human ovarian cancer cell lines and primary healthy tissues as a function of SLC1A5 RNA expression (RNA expression of human cell lines derived from Protein Atlas). R^2 from linear fit and p-value from non-zero slope test. Dashed lines represent 95% confidence interval of curve fit. (e) Fold increase in SLC1A5 RNA expression between tumor and healthy samples across various cancer types and highlighting high fold-changes in brain-derived cancers (data from GEPIA). (f) Fold increase in PLE-NP association relative to UL NPs in a library of glioblastoma cells lines against SLC1A5 gene expression. R^2 from linear fit and p-value from non-zero slope test. Dashed lines represent 95% confidence interval of curve fit.

Figure 9.6. PLD-coated NPs associate both glutamine transporters and anionic amino acid transporters. (a) Log-log plots of fold increase in PLE and PLD coated LbL-NPs relative to UL NPs in a library of ovarian cancer cells lines and primary healthy cells. R^2 from linear fit and p-value from non-zero slope test. Dashed lines represent 95% confidence interval of the curve fit. (b) same as (a) but on the library of glioblastoma cell lines. (c-e) HM-1 cells were plated in 96 well plates at 50 k cells/well and left to adhere overnight. Cells were then treated with either V9302 or TFB-TBOA for 15 minutes before NP dosing at varying concentrations. Two hours after NP treatment, cells were washed with PBS, and suspended for flow cytometry analysis of NP uptake. Shown are the percentage of NP-positive cells in PLD-treated HM-1s with 10 μM of V9302, 100 μM of V9302 or without V9302 (c), and the percentage of NP-positive cells in PLE-NP treated (d), or PLD-NP treated (e) HM-1s with or without 1 mM of TFB-TBOA. (f) Representative AlphaFold 3 model structure of SLC1A3 and PLE and SLC1A3 with PLD focused on the binding

pocket indicated by the dark shading. (g) AlphaFold 3 calculated chain-pair ipTM scores between SLC1A5 with PLD, SLC1A3 with PLD, and SLC1A3 with PLE. (h-i) The NP median fluorescence intensity (MFI) of PLD-NP treated cells was normalized to the MFI of PLE-treated cells and plotted against SLC1A3 expression of the cel line. Shown are the plots of the NP screen against ovarian cancer cells and primary healthy tissue (h) and on glioblastoma cells lines (i). R^2 from linear fit and p-value from non-zero slope test. Dashed lines represent 95% confidence interval of the curve fit.

Table A1: RP-HPLC conditions and gradient.

Table A2: Staggered dilution steps for QS-21 SMNP assembly.

Table A3: Critical Quality Attributes (CQAs) of SMNPs.

Figure A1: Protocols for generation of Quil-A based SMNPs fail to form ISCOMs when saponin is substituted for QS-21. (A) Chemical structure of the major isomer of QS-21. (B, C) DLS Z-avg, vol-avg, number-avg and PDI for attempts using dTFF (B) and low detergent dTFF (C) – error bars omitted for clarity. (D) DLS intensity-based and number-based distribution for standard dTFF and low detergent dTFF. (E) TEM micrographs of samples for standard dTFF before (top) and after (bottom) TFF process. (F) TEM micrographs of final product from low detergent dTFF.

Figure A2: Rapid dilution of lipid/QS-21/MEGA-10 mixture enables formation of large aggregates. TEM micrograph of sample rapidly diluted to below CMC.

Figure A3: Reverse-phase (RP) high-pressure liquid chromatography (HPLC) coupled with a evaporative light scattering detector enables quantification of each component in QS-21 SMNPs. (A) Representative chromatogram of QS-21 SMNP particles separated on a Jupiter C4 column with acetonitrile gradient ranging from 30 to 95%. (B) Representative chromatogram of QS-21 SMNP particles separated on a Accucore C8 column with ispopropanol gradient ranging from 5 to 95%.

Figure A4: TFF with 100 kDa membranes is an effective method for removal of MEGA-10 from QS-21 SMNPs. (A) Standard curve generated based on MEGA-10 absorbance at 205 nm. (B) Concentration of MEGA-10 in permeate from three independent batches of QS-21 SMNPs. Dashed lines indicate 95% confidence interval from fitted curves.

Figure A5: Room temperature (RT) QS-21 SMNPs can lead inhomogeneous preparations. (A) Diagram for QS-21 SMNP synthesis at room temperature (RT) through continuous dilution. (B) DLS Z-avg, and PDI for RT QS-21 SMNP samples from two independent batches. Serum IgG titer curves at week two (C) and week four (D) for particles generated via dialysis, dTFF with heating of QS-21 and two independent batches of dTFF SMNPs with QS-21 at room temperature for mice immunized with 2 μg of N332-GT2 trimer and 5 μg of SMNP. (E) Summary of serum IgG titers at week 2 and 4 from (C) and (D). (F) TEM micrograph showing SMNPs generated at RT with presence of lipidic vesicles. White arrows indicate lipid nanoparticles.

Figure A6: Staggered dilution enables proper assembly of QS-21 ISCOMs devoid of MPLA. A sample with 7.5% MEGA-10 and 5 mg/mL of QS-21-ISCOM components (QS-21, cholesterol and DPPC at a 5:1:1 mass ratio) was either rapidly diluted to final MEGA-10 concentrations or diluted via the staggered protocol of **Table S2.** DLS intensity-weighted size (Z-avg) and PDI were measured after overnight incubation for the fast diluted samples or after the appropriate incubation time for the staggered dilution protocol.

Figure B1. The chemical structure of components used to generate liposomes from dilution.

Figure B2. Representative cryo-TEM micrographs of 200 nm liposomes formed in region iii.

Figure B3. Detergent concentration after dilution controls the equilibrium size of liposomes. **(A)** DLS intensity-weighted size (Z-avg) and PDI after overnight incubation of a 10 mg/mL of 6:3:1 molar mixture of DSPC:cholesterol:POPG in 10% MEGA-10 diluted to various final detergent concentrations. **(B)** DLS intensity-weighted size (Z-avg) and PDI after overnight incubation of a 20 mg/mL of 6:3:1 molar mixture of DSPC:cholesterol:POPG in 10% octylglucoside diluted to various final detergent concentrations. **(C)** Effect of dilution samples equilibrated at 0.1% or

0.04% MEGA-10 overnight to 0.01% MEGA-10 on particle size (Z-avg) and PDI; samples were allowed to equilibrate at 0.01% overnight.

Figure B4. TFF of assembled lipid vesicles enables efficient removal of MEGA-10. **(A)** ELSD chromatogram of MEGA-10 at increasing concentrations. **(B)** ELSD of final purified particles incubated at either 0.1%, 0.02%, or 0.004% MEGA-10. Shaded regions indicate MEGA-10 elution times.

Figure B5. Characteristics of liposomes generated from lipid film hydration followed by extrusion with a 50 nm pore sized membrane. **(A)** DLS intensity-based and number-based size distribution. **(B)** Z-avg, number-average, and PDI. **(C)** Representative cryoTEM micrograph from liposomes generated via thin film hydration followed by extrusion on a 50 nm pore-sized membrane. **(D)** CryoTEM micrograph of extruded liposomes showing large (>50 nm) vesicles. **(E)** CryoTEM micrograph analysis of particle size from the extruded sample. Parenthesis indicates the total number of particles quantified and PDI based on the measured particle sizes from cryoTEM. **(F)** Normalized histograms of samples generated from detergent dilution into 0.1%, 0.02%, and 0.004% MEGA-10 then purified via TFF compared to liposomes generated via thin-film hydration followed by extrusion through 50 nm pore membrane.

Figure B6. Analysis of lipid exchange via FRET reveals that assembled liposomes in region iv are stable whereas particles in region iii have high rates of lipid exchange even after no change in particle size. Normalized FRET efficiency from samples containing 1mol% of dye diluted with PBS to various concentrations of MEGA-10 and mixed after set incubation periods.

Figure B7. Assessment of liposome assembly via cryo-TEM. **(A-D)** Cryo-TEM micrographs of 10 mg/mL 6:3:1 DSPC:Chol:POPG sample in 10% MEGA-10 rapidly diluted to 0.1% MEGA-10 with 10 mM HEPES 150 mM NaCl and frozen 5 minutes, 2 hours, 5 hours and 24 hours after dilution, respectively.

Figure B8. Diagram of the experimental protocol to determine the percentage of liposome fluorescence associated with macrophages.

Figure C1. **Chemical structure of components used for particle self-assembly.**

Figure C2. **Characterization of lisCNDs and high POPG composition diluted with PBS. (A)** Representative chromatograms from high-pressure liquid chromatography (HPLC) coupled with an evaporative light scattering detector (ELSD) for PBS only, 0.025 mg/mL sample in PBS, and samples allowed to be assembled at 0.1% MEGA-10 in 0 mM NaCl or 200 mM NaCl buffers then purified via TFF. **(B)** Z-avg, #-avg and PDI of purified samples allowed to assemble at 0.1% MEGA-10 in 200 mM NaCl, 0 mM NaCl, or 0 mM NaCl then exposed to 1X PBS after purification. **(C)** CryoTEM micrographs of purified samples from dilution of lipid/detergent micelles using 0 mM NaCl, but then added 1X PBS. **(D)** Size and PDI of lipid/detergent micelles with 3:3:4 molar ratios of DSPC:cholesterol:POPG diluted to 0.05% MEGA-10 then purified via TFF. Error bars represent SEM.

Figure C3. **Characteristics of LbL-CNDs and LbL-lisCNDs. (A)** Zeta potential of liposomes and CNDs upon layering with PLR and PLE. **(B)** Size and zeta potential of lisCNDs upon layering with PLR and PLE. **(C)** In vitro HM-1 association of NPs relative to liposomes 24 hrs after dosing cells. Error bars represent SEM. Statistical comparisons in C was performed using one-way analysis of variance (ANOVA) with Tukey's multiple-comparisons test. Asterisks denote p-values: ****$p < 0.0001$, ***$p < 0.001$, **$p < 0.01$, *$p < 0.05$.

Table D1: Lipid composition of nanoparticles and summary characteristics.

Table D2: Lipid composition of SAT NPs

Figure D1. Headgroup-modified lipids for IL-12 conjugation. a, Chemical structure of headgroup-modified lipids with either chelated nickel or N-aryl maleimide. N-aryl maleimide was employed to prevent potential thiosuccinimide retro-Michael addition and subsequent thiol-exchange, as this headgroup favors thiosuccinimide hydrolysis into sTable Duccinamic acid thioethers. **b**, IL-12 crystal structure derived from PDB 1F45 showing C-terminus used to engineered terminal poly-histidine (polyHis) tag and terminal cysteine. **c,** Reaction pathway for irreversible maleimide-based conjugation with thiols.

Figure D2. Synthesis of LbL-NPs conjugated with IL-12 via either maleimide-cysteine reaction or nickel-histidine interaction yield similar particle biophysical properties. a, Intensity-weighted hydrodynamic size (Z-avg), number average size (#-avg), and polydispersity index (PDI) of NPs during synthesis as measured via dynamic light scattering (mean ± s.d.). **b,** Zeta potential of NPs during synthesis as measured via electrophoretic mobility in deionized water (mean ± s.d.). **c,** Yield and weight loading of IL-12 for unlayered and layered particles with nickel-histidine linker (Ni-UL and Ni-LbL) and unlayered and layered particles with a maleimide-cysteine bond (Mal-UL and Mal-LbL) (mean ± s.e.m.). **d-e,** Negative-stain (NS) transmission electron microscopy (TEM) with phosphotungstic acid of particles during synthesis with nickel-containing lipids (**d**) and maleimide-containing lipids (**e**) - scale bars represent 200 nm. Unlayered (UL) NPs without IL-12 presented the typical low-contrast micrographs of liposomes. When conjugated with IL-12, however, a dark rim around the liposomes could be observed which became diffuse after LbL deposition, suggesting successful IL-12 conjugation and LbL coating. Data are presented as mean values ± error with $n = 3$ independent batches of NPs. Statistical comparisons in **c** were performed using two-way analysis of variance (ANOVA) with Tukey's multiple-comparisons test.

Figure D3. Polyelectrolyte film is partially released in buffers with physiological ionic strength and does not block IL-12 availability in LbL-NPs. A, Measurement of PLE or PLR release from LbL film on NPs incubated at 37 °C in 15 mM HEPES 150 mM NaCl (HEPES), 10%, or 100% FBS (mean ± s.e.m). **b,** Schematic for monoclonal antibody capture of NP-bound IL-12 and detection in varying buffer conditions. **c,** HEK-Blue IL-12 reporter cell line response to IL-12 in various formats (n>100 points per curve from 7 independent particle batches). (**d**) Calculated IL-12 EC_{50} from HEK-Blue IL12 response curves (mean ± s.e.m).

Figure D4. Characterization of metastatic ovarian cancer model - OV2944-HM1. a-b, B6C3F1 mice were inoculated with 10^6 HM-1-luc tumor cells i.p. on day 0 ($n = 40$) or left as naïve healthy animals ($n = 10$). Shown are representative, intestine, lung, omentum and UGT ex-vivo IVIS BLI images (**a**) and quantitation of BLI signal in healthy organs compared to organs two weeks after tumor inoculation (mean ± s.e.m, **b**). Statistical comparisons in **b** were performed

using the nonparametric Mean-Whitney test with correction for multiple comparisons based on a false discovery rate of 1% (q=0.0136).

Figure D5. Mice with complete remission of metastatic ovarian cancer demonstrate strong immune memory induction upon i.p. luc-HM-1 rechallenge. a-b, B6C3F1 mice (*n* = 10/group) inoculated with 10^6 HM-1-luc tumor cells on day 0 were treated on days 7 and 14 with 20 µg of IL-12 as a free cytokine or conjugated to NPs. On day 100, surviving Mal-LbL mine (*n* = 3) or naïve (*n* = 2) were injected with $3x10^5$ luc-HM-1 cells i.p. Shown are in vivo IVIS whole-animal i.p. BLI readings (mean ± s.e.m., **b**), and overall survival (**c**).

Figure D6. Intraperitoneal dosing of 20 µg of Mal-LbL NPs does not cause systemic toxicity. a-e, B6C3F1 mice inoculated with 10^6 HM-1 tumor cells on day 0 were treated on days 10 with 20 µg of IL-12 as a free cytokine or conjugated to Mal NPs (UL and LbL). Two days after dosing blood (n = 6/group) and spleens (n = 4/group) were harvested and sent for a complete blood panel or processed for flow cytometry analysis, respectively. Shown are serum levels of liver damage markers (alanine transaminase – ALT - and aspartate aminotransferase - AST) compared to healthy mice controls (*n* = 4, **a**), complete blood count panel (**b**), quantitation of live leukocyte ($CD45^+$) counts in spleen (**c**), and percentage of macrophage (**d**) and NK (**e**) cell in splenocytes. Statistical comparisons performed using two-way (**a,b**) or one-way (**c,d,e**) analysis of variance (ANOVA) with Tukey's multiple-comparisons (liver enzyme measurement was compared to healthy controls).

Figure D7. Immune phenotyping of cells in ascites fluid and tumor tissues. a-j, B6C3F1 mice inoculated with 10^6 HM-1 tumor cells on day 0 were treated on days 10 with 20 µg of IL-12 as a free cytokine or conjugated to Mal NPs (UL and LbL). Two days after dosing ascites (*n* = 6/group) and i.p. tumor nodules (primarly omentum tissue, *n* = 4/group) were harvested and processed for flow cytometry analysis. Shown are total counts of M1-like and M2-like macrophages **(a)**, logarithmic of M1-like to M2-like macrophages ratio (**b**), and total counts of PMN-MDSC (**c**), M-MDSC (**d)**, and NK cells (**e**) in ascites fluid. Also shown are total counts of PMN-MDSC (**f**) and M-MDSC (**g**), logarithmic of M1-like to M2-like macrophages ratio (**h**), and total counts of M1-like and M2-like macrophages (**i**), and NK cells (**j**) in tumor nodules. Statistical comparisons were

performed using two-way (**a,i**) or one-way (**b,c,d,e,h,j**) analysis of variance (ANOVA) with Tukey's multiple comparisons (liver enzyme measurement was compared to healthy controls).

Figure D8. Characterization of Mal IL-12 NPs composed of saturated (SAT) lipids. a, Illustration of liposome bilayer composition effect on lipid exchange rate with serum proteins. **b,** Intensity-weighted hydrodynamic size (Z-avg), number average size (#-avg), and PDI of NPs during synthesis as measured via DLS (mean ± s.d.). **c,** Zeta potential of NPs during synthesis as measured via electrophoretic mobility in deionized water (mean ± s.d.). **d,** Association of NP fluorescence with HM1 cells *in vitro* relative to unlayered NPs after 4 and 24 hours of incubation (mean ± s.d.). **e,** Representative confocal microscopy images of HM-1 cells dosed with SAT-LbL for 4 hours. **f,** Calculated IL-12 EC_{50} of IL-12 compared to SAT-LbL NPs from HEK-Blue IL-12 assay (mean ± s.e.m.). **g,** Assessment of de-quenching from fluorophore detachment from unsat and SAT NPs when incubated with 100% FBS at 37 °C – curves represent the best fit of a two-phase decay model. **h,** Quantification of IL-12 retention with Mal-LbL or SAT-LbL upon incubation with 100% FBS (mean ± s.e.m.) – curves represent the best fit of a two-phase decay model. Statistical comparisons performed in **d** using two-way analysis of variance (ANOVA) with Tukey's multiple-comparisons. Data are representative of at least two independent experiments.

Figure D9. Confocal microscopy analysis of histological cryosections of omentum tumor nodules demonstrates both Mal-LbL and SAT-LbL penetrate tumor tissue. a-b, B6C3F1 mice were inoculated with 10^6 HM-1-luc tumor cells on day 0 were administered fluorescently-tagged Mal-LbL of SAT-LbL NPs carrying 20 µg IL-12 on day 14. One day after dosing, animals were sacrificed, and the omentum containing tumor nodules was frozen in optimal cutting temperature (OCT) compound then frozen sectioned and stained for confocal microscopy analysis. Shown are representative confocal images of omental tumor nodules from Mal-LbL (**a**) and SAT-LbL (**b**) treated animals.

Figure D10. Flow cytometry cell gating strategy.

Figure E1. Microfluidic fluid mixing chips enable homogeneous LbL-NP assembly in optimized buffer solutions. (a) Z-avg size and PDI of NPs layered with increasing PLR-to-NP

wt. eq. in 25 mM HEPES and 20 mM NaCl. **(b)** Zeta potential of NPs layered with increasing PLR-to-NP wt. eq. in 25 mM HEPES and 20 mM NaCl. **(c)** Z-avg size, PDI, and zeta potential of NPs layered with PLR and PLE using small-scale bath sonication mixing of polymers and NPs. **(d)** Schematic, Z-avg size, PDI, and zeta potential of NPs layered with PLR and PLE using large-scale bath sonication mixing of polymers and NPs. **(e)** Schematic, Z-avg size, PDI, and zeta potential of NPs layered with PLR and PLE using MCF mixing of polymers and NPs.

Figure F1. Biophysical characterization of LbL-NP library assembled in DI or hNa. (a) Dynamic light scattering size and polydispersity index (PDI) measurements of LbL-NPs assembled either in deionized water (D) or in the presence of mild ionic strength (hNa). (b) Apparent surface zeta potential measurements of LbL-NPs assembled either in DI or hNa. (c) Diagram of salt stability assay. (d) HEK-Blue IL-12 derived EC_{50} of IL-12 in NP preparations. (e) Representative confocal microscopy image of HM-1 cells incubated with UL-NPs for 4 hrs.

Figure F2. Biophysical characterization of LbL-NP library composed of various polymer MWs. (a) Dynamic light scattering size and polydispersity measurements of LbL-NPs composed of various molecular weight (MW) polymers. (b) Apparent surface zeta potential measurements of LbL-NPs composed of low or high molecular weight (MW) polymers. (c) HEK-Blue IL-12 of panel of MWs.

Figure F3. Biodistribution study. (a) Treatment timeline of mice bearing HM-1-mCherry-luc tumors for biodistribution study. (b) Assessment of cellular fraction immune cells and tumor cells of ascites in HM-1 mice.

Figure G1. GSEA analysis of LbL-NP uptake. (a-d) Data from NanoPrism was used to rank cell lines based on their uptake of NPs, the median gene expression of the top 100 cell lines was compared to the median expression of the bottom 100 cell lines to derive the fold chance in gene expression for each formulation that was then used to perform gene-set enrichment analysis (GSEA) against the hallmark gene sets. Shown are the volcano plot for liposomal HA-NP (a), liposomal PAA-NP (b), PLE-coated PLGA NPs (c), and unlayered PLGA NPs (d) with the top 20 Hallmark gene sets hist. (e) The fold change in gene expression for PLE-coated PLGA NPs were

normalized to UL PLGA NPs derive gene expression signatures that corresponded to high LbL-film binding, but low binding towards the unlayered cores. Shown are the volcano plot of PLE coated PLGA-NPs after normalization to UL PLGA NPs.

Figure G2. System A amino acid transport inhibitor MeAIB does not impair PLE-NP binding. HM-1 cells were plated in 96 well plates at 50 k cells/well and left to adhere overnight. Cells were then treated with 10 or 100 mM of MeAIB for 15 minutes prior to NP dosing at varying concentrations. Two hours after NP treatment, cells were washed with PBS, and suspended for flow cytometry analysis of NP uptake. Shown are the percentage of NP+ cells at each concentration of NP dosed.

Figure G3. PLE coating is required for high colocalization of SLC1A5 with LbL-NPs. (a-b) HM-1 cells were plated in 8-well glass chamber slides at 10 k cells/well and left to adhere overnight. Cells were dosed with 1.5 μg/mL of NPs for 2 hrs. After NP treatment, cells were washed with PBS, fixed with PFA, and then rapidly permeabilized with saponin. Cells were then treated with primary antibodies for 2 hours followed by secondary antibodies for 30 minutes. Shown are HM-1 cells treated with PLE-NPs and stained with an anti-CD44 Ab or isotype control (a), and HM-1 cells treated with various outer layer LbL-NPs and stained with anti-SLC1A5 Abs (b). (c) The same protocol was followed as (a-b) but cells were treated with 13.5 μg/mL of PLE-NPs.

Figure G4. PLE-NPs associate primarily on the cell membrane. (a-b) HM-1 cells were plated in 8-well glass chamber slides at 10 k cells/well and left to adhere overnight. Cells were dosed with varying concentrations of NPs for 4 hrs. After NP treatment, cells were washed with PBS, fixed with PFA, and then stained with Hoechst 33342 and wheat germ agglutinin (WGA) and visualized on a confocal microscope. Shown are representative confocal images of HM-1 cells treated with various concentrations of PLE-NPs (a) and quantification of the fraction of NP pixel colocalized with cell membrane pixels (b).

Figure G5. 100 nm polystyrene PLE-NPs are retained at the cell membrane. HM-1 cells were plated in 8-well glass chamber slides at 10 k cells/well and left to adhere overnight. Cells were

dosed with 1 μg/mL of NPs for 4 hrs. After NP treatment, cells were washed with PBS, fixed with PFA, and then stained with Hoechst 33342 and wheat germ agglutinin (WGA) and visualized on a confocal microscope. Shown is a representative HM-1 cell dosed with 100 nm PLE-PS particles.

Figure G6. Modeling predictions. (a) Representative AlphaFold 3 model structure of SLC1A5 and PLQ bound to the outward or inward orientation of SLC1A5. (b) Representative AlphaFold 3 model structure of SLC1A5 and PLF binding to a transmembrane region. (c) patcHwork prediction of change in ionization states of amino acids in SLC1A5 from pH of 7.4 to pH of 6.0. (d) Representative AlphaFold 3 model structure of SLC38A2 and PLQ.

Figure G7. Analysis of hypoxia-related gene expression in ovarian cancer cell lines. (a) Heat map of Z-score for each gene across the cell lines and the "overall" hypoxia metric determined by the product of gene expression for each gene. (b) Z-score of the overall hypoxia expression levels. Expression levels extracted from the ProteinAtlas.

CHAPTER 1

Background: Engineering Strategies for Immunomodulatory Cytokine Therapies – Challenges and Clinical Progress

The work presented in this chapter has been adapted with permission from Pires, I. S., Hammond, P. T. & Irvine, D. J. Engineering Strategies for Immunomodulatory Cytokine Therapies: Challenges and Clinical Progress. *Adv Ther (Weinh)* 4, 2100035 (2021).

1.1 Introduction

The term cytokine originates from the combination of the Greek words "cyto" and "kine" which translates to "cellular movement". Coined by Stanley Cohen in 1974, it was used to describe cellular substances that induced immune cell-directed migration (chemotaxis) and activation.[1] Since that time, there have been many new insights into these molecules and cytokines are now defined as regulatory proteins that modulate the immune system and inflammation.[2] As immune regulators, cytokines have a major role as signaling molecules in response to danger, tissue damage, or injury.[3] Importantly, the vital role of the immune system in many pathologies make cytokines promising therapeutics for many disease states.

However, clinical use of cytokines has been restricted. This clinical translational challenge comes from two major characteristics of cytokines: 1) they are highly pleiotropic and 2) in normal physiology, they are generally produced and act very locally in tissues. Accordingly, systemic administration can lead to severe side effects. Given this challenge, cytokines present a promising opportunity for molecular and formulation engineering to improve their safety and therapeutic efficacy. Many of the drug delivery platforms presented here have been reviewed for general immunotherapy applications—focusing on the delivery of checkpoint inhibitors, engineered T cells, co-stimulatory receptor agonists, and cancer vaccines.[4–11] Here, we focus on the specific challenges presented by cytokine therapeutics, discuss the basic biology and clinical applications of key immunomodulatory cytokines, and review engineering strategies developed to increase their utility in therapeutic applications. To limit the scope of this review we focus on recombinant cytokine delivery; strategies involving cytokine-secreting cells (cellular vehicles) and gene therapy are only briefly introduced and cytokine inhibitor therapies are not covered here (we refer the interested reader to a number of recent reviews on these approaches[12–19]).

1.2 Cytokine Classification and Characteristics

Cytokines are cell-signaling proteins that perform their biological function via extracellular cell-membrane receptors.[20,21] This biological function may act on the cell that produces them (autocrine signaling) or on a different cell (paracrine signaling).[22] Accordingly, cytokines have similar characteristics to other soluble factors such as hormones, but some key differentiating factors of cytokines include local production and expression in response to specific stimuli.[21,22] Importantly, cytokines act primarily on the immune system while hormones primarily modulate the endocrine system.[23] Lastly, unlike hormones, baseline levels of cytokines in the circulation are typically low at steady state.[21] However, exceptions exist as some cytokines can act at distant sites (endocrine signaling) and some hormone-like substances—such as growth hormone, erythropoietin, thrombopoietin, and leptin can be categorized as cytokines.[22]

Albeit imperfect, there are various classifications of cytokines which aim to functionally distinguish these pleiotropic proteins. Some of the early functional classifications led to the naming of interleukins, which were thought to originate from and act on leukocytes[22]. Other functional groupings include colony-stimulating factors (GM-CSF, G-CSF) and interferons (IFN-α, IFN-β, IFN-γ).[24,25] However, these early historical classifications have become outdated as these factors are now known to be produced by many cell populations and have pleiotropic effects on various cell types[22,23]. For example, some cytokines (e.g., TNF-α, IL-1β, TGF-β, IL-6) are produced by or act on non-immune cells (e.g., fibroblasts, epithelial cells, and cancer cells). [26–28]

Cytokines may also be functionally classified as either pro-inflammatory or anti-inflammatory. Pro-inflammatory cytokines (e.g., IL-1α/β, TNF-α/β, IL-6, IL-11, IL-18, IFN-γ) up-regulate inflammatory reactions (i.e. tissue's catabolic reactions against pathogens including immune cell recruitment, infiltration, and stimulation), while anti-inflammatory cytokines (e.g., IL-10, IL-6, TGF-β, IL-27, IL-35) down-regulate inflammatory responses and promote tissue healing.[23,29] However, the cytokine-induced inflammatory response is highly context-dependent with the same cytokine inducing either pro- or anti-inflammatory reactions depending on factors such as the target cell, concentration, and presence of other cytokines.[30] A common example for the varying inflammatory response of cytokines is IL-6 which, in addition to its major role in initializing inflammatory responses (along with TNF-α and IL-1), is a potent stimulant of acute-

phase proteins in hepatocytes (an anti-inflammatory effect) and can inhibit TNF-α and IL-1 expression.[30].

More recent classifications have originated from the relation of cytokines to T cell responses. T cells can be biased into different functional states characterized by the production of certain groups of cytokines, e.g., Th1 cytokines (type 1 cytokines) such as IL-2, IL-12, and IFN-γ; Th2 cytokines (type 2 cytokines) such as IL-4, IL-5, IL-6, IL-10 and IL-13; or regulatory cytokines such as IL-10 and TGF-β[31]. Although other Th subsets exist, these three major classes provide a basic framework to understand diseases and potential therapeutic opportunities within them. In general, type 1 cytokines mediate the development of a strong cellular immune response while type 2 cytokines favor a strong humoral immune response.[32] Conversely, regulatory cytokines promote immune homeostasis, prevent autoimmunity, and moderate inflammation.[33] Importantly, cytokine groups exhibit cross-regulatory properties in which they not only favor a functional state but also suppresses the alternative states. Accordingly, high levels of one class of cytokines is indicative of a type of immune environment which could be reprogramed with cytokine therapies from other subsets. For example, in cancer, tumors are typically associated with tolerogenic and immunosuppressive microenvironments in which cytokine-mediated therapies primarily have aimed to deliver type 1 cytokines to stimulate an anti-cancer cellular immune response. On the other hand, some vaccine-based therapies may prefer type 2 cytokines as adjuvants base on their role in B cell maturation, while autoimmune conditions could benefit from regulatory cytokines. In many instances, however, these distinctions are insufficient to classify cytokines since their effects are highly context dependent. For example, IL-18 in isolation can promote Th2-biased cytokine production from T cells, but in the presence of IL-15 or IL-12, IL-18 leads to potent Th1-biased cytokine production.[34] Moreover, type 1 cytokines are not restricted to cellular immune responses as they aid in the development of certain antibody classes and functional differentiation of B cells. [35,36]

Lastly, more objective classifications exist such as those based on structural or receptor homology. This grouping includes type I cytokines (consisted of four α-helical bundle structures with an ‘up-up-down-down’ configuration) signaling through class I cytokine receptors (IL-6, IL-2, IL-4, IL-12, GM-CSF), type II cytokines signaling through class II cytokine receptors (IFNs, IL-10 family, IL-19 family), cytokines signaling through immunoglobulin superfamily cytokine receptors (MCSF, IL-1, IL-16) and the TNF family signaling through TNF receptors family (TNF-

α/β).[22,23] However, the wide-range of functions of cytokines within the same group make this classification less practical; therefore, it is less commonly used.

In addition to immunomodulatory substances, cytokines are sometimes defined to include growth factors (PDGF, EGF, FGF, NGF, IGFs, TGF (α/β), BMPs, and CNTF) and chemokines (IL-8, MIP, MRO, IP-10)[24]. Growth factors are primarily molecules regulating embryogenesis, tissue repair, and wound healing, while chemokines are primarily molecules directing cell migration[23]. Yet, these substances can also modulate immune cells and immune responses, leading to an overlap in classifications. For example, the growth factor TGF-β is commonly classified as an anti-inflammatory cytokine or T regulatory cytokine. IL-8, in addition to serving as a chemokine, has inflammatory effects on immune cells.[37]

With more than 300 known cytokines, chemokines, and growth factors, here we restrict our discussions to immunomodulatory cytokines with a focus on cytokines tested in clinical studies.[25] A diagram depicting the major immune cell targets of cytokines that have or are being evaluated in clinical trials is shown in **Figure 1.1**. Other cytokines, their targets, and functions can be found in the literature[31,38].

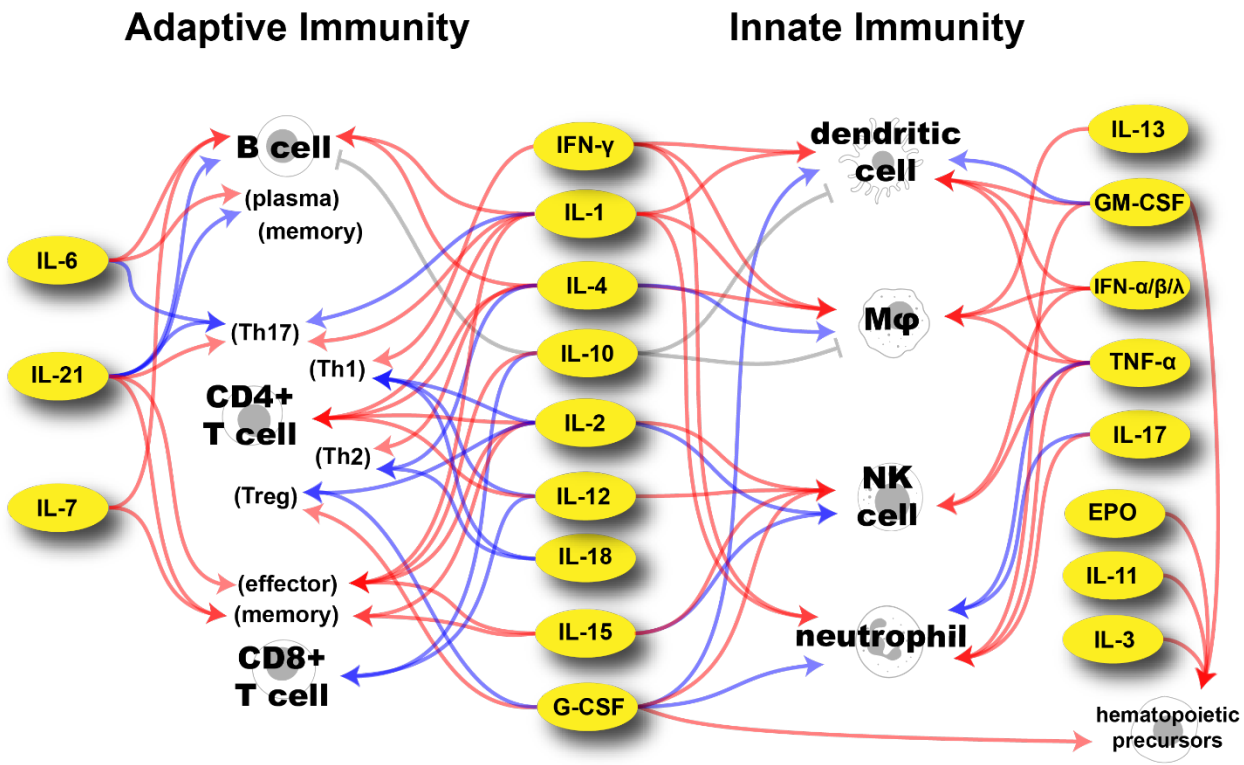

Figure 1.1. Major targets of cytokines used in clinical trials directed at immune cells involved in adaptive and innate immunity. Blue arrows indicate recruitment and differentiation. Red arrows indicate activation and expansion. Gray arrows indicate inhibition. IL-22 has been excluded here as its clinical trials have targeted its growth-factor properties and not its immunostimulant properties. TNF-related apoptosis-inducing ligand (TRAIL) is also excluded as its non-apoptotic role in immune-cells is not clearly understood.[39] The effects of IFN-λ are primarily on epithelial cells.[40]

Although not a comprehensive description of the effect of cytokines on immune cells, **Figure 1.1** clearly illustrates their pleiotropic nature. Other features of cytokines contributing to their complex activity include context dependency, cascading, antagonism, and feedback control. As previously mentioned, context-dependency implies that the settings of cytokine stimulus can regulate its responses such as the presence of cytokine combinations. Moreover, the cytokine concentration can alter their effects as shown by IL-2 where low doses preferentially stimulate regulatory T cells, while high doses activate $CD8^+$ T cells and NK cells.[41] The class of target cells, its environment, and time of cytokine activation are also contextual factors that can lead to altered responses of the same cytokine.[30] In addition to context-dependency, cytokines can have multiple effects based on the cascade of downstream cytokines produced in response to their stimulus. One such example is IFN-γ-mediated stimulation of activated macrophages leading to the release of IL-12 and TNF-α, both of which induce their own cascades.[35] As will be discussed in the **Clinical Perspective** section, this cytokine cascade effect is a crucial characteristic that hinders clinical translation as it expands the potential side effects of cytokine treatment. Conversely, antagonism refers to the property that a cytokine can restrict the effect or production of another such as IL-10-mediated inhibition proinflammatory cytokine production by macrophages or dendritic cells.[42] Finally, cytokine stimulation can be further enhanced (or downregulated) through feedback control mechanisms which can occur directly (e.g., macrophage auto-stimulation through TNF-α production) or indirectly (e.g., IFN-γ-mediated macrophage production of IL-12 leading to IFN-γ production via Th1 differentiated $CD4^+$ T cells).

1.3 History of Cytokines as Therapeutics

The first steps of cytokine discovery were taken in the 1920s, when it was shown that the mechanism underlying 'bacterial allergies' differed from protein anaphylaxis and that the supernatants of tissue sensitized to tuberculin amplified the reaction to old tuberculin[43,44].

Approximately thirty years later, the fundamental class of proteins leading to these phenomena started to be unraveled when the first individual cytokines were discovered as the 'endogenous pyrogen' (later classified as IL-1) and 'interferon' (later termed IFN-α) were isolated[43,45]. The potential clinical use of these substances was clear as 'interferon' interfered with viral infection. Furthermore, the 'endogenous pyrogen' was directly related to pathology as its effect was to induce fever in animals (*pyrogen* comes from the Greek word *pyro* meaning heat and *gen* meaning generating).[45]

By the 1970s and '80s, interest in therapeutic applications in cytokines increased as more cytokines were identified and the generation of recombinant proteins became possible.[34] During this time, interferon was found to have many other effects beyond preventing viral infection such as enhancement of cell function, immune system modulation, and inhibition of cell division with antitumor activity *in vivo.*[46] Based on these and other findings, the primary applications of cytokines began as immunostimulatory molecules (such as IL-1, IL-2 TNF-α) for immunodeficiencies (mainly AIDS), infections, and cancer treatment.[34] Since the initial burst of research, although many other cytokines and their mechanism have been identified and explored for therapeutic applications, only a select few have received regulatory approval as therapeutics. The cytokines currently approved as recombinant protein therapeutics, their indications, and administration routes are summarized in **Table 1.**

Table 1.1 Clinically approved recombinant cytokine therapies for *in vivo* immunomodulation.

Cytokine	Approval Indication (Year)	Other Indications	Adm. Route*	Ref
IFN-α IFN-α2a; IFN-α2b; peginterferon α2a; peginterferon α2b IFN-αn1; IFN-αn3	Hairy cell leukemia (1986)	Karposi's sarcoma, chronic myelogenous leukemia, metastatic malignant melanoma, follicular lymphoma hepatitis B and C, condyloma acuminate, labial and genital herpes, rhinoviruses	s.c. >TIM (Q1W PEG)	47,48
IFN-β IFN-β1a; IFN-β1b; peginterferon β1a; IFN-β (Soluferon)	Relapsing–remitting multiple sclerosis (1993)	-	s.c./i.m. QOD/Q1W (Q2W PEG)	49,50
IFN-γ IFN-γ1b	Chronic granulomatous disease (1990)	Malignant osteopetrosis	s.c. TIW	45,51
TNF-α tasonermin	Sarcoma (Europe, 1998) – application via isolated limb perfusion	Non-melanoma skin cancer– application via isolated limb perfusion	i.v.	52,53
IL-2 adesleukin	Metastatic renal cell carcinoma (1992)	Metastatic melanoma	i.v. Q8H	45,54
IL-11 oprelvekin	Chemotherapy-induced thrombocytopenia (1997)	-	s.c. QD	55

G-CSF filgrastim; lenograstim; pegfilgrastim	Prophylaxis of febrile neutropenia in patients receiving myelosuppressive chemotherapy (1991)	Accelerating neutrophil recovery after bone marrow transplantation, mobilizing peripheral-blood progenitor cells, and shortening the duration of neutropenia in patients receiving induction chemotherapy for acute myelogenous leukemia / reduce the incidence and sequelae of neutropenia in symptomatic patients with congenital, cyclic, or idiopathic neutropenia	i.v./s.c. QD (PEG s.c. >Q1W)	56
GM-CSF sargramostim; molgramostim	Accelerate myeloid recovery after autologous bone marrow transplantation and delayed or failed engraftment after allogeneic or autologous bone marrow transplantation (1991)	Accelerating neutrophil recovery after bone marrow transplantation, mobilizing peripheral-blood progenitor cells, and shortening the duration of neutropenia in patients receiving induction chemotherapy for acute myelogenous leukemia	i.v./s.c. QD	56
EPO epoetin alfa	Anemia associated with chronic renal failure (1989)	Anemia from Zidovudine used in HIV-infection, from myelosuppressive chemotherapy / reduction of allogenic red-blood cell transfusion in patients undergoing elective, noncardiac, nonvascular surgery	s.c./i.v. TIW or Q1W (PEG Q2W)	57,58

*Primary administration (Adm.) routes, some indications may differ. PEG – polyethylene glycol ; Parenthesis indicates any changes on the PEG-conjugated form of the cytokine

Abbreviations: s.c. - subcutaneous; i.m. – intramuscular; i.v. – intravenous; QD – every day; Q1W – every week; TIM – three times a week; Q8H – every eight hours; Q2W – every two weeks

As shown in **Table 1.1**, the approved indications for cytokine therapies have been cancer, viral infections (IFN-α), and immunodeficiencies (IFN-γ). Moreover, IFN-β is indicated as an anti-inflammatory agent for autoimmunity. The successful development of these treatments belies challenges even for these approved drugs. For example, IL-2 approval came even when >90% of patients had doses withheld during treatment due to toxicity.[59] Further, even though high-dose IL-2 therapy is still the first-line therapy for metastatic renal cell carcinoma, it is only applicable in selected patients (good organ function and performance status) and requires proper monitoring and management of the side-effects to reduce risks associated with the treatment.[60] As a second example, the approved TNF-α treatment in Europe for skin cancer is dosed via isolated limb perfusion to reduce systemic exposure to the drug.[61]

No regulatory approval for new cytokines has been made since the initial burst in the early 1990s. The chief advance since that time has been the approval of new forms of IFN-α, IFN-β, and G-CSF surface conjugated with polyethylene glycol (PEG) to extend their circulation half-life.[45,62] Despite these modifications, toxicity limitations have continued to restrict the expansion of already approved cytokines to new indications. For example, Type I IFN (α/β) could be clinically used in many other infections, but strategies to minimize systemic toxicity are needed.[50] Many more

preclinically promising therapeutic cytokines have not yet been clinically translated for similar reasons.[63] Nonetheless, great interest in expanding the use of cytokines as therapeutics remains, as indicated by the number of ongoing clinical trials (**Table 2.1**, compiled from *clinicaltrials.gov*).

Table 1.2. Current cytokine therapy clinical trials (parenthesis indicates number of trials still ongoing) and indications of active clinical trials (excluding approved indications).

Cytokine	Clinical Trial Phase				Total
	no record	1	2	3	
EPO	51 (6)	36 (3)	179 (18)	214 (18)	**480**
	Indic	*Phase 1:* healthy subjects, autoimmune hepatitis || *Phase 2:* bipolar disorder/unipolar depression/cognitive impairment, mantle cell lymphoma, premature infant, asthma, amyotrophic lateral sclerosis, eosinophilia/angioedema || *Phase 3:* anemia, chronic kidney disease, erythroblastosis fetalis, hypoxic-ischemic encephalopathy, intraventricular hemorrhage of prematurity, traumatic optic neuropathy, myelodysplastic syndromes			
G-CSF	24 (3)	28 (3)	97 (19)	51 (14)	**200**
	Indic.	*Phase 1:* solid tumor/ NSCLC/SCLC, advanced pancreatic cancer, postmenopausal symptoms || *Phase 2:* neurological diseases, multiple myeloma, lymphoma/leukemia, Fanconi anemia, early stage BC, Crohn's disease, heart failure || *Phase 3*: prostate cancer, liver cirrhosis/malnutrition, decompensated liver cirrhosis			
GM-CSF	18 (3)	43 (7)	130 (13)	18 (1)	**209**
	Indic.	*Phase 1*: prostate cancer, metastatic breast cancer || *Phase 2:* squamous cell carcinoma of the oral cavity, neuroblastoma, glioblastoma/gliosarcoma, recurrent neuroblastoma, colon cancer || *Phase 3:* pulmonary alveolar proteinosis			
IFN[a)]	15 (4)	9 (1)	59 (7)	29 (1)	**112**
	Indic.	*Phase 1:* various tumor malignancies || *Phase 2:* renal cell carcinoma/melanoma, lymphomatoid granulomatosis, chronic myeloid leukemia, breast cancer || *Phase 3:* malignant pleural mesothelioma			
IFN-α	45 (9)	82 (6)	360 (20)	259 (11)	**746**
	Indic.	*Phase 1:* Triple-negative BC || *Phase 2:* adverse effects of immunotherapy, squamous cell carcinoma, prostate cancer, recurrent ovarian cancer, myeloproliferative disorders, metastatic liver carcinoma, lymphoma, leukemia || *Phase 3:* polycythemia vera, melanoma, chronic myeloid leukemia, hepatitis, COVID-19			
IFN-β	4	30 (5)	40 (3)	49 (12)	**123**
	Indic.	*Phase 1:* solid tumor/NSCLC/SCLC, malignant solid tumors, endometrial clear cell adenocarcinoma, stage III melanoma, hepatocellular carcinoma || *Phase 3:* relapsing/remitting multiple sclerosis, COVID-19, MERS-CoV			
IFN-γ	8 (1)	16 (1)	40 (1)	15	**79**
	Indic.	*Phase 1:* ovarian cancer || *Phase 2:* breast cancer			
IFN-λ		1	7 (2)	7	**15**
	Indic.	*Phase 2:* hepatitis D, COVID-19			
IL-1	4	1	2		**7**
IL-10	2	1	1	1	**5**
IL-11		1	8	3 (1)	**12**
	Indic.	*Phase 3:* nasopharyngeal carcinoma			
IL-12	4	51 (5)	24 (1)		**79**
	Indic.	*Phase 1:* HIV, malignant epithelial tumors, solid tumors, acute myeloid leukemia || *Phase 2:* TNBC			
IL-13		1			**1**
IL-15		11 (4)	2		**13**
	Indic.	*Phase 1:* Relapsed T cell lymphoma, peripheral T cell lymphoma, metastatic solid tumors, leukemia			
IL-18		1	1		**2**
IL-2	16 (1)	95 (25)	233 (62)	27 (4)	**371**
	Indic.	*Phase 1:* ulcerative colitis, allotransplantation, solid tumors, recurrent or platinum resistant OC, metastatic colorectal carcinoma || *Phase 2:* type 1 diabetes, systemic lupus erythematosus, stage IV gastric carcinoma/stage IV nasopharyngeal carcinoma/lymphomas, autoimmune diseases, relapsing polychondritis, recurrent miscarriage, recurrent melanoma, recurrent acute myeloid leukemia, polymyalgia rheumatica, pleural mesothelioma, pemphigus vulgaris, NSCLC, metastatic OC, liver transplant, HIV, inflammatory myopathy, head and neck tumors, Crohn's disease, chronic graft versus host disease, bone sarcoma, Behcet's disease, amyotrophic lateral sclerosis , advanced plural mesothelioma, acute coronary syndromes || *Phase 3*: neuroblastoma			
IL-21		3	7		**10**
IL-22			1		**1**
IL-3		3			**3**
IL-4	1	3	3		**7**
IL-6		2			**2**

IL-7		6 (1)	19 (5)		**25**
	Indic.	*Phase 1:* acute myeloid leukemia || *Phase 2*: mycobacterium infections, metastatic bladder/renal urothelial carcinomas			
TNF-α	10	7	17	6	**40**
TRAIL		2 (2)	1		**3**
	Indic.	*Phase 1: malignant pleural effusion, peritoneal carcinomatosis*			
Total	**202 (27)**	**433 (63)**	**1231 (151)**	**679 (62)**	**2545**

Data obtained from searching *interferon, interleukin, tumor necrosis factor* and *colony-stimulating factor* in clinicaltrials.gov. Only interventional studies were included. Studies including the terms *anti, antagonist, inhibitor* or *cell* were excluded.
[a)] IFN type not specified in the intervention category for the clinical trial registry
Classification of early phase 1 as phase 1, phase1|phase2 as phase 2 and phase2|phase3 as phase 3
A total of 145 clinical trials used a combination of cytokines
Acronyms: BC – breast cancer; OC – ovarian cancer; TNBC – triple-negative breast cancer; NSCLC – non-small-cell lung carcinoma; SCLC – small cell lung cancer; HIV – human immunodeficiency virus; MERS-CoV – middle east respiratory syndrome coronavirus; COVID-19 – coronavirus disease 19

From **Table 1.2,** the major targeted indications for cytokine-based therapies continue to be cancer (~35%) and infections (~20%) with autoimmune conditions as the third most common class (~8%). Importantly, the use of cytokines in cancer has received renewed interest due to the success of checkpoint inhibitors (CPIs)[63]. The success of CPI treatment is highly dependent on immune infiltration of the tumor, which could be modulated via cytokine administration prior to or in combination with CPIs.[64] Combination treatments of highly immunostimulatory cytokines and CPIs are one of the main drivers for the recent increase in IL-2 clinical trials (indicated by the high fraction of active trials in **Table 1.1**). Furthermore, as will be noted in examples provided in this review, cytokine-based combination therapies also have therapeutic potential with radiotherapy, chemotherapy, cancer vaccines, and cellular therapies. [63,64]

In addition to the three major indication classes mentioned, there are many other potential applications for cytokine therapies. This is demonstrated by the various non-cancer indications in active clinical trials shown in **Table 1.2** such as neurological diseases, inflammatory diseases, fibrotic disease, and wound healing.[65]

1.4 Clinical Perspective

The basis for using cytokine therapies in the clinic is understanding their mechanism of action and toxicities. Many of the side effects from cytokine administration originate from the downstream cytokines released (i.e., the cytokine cascade). In the case of interferons or interleukins, the cytokine cascade is the cause of the most common adverse reactions of flu-like symptoms (fever, chills, myalgia, headache, and nausea). [66] These occur from the downstream expression of IL-1, IL-6, and TNF-α which can stimulate the hypothalamus leading to the various observed autonomic and behavioral effects.[67] The cytokine cascade can also stimulate autoimmune

conditions, affecting thyroid function and in some cases leading to psychiatric disorders such as depression. [67] Accordingly, combined with fatigue, even the more common systemic cytokine treatment toxicities can severely affect patient quality of life such that the therapeutic benefit is unsubstantiated. Further, under uncontrolled conditions, this cascade of cytokines released—termed 'cytokine storm'—is one of the leading causes of the more severe toxicities seen in cytokine-based therapies.

Unfortunately, it is difficult to prevent immune activation without subsequent expression of downstream cytokines. For example, i.v. administration of IL-2 will directly activate peripheral blood mononuclear cells (PBMC) expressing the IL-2R of which natural killer (NK) cells (~10% of PBMC) are the main elements.[68] Upon IL-2 stimulation, NK cells secrete IFN-γ, GM-CSF, and TNF-α, which in turn have downstream effects on a broad range of cell types. Moreover, although the downstream cytokines may lead to toxicities, they may also participate in the therapeutic effect. For example, IL-12-mediated toxicities are correlated with induction of high systemic IFN-γ levels.[69] Although these toxicities may be reduced via co-treatment with anti-IFN-γ antibodies, a reduction in therapeutic effect may also be seen as IFN-γ is a major driver of cellular immunity and macrophage activation.[70]

In addition to cytokine storms, another main concern with cytokine therapies is increased microvascular permeability, leading to vascular leak syndrome (VLS).[71] Typically associated with sepsis, VLS is characterized by the retention of extravascular fluid, hypotension, and multi-organ dysfunction. Although the mechanisms triggering VLS are not fully understood, it is likely mediated by multiple factors including increased vascular adhesion of activated immune cells, alterations in the endothelium due to inflammatory cytokines such as IFN-γ or TNF-α, and increased nitric oxide production in response to cytokine stimuli.[72] Although most deeply studied in the context of IL-2 administration where VLS is a chief toxicity, VLS is also associated with the administration of many other cytokines.[73] [71]

Given the issues with systemic administration of cytokines, one key goal for clinical development of cytokine therapies has been to minimize plasma exposure while maintaining efficacy, as high blood levels correlate with higher toxicities.[74] Indeed, preclinical studies that led to approval of aldesleukin demonstrated this effect when optimizing the IL-2 formulation and dose regimen.[75] Formulation of aldesleukin with albumin or bolus administration compared to short (5 to 15 minute) infusion led to increased total plasma exposure. In the case of albumin formulation,

there was a subsequent increase in toxicities and mortality in animals without improved therapeutic benefit. However, timing as well as peak plasma concentrations matter, as continuous dose regimens of IL-2 have a 10 fold lower maximum tolerated dose compared to a bolus i.v. administration.[68,76] Intriguingly, preclinical studies using bolus extended half-life IL-2 have indicated lower toxicities and improved efficacy compared to the native protein. [77,78]

Clinical development of cytokines is further hindered by limitations in preclinical animal models. For example, preclinical studies of cancer immunotherapies often require use of immunocompetent mouse models, but transplanted tumor models are characterized by very rapid tumor growth and the development of histopathology that often does not well replicate human cancer. These characteristics lead to different vascularization and immune infiltration which can have significant effects on the delivery or efficacy of cytokine treatment. Furthermore, the immune system of mice and humans has important differences in cellular makeup, receptor expression, and cytokine responses.[79] For example, human blood is neutrophil-rich (50-70% compared to 10-25% in mice). This difference can lead to an altered immune response from systemic cytokine administration since, for example, neutrophils play a major role in IL-2-induced capillary leak syndrome and IL-12 stimulation on human neutrophils leads to IFN-γ production.[80–82] Mice may lack a functioning intermediate IL-2Rβγ,[82] and this altered IL-2R biology could be a contributing reason for the increased toxicity noted when IL-2 immunocytokines were tested in humans compared to mouse models[83]. Importantly, these immunological differences are not restricted to mouse models as shown by the failed TGN1412 (a CD28 superagonist monoclonal antibody) Phase 1 trial in which differences in CD28 expression patterns between non-human primates and humans led to safe tests in cynomolgus and rhesus monkeys, but significant cytokine storms in humans.[84]

Some cytokine clinical trials have also failed to demonstrate clear relationships between administered dose and therapeutic effect.[85] This is likely due to marked patient-to-patient immune system heterogeneity. For example, in an IL-12 clinical trial, IL-12 failed to show a dose-response in IFN-γ induction.[85] Accordingly, understanding a patient's individual immune profile and monitoring the changes associated with the cytokine therapy are likely necessities for successful clinical cytokine therapies.

Given the pleiotropic characteristic of cytokines and their resulting clinical effects, the major challenges with the use of bolus or continuously-administered recombinant cytokines are

their high toxicity when administered systemically and poor pharmacokinetic profile. As signaling molecules for damage or danger, cytokines can cause serious side effects when present systemically by over-activating the immune system. Further, cytokine therapy suffers from poor pharmacokinetics as the small size of the proteins facilitates rapid vascular extravasation and kidney excretion. Thus, for conventional intravenous administration, large and frequent dose regimens are often required to reach therapeutic efficacy. However, these dosing regimens come at the expense of high toxicity risks which can outweigh the therapeutic benefit. Together, these challenges motivate the application of drug delivery technologies to enable the safe and effective use of these proteins therapeutically. Accordingly, many approaches have been developed to address the above challenges including protein engineering, polyethylene glycol (PEG) conjugation, fusion proteins, polymeric matrices, and particle-mediated delivery (micro- and nanoparticles). These engineering strategies and their clinical utility are described in this review. Other approaches for cytokine delivery such as cytokine-secreting cells and gene therapy are briefly introduced, but these approaches present distinct challenges beyond the scope of this review.

1.5 Protein Engineering Strategies for Cytokine Delivery

Sequence Modifications

One of the first engineering strategies that enabled the clinical translation of cytokines was mutations or modifications to the protein sequences for improved biologic manufacturability. More recently, mutated cytokine versions are being developed to reduce the pleiotropic nature of cytokines. Accordingly, these mutations are used to either enhance or diminish binding to cellular receptors, allowing for a more selective effect of the desired cytokine.

Enhanced protein folding and stability

Many of the cytokines discussed here are complex eukaryotic glycoproteins. Thus, to improve manufacturing, point mutations have been introduced to the sequence of approved products. For example, aldesleukin (IL-2) has a mutation replacing the 125-cysteine with serine to facilitate the folding to the proper conformation without affecting its bioactivity (aldesleukin also does not contain the N-terminal alanine of IL-2).[86] Similarly, the approved IFN-β expressed in *E. coli* (IFN-β-1b) has a cysteine substituted for serine in position 17.[87] Further, substitution of

hydrophobic residues for hydrophilic ones can improve bioavailability of non-glycosylated forms of these glycoproteins.[88]

Selective receptor binding

One of the first examples of sequence engineering to modulate cytokine receptor binding was the interferon alfacon-1. This synthetic protein contains the most common amino acids from the 14 IFN-α subtypes, yielding a non-natural protein with higher activity over IFN-α-2b (major subtype used in the clinic).[89] However, with the convenience of PEGylated IFN-α, this drug is currently restricted for treatment-failure patients dosed with peginterferon-α formulations.[90]

More recently, cytokine engineering has aimed to become more selective in modulating the receptor-binding properties of the cytokine. One of the most researched examples has been IL-2, which binds to two major forms of the IL-2 receptor (IL2R) in humans. One is an intermediate affinity receptor composed of IL2Rβ (CD122) and IL2Rγ (CD132) while the other a is high-affinity receptor containing IL2Rβ, IL2Rγ, and IL2Rα (CD25). Importantly, CD25 is upregulated on Tregs and activated T cells, while IL2Rβ and IL2Rγ are constitutively expressed in NK cells, macrophages, and T cells[91,92] Accordingly, there have been various engineered IL-2 muteins designed to preferentially bind to the IL2Rβγ complex and reduce Treg activation via IL-2Rα binding. For example, the IL-2v design employs three mutations in the CD25 binding interface, F42A, Y45A, and L72G, to restrict IL-2 binding to CD25.[93]

Interestingly, the opposite has also been attempted: a D20T mutation in IL-2 reduces intermediate affinity receptor binding but maintains high-affinity receptor (CD25) binding. This cytokine was designed to reduce systemic IL-2 toxicity by mutating a toxin-like motif involved in endothelial cell binding.[91] Reducing the affinity to the intermediate affinity receptor could also reduce systemic NK cell activation and its subsequent toxicities.[91] Although it could stimulate Tregs, it would serve to maintain activated T cells and was theorized to provide a potent anti-cancer response in combination with Treg depletion therapies.[91] However, this construct was discontinued for use in cancer treatment, potentially due to the low levels of CD25 expression in pulmonary endothelial cells, leading to toxicity or simply low potency in immune stimulation.[93] Importantly, although, selective CD25 binding IL-2 muteins have not to date had great success in cancer therapy, many of them remain under clinical investigation for immunodeficiencies (see **Fusion Protein** section for examples).

Modulation of cytokine-receptor interactions may also improve adoptive cell therapies. For example, an orthogonal pair of mutated IL-2 (*ortho*IL-2) and IL2Rβ (*ortho*IL2Rβ) were designed to have specific interactions without binding to the wild-type proteins.[94] When *ortho*IL2Rβ was expressed in engineered T cells, administration *ortho*IL-2 could selectively activate the transferred T cells without systemic immune activation and subsequent toxicity.[94]

Fusion Proteins

Fusion proteins consist of two or more proteins genetically linked to functionally enhance the resulting protein complex. The enhancement often originates from altered pharmacokinetics or targeted cytokine bioactivity. For pharmacokinetic alterations, cytokines fused to a partner protein have increased size, reducing kidney excretion and typically increasing the circulatory half-life of the protein. Moreover, the increased size can lower the interstitial transport rate, prolonging exposure once delivered to a site.[95] Cytokines can also be fused with targeting or functional proteins, to change their localization or introduce new functionalities to the protein. A variety of cytokine fusion protein constructs have reached clinical trials, including immunotoxins, tumor antigen cytokine fusion proteins, immunocytokines, non-antibody targeting motif fusion proteins, Fc-fusions, and albumin-fusions (**Figure 1.2**), These fusion proteins are discussed in this section.

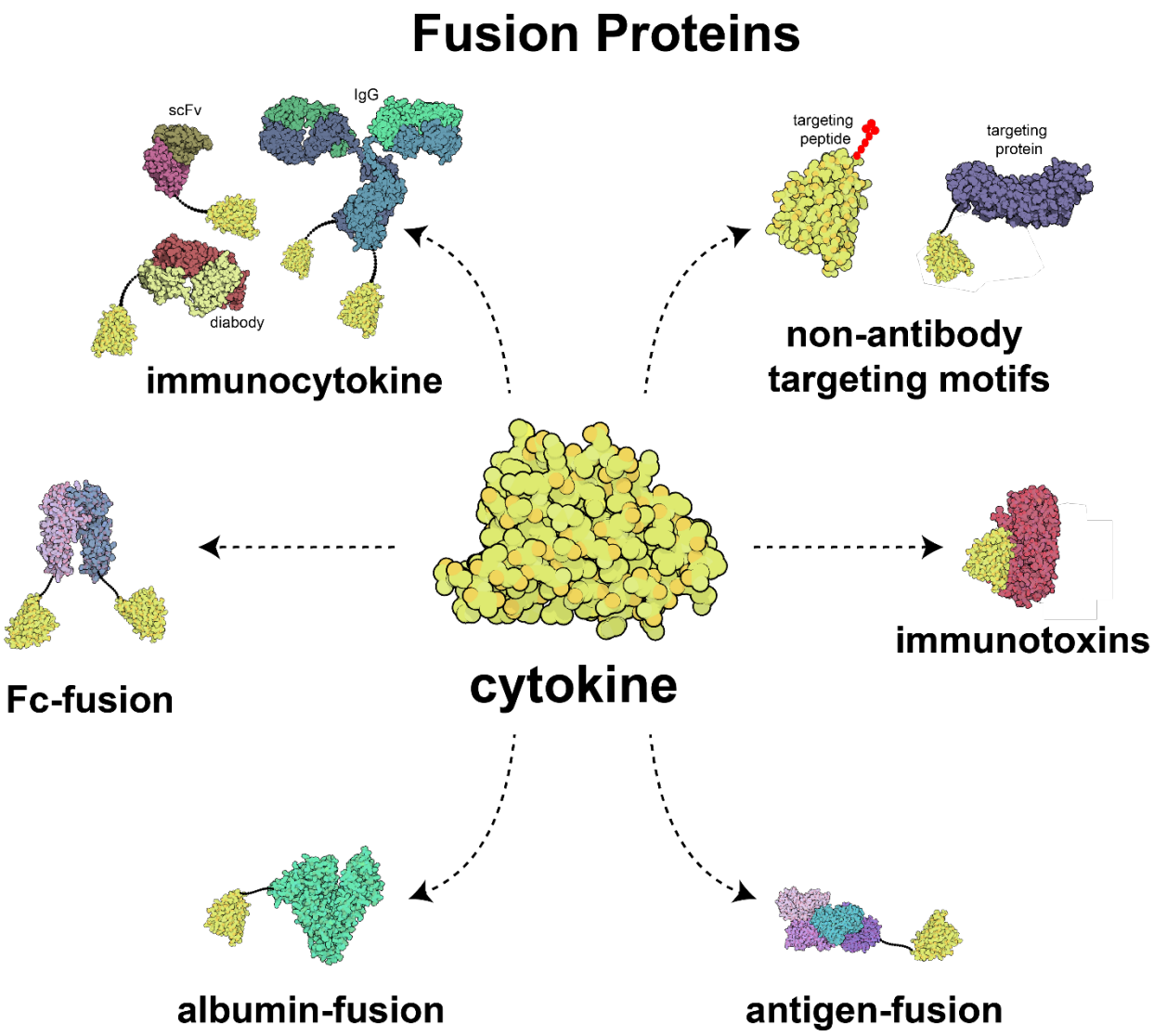

Figure 1.2. Illustration of major fusion proteins developed for cytokine delivery. The three-dimensional protein illustrations were generated in Qutemol[96] based on the Protein Data Bank structures of interleukin-2 (1M47), immunoglobin-G (1IGT), diabody scFv T84.66 (1MOE), scFv based on diabody structure (5GRV), human IgG1-Fc domain (5JII), diphtheria toxin (1F0L), prostatic acid phosphatase (1CVI), human serum albumin (1A06), and fibromodulin (5MX0).

Immunotoxins

Immunotoxins are fusions of cytokines with bacterial toxins designed to allow the specific killing of malignant cells that express a certain cytokine receptor. The first clinically approved immunotoxin consisted of IL-2 fused with the diphtheria toxin (DT) protein. This construct replaced the receptor-binding domain of diphtheria with IL-2, creating an IL-2 toxin directed at

cells expressing the IL-2R (primarily T cells).[97] This IL-2 toxin (denileukin diftitox, Ontak) received regulatory approval from the FDA in 1999 for persistent or recurrent cutaneous T cell lymphoma.[98] However, the treatment had severe side effects and complicated manufacturing which led to its discontinuation from clinical use.[98] Notably, other cytokines such as GM-CSF and IL-3 were also fused with DT for hematological malignancies.[99] Although GM-CSF-DT failed in Phase 1 trials due to liver toxicity, the IL-3 receptor-targeted version (Elzonris) received FDA approval in 2018 for blastic plasmacytoid dendritic cell neoplasm and is currently being tested in other myeloma malignancies.[99] Lastly, an IL-13 immunotoxin has also re-entered clinical trials for gliomas after it reached Phase 3 clinical trials for recurrent glioblastoma, but did not show survival benefit over standard-of-care carmustine wafers.[100]

Importantly, although these constructs were not designed as immunomodulators the potential to deplete certain immune cells can be used to alter the immune profile of a disease. Accordingly, more recent clinical trials have used denileukin diftitox to deplete Treg cells in tumors as these cells have high expression of the high affinity IL-2 receptor.[101] A better understanding of the full effects of the therapy are still needed as conflicting and unexpected results have been reported.[101] With the discontinuation of Ontak, safer and more reliable formulations of the drug are needed for further studies.[98] However, although new constructs can be developed, a major limitation in these class of fusion proteins is the high immunogenicity of the toxin moiety, which can greatly affect the pharmacokinetics and efficacy of the therapeutics.[102]

Antigen-cytokine fusion proteins

Another cytokine fusion protein strategy is the linkage of cytokines to antigens to provide enhanced antigen immunogenicity. This class of fusion protein has been clinically developed for prostate cancer treatment (tradename Sipuleucel-T) and was approved in 2011 as the first cancer vaccine treatment.[103] In this therapy, the patient's peripheral blood mononuclear cells (PBMCs) are treated *ex-vivo* with a fusion protein composed of prostatic acid phosphate (prostate cancer antigen) linked to GM-CSF. [103] Treatment with the fusion protein aims to enrich the autologous PBMC (mixture of lymphocytes, monocytes, and dendritic cells) with activated antigen-presenting cells (APCs) such as dendritic cells and monocytes. These fusion-protein-activated APCs are then reinjected into the patient to provide an immune response that prolonged survival by approximately 4 months in patients with asymptomatic or minimally symptomatic metastatic castrate resistant (hormone refractory) prostate cancer.[103] Importantly, the APC activation was enhanced with the

fusion protein over its separated constituents, enabling the development of the therapy. However, Sipuleucel-T has been under-applied in the clinic as it has a high cost, and traditional biomarkers of disease progression such as serum levels of prostate-specific antigen do not track well with activity of the therapy.[104,105]

Although Sipuleucel-T delivers the cytokine fusion protein *ex-vivo,* preclinical studies have used the same concept for *in vivo* cytokine delivery. For example, cytokine-neuroantigen fusion proteins have been used to induce a tolerogenic response to the antigen in models of multiple sclerosis. Several cytokines including IL-2, GM-CSF, M-CSF, IL-16, and IFN-β have been tested in these constructs.[106] Notably, GM-CSF showed the greatest tolerogenic effect due to its role in active induction of myeloid APCs and the targeting of the antigen to GM-CSFR expressed by APCs. Importantly, this fusion protein further illustrates the pleiotropic activity of cytokines as GM-CSF alone is known to exacerbate experimental autoimmune encephalomyelitis (EAE) but showed a tolerogenic (anti-inflammatory) effect in the fusion protein for EAE treatment. This anti-inflammatory response is also seen when GM-CSF is used in other animal models of autoimmunity such as type 1 diabetes, thyroiditis, and graft versus host disease.[107] This function is thought to occur through support of regulatory myeloid DCs and enhanced antigen presentation to Tregs.[107]

Immunocytokines

Another class of cytokine fusion proteins developed in the early stages of cytokine therapies are cytokine-antibody conjugates. These fusion proteins, termed immunocytokines, combine the targeting specificity of antibodies with the potency of cytokines aiming to elicit a local immune response while also modulating the pharmacokinetics and pharmacodynamics of the drug molecule (**Figure 1.2**). Interestingly, tumor-cell targeting immunocytokines may also bridge tumor cells and leukocytes, acting similarly to bispecific antibodies.[108] Given their potential for a localized immune response and enhanced pharmacokinetics, these constructs have been heavily researched for cytokine delivery in oncology and non-oncological diseases such as autoimmune or inflammatory conditions.[109] Immunocytokine candidates are in clinical trials for delivery of a variety of cytokines including IL-2, IL-10, IL-12, and TNF-α[110]. These fusion proteins and their current clinical stage are summarized in **Table 3**. Other immunocytokines have been developed in preclinical studies that have been reviewed previously.[111]

Table 1.3. Immunocytokines in clinical trials.

Immuno-cytokine	Cytokine	Route	Target / Ab	Combination	Clinical Trial Phase (indication)	Ref.
NHS-IL12	IL-12	s.c. Q4W	necrosis (histones)/IgG	avelumab (anti-PD-L1) -	Phase 1 (solid tumors) Phase 2 (Kaposi Sarcoma)	112
Hu14.18-IL2	IL-2	i.v. 3xQ1D	cell surface (GD2) / IgG	-	Phase 2 (neuroblastoma/ melanoma)	113
FAP-IL2v (RG7461)	IL-2 (↓CD25)	i.v. Q1W	Cell surface (FAP) / IgG (↓FcγR ↓C1q)	tecetriq, avastin, pembrolizumab (anti-PD1)	Phase 1 (melanoma/ RCN)	114
IL12-F8-F8 (Dodekin)	IL-12	-	vasculature / diabody	-	Phase 1	115
L19-IL2 (Darleukin)	IL-2	i.v. Q1W	vasculature (EDB) / diabody	SBRT rituximab (anti-CD20)	Phase 2 (NSCLC) Phase 1 (B cell lymphoma)	115
L19-TNF (Fibromun)	TNF-α	i.v Q2D	vasculature (EDB) / scFv	doxorubicin / dacarbazine -	Phase 3 EU / Phase 2 US (soft tissue sarcoma) Phase 2 US (glioma)	115
L19-IL2 + L19-TNF (Daromum)	IL-2 + TNF-α	i.t. Q1W	vasculature (EDB)	-	Phase 3 (Stage IIIB/C melanoma)	115
F16-IL2 (Teleukin)	IL-2	i.v. Q1W	vasculature (tenascin-C)/ diabody	anti-CD33 antibody	Phase 1 (AML)	115
F8-IL10 (Dekavil)	IL-10	s.c. Q1W	vasculature (EDA) / scFv	methotrexate	Phase 2 (RA and ulcerative colitis)	115
DI-Leu16-IL2	IL2	s.c. 3xQ1D	cell surface (CD20) / IgG	after rituximab (anti-CD20)	Phase 2 (Lymphoma)	116
CD20-IFNα (IGN002)	IFNα	i.v Q1W	cell surface (CD20) / IgG	-	Phase 1 (NHL)	117
Discontinued[a)]						
NHS-IL2T (Selectkine)	IL-2 (↑CD25)	i.v. Q3W	necrosis (histones)/IgG	SBRT/ipilimumab (anti-CTLA-4)	Phase 2 (melanoma)	118
CEA-IL2v	IL-2 (↓CD25)	i.v. Q1-3W	cell surface (CEA) / IgG (↓FcγR ↓C1q)	atezolizumab (anti-PDL1)	Phase 1 (advanced and/or metastatic tumors)	93
huKS-IL2	IL-2	i.v. 3xQ1D	EpCAM / IgG	cyclophosphamide	Phase 2 (SCLC)	119
BC1-IL12 (AS1409)	IL-12	i.v. Q1W	vasculature (B-FN) / IgG	-	Phase 1 (melanoma, RCN)	120

[a)]no active trials and/or removed from companies' pipeline

EDB: extra domain B of fibronectin; EDA: extra domain A of fibronectin; B-FN: isoform of fibronectin; FAP: Fibroblast activation protein alpha; CEA: Carcinoembryonic antigen; GD2: Disialoganglioside; RCN: renal cell carcinoma; SBRT: stereotactic body radiation therapy

As shown in **Table 1.3**, the antibody portion of the immunocytokine can be in various formats ranging from the full immunoglobulin G (IgG) to antibody fragments (**Figure 1.2** depicts some of these constructs).[109] These structural configurations as well as glycosylation patterns can modulate the circulatory half-life and residence time at the disease site.[108] For example, full IgG constructs have higher circulatory half-life over fragments, but a smaller immunocytokine with

fast extravasation may lead to a higher relative tumor to blood concentration (**Figure 1.3**), potentially minimizing systemic exposure while leading to similar tumor accumulation.[121]

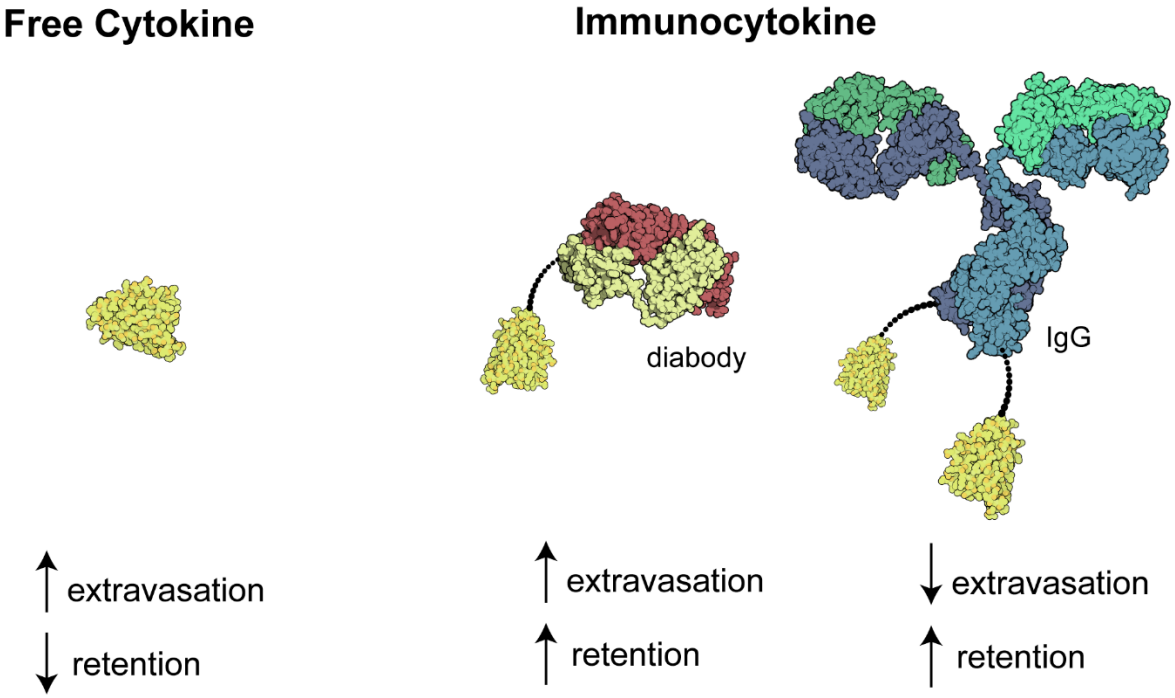

Figure 1.3. Selected formats of immunocytokines and their primary characteristics on vascular extravasation and tumor retention.

Although smaller immunocytokines can reduce systemic exposure, these fusion proteins need not be small to improve their therapeutic effect as size is only one of the factors that can alter its efficacy. For example, in addition to its structure, the site of linkage and type of linker can be used to modify pharmacokinetics and cytokine receptor binding properties.[122,123] Further, the use of an unmodified Fc region in immunocytokines mediates various effects such as antibody-dependent cell-mediated cytotoxicity, complement-dependent cytotoxicity, and extended half-life through the neonatal Fc receptor (FcRn) recycling.[121] Lastly, both the antibody and the cytokine may be mutated for altered receptor binding such as the FAP-IL2v which has a mutated IL-2 for lower CD25 binding and mutated IgG to restrict C1q and FcγR binding while maintaining FcRn recycling.[114] With these mutations, the therapy aims to prevent immunosuppression from IL-2-

mediated stimulation of $CD25^{hi}$ Tregs, and prevents induction of myeloid phagocytosis via FcγR or complement binding via C1q of the drug and its target. In a number of the clinical trials noted in **Table 1.3** the immunocytokine is given in combination with chemotherapy or CPIs. Promising results of combination therapies with CPIs have propelled research into immunocytokines targeting check-point markers such as fusion proteins of IL-15 and anti-PDL1 mAb (KD033)[124].

Although studied since the 1990s, most trials of immunocytokines are still in either Phase 1 or Phase 2. The greatest limitation with immunocytokines is the requirement of a tumor antigen to target. This requirement hinders the wide application of the therapy as *bona fide* tumor-specific antigens shared across patients are rare. Moreover, antigen loss by cancer cells can lead to tumor escape.[125] An alternative strategy has been to target tumor blood vessels or the tumor extracellular matrix, which is another major strategy currently used in clinical trials[108]. However, targeting of pro-inflammatory agents to blood vessels may lead to hypotension as a dose-limiting toxicity.[110] Moreover, for any of these antigen-targeted strategies, the therapy risks on-target toxicity. This occurs when these antigens are expressed at low levels in healthy tissues, promoting off-site targeting of the immune response. Further complicating their development is the observation that the cytokine payload of the fusion protein can compete with the variable region of the antibody by binding to cytokine receptors: rapid binding of the immunocytokine to cytokine $receptor^{+}$ immune cells in the blood can dominate the biodistribution of the fusion protein, limiting tumor accumulation.[121]

One strategy to minimize unspecific binding and systemic toxicity is intratumoral administration (also called intralesional).[121] Intralesional treatments aim to exert their effect locally, reducing systemic toxicity. Indeed this approach has shown encouraging clinical success when delivering IL-2 with high response rates and low toxicity, but the laborious administration schedule tempered its utility.[126] Immunocytokines are thus promising candidates due to their high retention, which enables more practical dose scheduling. In this area, the most clinically advanced immunocytokine treatment is a combination of IL-2 and TNF-α immunocytokines (Daromum) which uses L-19 diabodies (L19IL-2 and L19TNF) to target the tumor vasculature. These fusion proteins are in Phase 3 clinical trials as a neoadjuvant treatment for stage IIIB/C melanoma via intralesional delivery.[126] In animal studies, they were shown to have longer residence time within the treated lesion over free cytokine. Further, Phase 2 clinical studies showed an overall response rate of 55%, with reduction of untreated lesions ("abscopal effect") and minimal treatment-related

toxicity. Notably, the low toxicity of Daromum makes it a promising candidate for neoadjuvant immunotherapy as previous clinical trials with CPIs have shown high response rates but with significant toxicities .[126]

Albumin-Cytokine Fusion Proteins

Many proteins may be used to modulate the pharmacokinetics of fusion proteins. Another major class of fusion protein for this effect are albumin fusions, which prolong the circulatory half-life of fusion partners. The fusion increases molecular size and, similar to IgG fusion proteins, albumin is recycled through the FcRn which further enhances the half-life of albumin fusion proteins.[77] However, unlike other strategies for half-life extension such as PEGylation of other materials-based approaches, albumin fusion proteins are more readily synthesized at large-scales, providing more cost-effective methods for improving cytokine pharmacokinetics.[127] Accordingly, IL-2 was fused with albumin (Albuleukin) for a prolonged serum half-life and targeted biodistribution to spleen, liver, and lymph nodes which prompted its testing in Phase 1 clinical trials.[128] However, after an acquisition of the developing company, the project ended. [128]

Notably, promising candidates from this class were albinterferon alfa-2b (tradename Albuferon) and albumin-G-CSF fusion which had prolonged half-life and reached Phase 3 clinical trials.[129] However, although both Albuferon (albumin-IFN-α) and albumin-G-GCF were noninferior to the approved PEGylated versions of the cytokines, they did not reach clinical approval. Albuferon have higher toxicities compared to PEG-IFN-α while albumin-G-CSF was discontinued by the developing company.[90,130,131]

Importantly, although albumin-fusion proteins failed to reach clinical approval, preclinical studies are still looking to use albumin fusion cytokines. For example, canine IFN-γ-albumin fusion protein is being developed for veterinary medicine.[127] Moreover, recently, an albumin fused to GM-CSF (albGM-CSF) was shown in mice to control tuberculosis by prolonging GM-CSF half-life, increasing its bioactivity, and targeting the cytokine to the draining lymph nodes and lungs.[132] The albGM-CSF treatment increased DC count in the draining lymph nodes and elicited an antitubercular effect *ex vivo* and in mouse lungs. Notably, these effects may enhance first-line regimens for tuberculosis treatment or serve as a new adjuvant in cancer prevention or therapeutic vaccines. Lastly, there have been promising results using IL-2 fused to albumin in mouse models in combination with anti-tumor antibodies.[77,78]

Fc Fusion Proteins

Fusion of cytokines with the Fc domain of antibodies can be used to both enhance the circulation lifetime of cytokines and introduce antibody effector functions. For example, in addition to prolonged half-life, IL-2-Fc fusion proteins have been shown to deplete Tregs via the FcγR[133]. This mechanism may even have higher antitumor effect over the immune activation of IL-2 as a standard IL-2-Fc overperformed a mutated IL-2 with limited binding to Tregs.[133] However, combining mutations that limited IL-2 interaction with Tregs and enhanced T cell and NK activation have been shown to have enhanced antitumor immune effects over native Fc-IL2.[134] Clinically, a few cytokine-Fc fusion proteins are under investigation. These include a Phase 1 trial using Fc-IL-2 (CC 92252[135] and AMG592[136]) designed to have preferential binding to Tregs for autoimmune diseases and Phase 2 trials using Fc-IL-22 fusion proteins (UTTR1147A[137] and F-652[138]) for inflammatory diseases. Further, a non-specific IgG-IL2 construct which has increased Treg activation is also being developed[114]. Like some immunocytokines in **Table 3**, the IgG-IL2 fusion protein is also mutated to remove FcγR and C1q binding while retaining FcRn binding.

Fc fusions are also being developed for treatment of cancer. Fc-scTRAIL (ABBV-621) is in Phase 1 trials for solid tumors or hematologic malignancies.[139] Also for cancer therapy, an IL-12-Fc construct (DF6002) has recently started Phase 1/2 clinical trials delivered subcutaneously with CPI (anti-PD1) in advanced solid tumors (NCT04423029). Another promising Fc fusion protein is an IL-15 superagonist, N-803 (previously known as ALT-803). This drug molecule consists of a mutated IL-15 for increased IL15Rβ binding complexed with IL15Rα-Fc protein.[140] The IL15:IL15Rα (hetIL-15) complex in itself also has increased bioavailability and half-life and is in Phase 1 clinical trials (NIZ985) administered subcutaneously for metastatic and advanced solid tumors in combination with anti-PD-1 CPI[141]. Based on promising Phase 1 clinical results, N-803 is currently in Phase 2 clinical trials for various indications as a monotherapy or in combination immunotherapies administered subcutaneously. [141] A related construct, an IL-15-IL-15Rα fusion protein (SO-C101) is also in Phase 1 clinical trials for metastatic and advanced solid tumors as monotherapy or combination with CPI (NCT04234113). The concept of fusing the cytokine with its receptor is also being tested with an IL2-IL-2Rα construct (ALKS 4230) which is designed to prevent IL-2 from interacting with the endogenous IL2Rα and also increase its half-life.[142] Currently, ALKS 4230 is under investigation in Phase 1/2 clinical trials in advanced cancers as monotherapy or in combination with CPIs.[142] The IL-15 superagonist N-803 has also been

made into an immunocytokine by further fusion of anti-PDL1 scFv domains to the construct, yielding better results in animal models compared to N-803 in combination with anti-PDL1 mAb, which is currently being tested in the clinic.[143]

Non-antibody targeted fusion proteins

With the extensive experience and successes of monoclonal antibodies, immunocytokines have been the most studied class of targeted cytokine fusion proteins. However, in addition to antibodies, alternative mechanisms to enable targeted cytokine delivery have been developed including targeting peptides or targeting proteins. The most advanced and tested example of these constructs is the NGR-hTNF fusion proteins. This system uses the tumor vasculature targeting peptide Asn-Gly-Arg (NGR) to deliver TNF-α to tumor blood vessels.[144] The fusion with the targeting motif enabled a wider therapeutic window compared to the free cytokine.[144] Interestingly, it was observed that intermediate dose levels had diminished therapeutic efficacy compared to low or high dose treatments .[145] Mechanistic studies determined that the intermediate or high doses lead to the shedding of soluble TNFR which inhibited TNF-α activity. Thus, therapeutic efficacy was only seen when either low doses were administered to prevent soluble TNFR release or when high doses were used to overwhelm this counter-regulatory mechanism.[144] However, only low doses were likely to have selective interaction with tumor blood vessels as high doses lead to significant systemic toxicity. Importantly, TNF-α is not the only cytokine which can have its activity attenuated from the release of soluble receptors as it has been shown that IL-12 administration leads to an increase in soluble IFN-γ receptors.[85]

Currently, NGR-hTNF has completed various Phase 2 clinical trials with promising results in malignant mesothelioma and liver carcinoma. However, a Phase 3 clinical trial using NGR-hTNF as second line therapy for malignant plural mesothelioma did not reach its primary endpoint.[146] Interestingly, the results showed an overall survival and progression-free survival benefit for patients with short treatment-free intervals. Given that this patient subgroup had rapidly progressing tumors, this observation may be due to the high dependency of the proliferating cells on newly formed blood vessels which are the target of NRG-hTNF. [146] However, the data were not sufficient for EMA approval and NGR-hTNF needs to be further tested in clinical trials for mesothelioma.[147] Notably, NGR-hTNF has the potential to selectively increase vascular permeability as was demonstrated in a Phase 2 clinical trial in combination with an immune-

chemotherapy treatment of primary central nervous system lymphoma.[148] In this trial, pre-treatment with NGR-hTNF was safe and enhanced vascular permeability of the blood-brain barrier with a targeted effect in the tumor and peritumoral areas. Importantly, there are other targeting peptide sequences such as RGD, isoDGR, or RGR which can also be fused to cytokines for targeting.[144]

Other promising tumor-targeting cytokine fusion protein constructs are under investigation in pre-clinical studies targeting the tumor extracellular matrix. For example, the fusion of IL-2 or anti-PDL1 CPI with the A3 collagen-binding domain (CBD) of von Willebrand factor can reduce toxicity and improve antitumor immunity compared to the unmodified forms.[149] Further, when IL-12 was fused with CBD, the construct showed a potent effect in immunologically cold tumors and synergized with CPIs even in CPI-unresponsive mouse models.[150] Interestingly, this construct has an even lower plasma half-life compared to IL-12, but its tumor localization properties allowed for an effective immune response while the low plasma retention prevented systemic exposure to the cytokine (similar to the antibody fragment fusion proteins of **Figure 1.3**). Moreover, the CBD fusion protein was shown to be more effective when administered i.v. versus peritumorally. On the other hand, fusion of cytokines with lumican, a collagen-binding protein, was shown to provide enhanced tumor retention from i.t. administration.[151] Importantly, the retention of lumican fusion protein was further increased by generating a three-protein fusion protein construct composed of the cytokine, lumican, and albumin. This design was used to generate IL-2 and IL-12 fusion proteins which, when co-administered, enhanced various immunotherapies such as chimeric antigen receptor T cells, vaccines, tumor-targeting antibodies, and CPI.

Other Fusion Proteins

In addition to the designs discussed above, there are many other potential fusion protein constructs for cytokine delivery.[152] Notably, there have been cytokine-cytokine fusion proteins such as Pixykine that also showed some clinical success. Pixykine, a fusion protein of IL-3 with GM-CSF was capable of eliciting a 10-20 fold higher potency than GM-CSF or IL-3 alone *in vitro*, reaching Phase 3 clinical trials for treating neutropenia and thrombocytopenia.[153] However, its use was discontinued when it was not found to have superior effects compared to GM-CSF therapy alone in its Phase 3 clinical trial.[154] Similarly, GM-CSF has been linked to various other interleukins (IL-2, IL-15, IL-21) in preclinical studies to simultaneously stimulate the myeloid and

lymphoid immune system on an anticancer immune response.[153] Notably, GM-CSF-IL2 fusion proteins (GIFT-2) showed superior efficacy compared to the combination of individual cytokines while GIFT-15 showed an immune suppressive effect. Lastly, GIFT-21 had strong pro-inflammatory effects on monocytes, enabling DC differentiation *ex-vivo* which suppressed tumor growth *in vivo* when administered without antigen priming. [153]

Other interesting fusion protein concepts are cytokines linked to inhibitory molecules such as an scFv that prevents receptor binding of the cytokine.[155] In this construct, the linker between the cytokine to the inhibitory molecule is designed to be cleavable by enzymes overexpressed in some tumors such as matrix-metalloprotease 9. Accordingly, the cytokine is expected to remain inactive until it reaches the tumor microenvironment where the enzyme cleaves the linker, enabling the cytokine to elicit its effects. However, this technology has been primarily been tested *in vitro,* and future *in vivo* studies are needed to access its clinical potential.

Protein Engineering - Conclusion

Since its origins with sequence modifications for improved manufacturing, protein engineering has been continuously applied to improve cytokine-based therapies. As indicated by a late stage clinical trials and a number of on-going clinical trials, the field of cytokine fusion protein has many promising candidates. Further, many large biopharmaceutical companies are invested in immunocytokines or other types of fusion proteins.[156] As such, its real potential will be tested in the upcoming years and may lead to improved or new cytokine-based therapies.

1.6 Bioconjugation and Material-based Strategies for Cytokine Delivery

Polyethylene glycol (PEG) conjugation

Polyethylene glycol conjugation (PEGylation) is the most established technology to alter protein pharmacokinetics and pharmacodynamics.[157] Polyethylene glycol (PEG) is an amphiphilic non-ionic synthetic polymer that can be readily conjugated to cytokines. The hydrophilic nature of PEG facilitates the formation of an associated water layer around the polymer, which along with the entropic penalties of molecular adsorption to the PEG brush layer, reduces non-specific interactions of the conjugated protein with its surroundings.[158] Accordingly, PEGylation can shield the protein core from proteolytic enzymes, lower immunogenicity, increase stability and solubility, and prevent interactions with cell-surface proteins. [157] Moreover, the bound polymer and its water shell increase the hydrodynamic volume (i.e. size) of the resulting complex, preventing

extravasation and kidney filtration, increasing the conjugated protein's circulatory half-life.[157] Although there has been recent detection of anti-PEG antibodies in humans, PEG has no known biological receptors, allowing for modulation of the therapeutic properties with limited introduction of new side effects.

PEGylation may also lead to drug accumulation in tumors and at sites of inflammation due to the enhanced blood vessel permeability and tissue retention at these disease sites.[157] In cancer, this is termed the enhanced permeation and retention (EPR) effect, and is thought to occur due to alterations in tumor vasculature and tumor lymphatic drainage, leading to higher permeability and retention of macromolecules.[159] This is an important phenomenon that is commonly exploited for the delivery of nanosized molecules of particles in cancer, yet the actual mechanisms for accumulation and magnitude of enhancement are still debated.[160]

These collective properties have made PEGylation a common and viable method to enhance therapeutic efficacy and/or improve pharmacokinetics of cytokines. Notably, even without improvements in therapeutic efficacy, enhanced pharmacokinetics improves patient compliance and lowers administration costs as the patient needs to be dosed less frequently with therapy.[161] The first PEGylated protein was approved by the FDA in 1990, and research on its use with cytokines was not far behind, with the first approval of a PEGylated cytokine in 2000 (IFN-α2β , PegIntron). Notably, PegIntron and other PEGylated cytokines such as Pegasys (IFN-α2α), Mircera (erythropoietin), and Neulasta (G-CSF) have become blockbuster drugs.[162] These proteins showed great success due to their enhanced pharmacokinetic profiles. For example, PEGylation of IFN-α increased serum half-life (from 3-8 to 65 hrs) and lowered the clearance rate over 100-fold, eliciting the same response when administered once a week compared to thrice a week with unconjugated IFN-α in chronic hepatitis C[163,164] (other general changes in administration schedule on the PEGylated form of approved cytokines can be seen in **Table 1).**

Unfortunately, even on the approved PEGylated cytokines, there has not been a substantial reduction in toxicity. For example, the use of PEGylated IFN-α was approved due to its higher relapse-free survival (without significant improvement on overall survival), but treatment still leads to significantly decreased health-related quality of life due to its toxicity.[165,166] Further, although PEGylation provides a beneficial systemic administration pharmacokinetic profile, in general, PEGylation reduces protein activity by hindering binding to its receptor(s). However, the extent of activity loss has often been observed not to be significant enough to reduce the therapeutic

value of PEGylation. For example, peginterferon α-2a (Pegasys) retains less than 10% of the original *in vitro* cytokine activity, but its *in vivo* efficacy and improved administration schedule justified replacement over the unconjugated cytokine.[162,167]

In addition to the approved PEGylated cytokines in **Table 1**, IL-2 PEGylation has been widely explored in the literature, making it an excellent case to highlight the pros and cons of PEGylated cytokines. Preclinical studies showed that PEGylation enhanced the stability and solubility of recombinant IL-2 and lowered its immunogenicity.[168] However, even though human clinical trials with PEG-IL-2 showed enhanced plasma retention (10-20 fold increase in half-life), decreased clearance, and similar biological activity,[169] efficacy did not show significant differences over treatment with unconjugated IL-2 when administered after a single high dose in metastatic renal cell carcinoma and melanoma.[170] Furthermore, a Phase 2 trial with PEG-IL-2 treatment as monotherapy in renal-cell carcinoma showed high toxicities with lower response rates than unconjugated IL-2.[171] PEG-IL-2 was also used at low doses in clinical trials for HIV-infected patients in combination with antiretroviral therapy, leading to enhanced $CD4^+$ T cell counts, albeit not immediately restoring immune function.[172] However, this treatment also did not reach FDA approval likely due to the failure of the IL-2-mediated $CD4^+$ T cell increases to show a clinical benefit in HIV-positive patients.[173]

Importantly, various other cytokines have been PEGylated aiming to improve the therapeutic efficacy.[174] Yet, even though these typically had increased half-life, the results did not lead to clinical translation. Like PEG-IL-2, this may be attributed to the high levels of toxicity of treatment or lack of improved efficacy compared to unconjugated cytokine or standard-of-care treatments. Of note were the recent clinical trials using Pegilodecakin (PEG-IL-10) for cancer immunotherapy, which aimed to enhance anticancer $CD8^+$ T cell activity in immunologically "cold" cancers.[175] Although demonstrating promising preclinical and Phase 1 clinical results, PEG-IL-10 treatment for metastatic pancreatic cancer in combination with chemotherapy (FOLFOX) failed to promote overall survival in a Phase 3 clinical trial[176]. Moreover, the remaining two Phase 2 clinical trials that used PEG-IL-10 in combination with CPIs (pembrolizumab or nivolumab) for metastatic non-small cell lung cancer also did not reach their primary endpoints, ending a more than $1.5 billion dollar investment in the therapy.[177] While the full clinical data is still to be presented and more research is likely necessary to understand the failure of PEG-IL-10 despite its strong scientific rationale; the dose, activity or trafficking into the tumors may have hindered the

efficacy of the treatment in these immunosuppressive cancers.[178] These challenges may have been noted had there been more careful clinical data prior to hastening the therapy into Phase 3 for metastatic pancreatic cancer and the two Phase 2 studies after early efficacy results based on results from less than thirty patients on Phase 1.[178,179]

Despite the disappointing results discussed above, studies of PEGylated cytokines have continued to generate interest in clinical trials. An example are ongoing trials using an engineered PEG-IL-2 cytokine (Bempegaldesleukin, NKTR-214).[92] This drug has approximately six PEG chains attached to IL2Rα binding region of the protein, creating an inactive prodrug of IL-2 (**Figure 1.4**). The cytokine becomes active as the PEG linkers are gradually cleaved by hydrolysis revealing active forms of IL-2. Importantly, the active forms of Bempegaldesleukin (containing one to two PEG-chains attached to the protein) bias IL-2 binding to the IL2Rβγ receptor which should favor $CD8^+$ T cells and NK cell stimulation over Tregs.[180] Accordingly, preclinical results have shown that this drug can preferentially activate $CD8^+$ T cells over Tregs in tumors of mouse models and synergize with CIP therapy.[92,181] Phase 1 clinical studies have suggested similar effects in humans[182] with encouraging objective response rates when combined with CPIs that were independent of baseline tumor PD-L1 expression[183]. Based on these results, various Phase 2 and Phase 3 clinical trials are ongoing using Bempegaldesleukin in combination with CPIs[184]. The PEGylation strategy is also being used in another PEG-IL-2 construct (NKTR-358) to maintain higher relative binding to the high-affinity receptor (IL2Rαβγ), preferentially activating Treg cells.[185] This engineered protein should serve as a treatment for immune-inflammatory disorders and is currently under Phase 1 clinical trials.

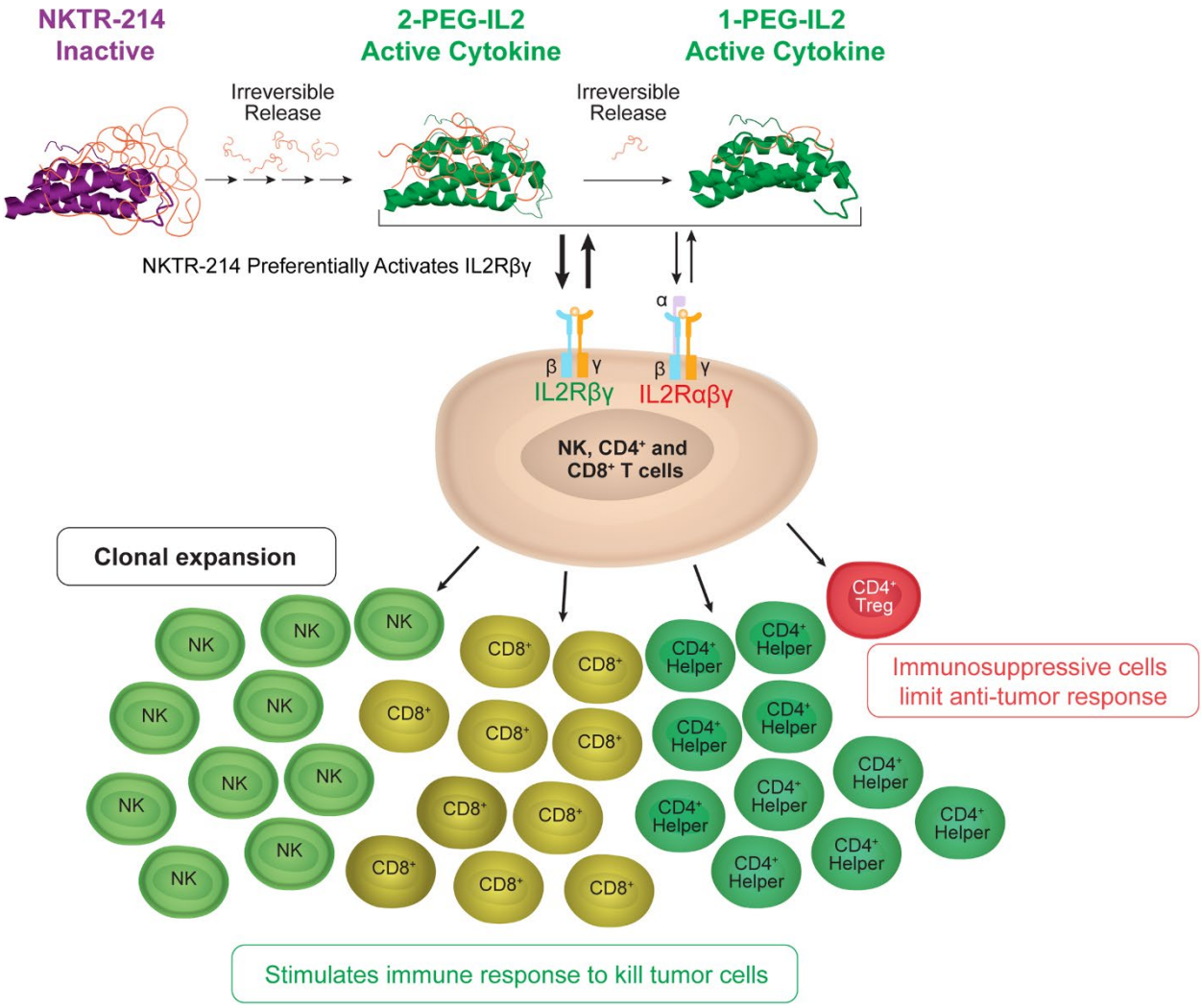

Figure 1.4. Representation of Bempegaldesleukin and its biased IL2Rβγ receptor binding for enhanced IL-2-mediated immunotherapy of cancer. Reproduced under the terms of the CC BY 4.0 license. [180] Copyright 2017, Charych et. al.

Other more recent strategies for PEGylation have included the use of non-natural amino acids, enabling site-specific chemical modification such as a recent PEG-IFN-β1b tested in a Phase 1 clinical trial. [186] This concept is also being used for site-specific PEG conjugation in IL-2 for preferential IL-2Rβγ binding (THOR-707) which is currently in a Phase 1/2 clinical study or lowered IL-2Rβγ (THOR-809).[187] Site-specific PEG-conjugated IL-15 and IL-10 are also in preclinical studies.[187]

Although the clinical history of PEG makes it one of the most widely used polymers for surface conjugation, there have been increasing concerns in its use. One issue is the recent findings

of anti-PEG antibodies present in the population or induced by the therapeutic administration.[158,186] When initially developed for bioconjugation, PEG was considered immunologically inert with 0.2% of the population possessing anti-PEG antibodies. However, recently, anti-PEG antibodies have been found in patients who became non-responsive to PEGylated forms of asparaginase and uricase.[186] Moreover, reassessment of the presence of anti-PEG antibodies in non-treated patients has shown a dramatic increase to more than 70% of the current population.[186] This rise in anti-PEG antibodies in treatment-naïve individuals has been attributed to the widespread use of PEG in household and hygiene products (shampoo, soap, toothpaste, lotion, etc.) and improved assay sensitivities.[158,186] As of yet, no direct negative relationship between the presence of anti-PEG antibodies and therapeutic efficacy with PEGylated cytokine therapies.[188] However, until recently, clinical trials with PEGylated therapeutics did not assay for the presence of anti-PEG antibodies, which may have obscured potential issues. A phase 1 study using PEG-IFN-β1b demonstrated a strong correlation between anti-PEG antibodies and accelerated blood clearance of the cytokine.[186] However, the approved formulation of PEG-IFN-β1a showed the development of neutralizing antibodies against the protein in only 1% of treated patients compared with 2.5% in the unconjugated protein.[188] Moreover, although total immunogenicity increased based on the development of anti-PEG antibodies in 7% of the patients, they were found to have no discernable impact on safety or clinical efficacy.[189]

Further hindering the use of PEG conjugates is their non-biodegradability which restricts elimination of the polymer to clearance via the kidneys.[190] This may lead to intracellular accumulation in the liver and tissue lysosomes, especially in chronically-administered PEGylated therapeutics. Accordingly, there have been various alternatives proposed. Of note have been the development in zwitterionic materials and use of polyaminoacids (polypeptides) as the conjugated polymer.[190] Notably, use of disordered biosynthetic polypeptides such as repeated proline, alanine, and/or serine (PAS) sequences may provide the benefits of PEG without the associated immunogenicity and non-degradability.[191]

Overall, after more than 20 years with PEGylation of cytokines, the results have shown some cases of enhanced pharmacokinetics with similar therapeutic efficacy and toxicity to that of unconjugated cytokines. However, PEGylation has not enabled clinical translation of new cytokines. While the reasons are not clear it may be that prolonged systemic exposure to the highly potent cytokines increases toxicity concurrently with the therapeutic efficacy, providing a similar

therapeutic window range compared to bolus administration. Moreover, in a clinical setting, the prolonged serum half-life can become a liability since it precludes the rapid reversal of toxicity which is commonly required for IL-2 treatment.[170] Lastly, PEGylation can also have significant effects on biodistribution, which need to be carefully considered for the desired cytokine effect.[192] Thus, new and rational strategies for cytokine delivery with or without polymer-drug conjugates still need to be developed.

Polymeric matrices

Polymeric matrices consist of polymer chains capable of entrapping the desired drug molecule. In the clinic, the matrix may be deployed at the desired site (e.g., near or in a tumor) or implanted after surgery (e.g. tumor resection), and often employs biodegradable polymers that will dissolve by hydrolysis over time. When a drug is loaded into these polymeric matrices, the diffusional barrier or the matrix degradation rate modulate the drug release rate. These parameters can be designed based primarily on the (i) polymer composition, (ii) the resulting water content within the matrix, (iii) the type of crosslinker and drug conjugation **(Figure 1.5**). Notably, the matrix may protect the loaded proteins from enzyme degradation and promote or diminish cellular interactions. Furthermore, these systems can be either externally-controlled or responsive to the local environment, allowing for even higher-order control of the delivery system.[193] Lastly, by using biodegradable polymers, the administered matrix may not require removal after completion of therapy.

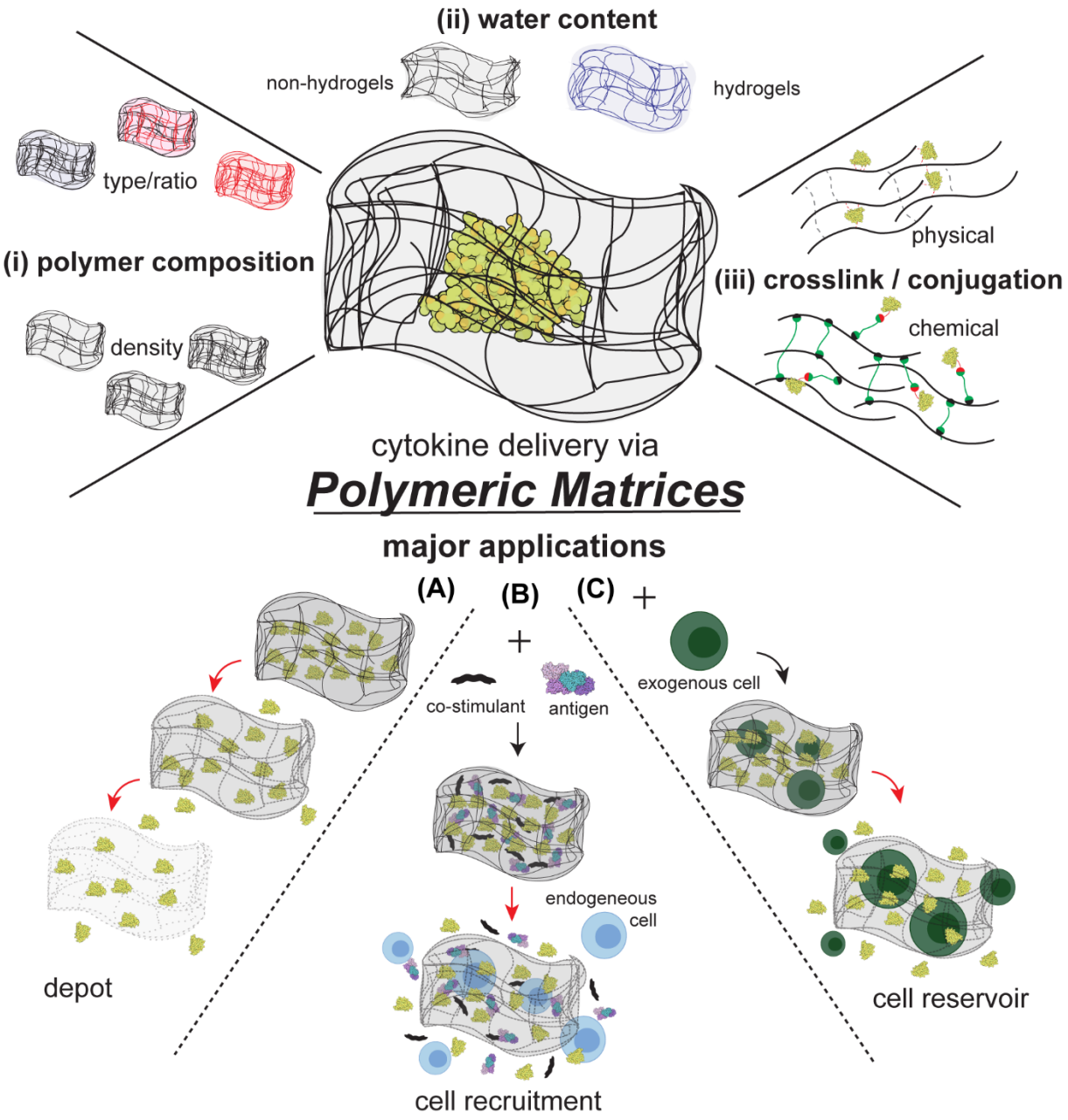

Figure 1.5. Major design parameters of polymeric matrices used in cytokine theraapies and their applications. Polymeric matrices can have varied properties by altering (i) the polymer composition, (ii) the resulting water content, and (iii) the type of crosslinker and/or conjugation. These matrices have been primarly used as (a) depots, (b) to promote endogenous cell recruitment, and (c) as exogenous cell resevoirs. Red arrows indicate progression of polymeric matrix systems after administration.

Polymer matrices can be composed of solid polymers or hydrogels. Hydrogels are three-dimensional polymeric matrices comprised of hydrophilic polymers swollen with large amounts of water (generally more than 50%). These polymer networks have solid-like behavior on the macroscale (i.e. contain a definitive shape and do not flow) and solution-like behavior on the molecular scale (water-soluble molecules can diffuse through the hydrogel).[194] Accordingly, hydrophilic drugs are easily loaded into these matrices without the requirement of harsh processing conditions, making them promising vehicles for protein delivery. Moreover, the structural similarity to that of macromolecular-based scaffolds in the body make these hydrogels generally biocompatible.[194]

Based on the modular design space of polymeric matrices, they have been used to enhance the therapeutic efficacy of cytokines by providing a spatiotemporal control over their release. As will be seen, polymeric matrices have shown great promise as modular systems to enhance cancer vaccines by serving as cytokine depots (**Figure 1.5A)** and for cellular-based immunotherapies **(Figure 1.5B-C)**.

Matrices releasing cytokines from a local site over prolonged periods have been extensively explored in applications for cancer vaccines or for intratumoral immunotherapy. To create enhanced cancer vaccines, one of the first approaches was based on the encapsulation and sustained release of tumor-associated antigens together with GM-CSF from hydrated polymer gel matrices derived from poly-N-acetyl glucosamine (p-GlcNAc).[195] Since its initial characterization, this gel matrix (F2 gel) has been used for not only combinations with tumor antigens for cancer vaccines, but also improved intratumoral cytokine monotherapy (GM-CSF, IL-2, IL-12, EPO).[196] Notably, co-formulation of cytokines with chitosan, a natural polymer composed of primarily deacetylated glucosamine polysaccharides, can also function as a controlled release platform due to the high viscosity of chitosan.[197] When IL-12 was formulated with chitosan, intravesical treatments were shown to eliminate up to 90% of tumors in orthotopic bladder cancer mouse models with induction of systemic immunity.[198,199] Furthermore, both the chitosan and p-GlcNAc matrices themselves are capable of inducing an immune response which may synergize with the cytokine effect. Importantly, p-GlcNAc and chitosan are biocompatible, biodegradable, and non-toxic with a p-GlcNAc-based hemostat already approved by the FDA.

A foundational study that propelled research into polymeric matrices for cytokine delivery was the use of a macroporous poly-lactide-*co*-glycolide (PLGA) scaffold to simultaneously deliver

GM-CSF, innate immune "danger signals", and cancer antigens (tumor cell lysate) for cancer vaccination.[200] This combination of molecules was chosen to mimic an infection when administered in which, a) the prolonged-release GM-CSF (~30 days) served as a cytokine gradient to attract dendritic cells, and b) the recruited dendritic cells were exposed to antigens and danger signals for antigen loading and maturation.[201] This concept is illustrated in **Figure 1.5B**. Notably, when implanted, GM-CSF released from the scaffold was shown to attract a similar number of dendritic cells to the scaffold as typical protocols for dendritic cell vaccines. The macroporous structure allowed for the dendritic cells to reside within the implant. Moreover, the design of the matrix could tune the number of dendritic cells recruited, activated and dispersed to local draining lymph nodes. Accordingly, this system could yield a robust immune response without the inherent difficulties with cellular therapeutics such as dendritic cell vaccines. In the poorly immunogenic B16-F10 murine melanoma model, the therapy yielded ~50% survival compared to 0% from GM-CSF-secreting tumor cells.[201] This therapeutic delivery system (termed WDVAX) is currently in Phase 1 clinical trials for melanoma treatment as the first-in-human biomaterial vaccine clinical trial. [201]

Notably, this concept of harboring and stimulating immune cells within a polymeric matrix via cytokines can also be used for enhanced cell therapies (**Figure 1.5B)**.[202] For example, a macroporous alginate scaffold was integrated with silica microparticles conjugated with T cell stimulatory antibodies (anti-CD3, anti-CD28, anti-CD137) and loaded with soluble IL-15 superagonist . The alginate scaffold was functionalized with a synthetic collagen-mimetic peptide to enhance T cell migration within the matrix. [202] Accordingly, when loaded with tumor-specific T cells, this system is designed to provide a local and prolonged adoptive T cell therapy (ACT), improving the efficacy of ACT in solid tumors. Experiments in animal models showed ~100-fold higher T cell proliferation at the injected site compared to prestimulated T cells in both an unresectable ovarian cancer model and an incompletely-resected breast cancer model. This enhanced T cell therapy prevented recurrence in 100% of animals in the breast cancer model and had complete tumor clearance in 6/10 animals in the unresectable ovarian cancer model which was significantly better to the 0% prevention of recurrence and 0% of complete tumor clearance in animals receiving pre-stimulated T cells alone. [202]

Importantly, traditional implants with specific shapes typically have limited methods for dosing and administration. Accordingly, injectable matrices, which normally either undergo *in situ*

chemical polymerization or sol-gel phase transitions, were developed and have been the main systems researched for polymeric matrix-mediated cytokine delivery.[203] These systems greatly facilitate clinical application as they do not require surgical application of the scaffold and can be designed to have similar performance to implantable materials. For example, prior to the WDVAX implant, it was shown that an injectable alginate gel loaded with CCL21 (a dendritic cell attractant cytokine) and activated dendritic cells was capable of sustained delivery of the chemokine and recruitment of the host dendritic cells and T cells into the injected matrix.[204] In this system, alginate microspheres containing calcium were mixed with an alginate solution to induce *in situ* gelation that occurred in ~60 min after s.c. administration. Alginate was chosen due to its biocompatibility and capability to electrostatically binding and retaining cytokines and chemokines that may be exogenously added or derived from immune cells. With this same *in situ* self-gelling system IL-2 and CpG oligonucleotides (immunostimulatory molecules) could be introduced into the injected matrix by electrostatically binding CpG to alginate microspheres and adding IL-2 to the alginate solution (**Figure 1.6**).[205] Peritumoral delivery of an IL-15 superagonist (see **Fusion Protein** section) combined with CpG via this matrix or two injections of IL-15 superagonist gel could elicit similar anti-tumor efficacy without exogeneous dendritic cells in the B16F10 melanoma mouse model.[206] In this construct the IL-15 superagonist was released *in vivo* over a period of a week with a ~40 fold higher peak cytokine concentration in the tumor and lower levels of the cytokine in circulation compared to systemic injection. Immune cell characterization revealed that the IL-15 superagonist recruited T cells into the matrix and tumor and reduced the relative frequency of regulatory T cells.

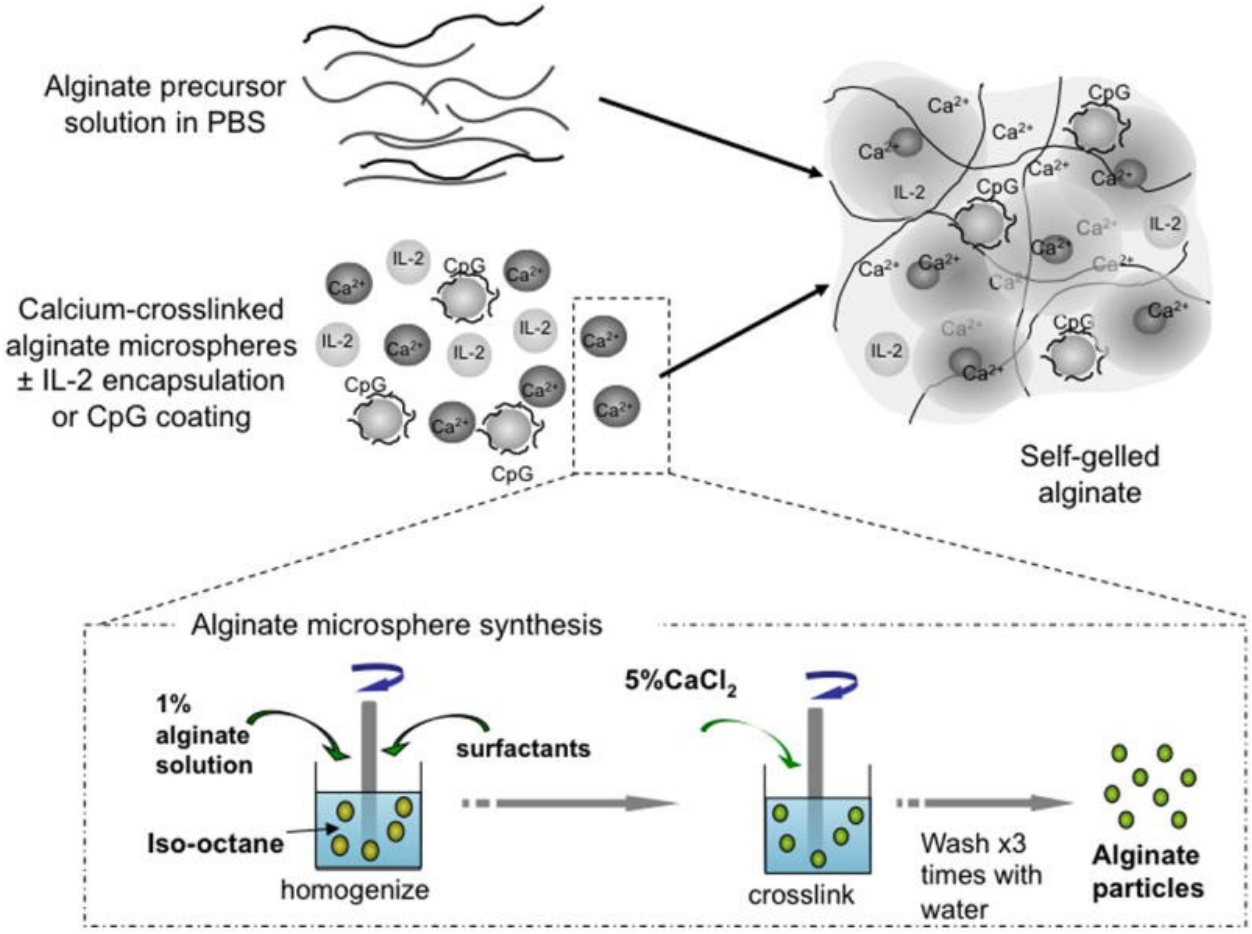

Figure 1.6. Schematic of an alginate-based polymeric matrix designed for in situ gelation to enable prolonged and dual release of IL-2 and CpG as well as harbor and attract immune cells. Reproduced with permission. [205] Copyright 2009, Elsevier.

Another promising example of injectable materials for cytokine delivery are self-assembling mesoporous silica rods.[207] In this system, high aspect ratio silica rods loaded with GM-CSF enabled prolonged release of the cytokine over more than 35 days. One key point in this strategy is that the biodegradable amorphous silica is generally recognized as safe by the FDA, enabling the potential future clinical translation of these materials. In animal models, therapeutic doses of mesoporous silica rods did not elicit noticeable adverse effects and degraded to an unmeasurable size within 25 days.[207]

Polymeric matrix-assisted cancer vaccine systems can also be made into injectable biomaterials hosting the tumor cells. For example, the combination of GM-CSF with CpG has been used in injectable cryogel systems co-loaded with irradiated tumor cells.[208] This system was

shown to out-perform bolus GM-CSF-secreting tumor cancer cells vaccination which enhanced spatiotemporal control of the vaccine delivery. However, the main limitation with such a system is the requirement of *ex-vivo* manipulations of autologous tumor cells which can alter their associated tumor antigen profile, as well as increased regulatory complexity of the therapy.

Injectable polymeric matrices have also been extensively used for as depots for cytokine monotherapy or combination therapies. [203] One of the first formulations for depot cytokine delivery was IL-2 loaded into a polyoxyethylene-polyoxypropylene block copolymer (F-127 gel).[209] The gel solidifies at physiological temperature providing prolonged released which prolonged survival in rat fibrosarcoma models.[209] In the case of combination therapies, an interesting example comprises the use of another thermo-sensitive polypeptide hydrogel for chemo-immunotherapy mediated by delivery of IL-2, doxorubicin, and IFN-γ:[210] This triple drug combination used poly(γ-ethyl-L-glutamate)-*b*-poly(ethylene glycol)-*b*-poly(γ-ethyl-L-glutamate) as a matrix which undergoes a thermally-induced sol-gel phase transition at body temperature, with good biocompatibility and biodegradability in mouse models. This scaffold yielded an improved anti-tumor response on the B16F10 melanoma mouse xenograft model over the free drug combination and had no observable systemic side-effects.

Lastly, in addition to depot function, engineered polymers can improve the therapeutic effect of cytokine-based therapies. One example was an injectable gel formed by a redox-active polyion complex which scavenges reactive oxygen species (ROS).[211] When delivered at the vicinity of tumors, the therapy elicited improved tumor growth-inhibition compared to IL-12 injection alone while also reducing toxicity from the IL-12 mediated ROS generation.

Fueled by a better understanding of immunology and chemistry of materials, there has been a recent surge in preclinical studies applying matrices for cytokine delivery. Some limitations encountered with clinical development of these scaffolds have been manufacturing, storage, regulatory complexity, and costs. Further, polymer degradation may yield unwanted effects such as acidification upon PLGA degradation. [212] However, a few hydrogel systems have recently been clinically translated, paving the way for future polymer-based drug delivery systems.[213]

Microparticles

Microparticles are large (>1 μm diameter) particles made of primarily polymers or lipids. In cytokine delivery, the most widely used microparticle system has been in the form of polymeric microparticles which, like the polymeric matrices, are used for spatiotemporal control of drug

release. Similarly, lipid-based systems such as multilamellar vesicles (MLVs) have also been made into microparticles for cytokine delivery. MLVs are spherical particles composed of multiple lipid bilayers with aqueous internal cavities that can increase an encapsulated drug's circulatory half-life and function as a depot for prolonged cytokine delivery.[214] These two main classes of microparticles are discussed in this section.

6.3.1. Lipid-based microparticles

Lipid-based microparticles were one of the first vehicles for cytokine delivery when macrophage-activating factor 'lymphokines' were encapsulated into large MLVs (average diameter of 1-2 μm) and shown to prevent pulmonary metastasis in mouse models of melanoma.[215,216] Later, more specific cytokine formulations containing IL-1α, TNF-α, IFN-α, and IL-2 were also tested in tumor models or as vaccine adjuvants.[217–219] Importantly, these formulations allowed for higher cytokine concentrations within tissues of the immune system such as lung, liver, spleen, and bone marrow over the free cytokine. Based on promising preclinical studies, IL-2 encapsulated in MLVs reached a preliminary Phase 1 clinical trial delivered i.v. to metastatic cancer patients, and showed immune activation with low toxicity in Phase 1 studies using aerosolized IL-2 MLVs for immunodeficiency and treatment of pulmonary metastases. [217,220,221] However, these MLV formulations did not process to further clinical trials, likely due to the fast clearance of these particles via the reticuloendothelial system (RES).

Notably, it was found that the interaction of IL-2 with small unilamellar vesicles (≤ 100 nm) of dimyristoylphophatigylcholine induced the formation of MLVs (> 1 μm). [222] This simple process allowed for >90% encapsulation of IL-2 and created large liposomal particles capable of targeting the immune cells of RES (primarily macrophages and monocytes) or to potentially serve as cytokine depots.[222] This IL-2 delivery vehicle is currently in clinical trials as a cancer vaccine by subcutaneously co-delivering autologous tumor lysates for lymphoma (Phase 2, NCT02194751) and leukemia (Phase 1, NCT01976520).

Although simple to fabricate, some of the processing conditions for these lipid-based microparticles such as heating, dehydration, or use of non-aqueous solvents can damage the activity of the loaded cytokine. Moreover, due to their fast RES clearance, MLVs tend to be limited for use as depots, but their high lipid contents lower the encapsulation efficiency of hydrophilic drugs. Lastly, lipid-based formations can be unstable in physiological conditions, can have difficult to control drug release rates and limited residence time of ~4 days as depots. [223] Thus, other depot

systems such as polymeric gels or polymeric microparticles have typically prevailed as more efficient prolonged delivery systems. Notably, to address some of the limitations with MLVs, multivesicular liposomes were developed which had greater improved residence time to serve as a depo.[223] However, limited studies have assessed their therapeutic benefit for cytokine delivery.[223]

6.3.2 Solid Polymeric Microparticles

Biodegradable polymeric microspheres were one of the first drug delivery systems to enable controlled release of cytokine with a successful therapeutic effect *in vivo*.[224] This was accomplished using phase-inversion nanoencapsulation to load IL-2 into poly(lactic acid) biodegradable microspheres which showed better therapeutic effect over PEG-IL2 in a human tumor xenograft mouse model.[224] Compared to encapsulation methods used until that point, the phase-inversion nanoencapsulation process produced a limited size distribution range (0.1-10 μm diameter spheres), had limited exposure of the cytokine to non-aqueous solvents, and did not require vigorous stirring or sonication. Accordingly, more of the protein was encapsulated in a bioactive form. Later studies showed that using the same process to encapsulate IL-12 and TNF-α could induce both a local and systemic immune response in a weakly immunogenic primary breast cancer model whereas either agent alone or IL-12 and GM-CSF were not as effective.[225]

Importantly, since the initial studies, many new microsphere designs and processes have been developed and tested in preclinical studies for cytokine delivery.[226] These systems have focused on using methods to retain the cytokine bioactivity during processing. Some examples in early works include the use of gelatin, chitosan, and bovine serum albumin substrates which have rapid degradation over poly(lactic acid), but gentle encapsulation. [226] Moreover, using a poly(ether ester) multiblock copolymer microsphere, a Phase 2 clinical trial was performed for delivery of IFN-α (Locteron) in patients with chronic hepatitis C genotype 1.[227] This system aimed to deliver unmodified IFN-α for prolonged periods to compete with the PEG-IFN-α versions which led to significant reductions in cytokine bioactivity after PEGylation. Although the Phase 2 studies showed equal efficacy and lower adverse effects from two week dosing of Locteron over weekly PEG-IFN-α, the therapy never reached Phase 3 clinical trials, likely due to failure of the developing company.[228]

More recently, designs have focused on combination therapy approaches. For example, using IL-12 and GM-CSF encapsulated into PLGA microspheres, 44% of FVBneuN mice with advanced spontaneous mammary tumors were completely cured if cyclophosphamide (CY) was

administered one day before cytokine treatment compared to 0% when only CY or microsphere-encapsulated cytokines were administered.[229] The cytotoxic CY chemotherapy was chosen due to its cytotoxic activity in Tregs which would enable a better anti-tumor immune response from the cytokine therapy. Notably, it was shown that the treatment yielded a 7-fold increase in $CD8^+$ cytotoxic T cell (CTL) to Treg ratio, 3-fold increase in CTL cytotoxicity and extended the effector window for $CD8^+$ T cell from 3 to 7 days. [229] In addition to immunochemotherapy approaches, the prolonged cytokine delivery from microspheres can be used in conjunction with radiation. Notably, the combination of stereotactic body radiation therapy (SBRT) with intratumorally administered IL-12 encapsulated in PLGA microspheres was capable of eliciting cures in preclinical mouse models of pancreatic ductal adenocarcinoma with abscopal effect.[230] In this study, SBRT was used to induce immune infiltration which, with the local and sustained IL-12 delivery, enabled the antitumor immune response.

Beyond simple slow-release matrices, more intricate delivery systems such as bio-responsive microspheres have also been developed. In depot formulations, these systems aim to have release of the therapeutic cytokine based on the degree of severity of the disease. For example, microspheres created by crosslinking of gelatin with genipin (a natural small molecule amine-amine crosslinker) yields negatively charged particles of ~10 μm on which positively charged cytokines such as IL-4, IL-10, and IL-13 are electrostatically bound for treatment of osteoarthritis **(Figure 1.7)**.[231] Their bio-responsiveness originates from the degradability of the microsphere when exposed to enzymes characteristically expressed in osteoarthritis. Accordingly, the cytokine release rate is linearly correlated with the concentration of enzymes in solution.

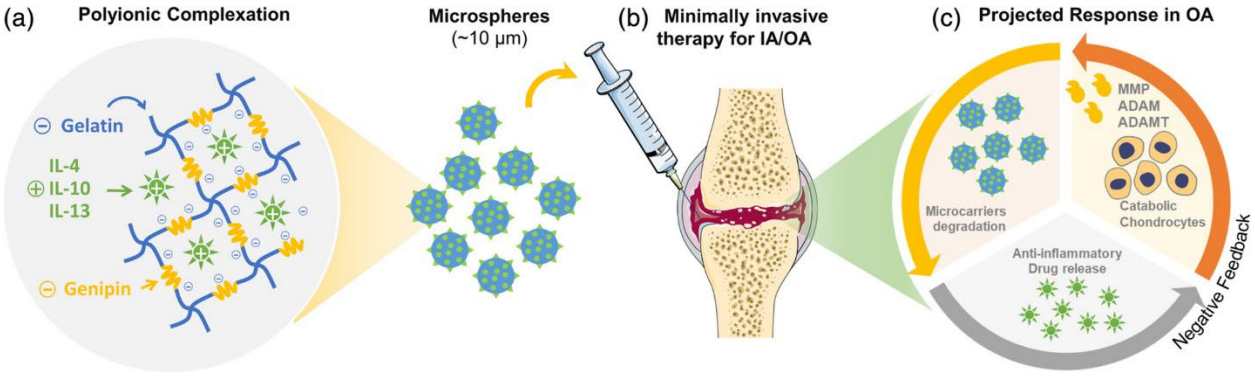

Figure 1.7. Bioresponsive polymeric microparticles for anti-inflammatory cytokine delivery to osteoarthritis. Reproduced with permission.[231] Copyright 2019, Wiley Periodicals, Inc.

Although most studies have been based on spherical microparticles, these need not be the only effective cytokine delivery vehicle; the shape is another physical property that can alter resulting *in vivo* effects. For example, soft discoidal microparticles were shown to provide prolonged *in vivo* cytokine exposure to phagocytic cell such as macrophages.[232] In this study, the discoidal microparticles were composed of an initial cell-adhesion layer followed by polyvinyl alcohol (PVA) layer in between PLGA layers. The hydrophilic PVA layer allowed for cytokine loading and PLGA provided structural support. The adhesive layer was synthesized via layer-by-layer assembly comprised of alternating layers of hyaluronic acid modified with aldehyde and poly(allylamine). This polyelectrolyte multilayer was designed to adhere to isolated macrophage cells. When loaded with IFN-γ, these cellular 'backpacks' were shown to alter macrophages to their antitumor phenotype (M1) *in vitro* and, more importantly, prevent differentiation from the M1 phenotype deep within the immunosuppressive environment of solid tumors from mouse 4T1 breast cancer model when delivered intratumorally.[232] Moreover, this treatment was shown to reprogram tumor-associated macrophages to the antitumor phenotype. Accordingly, treatment with the backpack-IFN-γ-loaded macrophages could slow tumor growth and reduce metastasis. Interestingly, the delivery of drug-loaded polymeric backpacks via monocytes has been previously shown to target inflamed tissues and may enable drug delivery further into the tumor cores.[233]

Although there has been great progress in the development of microparticles for drug delivery, they have not led to clinical translation of cytokine therapeutic. Some of the major limitations include ineffective drug loading, complex manufacturing, loss of cytokine bioactivity, biocompatibility and regulations.[226,234] However, these issues have begun to be addressed demonstrating *in-vivo* proof-of-concept of the effectiveness of these delivery vehicles.

Nanoparticles

Nanoparticles are small (typically 10-100 nm) particles that, due to their size, have special biophysical properties that enable the therapeutic enhancement of various drug molecules. Notably, nanoparticles have been extensively used to alter the pharmacokinetics and toxicity of drug agents, making them promising candidates for cytokine delivery.[10] Some of their benefits include increases in circulatory half-life and controlled drug release and/or activation. Moreover, either through the EPR effect or other properties, they can be used as targeting systems to the desired tissue or cell for targeted drug delivery. These benefits can be achieved through a variety of modifications including the material composition, charge, shape, and flexibility.[235] For example,

nanoparticles in the ~10-100 nm size range show preferential accumulation in lymph nodes following parenteral administration[10]. Furthermore, surface modifications such as PEGylation or conjugation of targeting motifs are also commonly employed to enhance the therapeutic efficacy of the loaded drug as they can prevent unwanted interactions or target certain interactions, respectively. Lastly, especially in the delivery of cytokines, nanoparticles are amenable for drug delivery either through encapsulation within the particle core or attached to the particle surface. As will be presented, in cytokine delivery, this surface attachment allows for presentation of cytokines to their receptors while retaining pharmacokinetics governed by the particle itself. Over the years, there have been many different classes of nanoparticles developed for cytokine delivery. In this section, we will focus on lipid-based nanoparticles and polymeric nanoparticles which have been the most widely studied classes of nanoparticles for cytokine delivery.

Notably, the approved formulation of IL-2 (aldesleukin) can be considered the first cytokine nanoparticle to reach the clinic. Aldeslueukin contains nanometer-sized (11-13 nm) 'microaggregates' composed of an average of 27 non-covalently bound IL-2 molecules complexed with sodium-dodecyl sulfate (SDS).[236] Initially described as a surfactant to solubilize the hydrophobic IL-2 molecules which, based on its FDA labeling, "may have an effect on the kinetic properties" of aldesleukin,[237] it was later disclosed that the concentration and formulation process of the SDS detergent were vital for the therapeutic efficacy of IL-2 due to the formation of these 'microaggregates'.[236] Importantly, the microaggregate formulation does not alter bioactivity of IL-2, but significantly alters the pharmacokinetics and biodistribution compared to monomeric IL-2. In rats, the clearance rate of IL-2 decreased ~30-fold, and the *in vivo* distribution altered from mainly the kidneys to lung, liver, and kidney. [236] Accordingly, when administered into animals, IL-2 microaggregates had superior efficacy at treating preventing lung metastasis compared to the monomeric cytokine. Importantly, this observation demonstrates the clinical potential of nanoparticle formulations for increased therapeutic efficacy. Moreover, likely due to the late disclosure, there have not been detailed studies on these IL-2 microaggregates in the literature and most IL-2 studies fail to discuss their significance. However, due to the altered clinical properties, new IL-2 therapeutics should be compared to the approved SDS/IL-2 microaggregates and not monomeric or other IL-2 formulations.

There are many techniques to synthesize lipid-based nanoparticles with controlled size and size distribution, making them attractive vehicles for nanomedicine. Notably, liposomes have been

one of the most studies class nanoparticles for drug delivery, making them the most common class of FDA-approved nanoparticles.[238] As discussed in the ***Microparticles*** section, early formulations of lipid-based particles were typically microns in size which, although useful as a depot, have very short circulatory half-lives due to rapid RES capture. [217] Accordingly, smaller liposome formulations were developed using PEG-lipids for even longer circulatory half-life. In an early example of employing liposomes for cytokine delivery, PEGylated 'stealth' liposomes were used to encapsulate IL-2, increasing the protein stability and its plasma half-life by 10-30 times over free IL-2, and eliciting superior anti-tumor effect compared to free IL-2 in combination with chemotherapy. [217]

Since these promising developments, many preclinical studies have pursued liposomal cytokine delivery in nanoparticle formulation. For example, attachment of IL-2-Fc fusion protein and anti-CD137 antibodies to liposomes (**Figure 1.8A**) enabled systemic administration of this potent combination therapy, eliciting an effective antitumor immune response with minimal toxicity.[239] In this design, the conjugated IL-2-Fc maintained its *in vitro* activity while conjugated anti-CD137 antibodies showed enhanced immune stimulation over the soluble antibody (**Figure 1.8B-D**). Further, the conjugated proteins had reduced circulatory half-life as the EPR effect concentrated the nanoparticle in the tumor, lowering the overall systemic exposure in circulation to the immunostimulant. Notably, an earlier study showed that intratumoral administration of the free immunomodulatory agents was too toxic for therapeutic use, corroborating the importance of anchoring the cytokines to the liposomes to prevent systemic exposure.[240]

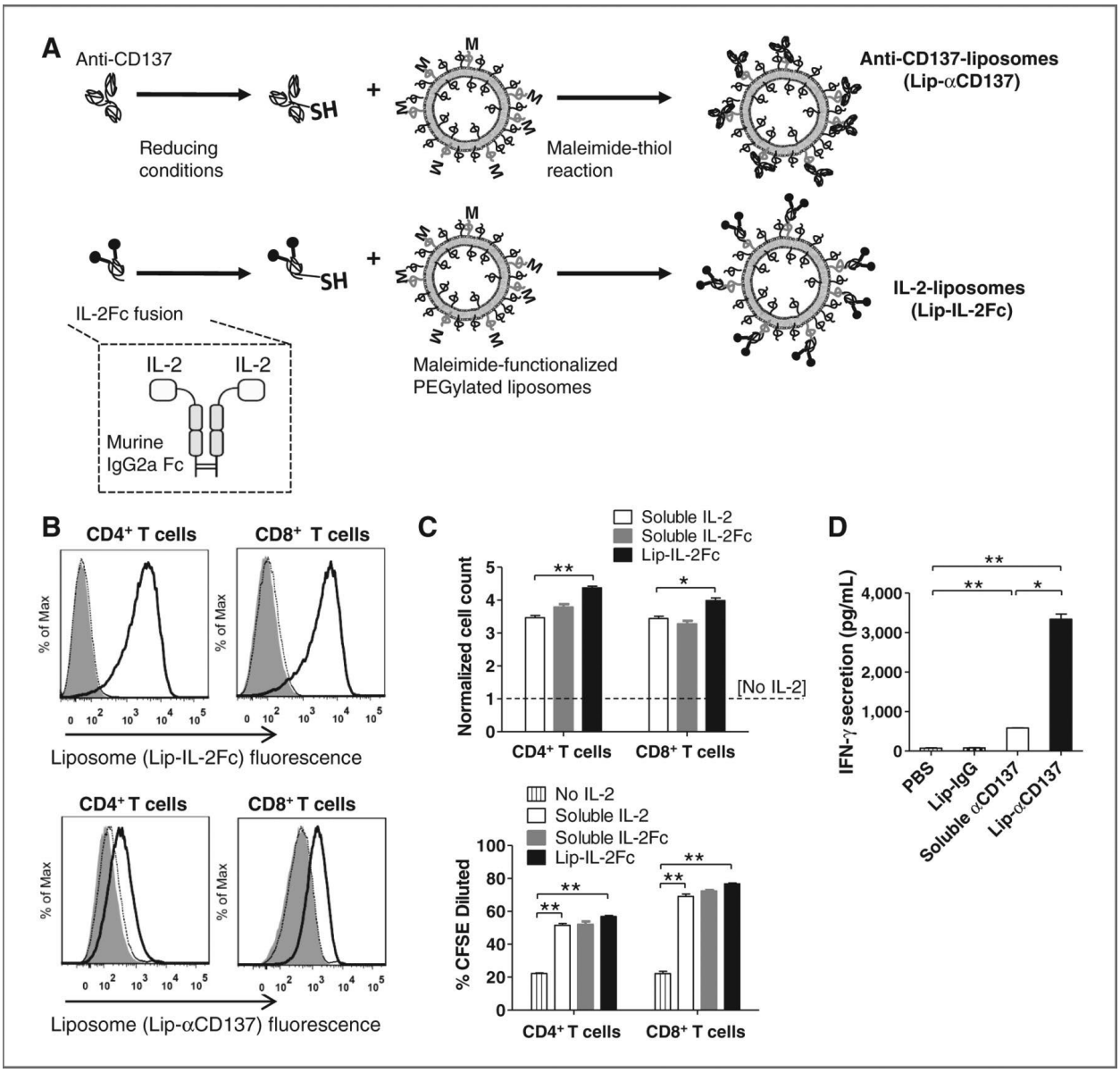

Figure 1.8. Synthesis and bioactivity of liposomes surface conjugated with anti-CD137 antibody or IL2-Fc fusion protein. **(A)** schematic for synthesis of liposomes. **(B)** Flow cytometry of $CD4^+$ and $CD8^+$ T cells incubated with fluorescently-labeled liposomes (solid), unconjugated liposomes (dashed), or no liposomes (grey area). **(C)** In vitro T cell proliferation normalized to unstimulated cells. **(D)** IFN-γ production by polyclonal T cells. Reproduced with permission.[240] Copyright 2013, American Association for Cancer Research.

Notably, the surface attachment of cytokines in liposomes may be combined with the external coating of the nanoparticle via the layer-by-layer technique. This approach can reduce exposure of the immunostimulatory protein in circulation but maintain immune activation at the desired tumor site.[241] Accordingly, when negatively charged liposomes were surface conjugated with IL-12 followed by deposition of a positively charged poly-L-arginine (PLR) and a terminal negative poly-L-glutamic acid (PLE) layers (**Figure 1.9)**, the IL-12 therapy showed reduced toxicity without loss of therapeutic efficacy in mouse models of ovarian (OV2944-HM-1) and colon (MC38) cancer when delivered intratumorally. In this system, the outer PLE layer was chosen due to its affinity for cancer cells with localization on the outer cellular membrane. Importantly, the modular nature of the layer-by-layer assembly tune the nanoparticle characteristics for improved therapeutic efficacy and equips the carrier for staged-release of combination treatments.[242]

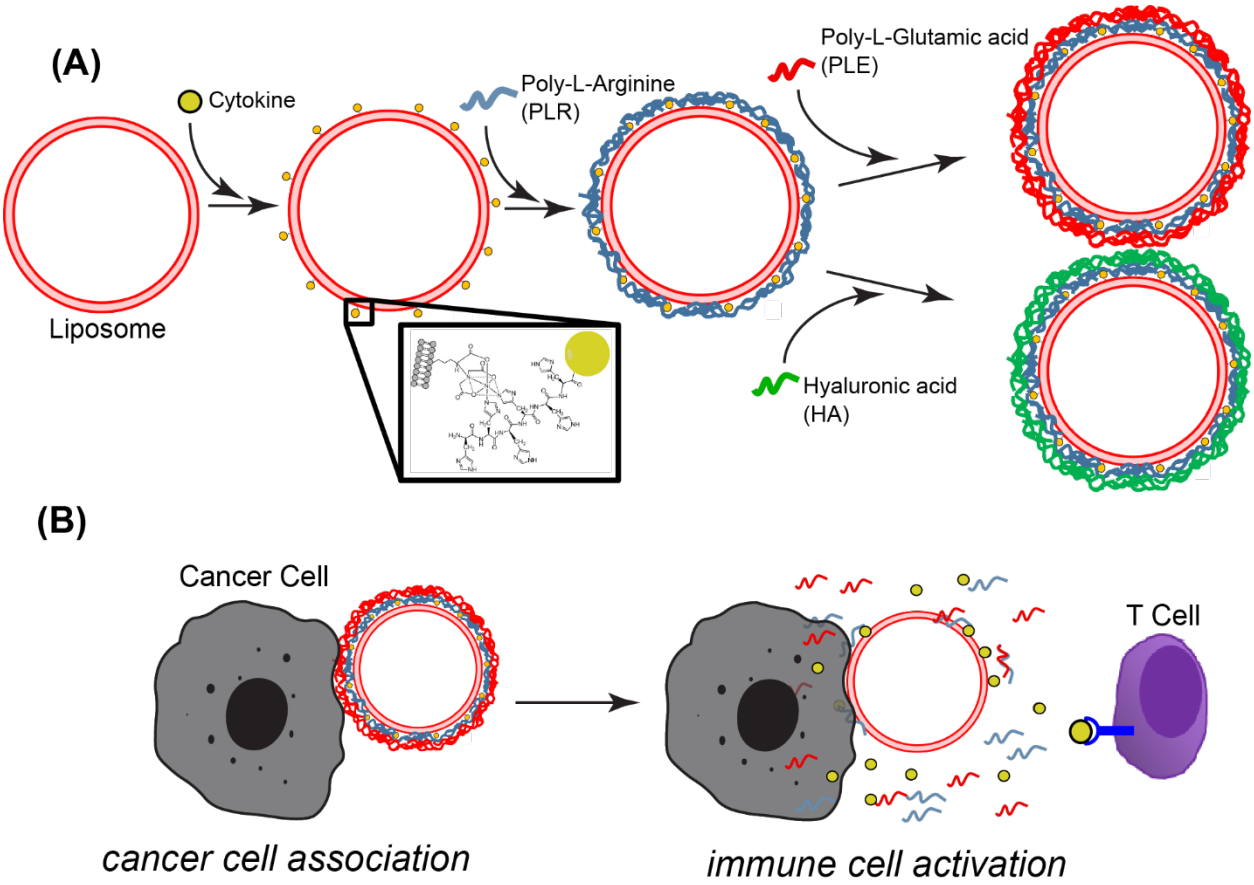

Figure 1.9. Cancer-cell targeting liposomal layer-by-layer nanoparticle containing surface conjugated IL-12. (A) Diagram for assembly of nanoparticle. (B) Cancer cell association and

subsequent targeted immune activation. Adapted with permission.[241] Copyright 2020, American Chemical Society.

However, although liposomes have low toxicity and low immunogenicity, efficient protein encapsulation in liposomes can be challenging, and release rates of encapsulated therapeutics can be difficult to tailor. Accordingly, other nanoparticle formulations have been developed that aim to address these limitations.

Polymeric nanoparticles are a second important class of materials explored for cytokine delivery. In these systems, polymer composition dictates the drug release rate which is typically longer than that of liposome-based nanoparticles. One example of PLGA-modification for enhanced encapsulation is the use of avidin-conjugated PLGA nanoparticles for co-encapsulation of IL-2 and TGF-β.[243] The avidin conjugation is used to both facilitate encapsulation of hydrophilic drugs as all as enable for surface conjugation of the PLGA nanoparticles as the protein is primarily present within the particle surface. In the IL-2 and TGF-β example, the avidin was used to conjugate biotin-anti-CD4 antibodies. This $CD4^+$ T cell-targeting construct was used to induce Treg differentiation mediated by the TGF-β followed by expansion of these regulatory cells via the IL-2. Accordingly, when administered *in vivo* these nanoparticles generated stable and functional Tregs for potential treatment of autoimmune disorders. Other approaches for chemoimmunotherapy using PLGA-based nanoparticle-mediated cytokine delivery include the use of "thermosponge" nanoparticles formulated from PEG-PLGA, PLGA, and F-127 gel. [244] In this system the hydrophobic PLGA core was used to load paclitaxel while a hydrophilic outer themosensitive F-127 shell was used for facile entrapment of IL-2 in an aqueous environment.[244]

Although PLGA is an attractive polymer for nanoparticles due to the history of use in FDA approved products, other polymers may be used with additional benefits. An example is pH-sensitive poly(β-amino ester)-based carriers that can exploit the lower pH of the tumor microenvironment for targeted release.[245] Using such a system for IL-12 delivery was shown to have anti-tumoral effects in B16F10 mouse model without signs of significant toxicity. [245] Notably, the antitumoral response was similar when the particles were injected i.t. or i.v. and attributable to the reprograming of tumor-associated macrophages from an M2 to M1 phenotype which is indicative of an anti-tumor immune response.

Importantly, the hydrophobicity of polymer-based nanoparticles can make encapsulation of hydrophilic proteins such as cytokines difficult. This challenge has prompted the development of nanogel-based delivery systems– hydrogels in the form of nano-sized particles. An interesting example of this class of nanomaterial employed reducible protein-based nanogels to create TCR-signaling-responsive delivery of IL-15 superagonist (N-803) to T cells during adoptive T cell therapy.[246] Notably, instead of using a polymer chain to yield the nanogels and carry the drug load, this design used a reducible small-molecule crosslinker connecting the IL-15 protein cargo itself to form the nanogel. Accordingly, compared to a traditional approach of encapsulating drug inside a lipid or polymeric nanoparticle, there was marked increase in drug loading. Moreover, by using a disulfide-containing cross-linkers, the nanogels had T cell activation responsive drug release due to the increased reduction rate of antigen-activated T cells over naïve T cells. Lastly, the nanogel was surface conjugated with PEG-b-poly(L-lysine) and anti-CD45 antibodies. The polymers provided a uniform positive charge that promoted an initial binding to cellular membrane while the anti-CD45 antibodies prevented intracellular uptake of the nanoparticles. Using this construct, a 16-fold increase in tumor T cell expansion was observed selectively in tumors, which enabled an increase in the therapeutic window of IL-15 superagonist adjuvant delivery in adoptive T cell therapy. [246]

There are many alternative nanoparticle formulations that may be used for cytokine delivery. Notably, the use of hybrid systems can enable for better controlled release of combination therapies by exploiting the properties of different materials. For example, the use of liposomal nanogels (nLG) enabled the co-delivery delivery of hydrophilic IL-2 hydrophilic and a hydrophobic small molecule TGF-β inhibitor while also incorporating the advantageous pharmacokinetic properties of PEGylated liposomes (**Figure 1.10**).[247] The liposomes also served as the molds for photo-crosslinking of the polymers to yield the hydrogel core which contained both IL-2 and the TGF-β inhibitor solubilized within methacrylate-conjugated β-cyclodextrins (**Figure 1.10A**). Using the combination therapy within the nLG for intratumoral treatment of metastatic melanoma, there was a marked increase in overall survival and reduction in tumor growth with 40% of animals having complete tumor regression (**Figure 1.10B-D**).[247] Importantly, neither the agents alone, their combination, nor the single agents in the nanoparticles yielded similar therapeutic efficacy. Moreover, a significant improvement in overall survival was also seen

in when the combination therapy nLG were administered systemically (i.v.) with reduction in lung metastatic tumor burden.

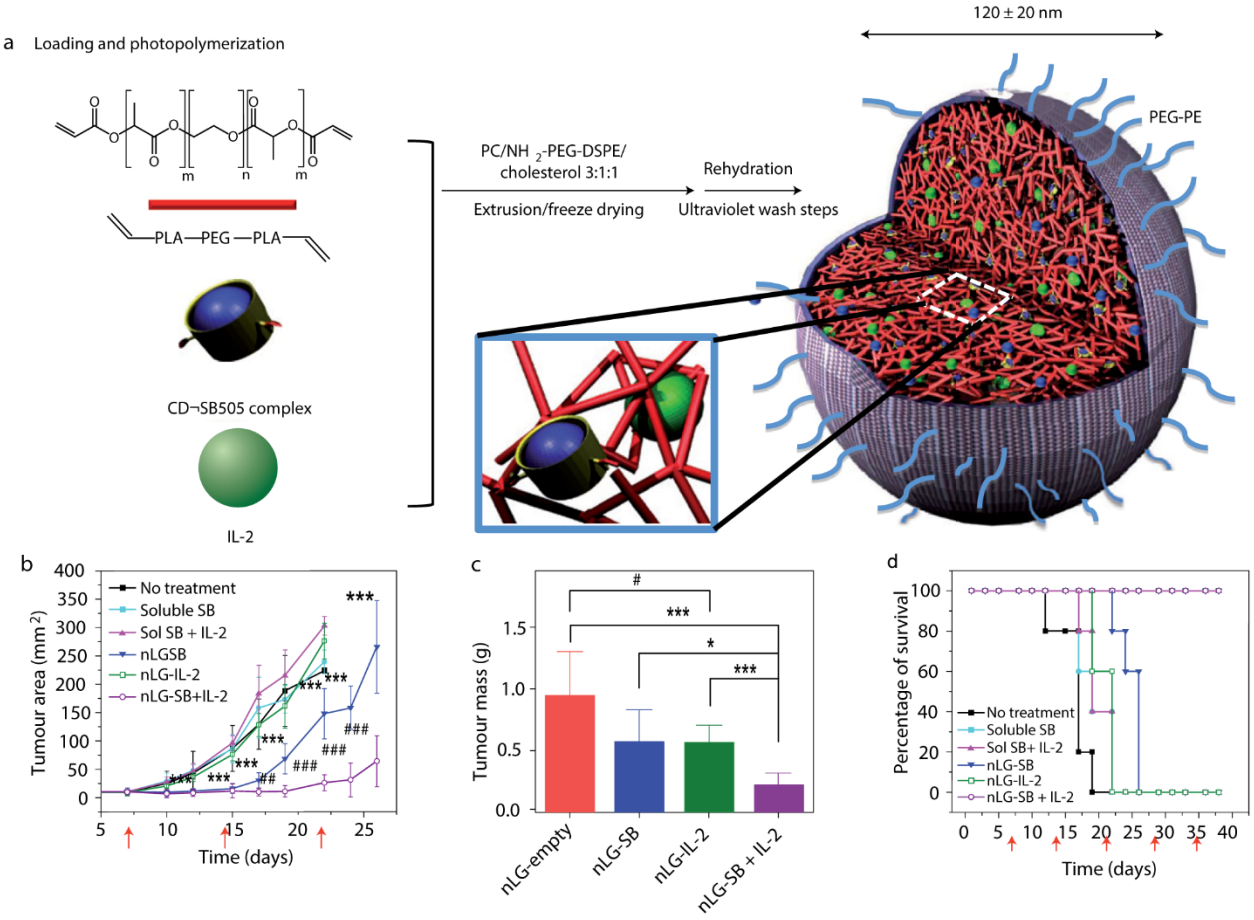

Figure 1.10. Schematic for synthesis of liposomal nanogel encapsulating a TGF-β inhibitor and IL-2 and its effects when intratumorally administered to a subcutaneous mouse metastatic melanoma model. **(a)** Components and final liposomal nanogel assembly. **(b)** Plot of tumor area versus time (day 0 was day of tumor inoculation). Red arrows indicate treatment. **(c)** Tumor masses after 7 days of treatment. **(d)** Survival plot of animals in **(b)**. Complete tumor regression and survival was obtained in 40% of the group after 60 days (data not shown). Adapted with permission.[247] Copyright 2012, Nature Publishing Group.

Beyond degradable polymers and lipids, many other nanomaterials may be used for immunotherapy that enable different mechanisms to improve the therapeutic efficacy of cytokines.[6] For example, dimercaptosuccinic acid (DMSA)-coated magnetite nanoparticles may be used for magnetically guided delivery of cytokines.[248] The DMSA serves as a functional group for cytokine

conjugation while the iron-based nanoparticle can have its biodistribution altered to accumulate in tumors via application of an external magnetic field.

Importantly, although nanoparticles have a highly modular assembly with many potential modifications, their clinical utility has been limited with no current clinical trials aiming at cytokine delivery.[238] This limited clinical success may be attributed to low targeting efficiency, manufacturing cost and complexity, and the currently limited design-space exploration.[160,249] Much of the fundamental understanding of physical parameters (e.g., size, shape, degradability, elasticity) still must be elucidated.[6] However, as demonstrated by the various examples presented here, nanoparticles have shown to be effective carriers for improvement of cytokine-based immunotherapy. Moreover, many of the other engineering strategies presented in this review can be combined with nanoparticle delivery as shown by Fc-fusion proteins or the antibody-mediated targeting. Accordingly, nanoparticles present themselves as one of the most promising approaches to enable future clinical translation of cytokines.

1.7 Other Cytokine Delivery Strategies

Other major classes of cytokine delivery strategies used in clinical trials have been mediated by advancements in genetic engineering. Initially, cytokine-secreting tumor cells were transfected *ex-vivo* then administered as a cancer vaccine, but had limited clinical success.[12] More recently, other cells such as mesenchymal stem cells (MSCs), dendritic cells, tumor infiltrating lymphocytes (TILs) and, chimeric antigen receptor T cell (CAR-T) have also been genetically modified for cytokine production with some clinical success.[14,250] However, cell-based therapies are still in early stages of clinical translation and have unique manufacturing and regulatory challenges prior to potential wide-scale use.[251]

One way to circumvent the limitations of cell-based therapies is use of gene therapy for *in vivo* transfection. However, gene therapy has been limited by efficient transfection of mammalian cells *in vivo* and control of dosing based on gene transcription[13]. Further, unlike the delivery of extracellular-targeting cytokine proteins, gene therapy requires the cargo to be intracellularly delivered for cytokine expression and subsequent secretion. Accordingly, there are many challenges with use of these system to which various technologies have been developed including viral and non-viral vectors systems as well as physical methods of gene insertion.[15] Although these three major gene therapy modalities have candidates in clinical trials, only an oncolytic viral vector

encoding for GM-CSF has been approved.[252–255] The modified virus, termed Talimogene laherparepvec (T-VEC), yielded significant and durable improvements when intratumorally delivered in advanced melanoma patients, making T-VEC the first oncolytic virus to obtain approval in 2015.[255]

1.8 Conclusions and Future in Cytokine Therapeutics

As detailed in this review, there have been many engineering strategies designed to improve the therapeutic applications of cytokines. These systems have mainly attempted to modulate the pharmacokinetics and pharmacodynamics to elicit a targeted effect and, therefore, reduce overall toxicity. Most designs have aimed at the localized delivery of cytokines as systemic exposure to the therapeutic cause dose-limiting toxicities. Importantly, these localized treatments have only recently garnered acceptance in clinical and surgical oncology as intralesional treatment was not always possible and surgical removal of primary lesions were prioritized over drug treatments.[256] Further, reluctance existed due to concerns that local injection could aid in metastasis through the needle track and have minimal effect on distal sites due to low systemic drug levels.[256] More recently, with technological developments and various clinical studies demonstrating the benefits of intralesional treatments, these hesitancies have greatly decreased.[256,257] However, the challenge in demonstrating systemic effects beyond homogenous tumors from preclinical animal models remains. Accordingly, as new fusion protein and nanoparticle designs have continued to show promising preclinical data, systemically administered cytokine therapeutics may find their way into clinical applications.

As these designs are developed, it will become important to fully understand their mechanisms to modulate therapeutic effect and toxicity. For example, even intratumoral injection does not prevent systemic leakage of cytokines.[258] Therefore, targeted or locally delivery strategies need to monitor the systemic levels of characteristic cytokines potentially released into circulation.[258] Unfortunately, many preclinical studies have failed to monitor for systemic leakage of the cytokine or its downstream induced signals. Further, protein engineering strategies and biomaterials-based approaches need to ensure that processing of a cytokine or its modifications are carefully characterized, to understand potential undesirable changes or losses in cytokine function. The sophisticated chemistry protocols required for these designs may also hinder manufacturing at the clinical scale and require powerful analytical tools to assess product quality.

Design considerations for clinical translation will also need to account for the pharmaceutical formulation challenges required to maintain drug stability in storage and their ease of administration. Optimization of protein formulation can be complex with additional regulatory complexity for introduction of any new excipient. Implementation of new delivery vehicles further complicates the problem as the vehicle's structure and composition also needs to be properly maintained. For example, lyophilization is employed in some approved cytokine formulations to maintain product stability, but could lead to changes in the physicochemical properties of liposome delivery systems.[259,260]

In addition to single-agent treatments, one of the more promising areas for cytokine therapeutics are combination therapies. These include use of cytokines as adjuvants for vaccines, CPIs, surgeries, chemotherapy or radiation therapy. Moreover, cytokine combinations with other immunostimulatory agents can also enable successful therapies. One example is the approval of dinutuximab in high-risk neuroblastoma in 2015 in which the anti-disialoganglioside GD2 antibody is combined with GM-CSF, IL-2 and isotretinoin. [261] Importantly, from a pharmaceutical perspective, the administration of two therapeutic agents may be cumbersome. Thus, fusion proteins or multi-therapeutic delivery systems to reduce toxicity ease the introduction of these combinations into the clinic. Moreover, whether in combination therapies or monotherapies, targeted delivery systems are demonstrating to be the necessary characteristics to mitigate the toxicities associated with cytokine delivery. Unfortunately, as the therapeutics become more complex, the more critical quality attributes are necessary for manufacturing, which delay development and increase costs of treatment.

In addition to the engineering design of the drug, the route and schedule of administration are major factors in the therapeutic efficacy. Variations in the administration route can dictate biodistributions, half-lives, and bioavailability.[262] Moreover, different administration schedules can elicit different immune responses due to varied concentration and duration of exposure of the immune cells to the therapeutics.[262] In the case of immunocytokines, there is initial clinical evidence that lower toxicities may be observed when administered at longer infusion rates, where the blood levels are sustained at a lower level.[110] These characteristics may be even more important in combination therapies as it has been shown that the sequence of combination therapies can be vital for their success. [263] For example, the administration IL-2 before IFN-α leads to severe toxicities that can be prevented via concurrent or after IFN-α.[264] These are crucial characteristics

that need to be considered and better understood in the design of controlled release systems for multiple immunostimulatory agents. The sequence is also important when immunotherapy is used in combination with surgeries as recent reports indicate that improved efficacy is seen in a neoadjuvant-based cytokine schedule. [265]

Although the unfavorable pharmacokinetic profile of cytokine therapeutics is a major hindrance for their clinical translation, the failure of Albuferon signals another crucial consideration in development of cytokine therapies: they must be more tolerable or more efficacious than current therapies. Mere improvement in the dosing convenience will be difficult to justify regulatory approval, especially if the new therapy has an increase in adverse events. [90] Moreover, modifications that aim to alter the pharmacokinetics need to be carefully designed as they can also alter the biodistribution, potentially reducing the therapeutic effect of the cytokine.

Overall, there are various engineering strategies for cytokine-based therapeutics. Many of these have had successes in preclinical and early clinical studies; however, full implementation of cytokines in the clinic will require a better understanding of immunology and how these designs modulate it to better develop systems that can effectively mimic or manipulate immune responses.

1.9 Thesis Overview

In this thesis, we sought to engineer LbL-NPs for the delivery of the potent immunostimulant: IL-12. We also explored methods to scale up the production of NP-based immunostimulants. Most of the work presented focuses on treatment of metastatic ovarian cancer which presents as a major clinical challenge.

In Chapter 2, we describe a scalable method to assemble an adjuvant lipid nanoparticle termed Saponin Monophosphoryl-lipid-A NanoParticles (SMNP) based on the controlled dilution of mixed micelles.

In Chapter 3, we exploit the same mixed micelle dilution approach to precisely control the size of liposomes.

In Chapter 4, we discover that exploiting the lipid headgroup charge valency allows us to assemble a new lipid-based nanodisc which we termed charge-stabilized nanodiscs (CNDs). We find that

CNDs have improved tumor accumulation compared to liposomes and yield increased association with cancer tissues in vivo when their surface is modified via the LbL technique.

In Chapter 5, we explore the delivery of IL-12 from liposomal LbL-NPs. We compare the surface conjugation methods to the lipid headgroup and NP lipid composition. Mechanistic investigations revealed that these LbL-NPs rapidly accumulated in tumor nodules upon intraperitoneal (i.p.) administration, wherein shedding of the LbL coating allowed for gradual release of IL-12-lipid conjugates via lipid extraction by serum proteins present in interstitial fluid. The optimized particle was capable of significantly outperforming the therapeutic efficacy of free cytokine without inducing toxicity. Further, we find that IL-12 delivery from LbL-NPs sensitizes a non-responsive model of metastatic ovarian cancer to immune checkpoint blockade resulting in complete responses.

In Chapter 6, we develop a new approach to assemble LbL films on NPs based on microfluidic mixing. In addition to the increased scale and throughput of polymer coating, we find that titration of polymer amount used for film assembly allows for LbL-NP production without time-consuming purification steps. The method is validated in vitro and in vivo using LbL-NPs to deliver IL-12.

In Chapter 7, we instigate the effects of polymer conformation during LbL assembly and polymer molecular weight (MW). We learn that thicker films generated upon LbL assembly in higher ionic strength conditions hinder the therapeutic efficacy of IL-12 delivered by LbL-NPs. However, increasing the polymer MW reduces polymer shedding upon LbL-NP contact with physiological buffers, leading to increased association with cancer cells and improved retention of LbL-NPs on the surface of cancer cells. Employing high MW polymers for delivery of IL-12 from LbL-NPs results in improved therapeutic efficacy compared to LbL-NPs composed of the small MW polymers used previously.

In Chapter 8, we devise a method to crosslink the polymers on the outer surface of LbL-NPs. This crosslinking stabilizes the film in LbL-NPs and can be used to regulate the surface exposure of conjugated IL-12.

In Chapter 9, we search for the binding targets of LbL-NPs to cancer cells with these NPs are coated with outer layers of poly-L-gluamate (PLE) and poly-L-aspartate (PLD). We determine that these polyamino acids retain the ability to bind to amino acid transporters overexpressed in cancer cells.

Finally, Chapter 10 concludes with the key findings from the work in this thesis and proposes future work.

1.10 References

[1] S. Cohen, P. E. Bigazzi, T. Yoshida, *Similarities of T cell function in cell-mediated immunity and antibody production*, Vol. 12, Academic Press, **1974**, pp. 150–159.

[2] Z. Kronfol, *Cytokines and mental health*, Kluwer Academic Pub, **2003**.

[3] M. A. Caligiuri, M. T. Lotze, *Cytokines in the genesis and treatment of cancer*, Humana Press, **2007**.

[4] C. Wang, Y. Ye, Q. Hu, A. Bellotti, Z. Gu, *Tailoring Biomaterials for Cancer Immunotherapy: Emerging Trends and Future Outlook*, Vol. 29, Wiley-VCH Verlag, **2017**.

[5] R. S. Riley, C. H. June, R. Langer, M. J. Mitchell, *Nat. Rev. Drug Discov.* **2019**, *18*, 175.

[6] C. W. Shields, L. L. Wang, M. A. Evans, S. Mitragotri, *Adv. Mater.* **2020**, *32*, 1901633.

[7] D. G. Leach, S. Young, J. D. Hartgerink, *Acta Biomater.* **2019**, *88*, 15.

[8] F. Yang, K. Shi, Y. peng Jia, Y. Hao, J. rong Peng, Z. yong Qian, *Advanced biomaterials for cancer immunotherapy*, Springer Nature, **2020**, pp. 1–17.

[9] M. S. Goldberg, *Improving cancer immunotherapy through nanotechnology*, Vol. 19, Nature Publishing Group, **2019**, pp. 587–602.

[10] D. J. Irvine, E. L. Dane, *Enhancing cancer immunotherapy with nanomedicine*, Nature Research, **2020**, pp. 1–14.

[11] M. O. Dellacherie, B. R. Seo, D. J. Mooney, *Macroscale biomaterials strategies for local immunomodulation*, Vol. 4, Nature Publishing Group, **2019**, pp. 379–397.

[12] R. I. Tepper, J. J. Mulé, *Hum. Gene Ther.* **1994**, *5*, 153.

[13] P. J. Wysocki, A. Karczewska-Dzionk, M. Mackiewicz-Wysocka, A. Mackiewicz, *Expert Opin. Biol. Ther.* **2004**, *4*, 1595.

[14] C. J. Dwyer, H. M. Knochelmann, A. S. Smith, M. M. Wyatt, G. O. Rangel Rivera, D. C. Arhontoulis, E. Bartee, Z. Li, M. P. Rubinstein, C. M. Paulos, *Front. Immunol.* **2019**, *10*.

[15] N. Bono, F. Ponti, D. Mantovani, G. Candiani, *Pharmaceutics* **2020**, *12*, 183.

[16] S. A. Shirley, In *Handbook of Electroporation*, Springer International Publishing, **2017**, pp. 1755–1768.

[17] Y. K. Sung, S. W. Kim, *Recent advances in the development of gene delivery systems*, Vol. 23, BioMed Central Ltd., **2019**, pp. 1–7.

[18] L. Liu, S. Wang, B. Shan, M. Sang, S. Liu, G. Wang, *Advances in viral-vector systemic cytokine gene therapy against cancer*, Vol. 28, Elsevier, **2010**, pp. 3883–3887.

[19] M. Feldmann, *J. Clin. Invest.* **2008**, *118*, 3533.

[20] W. E. Paul, *Fundamental immunology*, Wolters Kluwer/Lippincott Williams & Wilkins, **2008**.

[21] G. A. G. Morán, R. Parra-Medina, A. G. Cardona, P. Quintero-Ronderos, É. G. Rodríguez, In *Autoimmunity: From Bench to Bedside [Internet]* (Eds.: Anaya, J.-M.; Shoenfeld, Y.; Rojas-Villarraga, A.; Levy, R. A.; Cervera, R.), El Rosario University Press, Bogota, Colombia, **2013**.

[22] M. C. Horowitz, *The role of cytokines in bone remodeling*, Vol. 1, Humana Press, **1998**, pp. 187–198.

[23] M. D. Turner, B. Nedjai, T. Hurst, D. J. Pennington, *Biochim. Biophys. Acta - Mol. Cell Res.* **2014**, *1843*, 2563.

[24] J.-M. Zhang, J. An, *Int. Anesthesiol. Clin.* **2007**, *45*, 27.

[25] S. Setrerrahmane, H. Xu, *Tumor-related interleukins: Old validated targets for new anti-cancer drug development*, Vol. 16, BioMed Central Ltd., **2017**.

[26] M. Esquivel-Velázquez, P. Ostoa-Saloma, M. I. Palacios-Arreola, K. E. Nava-Castro, J. I. Castro, J. Morales-Montor, *J. Interf. Cytokine Res.* **2015**, *35*, 1.

[27] K. F. Chung, In *Asthma and COPD*, Elsevier Ltd, **2009**, pp. 327–341.

[28] J. M. Cavaillon, *Cell. Mol. Biol. (Noisy-le-grand).* **2001**, *47*, 695.

[29] C. A. Dinarello, *Eur. J. Immunol.* **2007**, *37*, S34.

[30] D. R. Lucey, M. Clerici, G. M. Shearer, *Clin. Microbiol. Rev.* **1996**, *9*, 532.

[31] D. A. A. Vignali, L. W. Collison, C. J. Workman, *Nat. Rev. Immunol.* **2008**, *8*, 523.

[32] L. Sompayrac, *How the immune system works*, 6th ed., Wiley-Blackwell, **2019**.

[33] F. E. Lund, T. D. Randall, *Nat. Rev. Immunol.* **2010**, *10*, 236.

[34] M. Baggiolini, I. Clark-Lewis, *Interleukin-8, a chemotactic and inflammatory cytokine*, Vol. 307, **1992**, pp. 97–101.

[35] D. Sag, Z. O. Ayyildiz, S. Gunalp, G. Wingender, *Cancers (Basel).* **2019**, *11*.

[36] N. E. Kelm, Z. Zhu, V. A. Ding, H. Xiao, M. R. Wakefield, Q. Bai, Y. Fang, *The role of IL-29 in immunity and cancer*, Vol. 106, Elsevier Ireland Ltd, **2016**, pp. 91–98.

[37] A. Kosmaczewska, *Low-dose interleukin-2 therapy: A driver of an imbalance between immune tolerance and autoimmunity*, Vol. 15, MDPI AG, **2014**, pp. 18574–18592.

[38] K. Asadullah, W. Sterry, H. D. Volk, *Interleukin-10 therapy - Review of a new approach*, Vol. 55, American Society for Pharmacology and Experimental Therapy, **2003**, pp. 241–269.

[39] J. M. Dayer, *From supernatants to cytokines: A personal view on the early history of IL-1, IL-1Ra, TNF and its inhibitor in rheumatology*, Vol. 20, BioMed Central Ltd., **2018**, p. 101.

[40] H. Zinsser, T. Tamiya, *J. Exp. Med.* **1926**, *44*, 753.

[41] J. Vilček, M. Feldmann, *Trends Pharmacol. Sci.* **2004**, *25*, 201.

[42] I. Gresser, *On the varied biologic effects of interferon*, Vol. 34, Academic Press, **1977**, pp. 406–415.

[43] R. A. Ningrum, *Scientifica (Cairo).* **2014**, *2014*.

[44] S. Pestka, C. D. Krause, M. R. Walter, *Immunol. Rev.* **2004**, *202*, 8.

[45] D. Jakimovski, C. Kolb, M. Ramanathan, R. Zivadinov, B. Weinstock-Guttman, *Interferon β for Multiple Sclerosis*, Vol. 8, NLM (Medline), **2018**, p. a032003.

[46] S. Spada, G. Walsh, *Directory of Approved Biopharmaceutical Products*, 1st ed., CRC PRESS, **2019**.

[47] A. M. M. Eggermont, J. H. W. de Wilt, T. L. M. ten Hagen, *Current uses of isolated limb perfusion in the clinic and a model system for new strategies*, Vol. 4, Lancet Publishing Group, **2003**, pp. 429–437.

[48] R. van Horssen, T. L. M. ten Hagen, A. M. M. Eggermont, *Oncologist* **2006**, *11*, 397.

[49] J. Clement, D. McDermott, *Clin. Genitourin. Cancer* **2009**, *7*, E7.

[50] National Institute of Diabetes and Digestive and Kidney Diseases, *Oprelvekin*, National Institute of Diabetes and Digestive and Kidney Diseases, **2012**.

[51] R. K. Sylvester, *Am. J. Heal. Pharm.* **2002**, *59*, S6.

[52] S. Fishbane, *Semin. Dial.* **2006**, *19*, 1.

[53] C. A. Blau, *Stem Cells* **2007**, *25*, 2094.

[54] Prometheus Laboratories, FDA, *PROLEUKIN ® (aldesleukin) Injection Label*, **2012**.

[55] A. Amin, R. L. White, *J. Kidney Cancer VHL* **2014**, *1*, 74.

[56] D. Metcalf, *The colony-stimulating factors and cancer*, Vol. 10, Nature Publishing Group, **2010**, pp. 425–434.

[57] P. Berraondo, M. F. Sanmamed, M. C. Ochoa, I. Etxeberria, M. A. Aznar, J. L. Pérez-Gracia, M. E. Rodríguez-Ruiz, M. Ponz-Sarvise, E. Castañón, I. Melero, *Br. J. Cancer* **2019**, *120*, 6.

[58] J. Galon, D. Bruni, *Approaches to treat immune hot, altered and cold tumours with combination immunotherapies*, Vol. 18, Nature Publishing Group, **2019**, pp. 197–218.

[59] S. Barrientos, O. Stojadinovic, M. S. Golinko, H. Brem, M. Tomic-Canic, *Wound Repair Regen.* **2008**, *16*, 585.

[60] K. Fent, G. Zbinden, *Trends Pharmacol. Sci.* **1987**, *8*, 100.

[61] S. Sleijfer, M. Bannink, A. R. Van Gool, W. H. J. Kruit, G. Stoter, *Side effects of interferon-α therapy*, Vol. 27, Springer, **2005**, pp. 423–431.

[62] K. Smith, *Blood* **1993**, *81*, 1414.

[63] J. P. Leonard, M. L. Sherman, G. L. Fisher, L. J. Buchanan, G. Larsen, M. B. Atkins, J. A. Sosman, J. P. Dutcher, N. J. Vogelzang, J. L. Ryan, *Blood* **1997**, *90*, 2541.

[64] W. Lasek, R. Zagożdżon, M. Jakobisiak, *Cancer Immunol. Immunother.* **2014**, *63*, 419.

[65] R. G. Baluna, In *Cytokines in Human Health*, Humana Press, Totowa, NJ, **2007**, pp. 205–231.

[66] A. Orucevic, P. K. Lala, *Role of nitric oxide in IL-2 therapy-induced capillary leak syndrome*, Vol. 17, Kluwer Academic Publishers, **1998**, pp. 127–142.

[67] J. P. Siegel, R. K. Puri, *J. Clin. Oncol.* **1991**, *9*, 694.

[68] C. Hutmacher, D. Neri, *Antibody-cytokine fusion proteins: Biopharmaceuticals with immunomodulatory properties for cancer therapy*, Vol. 141, Elsevier B.V., **2019**, pp. 67–91.

[69] U.S. Food and Drug Administration, *Proleukin Toxicologist's Review (PLA# 97-0501)*, **1998**.

[70] M. T. Lotze, Y. L. Matory, S. E. Ettinghausen, A. A. Rayner, S. O. Sharrow, C. A. Seipp, M. C. Custer, S. A. Rosenberg, *J. Immunol.* **1985**, *135*, 2865.

[71] E. F. Zhu, S. A. Gai, C. F. Opel, B. H. Kwan, R. Surana, M. C. Mihm, M. J. Kauke, K. D. Moynihan, A. Angelini, R. T. Williams, M. T. Stephan, J. S. Kim, M. B. Yaffe, D. J. Irvine, L. M. Weiner, G. Dranoff, K. D. Wittrup, *Cancer Cell* **2015**, *27*, 489.

[72] K. D. Moynihan, C. F. Opel, G. L. Szeto, A. Tzeng, E. F. Zhu, J. M. Engreitz, R. T. Williams, K. Rakhra, M. H. Zhang, A. M. Rothschilds, S. Kumari, R. L. Kelly, B. H. Kwan, W. Abraham, K. Hu, N. K. Mehta, M. J. Kauke, H. Suh, J. R. Cochran, D. A. Lauffenburger, K. D. Wittrup, D. J. Irvine, *Nat. Med.* **2016**, *22*, 1402.

[73] J. Mestas, C. C. W. Hughes, *J. Immunol.* **2004**, *172*, 2731.

[74] F. Ethuin, B. Gérard, J. E. Benna, A. Boutten, M. A. Gougereot-Pocidalo, L. Jacob, S. Chollet-Martin, *Lab. Investig.* **2004**, *84*, 1363.

[75] J. Li, S. Gyorffy, S. Lee, C. S. Kwok, *Inflammation* **1996**, *20*, 361.

[76] E. Assier, V. Jullien, J. Lefort, J. L. Moreau, B. B. Vargaftig, J. L. E. Jose Lapa, J. Thèze, *Cytokine* **2005**, *32*, 280.

[77] Z. Perez Horta, S. Saseedhar, A. L. Rakhmilevich, L. Carmichael, J. A. Hank, M. Boyden, S. D. Gillies, P. M. Sondel, *Oncoimmunology* **2019**, *8*.

[78] H. Attarwala, *J. Young Pharm.* **2010**, *2*, 332.

[79] N. Haicheur, B. Escudier, T. Dorval, S. Negrier, P. H. M. De Mulder, J. M. Dupuy, D. Novick, T. Guilloth, S. Wolf, P. Pouillart, W. H. Fridman, E. Tartour, *Clin. Exp. Immunol.* **2000**, *119*, 28.

[80] J. L. Winkelhake, S. S. Gauny, *Pharmacol. Rev.* **1990**, *42*.

[81] D. F. Mark, S. D. Lu, A. A. Creasey, R. Yamamoto, L. S. Lin, *Proc. Natl. Acad. Sci. U. S. A.* **1984**, *81*, 5662.

[82] Z. Zídek, P. Anzenbacher, E. Kmoníčková, *Br. J. Pharmacol.* **2009**, *157*, 342.

[83] E. B. Melian, G. L. Plosker, *Interferon alfacon-1: A review of its pharmacology and therapeutic efficacy in the treatment of chronic hepatitis C*, Vol. 61, Adis International Ltd, **2001**, pp. 1661–1691.

[84] P. J. Pockros, *Gastroenterology* **2010**, *139*, 1084.

[85] S. D. Gillies, Y. Lan, T. Hettmann, B. Brunkhorst, Y. Sun, S. O. Mueller, K. M. Lo, *Clin. Cancer Res.* **2011**, *17*, 3673.

[86] M. Sharma, H. Khong, F. Fa'ak, S. E. Bentebibel, L. M. E. Janssen, B. C. Chesson, C. A. Creasy, M. A. Forget, L. M. S. Kahn, B. Pazdrak, B. Karki, Y. Hailemichael, M. Singh, C. Vianden, S. Vennam, U. Bharadwaj, D. J. Tweardy, C. Haymaker, C. Bernatchez, S. Huang, K. Rajapakshe, C. Coarfa, M. E. Hurwitz, M. Sznol, P. Hwu, U. Hoch, M. Addepalli, D. H. Charych, J. Zalevsky, A. Diab, W. W. Overwijk, *Nat. Commun.* **2020**, *11*, 1.

[87] C. Klein, I. Waldhauer, V. G. Nicolini, A. Freimoser-Grundschober, T. Nayak, D. J. Vugts, C. Dunn, M. Bolijn, J. Benz, M. Stihle, S. Lang, M. Roemmele, T. Hofer, E. van Puijenbroek, D. Wittig, S. Moser, O. Ast, P. Brünker, I. H. Gorr, S. Neumann, M. C. de Vera Mudry, H. Hinton, F. Crameri, J. Saro, S. Evers, C. Gerdes, M. Bacac, G. van Dongen, E. Moessner, P. Umaña, *Oncoimmunology* **2017**, *6*.

[88] J. T. Sockolosky, E. Trotta, G. Parisi, L. Picton, L. L. Su, A. C. Le, A. Chhabra, S. L. Silveria, B. M. George, I. C. King, M. R. Tiffany, K. Jude, L. V. Sibener, D. Baker, J. A. Shizuru, A. Ribas, J. A. Bluestone, K. C. Garcia, *Science (80-.).* **2018**, *359*, 1037.

[89] M. R. Dreher, W. Liu, C. R. Michelich, M. W. Dewhirst, F. Yuan, A. Chilkoti, *JNCI J. Natl. Cancer Inst.* **2006**, *98*, 335.

[90] M. Tarini, P. Cignoni, C. Montani, *IEEE Trans. Vis. Comput. Graph.* **2006**, *12*, 1237.

[91] D. P. Williams, K. Parker, P. Bacha, W. Bishai, M. Borowski, F. Genbauffe, T. B. Strom, J. R. Murphy, *Protein Eng.* **1987**, *1*, 493.

[92] L. S. Cheung, J. Fu, P. Kumar, A. Kumar, M. E. Urbanowski, E. A. Ihms, S. Parveen, C. K. Bullen, G. J. Patrick, R. Harrison, J. R. Murphy, D. M. Pardoll, W. R. Bishai, *Proc. Natl. Acad. Sci. U. S. A.* **2019**, *116*, 3100.

[93] O. Alkharabsheh, A. E. Frankel, *Biomedicines* **2019**, *7*, 6.

[94] J. D. Heiss, A. Jamshidi, S. Shah, S. Martin, P. L. Wolters, D. P. Argersinger, K. E. Warren, R. R. Lonser, *J. Neurosurg. Pediatr.* **2019**, *23*, 333.

[95] A. S. Baur, M. B. Lutz, S. Schierer, L. Beltrame, G. Theiner, E. Zinser, C. Ostalecki, G. Heidkamp, I. Haendle, M. Erdmann, M. Wiesinger, W. Leisgang, S. Gross, A. J. Pommer, E. Kämpgen, D. Dudziak, A. Steinkasserer, D. Cavalieri, B. Schuler-Thurner, G. Schuler, *Blood* **2013**, *122*, 2185.

[96] B. Akbari, S. Farajnia, S. Ahdi Khosroshahi, F. Safari, M. Yousefi, H. Dariushnejad, L. Rahbarnia, *Int. Rev. Immunol.* **2017**, *36*, 207.

[97] R. B. Sims, *Vaccine* **2012**, *30*, 4394.

[98] E. K. Holl, M. A. McNamara, P. Healy, M. Anand, R. S. Concepcion, C. D. Breland, I. Dumbudze, R. Tutrone, N. Shore, A. J. Armstrong, M. Harrison, J. A. Wallace, Y. Wu, D. J. George, *Prostate Cancer Prostatic Dis.* **2019**, *22*, 588.

[99] C. M. Pieczonka, D. Telonis, V. Mouraviev, D. Albala, *Rev. Urol.* **2015**, *17*, 203.

[100] M. D. Mannie, J. L. Blanchfield, S. M. T. Islam, D. J. Abbott, *Front. Immunol.* **2012**, *3*, 255.

[101] C. D. Moorman, A. G. Bastian, K. B. DeOca, M. D. Mannie, *J. Neuroinflammation* **2020**, *17*, 180.

[102] D. Neri, P. M. Sondel, *Curr. Opin. Immunol.* **2016**, *40*, 96.

[103] F. Bootz, D. Neri, *Drug Discov. Today* **2016**, *21*, 180.

[104] N. Pasche, D. Neri, *Immunocytokines: A novel class of potent armed antibodies*, Vol. 17, Elsevier Current Trends, **2012**, pp. 583–590.

[105] J. Strauss, C. R. Heery, J. W. Kim, C. Jochems, R. N. Donahue, A. S. Montgomery, S. McMahon, E. Lamping, J. L. Marte, R. A. Madan, M. Bilusic, M. R. Silver, E. Bertotti, J. Schlom, J. L. Gulley, *Clin. Cancer Res.* **2019**, *25*, 99.

[106] R. K. Yang, I. B. Kuznetsov, E. A. Ranheim, J. S. Wei, S. Sindiri, B. E. Gryder, V. Gangalapudi, Y. K. Song, V. Patel, J. A. Hank, C. Zuleger, A. K. Erbe, Z. S. Morris, R. Quale, K. Kim, M. R. Albertini, J. Khan, P. M. Sondel, *Clin. Cancer Res.* **2020**.

[107] Roche, *Pipeline summary*, **2020**.

[108] Philogen, *PIPELINE - Philogen - innovating targeting*.

[109] V. Bachanova, F. Lansigan, D. P. Quick, D. Vlock, S. Gillies, R. Nakamura, *Blood* **2015**, *126*, 1533.

[110] P. A. Young, N. H. Dang, L. J. Nastoupil, D. Minning, M. J. Gresser, J. Timmerman, *J. Clin. Oncol.* **2016**, *34*, TPS3109.

[111] H. L. Kaufman, J. M. Mehnert, J.-M. Cuillerot, A. von Heydebreck, P. A. Ott, F. S. Hodi, *J. Clin. Oncol.* **2014**, *32*, TPS9107.

[112] O. Gladkov, M. Biakhov, R. Ramlau, P. Serwatowski, J. Milanowski, J. Tomeczko, P. B. Komarnitsky, L. Bernard, D. Kramer, M. J. Krzakowski, *J. Clin. Oncol.* **2012**, *30*, 7090.

[113] S. M. Rudman, M. B. Jameson, M. J. McKeage, P. Savage, D. I. Jodrell, M. Harries, G. Acton, F. Erlandsson, J. F. Spicer, *Clin. Cancer Res.* **2011**, *17*, 1998.

[114] A. Tzeng, B. H. Kwan, C. F. Opel, T. Navaratna, K. D. Wittrup, *Proc. Natl. Acad. Sci. U. S. A.* **2015**, *112*, 3320.

[115] S. D. Gillies, *Protein Eng. Des. Sel.* **2013**, *26*, 561.

[116] S. D. Gillies, K. M. Lo, Y. Lan, T. Dahl, W. K. Wong, C. Burger, *Clin. Cancer Res.* **2002**, *8*, 210.

[117] S. Martomo, D. Lu, Z. Polonskaya, X. Luna, F. Miyara, J. Patel, *Ann. Oncol.* **2019**, *30*, xi4.

[118] S. M. Amos, C. P. M. Duong, J. A. Westwood, D. S. Ritchie, R. P. Junghans, P. K. Darcy, M. H. Kershaw, *Autoimmunity associated with immunotherapy of cancer*, Vol. 118, American Society of Hematology, **2011**, pp. 499–509.

[119] J. T. Miura, J. S. Zager, *Futur. Oncol.* **2019**, *15*, 3665.

[120] B. Li, A. Chen, S. Zou, J. Wu, H. Wang, R. Chen, M. Luo, *Int. J. Pharm.* **2019**, *558*, 404.

[121] D. Skrombolas, J. G. Frelinger, *Expert Rev. Clin. Immunol.* **2014**, *10*, 207.

[122] V. K. Rustgi, *Curr. Med. Res. Opin.* **2009**, *25*, 991.

[123] Y. S. Huang, X. F. Wen, Z. Y. Yang, Y. L. Wu, Y. Lu, L. F. Zhou, R. H. Khan, *PLoS One* **2014**, *9*.

[124] O. Gladkov, V. Moiseyenko, I. N. Bondarenko, Y. Shparyk, S. Barash, L. Adar, N. Avisar, *Oncologist* **2016**, *21*, 7.

[125] Y. M. Chuang, L. He, M. L. Pinn, Y. C. Tsai, M. A. Cheng, E. Farmer, P. C. Karakousis, C. F. Hung, *Cell. Mol. Immunol.* **2020**, 1.

[126] R. Vazquez-Lombardi, C. Loetsch, D. Zinkl, J. Jackson, P. Schofield, E. K. Deenick, C. King, T. G. Phan, K. E. Webster, J. Sprent, D. Christ, *Nat. Commun.* **2017**, *8*, 1.

[127] Z. Sun, Z. Ren, K. Yang, Z. Liu, S. Cao, S. Deng, L. Xu, Y. Liang, J. Guo, Y. Bian, H. Xu, J. Shi, F. Wang, Y. X. Fu, H. Peng, *Nat. Commun.* **2019**, *10*, 1.

[128] Bristol Myers Squibb, *Pharmaceutical R&D Pipeline*, **2020**.

[129] N. Tchao, K. Gorski, T. Yuraszeck, S. Sohn, K. Ishida, H. Wong, K. Park, *Blood* **2017**, *130*, 696.

[130] Genentech, *Genentech: Our Pipeline*.

[131] Generon, *Generon Corporation (Shanghai) Ltd.*

[132] S. K. Tahir, M. L. Smith, L. R. Solomon, H. Zhang, J. C. Xue, Y. Xiao, D. Cheng, G. Buchanan, S. Morgan-Lappe, D. C. Phillips, *Blood* **2017**, *130*, 2812.

[133] J. M. Wrangle, V. Velcheti, M. R. Patel, E. Garrett-Mayer, E. G. Hill, J. G. Ravenel, J. S. Miller, M. Farhad, K. Anderton, K. Lindsey, M. Taffaro-Neskey, C. Sherman, S. Suriano, M. Swiderska-Syn, A. Sion, J. Harris, A. R. Edwards, J. A. Rytlewski, C. M. Sanders, E. C. Yusko, M. D. Robinson, C. Krieg, W. L. Redmond, J. O. Egan, P. R. Rhode, E. K. Jeng, A. D. Rock, H. C. Wong, M. P. Rubinstein, *Lancet Oncol.* **2018**, *19*, 694.

[134] K. M. Knudson, J. W. Hodge, J. Schlom, S. R. Gameiro, *Expert Opin. Biol. Ther.* **2020**, 1.

[135] J. E. Lopes, J. L. Fisher, H. L. Flick, C. Wang, L. Sun, M. S. Ernstoff, J. C. Alvarez, H. C. Losey, *J. Immunother. Cancer* **2020**, *8*, e000673.

[136] K. M. Knudson, K. C. Hicks, Y. Ozawa, J. Schlom, S. R. Gameiro, *J. Immunother. Cancer* **2020**, *8*.

[137] A. Corti, F. Curnis, G. Rossoni, F. Marcucci, V. Gregorc, *BioDrugs* **2013**, *27*, 591.

[138] F. Curnis, A. Sacchi, A. Corti, *J. Clin. Invest.* **2002**, *110*, 475.

[139] V. Gregorc, R. M. Gaafar, A. Favaretto, F. Grossi, J. Jassem, A. Polychronis, P. Bidoli, M. Tiseo, R. Shah, P. Taylor, S. Novello, A. Muzio, A. Bearz, L. Greillier, F. Fontana, G. Salini, A. Lambiase, M. O'Brien, *Lancet Oncol.* **2018**, *19*, 799.

[140] CHMP, *Withdrawal Assessment report - Zafiride*, **2017**.

[141] A. J. M. Ferreri, T. Calimeri, G. M. Conte, D. Cattaneo, F. Fallanca, M. Ponzoni, E. Scarano, F. Curnis, A. Nonis, P. Lopedote, G. Citterio, L. S. Politi, M. Foppoli, S. Girlanda, M. Sassone, S. Perrone, C. Cecchetti, F. Ciceri, C. Bordignon, A. Corti, N. Anzalone, *Blood* **2019**, *134*, 252.

[142] J. Ishihara, A. Ishihara, K. Sasaki, S. S.-Y. Lee, J.-M. Williford, M. Yasui, H. Abe, L. Potin, P. Hosseinchi, K. Fukunaga, M. M. Raczy, L. T. Gray, A. Mansurov, K. Katsumata, M. Fukayama, S. J. Kron, M. A. Swartz, J. A. Hubbell, *Sci. Transl. Med.* **2019**, *11*, eaau3259.

[143] A. Mansurov, J. Ishihara, P. Hosseinchi, L. Potin, T. M. Marchell, A. Ishihara, J. M. Williford, A. T. Alpar, M. M. Raczy, L. T. Gray, M. A. Swartz, J. A. Hubbell, *Nat. Biomed. Eng.* **2020**, *4*, 531.

[144] N. Momin, N. K. Mehta, N. R. Bennett, L. Ma, J. R. Palmeri, M. M. Chinn, E. A. Lutz, B. Kang, D. J. Irvine, S. Spranger, K. D. Wittrup, *Sci. Transl. Med.* **2019**, *11*.

[145] W. R. Strohl, *Fusion Proteins for Half-Life Extension of Biologics as a Strategy to Make Biobetters*, Vol. 29, Springer International Publishing, **2015**, pp. 215–239.

[146] P. Williams, J. Galipeau, *J. Immunol.* **2011**, *186*, 5527.

[147] J. O'Shaughnessy, A. Tolcher, D. Riseberg, D. Venzon, J. Zujewski, M. Noone, M. Gossard, D. Danforth, J. Jacobson, V. Chang, B. Goldspiel, P. Keegan, R. Giusti, K. Cowan, *Blood* **1996**, *87*, 2205.

[148] D. Skrombolas, M. Sullivan, J. G. Frelinger, *J. Interf. Cytokine Res.* **2019**, *39*, 233.

[149] D. Neri, *Cancer Immunol. Res.* **2019**, *7*, 348.

[150] V. Gupta, S. Bhavanasi, M. Quadir, K. Singh, G. Ghosh, K. Vasamreddy, A. Ghosh, T. J. Siahaan, S. Banerjee, S. K. Banerjee, *Protein PEGylation for cancer therapy: bench to bedside*, Vol. 13, Springer Netherlands, **2019**, pp. 319–330.

[151] Q. Yang, S. K. Lai, *Wiley Interdiscip. Rev. Nanomedicine Nanobiotechnology* **2015**, *7*, 655.

[152] H. Maeda, *Polymer therapeutics and the EPR effect*, Vol. 25, Taylor and Francis Ltd, **2017**, pp. 781–785.

[153] S. Sindhwani, A. M. Syed, J. Ngai, B. R. Kingston, L. Maiorino, J. Rothschild, P. MacMillan, Y. Zhang, N. U. Rajesh, T. Hoang, J. L. Y. Wu, S. Wilhelm, A. Zilman, S. Gadde, A. Sulaiman, B. Ouyang, Z. Lin, L. Wang, M. Egeblad, W. C. W. Chan, *Nat. Mater.* **2020**, 1.

[154] P. Bailon, C. Y. Won, *PEG-modified biopharmaceuticals*, Vol. 6, Taylor & Francis, **2009**, pp. 1–16.

[155] S. JevsÌ□evar, M. Kunstelj, V. G. Porekar, *Biotechnol. J.* **2010**, *5*, 113.

[156] S. Zeuzem, S. V. Feinman, J. Rasenack, E. J. Heathcote, M.-Y. Lai, E. Gane, J. O'Grady, J. Reichen, M. Diago, A. Lin, J. Hoffman, M. J. Brunda, *N. Engl. J. Med.* **2000**, *343*, 1666.

[157] K. Rajender Reddy, M. W. Modi, S. Pedder, *Adv. Drug Deliv. Rev.* **2002**, *54*, 571.

[158] A. Bottomley, C. Coens, S. Suciu, M. Santinami, W. Kruit, A. Testori, J. Marsden, C. Punt, F. Salès, M. Gore, R. Mackie, Z. Kusic, R. Dummer, P. Patel, D. Schadendorf, A. Spatz, U. Keilholz, A. Eggermont, *J. Clin. Oncol.* **2009**, *27*, 2916.

[159] T. M. Herndon, S. G. Demko, X. Jiang, K. He, J. E. Gootenberg, M. H. Cohen, P. Keegan, R. Pazdur, *Oncologist* **2012**, *17*, 1323.

[160] Z. Cao, S. Jiang, *Super-hydrophilic zwitterionic poly(carboxybetaine) and amphiphilic non-ionic poly(ethylene glycol) for stealth nanoparticles*, Vol. 7, Elsevier, **2012**, pp. 404–413.

[161] N. V Katre, *J. Immunol.* **1990**, *144*, 209.

[162] T. Menzel, A. Schomburg, A. Körfer, M. Hadam, M. Meffert, I. Dallmann, S. Casper, H. Kirchner, H. Poliwoda, J. Atzpodien, *Cancer Biother.* **1993**, *8*, 199.

[163] J. C. Yang, S. L. Topalian, D. J. Schwartzentruber, D. R. Parkinson, F. M. Marincola, J. S. Weber, C. A. Seipp, D. E. White, S. A. Rosenberg, *Cancer* **1995**, *76*, 687.

[164] R. M. Bukowski, J. Young, G. Goodman, F. Meyers, B. F. Issell, J. S. Sergi, D. McLain, G. Fyfe, J. Finke, *Invest. New Drugs* **1993**, *11*, 211.

[165] A. Carr, S. Emery, A. Lloyd, J. Hoy, R. Garsia, M. French, G. Stewart, G. Fyfe, D. A. Cooper, *J. Infect. Dis.* **1998**, *178*, 992.

[166] J. Onwumeh, C. I. Okwundu, T. Kredo, *Interleukin-2 as an adjunct to antiretroviral therapy for HIV-positive adults*, Vol. 2017, John Wiley and Sons Ltd, **2017**.

[167] J. F. Eliason, *BioDrugs* **2001**, *15*, 705.

[168] A. Naing, J. R. Infante, K. P. Papadopoulos, I. H. Chan, C. Shen, N. P. Ratti, B. Rojo, K. A. Autio, D. J. Wong, M. R. Patel, P. A. Ott, G. S. Falchook, S. Pant, A. Hung, K. L. Pekarek, V. Wu, M. Adamow, S. McCauley, J. B. Mumm, P. Wong, P. Van Vlasselaer, J. Leveque, N. M. Tannir, M. Oft, *Cancer Cell* **2018**, *34*, 775.

[169] J. R. Hecht, S. Lonardi, J. C. Bendell, H.-W. Sim, T. Macarulla, C. D. Lopez, E. Van Cutsem, A. J. M. Martin, J. O. Park, R. Greil, Y. Lin, S. Rao, B.-Y. Ryoo, *J. Clin. Oncol.* **2020**, *38*, 637.

[170] Eli Lilly, *TWENTY NINETEEN ELI LILLY AND COMPANY FINANCIAL REPORT*, **2020**.

[171] K. Nyberg, *Pegilodecakin Fails to Improve Survival When Added to Second-Line FOLFOX in PDAC*, **2020**.

[172] K. Autio, M. Oft, *Pegylated Interleukin-10: Clinical Development of an Immunoregulatory Cytokine for Use in Cancer Therapeutics*, Vol. 21, Current Medicine Group LLC 1, **2019**.

[173] D. Charych, S. Khalili, V. Dixit, P. Kirk, T. Chang, J. Langowski, W. Rubas, S. K. Doberstein, M. Eldon, U. Hoch, J. Zalevsky, *PLoS One* **2017**, *12*.

[174] D. H. Charych, U. Hoch, J. L. Langowski, S. R. Lee, M. K. Addepalli, P. B. Kirk, D. Sheng, X. Liu, P. W. Sims, L. A. VanderVeen, C. F. Ali, T. K. Chang, M. Konakova, R. L. Pena, R. S. Kanhere, Y. M. Kirksey, C. Ji, Y. Wang, J. Huang, T. D. Sweeney, S. S. Kantak, S. K. Doberstein, *Clin. Cancer Res.* **2016**, *22*, 680.

[175] S. E. Bentebibel, M. E. Hurwitz, C. Bernatchez, C. Haymaker, C. W. Hudgens, H. M. Kluger, M. T. Tetzlaff, M. A. Tagliaferri, J. Zalevsky, U. Hoch, C. Fanton, S. Aung, P. Hwu, B. D. Curti, N. M. Tannir, M. Sznol, A. Diab, *Cancer Discov.* **2019**, *9*, 711.

[176] A. Diab, N. M. Tannir, S.-E. Bentebibel, P. Hwu, V. Papadimitrakopoulou, C. Haymaker, H. M. Kluger, S. N. Gettinger, M. Sznol, S. S. Tykodi, B. D. Curti, M. A. Tagliaferri, J. Zalevsky, A. L. Hannah, U. Hoch, S. Aung, C. Fanton, A. Rizwan, E. Iacucci, Y. Liao, C. Bernatchez, M. E. Hurwitz, D. C. Cho, *Cancer Discov.* **2020**, *10*, 1158.

[177] S. K. Doberstein, *Expert Opin. Biol. Ther.* **2019**, *19*, 1223.

[178] J. L. Langowski, P. Kirk, M. Addepalli, T. Chang, V. Dixit, G. Kim, Y. Kirksey, P. Kuo, M. Lee, M. Maiti, W. Rubas, P. Sims, Y. Song, Y. Tang, L. Vanderveen, P. Zhang, S. K. Doberstein, J. Zalevsky, *NKTR-358: a selective, first-in-class IL-2 pathway agonist, which increases number and suppressive function of regulatory T cells for the treatment of immune innammatory disorders*.

[179] N. W. Nairn, K. Grabstein, K. D. Shanebeck, G. Li, A. Wang, In *Polymer-Protein Conjugates*, Elsevier, **2020**, pp. 317–349.

[180] Synthorx, *Scientific Publications - Synthorx*.

[181] J. R. Mora, J. T. White, S. L. DeWall, *AAPS J.* **2020**, *22*, 35.

[182] CHMP, *Committee for Medicinal Products for Human Use (CHMP) Assessment report Plegridy International non-proprietary name: peginterferon beta-1a*, **2014**.

[183] T. T. Hoang Thi, E. H. Pilkington, D. H. Nguyen, J. S. Lee, K. D. Park, N. P. Truong, *Polymers (Basel).* **2020**, *12*, 298.

[184] U. Binder, A. Skerra, *PASylation®: A versatile technology to extend drug delivery*, Vol. 31, Elsevier Ltd, **2017**, pp. 10–17.

[185] S. A. Chen, R. J. Sawchuk, R. C. Brundage, C. Horvath, H. V Mendenhall, R. A. Gunther, R. A. Braeckman, *J. Pharmacol. Exp. Ther.* **2000**, *293*, 248.

[186] S. Sershen, J. West, *Adv. Drug Deliv. Rev.* **2002**, *54*, 1225.

[187] K. Y. Lee, S. H. Yuk, *Polymeric protein delivery systems*, Vol. 32, Pergamon, **2007**, pp. 669–697.

[188] D. J. Cole, S. Gattoni-Celli, E. F. McClay, J. S. Metcalf, J. M. Brown, N. Nabavi, D. A. Newton, C. B. Woolhiser, M. C. Wilson, J. N. Vournakis, *Clin. Cancer Res.* **1997**, *3*, 867.

[189] M. L. Salem, W. E. Gillanders, A. N. Kadima, S. El-Naggar, M. P. Rubinstein, M. Demcheva, J. N. Vournakis, D. J. Cole, *J. Interf. Cytokine Res.* **2006**, *26*, 593.

[190] L. Yang, D. A. Zaharoff, *Biomaterials* **2013**, *34*, 3828.

[191] S. G. Smith, B. prasanth Koppolu, S. Ravindranathan, S. L. Kurtz, L. Yang, M. D. Katz, D. A. Zaharoff, *Cancer Immunol. Immunother.* **2015**, *64*, 689.

[192] S. G. Smith, J. L. Baltz, B. P. Koppolu, S. Ravindranathan, K. Nguyen, D. A. Zaharoff, *Oncoimmunology* **2017**, *6*, e1259050.

[193] O. A. Ali, N. Huebsch, L. Cao, G. Dranoff, D. J. Mooney, *Nat. Mater.* **2009**, *8*, 151.

[194] S. T. Koshy, D. J. Mooney, *Biomaterials for enhancing anti-cancer immunity*, Vol. 40, Elsevier Ltd, **2016**, pp. 1–8.

[195] S. B. Stephan, A. M. Taber, I. Jileaeva, E. P. Pegues, C. L. Sentman, M. T. Stephan, *Nat. Biotechnol.* **2015**, *33*, 97.

[196] Y. Chao, Q. Chen, Z. Liu, *Adv. Funct. Mater.* **2020**, *30*, 1902785.

[197] Y. Hori, A. M. Winans, C. C. Huang, E. M. Horrigan, D. J. Irvine, *Biomaterials* **2008**, *29*, 3671.

[198] Y. Hori, A. M. Winans, D. J. Irvine, *Acta Biomater.* **2009**, *5*, 969.

[199] Y. Hori, P. J. Stern, R. O. Hynes, D. J. Irvine, *Biomaterials* **2009**, *30*, 6757.

[200] J. Kim, W. A. Li, Y. Choi, S. A. Lewin, C. S. Verbeke, G. Dranoff, D. J. Mooney, *Nat. Biotechnol.* **2015**, *33*, 64.

[201] S. A. Bencherif, R. W. Sands, O. A. Ali, W. A. Li, S. A. Lewin, T. M. Braschler, T. Y. Shih, C. S. Verbeke, D. Bhatta, G. Dranoff, D. J. Mooney, *Nat. Commun.* **2015**, *6*, 1.

[202] K. Morikawa, F. Okada, M. Hosokawa, H. Kobayashi, *Cancer Res.* **1987**, *47*.

[203] Q. Lv, C. He, F. Quan, S. Yu, X. Chen, *Bioact. Mater.* **2018**, *3*, 118.

[204] S. Ishii, J. Kaneko, Y. Nagasaki, *Biomaterials* **2016**, *84*, 210.

[205] V. R. Sinha, A. Trehan, *Biodegradable microspheres for protein delivery*, Vol. 90, Elsevier, **2003**, pp. 261–280.

[206] J. Li, D. J. Mooney, *Nat. Rev. Mater.* **2016**, *1*, 16071.

[207] P. M. Anderson, E. Katsanis, S. F. Sencer, D. Hasz, A. C. Ochoa, B. Bostrom, *J. Immunother.* **1992**, *12*, 3.

[208] I. J. Fidler, *Science (80-.).* **1980**, *208*, 1469.

[209] I. J. Fidler, A. Raz, W. E. Fogler, G. Poste, In *Cancer Chemo- and Immunopharmacology* (Eds.: Mathé, G.; Muggia, F. M.), Springer-Verlag Berlin Heidelberg, **1980**, pp. 246–251.

[210] E. Kedar, Y. Rutkowski, E. Braun, N. Emanuel, Y. Barenholz, *J. Immunother.* **1994**, *16*, 47.

[211] I. Babai, S. Samira, Y. Barenholz, Z. Zakay-Rones, E. Kedar, *Vaccine* **1999**, *17*, 1223.

[212] D. A. Christian, C. A. Hunter, *Immunotherapy* **2012**, *4*, 425.

[213] K. M. Skubitz, P. M. Anderson, *Anticancer. Drugs* **2000**, *11*, 555.

[214] R. M. Ten, P. M. Anderson, N. N. Zein, Z. Temesgen, M. Lou Clawson, W. Weiss, *Int. Immunopharmacol.* **2002**, *2*, 333.

[215] L. T. Boni, M. M. Batenjany, M. E. Neville, Y. Guo, L. Xu, F. Wu, J. T. Mason, R. J. Robb, M. C. Popescu, *Biochim. Biophys. Acta - Biomembr.* **2001**, *1514*, 127.

[216] N. V. Katre, *Am. J. Drug Deliv.* **2004**, *2*, 213.

[217] N. K. Egilmez, Y. S. Jong, Y. Iwanuma, J. S. Jacob, C. A. Santos, F. A. Chen, E. Mathiowitz, R. B. Bankert, *Cancer Immunol. Immunother.* **1998**, *46*, 21.

[218] M. S. Sabel, J. Skitzki, L. Stoolman, N. K. Egilmez, E. Mathiowitz, N. Bailey, W. J. Chang, A. E. Chang, *Ann. Surg. Oncol.* **2004**, *11*, 147.

[219] N. K. Egilmez, *Immunol. Invest.* **2020**, 1.

[220] I. Dzyublyk, T. Yegorova, L. Moroz, O. Popovych, I. Zaytsev, V. Miroshnichenko, A. Kromminga, M. M. Wilkes, E. J. Van Hoogdalem, J. E. Humphries, *J. Viral Hepat.* **2011**, *18*, 271.

[221] Biolex, *Locteron, controlled-release interferon alpha 2b, 3 studies at EASL 2010 Vienna - 3 company press releases*, **2010**.

[222] R. B. Rowswell-Turner, J. L. Harden, R. E. Nair, T. Gu, M. O. Kilinc, N. K. Egilmez, *J. Immunol.* **2011**, *187*, 4109.

[223] B. N. Mills, K. A. Connolly, J. Ye, J. D. Murphy, T. P. Uccello, B. J. Han, T. Zhao, M. G. Drage, A. Murthy, H. Qiu, A. Patel, N. M. Figueroa, C. J. Johnston, P. A. Prieto, N. K. Egilmez, B. A. Belt, E. M. Lord, D. C. Linehan, S. A. Gerber, *Cell Rep.* **2019**, *29*, 406.

[224] E. Park, M. L. Hart, B. Rolauffs, J. P. Stegemann, R. T. Annamalai, *J. Biomed. Mater. Res. Part A* **2020**, *108*, 722.

[225] C. Wyatt Shields, M. A. Evans, L. L. W. Wang, N. Baugh, S. Iyer, D. Wu, Z. Zhao, A. Pusuluri, A. Ukidve, D. C. Pan, S. Mitragotri, *Sci. Adv.* **2020**, *6*, eaaz6579.

[226] A. C. Anselmo, J. B. Gilbert, S. Kumar, V. Gupta, R. E. Cohen, M. F. Rubner, S. Mitragotri, *J. Control. Release* **2015**, *199*, 29.

[227] J. L. Cleland, A. Daugherty, R. Mrsny, *Emerging protein delivery methods*, Vol. 12, Elsevier Ltd, **2001**, pp. 212–219.

[228] Z. Zhao, A. Ukidve, V. Krishnan, S. Mitragotri, *Adv. Drug Deliv. Rev.* **2019**, *143*, 3.

[229] Maninder C/O Chiron Corporation Hora, *Preparing aldesleukin for pharmaceutical use*, European Patent Office, **2006**.

[230] J. Geigert, N. Solli, P. Woehleke, S. Vemuri, In *Stability and Characterization of Protein and Peptide Drugs* (Eds.: Pearlman, R.; Wang, Y. J.), Springer, **1993**, pp. 249–262.

[231] A. C. Anselmo, S. Mitragotri, *Bioeng. Transl. Med.* **2019**, *4*.

[232] Y. Zhang, N. Li, H. Suh, D. J. Irvine, *Nat. Commun.* **2018**, *9*, 1.

[233] B. Kwong, S. A. Gai, J. Elkhader, K. D. Wittrup, D. J. Irvine, *Cancer Res.* **2013**, *73*, 1547.

[234] A. E. Barberio, S. G. Smith, S. Correa, C. Nguyen, B. Nhan, M. Melo, T. Tokatlian, H. Suh, D. J. Irvine, P. T. Hammond, *ACS Nano* **2020**, *14*, 11238.

[235] D. Alkekhia, P. T. Hammond, A. Shukla, *Annu. Rev. Biomed. Eng.* **2020**, *22*, 1.

[236] M. D. McHugh, J. Park, R. Uhrich, W. Gao, D. A. Horwitz, T. M. Fahmy, *Biomaterials* **2015**, *59*, 172.

[237] Y. Zhao, Q. Song, Y. Yin, T. Wu, X. Hu, X. Gao, G. Li, S. Tan, Z. Zhang, *J. Control. Release* **2018**, *269*, 322.

[238] Y. Wang, Y. X. Lin, S. L. Qiao, H. W. An, Y. Ma, Z. Y. Qiao, R. P. Y. J. Rajapaksha, H. Wang, *Biomaterials* **2017**, *112*, 153.

[239] L. Tang, Y. Zheng, M. B. Melo, L. Mabardi, A. P. Castaño, Y. Q. Xie, N. Li, S. B. Kudchodkar, H. C. Wong, E. K. Jeng, M. V. Maus, D. J. Irvine, *Nat. Biotechnol.* **2018**, *36*, 707.

[240] J. Park, S. H. Wrzesinski, E. Stern, M. Look, J. Criscione, R. Ragheb, S. M. Jay, S. L. Demento, A. Agawu, P. Licona Limon, A. F. Ferrandino, D. Gonzalez, A. Habermann, R. A. Flavell, T. M. Fahmy, *Nat. Mater.* **2012**, *11*, 895.

[241] R. Mejías, S. Pérez-Yagüe, L. Gutiérrez, L. I. Cabrera, R. Spada, P. Acedo, C. J. Serna, F. J. Lázaro, Á. Villanueva, M. del P. Morales, D. F. Barber, *Biomaterials* **2011**, *32*, 2938.

[242] A. C. Anselmo, S. Mitragotri, *Bioeng. Transl. Med.* **2016**, *1*, 10.

[243] A. A. Hombach, U. Geumann, C. Günther, F. G. Hermann, H. Abken, *Cells* **2020**, *9*, 873.

[244] T. R. Heathman, A. W. Nienow, M. J. McCall, K. Coopman, B. Kara, C. J. Hewitt, *The translation of cell-based therapies: Clinical landscape and manufacturing challenges*, Vol. 10, Future Medicine Ltd., **2015**, pp. 49–64.

[245] V. Cervera-Carrascon, R. Havunen, A. Hemminki, *Expert Opin. Biol. Ther.* **2019**, *19*, 443.

[246] S. L. Hewitt, A. Bai, D. Bailey, K. Ichikawa, J. Zielinski, R. Karp, A. Apte, K. Arnold, S. J. Zacharek, M. S. Iliou, K. Bhatt, M. Garnaas, F. Musenge, A. Davis, N. Khatwani, S. V. Su, G. MacLean, S. J. Farlow, K. Burke, J. P. Frederick, *Sci. Transl. Med.* **2019**, *11*.

[247] S. Bhatia, N. V. Longino, N. J. Miller, R. Kulikauskas, J. G. Iyer, D. Ibrani, A. Blom, D. R. Byrd, U. Parvathaneni, C. G. Twitty, J. S. Campbell, M. H. Le, S. Gargosky, R. H. Pierce, R. Heller, A. I. Daud, P. Nghiem, *Clin. Cancer Res.* **2020**, *26*, 598.

[248] H. Rehman, A. W. Silk, M. P. Kane, H. L. Kaufman, *J. Immunother. Cancer* **2016**, *4*, 53.

[249] E. P. Goldberg, A. R. Hadba, B. A. Almond, J. S. Marotta, *J. Pharm. Pharmacol.* **2002**, *54*, 159.

[250] A. Marabelle, R. Andtbacka, K. Harrington, I. Melero, R. Leidner, T. De Baere, C. Robert, P. A. Ascierto, J. F. Baurain, M. Imperiale, S. Rahimian, D. Tersago, E. Klumper, M. Hendriks, R. Kumar, M. Stern, K. Öhrling, C. Massacesi, I. Tchakov, A. Tse, J. Y. Douillard, J. Tabernero, J. Haanen, J. Brody, *Ann. Oncol.* **2018**, *29*, 2163.

[251] B. Kwong, Liposome-Anchored Local Delivery of Immunomodulatory Agents for Tumor Therapy, Massachusetts Institute of Technology, **2012**.

[252] S. Franzé, F. Selmin, E. Samaritani, P. Minghetti, F. Cilurzo, *Pharmaceutics* **2018**, *10*, 139.

[253] T. Lipiäinen, M. Peltoniemi, S. Sarkhel, T. Yrjönen, H. Vuorela, A. Urtti, A. Juppo, *J. Pharm. Sci.* **2015**, *104*, 307.

[254] M. E. Keyel, C. P. Reynolds, *Spotlight on dinutuximab in the treatment of high-risk neuroblastoma: Development and place in therapy*, Vol. 13, Dove Medical Press Ltd., **2019**, pp. 1–12.

[255] M. A. Shaker, H. M. Younes, *J. Pharm. Sci.* **2009**, *98*, 2268.

[256] A. M. Rothschilds, K. D. Wittrup, *What, Why, Where, and When: Bringing Timing to Immuno-Oncology*, Vol. 40, Elsevier Ltd, **2019**, pp. 12–21.

[257] A. Rothschilds, A. Tzeng, N. K. Mehta, K. D. Moynihan, D. J. Irvine, K. D. Wittrup, *Oncoimmunology* **2019**, *8*.

[258] J. Liu, S. J. Blake, M. C. R. Yong, H. Harjunpää, S. F. Ngiow, K. Takeda, A. Young, J. S. O'Donnell, S. Allen, M. J. Smyth, M. W. L. Teng, *Cancer Discov.* **2016**, *6*, 1382.

CHAPTER 2
Controlled lipid self-assembly for scalable manufacturing of next-generation immune stimulating complexes

---

The work presented in this chapter has been adapted with permission from Pires, I. S., Ni, K., Melo, M. B., Li, N., Ben-Akiva, E., Maiorino, L., ... & Irvine, D. J. (2023). Controlled lipid self-assembly for scalable manufacturing of next-generation immune stimulating complexes. *Chemical Engineering Journal*, *464*, 142664.

2.1 Introduction

Immune stimulating complexes (ISCOMs) are nanoparticles generated by the self-assembly of cholesterol and phospholipids with saponins. Saponins are triterpene glycosides typically isolated from the soapbark tree *Quillaja saponaria Molina* that have strong immunostimulatory properties.[1] The resulting 30-40 nm diam. particles have a cage-like structure that have potent activity as vaccine adjuvants in preclinical animal models and humans.[2] ISCOMs were initially studied by assembling saponin/lipids in the presence of antigens in order to embed antigen within the particles, but it was later found that physical association with antigens was not necessary for adjuvant activity. This finding led to use of ISCOM matrices (hereafter, ISCOMs for simplicity) as adjuvants admixed with antigens, which have undergone extensive preclinical and clinical development as vaccine adjuvants over the past 30 years.[3] In 2021, the European Medicines Agency (EMA) granted a conditional marketing authorization to Nuvaxovid (NVX-CoV2373), a COVID-19 vaccine comprised of SARS-CoV-2 spike glycoprotein nanoparticle antigen mixed with an ISCOM adjuvant termed Matrix-M.[4] Currently, Nuvaxovid is used by more than 35 countries and has been approved by the United States Food and Drug Administration (FDA) under Emergency Use Authorization.[5] ISCOM-adjuvanted vaccine formulations are also in current clinical development for various other viral infections such as seasonal influenza and respiratory syncytial virus (RSV).[6] Aiming to improve adjuvant activity with ISCOMs, we recently reported generation of ISCOM particles incorporating an additional innate immune activator, monophosphoryl lipid A (MPLA), a Toll-like receptor 4 agonist.[2] These novel ISCOM particles, which we term Saponin-MPLA NanoParticles (SMNP), have enhanced adjuvant activity, making them promising next-generation vaccine adjuvants.[2]

Several methods have been described in the literature for the manufacture of ISCOMs. The most commonly employed approach is to solubilize lipids, cholesterol, and saponin in a high concentration of a non-ionic detergent (typically MEGA-10), followed by detergent removal via ultracentrifugation or dialysis. While dialysis is a simple method leading to uniform ISCOM particle formation, the procedure generally requires more than three days.[7] Further, neither dialysis nor ultracentrifugation are readily amenable to large-scale manufacturing. More recently, lipid film hydration, ethanol injection and ether injection methods have been developed aimed at improving the scalability of ISCOM processing.[8] However, these methods have either led to more heterogeneous formulations, require altered sample composition, prolonged exposure of saponin to high temperatures, or have only been employed using hydrophilic saponin fractions. Some reports have indicated the use of ultrafiltration for large-scale production of ISCOMs under Good Manufacturing Practice (GMP) conditions.[9] However, to our knowledge there are no descriptions of this technique presented in the literature other than dialysis. Here, a scalable and facile process for manufacturing of ISCOMs and SMNP via tangential flow filtration (TFF) is presented and characterized, providing insights into the mechanism for ISCOM self-assembly from detergent micelles. TFF is a linearly scalable size-based separations technique that should enable GMP production of ISCOMs at clinically relevant scales. The process was developed starting with the commonly used Quil-A saponin fraction, a mixture of saponins with acceptable quality for veterinary vaccines, and then optimized for use with QS-21, a purified hydrophobic saponin fraction derived from Quil-A which is used in human saponin-based vaccine adjuvant formulations.

2.2 Materials and Methods

2.2.1 Generation of saponin and detergent/lipid mixture

ISCOM and SMNP adjuvants was prepared as previously described.[2] Briefly, solutions of cholesterol (Avanti Polar Lipids Cat# 700000) and DPPC (Avanti Polar Lipids Cat# 850355) were prepared in Milli-Q water containing 20% w/vol MEGA-10 (Sigma D6277) detergent at 60 °C. Quil-A saponin (InvivoGen; vac-quil) was dissolved in either Milli-Q water or 20% w/vol MEGA-10 to compare processing to QS-21 (Desert King) which was soluble in 20% MEGA-10. Saponin solutions were solubilized at 37 °C expect for the room temperature QS-21 preparations. For ISCOMs, all components were mixed at mass ratio of 5:1:1 (saponin:chol:DPPC) at 60 °C

followed by dilution with pre-heated PBS to a final concentration of 5 mg/ml saponin and 7.5% MEGA-10. SMNP was formulated in a similar manner but included MPLA (Avanti Polar Lipids 699800P) at a mass ratio of 10:2:1:1 (saponin:chol:DPPC:MPLA). MPLA stock solutions were generated in 20% MEGA-10 at 10 mg/mL by with heating at 37 °C. ISCOMs and SMNP concentrations are reported in terms of the amount of saponin. For *in vivo* studies, saponin content was calculated by measuring the concentration of cholesterol (Cholesterol Quantitation kit; Millipore Sigma; Cat# MAK043) in the preparation and assuming all lipids incorporated in proportion to their relative amounts included in the synthesis. Prior to removing detergent through dialysis or TFF, the mixture was allowed to equilibrate at room temperature for at least two hours. Dilution for Quil-A SMNPs was performed in less than one minute to reach 0.15% MEGA-10. For "low detergent" synthesis of Quil-A SMNP, the initial lipid mixture was prepared with 5% MEGA-10 at a 1:1.5 mass ratio of MEGA-10 to saponin. For overnight QS-21 SMNP dilution, buffer was dropwise added to the sample at a rate to achieve 10X/hr for 10 hours. Staggered dilution was performed by diluting in a series of steps relative to the initial volume and allowing samples to equilibrate before performing the next dilution step (see **Supplementary Table A2**).

2.2.2 ISCOM/SMNP self-assembly via dialysis

The saponin and lipid mixture was placed in 10 kDa molecular weight cut-off (MWCO) dialysis membranes (ThermoFisher, Slide-A-Lyzer) and extensively dialyzed against PBS for five days at 25 °C with buffer changes at least once a day. The adjuvant solution was passed through an 0.2 µm sterile filter, and concentrated using 50K MWCO Amicron Ultra (Sigma) spin filters. Quil-A preparations were further purified by FPLC using a Sephacryl S-500 HR size exclusion column.

2.2.3 ISCOM/SMNP self-assembly via TFF

The saponin and lipid mixtures were diluted with PBS at room temperature (20-25 °C) until stable ISCOM formation was observed (expect for low detergent Quil-A SMNP in which dilution was done at 60 °C). For QS-21 SMNP, the dilution rate was controlled to occur at a rate of 10-fold per hour. Samples were then placed on a KrosFlo KR2i tangential flow filtration system (Repligen) using 20 cm^2 100 kDa MWCO mPES membranes. QS-21 and Quil-A batch sizes ranged from 1 to 15 mg of QS-21 using the 20 cm^2 membrane. The "low detergent" Quil-A batch size was increased to 50 mg of Quil-A. For processing, the samples were concentrated to approximately 1

mg/mL prior to having MEGA-10 removed by performing 10 diafiltration volumes against PBS. Concentration of MEGA-10 in the permeate was estimated based on its absorbance at 205 nm with an empirically determined mass extinction coefficient of 20 $mg^{-1}cm^{-1}$ (**Figure A4A**). After TFF, Quil-A ISCOM and SMNP preparations were further purified by FPLC using a Sephacryl S-500 HR size exclusion column.

2.2.4 Characterization of particle preparation

Dynamic light scattering (DLS) and zeta potential measurements were made on a Zetasizer Nano ZSP (Malvern). Nanoparticle micrographs were acquired using Transmission Electron Microscopy (TEM) on a JEOL 2100F microscope (200 kV) or on a The FEI Tecnai (120 kV). The microscopes were with a magnification range of 10,000-60,000X.

2.2.5 Modeling of TFF with detergent micelle

The surfactant monomer-micelle equilibrium was represented by the closed-association model in which *n* detergent monomers associate into one detergent micelle as shown in **Equation 1**.[10]

$$nM \leftrightarrow M_n \qquad (1)$$

Where M is the concentration of surfactant monomers, M_n is the concentration of detergent micelles and n is the surfactant aggregation number, which was assumed to be 150 for MEGA-10.[11,12] Based on this model, the association of detergent monomers into micelles is governed by **Equation 2**.

$$K_n = \frac{M_n}{M^n} \qquad (2)$$

In which K_n is the equilibrium constant which can be calculated from the detergent CMC (set at 5 mM for MEGA-10[11–13]) through **Equation 3**.

$$CMC = (nK_n)^{-\frac{1}{n}} \qquad (3)$$

TFF was modeled based on previously described mathematical expressions.[14] Briefly, the system (sample container, tubes and internal filter contents) were assumed to be well mixed. Further, the total sample volume (V) was assumed to be constant such that the feed flow rate (F) and permeate flow rates (P) were equal. Both the detergent micelles (M_n) and saponin (S) were assumed to not permeate the membrane such that the only species in the permeate were detergent monomers whose concentration (C_M^{perm}) can be determined based on **Equation 4**.

$$C_M^{perm} = M * (1 - R_M) \quad (4)$$

In which R_M is the retention factor of surfactant monomers for each membrane which was set to be 10% for the 10 kDa membrane and 5% for the 100 kDa membrane.

To determine the concentration of material overtime in the TFF system, a mass balance can be done yielding **Equation 5**.

$$\frac{dC_i^{vessel}}{dt} = \left(C_i^{feed} - C_i^{perm}\right) * {}^{F}/_{V} \quad (5)$$

In which C_i^{vessel}, C_i^{feed} and C_i^{perm} are the concentration of species *i* in the system, feed and permeate, respectively, and *t* is the process time. **Equation 5** may be simplified by normalizing the processing time by the characteristic time for a diafiltration volume ($\tau = {}^{V}/_{P} = {}^{V}/_{F}$) yielding **Equation 6**.

$$\frac{dC_i^{vessel}}{dt_D} = \left(C_i^{feed} - C_i^{perm}\right) \quad (6)$$

Combining **Equations 2, 4 and 6** yields a differential-algebraic system of equations (DAE) (**Figure 2.2C**) that may be solved using MATLABs *ode15s* function. The concentration step for the 100 kDa membrane model was modeled as a system in which the diluted material was fed into the system until reaching the initial saponin concentration. Purification was modeled by feeding in buffer (i.e., concentration of all species in feed was zero).

2.2.6 Quantification of particle composition and component

QS-21 SMNP particles were characterized via Reverse-Phase High Pressure Liquid Chromatography (RP-HPLC) to quantify each of its components. SMNPs were diluted 10X in 9:1 (v/v) 2-propanol:chloroform then separated on either a Jupiter C4 column (5 µm particles, 300 Å – Phenomenex P/N: 00G-4167-E0) or an Accucore C8 column (ThermoFisher). Detection was performed via low temperature evaporative light scattering detector (ELSD) on an ELSD-LT III (Shimadzu). Gradient times and operating conditions are shown in **Table S1**.

2.2.7 Animal Studies

Mouse experiments were performed at Massachusetts Institute of Technology (MIT). All experimental procedures were approved by Institutional Animal Care and Use Committees (IACUCs). Experiments were done using sex- and age-matched female mice between 6 and 12

weeks of age. C57Bl/6J mice (strain 000664) and BALB/c (strain 000651) were purchased form the Jackson Laboratory. For immunizations, mice were injected with 2 μg of recombinant N332-GT2 HIV Env gp140 trimer antigen and 5 μg of SMNP, subcutaneously (s.c.) bilaterally with half of the dose administered on each side of the tail base. Serum was collected 2-6 weeks after dosing and characterized for presence of antibodies against N332-GT2 trimer via enzyme-linked immunosorbent assays (ELISAs) as previously described.[2]

2.2.8 Enzyme-linked immunosorbent spot (ELISpot) assay

*S*pleens were harvested 2 weeks after immunization. Splenocytes were isolated by mechanical dissociation of the spleen and erythrocytes were lysed using the Gibco Ammonium-Chloride-Potassium buffer (Thermo Fisher Scientific). ELISpot was conducted using the mouse IFN-γ ELISPOT Kit (BD Biosciences) per manufacturer's instructions. Briefly, cells were seeded on IFN-γ-coated wells at 10^6 cells/well in triplicate and stimulated overnight at 37 °C with a single pools of N332-GT2 trimer peptides at 6 μg/mL. Plates were scanned using the CTL-ImmunoSpot Plate Reader, and data were analyzed using CTL ImmunoSpot Software.

2.3 Results and Discussion

2.3.1 Dilution of saponin and lipids in detergent micelles allows for self-assembly of ISCOMs without compromising TFF efficiency

Production of ISCOMs through dialysis is typically performed by solubilizing phospholipids, cholesterol, and saponin in detergent micelles, followed by removal of the detergent by dialysis using low molecular weight cutoff (MWCO) membranes (e.g., 10 kDa). These membranes allow for detergent monomers (<1 kDa) to permeate but retain the detergent micelles containing ISCOM components. These micelles persist until the detergent concentration falls below its critical micelle concentration (CMC), at this point the lipids and saponin self-assemble into their cage-like structure. Accordingly, as a first attempt for scalable manufacturing of ISCOMs, we attempted to process a solution of Quil-A-based ISCOM components (Quil-A saponin, cholesterol, and 1,2-dipalmitoyl-*sn*-glycero-3-phosphocholine [DPPC]) in MEGA-10 micelles through a 10 kDa MWCO hollow fiber TFF filter. However, as most of the detergent was in micellar form, filtration was ineffective with high operating pressures and low permeate fluxes

due to the high concentration of material. This observation may explain why prolonged dialysis times are reported as necessary for ISCOM synthesis (3-5 days).[2,15] As an alternative, we tested whether ISCOM particles could be formed by diluting the micellar solution prior to TFF, such that high MWCO membranes could be used to facilitate detergent removal (**Figure 2.1A**). In order to validate this idea, we first explored the equilibrium of detergent micelles and ISCOMs by characterizing a 2% MEGA-10 micelle sample with or without added ISCOM components via dynamic light scattering (DLS). As shown in **Figure 2.1B**, at high concentration of detergent (2%), lipid/saponin/MEGA-10 mixtures showed particle sizes indicative of material being largely localized in MEGA-10 micelles. However, when diluted below the detergent CMC (~0.2-0.1% for MEGA-10[13]), the detergent micelles disassembled into monomers, such that DLS measurements either detected detergent monomers (for the surfactant-only solution) or ISCOMs (40 nm particles).

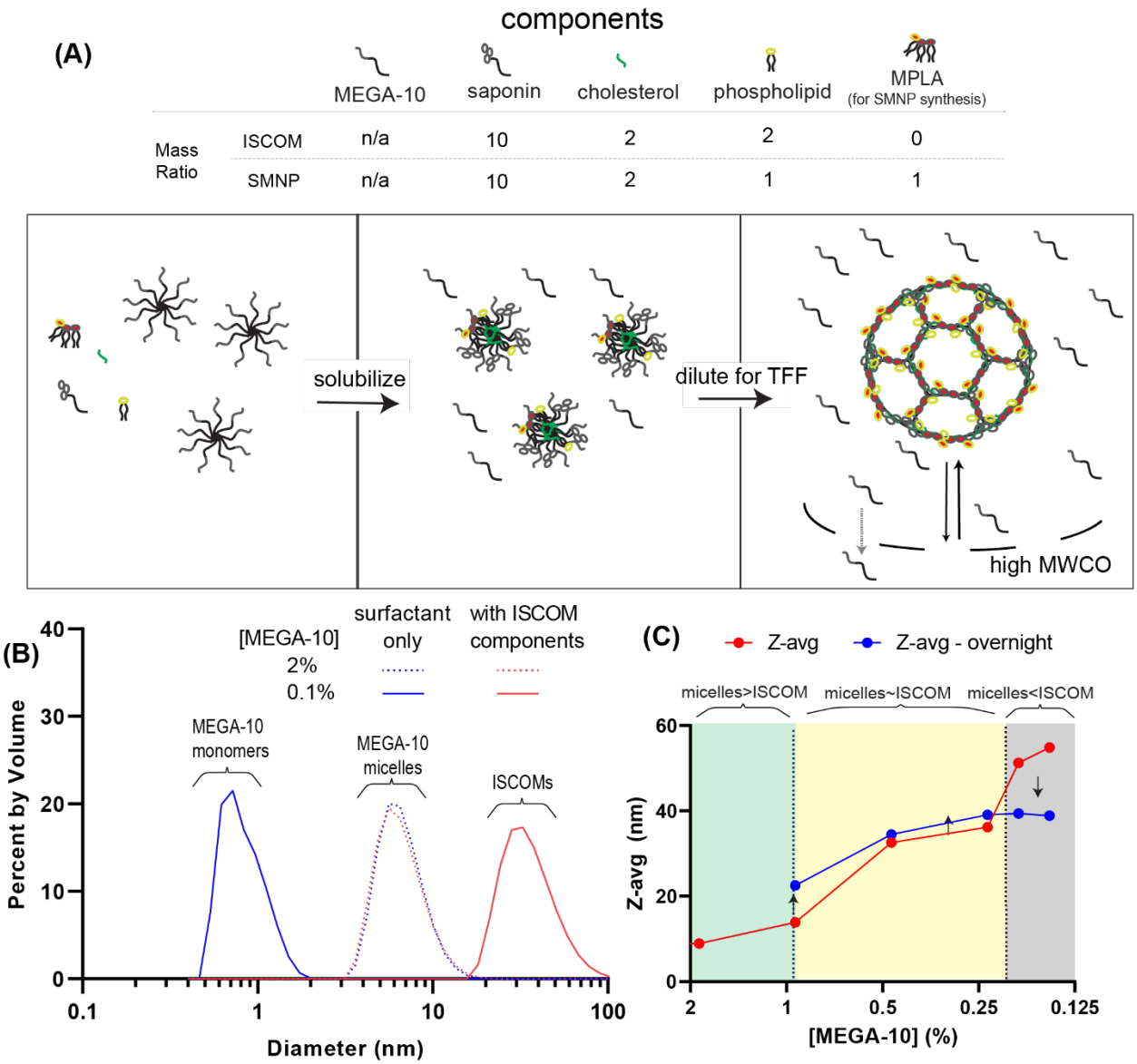

Figure 2.1: Critical micelle concentration (CMC) of detergent controls self-assembly of ISCOMs. (A) Schematic illustrating strategy of micelle dilution for ISCOM assembly. (B) DLS volume-based size distribution of MEGA-10 detergent at various concentrations in the presence or absence of ISCOM components. (C) DLS intensity-weighted size measurements (Z-avg) and polydispersity index (PDI) of 5 mg/mL ISCOMs rapidly diluted from an initial 7.5% (w/v) MEGA-10 to the indicated final concentrations of surfactant (arrows indicate change in size after incubation sample overnight at room temperature).

This result indicated that we could generate ISCOMs prior to TFF by diluting the detergent mixture to below its CMC. We repeated this process using the same initial solution composition that has been used for dialysis-based ISCOM preparation (5 mg/mL ISCOM components in 7.5% MEGA-10[2]), and carried out DLS analysis of solutions rapidly diluted to different final concentrations, aiming to determine the optimal dilution conditions for ISCOM formation (**Figure 2.1C**). Three regions of solution behavior were identified as a function of detergent final concentration: (1) At high MEGA-10 concentrations (>1%), micelles dominated with sizes of ~10 nm that did not change after overnight incubation. (2) At intermediate MEGA-10 concentrations (1%-0.2%), both micelles and ISCOMs were likely present, and DLS measured intermediate sizes between micelles and ISCOMs (10-40 nm), with minor increases in particle size after overnight incubation indicating the formation of ISCOMs. (3) At low MEGA-10 concentrations (<0.2%), the low micelle content due to proximity to the detergent CMC led to formation of larger species (~60 nm) that tended to condense into the expected ~40 nm diameter size of ISCOMs after overnight incubation.

Given that we could generate ISCOMs by diluting the detergent mixture to below its CMC, we next tested if TFF could be used to process the pre-formed ISCOMs formed in diluted detergent to remove the MEGA-10. It is generally preferable to operate TFF at high concentrations to increase total mass of impurities removed per unit volume in the permeate. To gain insight into the relevant process parameters, we developed a simple mathematical model to determine how many diafiltration volumes (i.e., total permeate volume relative to sample volume) would be required to remove 7.5% of MEGA-10 through TFF from 5 mg/mL of saponin. Two scenarios were explored - constant volume diafiltration on a 10 kDa membrane with a high detergent concentration mixture (resembling the dialysis procedure) or dilution of the detergent mixture to below its CMC followed by a concentration step to its starting saponin concentration and constant volume diafiltration on a 100 kDa membrane. The detergent monomer to micelle equilibrium was represented through the closed-association model (**Figure 2.2A**)[10] and TFF was modeled based on previously described mathematical expressions derived from mass balances on the TFF system (**Figure 2.2B**).[14] The resulting set of differential algebraic equations (see **Methods**) were solved in MATLAB to determine the concentration of each species during TFF processing.

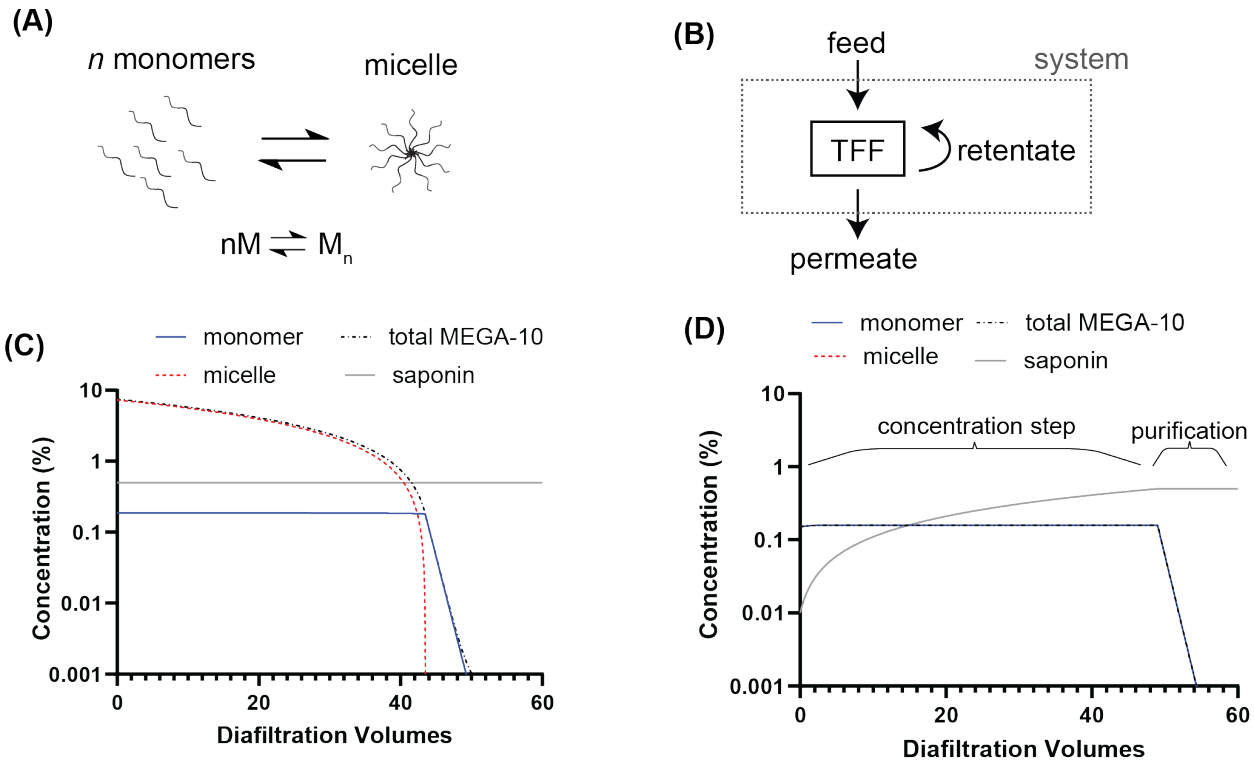

Figure 2.2: Analytical modeling predicts that dilution of surfactants to CMC prior to TFF does not significantly affect filtration performance. (A) Schematic depicting the close-association model of micelle-monomer equilibrium. (B) Simplified schematic TFF system used to derive mass balance equations. (C) Concentration over time from TFF model using a 10 kDa membrane to remove detergent monomers from a mixture with 7.5% MEGA-10 and 5 mg/mL saponin. (D) Concentration over time from TFF model using a 100 kDa membrane to first concentrate a mixture with 0.15% MEGA-10 and 0.1 mg/mL saponin to 5 mg/mL saponin then purify mixture from detergent monomers.

The model predicted that when processed through TFF on a 10 kDa membrane, the 7.5% MEGA-10 with 5 mg/mL saponin required approximately 50 diafiltration volumes to reduce the MEGA-10 content to 0.001% (**Figures 2C**). While a 1000-fold reduction of a small MW impurity such as the detergent should be achieved in ~10 diafiltrations, the detergent-micelle equilibrium limited the monomer concentration in solution to the detergent CMC, limiting the concentration of MEGA-10 in the permeate. Therefore, even though a 50X dilution to 0.15% MEGA-10 was performed in the second case, the concentration of detergent monomers in the permeate was similar in both scenarios such that concentrating prior to TFF achieved the same level of MEGA-10

reduction in ~55 diafiltration volumes (**Figure 2.2D**). Importantly, since the detergent monomer easily permeated the membrane, the concentration of detergent did not increase during the sample concentration step such that only the saponin concentration increased. In this scenario, 49 diafiltrations volume equivalents were performed for concentrating the saponin and 6 for purification. Although this indicated a slight increase in total buffer processing by diluting the sample prior to processing, the 100 kDa membranes are shown to have more than 10-fold higher normalized water permeability relative to 10 kDa membranes, thus the dilution prior to TFF processing could reduce processing time by more than an order of magnitude.[16] Further, as mentioned, the 7.5% MEGA-10 solution was impractical to process via TFF due to the high concentration of detergent, thus the dilution step should greatly facilitate TFF filtration. Based on these observations, we aimed to develop a complete ISCOM production process by first diluting the MEGA-10/lipids solution below the detergent CMC to generate ISCOMs, followed by use of a large MWCO membrane to easily concentrate the material and purify detergent monomers from ISCOMs.

2.3.2 Dilution prior to ultrafiltration yields biophysically similar ISCOM and SMNP particles compared to dialysis

We next sought to compare whether ISCOMs and SMNP generated via dilution followed by TFF (dTFF) were structurally and biologically similar to particles formed by the standard dialysis protocol. We solubilized all saponin and lipid components in 20% MEGA-10 at 60 °C and mixed with PBS to generate a 5 mg/mL solution of Quil-A saponin (together with the other ISCOM/SMNP components at the mass ratios indicated in **Figure 2.1A**) in 7.5% MEGA-10 as previously described for dialysis-based ISCOM synthesis.[2] This mixture was then either dialyzed ("dialysis") or diluted to 0.15% MEGA-10 to induce ISCOM formation prior to TFF ("dilution followed by TFF (dTFF)", **Figure 2.3A)**. In addition, to minimize the processing volume for TFF, we carried out a second TFF-based procedure where we attempted to reduce the total amount of detergent used for SMNP production 10-fold, by solubilizing 33.3 mg/mL of Quil-A saponin in 5% MEGA-10 at 60 °C, then diluting the mixture to the same final concentration of MEGA-10 (0.15%) ("low detergent dTFF", **Figure 2.3A**). After ISCOM formation, samples were processed

on 100 kDa hollow fiber TFF membranes to concentrate particles to 1 mg/mL saponin then remove detergent monomers via continuous diafiltration for 10 diafiltration volumes.

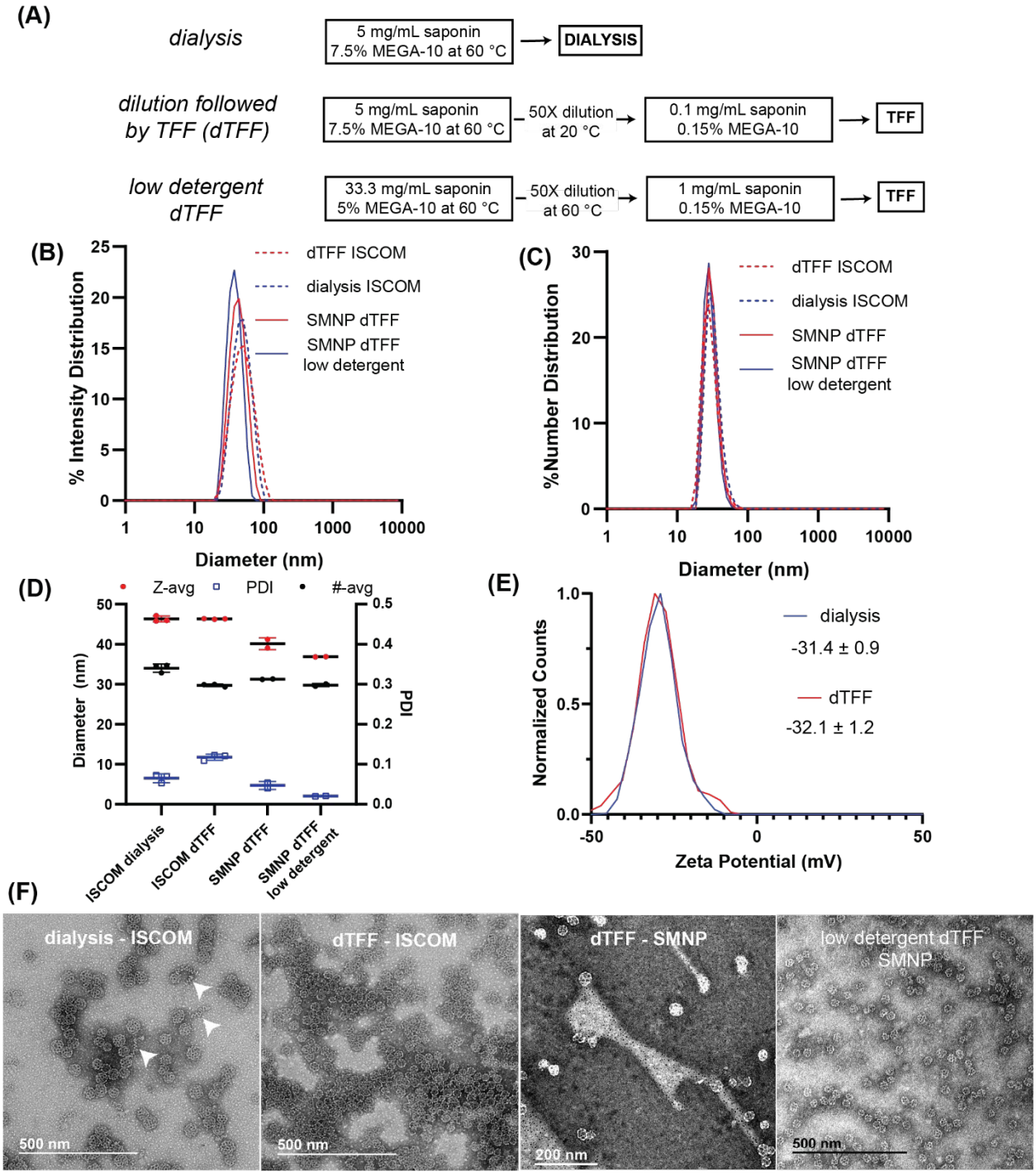

Figure 2.3: Comparison of Quil-A ISCOMs and SMNP generated via dialysis or dTFF. (A) Schematic for process to generate ISCOMs via dialysis, standard dTFF or low detergent dTFF. (B) DLS intensity-based distribution of final particles. (C) DLS number-based distribution of final particles. (D) DLS Z-avg, number average (#-avg) and PDI of final particles. (E) Representative Zeta Potential distribution of SMNP particles generated via dialysis of dTFF with average and standard deviation provided of three measurements. (F) TEM micrograph of ISCOMs or SMNPs generated via dialysis, dTFF or LD-dTFF. White arrowheads indicate worm-like species.

ISCOMs or SMNP generated via either dialysis, dTFF, or low detergent-dTFF were indistinguishable based on DLS measurements (**Figures 3B-D**). As SMNP requires incorporation of the negatively charged MPLA phospholipid, we also characterized their zeta potential and found no difference between dialysis- or dTFF-produced SMNP (**Figure 2.3E**). When assessed via TEM, all preparations yielded the characteristic cage-like morphology of ISCOMs or SMNP (**Figure 2.3F**). Interestingly, we noted that ISCOMs prepared by dialysis contained a small proportion of worm-like species (indicated with white arrowheads in the dialysis ISCOM sample in **Figure 2.3F**) that were not seen in the dTFF material, potentially indicating an improved robustness of ISCOM production via dTFF. We then sought to evaluate whether any changes in the biological adjuvant activity of the SMNP preparations were observed *in vivo* by immunizing mice with a human immunodeficiency virus (HIV) Env trimer antigen N332-GT2.[17] Mice were injected with a mixture of the antigen and the different SMNP adjuvant formulations and antigen-specific serum IgG responses were analyzed by ELISA (**Figure 2.4A**). As shown in **Figure 2.4B-C**, immunizations adjuvanted with Quil-A SMNP generated via dialysis, dTFF or low detergent dTFF elicited indistinguishable anti-HIV antigen IgG responses in mice.

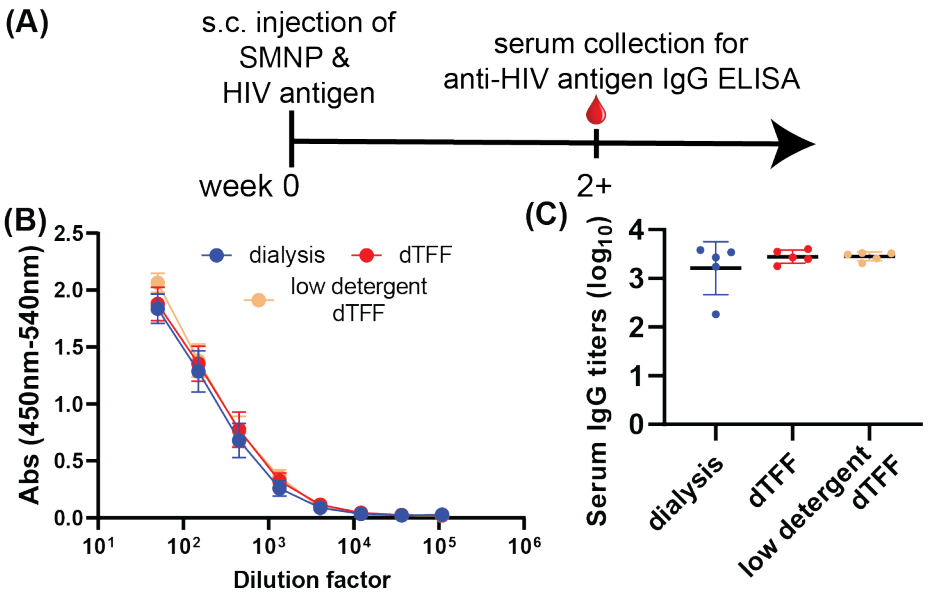

Figure 2.4: Quil-A SMNP generated via dialysis or dTFF have indistinguishable biological adjuvant activity in vivo. (A) Timeline of immunizations with SMNP and HIV Env trimer antigen N332-GT2. (B) ELISA analysis of serum IgG response at week 4 for mice immunized with 2 µg of N332-GT2 trimer and 5 µg of SMNP from the different preparations. (C) Serum titers of IgG measured from curves in (B).

2.3.2 Generation of QS-21 SMNP requires control over dilution rates to generate ISCOMs

While Quil-A is widely used in many preclinical studies and is used in an approved equine vaccine[18], Quil-A is a mixture of more than 20 different saponin components.[19] When separated via reverse-phase chromatography, the 21st peak - termed QS-21 - was found to be very potent without high toxicity, making QS-21 a promising material for the development of saponin-based adjuvants for human use.[20] Indeed, QS-21 is used in the adjuvant formulation of two approved human vaccines - Shingrix® against herpes zoster by the US FDA and Mosquirix® against malaria approved by the European Medicines Agency.[21] QS-21 is also used in a commercially available feline leukemia virus vaccine.[19] We previously showed that SMNP prepared by dialysis using QS-21 or Quil-A had similar adjuvant activity *in vivo*.[2] Thus, in order to facilitate scalable manufacturing of QS-21 SMNP for human clinical studies, we sought to use the standard dTFF protocol and the low detergent dTFF protocols developed with Quil-A to generate QS-21 SMNP. As a terminal size exclusion chromatography step used in Quil-A preparations was not scalable

and found to not lead to major changes in SMNP quality it was omitted during QS-21 SMNP development.

Surprisingly, when we attempted to replicate the process used for Quil-A SMNP synthesis with QS-21 (**Figure A1A**), we did not observe proper ISCOM formation. After solubilizing QS-21, cholesterol, MPLA, and lipid in MEGA-10 to generate a 7.5% MEGA-10 solution with 5 mg/mL QS-21, DLS measurements indicated the formation of species larger than ISCOMs (>60 nm), with the sample PDI (> 0.2) indicating a polydisperse mixture upon dilution with PBS (**Figure A1B-C**). After TFF processing, while the final products had the expected number average size of ~30 nm, the DLS intensity distribution showed a skew towards larger species (**Figure A1D**). TEM revealed that the SMNP components did not properly interact as lipid particles and ring-like micelles were prevalent on the TEM micrographs either before or after TFF (**Figure A1E**). Prior studies have shown that the ring-like micelles and worm-like micelles are primarily composed of saponin and cholesterol indicating that the lipidic components did not properly interact leading to self-assembly of two separate species.[15,22] Similarly, the low detergent dTFF product was found to contain ring-like micelles and lipid particles (**Figure A1F**). We also noted formation of rod-like structures in the low detergent dTFF product which are also known to be favored when the mole fraction of cholesterol is increased in ISCOM formulations.[8] However, unlike the standard dTFF particle, almost no cage-like particles were seen on TEM of the low detergent dTFF QS-21 SMNP. We interpret these results to indicate that QS-21 preparations require a higher amount of detergent to generate the expected cage-like SMNP particle structure, likely due to an incomplete solubilization of QS-21 into MEGA-10 micelles. While QS-21 is one of the more hydrophobic fractions contained in Quil-A, we did not expect such significant formulation differences as QS-21 is known to form micelles of ~7 nm in aqueous solutions with solubility of up to 30 mg/mL in PBS (Quil-A also forms micelles and is soluble at >100 mg/mL).[23] This hydrophobicity originates from the fatty acid chain attached to the 4-position in the triterpenoid aglycone of saponins that is present in many of the saponin species of Quil-A.[24]

Based on these observations, we characterized the dilution behavior of the lipid/QS-21/MEGA-10 mixture, starting from the 5 mg/mL of QS-21 in 7.5% MEGA-10 and rapidly diluting to different endpoint MEGA-10 concentrations as was done for Quil-A. We focused on the "standard" dTFF protocol rather than the low-detergent method, as the standard procedure generated some cage-like particles whereas low detergent dTFF material consisted mostly of

unwanted species. As shown in **Figure 2.5A**, similar to the Quil-A ISCOMs, three regions of self-assembly were identified with lowering MEGA-10 concentration. However, unlike Quil-A samples which were capable of properly forming ISCOMs in the "low micelle concentration" region (<0.2% MEGA-10), QS-21 preparations rapidly diluted to these concentrations formed particles with initial mean sizes of more than 250 nm, which lowered to ~100 nm after overnight incubation. Moreover, upon reducing MEGA-10 concentration further to less than ~0.125% MEGA-10, we observed a fourth regime in which, instead of particles reorganizing during overnight incubation, aggregates were kinetically trapped due to the low micelle concentration, and further aggregated into micron-sized species upon overnight incubation. TEM micrographs revealed some cage-like particles in the preparations, but most of the sample was present in large lipidic-saponin aggregates (**Figure A2**). Similar observations were made in previous attempts to generate QS-21 ISCOMs.[25]

To overcome this limitation with QS-21 and better recapitulate the process of dialysis previously used to generate QS-21 SMNP, we attempted to slowly dilute the QS-21 mixture containing 5 mg/mL QS-21, 7.5% MEGA-10 and the other SMNP components. This dilution was performed at a rate of 10-fold per hour, to gradually move from the starting solution into the "low micelle concentration" region (0.075%), with the goal of allowing the ISCOM components to reach their equilibrium assembly state before becoming trapped in their final structures as the MEGA-10 concentration dropped (**Figure 2.5B**). Dialysis of the QS-21 SMNP components was also performed to compare to the product generated via dTFF.

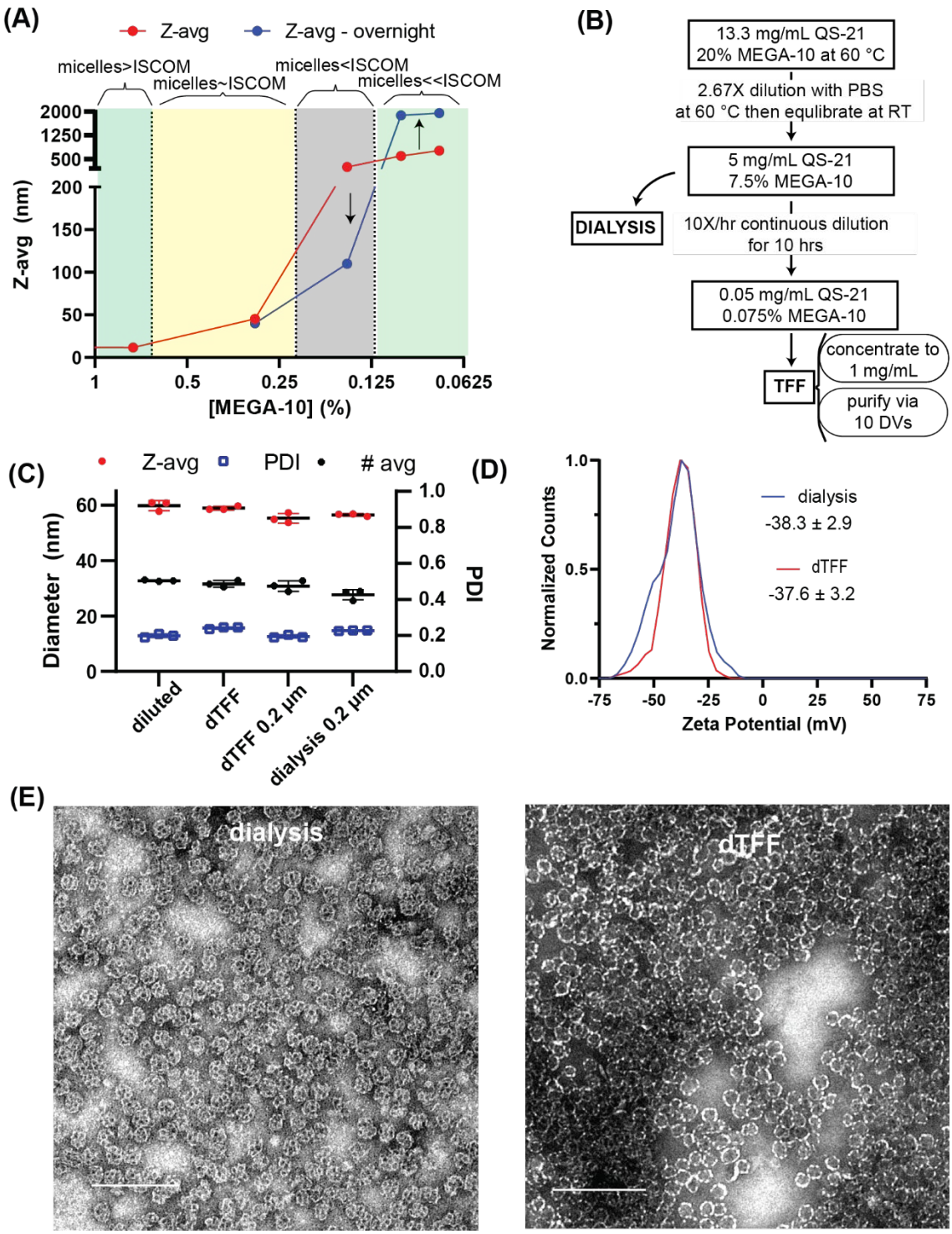

Figure 2.5: Slow dilution of QS-21 SMNP components in surfactant enables well-defined ISCOM self-assembly. (A) DLS Z-avg size measurements and PDI of 5 mg/mL of QS-21 SMNPs in 7.5% MEGA-10 at various dilutions. (B) Diagram illustrating slow dilution at room temperature to generate SMNP. (C) DLS Z-avg, number-avg and PDI for QS-21 SMNP samples slowly diluted

continuously then processed via TFF (dTFF) compared to QS-21 SMNP generated via dialysis. (D) Representative zeta potential distribution of QS-21 SMNP generated via dTFF or dialysis with average zeta potential of three measurements displayed. (E) TEM micrographs of samples QS-21 SMNPs generated via dialysis (left) or via dTFF (right). Scale bars indicate 200 nm.

We found that well-structured QS-21 SMNP particles could be formed and processed via dTFF using this slow continuous dilution approach (**Figures 2.5C-E**). Size **(Figure 2.5C**) and zeta-potential (**Figure 2.5D**) measurements showed indistinguishable physical properties of the final products generated via either dTFF or dialysis. TEM imaging revealed a homogeneous cage-like particle morphology for dTFF QS-21 SMNP (**Figure 2.5E**). We also assessed the composition of particles prepared by the dTFF or dialysis process using reverse phase HPLC (RP-HPLC). As shown in **Table 2.1**, the final composition of QS-21 SMNP particles generated with dTFF closely mirrored the input 10:2:1:1 saponin:cholesterol:DPPC:MPLA (by mass) feed ratio added to the synthesis. Representative RP-HPLC chromatograms for QS-21 SMNP with identified peaks are shown in **Figure A3**. Further, both methods led to high yields (70-80% by QS-21 content) as determined via RP-HPLC. Using either dialysis or dTFF preparation, no MEGA-10 was detectable via RP-HPLC, in agreement with quantification of MEGA-10 in the permeate via spectrophotometry (**Figure A4A-B**).

Table 2.1: Mass ratio of QS-21 SMNPs components relative to saponin. Values indicate average of three independent batches and standard deviation.

Stage	**Component**			
	QS-21	**Cholesterol**	**DPPC**	**MPLA**
starting mixture	10	2	1	1
dTFF	10	1.95 ± 0.11	1.03 ± 0.15	1.02 ± 0.24
yield (based on QS-21)	77 ± 3 %			

2.3.3 QS-21 SMNP generated through dilution and ultrafiltration is bioactive and stable to freezing

With a scalable process to generate clinical grade SMNP developed, we next turned to evaluate the bioactivity of the material and its stability when frozen at -20 °C or -80 °C to enable long term storage and transport of material (**Figure 2.6**). In order to minimize sample formulation complexity, we evaluated the stability of QS-21 SMNP frozen without additional cryoprotectants.

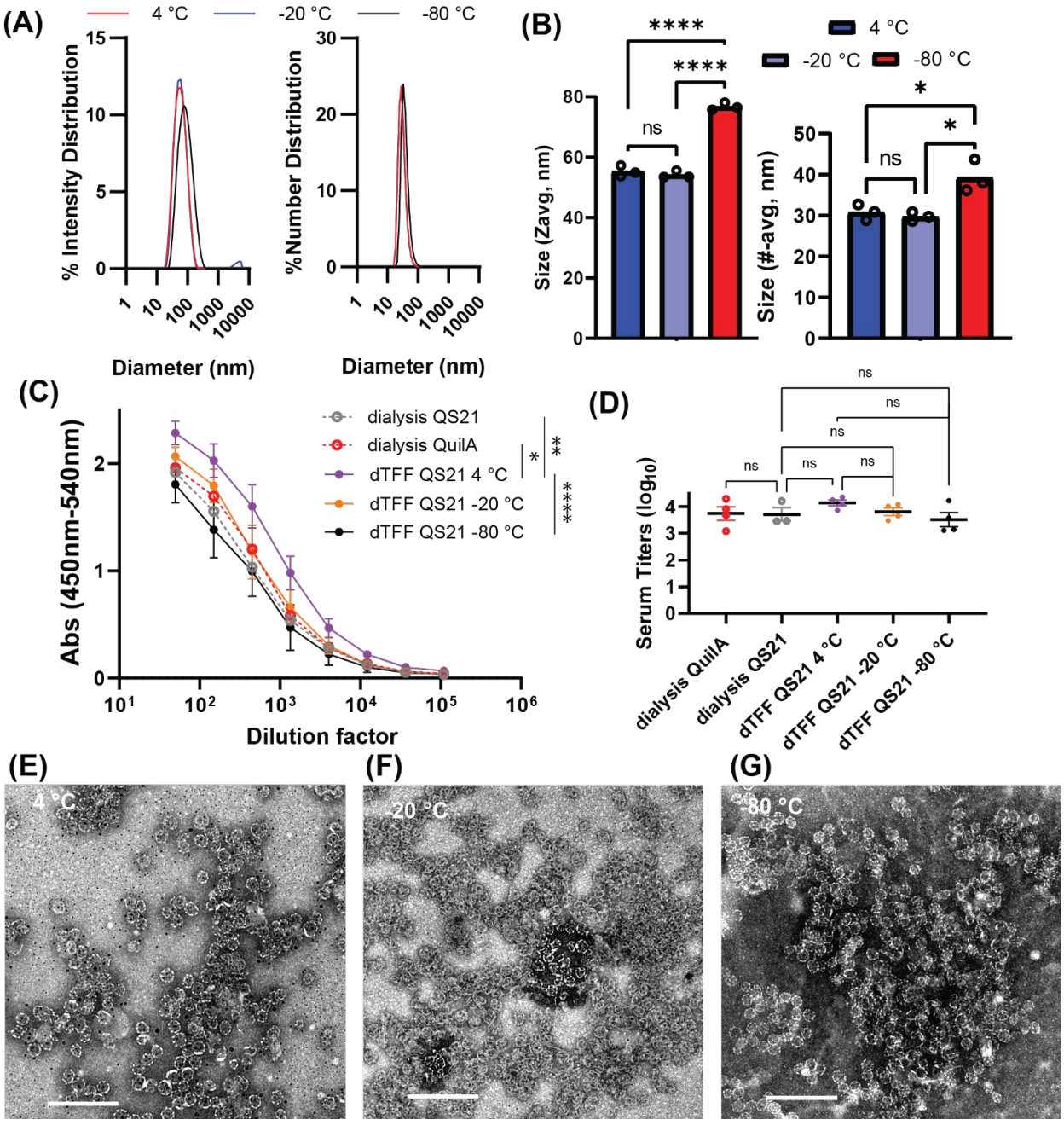

Figure 2.6: QS-21 SMNP is bioactive and stable when stored at -20 °C without use of cryoprotectants. (A) Representative DLS intensity-based and number-based distribution of QS-21 SMNP particles stored at 4 °C or frozen at -20 °C or -80 °C then thawed at room temperature. (B) DLS Z-avg, and number-avg for QS-21 SMNP samples stored at 4 °C or frozen at -20 °C or -80 °C then thawed at room temperature. (C) ELISA analysis of serum IgG response at week 6 for mice immunized with 2 µg of N332-GT2 trimer and 5 µg of SMNP stored at 4 °C or frozen at -20

°C or -80 °C then thawed at room temperature. (D) Serum titer from ELISA curves in (C). TEM micrographs of QS-21 SMNP stored at 4 °C (E) or frozen at -20 °C (F) or -80 °C (G) then thawed at room temperature. Scale bars indicate 200 nm.

As shown in **Figure 2.6A-B**, when frozen at -20 °C, QS-21 SMNP particles did not exhibit any changes in their size even without the presence of cryoprotectants. Only when frozen at -80 °C was there a noticeable increase in particle size. Interestingly, we found that QS-21 SMNP particles generated via dTFF had slightly improved adjuvant activity *in vivo* compared to either Quil-A or QS-21 SMNP generated via dialysis based on their serum IgG ELISA curves **(Figure 2.6C**), though this did not equate to a statistically significant difference in endpoint serum IgG titers (**Figure 2.6D**). Although QS-21 SMNP frozen at -80 °C showed some aggregation and a lower serum IgG titer curve than QS-21 SMNP at 4 °C **(Figure 2.6C**), there was no difference in endpoint serum IgG titers for dTFF samples frozen at -20 °C or -80 °C compared to dialysis or dTFF samples stored at 4°C (**Figure 2.6C-D**). When assessed via TEM, particles kept at 4 °C or frozen were found to maintain the cage-like morphology and sample homogeneity (**Figure 2.6E-G**). These results indicated that biologically active QS-21 SMNP could be generated through dTFF and that they may be readily frozen and transported at -20 °C without loss of its biological adjuvant properties.

2.3.4 Staggered discontinuous dilution improves particle quality and enables room temperature QS-21 SMNP synthesis

In our initial QS-21 SMNP process development, we used high temperature mixing at 60 °C to enable a fully dissolved initial lipid/MEGA-10 solution to be prepared. As QS-21 may undergo temperature-driven hydrolysis of its ester bond between the fucose and the fatty acid domain leading to inactivation,[23] we finally sought to remove the need for this high temperature mixing step. We maintained heating of DPPC and cholesterol at 60 °C and MPLA at 37 °C to facilitate solubilization into MEGA-10 micelles as these materials should not be prone to rapid degradation in aqueous solutions (**Figure A5A**). Unfortunately, while it was possible to generate QS-21 SMNP by simply mixing all MEGA-10-solubilized components at room temperature followed by continuous dilution and TFF, the sample homogeneity was reduced relative to our prior preparations, based on a Z-avg size larger than 60 nm and PDI greater than 0.2 (**Figure A5B**).

In order to explore whether these inhomogeneities had an effect on the biological adjuvant activity of SMNPs, we tested *in vivo* two room temperature dTFF SMNP batches – one with highest homogeneity (dTFF-RT#1) and one with lowest (dTFF-RT#2). While dTFF-RT#1 batch was similar to heated dTFF SMNP or SMNP generated via dialysis, the preparation with largest Z-avg and PDI was found to have diminished serum IgG titers at week 2 compared to SMNP prepared by dialysis or the dTFF preparations (**Figure A5C and S5E**). However, antibody responses reached similar levels by 4 weeks (**Figure A5D and S5E**) and showed improved serum IgG curves from heated dTFF samples or the high-homogeneity room temperature dTFF relative to dialysis preparations. TEM micrographs analysis (**Figure A5F**) revealed a notable presence of lipid vesicles in these SMNP preparations, suggesting incomplete complexing of saponin with phospholipids during the gradual dilution procedure.

In order to overcome this issue, we discovered that the sample homogeneity could be improved by diluting the MEGA-10/QS-21/lipid/cholesterol mixture in staggered steps instead of continuously (**Figure 2.7A, Supplementary Table A2**). We theorize that this improved self-assembly may be due to particles existing at the "intermediate" MEGA-10 concentrations in which micelles co-exist with ISCOMs which favor proper ISCOM particle formation. In the continuous dilution, the sample never reached equilibrium during its dilution as buffer was constantly added. In the staggered dilution, the sample was allowed to equilibrate after every dilution step such that a more complete complexing of saponin with phospholipids could be achieved. Notably, this new dilution protocol enabled homogenous QS-21 SMNP preparations with Z-avg size and PDI similar to QS-21 SMNPs processed through SEC-FPLC after dialysis synthesis (**Figure 2.7B**). Further, TEM micrographs revealed the desired prominent cage-like particle morphology (**Figure 2.7C**). The same protocol enabled synthesis of QS-21 ISCOMs (**Figure A6**) indicating that the MPLA component of SMNPs was not the driver for the aggregates formed via rapid dilution.

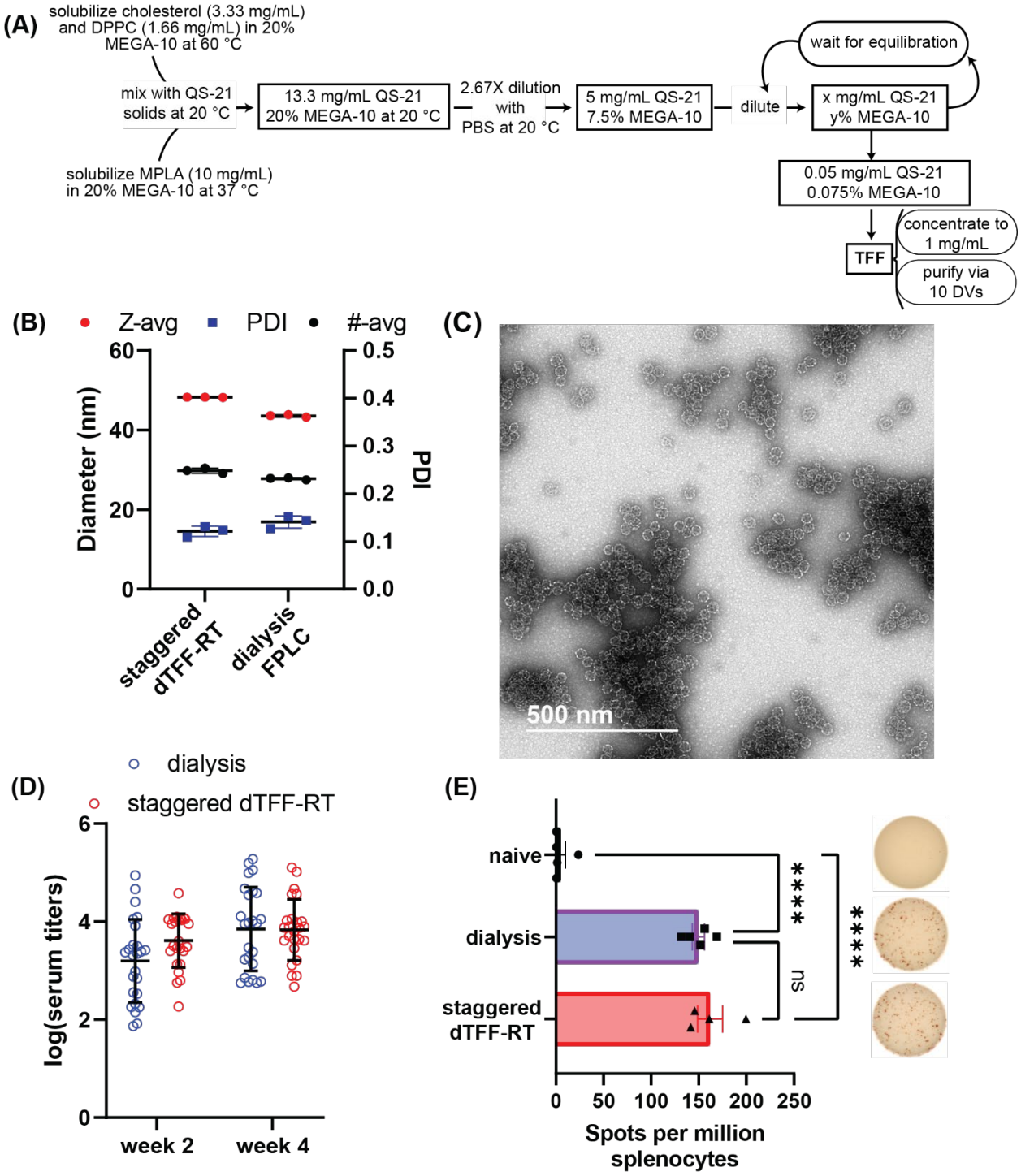

Figure 2.7: Room temperature QS-21 SMNPs synthesis is facilitated through staggered dilution. (A) Diagram for staggered room temperature (RT) dilution where the sample is repeatedly partially diluted then let sit until fully equilibrated (equilibration times and dilution factors at for each step shown in **Supplementary Table A2**). (B) DLS Z-avg, PDI and number-

avg for room temperature QS-21 SMNP samples synthesized via staggered dilution compared to FPLC purified SMNPs from dialysis synthesis. (C) TEM micrographs of QS-21 SMNP generated at room temperature through the staggered dilution protocol. (D) Summary of serum IgG titers at week 2 and week 4 from mice immunized with 2 μg of N332-GT2 trimer and 5 μg of SMNP using the staggered dilution room temperature protocol (E) IFN-γ ELISpot of splenocytes harvested two weeks after immunization and stimulated with a pool of N332-GT2 trimer peptides.

To more completely assess any differences between dialysis-generated QS-21 SMNP and staggered-dTFF QS-21 SMNP, three independent batches of each were tested *in vivo* for their effect on seroconversion following immunization. No significant differences were observed on the particle adjuvant performance in mouse immunizations (**Figure 2.7D**). Moreover, we evaluated the cellular immune response via IFN-γ an enzyme-linked immunosorbent spot (ELISpot) assay and did not find any differences (**Figure 2.7E**), confirming that the QS-21 SMNP could be synthesized at room temperature and processed via dTFF to yield biologically active and homogeneous QS-21 SMNP product. Notably, while most experiments presented here were performed at 5-15 mg scales of QS-21, this method has been successfully scaled to 50 mg and 500 mg batches of QS-21 SMNPs without processing changes except increasing TFF filter surface area and total processing volumes. Based on the experience gained from these experiments, we defined a set of target Critical Quality Attributes (CQAs, **Supplementary Table A3**) for SMNPs.

2.4 Conclusions

The next-generation ISCOM-like adjuvant termed SMNP has demonstrated promising preclinical adjuvant activity in mice, rabbits, and non-human primates. However, dialysis-based processing that is not easily adapted to GMP scale-up manufacturing was used to synthesize SMNP particles in preclinical studies. In this study we successfully developed a scalable method to generate Quil-A and QS-21 SMNPs via controlled dilution followed by TFF. While it is known that lipid and buffer composition can affect saponin-based particle morphology, we demonstrated that the dilution rate is another critical process parameter for proper assembly of QS-21 based ISCOMs.[8,15,22] In addition to improved sample homogeneity, the controlled self-assembly of ISCOMs or SMNP through the method presented here may facilitate use of saponin fractions previously found to be very potent but that were difficult to generate into the cage-like particles.

For example, when initially attempted to generate ISCOMs with the QS-21 fraction, they were found to form into >1 μm particles with some cage-like structures present similar to rapidly diluted samples (**Figure 2.5A and A2**). [25] Further, other Quil-A fractions such as QHB and QHC which are in formulations for clinical development were reported to have a lower ISCOM forming ability.[26] This lower propensity to form ISCOMs may originate from the higher hydrophobicity of these fractions, which we show here may be overcome by increasing residence time at "intermediate" detergent concentrations required for proper ISCOM self-assembly.[27] Importantly, SMNP elicited higher antibody titers as well as higher antigen-specific $CD4^+$ T cell production of IFN-γ and IL-21 compared to the potent liposomal saponin/MPLA adjuvant $AS01_B$.[2] These results suggest that the unique cage-like assembly of ISCOMs may play an important role in maximizing adjuvant activity, such that processes for its production need to ensure preservation of the particle structure. Future studies are needed to explore whether structural differences such as the ones from rapid dilution or compositional differences can affect the bioactivity of saponin/MPLA-based adjuvants. Overall, the methods presented here for controlled lipid self-assembly may also have utility for the synthesis of other soft matter assemblies of interest for broad applications in medicine and beyond.

2.5 References

1. Morein, B. & Bengtsson, K. L. Functional aspects of iscoms. *Immunol Cell Biol* **76**, 295–299 (1998).

2. Silva, M. *et al.* A particulate saponin/TLR agonist vaccine adjuvant alters lymph flow and modulates adaptive immunity. *Sci Immunol* **6**, (2021).

3. Lövgren Bengtsson, K., Morein, B. & Osterhaus, A. D. ISCOM technology-based Matrix M^{TM} adjuvant: success in future vaccines relies on formulation. *Expert Rev Vaccines* **10**, 401–403 (2011).

4. Dunkle, L. M. *et al.* Efficacy and Safety of NVX-CoV2373 in Adults in the United States and Mexico. *New England Journal of Medicine* **386**, 531–543 (2022).

5. FDA. Novavax Letter of Authorization 10192022. *fda.gov* https://www.fda.gov/media/159902/download (2022).

6. Keech, C. *et al.* Phase 1–2 Trial of a SARS-CoV-2 Recombinant Spike Protein Nanoparticle Vaccine. *New England Journal of Medicine* **383**, 2320–2332 (2020).

7. Sun, H.-X., Xie, Y. & Ye, Y.-P. ISCOMs and ISCOMATRIX^{TM}. *Vaccine* **27**, 4388–4401 (2009).

8. Pham, H. L., Shaw, P. N. & Davies, N. M. Preparation of immuno-stimulating complexes (ISCOMs) by ether injection. *Int J Pharm* **310**, 196–202 (2006).

9. Sjölander, A. *et al.* Immune responses to ISCOM® formulations in animal and primate models. *Vaccine* **19**, 2661–2665 (2001).

10. Nyrkova, I. A. & Semenov, A. N. Multimerization: Closed or open association scenario? *The European Physical Journal E* **17**, 327–337 (2005).

11. Lee, M.-T., Vishnyakov, A. & Neimark, A. V. Calculations of Critical Micelle Concentration by Dissipative Particle Dynamics Simulations: The Role of Chain Rigidity. *J Phys Chem B* **117**, 10304–10310 (2013).

12. Sulthana, S. B. *et al.* Solution Properties of Nonionic Surfactants and Their Mixtures: Polyoxyethylene (10) Alkyl Ether [C n E 10] and MEGA-10. *Langmuir* **16**, 980–987 (2000).

13. Walter, A., Suchy, S. E. & Vinson, P. K. Solubility properties of the alkylmethylglucamide surfactants. *Biochimica et Biophysica Acta (BBA) - Biomembranes* **1029**, 67–74 (1990).

14. Pires, I. S. & Palmer, A. F. Selective protein purification via tangential flow filtration – Exploiting protein-protein complexes to enable size-based separations. *J Memb Sci* **618**, 118712 (2021).

15. Sun, H.-X., Xie, Y. & Ye, Y.-P. ISCOMs and ISCOMATRIX^{TM}. *Vaccine* **27**, 4388–4401 (2009).

16. Repligen. *Spectrum® MPES Hollow Fiber Filter Modules*. (2021).

17. Steichen, J. M. *et al.* A generalized HIV vaccine design strategy for priming of broadly neutralizing antibody responses. *Science (1979)* **366**, (2019).

18. Oladunni, F. S., Oseni, S. O., Martinez-Sobrido, L. & Chambers, T. M. Equine Influenza Virus and Vaccines. *Viruses* **13**, 1657 (2021).

19. Wenbin Tuo, D. Z. QS-21: A Potent Vaccine Adjuvant. *Nat Prod Chem Res* **03**, (2015).

20. Kensil, C. R., Patel, U., Lennick, M. & Marciani, D. Separation and characterization of saponins with adjuvant activity from Quillaja saponaria Molina cortex. *The Journal of Immunology* **146**, (1991).

21. Wang, P. Natural and Synthetic Saponins as Vaccine Adjuvants. *Vaccines (Basel)* **9**, 222 (2021).

22. Demana, P. H., Berger, B., Vosgerau, U., Rades, T. & Davies, N. M. A comparison of pseudo-ternary diagrams of aqueous mixtures of Quil A, cholesterol and phospholipid prepared by lipid-film hydration and dialysis. *Journal of Pharmacy and Pharmacology* **56**, 573–580 (2010).

23. Kensil, C. R., Wu, J. Y. & Soltysik, S. Structural and immunological characterization of the vaccine adjuvant QS-21. *Pharm Biotechnol* **6**, 525–541 (1995).

24. Morein, B., Berenjian, S. & Hu, K. Nanoparticles, process for preparation and use thereof as carrier for amphipatic and hydrophobic molecules in fields of medicine including cancer treatment and food related compounds. (2017).

25. ANNE, K. G. F., ARJEN, S., GERRIT, V. D. W. & COEN, B. E. IMMUNOGENIC COMPLEXES, IN PARTICULAR ISCOMS. (1991).

26. COOPER, C. J., ROBERT, C., ALAN; BROR, M., KARIN, L.-B. & BO, S. SAPONIN PREPARATIONS AND USE THEREOF IN ISCOMS. (1996).

27. BROR, M. & KARIN, L. Pharmaceutical Carrier. (1992).

CHAPTER 3

Surfactant-mediated assembly of precision-size liposomes

The work presented in this chapter has been adapted with permission from Pires, I. S., Suggs, J. R., Carlo, I. S., DongSoo, Y., Hammond, P. T. & Irvine, D. J. (2024). Surfactant-mediated assembly of precision-size liposomes. *Chemistry of Materials*. (in press)

3.1 Introduction

Lipid-based nanoparticles such as liposomes are effective vehicles for the delivery of therapeutic agents. Since their first Food and Drug Administration (FDA) approval in 1995 for the drug Doxil®[1], the development of these nanocarriers has greatly expanded owing to their ability to efficiently package therapeutics and improve accumulation in target tissues.[2,3] While there are many strategies to generate lipid vesicles, most methods involve kinetically trapped species which often limits control over their size and polydispersity.[4–6] Moreover, the requirement of rapid mixing in many of these systems presents a significant challenge to scale-up manufacturing.[4]

One of the earlier reported methods to generate liposomes is based on solubilizing lipid components into detergent micelles followed by either dialysis or gel filtration chromatography to remove detergent.[7,8] While this method is still commonly used for proteoliposome synthesis,[9] for laboratory studies this approach has been largely displaced by solvent dispersion or thin film hydration methods that do not require tedious and time-consuming purification steps.[8,10] However, advancements in size-exclusion methods such as tangential flow filtration (TFF) have made size-based separations a faster and scalable process.[11] Indeed, we previously showed that dilution of mixed detergent/lipid micelles followed by TFF enabled controlled self-assembly of immune-stimulating complexes (ISCOMs) that can be readily produced at clinical lot scales.[12]

We hypothesized that an improved method to manipulate lipid self-assembly from detergent micelles could enable liposome generation with more precise particle size control and lower polydispersity relative to commonly used approaches. In this study, we revisited the detergent removal method for liposome synthesis using TFF for rapid concentration of samples and removal of detergent and determined key parameters controlling liposome self-assembly. Vesicle formation was induced by diluting a lipid/detergent mixture (mixed micelles) below the critical micelle concentration (CMC) of the detergent. We discovered that the concentration of detergent during self-assembly allowed for precise control of liposome size from ~1 μm down to

50 nm, with low polydispersity (polydispersity indices below 0.1). To understand this process, we developed a model for the growth of liposomes based on phase separation of lipid-rich and detergent-rich phases in solution during detergent removal that enabled large liposome assembly. Finally, we demonstrate the utility of controlled liposome assembly by validating that liposomes produced by this process are differentially recognized by macrophages as a function of particle size.

3.2 Methods

3.2.1 Materials

1,2-distearoyl-sn-glycero-3-phosphocholine (DSPC), Cholesterol, 1-palmitoyl-2-oleoyl-sn-glycero-3-phospho-(1'-rac-glycerol) (sodium salt) (POPG), 1,2-dioleoyl-sn-glycero-3-phosphoethanolamine-N-(glutaryl) (sodium salt) (DOPE-glutaryl), 1,2-dioleoyl-sn-glycero-3-phosphoethanolamine-N-dibenzocyclooctyl (DOPE-DBCO), and 1,2-distearoyl-sn-glycero-3-phospho-(1'-rac-glycerol) (DSPG) were purchased from Avanti Polar Lipids. N-decanoyl-N-methylglucamine (MEGA-10) and n-octyl-β-d-glucoside (octylglucoside) were purchased from Sigma Aldrich. For fluorescence measurements, borondipyrromethene (BDP) tetramethylrhodamine (TMR) azide (Lumiprobe) and BDP 630/650 azide (Lumiprobe) were reacted with DOPE-DBCO in chloroform to generate DOPE-TMR and DOPE-630/650. Successful conjugation was validated via thin-layer chromatography which indicated <1% free dye.

3.2.2 Generation of detergent/lipid mixtures

Lipid stock solutions were made in chloroform and then measured into glass vials and left drying on a desiccator overnight. For solubilization in MEGA-10 micelles, a 10% MEGA-10 solution was made in deionized water. The 10% MEGA-10 solution was then added to the dried lipids and left in a water bath sonicator at 50 to 60 °C until all lipids were solubilized. The lipid/detergent mixture was allowed to equilibrate at 25°C prior to dilution. The same process was followed for experiments using octylglucoside instead of MEGA-10.

3.2.3 Synthesis of nanoparticles via dilution

Lipid/detergent micelles were diluted by adding buffer to the micelles to reach the target detergent concentration. For small-scale samples (<2 mL), the mixed micelle mixture was added to a container, and then buffer was added and mixed with a 1 mL pipette. No major difference in

particle size was observed when mixed micelles were directly added to the buffer instead. For larger scales (>2 mL), the mixed micelles were added to the bottom of a container that could house the full dilution volume. Then the buffer was added to the sides of the vessel with a serological pipette gun while the sample was swirled. Upon full dilution, the sample was further mixed with the serological pipette gun. The samples were then allowed to equilibrate at 25 °C.

3.2.4 Purification via TFF

Generally, 5 mg of the lipid/detergent mixtures were diluted to the target MEGA-10 concentration and left to self-assemble overnight. Then samples were diluted to 0.02% MEGA-10 to ensure minimal effects of the detergent on the assembled lipid structures. Samples were then placed on a KrosFlo KR2i TFF system (Repligen) system using a 100 kDa mPES membrane with a surface area of 115 cm^2. Samples underwent 10 diafiltration volumes against the buffer used for their assembly. Particle yield was either accessed based on recovered nanoparticle fluorescence or total lipid content measured via the Steward assay.[13] For cryo-TEM analysis, samples underwent 5 diafiltration volumes against deionized water to remove salts.

3.2.5 Analysis of lipid transfer via FRET

Lipid/detergent micelles of the desired composition were generated by replacing 1 mol% of DSPC with 1 mol% of either DOPE-TMR (donor-micelles) or DOPE-630/650 (acceptor-micelles). For FRET-micelles, donor micelles and acceptor micelles were mixed 1:1. FRET-micelles, donor-micelles, and acceptor-micelles were diluted to the target MEGA-10 concentration. After dilution of donor and acceptor micelles, the diluted samples of equal final MEGA-10 concentration were mixed at 0 hr, 1 hr, and 24 hrs after dilution. FRET efficiency was then measured at 0 hr, 1 hr, 24 and 48 hrs after mixing of donor and acceptor micelles. Fluorescence values were measured in a 384-well plate in a Tecan Infinite 200. FRET efficiency was calculated based on the equation for the corrected FRET efficiency ($FRET_N$) described previously.[14] Briefly, acceptor-only and donor-only controls were evaluated for their emission in the donor (530 nm excitation/570 nm emission), acceptor (610 nm excitation/650 nm emission), and FRET (530 nm excitation/650 nm emission) channels. For FRET efficiency measurements, the acceptor fluorescence channel was used to correct the donor channel fluorescence. Then both acceptor channel fluorescence and corrected donor channel fluorescence were used to correct the FRET channel fluorescence for any contribution of donor or acceptor emission in the channel so that only energy transfer was

measured. FRET efficiency was then calculated based on the ratio of corrected FRET channel measurement relative to the corrected donor channel fluorescence.

3.2.6 Characterization of particle preparations

Dynamic light scattering (DLS) and zeta potential measurements were made on a Zetasizer Nano ZSP (Malvern). Nanoparticle micrographs were acquired using Cryogenic Transmission Electron Microscopy (cryo-TEM) on a JEOL 2100 FEG microscope (200 kV). For cryo-TEM, particles were buffer exchanged into deionized water via either dialysis or TFF unless otherwise indicated. For grid preparation, 3 μL of the sample was dropped on a lacey copper grid coated with a continuous carbon film and blotted to remove excess sample without damaging the carbon layer by Gatan Cryo Plunge III. The grid was then mounted on a Gatan 626 single-tilt cryo-holder equipped in the TEM column. The specimen and holder tip were frozen and cooled down by liquid nitrogen, and the temperature was maintained during transfer into the microscope and subsequent imaging. Images were collected with a magnification range of 10,000-60,000X. Cryo-TEM micrographs were analyzed on ImageJ to measure particle diameter. Polydispersity index (PDI) from diameter distribution was determine based on the PDI equation used for dynamic light scattering: $PDI = \left(\frac{\sigma}{\mu}\right)^2$, where σ is the standard deviation of the particle diameter and μ is the average diameter.

3.2.7 Cell Culture

RAW 264.7 macrophages (ATCC) were cultured in DMEM. Cell media was supplemented with 10% FBS and penicillin/streptomycin with cells incubated in a 5% CO_2 humidified atmosphere at 37 °C. All cell lines were murine pathogen tested and confirmed mycoplasma negative by Lonza MycoAlert™ Mycoplasma Detection Kit.

3.2.8 In vitro cellular association

Liposomes were generated with 0.2 mol% of DOPE-630/650 which is composed of a dye relatively insensitive to the polarity and pH of the environment.[15] The day before dosing, RAW 264.7 cells were plated on a tissue-culture 96-well plate at a density of 25k cells per well. The next day, wells were dosed with liposomes at 0.01 mg/mL and left for the target incubation time (4 hrs or 24 hrs). To determine the percentage of liposomes associated with macrophages, a sample of the of the supernatant was removed from the well and diluted 5X with dimethyl sulfoxide (DMSO). Cells were then washed three times with PBS and then scraped and dissolved with DMSO to

homogenize and extract all fluorescent lipids from the cell. Fluorescence of the liposomes remaining in the supernatant and fluorescence of liposomes associated with macrophages were then measured using a fluorescence plate reader (TECAN Infinite 200).

3.3 Results and Discussion

3.3.1 Concentration of detergent enables precise control of varied liposome size with low polydispersity

Liposome assembly from mixed micelles derived from surfactants and lipids occurs by depleting detergent molecules from micellar structures, leading to lipid aggregate coalescence into bilayer vesicles.[16,17] Prior studies on liposome formation from nonionic detergent micelles have focused on the rate of detergent removal from the sample to control the final liposome size.[7,18] We hypothesized that the final detergent concentration could control self-assembly due to both the kinetics and equilibrium partitioning of the detergent into the aqueous phase. To test this idea, we evaluated liposome assemblies formed following rapid dilution of lipid/detergent micelles followed by overnight equilibration at different final total detergent concentrations (**Figure 3.1A**). As a model system, we used lipid mixtures with a 6:3:1 molar ratio of 1,2-distearoyl-sn-glycero-3-phosphocholine (DSPC), cholesterol, and 1-palmitoyl-2-oleoyl-sn-glycero-3-phospho-(1'-rac-glycerol) (POPG), as we and others have used similar formulations for therapeutic liposomes (see component structures in **Figure B1**).[19–23] The detergent, N-decanoyl-N-methylglucamine (MEGA-10), at an initial concentration of 10 wt% was chosen due to its high critical micelle concentration (CMC, ~0.2-0.1%[24]), which facilitates surfactant removal; and samples were diluted with pH 7.4 phosphate-buffered saline (PBS), a physiological buffer. After rapid dilution of MEGA-10/lipid solutions to varying final detergent concentrations, sample size and polydispersity index (PDI) were measured via dynamic light scattering (DLS) before and after overnight incubation to ensure final self-assembly.

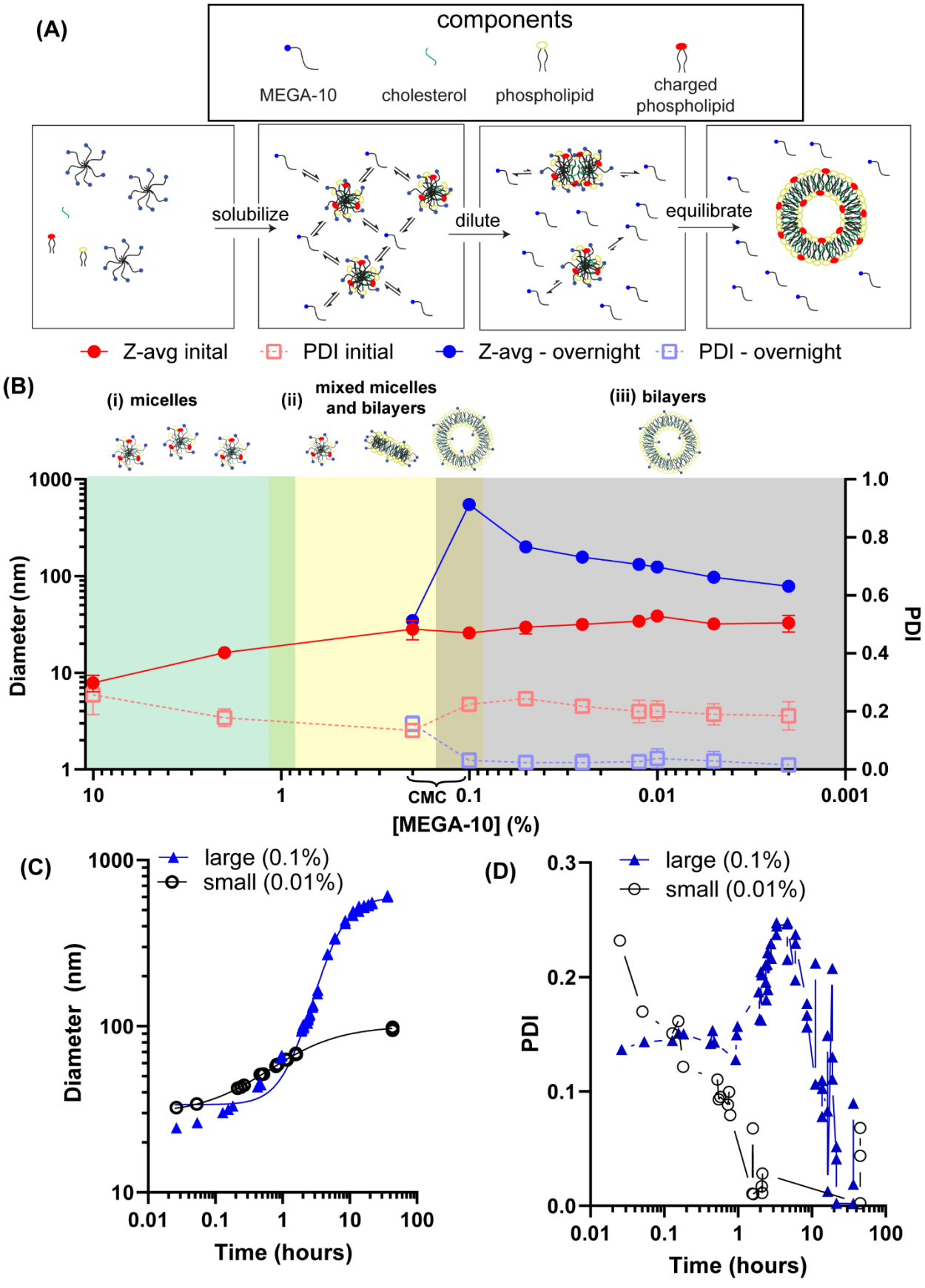
(A)
components
MEGA-10
cholesterol
phospholipid
charged phospholipid
solubilize
dilute
equilibrate
Z-avg inital
PDI initial
Z-avg - overnight
PDI - overnight
(B)
(i) micelles
(ii) mixed micelles and bilayers
(iii) bilayers
Diameter (nm)
PDI
CMC
[MEGA-10] (%)
(C)
large (0.1%)
small (0.01%)
Diameter (nm)
Time (hours)
(D)
large (0.1%)
small (0.01%)
PDI
Time (hours)

Figure 3.1. Detergent concentration during nanoparticle formation dictates equilibrium size of nanoparticles. **(A)** Schematic of liposome assembly from mixed micelle dilution. **(B)** Particle size determined by DLS of samples diluted with PBS to various final concentrations of MEGA-10 starting from an initial mixture of 10 mg/mL of 6:3:1 molar mixture of DSPC:cholesterol:POPG in 10% MEGA-10. **(C)** Particle size evolution over time determined by DLS for mixed micelles diluted to 0.1% and 0.01% MEGA-10. **(D)** Polydispersity index (PDI) kinetics for mixed micelles diluted to 0.1% and 0.01% MEGA-10.

Immediately following dilution, no major changes in particle size were observed even at detergent concentrations far below the CMC (**Figure 3.1B**, Z-Avg initial). However, after 18 hr incubation at dilutions below the detergent CMC, particles were detected by DLS with mean sizes ranging from 50-500 nm (**Figure 3.1B**, Z-Avg overnight). Particle size was determined by the final concentration of MEGA-10, even though no detergent molecules were removed, and all samples were diluted at the same rate. Unexpectedly, we were able to achieve more than one order of magnitude variation in final particle size with very low polydispersity. We confirmed that these resulting particles were spherical unilamellar liposomes via cryo-transmission electron microscopy (cryo-TEM, **Figure B2**). Previous work on mixed micelles has suggested the presence of three phases during the transition between micelles to vesicles that help explain the observed size changes.[25] At high concentrations of detergent, a small spherical micelle-predominant region exists (region i) that transitions into a mixed micelle region (region ii) followed by a final bilayer-predominant (vesicle) region at detergent concentrations below the CMC (region iii). In region ii, mixed micelle structures may include disc-like bicelles or cylindrical worm-like micelles that coexist with vesicles.[26]

Given the unusual low polydispersity when large (>200 nm) particles were formed near the detergent CMC, we first explored the limits of final vesicle size.[27] By slightly increasing the MEGA-10 concentration from 0.1% MEGA-10, it was possible to achieve >1 μm particles with polydispersity indices (PDI) below 0.1, indicative of a monodisperse population (**Figure B3A**).[20] To validate that this observed size control was not restricted to MEGA-10, we tested the same protocol using a different nonionic surfactant, n-octyl-β-d-glucoside, (octylglucoside, CMC~0.6-0.7%). Like MEGA-10 mixed micelle dilution, we observed the three distinct regions of lipid assembly and the formation of large monodisperse particles below the CMC (**Figure B3B**).

Moreover, to ensure that the particle size was not dependent on residual detergent in the bilayer, we further diluted equilibrated samples and found no change in size or polydispersity, suggesting that stable lipid assemblies had been formed (**Figure B3C**).

We next characterized the kinetics of lipid vesicle assembly at 0.1% MEGA-10 and compared to smaller vesicles formed at 0.01% MEGA-1. While self-assembly at 0.01% MEGA-10 was rapid, reaching near final sizes within ~3 hrs, self-assembly at 0.1% MEGA-10 required >10 hrs to approach equilibrium (**Figure 3.1C**). The observed kinetic curves could be well described by the Hill Equation which indicated cooperative assembly ($n > 1$[28]) at 0.1% MEGA-10 (n~2), but not at 0.01% MEGA-10 (n=0.9)[23]. Further, while the PDI of particles formed at 0.01% MEGA-10 decreased monotonically with time, at 0.1% MEGA-10, a transient transition into a polydisperse sample was observed (**Figure 3.1D**), and the PDI did not begin decreasing until ~10 hr of incubation for self-assembly had passed. We hypothesize this decrease in PDI during overnight incubation was represents a gradual transition of small heterogeneous mixed micelles into uniform lipid vesicles as these lipid assemblies slowly equilibrate.

3.3.2 Purification of assembled nanoparticles via tangential flow filtration (TFF) removes detergent without affecting liposome structure

Having observed an unexpected wide range of control over monodisperse liposome assembly using detergent dilution, we next sought to assess removal of the surfactant using TFF, as residual detergent could be a potential source of toxicity and interfere with liposome behavior. In addition, TFF provides a convenient means to concentrate the particles. We tested purification of samples equilibrated at 0.1%, 0.02%, or 0.004% MEGA-10 to form vesicles of three distinct sizes (**Figures 2A-B**). Detergent was removed by concentrating the samples to 0.25 mg/mL of lipids then purifying via 10 diafiltration volumes through a 100 kDa MWCO TFF membrane. Analysis of the purified vesicles via reverse-phase high-pressure liquid-chromatography (RP-HPLC) coupled with evaporative light scattering detector (ELSD) showed no detectable levels of MEGA-10 (<1% mass composition out of the total lipid components), indicating removal of greater than 99.9% of MEGA-10 from the sample (**Figure B4A-B**). We also found no appreciable difference in the final particle size of small-scale (~0.05 mg) or larger batches (5 mg) prepared by this process and particles maintained their size and monodispersity with yields of 70-80% after purification (data not shown). Zeta potential measurements indicated the expected negative surface charge on these

particles due to the presence of POPG (**Figure 3.2C**). Analysis via cryo-TEM revealed that the vesicles were primarily unilamellar liposomes with narrow polydispersity (**Figure 3.2D-H**). Compared to conventional thin-film hydration followed by extrusion through a 50 nm pore-sized membrane (**Figure B5A-D**), detergent dilution and TFF purification enabled even large liposomes of ~500 nm mean diameter to be prepared with lower polydispersity (**Figure B5E-F**).

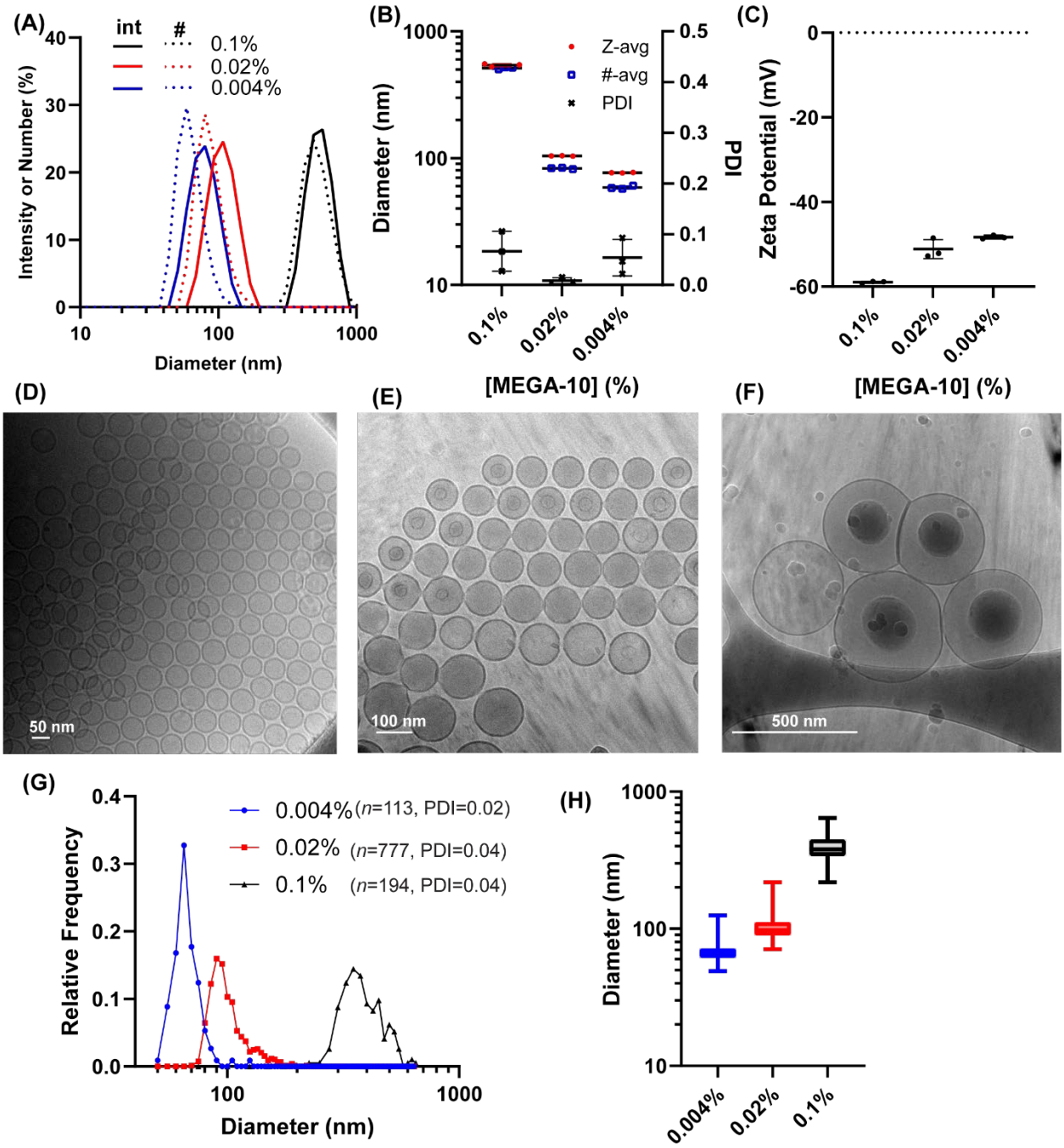

Figure 3.2. Purified lipid nanoparticles maintain size and monodispersity. **(A)** DLS intensity and number distribution for liposomes generated by diluting a lipid mix (of 10 mg/mL of 6:3:1 molar mixture of DSPC:cholesterol:POPG in 10% MEGA-10) to 0.1%, 0.02% and 0.004% of detergent. **(B)** Size and PDI of samples from **(A)**. **(C)** Zeta potential of samples from **(A)** - the variation in measured zeta potentials can be explained by the approximation of the Henry's function as a

constant in our instrument given that for a given zeta potential, increased particle size increases electrophoretic mobility.[29] Representative cryoTEM images of samples from samples generated at **(D)** 0.004%, **(E)** 0.02%, **(F)** and 0.1% – internal shading on large liposomes are due to particle protrusion from ice.[30] **(G)** Histograms of particles measured on cryoTEM micrographs from samples in **(A)** – parenthesis indicates the total number of particles quantified and PDI based on the measured particle sizes from cryoTEM. **(H)** Box and whiskers plot of size distribution from **(G)**.

3.3.3 Electrostatic interactions and lipid membrane rigidity enable controlled growth of liposomes

To explore the system characteristics that enabled a wide range of liposome size control, we first assessed whether the ionic strength of the dilution buffer affected equilibrated particle size, by carrying out rapid dilution to varying concentrations of detergent using a lower ionic strength buffer (10 mM HEPES). In these low ionic strength conditions, there was no appreciable change in the size of mixed micelles regardless of final detergent concentration over 18 hr (**Figure 3.3A**), indicating that the high electrostatic repulsion between micelles limited the growth of larger species. To test whether electrostatic interactions played a role in achieving monodisperse vesicle assembly, we evaluated liposome assembly from mixed micelles lacking the charged POPG lipid (i.e. neutral DSPC:chol liposomes) in PBS or HEPES. With this formulation it was possible to generate small vesicles with low polydispersity using both buffers and the transition from small mixed micelles to larger particles occurred at similar MEGA-10 concentrations (0.2-0.1 wt%, **Figure 3.3B**). However, the size control was limited as vesicles >200 nm in diam. formed at lower MEGA-10 dilutions had high polydispersity, indicating that a balance of charge repulsion and particle coalescence was important for the controlled formation of large monodisperse vesicles (**Figure 3.3B**).

As lipid unsaturation and the presence of cholesterol are known to promote liposome fusion as well as alter lipid bilayer rigidity[31,32], we next evaluated the effect of lipid composition by removing cholesterol (chol) or replacing POPG with 1,2-distearoyl-sn-glycero-3-phospho-(1'-rac-glycerol) (DSPG), a saturated anionic lipid. Dilution of DSPG/DSPC/chol mixed micelles with either PBS of HEPES-only buffer behaved like POPG/DSPC/chol mixed micelles (**Figure 3.3C**), but with lower overall liposome sizes. On the other hand, removal of cholesterol from the

unsaturated (unsat) formulation (DSPC/POPG mixture only) fully prevented formation of large vesicles at 0.1% MEGA-10 and yielded polydisperse samples at low MEGA-10 concentrations (**Figure 3.3D**). Dilution of saturated (sat) lipid compositions devoid of cholesterol yielded only large polydisperse species (**Figure 3.3D**). Thus, control over liposome size required the presence of cholesterol and was facilitated by lipid unsaturation, consistent with properties that promote bilayer fusion.

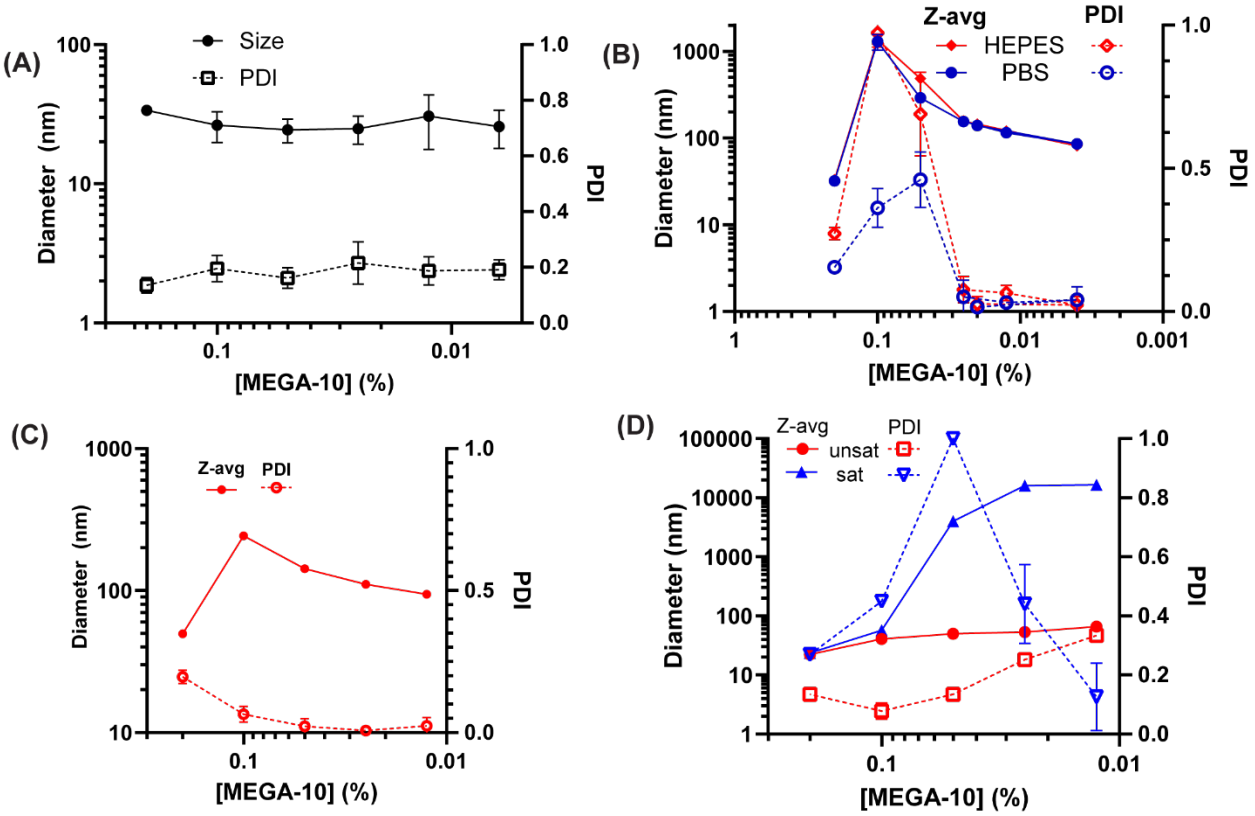

Figure 3.3. Solution ionic strength and lipid composition regulates the self-assembly from lipid/detergent micelles into liposomes. **(A)** Particle size (Z-avg) and PDI after lipid/detergent micelle dilution (10 mg/mL of 6:3:1 molar mixture of DSPC:cholesterol:POPG in 10% MEGA-10) with 10 mM HEPES and overnight incubation. **(B)** Z-avg and PDI of neutral lipid/detergent micelles (10 mg/mL of 7:3 molar mixture of DSPC:cholesterol in 10% MEGA-10) diluted with either PBS or 10 mM HEPES. **(C)** Z-avg and PDI of anionic lipid/detergent micelles charged with DSPG either containing or lacking cholesterol (10 mg/mL of either 6:3:1 or 9:1 molar mixture of DSPC:cholesterol:DPSG or DSPC:DSPG in 10% MEGA-10) diluted with PBS. **(D)** Z-avg and PDI of cholesterol-free unsaturated (unsat) mixed micelles (9:1 DSPC:POPG) and saturated (sat)

mixed micelles (9:1 DSPC:DSPG) diluted with PBS to various final MEGA-10 concentration and allowed to incubate overnight at room temperature.

3.3.4 Self-assembly of large liposomes occurs through phase separation into lipid-rich and detergent-rich phases

Given the possibility of micelle and bilayer coexistence near the detergent's CMC of mixed micelles[25,27], which should result in enhanced lipid transfer between both bilayers and micelles,[33,34] we turned to the use of fluorescence resonance energy transfer (FRET) to evaluate if lipid exchange was occurring during vesicle self-assembly at various detergent concentrations. We first evaluated FRET during self-assembly from mixed micelles (6:3:1 molar ratio of DSPC:chol:POPG) containing both donor and acceptor fluorescently-tagged lipids (FRET micelles, **Figure 3.4A**). To assess if lipid mixing could occur at various stages of vesicle self-assembly, we separately diluted mixed micelles containing either donor-only or acceptor-only fluorescently tagged lipids (sepFRET micelles). After a given time for self-assembly, samples at the same concentration of MEGA-10 were mixed to evaluate changes in FRET efficiency (**Figure 3.4B**).

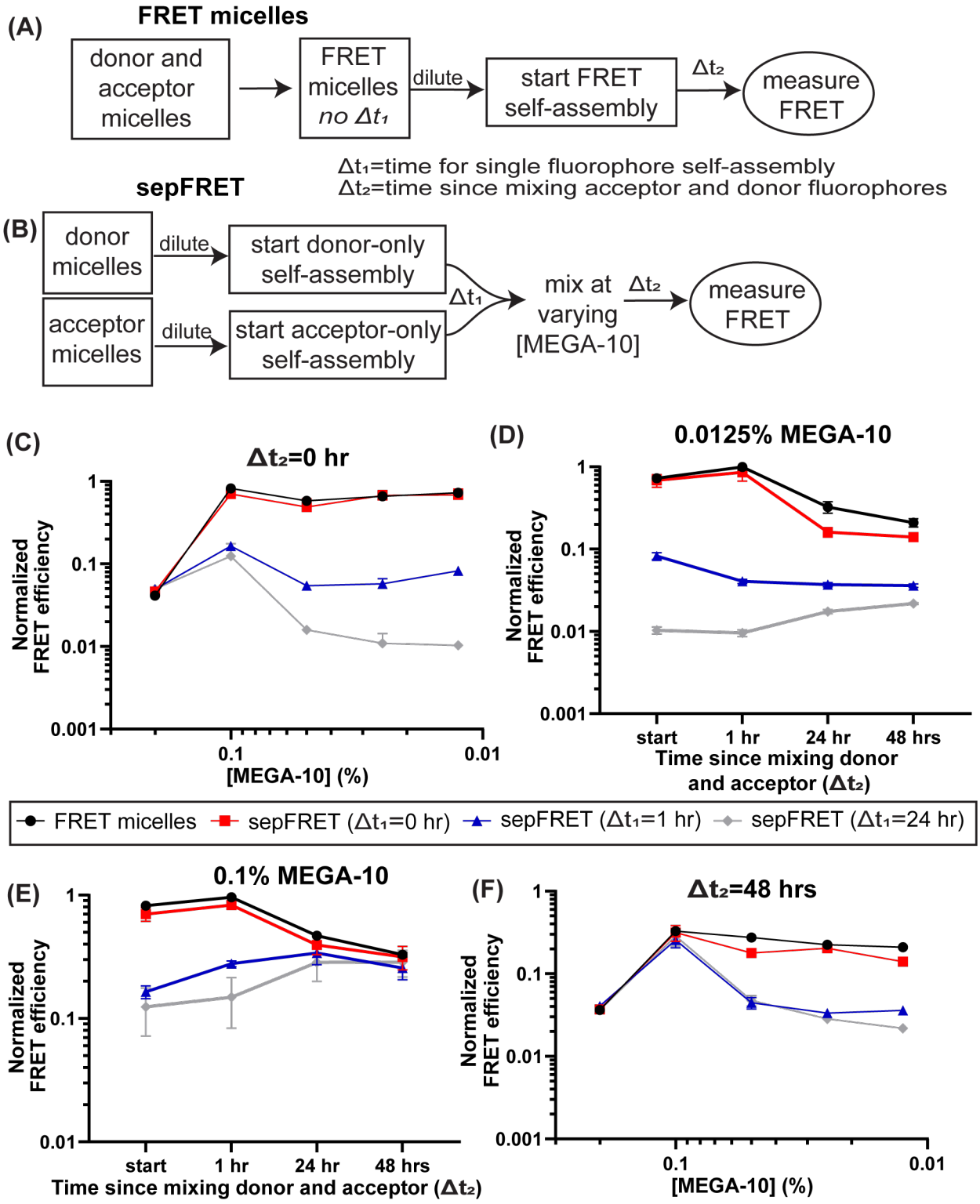

Figure 3.4. FRET of diluted mixed micelles reveals intermediates with high rates of lipid exchange. **(A)** Schematic for dilution of FRET micelles. **(B)** Schematic for separately diluting

donor-only or acceptor-only micelles and then mixing the diluted samples (sepFRET). **(C)** Normalized FRET efficiency of FRET micelles and sepFRET micelles right after mixing donor and acceptor (0 hr). **(D)** Time course of normalized FRET efficiency since mixing donor and acceptor micelles at 0.0125% MEGA-10 for FRET micelles and sepFRET micelles. **(E)** Time course of normalized FRET efficiency since mixing donor and acceptor micelles at 0.1% MEGA-10 for FRET micelles and sepFRET micelles. **(F)** Normalized FRET efficiency of FRET micelles and sepFRET micelles two days after mixing donor and acceptor (48 hrs).

When donor and acceptor micelles were mixed at 10% MEGA-10 a low energy transfer was measured (~0.05 normalized FRET efficiency). Yet when FRET micelles were diluted to 0.2% MEGA-10 or lower, a marked increase in FRET efficiency was observed (**Figure 3.4C**, **Figure B6**). Further, sepFRET micelles behaved similar to FRET micelles when donors and acceptors were mixed right after dilution (sepFRET-0h), indicating that the initial intermediates generated upon dilution undergo rapid lipid mixing during self-assembly. However, after one hour or more of independent self-assembly of donor and acceptor samples (sepFRET >1hr) no major increase in FRET efficiency could be seen below 0.1% MEGA-10, indicating that the later intermediates in region (iii) did not undergo rapid lipid mixing events. Indeed, sepFRET samples allowed to assemble for one or more hours maintained low FRET efficiency for 48 hours which is consistent with the expected low lipid exchange rate of assembled liposomes (**Figure 3.4D**). However, at 0.1% MEGA-10, all sepFRET groups converged to similar FRET efficiency levels as that of FRET micelles (**Figure 3.4E**) which was not observed for lower concentrations of MEGA-10 (**Figure 3.4F**). The high rate of lipid exchange at 0.1% MEGA-10 after 24 hrs of sepFRET assembly suggested that the large species formed at 0.1% MEGA-10 were in a state of dynamic equilibrium likely due to the coexistence of mixed micelles and bilayers.

We next used cryo-TEM to visualize intermediates that allowed for assembly of large liposomes. We diluted mixed micelles with 10 mM HEPES and 150 mM NaCl (HEPES was used instead of PBS as phosphates can interfere with cryo-TEM imaging) to 0.1% MEGA-10 and processed samples for cryo-TEM analysis after 5 minutes, 2 hours, 5 hours, or 24 hours of incubation at 25 °C. Upon dilution, the sample started as small (~15 nm) spherical micelles and disc-like or worm-like structures (**Figure 3.5A**, **Figure B7A**) that accumulated at the carbon region of the TEM grid likely due to their small size and low concentration.[35] These small micellar

structures coalesced to larger (>100 nm) bilayer discs and liposomes within 1-2 hours (**Figure 3.5B**, **Figure B7B**). At 5 hours, smaller discs were no longer seen, and the sample was composed of primarily large (>300 nm) discs and liposomes (**Figure 3.5C**, **Figure B7C**). Finally, after 24 hours, only large liposomal species could be seen as well as micellar aggregates[36] (**Figure 3.5D**, **Figure B7D**). The presence of these micellar aggregates in cryoTEM micrographs confirmed the expectation of mixed micelle coexistence with bilayers.

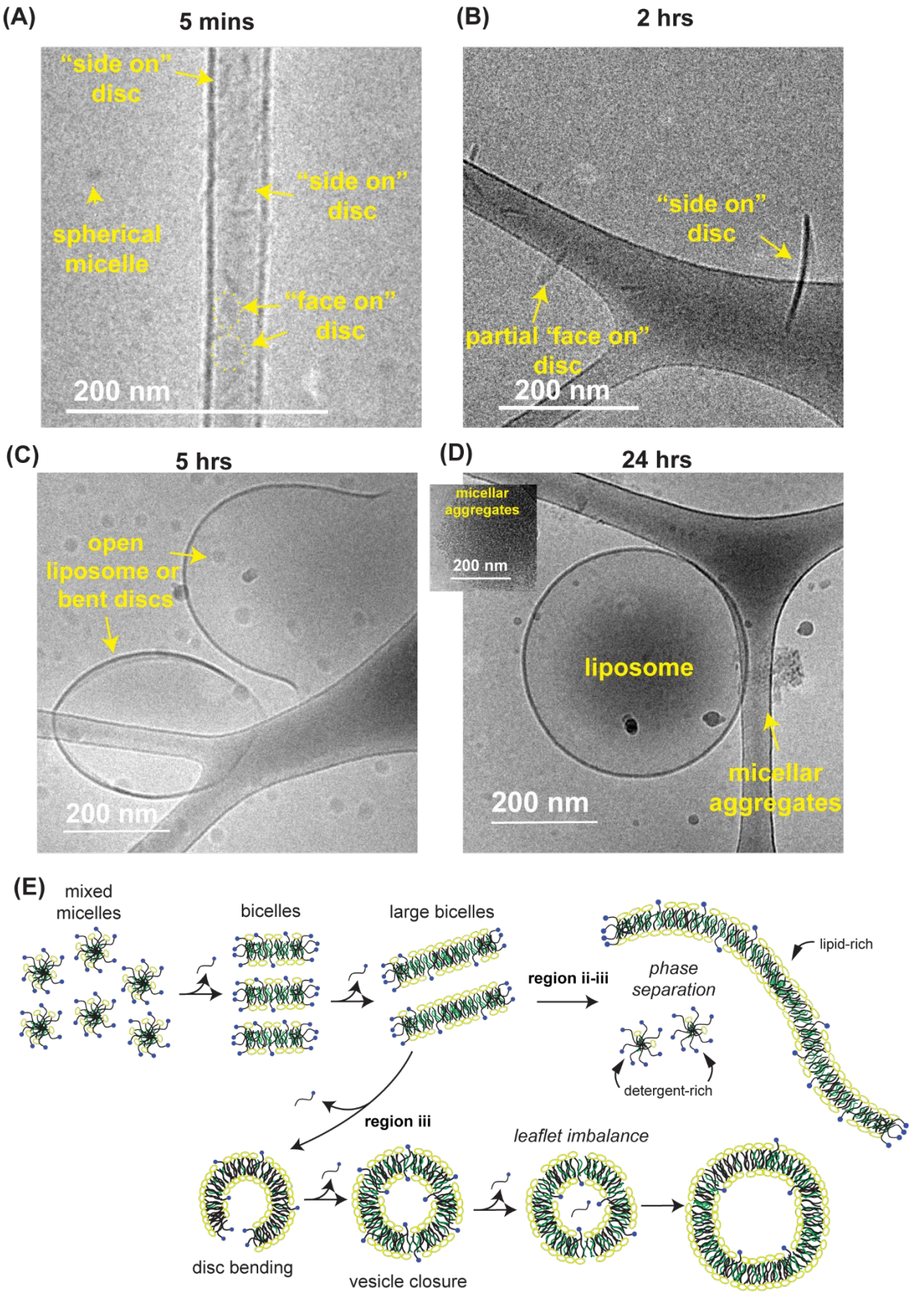
(A)
5 mins
"side on" disc
"side on" disc
spherical micelle
"face on" disc
200 nm
(B)
2 hrs
"side on" disc
partial "face on" disc
200 nm
(C)
5 hrs
open liposome or bent discs
200 nm
(D)
24 hrs
micellar aggregates
200 nm
liposome
micellar aggregates
200 nm
(E)
mixed micelles
bicelles
large bicelles
region ii-iii
phase separation
lipid-rich
detergent-rich
region iii
leaflet imbalance
disc bending
vesicle closure

Figure 3.5. Cryo-TEM micrographs of particles incubated in 0.1% MEGA-10 reveal formation of large disc assemblies and coexistence of micelles with fully assembled bilayer vesicles. **(A-D)** Cryo-TEM micrograph of 10 mg/mL 6:3:1 DSPC:Chol:POPG sample in 10% MEGA-10 rapidly diluted to 0.1% MEGA-10 with 10 mM HEPES 150 mM NaCl and frozen 5 minutes, 2 hours, 5 hours and 24 hours after dilution, respectively. **(E)** Schematic for the two proposed main driving mechanism of particle coalescence and growth upon mixed micelle dilution.

Based on these results, we proposed two distinct mechanisms for particle coalescence and growth (**Figure 3.5E**). When diluted to the interface between region ii and region iii where bilayers and mixed micelles may coexist (~0.1% MEGA-10, see **Figure 3.1B**), bicelles (surfactant-stabilized bilayer nanodiscs) initially form. As further detergent partitions into the aqueous phase, bicelle fusion is driven, as less detergent is available to stabilize the outer edges of discoidal assemblies. However, when the detergent monomers begin to equilibrate with the aqueous phase, there is still sufficient detergent incorporated into the bilayers to prevent complete stable vesicle closure. Instead, the detergent partitions into lipid-rich and detergent-rich phases driven by the curvature preference of the surfactant molecules. As large bilayer discs start to form, less detergent is freed from the discoidal rims upon further fusion and charge repulsion between particles increases, enabling the system to reach a terminal size.

If vesicles are formed prior to detergent equilibration with the aqueous phase, detergents released into the internal aqueous volume of the liposome cannot freely diffuse to the external volume, whereas outer leaflet detergent molecules are continuously depleted, leading to an imbalance on the required number of molecules between the inner and outer leaflet (**Figure 3.5E**).[26,37] These imbalances are known to promote fusion or vesicle rupture, and its effect becomes more pronounced as the size of the vesicle grows.[37] This leaflet imbalance-driven particle coalescence is likely the primary cause for liposome fusion when diluted to lower detergent concentrations of region iii due to rapid detergent depletion from bilayers (i.e., lack of detergent-stabilized bicelles) and lack of mixed micelle coexistence.[16] Under this scenario, the final liposome size is dictated by the number of fusion events required to normalize the leaflet imbalances such that higher dilutions increase the rate of detergent partitioning into the aqueous phase prior to vesicle closure and subsequently, smaller liposome size.

3.3.5 Purified liposomes maintain expected biophysical interactions with macrophages

Different-sized nanoparticles have different biophysical interactions with cells. Thus, we next wanted to validate that the method for liposome assembly presented here could be used to probe such interactions. While conflicting results have been presented,[38] most studies have indicated that macrophages preferentially uptake larger liposomes *in vitro*.[39–42] Unlike most normal cells, macrophages are known as professional phagocytes which enable them to efficiently uptake particles with diameters above 200 nm.[43,44] However, prior work has failed to present a clear relationship between liposome size and uptake, potentially due to the use of thin film hydration followed by extrusion, where it is difficult to control liposome size and lamellarity. Given that the method presented here enabled the synthesis of large and monodisperse unilamellar liposomes, we decided to evaluate the effect of liposome size on macrophage uptake.

To investigate this trend, we first generated a library of varied-sized liposomes, comprised of 14 samples with sizes spanning from ~100 nm diam. to ~1 μm, all with low polydispersity– this size series demonstrates the high degree of control that this process provides over vesicle generation (**Figure 3.6A**). We then dosed RAW 264.7 macrophages with equal mass concentrations of each particle (i.e., an equal amount of total fluorescence lipids). As equal mass of lipids were dosed, increasing the particle size effectively reduced the number of liposomes per well, but maintained the total particle surface area as liposomes are 2D assemblies. After 4 hrs or 24 hrs of incubation, the remaining liposome signal in the supernatant and liposome signal associated with macrophages were measured to determine a percentage of vesicle uptake (**Figure B8**). As expected, macrophages were found to have increased uptake of large liposomes (**Figure 3.6A**). Importantly, however, through our assembly method, we could see that there was a clear linear relationship between liposome size and liposome uptake at either 4 or 24 hours of incubation (**Figure 3.6B**). Thus, the generation of monodisperse liposomes allows biological interactions with cells to be more clearly assessed.

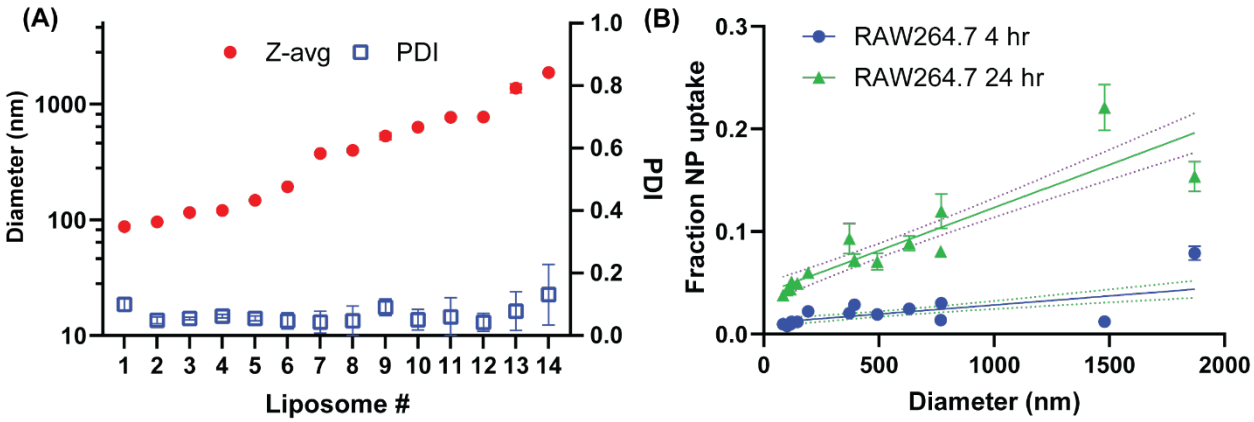

Figure 3.6. Controlled assembly of liposomes reveals a linear size-dependence effect on NP uptake in macrophages *in vitro*. **(A)** Intensity weighted size (Z-avg) and PDI of liposomes generated for this experiment. **(B)** NP uptake on RAW264.7 macrophage cells after 4 or 24 hours of incubation with NPs. Dashed lines indicate 95% confidence interval of linear fit.

3.4 Conclusions

Liposomes are important delivery vehicles for both the current and next generation of therapeutics. Here we show that, through the rational disassembly of mixed micelles, we can precisely control the size of charged liposomes.[26] Although previous work using glycocholate and egg phosphatidylcholine similarly found that dilution of micellar mixtures could control liposome size, these studies only achieved size ranges of only ~50-100 nm.[27,45]

Through a combined assessment of the assembly kinetics, lipid composition effects, and lipid exchange rates at each detergent concentration, we were able to propose qualitative models to describe the size control, which has been lacking in the literature.[26] The models combine and build upon prior work which has described phase separation at the transition between mixed micelles and bilayer,[25,26] the potential for detergent entrapment in the inner core of vesicles upon disc closure,[25] and how leaflet imbalances induce bilayer fusion.[37]

Furthermore, while our results contradict the idea that the rate of detergent removal either via controlled dilution or controlled dialysis governs final liposome size,[7,18,46,47] the rate of detergent removal likely alters the residence time of the lipidic mixture at each concentration of detergent, leading to the control in liposome size observed previously. Future studies are also needed to validate the models presented here as we are unable to make conclusions on the system reaching full chemical equilibrium.

Taken together, the findings presented here demonstrate a promising new method of detergent-aided assembly of monodisperse liposomes with controlled via scalable techniques. The benefits of generating particles across a wide range of sizes and with little variance open the doors to accurate investigations of the effect of liposome size in biological systems as well as highly implementable manufacturing approaches for nanotherapeutics with a new level of precision. Further, the techniques and insights presented may facilitate the generation of new and more controlled lipid-based assemblies.

3.5 References

(1) Barenholz, Y. (Chezy). Doxil® — The First FDA-Approved Nano-Drug: Lessons Learned. *Journal of Controlled Release* **2012**, *160* (2), 117–134. https://doi.org/10.1016/j.jconrel.2012.03.020.

(2) Hou, X.; Zaks, T.; Langer, R.; Dong, Y. Lipid Nanoparticles for MRNA Delivery. *Nat Rev Mater* **2021**, *6* (12), 1078–1094. https://doi.org/10.1038/s41578-021-00358-0.

(3) Mitchell, M. J.; Billingsley, M. M.; Haley, R. M.; Wechsler, M. E.; Peppas, N. A.; Langer, R. Engineering Precision Nanoparticles for Drug Delivery. *Nat Rev Drug Discov* **2021**, *20* (2), 101–124. https://doi.org/10.1038/s41573-020-0090-8.

(4) Xu, L.; Wang, X.; Liu, Y.; Yang, G.; Falconer, R. J.; Zhao, C.-X. Lipid Nanoparticles for Drug Delivery. *Adv Nanobiomed Res* **2022**, *2* (2), 2100109. https://doi.org/10.1002/anbr.202100109.

(5) Liu, P.; Chen, G.; Zhang, J. A Review of Liposomes as a Drug Delivery System: Current Status of Approved Products, Regulatory Environments, and Future Perspectives. *Molecules* **2022**, *27* (4), 1372. https://doi.org/10.3390/molecules27041372.

(6) Akbarzadeh, A.; Rezaei-Sadabady, R.; Davaran, S.; Joo, S. W.; Zarghami, N.; Hanifehpour, Y.; Samiei, M.; Kouhi, M.; Nejati-Koshki, K. Liposome: Classification, Preparation, and Applications. *Nanoscale Res Lett* **2013**, *8* (1), 102. https://doi.org/10.1186/1556-276X-8-102.

(7) Schwendener, R. A.; Asanger, M.; Weder, H. G. N-Alkyl-Glucosides as Detergents for the Preparation of Highly Homogeneous Bilayer Liposomes of Variable Sizes (60–240 Nm φ) Applying Defined Rates of Detergent Removal by Dialysis. *Biochem Biophys Res Commun* **1981**, *100* (3), 1055–1062. https://doi.org/10.1016/0006-291X(81)91930-6.

(8) Akbarzadeh, A.; Rezaei-Sadabady, R.; Davaran, S.; Joo, S. W.; Zarghami, N.; Hanifehpour, Y.; Samiei, M.; Kouhi, M.; Nejati-Koshki, K. Liposome: Classification, Preparation, and Applications. *Nanoscale Res Lett* **2013**, *8* (1), 102. https://doi.org/10.1186/1556-276X-8-102.

(9) Crouch, C.; Bost, M.; Kim, T.; Green, B.; Arbuckle, D.; Grossman, C.; Howard, K. Optimization of Detergent-Mediated Reconstitution of Influenza A M2 Protein into Proteoliposomes. *Membranes (Basel)* **2018**, *8* (4), 103. https://doi.org/10.3390/membranes8040103.

(10) Jeffs, L. B.; Palmer, L. R.; Ambegia, E. G.; Giesbrecht, C.; Ewanick, S.; MacLachlan, I. A Scalable, Extrusion-Free Method for Efficient Liposomal Encapsulation of Plasmid DNA. *Pharm Res* **2005**, *22* (3), 362–372. https://doi.org/10.1007/s11095-004-1873-z.

(11) Pires, I. S.; Palmer, A. F. Selective Protein Purification via Tangential Flow Filtration – Exploiting Protein-Protein Complexes to Enable Size-Based Separations. *J Memb Sci* **2021**, *618*, 118712. https://doi.org/10.1016/j.memsci.2020.118712.

(12) Pires, I. S.; Ni, K.; Melo, M. B.; Li, N.; Ben-Akiva, E.; Maiorino, L.; Dye, J.; Rodrigues, K. A.; Yun, D.; Kim, B.; Hosn, R. R.; Hammond, P. T.; Irvine, D. J. Controlled Lipid Self-Assembly for Scalable Manufacturing of next-Generation Immune Stimulating Complexes. *Chemical Engineering Journal* **2023**, *464*, 142664. https://doi.org/10.1016/j.cej.2023.142664.

(13) Stewart, J. C. M. Colorimetric Determination of Phospholipids with Ammonium Ferrothiocyanate. *Anal Biochem* **1980**, *104* (1), 10–14. https://doi.org/10.1016/0003-2697(80)90269-9.

(14) Edidin, M. Fluorescence Resonance Energy Transfer: Techniques for Measuring Molecular Conformation and Molecular Proximity. *Curr Protoc Immunol* **2003**, *57* (1). https://doi.org/10.1002/0471142735.im1810s52.

(15) Loudet, A.; Burgess, K. BODIPY Dyes and Their Derivatives: Syntheses and Spectroscopic Properties. *Chem Rev* **2007**, *107* (11), 4891–4932. https://doi.org/10.1021/cr078381n.

(16) Ollivon, M.; Lesieur, S.; Grabielle-Madelmont, C.; Paternostre, M. Vesicle Reconstitution from Lipid–Detergent Mixed Micelles. *Biochimica et Biophysica Acta (BBA) - Biomembranes* **2000**, *1508* (1–2), 34–50. https://doi.org/10.1016/S0304-4157(00)00006-X.

(17) Has, C.; Pan, S. Vesicle Formation Mechanisms: An Overview. *J Liposome Res* **2021**, *31* (1), 90–111. https://doi.org/10.1080/08982104.2020.1730401.

(18) Milsmann, M. H. W.; Schwendener, R. A.; Weder, H.-G. The Preparation of Large Single Bilayer Liposomes by a Fast and Controlled Dialysis. *Biochimica et Biophysica Acta (BBA) - Biomembranes* **1978**, *512* (1), 147–155. https://doi.org/10.1016/0005-2736(78)90225-0.

(19) Barberio, A. E.; Smith, S. G.; Pires, I. S.; Iyer, S.; Reinhardt, F.; Melo, M. B.; Suh, H.; Weinberg, R. A.; Irvine, D. J.; Hammond, P. T. <scp>Layer-by-layer</Scp> Interleukin-12 Nanoparticles Drive a Safe and Effective Response in Ovarian Tumors. *Bioeng Transl Med* **2022**. https://doi.org/10.1002/btm2.10453.

(20) Barberio, A. E.; Smith, S. G.; Correa, S.; Nguyen, C.; Nhan, B.; Melo, M.; Tokatlian, T.; Suh, H.; Irvine, D. J.; Hammond, P. T. Cancer Cell Coating Nanoparticles for Optimal Tumor-Specific Cytokine Delivery. *ACS Nano* **2020**, *14* (9), 11238–11253. https://doi.org/10.1021/acsnano.0c03109.

(21) Correa, S.; Choi, K. Y.; Dreaden, E. C.; Renggli, K.; Shi, A.; Gu, L.; Shopsowitz, K. E.; Quadir, M. A.; Ben-Akiva, E.; Hammond, P. T. Highly Scalable, Closed-Loop Synthesis of Drug-Loaded, Layer-by-Layer Nanoparticles. *Adv Funct Mater* **2016**, *26* (7), 991–1003. https://doi.org/10.1002/adfm.201504385.

(22) Østrem, R. G.; Parhamifar, L.; Pourhassan, H.; Clergeaud, G.; Nielsen, O. L.; Kjær, A.; Hansen, A. E.; Andresen, T. L. Secretory Phospholipase A 2 Responsive Liposomes Exhibit a Potent Anti-Neoplastic Effect in Vitro , but Induce Unforeseen Severe Toxicity in Vivo. *Journal of Controlled Release* **2017**, *262*, 212–221. https://doi.org/10.1016/j.jconrel.2017.07.031.

(23) Eliaz, R. E.; Szoka, F. C. Liposome-Encapsulated Doxorubicin Targeted to CD44: A Strategy to Kill CD44-Overexpressing Tumor Cells. *Cancer Res* **2001**, *61* (6), 2592–2601.

(24) Walter, A.; Suchy, S. E.; Vinson, P. K. Solubility Properties of the Alkylmethylglucamide Surfactants. *Biochimica et Biophysica Acta (BBA) - Biomembranes* **1990**, *1029* (1), 67–74. https://doi.org/10.1016/0005-2736(90)90437-S.

(25) Lichtenberg, D.; Ahyayauch, H.; Goñi, F. M. The Mechanism of Detergent Solubilization of Lipid Bilayers. *Biophys J* **2013**, *105* (2), 289–299. https://doi.org/10.1016/j.bpj.2013.06.007.

(26) Ollivon, M.; Lesieur, S.; Grabielle-Madelmont, C.; Paternostre, M. Vesicle Reconstitution from Lipid–Detergent Mixed Micelles. *Biochimica et Biophysica Acta (BBA) - Biomembranes* **2000**, *1508* (1–2), 34–50. https://doi.org/10.1016/S0304-4157(00)00006-X.

(27) Schurtenberger, P.; Mazer, N.; Kaenzig, W. Micelle to Vesicle Transition in Aqueous Solutions of Bile Salt and Lecithin. *J Phys Chem* **1985**, *89* (6), 1042–1049. https://doi.org/10.1021/j100252a031.

(28) Stefan, M. I.; Le Novère, N. Cooperative Binding. *PLoS Comput Biol* **2013**, *9* (6), e1003106. https://doi.org/10.1371/journal.pcbi.1003106.

(29) O'Brien, R. W.; White, L. R. Electrophoretic Mobility of a Spherical Colloidal Particle. *Journal of the Chemical Society, Faraday Transactions 2* **1978**, *74*, 1607. https://doi.org/10.1039/f29787401607.

(30) Almgren, M.; Edwards, K.; Karlsson, G. Cryo Transmission Electron Microscopy of Liposomes and Related Structures. *Colloids Surf A Physicochem Eng Asp* **2000**, *174* (1–2), 3–21. https://doi.org/10.1016/S0927-7757(00)00516-1.

(31) Poojari, C. S.; Scherer, K. C.; Hub, J. S. Free Energies of Membrane Stalk Formation from a Lipidomics Perspective. *Nat Commun* **2021**, *12* (1), 6594. https://doi.org/10.1038/s41467-021-26924-2.

(32) Chernomordik, L. v.; Kozlov, M. M. Protein-Lipid Interplay in Fusion and Fission of Biological Membranes. *Annu Rev Biochem* **2003**, *72* (1), 175–207. https://doi.org/10.1146/annurev.biochem.72.121801.161504.

(33) Shoemaker, D. G.; Nichols, J. W. Interaction of Lysophospholipid/Taurodeoxycholate Submicellar Aggregates with Phospholipid Bilayers. *Biochemistry* **1992**, *31* (13), 3414–3420. https://doi.org/10.1021/bi00128a016.

(34) Fullington, D. A.; Shoemaker, D. G.; Nichols, J. W. Characterization of Phospholipid Transfer between Mixed Phospholipid-Bile Salt Micelles. *Biochemistry* **1990**, *29* (4), 879–886. https://doi.org/10.1021/bi00456a005.

(35) Tonggu, L.; Wang, L. Cryo-EM Sample Preparation Method for Extremely Low Concentration Liposomes. *Ultramicroscopy* **2020**, *208*, 112849. https://doi.org/10.1016/j.ultramic.2019.112849.

(36) Stuart, M. C. A.; Boekema, E. J. Two Distinct Mechanisms of Vesicle-to-Micelle and Micelle-to-Vesicle Transition Are Mediated by the Packing Parameter of Phospholipid–Detergent Systems. *Biochimica et Biophysica Acta (BBA) - Biomembranes* **2007**, *1768* (11), 2681–2689. https://doi.org/10.1016/j.bbamem.2007.06.024.

(37) Devaux, P. F. Is Lipid Translocation Involved during Endo- and Exocytosis? *Biochimie* **2000**, *82* (5), 497–509. https://doi.org/10.1016/S0300-9084(00)00209-1.

(38) Allen, T. M.; Austin, G. A.; Chonn, A.; Lin, L.; Lee, K. C. Uptake of Liposomes by Cultured Mouse Bone Marrow Macrophages: Influence of Liposome Composition and Size. *Biochimica et Biophysica Acta (BBA) - Biomembranes* **1991**, *1061* (1), 56–64. https://doi.org/10.1016/0005-2736(91)90268-D.

(39) Kelly, C.; Jefferies, C.; Cryan, S.-A. Targeted Liposomal Drug Delivery to Monocytes and Macrophages. *J Drug Deliv* **2011**, *2011*, 1–11. https://doi.org/10.1155/2011/727241.

(40) Epstein-Barash, H.; Gutman, D.; Markovsky, E.; Mishan-Eisenberg, G.; Koroukhov, N.; Szebeni, J.; Golomb, G. Physicochemical Parameters Affecting Liposomal Bisphosphonates Bioactivity for Restenosis Therapy: Internalization, Cell Inhibition, Activation of Cytokines and Complement, and Mechanism of Cell Death. *Journal of Controlled Release* **2010**, *146* (2), 182–195. https://doi.org/10.1016/j.jconrel.2010.03.011.

(41) Chono, S.; Tanino, T.; Seki, T.; Morimoto, K. Uptake Characteristics of Liposomes by Rat Alveolar Macrophages: Influence of Particle Size and Surface Mannose Modification. *Journal of Pharmacy and Pharmacology* **2010**, *59* (1), 75–80. https://doi.org/10.1211/jpp.59.1.0010.

(42) Chono, S.; Tanino, T.; Seki, T.; Morimoto, K. Influence of Particle Size on Drug Delivery to Rat Alveolar Macrophages Following Pulmonary Administration of Ciprofloxacin Incorporated into Liposomes. *J Drug Target* **2006**, *14* (8), 557–566. https://doi.org/10.1080/10611860600834375.

(43) Petithory, T.; Pieuchot, L.; Josien, L.; Ponche, A.; Anselme, K.; Vonna, L. Size-Dependent Internalization Efficiency of Macrophages from Adsorbed Nanoparticle-Based Monolayers. *Nanomaterials* **2021**, *11* (8), 1963. https://doi.org/10.3390/nano11081963.

(44) Aderem, A.; Underhill, D. M. MECHANISMS OF PHAGOCYTOSIS IN MACROPHAGES. *Annu Rev Immunol* **1999**, *17* (1), 593–623. https://doi.org/10.1146/annurev.immunol.17.1.593.

(45) Mazer, N. A.; Benedek, G. B.; Carey, M. C. Quasielastic Light-Scattering Studies of Aqueous Biliary Lipid Systems. Mixed Micelle Formation in Bile Salt-Lecithin Solutions. *Biochemistry* **1980**, *19* (4), 601–615. https://doi.org/10.1021/bi00545a001.

(46) Jiskoot, W.; Teerlink, T.; Beuvery, E. C.; Crommelin, D. J. A. Preparation of Liposomes via Detergent Removal from Mixed Micelles by Dilution. *Pharm Weekbl Sci* **1986**, *8* (5), 259–265. https://doi.org/10.1007/BF01960070.

(47) Seras, M.; Ollivon, M.; Edwards, K.; Lesieur, S. Reconstitution of Non-Ionic Monoalkyl Amphiphile-Cholesterol Vesicles by Dilution of Lipids-Octylglucoside Mixed Micelles. *Chem Phys Lipids* **1993**, *66* (1–2), 93–109. https://doi.org/10.1016/0009-3084(93)90035-2.

CHAPTER 4

Charge-stabilized nanodiscs as a new class of lipid nanoparticles

4.1 Introduction

Nanomedicine is a promising field that employs nanoscale materials for disease diagnosis and treatment.[1] Nanoparticles (NP) can serve as carriers for insoluble drugs or as therapeutic delivery vehicles for substances that have inherently poor pharmacokinetic properties. Further, NPs can passively accumulate in certain tissues with high vascular permeability such as tumors, lymph nodes, sites of infection, or atherosclerosis.[2] These effects may be enhanced through rational functionalization of NPs with targeting motifs. Accordingly, NPs serve to improve the effectiveness of a drug while also potentially mitigating side effects by accumulating in the disease site while sparing healthy tissue.

The size, shape, rigidity, and surface chemistry of NPs are all key parameters that regulate their pharmacokinetics, biodistribution, tissue penetration, and cellular uptake.[3–6] In the setting of cancer treatment, a major limitation of NPs is their poor tumor penetration as particles tend to accumulate perivascularly just outside tumor vessels with limited transport deeper into tumors.[5,7] To overcome this issue, recent studies have indicated that sub-100 nm particles with high aspect ratio morphologies can significantly improve tumor penetration.[5,7–11] Yet the most widely studied cancer nanomedicines have consisted of spherical nanoparticles.[5] In the case of lipid-based nanocarriers, this is in part due to the difficulties in controlling the self-assembly of lipids into non-spherical shapes. Some approaches to alter lipid-based nanoparticles from spherical to discoidal have included the addition of lipid-polymer conjugates, proteins, synthetic amphiphilic polymers, and mixtures of surfactant tail lengths.[8,12–15] For example, we recently demonstrated that PEGylated lipid nanodics (LNDs) have significantly greater tumor penetration and accumulation *in vivo* compared to state-of-the-art spherical liposomes.[8] However, the use of polymer conjugates such as polyethylene glycol (PEG) or other additives to induce disc formation may introduce additional challenges such as increased immunogenicity, complement activation, or potential for allergic or hypersensitivity reactions.[15–18]

In this study, we employed a bottom-up approach to generate a new class of lipid nanodiscs starting from detergent micelles. While dilution of lipid/detergent mixture (mixed micelles) is a commonly used method to form liposomes[19], we discovered that the lipid head group charge could

stabilize lipid nanodisc structures depending on the buffer ionic strength or the lipid headgroup charge valency. We show that using tangential flow filtration (TFF), a scalable size-based separations technique, we can remove excess detergent to yield discoidal lipid nanoparticles which we termed charge-stabilized nanodiscs (CNDs).[20]We validate that CNDs have better tumor accumulation properties than liposomes. Further, we exploit the increased NP surface area of discoidal assemblies to modify CNDs with the layer-by-layer (LbL) technique to further improve their tumor targeting properties in a metastatic model of ovarian cancer.

4.2 Methods

4.2.1 Materials

1,2-distearoyl-sn-glycero-3-phosphocholine (DSPC), Cholesterol, 1-palmitoyl-2-oleoyl-sn-glycero-3-phospho-(1'-rac-glycerol) (sodium salt) (POPG), 1,2-dioleoyl-sn-glycero-3-phosphoethanolamine-N-(glutaryl) (sodium salt) (DOPE-glutaryl), 1,2-dioleoyl-sn-glycero-3-phosphoethanolamine-N-dibenzocyclooctyl (DOPE-DBCO), 1,2-distearoyl-sn-glycero-3-phospho-(1'-rac-glycerol) (DSPG), and 1,2-distearoyl-sn-glycero-3-phosphoethanolamine-N-(Cyanine 5) (DSPE-cy5) were purchased from Avanti Polar Lipids. Poly-L-arginine (PLR) with a molecular weight (MW) of 9.6 kDa and poly-L-glutamic acid (PLE) with a MW of 15 kDa were purchased from Alamanda Polymers. N-decanoyl-N-methylglucamine (MEGA-10) and n-octyl-β-d-glucoside (octylglucoside) were purchased from Sigma Aldrich. For fluorescence measurements with lisCND samples, borondipyrromethene 630/650 (BDP 630/650) azide (Lumiprobe) were reacted with DOPE-DBCO in chloroform to generate DOPE-630/650. Successful conjugation was validated via thin-layer chromatography which indicated <1% free dye.

4.2.2 Generation of detergent/lipid mixture

Lipid stock solutions were made in chloroform and them measured into glass vials and left drying on a desiccator overnight. For solubilization in MEGA-10 micelles, a 10% MEGA-10 solution was made in deionized water. The 10% MEGA-10 solution was then added to the dried lipids and left in a water bath sonicator at 50 to 60 °C until all lipids were solubilized. The lipid/detergent mixture was allowed to equilibrate at room temperature prior to dilution.

4.2.3 Synthesis of nanoparticles via dilution

The lipid/detergent micelles were diluted by rapidly adding buffer to the micelles to reach the target detergent concentration. The samples were then allowed to equilibrate at 25 °C.

4.2.4 Purification via TFF

Generally, 5 mg of the lipid nanoparticle mixtures were diluted to the target MEGA-10 concentration and left to self-assemble overnight. Then samples were diluted to a minimum of 0.02% MEGA-10 to ensure minimal effect of the detergent on the NPs. Samples were then placed on a KrosFlo KR2i TFF system (Repligen) system using either a 50 kDa molecular weight cutoff (MWCO) mPES membrane with a surface area of 75 cm^2 (D02-E050-10-N) for particles <100 nm or a 100 kDa MWCO mPES membrane with a surface area of 115 cm^2 for particles >100 nm (D02-E100-05-N). Samples underwent 10 diafiltration volumes against the buffer used for their self-assembly.

4.2.5 Layer by Layer (LbL) deposition

LbL-lisCND particles were generated by mixing lisCND particles at 0.5 mg/mL lipids with 5 weight equivalents (wt. eq.) of polymers in 10 mM HEPES. After polymer mixing, particles were allowed to incubate on ice for at least 30 minutes before TFF purification as described previously.[20] LbL-CND particles were generated by first buffer exchanging the sample samples into 50 mM HEPES and 40 mM NaCl via TFF. Then particles at 0.5 mg/mL were mixed with 5 wt. eq. of PLR in deionized water. After PLR deposition, samples were incubated for 30 minutes on ice and then purified by TFF into deionized water. After purification, PLR-coated CNDs at 0.5 mg/mL lipids were mixed with 5 wt. eq. PLE, incubated for 30 min on ice, and then purified by TFF into deionized water. Control LbL-liposomes for either lisCND or CND were generated using the same conditions. PLR purification was performed on a 30 kDa mPES membrane with a surface area of 20 cm^2 (C02-E030-05-N, Repligen) while PLE purification was performed on a 50 kDa mPES membrane with a surface area of 75 cm^2 (D02-E050-10-N, Repligen). Purification was completed once samples underwent 10 diafiltration volumes. Fluorescently-labeled lisCNDs contained 0.2 mol% of DOPE-630/650 while CNDs contained 1 mol% of DSPE-cy5.

4.2.6 Characterization of particle preparations

Dynamic light scattering (DLS) and zeta potential measurements were made on a Zetasizer Nano ZSP (Malvern). Nanoparticle micrographs were acquired using Transmission Electron Microscopy (TEM) on a JEOL 2100F microscope (200 kV). For cryo-TEM, particles were buffer exchanged into deionized water via either dialysis or TFF. The microscopes were with a magnification range of 10,000-60,000X. Cryo-TEM micrographs were analyzed on ImageJ to measure particles diameter. Particles with 1 mol% DSPE-cy5 were characterized on a Wyatt Dyna Pro Plate Reader.

4.2.7 Cell Culture

OV2944-HM-1 cells (female origin) were acquired through Riken BRC and were cultured in α-MEM (Gibco) while MC38 (female origin, a gift from the laboratory of Karl Dane Wittrup) were cultured in DMEM (Corning). Cell media was also supplemented with 10% FBS and penicillin/streptomycin with cells incubated in a 5% CO2 humidified atmosphere at 37 °C. All cell lines were murine pathogen tested and confirmed mycoplasma negative by Lonza MycoAlert™ Mycoplasma Detection Kit. Passage number was maintained below 20.

4.2.8 In vitro cellular association

The day before dosing, HM-1 cells were plated on a tissue-culture 96-well plate at a density of 50k cells per well. The next day, wells were dosed with NPs to 0.05 mg/mL and left for the target incubation time (4 hrs or 24 hrs). For analysis of association, the supernatant was removed from the well and diluted 10X with DMSO. Cells were then washed three times with PBS then dissolved with DMSO. Fluorescence of NPs associated with cells was then normalized to supernatant fluorescence. The relative fluorescence of each formulation was then compared to an unlayered liposome control containing the same fluorophore. For confocal imaging, 8-well chambered coverglass (Nunc Lab-Tek II, Thermo Scientific) were treated with rat tail collagen type I (Sigma-Aldrich) per manufacturer's instructions. HM-1 cells were plated onto wells at a density of 10k/well and left to adhere overnight prior to NP treatment. After the desired incubation time with NPs, cells were washed 3x with PBS. After washing, cells were fixed in 4% paraformaldehyde for 10 minutes then washed (3x with PBS) and stained with wheat germ agglutinin (WGA) conjugated to Alexa Fluor488 (Invitrogen) and hoechst 33342 (Thermo Scientific) following manufacturer instructions. Images were analyzed using ImageJ. Slides were imaged on a Olympus FV1200 Laser Scanning Confocal Microscope.

4.2.9 Mice

C57Bl/6 and B6C3F1 mice were purchased from Jackson Laboratories. Female mice were used between 8-12 weeks of age unless otherwise noted with weights of 20-25 g. All animal work was conducted under the approval of the Massachusetts Institute of Technology Division of Comparative Medicine (Committee on Animal Care protocol number 2303000488) in accordance with federal, state, and local guidelines. Subcutaneous, intravenous, and intraperitoneal injections were performed with volumes of 100, 100, and 200 µL, respectively. Mice were randomly divided

prior to treatments. Before mouse treatments or imaging, mice were anesthetized with 2-3% isoflurane.

4.2.10 Subcutaneous tumor model

C57Bl/6 mice were implanted with subcutaneous MC38 tumors by injecting 10^6 cells into the right flank. One week after tumor inoculation, mice were injected intravenously via the tail vein with NPs containing 1 mol% DSPE-cyanine5 (1 nmol dye injected per mouse). *In vivo* tumor radiant efficiency was measured on an In Vivo Imaging System Spectrum CT (IVIS, Perkin Elmer) and serum was collected via cheek bleeds. After the final timepoint (24 hrs), mice were euthanized and the major NP clearance organs – liver and spleen – as well as tumor were removed and had their radiant efficiency measured *ex vivo* by IVIS. Data were analyzed using Living Image software. Background fluorescence measurements were made for each organ based on signal from mice treated with PBS. Recovered fluorescence efficiency was calculated as described previously.[21]

4.2.11 Intraperitoneal ovarian cancer model

B6C3F1 mice were inoculated with firefly luciferase-expressing OV2944-HM1 (HM-1-luc) cells through intraperitoneal (i.p.) injection of 10^6 cells in PBS. Two weeks after tumor inoculation, mice were injected with 0.75 nmol of 1 mol% DSPE-cy5 NPs. Analysis was done similar to subcutaneous tumor model with the exception that peritoneal radiant efficiency was measured instead of tumor fluorescence. For correlation analysis, the weight-normalized bioluminescence flux (p/s/g) and radiant efficiency ([p/s] / [μW/cm²]/g) for each organ (excluding main tumor) were analyzed on Graphpad Prism 9 for their correlation via the Pearson's coefficient.

4.2.12 Statistical Analysis

GraphPad PRISM 10 was used to perform statistical analyses. Comparisons between two groups was performed via unpaired t-tests. For multiple groups or multiple variable analysis, one-way, or two-way ANOVAs were used with Tukey's posthoc correction.

4.3 Results and Discussion

4.3.1 Monovalent lipids fail to generate charged nanodiscs stable in physiological ionic strength solutions.

Upon dilution of mixed micelles (lipid/detergent mixtures) to below the detergent critical micelle concentration (CMC), liposomes are generally formed.[19] Given that liposome formation from mixed micelles occurs through discoidal intermediates[22,23] (**Figure 4.1A**), we theorized that we

could stabilize these intermediates by increasing electrostatic repulsion between lipid assemblies, and thereby prevent particle disc coalescence into liposomes. To evaluate this idea, we used buffers with decreasing ionic strength to dilute an anionic mixed micelle mixture [6:3:1 molar ratio of 1,2-distearoyl-sn-glycero-3-phosphocholine (DSPC), cholesterol, and 1-palmitoyl-2-oleoyl-sn-glycero-3-phospho-(1'-rac-glycerol) (POPG) solubilized at 10 mg/mL in 10% (w/v) of the detergent N-decanoyl-N-methylglucamine (MEGA-10)] to various final MEGA-10 concentrations and allowed them to equilibrate overnight (see **Figure C1** for chemical structure of each component). MEGA-10 was chosen due to its high critical micelle concentration (CMC) which facilitates detergent removal.

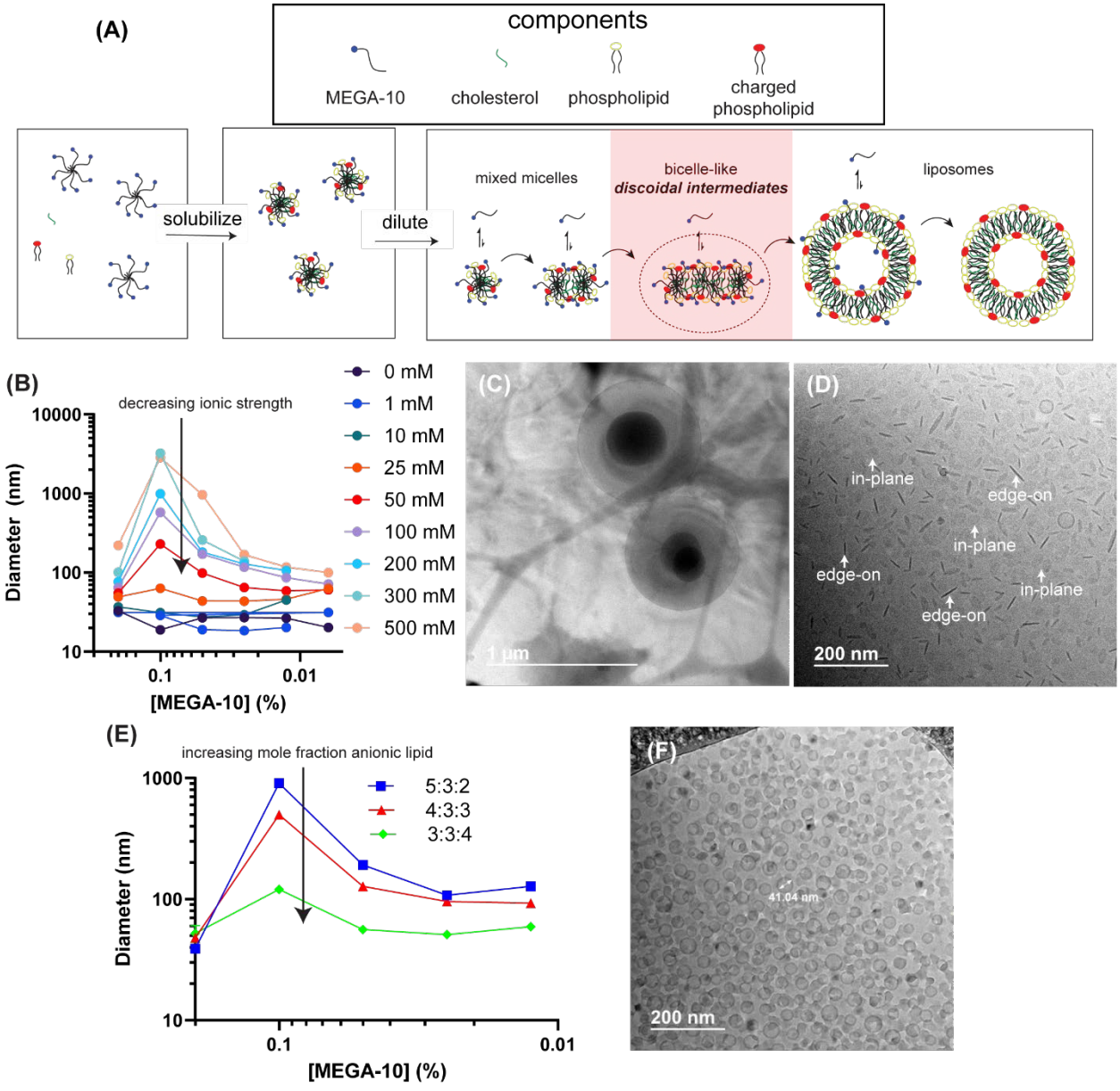

Figure 4.1. **Charge-stabilized nanodiscs (CND) with monovalent lipids are unstable in physiological ionic strength media. (A)** Schematic process for dilution of mixed micelles to generate discoidal lipid assemblies or liposomes. **(B)** Lipid/detergent micelles (10 mg/mL of 6:3:1 molar mixture of DSPC:cholesterol:POPG in 10% MEGA-10) in 10 mM HEPES buffer with different concentration of NaCl were diluted to indicated final MEGA-10 concentrations and particle sizes (hydrodynamic Z-avg) were assessed by DLS. (**C, D**) CryoTEM micrographs of purified samples from dilution of lipid/detergent micelles using **(C)** 200 mM NaCl and **(D)** 0 mM NaCl. **(E)** Intensity-weighted diameter (Z-avg) of PBS-diluted lipid/detergent micelles containing 10 mg/mL of lipids in 10% MEGA-10 composed of either 5:3:2, 4:3:3, or 3:3:4 molar ratios of DSPC:cholesterol:POPG. **(F)** Representative cryoTEM micrograph of a 3:3:4 molar composition (DSPC:cholesterol:POPG) of mixed micelles allowed to equilibrate at 0.05% MEGA-10 overnight then purified via TFF to remove MEGA-10.

Dynamic light scattering (DLS) analysis of samples appeared to indicate that no liposomes were forming at low ionic strength conditions (<25 mM NaCl), due to the lack of particle size change upon dilution of lipid/MEGA-10 solutions below the MEGA-10 CMC **(**~0.2-0.1 wt%[24] , **Figure 4.1B**). By contrast, at higher ionic strengths, liposomes appeared to form which had increasing size as ionic strength increased, consistent with reduced electrostatic repulsion enabling increased particle coalescence. We next used cryogenic transmission electron micrography (cryoTEM) to evaluate sample morphology differences induced by changes in buffer ionic strength. Lipid/detergent mixtures were diluted to 0.1% MEGA-10 in low (0 mM) or high (200 mM) NaCl for self-assembly for 18 hr, then further diluted to 0.02% MEGA-10 before purification to fully remove detergent via tangential flow filtration (TFF). High-pressure liquid chromatography (HPLC) coupled with an evaporative light scattering detector confirmed the removal of >99.9% of detergent from samples via this approach (**Figure C2A**). CryoTEM imaging confirmed that in high ionic strength buffers, unilamellar liposomes were formed **(Figure 4.1C)**. However, particles diluted with low ionic strength buffer appeared to be primarily discoidal assemblies (captured either in the plane or viewed edge-on, **Figure 4.1D**). This high homogeneity was surprising as previous work has only generated heterogeneous mixtures of liposomes, micelles, and discs with monovalent charged headgroups even when 80% of the lipids were charged in the composition.[25] For biomedical applications, particles require colloidal stability;

unfortunately, these species coalesced into liposomes when exposed to a physiological buffer – 10 mM pH 7.4 phosphate-buffered saline (PBS) - leading us to term these as low ionic strength charge stabilized nanodiscs (lisCND, **Figure C2B-C**).

To generate discoidal particles that would be stable in physiological buffers, we attempted to increase the mole fraction of anionic lipid instead of reducing the buffer ionic strength to potentially increase particle-particle charge repulsion in high ionic strength solutions. We generated MEGA-10 mixed micelles with molar lipid compositions of 5:3:2, 4:3:3, and 3:3:4 of DSPC:cholesterol:POPG and diluted them with PBS. The formulation with 3:3:4 yielded sub-100 nm particles when diluted below the MEGA-10 CMC, which would be indicative of reduced particle coalescence and potential discoidal assemblies (**Figure 4.1E**). We thus purified particles generated at 0.05% MEGA-10 **(Figure C2D**), but cryoTEM revealed that the sample was composed entirely of very small unilamellar liposomes (**Figure 4.1F**), indicating that monovalent surface charges alone were not sufficient to stabilize a disc morphology.

4.3.2 Increased lipid charge valency enables synthesis of CNDs stable in physiological buffers

We theorized that charged lipids promoted the formation of nanodiscs through lipid-lipid repulsion at the disc edges, similar to how PEGylated lipids stabilize the edges of LNDs when a sufficient amount of PEGylated lipid is incorporated into the bilayer.[26] In this scenario, increasing ionic strength would screen the stabilizing charges and destabilize the disc morphology. To overcome this issue, we posited that lipids containing two charges in close proximity could increase the lipid headgroup charge density and enable nanodiscs to remain stable in physiological ionic strength buffers.

To test this idea, we replaced POPG with the di-anionic headgroup lipid 1,2-dioleoyl-sn-glycero-3-phosphoethanolamine-N-(glutaryl) (DOPE-glutaryl, **Figure 4.2A**), and tested mixtures where the mole fraction of cholesterol was fixed and the amount of DPSC replaced by the anionic lipid was varied. Using the same detergent-dilution method for controlling lipid self-assembly, we used PBS to dilute samples to 0.1% MEGA-10, as we found that samples that had large size (>100 nm) in these conditions were indicative of disc coalescence and liposome formation. While the inclusion of low amounts of DOPE-glutaryl (<2.5 mol%) yielded large particles (>100 nm), increasing the DOPE-glutaryl content above 5 mol% gave small particles (Z-avg < 50 nm, **Figure**

4.2B). To better characterize these assemblies, we synthesized a larger batch size of 10 mol% DOPE-glutaryl NPs. After overnight incubation at 0.1% MEGA-10 to allow self-assembly, the sample was further diluted to 0.02% MEGA-10 and purified via TFF to remove the detergent. If these charged lipids are assembled into nanodiscs, we would predict a higher degree of anisotropy in light scattering from the particles.[27] Indeed, we found that evaluating the contribution of polarized (vertical) versus horizontal (depolarized) scattered light to sample counts in dynamic light scattering, the particles formed with DOPE-glutaryl had relatively high depolarized scattering compared to liposomes formed with 10% POPG (**Figure 4.2C**). Similar to 10% POPG liposomes, the purified particles exhibited negative zeta potential (**Figure 4.2D**). Negative stain TEM imaging showed that DOPE-glutaryl particles indeed had a nanodisc morphology based on the presence of the disc-like structures in characteristic "edge-on" and "face-on" orientations (**Figure 4.2E**).[28] Given that these particles were stable in a physiological buffer (PBS), we termed them simply charge-stabilized nanodiscs (CNDs) and show their proposed structure in **Figure 4.2F**.

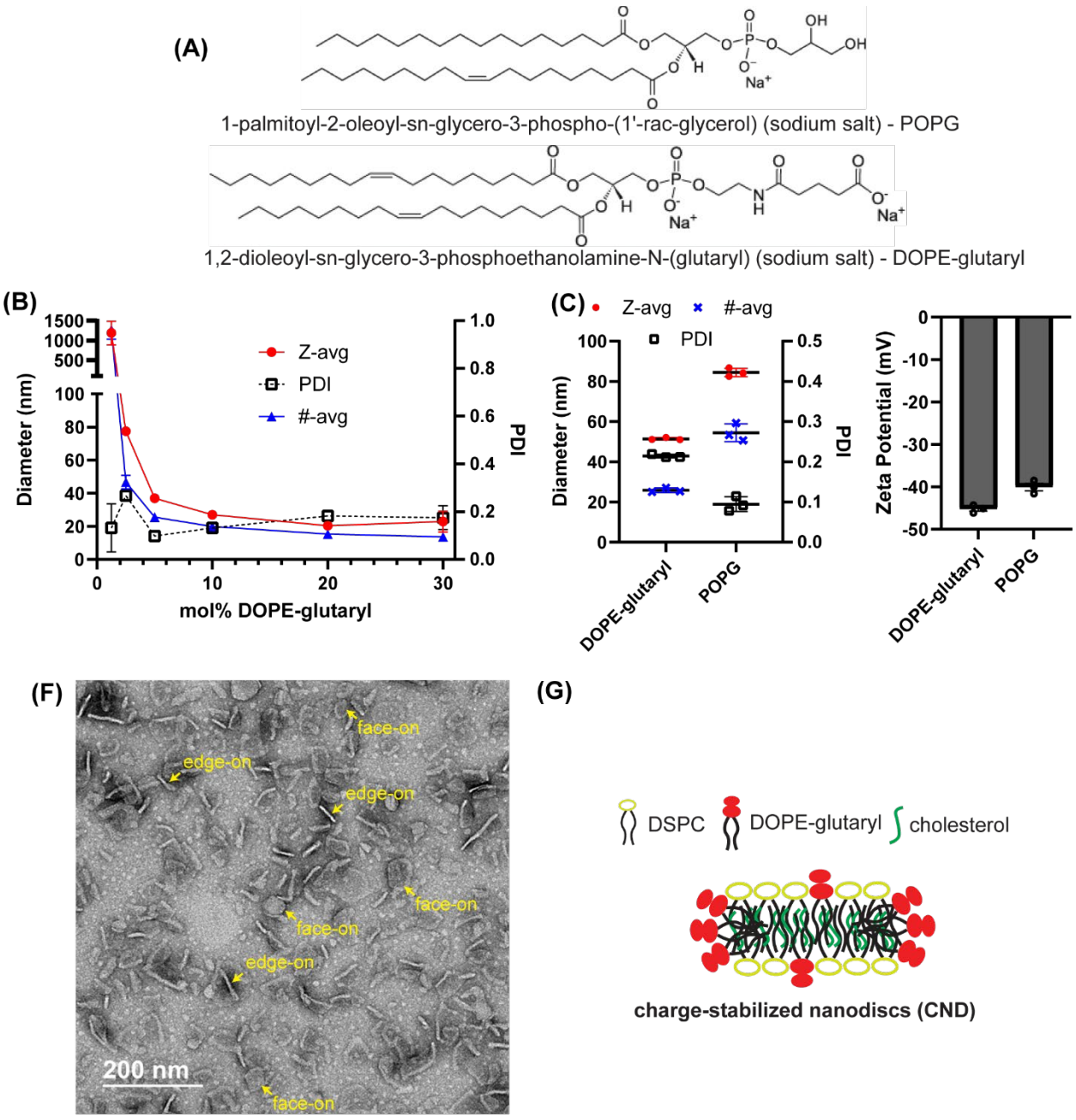

Figure 4.2. Charge density of anionic lipid DOPE-glutaryl enables synthesis of CNDs stable at physiological ionic strength buffers. (A) Chemical structure of POPG and DOPE-glutaryl. **(B)** DLS size (Z-avg, and #-avg) and polydispersity index (PDI) of particles assembled from varying compositions of DPSC, cholesterol, and DOPE-glutaryl diluted in PBS to 0.1% MEGA-10 concentrations (all samples contained 30 mol% cholesterol and the mol% indicated of DOPE-glutaryl with the remainder being DSPC). **(C)** DLS count rate with or without polarized light filters. **(D)** Zeta potential of CNDs composed with 10 mol% DOPE-glutaryl compared to

extrusion-based liposomes with 10 mol% POPG (both samples contained 30% cholesterol and 60% DSPC). **(E)** Representative negative stain TEM (NS-TEM) micrograph of purified CNDs from (C). **(F)** Proposed structure of CNDs composed of DOPE-glutaryl, DSPC, and cholesterol.

4.3.3 CNDs have higher tumor accumulation in vivo compared to liposomes

Anisotropic particles such as worm-like micelles and nanodiscs have been reported to exhibit a higher degree of tumor accumulation than traditional liposomes[8]. To determine if CNDs could exhibit similar tumor uptake, we compared intravenous injection of anionic DOPE-glutaryl CNDs to anionic POPG liposomes in mice bearing subcutaneous tumors (**Figure 4.3A-B**). While the liposomes were larger than CNDs, 50-60 nm liposomes are one of the most common NPs for drug delivery and we could not generate smaller liposomes without substantially altering their composition, consistent with the poor stability of liposomes smaller than ~40 nm.[29] As shown in **Figures 3C-D**, there was a significant increase in the tumor accumulation of CNDs compared to liposomes, even though levels of the two particle types in blood were similar over time (**Figure 4.3E**). Moreover, while there was no significant difference in NP accumulation in major clearance organs (liver and spleen), CNDs were able to preferentially accumulate in tumors (**Figure 4.3F**). These results further validate that anisotropic structures such as CNDs can achieve better tumor accumulation *in vivo* compared to spherical state-of-the-art liposomes.[6,8,30–32]

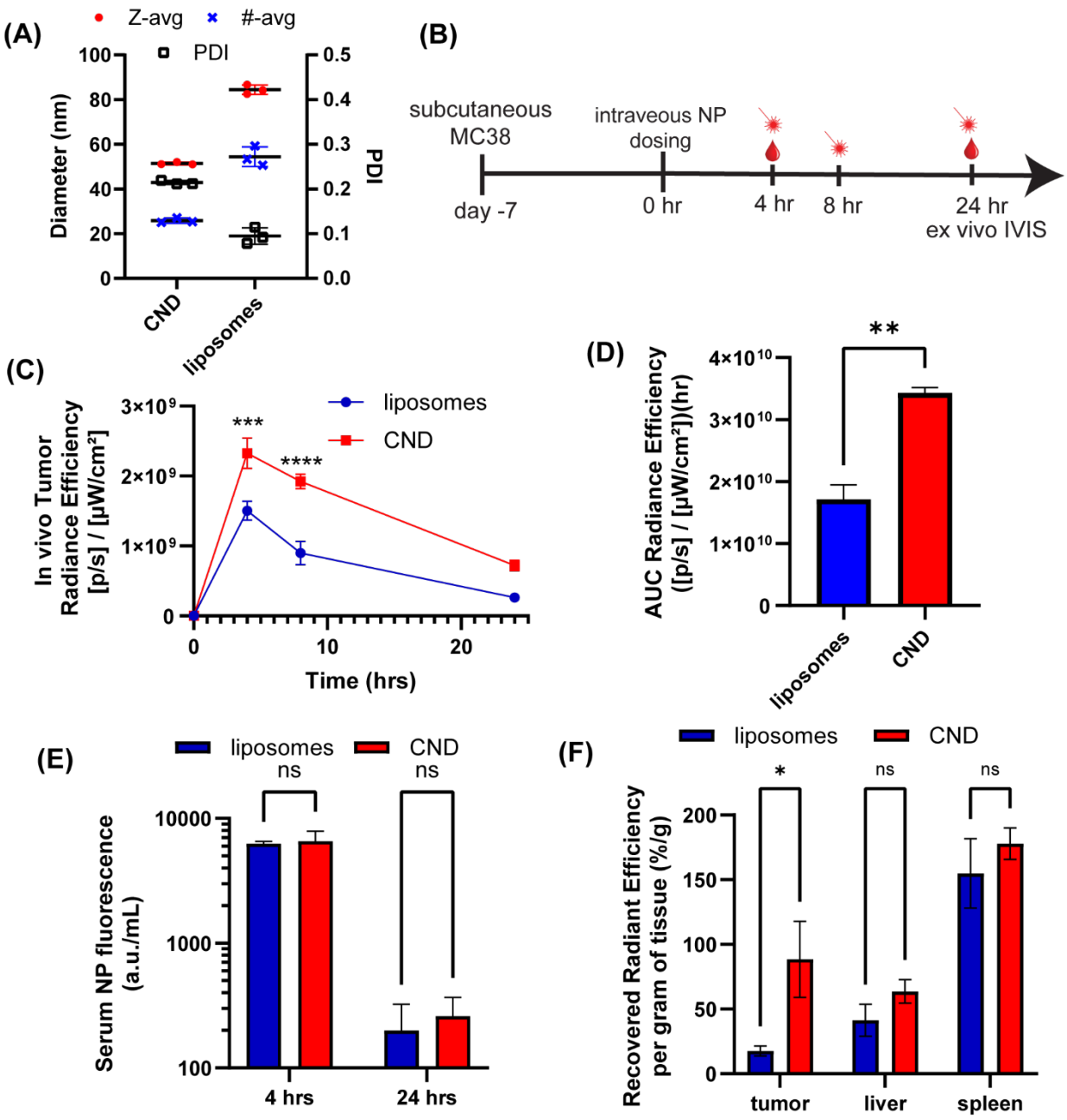

Figure 4.3. **CNDs show greater tumor accumulation than liposomes in solid tumors. (A)** DLS Z-avg, #-avg, and PDI of purified CNDs composed with 10 mol% DOPE-glutaryl compared to extrusion-based liposomes with 10 mol% POPG (both samples contained 30% cholesterol and 60% DSPC). **(B)** In vivo study timeline in which mice were inoculated subcutaneously with 10^6 MC38 cells and then dosed intravenously on day 7 with 1 nmol of cyanine-5 labeled NPs (1 mol%). **(C)** Tumor radiant efficiency measured in vivo via IVIS. **(D)** Area under the curve (AUC) or data

from (H). **(E)** Serum fluorescence of CNDs and liposome dosed animals at 4 and 16 hours after dosing. **(F)** Recovered radiant efficiency from tumor, liver and spleen 24 hours after dosing mice with either CNDs or liposomes. Error bars represent SEM (n = 3 for C-D and n = 4 for E-F). Statistical comparisons in C, E and F were performed using two-way analysis of variance (ANOVA), with Tukey's multiple-comparisons test and an unpaired two-tailed t-test was performed for D. Asterisks denote p-values: ****$p < 0.0001$, ***$p < 0.001$, **$p < 0.01$, *$p < 0.05$.

4.3.4 Deposition of thin polyelectrolyte films via layer-by-layer (LbL) technique enables increased tumor cell association of LbL-CNDs compared to LbL-liposomes in vitro

Previous work has shown that the deposition of thin polymer films onto nanoparticles via the layer-by-layer (LbL) technique can enable controlled drug release and tumor targeting.[33–35] The choice of polymer chemistry regulates the overall LbL-NP properties, enabling a wide range of particle characteristics.[21] Given that the association of LbL-NPs with cells is a surface-driven phenomena, we theorized that the increased surface area of CNDs could generate improved LbL-NP formulations relative to spherical liposomes. We previously showed that depositing a bilayer of poly-L-arginine (PLR) and poly-L-glutamate (PLE) onto NPs promotes binding of the particles to the surface of ovarian cancer cells without triggering endocytosis, such that PLE-coated NPs accumulate on the cell surface.[21,36,37] Thus, we next attempted to layer CNDs with PLR and PLE and compared the resulting nanoparticles to layered liposomes (**Figure 4.4A**). Layering was performed by rapidly mixing particles with excess polymers and then purifying via TFF.

As expected, addition of the polyelectrolyte layers led to characteristic changes in zeta potential of both CNDs and liposomes as the polymers were layered (**Figure C3A).** Both liposomes and CNDs exhibited increases in hydrodynamic size following layering, but maintained low PDIs (PDI < 0.2, **Figure 4.4B**). Following incubation of fluorescently-tagged particles with HM-1 ovarian cancer cells, both LbL-liposomes and LbL-CNDs yielded the expected increase in cancer cell association relative to bare POPG liposomes (**Figure 4.4C**). However, LbL-CNDs increased ovarian cancer cell binding by ~3-fold relative to LbL-liposomes (**Figure 4.5C**). Interestingly, while lisCNDs (nanodisc structures formed from POPG formulations in low ionic strength) could also be modified via the LbL technique (**Figure C3B**), only LbL-CNDs presented an improved association with ovarian cancer cells *in vitro* relative to LbL-liposomes (**Figure C3C**). This could be due to the instability of lisCND which were found to have lower uptake than

unlayered liposomes whereas CND had equal or higher uptake by ovarian cancer cells. Similar to the behavior we previously reported for anionic liposomes, confocal imaging revealed that “bare” CNDs were endocytosed by the tumor cells, while LbL-CNDs remained at the cell surface for at least 4 hrs (**Figure 4.4D**).

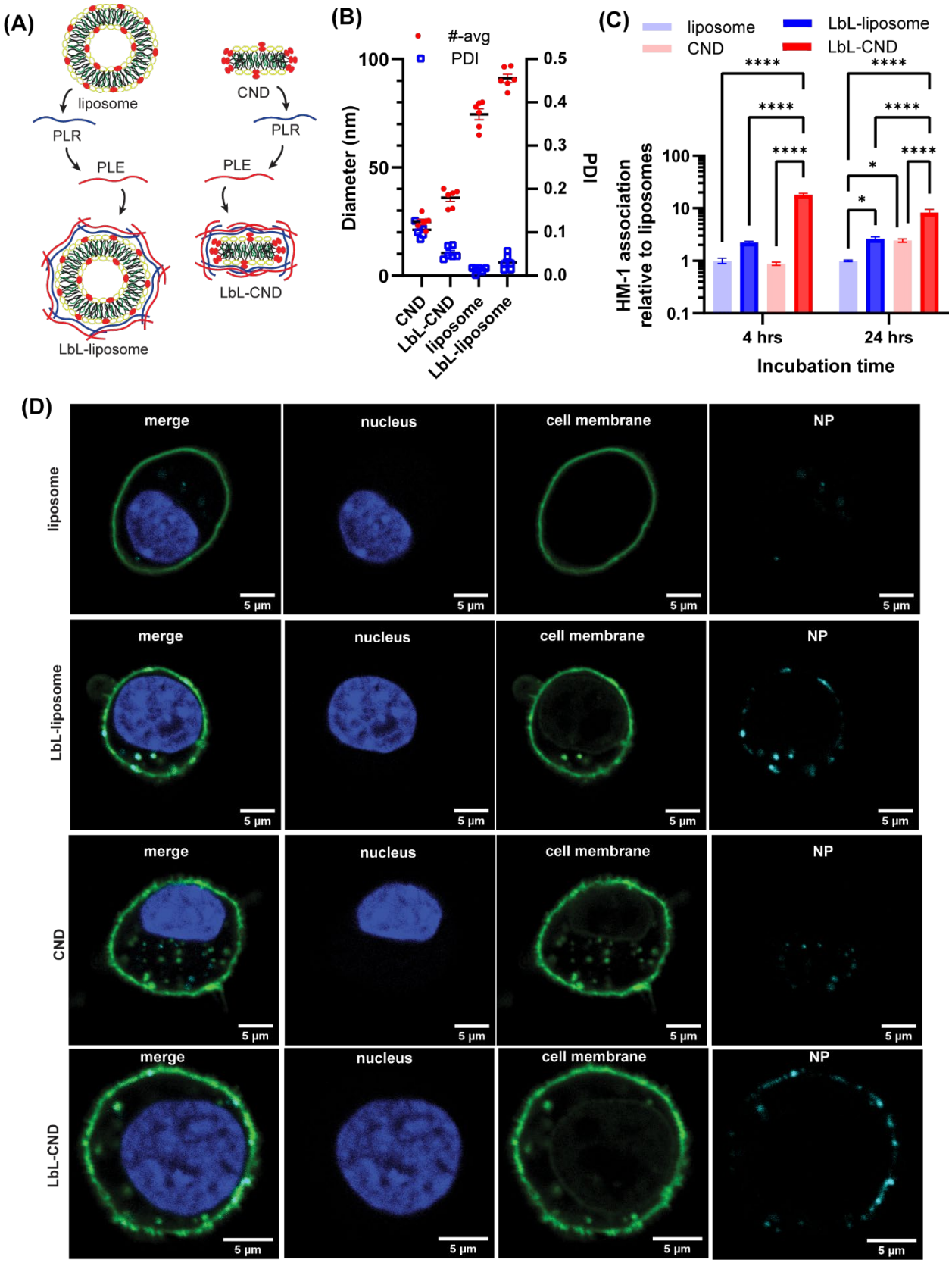
(A)
liposome
PLR
PLE
LbL-liposome
CND
PLR
PLE
LbL-CND
(B)
#-avg
PDI
Diameter (nm)
PDI
100
50
0
0.5
0.4
0.3
0.2
0.1
0.0
CND
LbL-CND
liposome
LbL-liposome
(C)
liposome
CND
LbL-liposome
LbL-CND
HM-1 association relative to liposomes
100
10
1
0.1
****
*
4 hrs
24 hrs
Incubation time
(D)
merge
nucleus
cell membrane
NP
liposome
LbL-liposome
CND
LbL-CND
5 μm

Figure 4.4. **Deposition of polyelectrolyte layers composed of PLR and PLE onto CNDs enables improved association of CNDs with ovarian cancer cells *in vitro*. (A)** Schematic of LbL technique to generate LbL-liposomes and LbL-CNDs. **(B)** Size and PDI of CND and liposomes before and after LbL modification. **(C)** In vitro measurement of total HM-1-associated NP fluorescence relative to liposomes using a plate reader after 4 or 24 hours of incubation. **(D)** Confocal images of HM-1 cells after 4 hrs of incubation with NPs. Error bars represent SEM. Statistical comparisons in C was performed using two-way analysis of variance (ANOVA), with Tukey's multiple-comparisons. Asterisks denote p-values: ****$p < 0.0001$, ***$p < 0.001$, **$p < 0.01$, *$p < 0.05$.

4.3.5 Deposition of thin polyelectrolyte films via layer-by-layer (LbL) technique enables increased tumor cell association of LbL-CNDs compared to LbL-liposomes in vivo

Based on the improved *in vitro* ovarian cancer binding of LbL-CNDs compared to LbL-liposomes, we next examined the *in vivo* tumor-targeting properties of LbL-CNDs in a model of metastatic ovarian cancer. Luciferase-expressing HM-1 cells were injected intraperitoneally (i.p.) into mice and allowed to establish for 14 days, followed by i.p. administration of fluorescent liposomes or CNDs, with or without the LbL coating (**Figure 4.5A**).

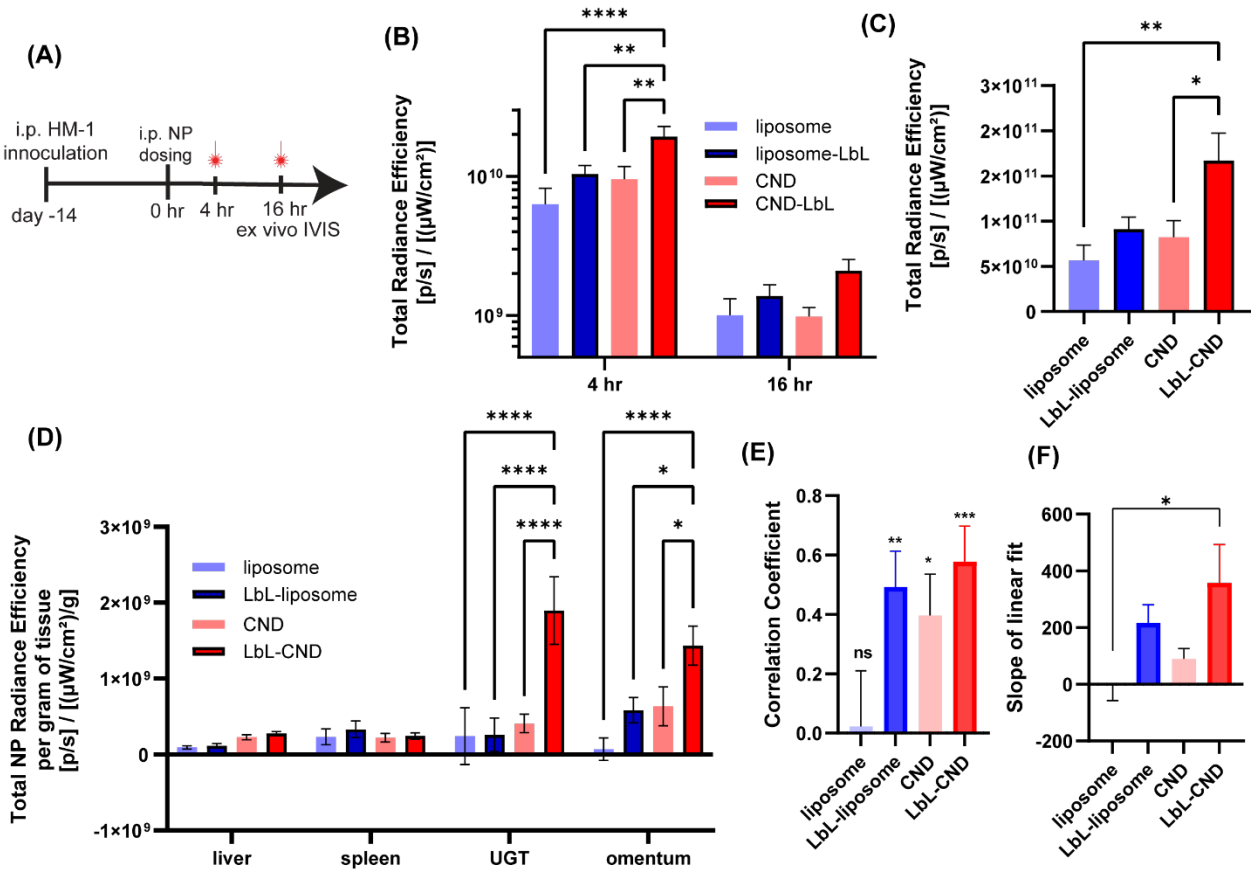

Figure 4.5. LbL-CNDs NPs efficiently target metastatic ovarian cancer in vivo. (A) In vivo timeline for treatment of fluorescently-labeled NPs i.p. in ovarian cancer model. Mice were inoculated with 10^6 HM-1-luc cells i.p. and dosed with NPs 14 days later. **(B)** Total radiant efficiency of NP fluorescence from peritoneum. **(C)** AUC of peritoneal fluorescence readings from B. **(D)** *Ex vivo* weight normalized NP fluorescence in liver, spleen, UGT, and omentum. **(E)** Spearman's correlation coefficient between weight-normalized NP fluorescence and weight-normalized BLI readings. Error bars (s.e.m.) derived from parameter estimates for each group. **(F)** Slope of linear fit between weight-normalized NP fluorescence and weight-normalized BLI readings. Error bars (s.e.m.) represent variation between each animal in respective treatment groups (n = 4 mice/group). Statistical comparisons in B and D were performed using two-way analysis of variance (ANOVA) one-way ANOVA was used in C and F with Tukey's multiple-comparisons test. Spearman's correlation significance for E was performed based on a t-test analysis with the null hypothesis of no (r=0) correlation. Asterisks denote p-values: ****p < 0.0001, ***p < 0.001, **p < 0.01, *p < 0.05.

Mice given LbL-CNDs had significantly higher (~2-fold) *in vivo* peritoneal fluorescence 4 hours after dosing compared to other groups indicating a better retention of NPs in the i.p. space (**Figure 4.5B-C**). While accumulation in the major clearance tissues (spleen and liver) was low, *ex vivo* measurement of total NP fluorescence in the main sites of metastasis development (i.e., omentum and UGT [38]) revealed a significantly improved accumulation of LbL-CNDs in tumor tissue with a 10-fold or more increase relative to bare liposomes (**Figure 4.5D**). Further, as all peritoneal organs present some level of tumor burden which could be measured via bioluminescence intensity (BLI) readings, we analyzed the correlation between the tumor burden of an organ to its NP fluorescence reading. While bare liposome fluorescence did not correlate with tissue tumor burden, LbL-liposomes showed a significant correlation, consistent with the tumor-targeting properties of LbL-coated NPs (**Figure 4.5E**). Moreover, both CND and LbL-CND accumulation were correlated with tumor burden, albeit CND-LbL treatment yielded a more confident fit. Indeed, LbL modification of CNDs increased the amount of NP accumulation per BLI reading ~4-fold (**Figure 4.5F**). These results indicate that combining the nanodisc morphology with an ovarian cancer-targeting LbL coating substantially enhances the delivery of lipid nanoparticles to metastatic ovarian cancer.

4.4 Conclusions

Lipid nanoparticles are important delivery vehicles for current and new-generation therapeutics. Here we have shown that through the rational disassembly of mixed micelles, we can stabilize nanodisc intermediates to generate a new class of lipid nanoparticles – charge-stabilized nanodiscs (CNDs). We also found that assembly from detergent micelles enabled the synthesis of minute liposomes. While not the focus of the present paper, these minute liposomes with minimal polydispersity are close to the limit in size of nanoliposomal systems which have great potential for biomedical applications.[39] Achieving such small liposome sizes (30-40 m) via conventional methods has been challenging.[40] Even with optimized conditions, previously reported limit-size nanoliposomes have exhibited high polydispersity (PDI>0.1).[39,40]

Importantly, CNDs demonstrated improved tumor accumulating properties compared to standard liposomes and could be surface modified via the LbL technique to further promote tumor targeting. Previous studies have shown that PEG, proteins, synthetic polymers, or mixtures of short and long-tailed surfactants (such as detergents and lipids) can generate disc-like structures.[8,12–14]

However, these added components can alter the particle characteristics and in the case of bicelles, they are limited by their sensitivity to dilution which did not occur with CNDs.[13] Further, while it has been shown that lipids with charged dendritic headgroups (>5*e*) can yield disc-like micellar structures, they are limited to formulations in high-resistivity water, require more than 50 mol% of the charged lipid in the composition, and need sonication to reduce particle size.[25,41] Moreover, the additional components previously used to assemble discs increase the risks of immunogenicity and allergen sensitivity. Through the readily scalable method presented here, the resulting CNDs were stable in a physiological buffer and required less than 10 mol% of a bivalent charged lipid. Taken together, we demonstrate that the novel Layer-by-Layer CND assemblies have great potential for use in biomedical applications. CNDs may also be valuable in structural and functional studies of membrane proteins given the lack of synthetic constituents. [42–44] Further, the techniques and discoveries presented here may facilitate the generation of new and more controlled lipid-based assemblies.

4.5 References

1. Mundekkad, D. & Cho, W. C. Nanoparticles in Clinical Translation for Cancer Therapy. *Int J Mol Sci* **23**, 1685 (2022).

2. Durymanov, M., Kamaletdinova, T., Lehmann, S. E. & Reineke, J. Exploiting passive nanomedicine accumulation at sites of enhanced vascular permeability for non-cancerous applications. *Journal of Controlled Release* **261**, 10–22 (2017).

3. Albanese, A., Tang, P. S. & Chan, W. C. W. The Effect of Nanoparticle Size, Shape, and Surface Chemistry on Biological Systems. *Annu Rev Biomed Eng* **14**, 1–16 (2012).

4. Zhu, X., Vo, C., Taylor, M. & Smith, B. R. Non-spherical micro- and nanoparticles in nanomedicine. *Mater Horiz* **6**, 1094–1121 (2019).

5. Ding, J. *et al.* Engineered nanomedicines with enhanced tumor penetration. *Nano Today* **29**, 100800 (2019).

6. Kapate, N., Clegg, J. R. & Mitragotri, S. Non-spherical micro- and nanoparticles for drug delivery: Progress over 15 years. *Adv Drug Deliv Rev* **177**, 113807 (2021).

7. Sun, Q., Ojha, T., Kiessling, F., Lammers, T. & Shi, Y. Enhancing Tumor Penetration of Nanomedicines. *Biomacromolecules* **18**, 1449–1459 (2017).

8. Dane, E. L. *et al.* STING agonist delivery by tumour-penetrating PEG-lipid nanodiscs primes robust anticancer immunity. *Nat Mater* **21**, 710–720 (2022).

9. Smith, B. R. *et al.* Shape Matters: Intravital Microscopy Reveals Surprising Geometrical Dependence for Nanoparticles in Tumor Models of Extravasation. *Nano Lett* **12**, 3369–3377 (2012).

10. Geng, Y. *et al.* Shape effects of filaments versus spherical particles in flow and drug delivery. *Nat Nanotechnol* **2**, 249–255 (2007).

11. Niora, M. *et al.* Head-to-Head Comparison of the Penetration Efficiency of Lipid-Based Nanoparticles into Tumor Spheroids. *ACS Omega* **5**, 21162–21171 (2020).

12. Smith, A. A. A. *et al.* Lipid Nanodiscs via Ordered Copolymers. *Chem* **6**, 2782–2795 (2020).

13. Lu, Z. *et al.* Bicelles at Low Concentrations. *Mol Pharm* **9**, 752–761 (2012).

14. Patel, H. *et al.* Characterization of apolipoprotein A-I peptide phospholipid interaction and its effect on HDL nanodisc assembly . *Int J Nanomedicine* **Volume 14**, 3069–3086 (2019).

15. Bariwal, J., Ma, H., Altenberg, G. A. & Liang, H. Nanodiscs: a versatile nanocarrier platform for cancer diagnosis and treatment. *Chem Soc Rev* **51**, 1702–1728 (2022).

16. Kozma, G. T., Shimizu, T., Ishida, T. & Szebeni, J. Anti-PEG antibodies: Properties, formation, testing and role in adverse immune reactions to PEGylated nano-biopharmaceuticals. *Adv Drug Deliv Rev* **154–155**, 163–175 (2020).

17. Bigini, P. *et al.* The role and impact of polyethylene glycol on anaphylactic reactions to COVID-19 nano-vaccines. *Nat Nanotechnol* **16**, 1169–1171 (2021).

18. Wenande, E. & Garvey, L. H. Immediate-type hypersensitivity to polyethylene glycols: a review. *Clinical & Experimental Allergy* **46**, 907–922 (2016).

19. Jiskoot, W., Teerlink, T., Beuvery, E. C. & Crommelin, D. J. A. Preparation of liposomes via detergent removal from mixed micelles by dilution. *Pharm Weekbl Sci* **8**, 259–265 (1986).

20. Correa, S. *et al.* Highly Scalable, Closed-Loop Synthesis of Drug-Loaded, Layer-by-Layer Nanoparticles. *Adv Funct Mater* **26**, 991–1003 (2016).

21. Correa, S. *et al.* Tuning Nanoparticle Interactions with Ovarian Cancer through Layer-by-Layer Modification of Surface Chemistry. *ACS Nano* **14**, 2224–2237 (2020).

22. Ollivon, M., Lesieur, S., Grabielle-Madelmont, C. & Paternostre, M. Vesicle reconstitution from lipid–detergent mixed micelles. *Biochimica et Biophysica Acta (BBA) - Biomembranes* **1508**, 34–50 (2000).

23. Lasič, D. D. A general model of vesicle formation. *J Theor Biol* **124**, 35–41 (1987).

24. Walter, A., Suchy, S. E. & Vinson, P. K. Solubility properties of the alkylmethylglucamide surfactants. *Biochimica et Biophysica Acta (BBA) - Biomembranes* **1029**, 67–74 (1990).

25. Steffes, V. M., Zhang, Z., Ewert, K. K. & Safinya, C. R. Cryo-TEM Reveals the Influence of Multivalent Charge and PEGylation on Shape Transitions in Fluid Lipid Assemblies: From Vesicles to Discs, Rods, and Spheres. *Langmuir* **39**, 18424–18436 (2023).

26. Viitala, L. *et al.* Shape and Phase Transitions in a PEGylated Phospholipid System. *Langmuir* **35**, 3999–4010 (2019).

27. Lehner, D., Lindner, H. & Glatter, O. Determination of the Translational and Rotational Diffusion Coefficients of Rodlike Particles Using Depolarized Dynamic Light Scattering. *Langmuir* **16**, 1689–1695 (2000).

28. Asadi, J. *et al.* Enhanced imaging of lipid rich nanoparticles embedded in methylcellulose films for transmission electron microscopy using mixtures of heavy metals. *Micron* **99**, 40–48 (2017).

29. Zhigaltsev, I. V., Tam, Y. K., Leung, A. K. K. & Cullis, P. R. Production of limit size nanoliposomal systems with potential utility as ultra-small drug delivery agents. *J Liposome Res* 1–7 (2015) doi:10.3109/08982104.2015.1025411.

30. Shamul, J. G. *et al.* Verteporfin-Loaded Anisotropic Poly(Beta-Amino Ester)-Based Micelles Demonstrate Brain Cancer-Selective Cytotoxicity and Enhanced Pharmacokinetics . *Int J Nanomedicine* **Volume 14**, 10047–10060 (2019).

31. Wang, L. *et al.* Novel fibronectin-targeted nanodisk drug delivery system displayed superior efficacy against prostate cancer compared with nanospheres. *Nano Res* **12**, 2451–2459 (2019).

32. Chu, K. S. *et al.* Plasma, tumor and tissue pharmacokinetics of Docetaxel delivered via nanoparticles of different sizes and shapes in mice bearing SKOV-3 human ovarian carcinoma xenograft. *Nanomedicine* **9**, 686–693 (2013).

33. Correa, S. *et al.* Tuning Nanoparticle Interactions with Ovarian Cancer through Layer-by-Layer Modification of Surface Chemistry. *ACS Nano* **14**, 2224–2237 (2020).

34. Deng, Z. J. *et al.* Layer-by-Layer Nanoparticles for Systemic Codelivery of an Anticancer Drug and siRNA for Potential Triple-Negative Breast Cancer Treatment. *ACS Nano* **7**, 9571–9584 (2013).

35. Correa, S., Dreaden, E. C., Gu, L. & Hammond, P. T. Engineering nanolayered particles for modular drug delivery. *Journal of Controlled Release* **240**, 364–386 (2016).

36. Barberio, A. E. *et al.* <scp>Layer-by-layer</scp> interleukin-12 nanoparticles drive a safe and effective response in ovarian tumors. *Bioeng Transl Med* (2022) doi:10.1002/btm2.10453.

37. Barberio, A. E. *et al.* Cancer Cell Coating Nanoparticles for Optimal Tumor-Specific Cytokine Delivery. *ACS Nano* **14**, 11238–11253 (2020).

38. Krishnan, V. *et al.* Omental macrophages secrete chemokine ligands that promote ovarian cancer colonization of the omentum via CCR1. *Commun Biol* **3**, 524 (2020).

39. Zhigaltsev, I. V., Tam, Y. K., Leung, A. K. K. & Cullis, P. R. Production of limit size nanoliposomal systems with potential utility as ultra-small drug delivery agents. *J Liposome Res* 1–7 (2015) doi:10.3109/08982104.2015.1025411.

40. Zhigaltsev, I. V. *et al.* Bottom-Up Design and Synthesis of Limit Size Lipid Nanoparticle Systems with Aqueous and Triglyceride Cores Using Millisecond Microfluidic Mixing. *Langmuir* **28**, 3633–3640 (2012).

41. Zidovska, A. *et al.* Liquid Crystalline Phases of Dendritic Lipid−DNA Self-Assemblies: Lamellar, Hexagonal, and DNA Bundles. *J Phys Chem B* **113**, 3694–3703 (2009).

42. Dalal, V. *et al.* Lipid nanodisc scaffold and size alter the structure of a pentameric ligand-gated ion channel. *Nat Commun* **15**, 25 (2024).

43. Denisov, I. G. & Sligar, S. G. Nanodiscs for structural and functional studies of membrane proteins. *Nat Struct Mol Biol* **23**, 481–486 (2016).

44. Elzoghby, A. O. *et al.* Nanodiscs: Game changer nano-therapeutics and structural biology tools. *Nano Today* **53**, 102026 (2023).

CHAPTER 5

"Target-and-release" nanoparticles for effective immunotherapy of metastatic ovarian cancer

5.1 Introduction

Ovarian cancer (OC) treatment is particularly challenging due to late diagnosis and metastatic spread.[1,2] A promising approach for late-stage cancer treatment is immunotherapy.[3–5] However, poor baseline lymphocyte infiltration and an immunosuppressive tumor microenvironment (TME) have correlated with limited benefits of immunotherapy in OC patients.[6,7] Immunostimulatory agents such as cytokines and costimulatory antibodies may have the potential to overcome these limitations, but systemic administration of these therapeutics is severely limited by dose-limiting toxicities.[8,9]

Nanoparticles (NPs) are promising vehicles to deliver immunotherapeutics.[1011] In OC, NPs have been used to deliver various immunomodulatory agents such as nucleic acids[12,13], proteins[14], and small molecules[15,16]. We previously reported that NPs coated with poly-L-arginine (PLR)/poly-L-glutamate (PLE) bilayers via layer-by-layer (LbL) deposition showed selective binding to the surface of OC cells.[17] In mouse OC models, administration of liposomal LbL-NPs carrying the potent immunostimulatory cytokine interleukin-12 (IL-12) showed reduced toxicity over systemic IL-12 dosing but only modest therapeutic efficacy.[18,19] We hypothesized that the non-covalent nickel-histidine interaction used to tether IL-12 to these particles was very short-lived *in vivo*,[20,21] leading to premature release of the cytokine before uptake in tumors.

Here, we demonstrate that covalent conjugation of IL-12 to the liposomal core of LbL-NPs greatly improves targeting and retention of IL-12 in peritoneally-disseminated OC tumors, enabling immunological and therapeutic effects not observed with free cytokine treatment. Mechanistic investigations revealed that these LbL-NPs rapidly accumulated in tumor nodules upon intraperitoneal (i.p.) administration, followed by shedding of the LbL coating and gradual release of IL-12-lipid conjugates via lipid extraction by serum proteins present in interstitial fluid. Both rapid LbL-mediated cancer cell targeting and slow cytokine release with sustained retention on cell membrane surfaces were crucial for therapeutic efficacy. These findings demonstrate the

potential of “target and release” NP designs to effectively concentrate cytokine in disseminated ovarian cancer lesions and promote robust anti-tumor immunity.

5.2 Methods

5.2.1 Materials

1,2-distearoyl-sn-glycero-3-phosphocholine (DSPC), 1,2-dioleoyl-sn-glycero-3-[(N-(5-amino-1-carboxypentyl)iminodiacetic acid)succinyl] (nickel salt) (18:1 (Ni)NTA-DGS), 1,2-dioleoyl-sn-glycero-3-phosphoethanolamine-N-[4-(p-maleimidophenyl)butyramide] (sodium salt) (18:1 MPB-PE), 1-palmitoyl-2-oleoyl-sn-glycero-3-phospho-(1’-rac-glycerol) (sodium salt) (POPG), 1,2-dioleoyl-sn-glycero-3-phosphoethanolamine-N-dibenzocyclooctyl (DOPE-DBCO), 1,2-distearoyl-sn-glycero-3-phospho-(1'-rac-glycerol) (sodium salt) (DSPG), 1,2-dipalmitoyl-sn-glycero-3-phosphoethanolamine-N-[4-(p-maleimidophenyl)butyramide] (sodium salt) (16:0 MPB-PE), 1,2-dipalmitoyl-sn-glycero-3-phosphoethanolamine-N-dibenzocyclooctyl (16:0 DBCO PE), and cholesterol were purchased from Avanti Polar Lipids. Poly-L-arginine (PLR) with a molecular weight (MW) of 9.6 kDa and poly-L-glutamic acid (PLE) with a MW of 15 kDa were purchased from Alamanda Polymers. BDP TMR azide (Lumiprobe) and BDP 630/650 azide (Lumiprobe) were conjugated to DOPE-DBCO or 18:0 DBCO-PE in chloroform to generate fluorescently labeled lipids. Successful conjugation was validated via thin-layer chromatography which indicated <1% free dye. For immunophenotyping (all mouse targets), antibodies for CD3e (clone 145-2C11, FITC), CD49b (clone DX5, PE), CD45 (close 30-F11, PE-Cy5.5), F4/80 (clone T45-2342, PE), CD80 (clone 16-10A1, FITC), CD11b (clone M1/70, FITC), and Ly6C (clone AL-21, PE) were purchased from BD Biosciences. Antibodies for CD4 (clone GK1.5, APC-Cy7), CD8a (clone 53-6.7, PE), CD206 (clone C068C2, PE-Cy5), and Ly6G (clone 1A8, APC) were purchased from BioLegend. Deionized water was of ultrapure grade obtained through a Milli-Q water system (EMD Millipore).

5.2.2 Recombinant single-chain IL-12 production

Single-chain IL-12 sequence[22] was synthesized as a genomic block (Integrated DNA Technologies) and cloned into gWIZ expression vector (Genlantis). Plasmids were transiently transfected into Expi293 cells (ThermoFisher Scientific). After 5 days, cell culture supernatants were collected and protein was purified in an ÄKTA pure chromatography system using HiTrap HP Niquel sepharose affinity column, followed by size exclusion using Superdex 200 Increase

10/300 GL column (GE Healthcare Life Sciences). Endotoxin levels in purified protein was measured using Endosafe Nexgen-PTS system (Charles River) and assured to be <5 EU/mg protein.

5.2.3 Liposome synthesis

A lipid solution was prepared by mixing (all mole %) 65% DSPC (25 mg/mL), 24% cholesterol (25 mg/mL), 6% POPG (25 mg/mL) and 5% of either 18:1 (Ni)NTA-DGS (5 mg/mL) or 18:1 MPB-PE (5 mg/L) then formed into a thin film using a rotary evaporator (Buchi). Lipid films were allowed to further dry overnight in a desiccator, then were hydrated at 0.5-1 mg/mL using deionized water and sonicated for 3-5 minutes at 65 °C then extruded (Avestin Liposofast LF-50) once at 65 °C through a 100 nm membrane (Cytiva Nuclepore) then 3X through 50 nm membranes (Cytiva Nuclepore) . Extruded liposomes were added to an ice bath. SAT NPs were generated with the same procedure as Mal NPs, but its composition (all mole %) was 65% DSPC (25 mg/mL), 24% Cholesterol (25 mg/mL), 6% DSPG (25 mg/mL) and 5% of 16:0 MPB-PE (5 mg/mL). Lipid were stored at -20 °C in amber vials in chloroform except DSPG which was stored in a 1:1 (v/v) mixture of chloroform and methanol instead of pure chloroform.

For coupling of scIL-12 via Ni-histag interactions, scIL-12 was added to 0.5 mg/mL Ni(NTA)-DGS liposomes at a molar ratio of 28:1 of Ni(NTA)-DGS lipids to IL-12. After incubation with IL-12 at 4 °C for 18 hr, Ni-UL liposomes were purified via tangential flow filtration on a 100 kDa mPES membranes (Repligen) against 6 diafiltration volumes of deionized water.

For covalent linkage of scIL-12 to Mal-liposomes, the solution pH of MPB-PE liposomes was adjusted to pH 5 with hydrochloric acid prior to lipid film hydration, and following membrane extrusion, liposomes at 0.33 mg/mL were adjusted to pH 7.0 with 10 mM HEPES prior followed by addition of scIL-12 containing a terminal cysteine residue at a molar ratio of 25:1 of MPB-PE lipid to protein for at least 12 hours at 4 °C in a rotating mixed. Any remaining maleimides were quenched with a 100-fold molar excess of L-cysteine (Sigma) for 1.5 hrs on ice.

For fluorescence labeling of liposomes, 0.2 mol% of DSPC content was replaced by either DOPE-TMR or DOPE-630/650. IL-12 concentrations were measured via enzyme-linked immunoassay (ELISA) (Peprotech) and lipid content was quantified via the Stewart Assay.[23]

5.2.4 Layer-by-Layer (LbL) film deposition onto NPs

Assembly of polyelectrolyte layers was performed by adding unlayered particles to a diH_2O solution with 0.3-0.4 weight equivalents (wt.eq.) of PLR relative to lipid in a glass vial under sonication and incubating on ice for at least 30 min. Excess PLR polymer was purified by TFF through a 100 kDa mPES membrane (Repligen) pre-treated with a 10 mg/mL solution of free PLR. For the terminal PLE layer, purified particles coated with PLR were added to a diH_2O solution with PLE in a glass vial under sonication at 1 wt.eq. of polymer to lipid. LbL particles were then purified by TFF on a separate 100 kDa mPES membrane (Repligen) to remove any excess PLE.

5.2.5 Characterization of particle preparations

Dynamic light scattering (DLS) and zeta potential measurements were made on a Zetasizer Nano ZSP (Malvern). Nanoparticle micrographs were acquired using Transmission Electron Microscopy (TEM) on a JEOL 2100F microscope (200 kV) with a magnification range of 10,000-60,000X. All images were recorded on a Gatan 2kx2k UltraScan CCD camera. Negative-stain sample preparation was performed by adding 10 μL of NPs on a 200 meshes copper grid coated with a continuous carbon film and allowing for sample adsorption for 60 seconds. Excess solution was then removed by touching the grid with a kimwipe. The grid was then quickly washed by adding 10 μL of negative staining solution, phosphotungstic acid (PTA), 1% aqueous solution then removing excess by touching the grid with a kimwipe. Then, the grid was mounted on a JEOL single tilt holder equipped in the TEM column for image capture.

5.2.6 Fluorescent labeling of polymers

PLR was solubilized at 100 mg/mL in diH_2O then mixed with 2 molar equivalents of BDP-TR-NHS-ester (Lumiprobe) in DMSO to generate a 15 mg/mL PLR solution. The reaction was catalyzed with ten molar equivalent of triethylamine (TEA) and allowed to react for 4 hrs at room temperature then overnight at 4 °C. PLR-TR was purified via Reverse-Phase High Pressure Liquid Chromatography (RP-HPLC) on a Jupiter C4 column (5 μm particles, 300 Å – Phenomenex) using a water:acetonitrile gradient which started at 20% actetonitrile for 5 minutes, then increased to 35% in a linear gradient until 10 minutes. Isocratic elution at 35% was performed for 30 minutes then the elution buffer was increased to 95% to clean out the column for 10 minutes then dropped back to 20% acetonitrile to re-equilibrate the column for 5 minutes. Collected purified PLR-TR fractions were then diluted 10-fold with diH_2O then lyophilized. PLE at 10 mg/mL was labeled by

reacting with 5 molar equivalents of sulfo-cyanine3 NHS ester (Lumibrobe) in PBS adjusted to pH ~8.5 with 0.1 M sodium bicarbonate. Excess dye was removed via extensive 0.9wt% NaCldialysis followed by extensive diH_2O dialysis using a 3 kDa regenerated cellulose membrane (Repligen) and the purified PLE-cy3 was lyophilized until use.

5.2.7 Analysis of LbL film stability

For PLR stability, PLR/PLE films were assembled onto Mal-UL NPs as described in *Layer-by-Layer (LbL) film deposition onto NPs,* but the PLR solution was doped with 30% PLR-TR. For PLE stability, the PLE solution was doped with 50% PLE-cy3. Particles were incubated in various buffer solutions at 0.1 mg/mL in a shaker at 37 °C. At defined intervals, aliquots were extracted from the incubation solution and free polymers were separated from the NP. For PLE separation, samples were spun on a 300 kDa centrifugal filter (VivaSpin500, Sartorius) at 10x*g* for 15 min and the permeate fluorescence was compared to the fluorescence of the initial sample. For PLR separation, the NPs in the sample were pelleted by centrifuging at 25000x*g* for 30 min and the supernatant PLR fluorescence was compared to the initial sample PLR fluorescence. Particles were validated to lack free polymers by centrifuging in diH_2O. Fluorescence was measured on 96 well plates using a plate reader (Tecan Infinite 200).

5.2.8 IL-12 accessibility via monoclonal antibody binding

IL-12 accessibility to monoclonal antibody binding was determined by using the antibodies in an IL-12 sandwich ELISA kit (Peprotech). After coating a 96 well plate with anti-IL-12 antibodies and blocking the plate with bovine serum albumin according to the manufacturer protocol, Mal-UL or Mal-LbL NPs were captured onto the plate by incubating the samples for two hours in either diH_2O or HEPES buffered saline solution supplemented with 10% FBS. After sample incubation with capture antibodies, plates were washed and total captured IL-12 was determined following the manufacturer's protocol.

5.2.9 Cell Culture

OV2944-HM-1 cells were acquired through Riken BRC and were cultured in α-MEM. HEK-Blue IL-12 (InvivoGen) cells were cultured and used for IL-12 bioactivity assessment according to the manufacturer's instructions. Cell media was also supplemented with 10% FBS and penicillin/streptomycin with cells incubated in a 5% carbon dioxide humidified atmosphere at 37 °C. All cell lines were murine pathogen tested and confirmed mycoplasma negative by Lonza MycoAlert™ Mycoplasma Detection Kit.

5.2.10 In vitro cellular association

HM-1 cells were plated on a tissue-culture 96-well plate at a density of 50K cells per well. The next day, wells were dosed with NPs and left for the target incubation time (4 hrs or 24 hrs). For analysis via flow cytometry, NPs were dosed at 0.02 mg/mL and allowed to incubate with cells for 4 hours at 37°C. Cells were washed with PBS then detached from the plates using 0.25% trypsin and stained with DAPI (15 min incubation) for viability assessment and fixed with 2% paraformaldehyde (30 min incubation) until analysis by flow cytometry using an LSR Fortessa (BD Biosciences). For assessment of NP-associated fluorescence in a fluorescence plate reader, a dose of 0.05 mg/mL was used and before cell washing with PBS, the supernatant was removed from the well and diluted 10X with DMSO. Cells were then washed three times with PBS and disrupted with DMSO. Fluorescence of NPs associated with cells was then normalized to supernatant fluorescence. The relative fluorescence of each formulation was then compared to an unlayered liposome control containing the same fluorophore. For confocal imaging, 8-well chambered coverglasses (Nunc Lab-Tek II, Thermo Scientific) were coated with rat tail collagen type I (Sigma-Aldrich) per the manufacturer's instructions. HM-1 cells were plated into the wells at a density of 10K/well and left to adhere overnight prior to NP treatment. After the desired incubation time with NPs, cells were washed 3x with PBS. After washing, cells were fixed in 4% paraformaldehyde for 10 minutes then washed (3x with PBS) and stained with wheat germ agglutinin (WGA) conjugated to Alexa Fluor488 (Invitrogen) and Hoechst 33342 (Thermo Scientific) following manufacturer's instructions. Images were analyzed using ImageJ. Slides were imaged on an Olympus FV1200 Laser Scanning Confocal Microscope.

5.2.11 Fluorescent labeling of IL-12

IL-12 was labeled with indocyanine green (ICG) tetrafluorophenyl (TFP) ester (AAT Bioquest) by solubilizing the dye in dimethyl sulfoxide at 1 mg/mL and adding it to IL-12 at 3 mg/mL in phosphate buffered saline (PBS) supplemented with 0.1 M sodium bicarbonate at a 1.2:1 molar ratio of dye to protein. Excess dye was removed via 7 kDa desalting columns (Zeba Spin, ThermoFisher) and validated via thin-layer chromatography.

5.2.12 IL-12 release assay

IL-12 release from liposomes was quantified using the same procedure as quantification of PLE stability.

5.2.13 Serum-induced lipid exchange

Lipid release from NPs was assessed by generating liposomes with a high density (1 mol%) of DOPE-630-650 (for Mal-LbL) or DPPE-630/650 (for SAT-LbL) to induce fluorescence quenching. Particles were then mixed with 100% FBS solution supplemented with penicillin/streptomycin and incubated in 96 well plates in a shaker at 37 °C. At certain intervals, dye fluorescence was measured (ex: 610 nm/ em: 650 nm) on a plate reader (Tecan Infinite200) and compared to total dye fluorescence which was obtained by dissolving the NPs in DMSO.

5.2.14 Animals

All animal work was conducted under the approval of the Massachusetts Institute of Technology Division of Comparative Medicine IACUC in accordance with federal, state, and local guidelines. B6C3F1 mice were purchased from Jackson Laboratories. Female mice were used between 8-12 weeks of age unless otherwise noted.

5.2.15 Kinetics of NP association with high tumor burden tissues in metastatic ovarian cancer model

B6C3F1 mice were inoculated with firefly luciferase-expressing OV2944-HM1 (HM-1-luc) cells through intraperitoneal (i.p.) injection of 10^6 cells in PBS. For kinetics of LbL-NP association, two weeks after tumor inoculation, mice were injected with NPs containing fluorescently labeled lipid (DOPE-630/650, 0.2 mol%) and euthanized 1, 2, 4, 12 and 24 hrs after dosing. UGT and omentum tissues were extracted and placed in PBS under ice. Tissues were then transferred to an In Vivo Imaging System (IVIS, Perkin Elmer) to quantify ex-vivo tissue NP fluorescence. Data were analyzed using Living Image software. Background fluorescence measurements were made for each organ based on signal from mice treated with dextrose and measurements were normalized to tissue weight.

5.2.16 Pharmacokinetic and biodistribution in metastatic ovarian cancer model

B6C3F1 mice were inoculated with firefly luciferase-expressing OV2944-HM1 (HM-1-luc) cells through intraperitoneal (i.p.) injection of 10^6 cells in PBS. Two weeks after tumor inoculation, mice were injected with NPs containing fluorescently labeled lipid (DOPE-630/650, 0.2 mol%) and IL-12-ICG. The same IL-12-ICG was used for all groups to avoid labeling efficiency differences and groups were dosed intraperitoneally with 20 μg of IL-12. *In vivo* tumor radiant efficiency was measured on an IVIS by imaging the mice i.p. region. After the final timepoint (4 hrs or 24 hrs), mice were euthanized, organs were removed and placed in PBS under

ice. Organs were then transferred to a 1 mg/mL D-luciferin solution in PBS and incubated for 5 minutes then placed in an IVIS to determine each organ's BLI, NP fluorescence and IL-12 fluorescence. Data were analyzed using Living Image software. Background fluorescence measurements were made for each organ based on signal from mice treated with dextrose. For correlation analysis, the weight-normalized bioluminescence flux (p/s/g) and radiant efficiency ([p/s] / [μW/cm²]/g) for each organ were analyzed on Graphpad Prism 9 for their correlation via the Pearson's correlation coefficient.

5.2.17 IVIS image pixel correlation analysis

IVIS images were extracted from the Living Image software using the same range of BLI and IL-12 fluorescence values. Pixel intensity values for all tissues of each mouse were extracted using ImageJ and then analyzed for Spearman's correlation between BLI and IL-12 using GraphPad Prism 9.

5.2.18 Cryogenic freezing of omentum tumors

Omentum tissue from the biodistribution study was added to optimal cutting temperature (OCT) compound and rapidly frozen in cryomolds using isopentane with dry ice. Samples were sectioned in 10 μm slices on a microtome-cryostat onto Tissue Path Superfrost Plus Gold Slides (Fisherbrand) and stored in -80 °C. For staining, slides were rapidly fixed with ice-cold 4% methanol-free formaldehyde for 10 minutes then washed with PBS and blocked with 10% goat serum for 1 hr. The samples were then incubated with PE anti-IL-12/IL-23 p40 antibody (Biolegend) overnight at 4 °C in 1% bovine serum albumin (BSA) PBS buffer. After overnight incubation, Hoechst 33342 (ThermoFisher) and WGA-alexafluor488 (ThermoFisher) were added and allowed to incubate for 30 minutes at room temperature. Samples were then washed with PBS then were mounted with a coverslip using ProLong Gold (ThermoFisher) and stored at 4 °C after drying. Slides were imaged on an Olympus FV1200 Laser Scanning Confocal Microscope.

5.2.19 Immunophenotyping via flow cytometry and blood panel analysis

B6C3F1 mice were inoculated intraperitoneally with 10^6 cells of HM-1 in PBS. Ten days after tumor inoculation, mice were treated with either dextrose (vehicle control) or 20 μg of IL-12 in free, Mal-UL, or Mal-LbL formats. Two days after dosing, mice were bled retro-orbitally and then euthanized to extract ascites cells via peritoneal lavage with PBS. Peritoneal tumor nodules and spleen were also collected. Part of the blood samples were submitted to The Division of Comparative Medicine at MIT to perform a complete blood count and analysis of liver function

and the remainder was processed with ACK lysing buffer (Gibco) to isolate PBMCs. Spleens were processed on a 70 μm cell strainer with a syringe plunger then exposed to ACK lysing buffer to lyse red blood cells (RBCs). Tumor nodules from each mouse were diced with scissors then incubated for one hour at 37 °C in 2 mL of 1 mg/mL collagenase type IV (Sigma) in RPMI media. After collagenase incubation, tumors were processed on a 70 μm cell strainer then collected with an insulin syringe into falcon tubes to pellet tumor cells and wash out collagenase solution. For cell staining with antibodies, samples were placed in 96 well plates, then centrifuged and resuspended in Fc block solution (BD Biosciences) for 5 minutes. Freshly prepared antibody panels were then mixed with the samples and allowed to react for 20 minutes. Finally, DAPI (BD Biosciences) was added to each well (at 2 μg/mL) and allowed to react for 5 minutes. Stained cells were washed twice with flow cytometry buffer (PBS with 0.5% BSA and 2 mM EDTA), then resuspended in 2% PFA in PBS for 30 minutes, washed and stored at 4 °C for analysis the next day on a on a flow cytometry instrument (LSR Fortessa, BD Biosciences). Flow cytometry buffer was used to prepare Fc block and antibody solutions. The gating strategy for flow cytometry analysis with each antibody used is shown in **Figure D10**.

5.2.20 Efficacy studies with metastatic ovarian cancer model

B6C3F1 mice were inoculated intraperitoneally with 10^6 cells of HM-1-luc in PBS. One week after inoculation, treatment was initiated as indicated on each figure. All treatments included the same IL-12 dose. For combination with immune checkpoint inhibitors, mice received 250 μg of anti-PD1 antibody (clone 29F.1A12, BioXCell) and 100 μg of anti-CLTA4 antibody (clone 9D9, BioXCell) i.p. one day after treatment with IL-12 constructs. Animal weights were tracked daily after treatments for signs of toxicity. Bioluminescence was measured on a IVIS 10 minutes after i.p. injection of 3 μg of D-luciferin sodium salt (GoldBio) for 30 days after tumor inoculation or as needed to track tumor burden.

5.2.21 IFN-γ ELISPOT

Blood was collected from mice via sub-mandibular bleeding and lysed in ACK Lysis Buffer then placed in RPMI supplemented with 10% FBS, 1% penicillin–streptomycin, 1× non-essential amino acids (Invitrogen), 1× sodium pyruvate (Invitrogen) and 1× 2-mercaptoethanol (Invitrogen). On the same day, HM-1-luc cells (treated with 500 U ml−1 IFN-γ overnight) were subjected to 120 Gy radiation and trypsinized into a single-cell suspension in the same supplemented RPMI. Then, 25,000 irradiated HM-1-luc cells were mixed with 3×10^5 PBMCs per sample and seeded

in a 96-well ELISPOT plate (BD Biosciences) that was pre-coated with IFN-γ capture antibody (BD Biosciences). Plates were cultured for 24 h in a 37 °C incubator, then developed according to the manufacturer's protocol. Plates were scanned using a CTL-ImmunoSpot Plate Reader, and data were analysed using CTL ImmunoSpot Software.

5.2.22 Statistical Analysis

GraphPad PRISM 9 was used to perform statistical analyses. Comparisons between two groups was performed via unpaired t-tests. For multiple groups or multiple variable analysis, one-way, or two-way ANOVAs were used with Tukey's posthoc correction for time-based analysis or Sidak posthoc for other ANOVA analysis.

5.3 Results

5.3.1 Dynamics of IL-12-conjugated LbL-NPs on contact with physiologic fluids

The overall design of the LbL-NP system is shown in **Figure 5.1a**. An immunostimulatory payload (here, a single-chain version of the potent cytokine IL-12) is linked to the surface of a liposomal core particle, followed by sequential LbL deposition of a layer of positively charged poly-L-arginine (PLR) and then a layer of negatively-charged poly-L-glutamate (PLE). To understand how the stability of the IL-12/NP association impacts the efficacy of this system, we compared the previously employed non-covalent nickel:polyhistidine (Ni) interaction[18] to a new formulation with a N-aryl maleimide (Mal)-cysteine linkage of IL-12 to the particles which forms a stable covalent bond[24] (**Supplementary Table 1, Figure D1a-c**). IL-12-conjugated NPs were synthesized with both linker chemistries (Ni or Mal) in either unlayered (UL) or PLR/PLE-layered (LbL) formats. Ni and Mal NPs had similar sizes (**Figure D2a**), zeta potentials (**Figure D2b**), yields (>70%), and loadings of IL-12 (~10-13 wt%, corresponding to ~50 IL-12 molecules/particle[18] , **Figure D2c-e**).

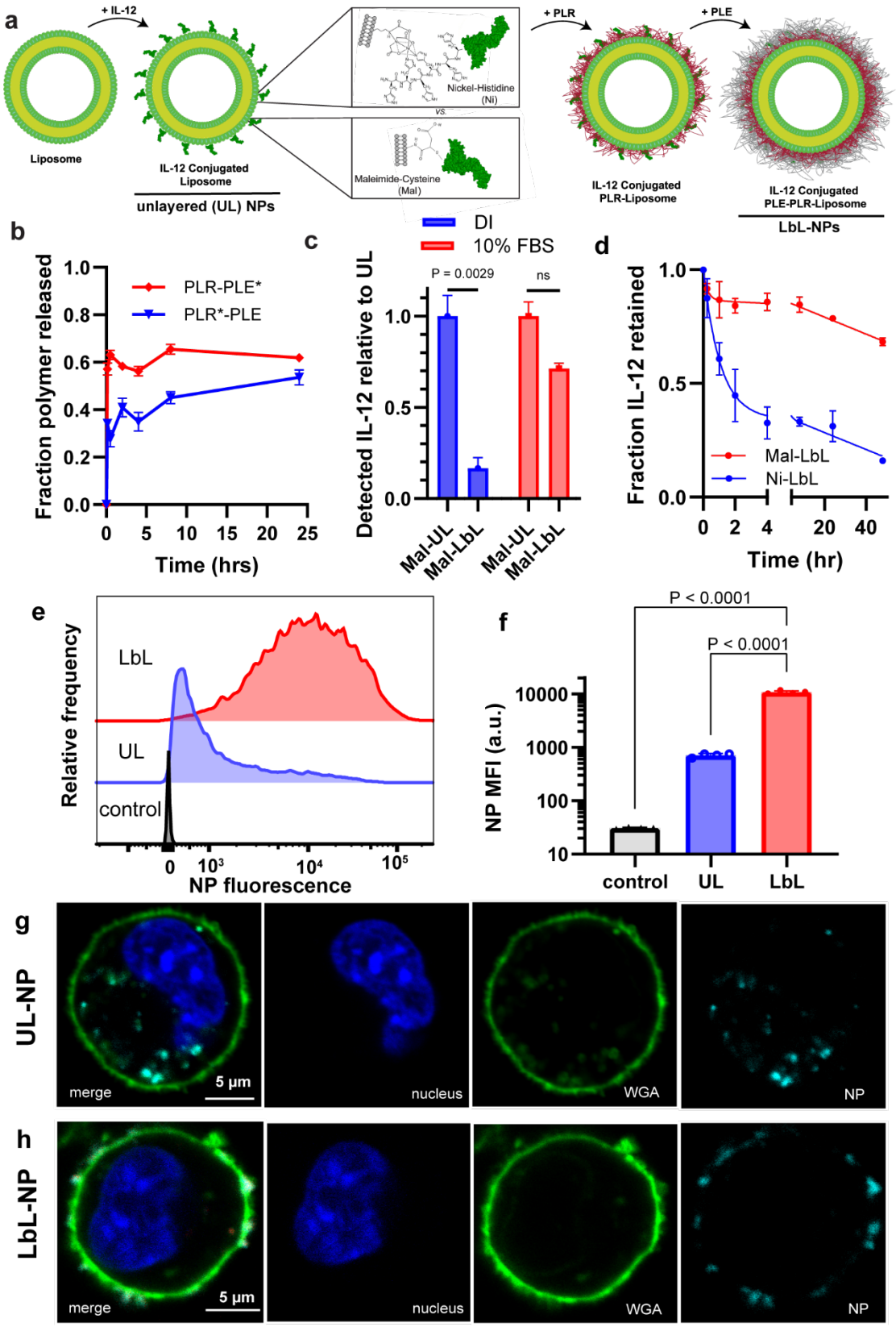
a
+ IL-12
Liposome
IL-12 Conjugated Liposome
unlayered (UL) NPs
Nickel-Histidine (Ni)
vs.
Maleimide-Cysteine (Mal)
+ PLR
+ PLE
IL-12 Conjugated PLR-Liposome
IL-12 Conjugated PLE-PLR-Liposome
LbL-NPs
b
Fraction polymer released
PLR-PLE*
PLR*-PLE
Time (hrs)
c
DI
10% FBS
Detected IL-12 relative to UL
P = 0.0029
ns
Mal-UL
Mal-LbL
d
Fraction IL-12 retained
Mal-LbL
Ni-LbL
Time (hr)
e
Relative frequency
LbL
UL
control
NP fluorescence
f
P < 0.0001
P < 0.0001
NP MFI (a.u.)
control
UL
LbL
g
UL-NP
merge
5 µm
nucleus
WGA
NP
h
LbL-NP
merge
5 µm
nucleus
WGA
NP

Figure 5.1. LbL NPs undergo dynamic reorganization on contact with physiologic fluids. a, Schematic for assembly of LbL- NPs with either Mal or Ni linker chemistries for conjugation of IL-12 onto NPs. **b,** Quantification of total PLE and PLR retained with LbL-NPs upon incubation in cell-free ascites fluid at 37 °C (* indicates fluorophore tagged polymer) (mean ± s.e.m.). **c,** Quantification of total IL-12 available for monoclonal antibody binding from Mal NPs either in diH_2O or 10% FBS media (mean ± s.e.m.). **d,** Quantification of total IL-12 released from LbL-NPs upon incubation in cell-free ascites fluid at 37 °C (mean ± s.e.m.). **e,** Representative flow cytometry fluorescence histogram of HM-1 cells incubated with unlayered (UL) or PLE-coated LbL-NPs for 4 hours *in vitro*. **f,** Quantification of median fluorescence intensity (MFI) of treated HM-1 cells from e (mean ± s.d.). **g-h,** Representative confocal images of HM-1 cells incubated with UL (**g**) or LbL NPs (**h**) for 4 hours – UL images adjusted relative to LbL to visualize internalized NPs (blue, Hoechst 33342 nuclear stain; green , wheat germ agglutinin (WGA) cell surface stain; cyan, nanoparticles). Data are representative of at least two independent experiments. Statistical comparisons in **c** and **f** were performed using two and one-way analysis of variance (ANOVA), respectively, with Tukey's multiple-comparisons test.

LbL-NPs of this type are stored in deionized water (diH_2O) to maintain colloidal stability and are diluted in 5% dextrose for isosmotic *in vivo* administration.[17,19,25] However, we expect rearrangements in the LbL film to occur *in vivo* due to the high ionic strength of the intraperitoneal fluid. To simulate the exposure of NPs to the tumor-bearing peritoneal space, we incubated LbL-NPs in cell-free ascites fluid collected from mice bearing tumors formed from the highly metastatic OC cell line OV2944-HM1 (HM-1).[26] Using fluorescently-labeled polymers to assess the release of the LbL components, we found both PLR and PLE exhibited a burst release in the presence of ascites fluid from the particles of ~40% and ~60%, respectively; following this initial rearrangement the remaining LbL film was stable for at least 24 hr (**Figure 5.1b**). Similar PLE release profiles were observed when particles were incubated in HEPES-buffered saline solution with or without serum supplementation (**Figure D3a**), suggesting that this partial polymer shedding was driven by the change in ionic strength from assembly and storage in diH_2O.

Given this reorganization of the LbL film on contact with physiological fluids, we next evaluated the accessibility of particle-bound IL-12 by capturing Mal NPs on microtiter plates and testing binding of an IL-12-specific monoclonal antibody via an enzyme-linked immunosorbent

assay (ELISA, **Figure D3b**). LbL coating of IL-12-conjugated liposomes reduced the accessibility of IL-12 conjugated to the as-synthesized particles in diH_2O by ~90%, but on exposure to serum-containing buffer, the majority of particle-bound cytokine was accessible to the anti-IL-12 antibody (**Figure 5.1c**). Further, addition of either UL or LbL NPs to IL-12 reporter cells in the presence of serum elicited roughly equivalent IL-12 signaling (**Figure D3c-d**). Exposure of NP-bound IL-12 enables IL-12 signaling and also opens the potential for release of the IL-12 from the particle core over time, either due to disruption of the Ni/his-tag interaction (for Ni particles) or via protein-mediated extraction of lipid-anchored IL-12 from the core liposomal bilayer (for Mal particles). We incubated LbL-NPs carrying fluorescently tagged IL-12 with ascites fluid collected from HM-1 tumor-bearing mice, and IL-12 release from the particles was measured over time. While Ni-LbL particles released more than 50% of their IL-12 payload in 2 hr, cytokine release from Mal-LbL particles was much slower, with ~70% of the payload still bound to the particles at 48 hr (**Figure 5.1d**). Finally, we assessed whether the LbL-NPs retained effective cancer cell targeting on exposure to physiologic conditions. When incubated with HM-1 cells in the presence of complete cell culture media, LbL-coated NPs showed a >10-fold increased association with the cancer cells relative to uncoated particles (**Figure 5.1e-f**). We previously showed that LbL-NPs selectively bind to OC cells over healthy cells.[17,27,28] Confocal imaging confirmed that Mal-LbL NPs were primarily located on the cell membrane 4 hours after NP dosing, while Mal-UL NPs were internalized in the same time frame, consistent with our prior studies of NPs carrying Ni-anchored IL-12 and suggesting that despite the initial partial shedding of polymer from the layered particles, the remaining LbL film still effectively mediated cancer cell surface targeting (**Figure 5.1g-h**).

Altogether, these analyses predict a dynamic process of rapid LbL coating reorganization on injection *in vivo*, enabling IL-12 exposure that could promote immune engagement while retaining effective OC cell surface targeting. Linkage of the cytokine to particles via Ni:histag interactions will simultaneously lead to rapid release of IL-12 from the particle carrier, while covalently anchored IL-12 is predicted to exhibit a much slower release of lipid-bound IL-12.

5.3.2 LbL-NPs rapidly associate with tumor tissue in vivo and covalent IL-12 conjugation enables prolonged cytokine retention in tumors

We next characterized the *in vivo* pharmacokinetics of IL-12 delivery via LbL-NPs in a model of disseminated OC.[26] In this model, 7 days after i.p. inoculation of luciferase-expressing HM-1 cells (HM-1-luc), tumor nodules are detected across the intestines, omentum, and urogenital tract (UGT), with a preference for the omentum and UGT as is clinically observed with metastatic OC (**Figure D4a-b**).[29] Employing fluorescently tagged IL-12 and fluorescently labeled lipids in the NP formulations, we tracked the kinetics of NP and IL-12 clearance from the i.p. space using whole-animal fluorescence imaging. UL-NPs exhibited an exponential decay in NP signal over time, but LbL-NPs, by contrast, showed a partial clearance over 24 hr, followed by prolonged retention of ~10% of particles from 24 hrs to 4 days (**Figure 5.2a**). The kinetics of IL-12 clearance were affected both by the presence of the LbL coating and chemistry of NP linkage: IL-12 loaded on Ni-UL NPs cleared with kinetics identical to free IL-12 injected i.p., suggesting rapid release of the cytokine from the Ni-UL carrier (**Fig 2b)**. LbL coating of Ni NPs prolonged IL-12 persistence, but interestingly Mal-UL NPs provided a similar IL-12 retention in the i.p. space (**Figure 5.2b-c**). Mal-LbL NPs exhibited the slowest IL-12 clearance, with ~50% of the cytokine signal still present at 4 days post injection (**Figure 5.2c**). Notably, IL-12 administered as Mal-LbL NPs had slower clearance than its lipid carrier, suggesting dissociation of the cytokine payload from the carrier particles over time, consistent with our *in vitro* analyses of NP stability.

To define the kinetics of NP accumulation at the major sites of tumor dissemination, fluorescently labeled UL or LbL-NPs devoid of IL-12 were injected i.p. in mice bearing HM-1-luc tumors, and tumor-bearing tissues were extracted at various time points post-administration for *ex vivo* NP signal measurement. LbL-NPs showed rapid association with high tumor-burdened tissues (**Figure 5.2d-e**) with peak NP fluorescence signal within ~1 or 2 hours after injection for the UGT and omentum, respectively, at 2-5-fold higher levels than UL NPs. Evaluating Ni or Mal NPs distribution at 4 hrs post-injection showed low uptake in other organs (**Figure 5.2f**) with only LbL-NPs exhibiting significant correlation between tumor bioluminescence intensity (BLI) and NP fluorescence (**Figure 5.2g-h**), consistent with LbL-NP targeting of disseminated tumors.

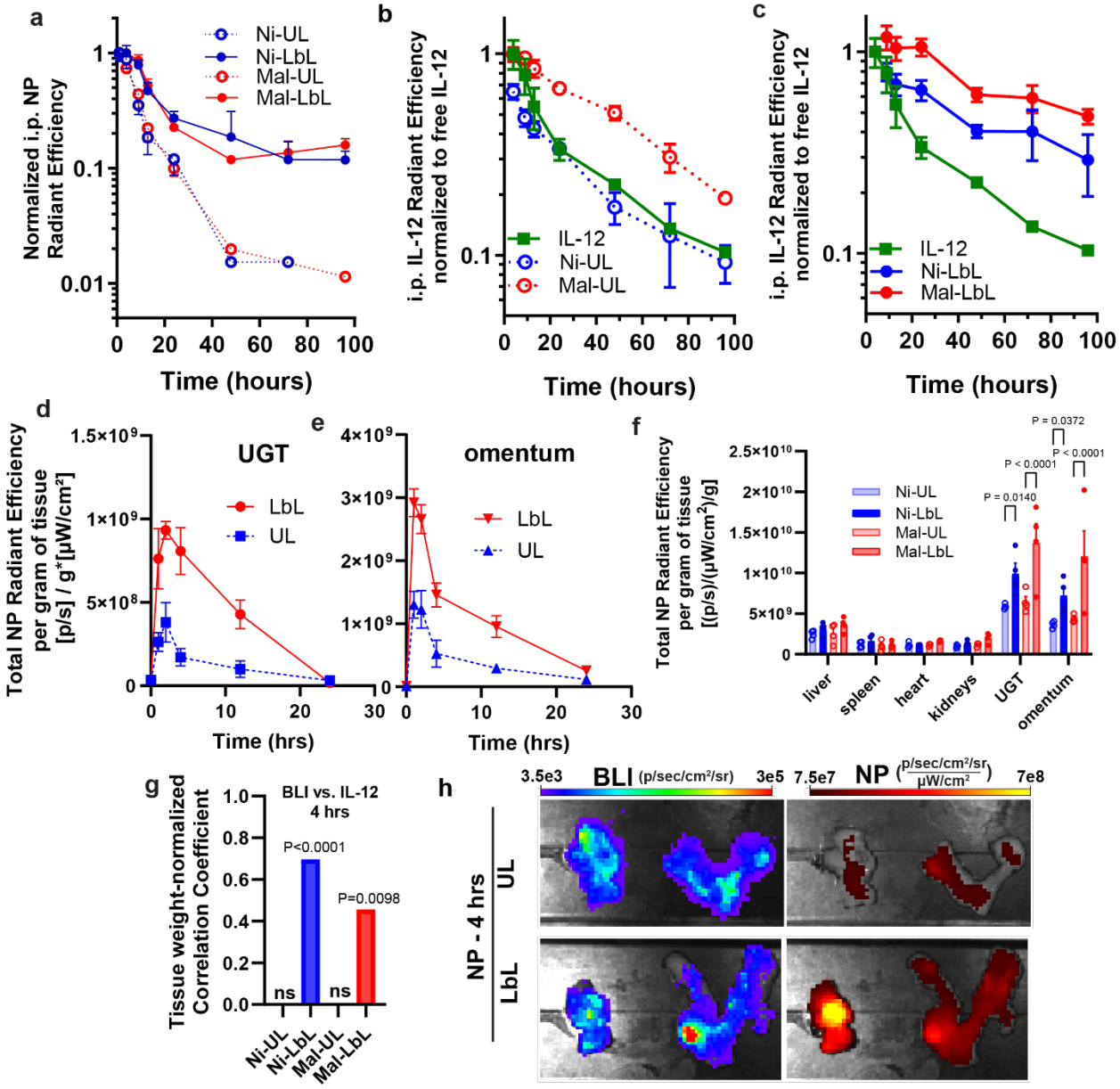

Figure 5.2. LbL coating enables targeting of tumor tissue *in vivo* and enhanced i.p. retention of NPs and IL-12. **a-c,** B6C3F1 mice (*n*=8/group for 0-24 hrs and n=3/group for 24-96 hrs) inoculated with 10^6 HM-1-luc tumor cells on day 0 were administered fluorescently-tagged NPs carrying 20 μg IL-12 (or an equivalent dose of free IL-12) on day 14. Shown are whole-animal imaging NP fluorescence **(a)** and IL-12 fluorescence **(b, c)** from the i.p. space collected over time post dosing (mean ± s.e.m.). **d-e,** B6C3F1 mice (n=4/group) inoculated with 10^6 HM-1-luc tumor cells on day 0 were administered 100 μg fluorescently-tagged LbL-NPs or UL-NPs (devoid of IL-12) on day 14. UGT and omentum tissue were harvested at 1, 2, 4, 12 and 24 hrs after dosing and

imaged ex-vivo via IVIS. Shown are weight-normalized tissue NP fluorescence in **d** UGT and **e** omentum (mean ± s.e.m.). **f-h,** B6C3F1 mice (*n*=4/group) were treated as **a-c**. Four hours after dosing, animals were sacrificed, and tissues were analyzed ex-vivo via IVIS. Shown are weight-normalized tissue NP fluorescence (mean ± s.e.m., **f**), Pearson's correlation coefficient for groups with significant ($p<0.05$) correlation between weight-normalized tissue NP fluorescence and BLI 4 hours after dosing **(g),** and representative omentum and UGT tissue IVIS BLI and NP fluorescence images for LbL NPs and UL NPs **(h)**. Correlation significance performed based on a t-test analysis with the null hypothesis of no ($r=0$) correlation. Group statistical comparisons in **f** were performed using a two-way ANOVA with Tukey's multiple-comparisons test.

We next examined the distribution of IL-12 in OC-bearing tissues and its spatial relationship with the NP carrier. Near the timepoint of peak NP accumulation in the UGT and omentum tissues (4 hrs), only Mal-LbL NPs exhibited a significant correlation between NP and IL-12 tissue fluorescence (**Figure 5.3a**), indicating that neither the LbL film of Ni-LbL or the covalent conjugation of Mal-UL alone enabled retention of the cytokine on the particle carrier over this time course *in vivo*. At 24 hr post-dosing, animals receiving Mal-LbL NPs showed increased cytokine retention in the high tumor burdened UGT and omentum, 5- and 10-fold increased over free cytokine, respectively (**Figure 5.3b**). Importantly, the fluorescence signal of IL-12 delivered via Mal-LbL NPs showed a significant correlation with tumor BLI, indicating the ability of the LbL-NPs to target disseminated OC and increase IL-12 retention in tumor tissue relative to UL or Ni NPs (**Figure 5.3c**). We also assessed *ex-vivo* IVIS images for a pixel-by-pixel correlation between tumor BLI and IL-12 fluorescence. While most IL-12 treatments had a negative correlation, Mal-LbL NP delivery of the cytokine showed a positive correlation between tumor BLI and IL-12 fluorescence, suggesting improved IL-12 tumor targeting and retention with this construct (**Figure 5.3d-e).**

Histological analysis of omental tumor nodules 24 hours after dosing revealed that the Mal-LbL NPs could efficiently penetrate tumor tissue and disseminate IL-12 (**Figure 5.3f**). Consistent with the expected lipid-IL-12-conjugate release from Mal-LbL, while NP and IL-12 signals were mostly correlated across the tissue, we could observe regions with only IL-12 or only NP signal. Furthermore, at high magnification we could observe that the Mal-LbL NPs appeared to diffusely stain the membrane of cells in the tumor with patches of high IL-12 or high NP signal (**Figure**

5.3g). These segregating signals suggest the release of IL-12 from the NP cores over time, on a timescale substantially slower than the time required for the NPs to effectively localize to tumor nodules.

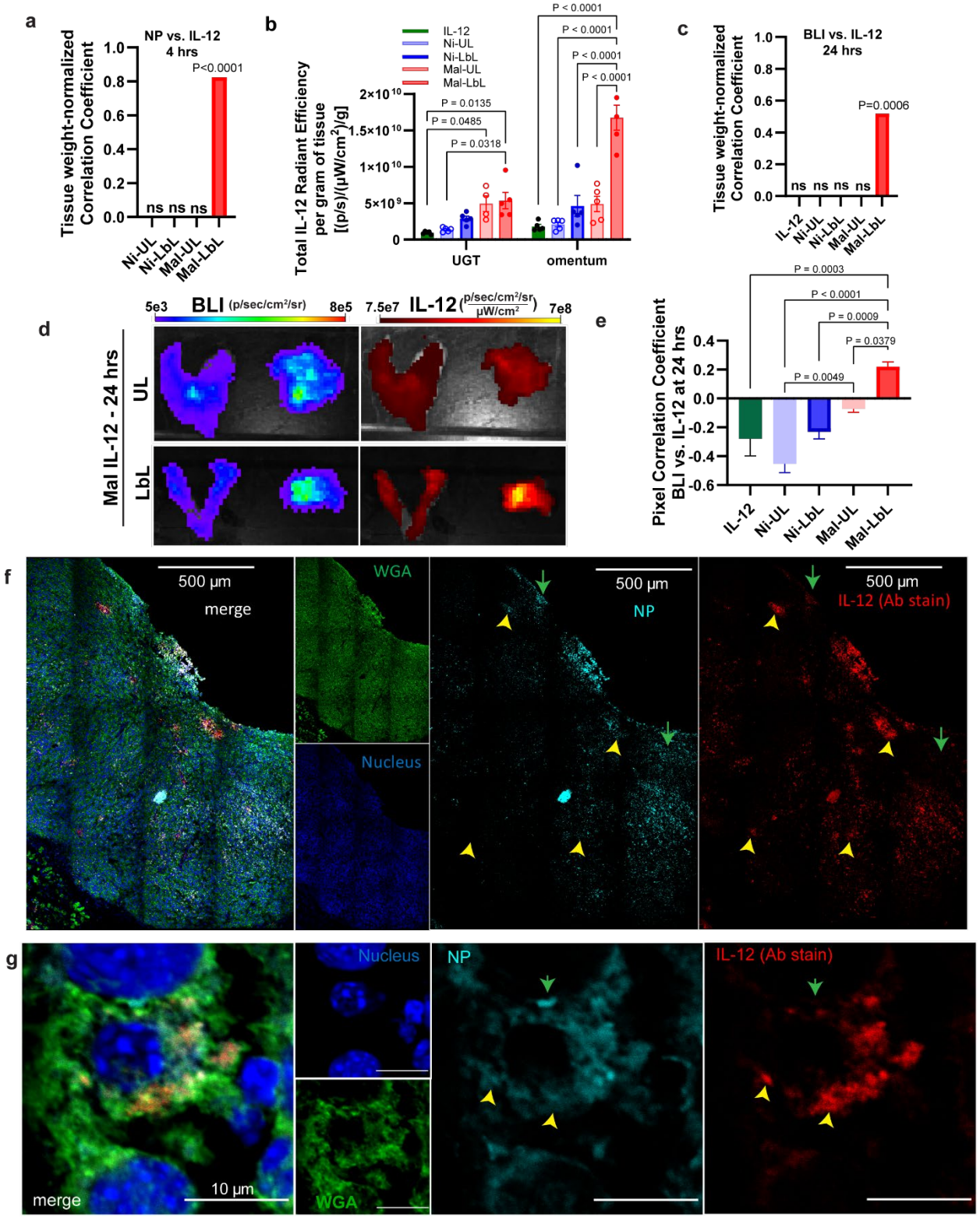

Figure 5.3. Mal-LbL NPs efficiently target and deliver IL-12 to ovarian cancer tumor nodules. A-e, B6C3F1 mice (n=4-5/group) inoculated with 10^6 HM-1-luc tumor cells on day 0 were administered fluorescently-tagged NPs carrying 20 μg IL-12 on day 14. Four hours or one day after dosing, animals were sacrificed, and tissues were analyzed ex-vivo via IVIS. Shown are Pearson's correlation coefficient for groups with significant ($p<0.05$) correlation between weight-normalized tissue NP fluorescence and IL-12 fluorescence 4 hours after dosing **(a)**, weight-normalized tissue IL-12 fluorescence one day after dosing in UGT and omentum (mean ± s.e.m., **b**), Pearson's correlation coefficient for groups with significant ($p<0.05$) correlation between weight-normalized tissue IL-12 fluorescence and BLI one day after dosing **(c)**, representative omentum and UGT tissue IVIS BLI and IL-12 fluorescence images for Mal-UL and Mal-LbL **(d)**, and pixel-by-pixel Spearman's correlation coefficient between IL-12 fluorescence and BLI one day after dosing from IVIS images. **E-f,** B6C3F1 mice were treated as in **a**. One day after dosing, Mal-LbL NP animals were sacrificed, and the omentum containing tumor nodules was frozen in optimal cutting temperature (OCT) compound then frozen sectioned and stained for confocal microscopy analysis. Shown are representative confocal microscopy images of tumor nodules in omental tissue at low **(f)** and high magnification **(g)**. Green arrows indicate areas with high NP signal relative to IL-12 whereas yellow arrowheads indicate areas with high IL-12 relative to NP. Correlation significance was performed based on a t-test analysis with the null hypothesis of no ($r=0$) correlation. Group statistical comparisons were performed using two-way ANOVA for **b** and one-way ANOVA for **e** with Tukey's multiple-comparisons test.

5.3.3 Tumor-targeted delivery of IL-12 is non-toxic and enhances therapeutic responses against metastatic ovarian cancer

To assess the therapeutic impact of enhanced IL-12 targeting to ovarian tumors achieved by Mal-LbL NPs, HM-1-luc tumor-bearing mice were treated with 20 μg of IL-12 administered as free cytokine or nanoparticle formulations at days 7 and 14, or a 5X higher dose of the free cytokine (to determine whether higher dosing of free cytokine could compensate for its rapid clearance, **Figure 5.4a**). Three days following the first dose, a dramatic drop in tumor BLI was observed for all IL-12 treatments (**Figure 5.4b**). However, except for the Mal-LbL NP-treated group, tumor

signals began to rebound by day 24, ultimately leading to similar increases in median survival of ~33 days, compared to 23 days for the untreated tumors (**Figure 5.4c**). By contrast, Mal-LbL NPs delayed tumor recurrence, increasing the median survival to 44 days, with ~30% of the animals achieving complete tumor clearance. IFN-γ ELISPOT analysis of peripheral blood lymphocytes on day 30 revealed a stronger tumor-specific T cell response induced by Mal-LbL NP treatment compared to all other groups (**Figure 5.4d**). When mice that rejected their tumors were rechallenged i.p. with fresh tumor cells on day 100, all animals showed rapid tumor clearance (**Figure D5a**) and survived whereas all naïve mice succumbed to the tumor challenge (**Figure D5b**), indicating successful development of protective anti-tumor memory.

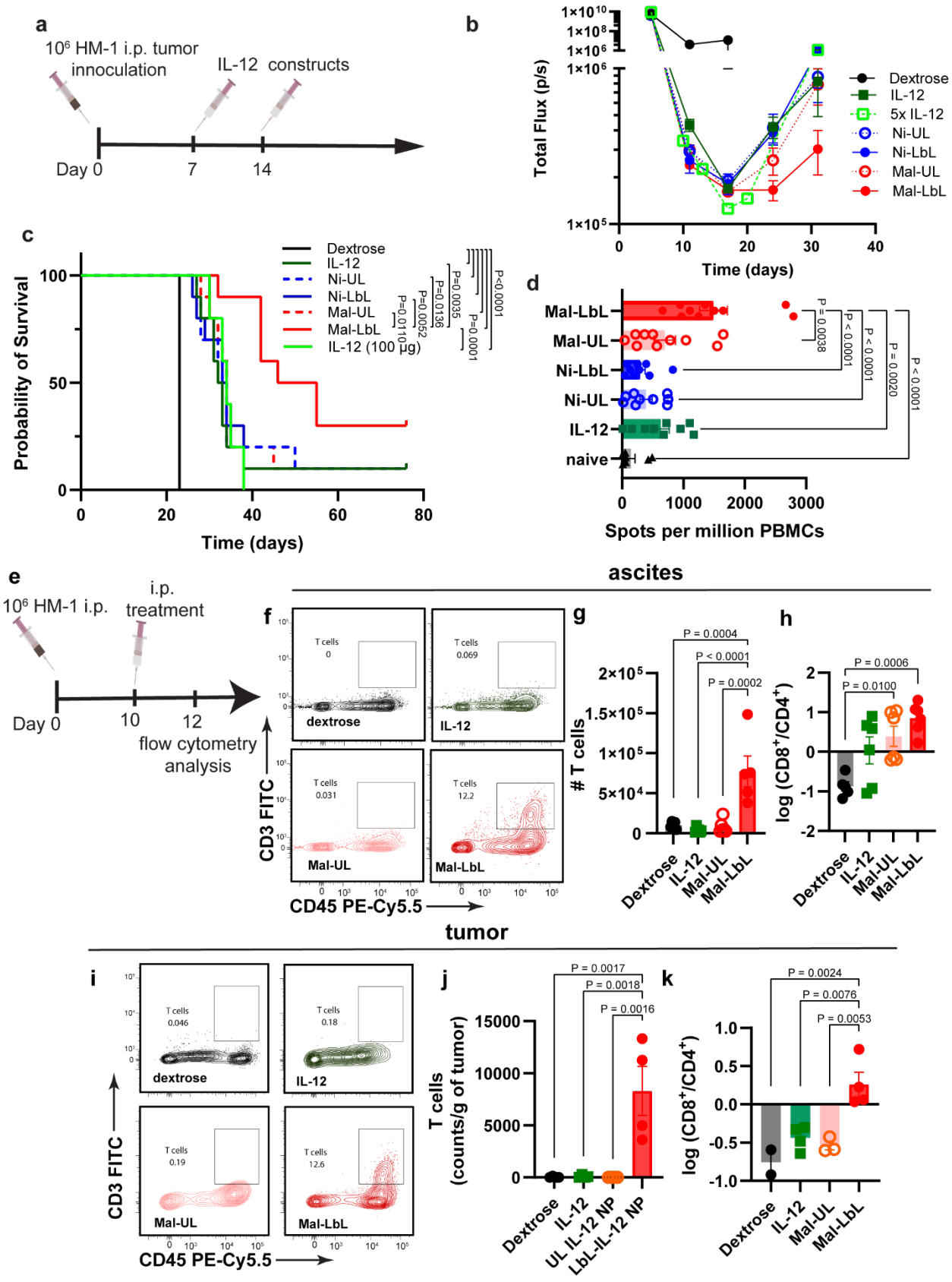
a
10⁶ HM-1 i.p. tumor innoculation
IL-12 constructs
Day 0
7
14
b
Total Flux (p/s)
Time (days)
Dextrose
IL-12
5x IL-12
Ni-UL
Ni-LbL
Mal-UL
Mal-LbL
c
Probability of Survival
Time (days)
Dextrose
IL-12
Ni-UL
Ni-LbL
Mal-UL
Mal-LbL
IL-12 (100 µg)
P=0.0110
P=0.0052
P=0.0136
P=0.0035
P=0.0001
P<0.0001
d
Mal-LbL
Mal-UL
Ni-LbL
Ni-UL
IL-12
naive
P = 0.0038
P < 0.0001
P < 0.0001
P = 0.0020
P < 0.0001
Spots per million PBMCs
e
10⁶ HM-1 i.p.
i.p. treatment
Day 0
10
12
flow cytometry analysis
ascites
f
T cells 0
dextrose
T cells 0.069
IL-12
T cells 0.031
Mal-UL
T cells 12.2
Mal-LbL
CD3 FITC
CD45 PE-Cy5.5
g
P = 0.0004
P < 0.0001
P = 0.0002
# T cells
Dextrose
IL-12
Mal-UL
Mal-LbL
h
P = 0.0006
P = 0.0100
log (CD8⁺/CD4⁺)
Dextrose
IL-12
Mal-UL
Mal-LbL
tumor
i
T cells 0.046
dextrose
T cells 0.18
IL-12
T cells 0.19
Mal-UL
T cells 12.6
Mal-LbL
CD3 FITC
CD45 PE-Cy5.5
j
P = 0.0017
P = 0.0018
P = 0.0016
T cells (counts/g of tumor)
Dextrose
IL-12
UL IL-12 NP
LbL-IL-12 NP
k
P = 0.0024
P = 0.0076
P = 0.0053
log (CD8⁺/CD4⁺)
Dextrose
IL-12
Mal-UL
Mal-LbL

Figure 5.4. IL-12 delivered by Mal-LbL NPs exhibits potent anti-tumor activity and enhances T cell infiltration of tumors. a-d, B6C3F1 mice (*n* = 10/group) inoculated with 10^6 HM-1-luc tumor cells on day 0 were treated on days 7 and 14 with 20 μg of IL-12 as a free cytokine or conjugated to NPs. Shown are the experimental timeline **(a),** in vivo IVIS whole-animal i.p. BLI readings (mean ± s.e.m., **b)**, and overall survival **(c)**. On day 30, peripheral blood mononuclear cells (PBMCs) of surviving and naïve mice (n = 5) were analyzed via IFN-γ ELISpot restimulated with HM-1-luc tumor cells. Shown are quantitation of spots detected (mean ± s.e.m., **d**). **e-k**, B6C3F1 mice inoculated with 10^6 HM-1 tumor cells on day 0 were treated on days 10 with 20 μg of IL-12 as a free cytokine or conjugated to Mal NPs (UL and LbL). Two days after dosing ascites (*n* = 6/group) and i.p. tumor nodules (primarily omentum tissue, *n* = 4/group) were harvested and processed for flow cytometry analysis. Show are timeline for experiment (**e**), representative flow plots of T cell ($CD45^+CD3^+$) in ascites fluid (**f**), quantitation of T cells in ascites fluid (**g**), quantitation of $CD8^+$ to $CD4^+$ T cell ratio in ascites fluid (**h**), representative flow plots of T cell ($CD45^+CD3^+$) in tumor nodules (**i**), quantitation of T cells in tumor nodules (**j**), quantitation of $CD8^+$ to $CD4^+$ T cell ratio in tumor nodules (**k**). *P* values were determined by the log-rank (Mantel–Cox) test **(c)** and one-way ANOVA followed by Tukey's multiple comparison test (**d, g, h, j, k**).

We next sought to determine the safety of this treatment. Mice bearing 10-day old HM-1 i.p. tumors were dosed with 20 μg IL-12 in either free form or conjugated to Mal-UL or Mal-LbL NPs. Two days after dosing, blood was collected, and spleen was processed via flow cytometry (**Figure 5.4e**). Systemic IL-12 administration is known to increase markers of liver toxicity, induce transient cytopenia, and alter the splenic immune cell profile.[30–36] While none of the treatments caused major liver damage as measured by liver enzyme activities, Mal-UL increased levels compared to healthy controls (**Figure D6a**). Both free IL-12 and Mal-UL reduced white blood cell (WBC) counts compared to vehicle control mice, which was not observed with Mal-LbL treatment (**Figure D6b)**. Untargeted IL-12 treatments also induced reduced leukocyte counts in the spleen and Mal-UL NPs elevated levels of splenic macrophage and NK cells, consistent with the expected effects of systemic IL-12 exposure (**Figure D6d-e**).

To examine the effects of IL-12 therapy on the immune response in the local tissue, we next analyzed leukocytes in the ascites (peritoneal fluid) and tumor nodules via flow cytometry two days following a single dose of free IL-12 or IL-12 NPs at day 10 post HM-1 inoculation (**Figure 5.4e**). Within the ascites, all IL-12 treatments depleted protumorigenic $CD206^{+}CD80^{-}$ (M2-like) macrophages (**Figure D7a**), shifting the macrophage population towards a predominantly tumoricidal $CD206^{-}CD80^{+}$ M1-like phenotype (**Figure D7b**). Polymorphonuclear and monocyte-related myeloid-derived suppressor cells (MDSCs) in the ascites, which can hinder the development of an effective immune response,[37] were also reduced for all IL-12 treatment groups (**Figure D7c-d**), while levels of natural killer (NK) cells increased (**Figure D7e**). However, only Mal-LbL treatment substantially increased T cell accumulation in the ascites fluid (**Figure 5.4f-g**). Characterization of the T-cell subtypes revealed a shift towards an increased CD8:CD4 ratio (**Figure 5.4h**) which is associated with improved outcomes in human OC patients.[38]

In extracted tumor nodules, IL-12 treatments did not cause major effects in either PMN-MDSCs (**Figure D7f**) or M-MDSCs levels (**Figure D7g**). All IL-12-based treatments polarized the macrophage population from a predominantly M2-like towards a predominantly M1-like phenotype (**Figure D7h**). However, only free IL-12 treatment led to a substantial increase in the number of M1-like tumoricidal macrophages (**Fig S7i**), suggesting a bias towards monocyte-driven immune response from systemic IL-12 treatment. On the other hand, Mal-LbL NPs increased NK cell infiltration (**Figure D7j**). Moreover, Mal-LbL NP treatment triggered a dramatic ~50-fold increase in T cell infiltration in tumor nodules and increase in the ratio of $CD8^{+}$ to $CD4^{+}$ T cells, which was not observed for free IL-12 or unlayered particles (**Figure 5.4i-k**). These results demonstrate the importance of targeting the cytokine to cancer cells to modulate immune infiltration of lymphocytes into tumors which is not achievable by free cytokine administration.

5.3.4 Efficacy of tumor-targeted IL-12 delivery from LbL-NPs is dependent on a fluid membrane composition of the liposomal core.

Membrane lipids *in vivo* can be extracted from bilayers by albumin and other serum components and undergo constant exchange with serum lipids.[39–42] We hypothesized that the gradual release of IL-12-lipid-conjugates from Mal-LbL NPs through this process was important for optimal cytokine activity, as this could promote dissemination of the cytokine throughout the tumor bed to engage with immune cells, while simultaneously promoting prolonged retention in

the tumor via insertion of the lipid tails of the conjugate in cell membranes in the local microenvironment (**Figure 5.5a**). To test if IL-12-lipid conjugate release from the NP core was important for the therapeutic efficacy of Mal-LbL particles, we prepared NPs incorporating exclusively saturated lipids. Unlike Mal-LbL which contained unsaturated lipids, fully saturated lipids exhibit increased resistance to extraction by serum components *in vivo* due to their gel-phase state at physiologic temperatures (**Table S2, Figure D8a**).[43–45] These fully saturated LbL-NPs (SAT-LbL) carrying covalently-linked IL-12 had the same size and zeta potential as Mal-LbL particles, showed identical binding to HM-1 cells *in vitro*, and maintained IL-12 bioactivity against reporter cells (**Figure D8b-f)**. However, SAT-LbL NPs were substantially more resistant to the extraction of fluorophore tagged lipids in serum compared to Mal-LbL (**Figure D8g)** and showed reduced IL-12 release in serum compared to Mal-LbL NPs (**Figure D8h)**.

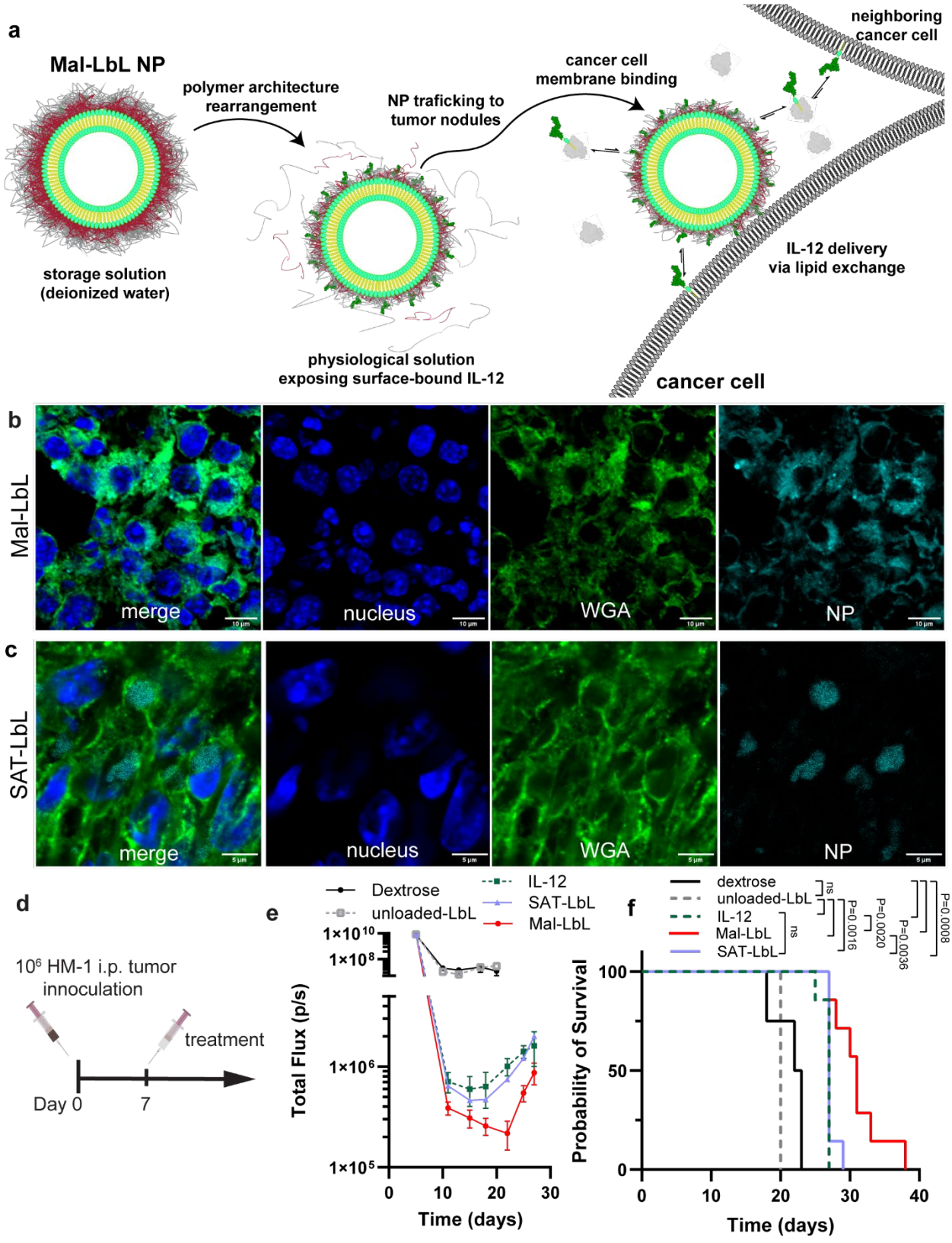
a
Mal-LbL NP
polymer architecture rearrangement
NP trafficking to tumor nodules
cancer cell membrane binding
neighboring cancer cell
storage solution (deionized water)
physiological solution exposing surface-bound IL-12
IL-12 delivery via lipid exchange
cancer cell
b
Mal-LbL
merge
nucleus
WGA
NP
c
SAT-LbL
merge
nucleus
WGA
NP
d
10⁶ HM-1 i.p. tumor innoculation
treatment
Day 0
7
e
Dextrose
unloaded-LbL
IL-12
SAT-LbL
Mal-LbL
Total Flux (p/s)
Time (days)
f
dextrose
unloaded-LbL
IL-12
Mal-LbL
SAT-LbL
ns
P=0.0016
P=0.0020
P=0.0036
P=0.0008
Probability of Survival
Time (days)

Figure 5.5. Efficacy of Mal-LbL NPs is dependent on lipid exchange properties which alter lipid distribution inside tumor nodules. a, Schematic of proposed mechanism of tumor targeted IL-12 lipid-conjugate dissemination from Mal-LbL NPs. **b-c**, B6C3F1 mice were inoculated with 10^6 HM-1-luc tumor cells on day 0 were administered fluorescently-tagged Mal-LbL of SAT-LbL NPs carrying 20 μg IL-12 on day 14. One day after dosing, animals were sacrificed, and the omentum containing tumor nodules was frozen in optimal cutting temperature (OCT) compound then frozen sectioned and stained for confocal microscopy analysis. Shown are representative high-magnification confocal images of omental tumor nodules from Mal-LbL (**b**) and SAT-LbL (**c**). **d-f**, B6C3F1 mice (n = 7/group) inoculated with 10^6 HM-1-luc tumor cells on day 0 were treated on days 7 with NP vehicle control (unloaded-LbL), 20 μg of IL-12 as a free cytokine or conjugated to Mal-LbL or SAT-LbL. Shown are the experimental timeline **(d),** in vivo IVIS whole-animal i.p. BLI readings **(**mean ± s.e.m., **e)**, and overall survival **(f)**. Statistical comparisons between survival curves were performed using a log-rank (Mantel–Cox) test.

To determine whether membrane composition impacts the biodistribution of lipids initially incorporated into the liposomal core, we treated HM-1 tumor-bearing mice with either Mal-LbL or SAT-LbL NPs carrying fluorescent phosphatidylethanolamine (PE) lipids. One day after dosing, we extracted the omentum tumor nodules for histological assessment via confocal microscopy. Both SAT-LbL and Mal-LbL NPs efficiently penetrated tumors (**Figure D9a-b**). Strikingly, the membrane composition of the NPs directly impacted the pattern of fluorescent-lipid distribution in tumor nodules: fluorophore-lipids delivered by Mal-LbL NPs localized in regions showing high staining for cell membranes and extracellular matrix (wheat germ agglutinin, WGA), while fluorescent lipids delivered as part of SAT-LbL NPs localized in pockets devoid of WGA staining **(Figure 5.5b-c**), suggesting that SAT-LbL particles (and their associated fluorescent-lipid cargo) might be ultimately internalized by cells in the tissue.

We next carried out a therapeutic study administering a single dose of 20 μg IL-12 as free cytokine, Mal-LbL NPs, SAT-LbL NPs, or a control LbL-NP lacking IL-12 (unloaded-LbL, **Figure 5.5d**). Unloaded-LbL NPs had no impact on tumor BLI and did not induce any therapeutic benefit compared to vehicle control mice (**Figure 5.5e-f**). As seen in the two-dose setting, a single administration of Mal-LbL NPs dramatically reduced tumor BLI by 3 days post dosing, which did

not begin to relapse until after day 22 and extended median survival to 31 days. Interestingly, free IL-12 and SAT-LbL NPs elicited very similar tumor BLI reduction/relapse and overall survival, with relapse evidence after day 18 and median survival of only 27 days (**Figure 5.5e-f**). These data suggest that the lipid-exchange properties of Mal-LbL NPs enabling slow release of lipid-conjugate IL-12 are important for the improved therapeutic benefit seen with this formulation.

5.3.5 Mal-LbL NPs sensitize metastatic ovarian cancer to immune checkpoint inhibitors therapy

Checkpoint inhibitors (CPI), such as antibodies blocking the negative regulatory receptors PD-1 and CTLA-4 expressed by T cells, are currently the most broadly effective class of immunotherapy agents clinically, but CPIs have failed to show substantial benefit in OC.[46,47] Responsiveness to checkpoint blockade correlates with the presence of pre-existing CD8 T cell infiltrates in patient tumors,[48] and thus we hypothesized that enhanced T cell infiltration driven by LbL-NPs could increase the responsiveness of OC to checkpoint inhibition. Moreover, IL-12 induces strong IFN-γ expression in T cells and NK cells, which will in turn upregulate expression of PD-L1 on tumor cells, a phenomenon termed adaptive resistance.[49] We thus theorized that Mal-LbL treatment may sensitize OC to CPI therapy. To test this idea, we evaluated treatment of HM-1-luc tumors with systemic anti-PD-1 + anti-CTLA-4 CPI therapy alone or combined with two weekly doses of IL-12 in free or NP form (**Figure 5.6a**). Analysis of tumor burden via BLI clearly showed that CPIs alone could only mildly and transiently control tumor growth (**Figure 5.6b**). On the other hand, there was a marked synergism when any form of IL-12 was included in the treatment, reducing tumor BLI to baseline for one month after tumor inoculation. CPI therapy alone had only marginal survival benefit over untreated controls, similar to what has been observed with OC in the clinic (**Figure 5.6c).**[47] Combining CPI with free IL-12 showed some efficacy, reducing tumor BLI to baseline for ~25 days and curing 20% of treated animals (**Figure 5.6b-c**). Ni-LbL also synergized with CPI treatment, showing a significant extension in survival compared to free IL-12 and CPI but ultimately resulted in only a 30% long-term survivor rate. Strikingly, however, Mal-LbL showed a remarkable sensitization effect, achieving 100% cures with this treatment schedule (**Figure 5.6c**). When challenged with fresh tumor cells at day 150, all Mal-LbL NP-treated mice rejected the rechallenge (**Figure 5.6d-e**), demonstrating induction of a strong memory response. Thus, engineering the rapid targeting and slow local release of IL-12 in ovarian

tumor nodules using LbL-NPs dramatically sensitizes tumors to clinically approved CPI combination therapy.

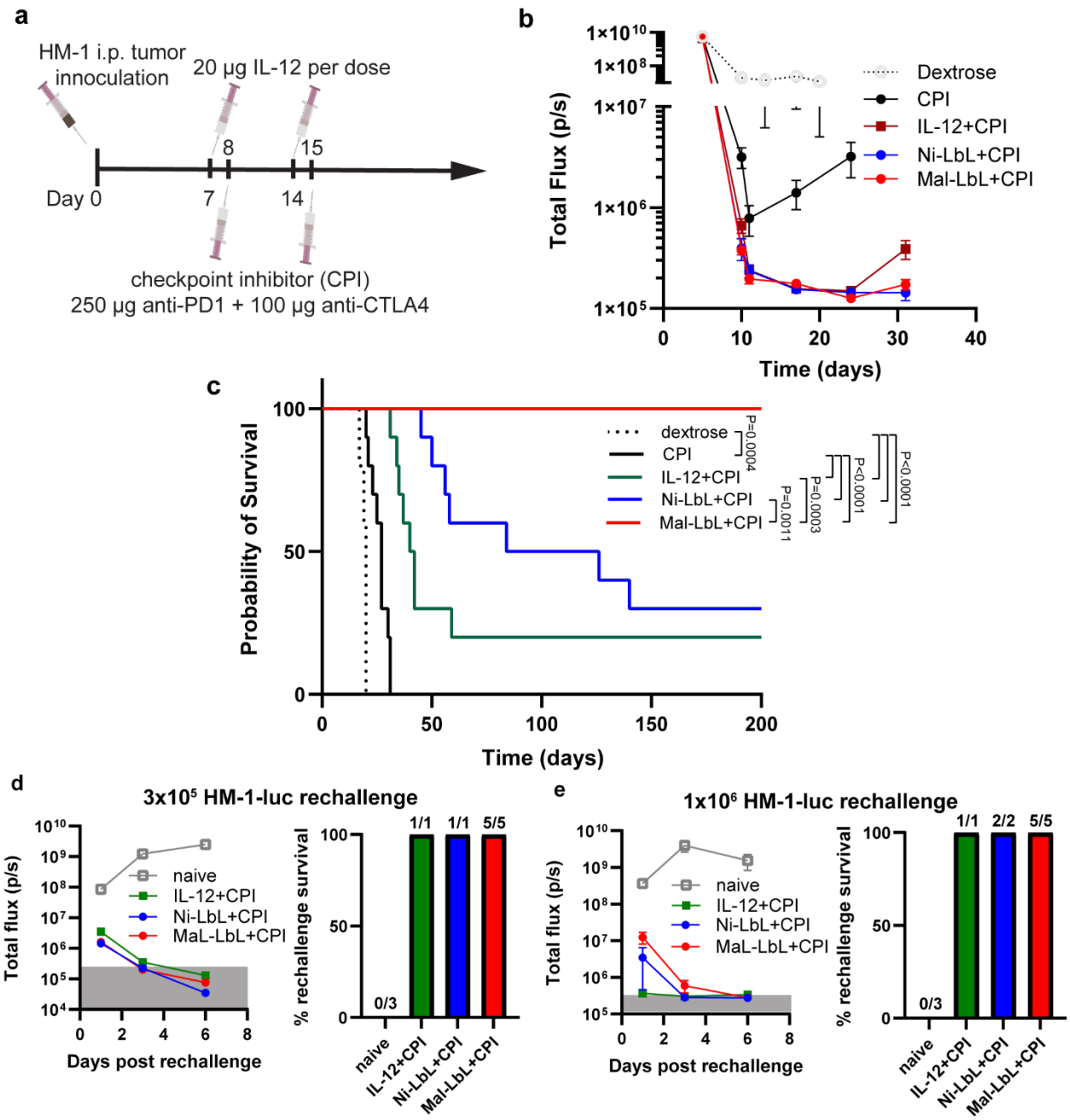

Figure 5.6. Combination of immune checkpoint inhibitors with two dose treatment of Mal-LbL eradicates metastatic ovarian cancer. a-e, B6C3F1 mice (n = 10/group) inoculated with 10^6 HM-1-luc tumor cells on day 0 were treated on days 7 and 14 with 20 µg of IL-12 as a free

cytokine or conjugated to Mal-LbL or Ni-LbL. Mice were also treated with 250 µg of anti-PD1 and 100 µg of anti-CTLA4 i.p. on days 8 and 15. Shown are the experimental timeline **(a),** *in vivo* IVIS whole-animal i.p. BLI readings **(**mean ± s.e.m., **b)**, and overall survival **(c)**. On day 150, surviving mice were rechallenged with either $3x10^5$ (**d**) or 10^6 (**e**) HM-1-luc tumor cells i.p. Shown are in vivo IVIS whole-animal i.p. BLI readings post rechallenge **(**mean ± s.e.m) and the percentage of mice per group that survived rechallenge. Statistical comparisons between survival curves were performed using a log-rank (Mantel–Cox) test.

5.4 Discussion

Cytokine therapies have been challenging to develop and achieve regulatory approval.[9,50] IL-12 has long been viewed as an attractive candidate cytokine to drive ant-tumor immunity, but has failed to progress clinically due to its low therapeutic index when administered as a free protein drug.[51] Here we report the use of LbL-NPs capable of targeting and attaching to cancer cell membranes to deliver IL-12 in peritoneally-disseminated metastatic OC. We demonstrate that optimized LbL-IL-12-NPs are non-toxic, elicit strong systemic anti-tumor immunity, drive remodeling of the TME, and strongly sensitize ovarian tumors to CPI therapy. Importantly, we demonstrate that the efficacy of LbL-IL-12-NPs is dependent on both covalent conjugation of the cytokine payload to lipids and lipid extraction, a known but relatively unexplored property of lipid-based nanoparticles. It is also clear that targeting the LbL-NPs to the tumor cell membrane surface is a critical aspect of this approach. In addition to delayed lipid-conjugate release from the NP, such a mechanism may promote trafficking of therapeutic payloads to tumor-draining lymph nodes.[52]

Although other approaches exist to augment cytokine delivery in cancer, most rely on local (intratumoral, i.t.) administration to increase tumor drug concentration while minimizing systemic exposure.[53] However, such approaches would be impractical to implement in metastatic OC due to difficulties with administration into small, disseminated legions in the i.p. space. Moreover, while NPs have previously been explored for cytokine delivery, they have primarily relied on passive tumor targeting through the enhanced permeability and retention (EPR) effect by extending NP circulatory half-life via polyethylene glycol (PEG) decoration.[8] However, in addition to concerns with anti-PEG immune responses[54], increased half-life also increases

systemic exposure and subsequent toxicity and the lack of specific tumor interactions would facilitate clearance from the peritoneal cavity after i.p. administration.[17]

In summary, this study demonstrates that engineering PLE-coated LbL-NPs carrying IL-12 can facilitate both tumor-targeted delivery and sustained cytokine release within disseminated tumor nodules. Combining tumor targeting with localized cytokine dissemination in the tumor microenvironment significantly improves the efficacy of this immunotherapy against metastatic ovarian cancer. Importantly, optimized LbL-NPs exhibited strong synergy with checkpoint blockade, the current gold standard for cancer immunotherapy in the clinic.

5.5 References

1. Arora, T., Mullangi, S. & Lekkala, M. R. *Ovarian Cancer*. (2023).

2. Lheureux, S., Braunstein, M. & Oza, A. M. Epithelial ovarian cancer: Evolution of management in the era of precision medicine. *CA Cancer J Clin* caac.21559 (2019) doi:10.3322/caac.21559.

3. Esfahani, K. *et al.* A Review of Cancer Immunotherapy: From the Past, to the Present, to the Future. *Current Oncology* **27**, 87–97 (2020).

4. Korman, A. J., Garrett-Thomson, S. C. & Lonberg, N. The foundations of immune checkpoint blockade and the ipilimumab approval decennial. *Nat Rev Drug Discov* **21**, 509–528 (2022).

5. Upadhaya, S., Neftelinov, S. T., Hodge, J. & Campbell, J. Challenges and opportunities in the PD1/PDL1 inhibitor clinical trial landscape. *Nat Rev Drug Discov* **21**, 482–483 (2022).

6. Chardin, L. & Leary, A. Immunotherapy in Ovarian Cancer: Thinking Beyond PD-1/PD-L1. *Front Oncol* **11**, (2021).

7. Anderson, K. G., Stromnes, I. M. & Greenberg, P. D. Obstacles Posed by the Tumor Microenvironment to T cell Activity: A Case for Synergistic Therapies. *Cancer Cell* **31**, 311–325 (2017).

8. Pires, I. S., Hammond, P. T. & Irvine, D. J. Engineering Strategies for Immunomodulatory Cytokine Therapies: Challenges and Clinical Progress. *Adv Ther (Weinh)* **4**, 2100035 (2021).

9. Agarwal, Y. *et al.* Intratumourally injected alum-tethered cytokines elicit potent and safer local and systemic anticancer immunity. *Nat Biomed Eng* **6**, 129–143 (2022).

10. Irvine, D. J. & Dane, E. L. Enhancing cancer immunotherapy with nanomedicine. *Nature Reviews Immunology* 1–14 Preprint at https://doi.org/10.1038/s41577-019-0269-6 (2020).

11. Yang, Y. *et al.* Nanomedicine Strategies for Heating "Cold" Ovarian Cancer (OC): Next Evolution in Immunotherapy of OC. *Advanced Science* **9**, (2022).

12. Thaker, P. H., Borys, N., Fewell, J. & Anwer, K. GEN-1 immunotherapy for the treatment of ovarian cancer. *Future Oncology* **15**, 421–438 (2019).

13. Lin, Y. *et al.* Immunostimulatory gene therapy combined with checkpoint blockade reshapes tumor microenvironment and enhances ovarian cancer immunotherapy. *Acta Pharm Sin B* **14**, 854–868 (2024).

14. Wimalachandra, D. C. *et al.* Microfluidic-Based Immunomodulation of Immune Cells Using Upconversion Nanoparticles in Simulated Blood Vessel–Tumor System. *ACS Appl Mater Interfaces* **11**, 37513–37523 (2019).

15. Mei, K.-C. *et al.* Liposomal Delivery of Mitoxantrone and a Cholesteryl Indoximod Prodrug Provides Effective Chemo-immunotherapy in Multiple Solid Tumors. *ACS Nano* **14**, 13343–13366 (2020).

16. Kang, Y. *et al.* Large, Anionic Liposomes Enable Targeted Intraperitoneal Delivery of a TLR 7/8 Agonist To Repolarize Ovarian Tumors' Microenvironment. *Bioconjug Chem* **32**, 1581–1592 (2021).

17. Correa, S. *et al.* Tuning Nanoparticle Interactions with Ovarian Cancer through Layer-by-Layer Modification of Surface Chemistry. *ACS Nano* **14**, 2224–2237 (2020).

18. Barberio, A. E. *et al.* Cancer Cell Coating Nanoparticles for Optimal Tumor-Specific Cytokine Delivery. *ACS Nano* **14**, 11238–11253 (2020).

19. Barberio, A. E. *et al.* <scp>Layer-by-layer</scp> interleukin-12 nanoparticles drive a safe and effective response in ovarian tumors. *Bioeng Transl Med* (2022) doi:10.1002/btm2.10453.

20. Rüger, R., Müller, D., Fahr, A. & Kontermann, R. E. *In vitro* characterization of binding and stability of single-chain Fv Ni-NTA-liposomes. *J Drug Target* **14**, 576–582 (2006).

21. Platt, V. *et al.* Influence of Multivalent Nitrilotriacetic Acid Lipid−Ligand Affinity on the Circulation Half-Life in Mice of a Liposome-Attached His_6-Protein. *Bioconjug Chem* **21**, 892–902 (2010).

22. Lieschke, G. J., Rao, P. K., Gately, M. K. & Mulligan, R. C. Bioactive murine and human interleukin-12 fusion proteins which retain antitumor activity in vivo. *Nat Biotechnol* **15**, 35–40 (1997).

23. Stewart, J. C. M. Colorimetric determination of phospholipids with ammonium ferrothiocyanate. *Anal Biochem* **104**, 10–14 (1980).

24. Ravasco, J. M. J. M., Faustino, H., Trindade, A. & Gois, P. M. P. Bioconjugation with Maleimides: A Useful Tool for Chemical Biology. *Chemistry – A European Journal* **25**, 43–59 (2019).

25. Correa, S., Boehnke, N., Deiss-Yehiely, E. & Hammond, P. T. Solution Conditions Tune and Optimize Loading of Therapeutic Polyelectrolytes into Layer-by-Layer Functionalized Liposomes. *ACS Nano* **13**, 5623–5634 (2019).

26. Hashimoto, M., Niwa, O., Nitta, Y., Takeichi, M. & Yokoro, K. Unstable Expression of E-Cadherin Adhesion Molecules in Metastatic Ovarian Tumor Cells. *Japanese Journal of Cancer Research* **80**, 459–463 (1989).

27. Pickering, A. J. *et al.* Layer-by-Layer Polymer Functionalization Improves Nanoparticle Penetration and Glioblastoma Targeting in the Brain. *ACS Nano* (2023) doi:10.1021/acsnano.3c09273.

28. Tošić, I. *et al.* Lipidome-based Targeting of STAT3-driven Breast Cancer Cells Using Poly- <scp>l</scp> -glutamic Acid–coated Layer-by-Layer Nanoparticles. *Mol Cancer Ther* **20**, 726–738 (2021).

29. Iwagoi, Y. *et al.* Omental metastasis as a predictive risk factor for unfavorable prognosis in patients with stage III–IV epithelial ovarian cancer. *Int J Clin Oncol* **26**, 995–1004 (2021).

30. Gokhale, M. S. *et al.* Single low-dose rHuIL-12 safely triggers multilineage hematopoietic and immune-mediated effects. *Exp Hematol Oncol* **3**, 11 (2014).

31. Eng, V. M. *et al.* The stimulatory effects of interleukin (IL)-12 on hematopoiesis are antagonized by IL-12-induced interferon gamma in vivo. *J Exp Med* **181**, 1893–1898 (1995).

32. Car, B. D. *et al.* Role of interferon-gamma in interleukin 12-induced pathology in mice. *Am J Pathol* **147**, 1693–707 (1995).

33. Grigorian, A. & O'Brien, C. B. Hepatotoxicity Secondary to Chemotherapy. *J Clin Transl Hepatol* **2**, (2014).

34. Gollob, J. A. *et al.* Phase I Trial of Concurrent Twice-Weekly Recombinant Human Interleukin-12 Plus Low-Dose IL-2 in Patients With Melanoma or Renal Cell Carcinoma. *Journal of Clinical Oncology* **21**, 2564–2573 (2003).

35. Orange, J. S., Wolf, S. F. & Biron, C. A. Effects of IL-12 on the response and susceptibility to experimental viral infections. *The Journal of Immunology* **152**, 1253–1264 (1994).

36. Mansurov, A. *et al.* Masking the immunotoxicity of interleukin-12 by fusing it with a domain of its receptor via a tumour-protease-cleavable linker. *Nat Biomed Eng* **6**, 819–829 (2022).

37. Okła, K. Myeloid-Derived Suppressor Cells (MDSCs) in Ovarian Cancer—Looking Back and Forward. *Cells* **12**, 1912 (2023).

38. Giuntoli, R. L. *et al.* Ovarian cancer-associated ascites demonstrates altered immune environment: implications for antitumor immunity. *Anticancer Res* **29**, 2875–84 (2009).

39. Wirtz, K. W. A. Transfer of phospholipids between membrane. *Biochimica et Biophysica Acta (BBA) - Reviews on Biomembranes* **344**, 95–117 (1974).

40. Abreu, M. S. C., Estronca, L. M. B. B., Moreno, M. J. & Vaz, W. L. C. Binding of a Fluorescent Lipid Amphiphile to Albumin and its Transfer to Lipid Bilayer Membranes. *Biophys J* **84**, 386–399 (2003).

41. Doktorova, M. *et al.* Preparation of asymmetric phospholipid vesicles for use as cell membrane models. *Nat Protoc* **13**, 2086–2101 (2018).

42. Wolfbauer, G., Albers, J. J. & Oram, J. F. Phospholipid transfer protein enhances removal of cellular cholesterol and phospholipids by high-density lipoprotein apolipoproteins. *Biochimica et Biophysica Acta (BBA) - Molecular and Cell Biology of Lipids* **1439**, 65–76 (1999).

43. Slater, S. J., Ho, C., Taddeo, F. J., Kelly, M. B. & Stubbs, C. D. Contribution of hydrogen bonding to lipid-lipid interactions in membranes and the role of lipid order: Effects of cholesterol, increased phospholipid unsaturation, and ethanol. *Biochemistry* **32**, 3714–3721 (1993).

44. Zhu, X. *et al.* Surface De-PEGylation Controls Nanoparticle-Mediated siRNA Delivery *In Vitro* and *In Vivo*. *Theranostics* **7**, 1990–2002 (2017).

45. Münter, R. *et al.* Dissociation of fluorescently labeled lipids from liposomes in biological environments challenges the interpretation of uptake studies. *Nanoscale* **10**, 22720–22724 (2018).

46. Hamanishi, J. *et al.* Nivolumab Versus Gemcitabine or Pegylated Liposomal Doxorubicin for Patients With Platinum-Resistant Ovarian Cancer: Open-Label, Randomized Trial in Japan (NINJA). *Journal of Clinical Oncology* **39**, 3671–3681 (2021).

47. Zamarin, D. *et al.* Randomized Phase II Trial of Nivolumab Versus Nivolumab and Ipilimumab for Recurrent or Persistent Ovarian Cancer: An NRG Oncology Study. *Journal of Clinical Oncology* **38**, 1814–1823 (2020).

48. Li, F. *et al.* The association between CD8+ tumor-infiltrating lymphocytes and the clinical outcome of cancer immunotherapy: A systematic review and meta-analysis. *EClinicalMedicine* **41**, 101134 (2021).

49. Spranger, S. *et al.* Up-Regulation of PD-L1, IDO, and T_{regs} in the Melanoma Tumor Microenvironment Is Driven by $CD8^+$ T Cells. *Sci Transl Med* **5**, (2013).

50. Riley, R. S., June, C. H., Langer, R. & Mitchell, M. J. Delivery technologies for cancer immunotherapy. *Nat Rev Drug Discov* **18**, 175–196 (2019).

51. Lasek, W., Zagożdżon, R. & Jakobisiak, M. Interleukin 12: still a promising candidate for tumor immunotherapy? *Cancer Immunology, Immunotherapy* **63**, 419–435 (2014).

52. Liu, H. *et al.* Structure-based programming of lymph-node targeting in molecular vaccines. *Nature* **507**, 519–522 (2014).

53. Nguyen, K. G. *et al.* Localized Interleukin-12 for Cancer Immunotherapy. *Front Immunol* **11**, (2020).

54. Chen, B.-M., Cheng, T.-L. & Roffler, S. R. Polyethylene Glycol Immunogenicity: Theoretical, Clinical, and Practical Aspects of Anti-Polyethylene Glycol Antibodies. *ACS Nano* **15**, 14022–14048 (2021).

CHAPTER 6
High-Throughput Microfluidic-Mediated Assembly of Layer-by-Layer Nanoparticles

6.1 Introduction

Spatiotemporal control of drug delivery has been a major objective of new therapeutic platforms.[1] Nanoparticles (NPs) have been extensively studied as drug carriers to alter the pharmacokinetics and pharmacodynamics of therapeutics, with engineering of NP surface chemistry representing an important strategy to optimize delivery of drugs to disease sites and/or avoid off-target tissue uptake.[2,3] A versatile approach to engineer surface chemistry is via layer-by-layer (LbL) assembly of polymer coatings on nanoparticles. The LbL technique consists of the deposition of nanoscale polymer films on surfaces through alternating adsorption of molecular layers of complementary polymers, such as polycations and polyanions.[4,5] The resulting multilayer assemblies enable controlled drug release as well as modulation of surface properties and the resulting interactions with biological interfaces.[4,6] Based on these promising properties, we and others have successfully demonstrated the utility of LbL-NPs for targeted drug delivery and controlled drug release in many applications.[5,7,8] Assembly of polymer films on NPs can yield increased NP plasma half-life and stability, tumor targeting, and control over the subcellular localization of NPs.[6,9–15] LbL-NPs have been used to effectively deliver small-molecule therapeutics[16–22] or nucleic acids[23–28] which can be loaded into the polymer film in the NP. The high versatility of this platform approach enables the facile assembly of combination therapies to target diverse diseases.

A challenge of LbL-NP synthesis is the serial nature of the layer deposition process. While there have been efforts to improve LbL-NP assembly at the lab scale, these approaches have still required multiple purification steps as well as hard-to-scale methods of mixing polymers and NPs such as the use of sonication or vortex mixers.[5,29] Membrane-based purification approaches also suffer from potential interactions of NPs with the membrane.[29] Here we demonstrate a novel approach for multilayer assembly on NPs using microfluidic (MCF) mixing technology. MCF mixing is scalable and readily implemented under cGMP conditions for clinical-grade NP production.[30–34] As a test case for this new manufacturing method, we synthesized LbL-NPs composed of an interleukin-12 (IL-12)-conjugated liposomal core layered with polyamino acid polymers, which has shown promising therapeutic efficacy in preclinical mouse models of

metastatic ovarian cancer.[6,35,36] We show that by rational selection of polymer-to-NP ratios for surface charge conversion without the addition of excess polymers, this approach enables LbL films to be constructed without the need for time-consuming purification steps, greatly simplifying LbL-NP preparation.

6.2 Methods

6.2.1 Materials

1,2-distearoyl-sn-glycero-3-phosphocholine (DSPC), 1-palmitoyl-2-oleoyl-sn-glycero-3-phospho-(1'-rac-glycerol) (sodium salt) (POPG), 1,2-distearoyl-sn-glycero-3-phospho-(1'-rac-glycerol) (sodium salt) (DSPG), 1,2-dioleoyl-sn-glycero-3-phosphoethanolamine-N-[4-(p-maleimidophenyl)butyramide] (sodium salt) (18:1 MPB-PE), 1,2-dioleoyl-sn-glycero-3-phosphoethanolamine-N-dibenzocyclooctyl (DOPE-DBCO), and cholesterol were purchased from Avanti Polar Lipids. Poly-L-arginine (PLR) with a molecular weight (MW) of 9.6 kDa and poly-L-glutamic acid (PLE) with a MW of 15 kDa were purchased from Alamanda Polymers. Borondipyrromethene tetramethylrhodamine (BDP TMR) azide (Lumiprobe) and BDP 630/650 azide (Lumiprobe) were conjugated to DOPE-DBCO in chloroform to generate DOPE-TMR and DOPE-630/650. Successful conjugation was validated via thin-layer chromatography which indicated <1% free dye.

6.2.2 Recombinant single-chain IL-12 production

Single-chain IL-12 sequence[37] was synthesized as a genomic block (Integrated DNA Technologies) and cloned into gWIZ expression vector (Genlantis). Plasmids were transiently transfected into Expi293 cells (ThermoFisher Scientific). After 5 days, cell culture supernatants were collected and protein was purified in an ÄKTA pure chromatography system using HiTrap HP Niquel sepharose affinity column, followed by size exclusion using Superdex 200 Increase 10/300 GL column (GE Healthcare Life Sciences). Endotoxin levels in purified protein was measured using Endosafe Nexgen-PTS system (Charles River) and assured to be <5 EU/mg protein.

6.2.3 IL-12 conjugated liposome synthesis

Lipid solution composed of 65 mol% DSPC, 24 mol% Cholesterol, 6 mol% POPG and 5 mol% of MPB-PE were made in chloroform and dried into a thin film using a rotovap, and then further dried overnight in a desiccator. Lipid films were then hydrated at 0.5-1 mg/mL using pH 5 deionized water and sonicated for 5 minutes at 65 °C then extruded (Avestin Liposofast-50) at 65°C one time through a 100 nm membrane then three times through 50 nm membranes. Extruded liposomes were added to an ice bath and the pH was adjusted to pH 7.0 with 10 mM HEPES buffer prior to the addition of scIL-12 containing a terminal cysteine residue at 0.17 wt.eq. with liposomes at 0.33 mg/mL. After overnight incubation with IL-12 at 4 °C, any remaining maleimides were quenched with 100-fold molar excess of L-cysteine (Sigma) for 1.5 hrs on ice. For fluorescence labeling of liposomes, 0.2 mol% of DSPC content was replaced by either DOPE-TMR or DOPE-630/650. IL-12 concentration was measured via enzyme-linked immunoassay (ELISA) (Peprotech) and lipid content was quantified via fluorescence. IL-12 free liposomes were made with a 33 mol% DSPC, 33 mol% DSPG, and 33 nol% cholesterol and hydrated and extruded as described previously.[27]

6.2.4 Small-scale layer-by-layer (LbL) assembly

For small-scale (~50 μL) polymer adsorption onto NP surfaces, polymer solution was added to a 1.7 mL tube. The container was then placed under bath sonication (Branson 2510) and the NPs were quickly (<1 s) added to the polymer solution. Samples were allowed to incubate for 5 minutes analysis. Any subsequent layers were deposited without any purification unless otherwise indicated.

6.2.5 Large-scale LbL assembly and purification via tangential flow filtration (TFF)

Assembly of polyelectrolyte layers at larger scale (>1 mL) was performed as described previously.[29] Briefly, unlayered liposomes were added to a solution with 0.3-0.4 wt.eq. of PLR relative to lipid in a glass Erlenmeyer flask under sonication. After 30 minutes incubation on ice, excess PLR polymer was removed by tangential-flow filtration (TFF) through a 100 kDa mPES membrane (Repligen) pre-treated with a 10 mg/mL solution of free PLR. For the terminal PLE layer, purified particles coated with PLR were added to a solution with PLE in a glass flask under sonication at 1 wt.eq. of polymer to lipid. Particles coated with both PLR and PLE were then

purified by TFF on a separate 100 kDa mPES membrane (Repligen) to remove any excess PLE. For layering, a glass Erlenmeyer flask with <30% of its rated volume was used to facilitate homogeneous NP distribution over the polymer solution and minimize the chance of inhomogeneities in the sample

6.2.6 Microfluidics LbL assembly

Microfluidic mixing was performed on a NanoAssblr Ignite (Precision Nanosystems) mixing chip. Luer lock syringes were separately filled with either polymer solution or liposomes and attached to the microfluidics chip. A syringe pump (Pump 11 Elite, Harvard Apparatus) was then used to control the fluid flow rate into the mixing chip.

6.2.7 Characterization of particle preparations

Dynamic light scattering (DLS) and zeta potential measurements were made on a Zetasizer Nano ZSP (Malvern). Nanoparticle micrographs were acquired using Transmission Electron Microscopy (TEM) on a JEOL 2100F microscope operated at 200 kV with a magnification range of 10,000-60,000X.

6.2.8 Fluorescent polymer synthesis

PLR was reacted with 2 molar equivalents of BDP-Texas Red (TR)-NHS-ester (Lumiprobe) in DMSO catalyzed with one molar equivalent of triethylamine (TEA). The resulting PLR-TR conjugate was purified via Reverse-Phase High Pressure Liquid Chromatography (RP-HPLC) on a Jupiter C4 column (5 μm particles, 300 Å – Phenomenex), then lyophilized and stored at -20 °C. PLE was reacted with 5 molar excess of sulfo-cy3-NHS-ester (Lumiprobe) in pH 9 PBS (adjusted by adding 0.1 M sodium bicarbonate) for 3 hours at 25°C then left 18 hr at 4 °C. Excess dye was removed via extensive dialysis (3 kDa, Spectrum) against 0.9% NaCl, and then dialyzed against deionized water to remove salts. The resulting PLE-cy3 polymer was lyophilized and stored at -20 °C.

6.2.9 Polymer retention quantification

To assess the amount of polymer retained on LbL-NPs after TFF processing, IL-12 NPs with 0.2 mol% of DOPE-630/650 was layered with 0.3 wt. eq. of a PLR solution composed of 50% PLR

and 50% PLR-TR. After purification of excess PLR/PLR-TR via TFF, particles were layered with 1 wt. eq. of a PLE solution composed of 50% of PLE and 50% PLE-cy3. After purification of excess PLE/PLE-cy3 via TFF, the sample was diluted 10x into dimethyl sulfoxide (DMSO) to disrupt the NPs. The fluorescence of lipids and polymers were separately quantified on a plate reader (TECAN) compared to standard curves to determine the polymer-to-NP wt. eq. of the purified NPs.

6.2.10 Excess polymer quantification

IL-12 NPs were generated via either the standard TFF-based LbL protocol or the MCF protocol, but with the PLE layering solution having 50% PLE-cy3. Free polymers were separated from NPs on a 300 kDa centrifugal filter (Vivaspin500, Sartorius) at 30 xg for 20 min. Polymer fluorescence oi the permeate fluid was then compared to that of the initial sample to determine the fraction of polymer bound to NPs.

6.2.11 Cell Culture

OV2944-HM-1 cells were acquired through Riken BRC and were cultured in α-MEM. Cell media was also supplemented with 10% FBS and penicillin/streptomycin with cells incubated in a 5% CO2 humidified atmosphere at 37 °C. All cell lines were murine pathogen tested and confirmed mycoplasma negative by Lonza MycoAlert™ Mycoplasma Detection Kit.

6.2.12 In vitro cellular association

The day before dosing, HM-1 cells were plated on a tissue-culture 96-well plate at a density of 50k cells per well. The next day, wells were dosed with NPs to 0.05 mg/mL and left for the target incubation time (4 hrs or 24 hrs). For analysis of association, the supernatant was removed from the well and diluted 10X with DMSO. Cells were then washed three times with PBS then dissolved with DMSO. Fluorescence of NPs associated with cells was then normalized to supernatant fluorescence. The relative fluorescence of each formulation was then compared to an unlayered liposome control containing the same fluorophore. For confocal imaging, 8-well chambered coverglass (Nunc Lab-Tek II, Thermo Scientific) were treated with rat tail collagen type I (Sigma-Aldrich) per manufacturer's instructions. HM-1 cells were plated onto wells at a density of 10k/well and left to adhere overnight prior to NP treatment. After the desired incubation time with

NPs, cells were washed 3x with PBS. After washing, cells were fixed in 4% paraformaldehyde for 10 minutes then washed (3x with PBS) and stained with wheat germ agglutinin (WGA) conjugated to Alexa Fluor488 (Invitrogen) and hoechst 33342 (Thermo Scientific) following manufacturer instructions. Images were analyzed using ImageJ. Slides were imaged on an Olympus FV1200 Laser Scanning Confocal Microscope. FRET studies were performed on a Leica SP8 Spectral Confocal Microscope.

6.2.13 Animals

B6C3F1 mice were purchased from Jackson Laboratories. Female mice were used between 8-12 weeks of age unless otherwise noted. All animal work was conducted under the approval of the Massachusetts Institute of Technology Division of Comparative Medicine in accordance with federal, state, and local guidelines.

6.2.14 Efficacy studies with metastatic ovarian cancer model

B6C3F1 mice were inoculated intraperitoneally with 10^6 cells of HM-1-luc in PBS. One week after inoculation, treatment was initiated as indicated on each figure. Mice weights were tracked daily after treatments for signs of toxicity. For HM-1-luc tumors, bioluminescence was measured on an IVIS Spectrum imaging system 10 minutes after i.p. injection of 3 μg of D-luciferin sodium salt (GoldBio) for 30 days after tumor inoculation or as needed to track tumor burden.

6.2.15 Statistical Analysis

GraphPad PRISM 10 was used to perform statistical analyses. Comparisons between two groups was performed via unpaired t-tests. For multiple groups or multiple variable analysis, one-way, or two-way ANOVAs were used with Tukey's posthoc correction for time-based analysis or Sidak posthoc for other ANOVA analysis.

6.3 Results and Discussion

6.3.1 Titration of polyelectrolyte deposition onto nanoparticle surfaces suggests excess polymer is required for LbL assembly without particle aggregation

As a model system with relevance for targeted immunotherapy delivery to cancer cells, we studied anionic liposomes that were surface-conjugated with the potent cytokine IL-12 (IL-12 NPs), and

subsequently coated by alternating layers of poly(L-arginine) (PLR) and poly(L-glutamate) (PLE). LbL assembly is performed by alternating sequential incubations of the liposomal core particle with excess PLR and PLE in a low ionic strength buffer. Under these typical self-assembly conditions, each step of polyelectrolyte adsorption must be accompanied by extensive washing/purification to remove excess unbound polymer from the coated particles. To develop a continuous process for LbL assembly, we first sought to define how the polymer:particle weight ratio during impacted nanolayer deposition. Unlayered anionic IL-12 NPs were incubated with increasing PLR weight equivalents (wt. eq.), or alternatively, purified PLR-coated cationic IL-12-NPs (PLR/NPs) were incubated with increasing PLE wt. eq. After polymer and NP mixing, we characterized the resulting unpurified polymer-NP assemblies' size and charge via dynamic light scattering (DLS) and electrophoretic mobility, respectively. Starting from very low polymer concentrations, increasing the polymer-to-NP wt. eq. led to increasing NP charge up to a charge neutralization point (isoelectric point), at which particles rapidly aggregated due to a lack of charge-charge repulsion (**Figure 6.1a-b**). Further increases in polymer-to-NP wt. eq. led to reductions in particle size as the overall NP charge inverted, and the particle zeta potentials plateaued as complete charge reversal was achieved. Yet, further increases in the polymer-to-NP wt. eq. beyond the zeta potential plateau onset point (POP) was required to form polymer-coated NPs with the lowest overall size and PDI. Due to this reduced size and increased homogeneity, polymer:NP wt. equivalents beyond 0.3 and 1 for PLR and PLE, respectively, have been used for LbL-NP synthesis.[27] As polymer deposition onto NP surfaces is a kinetically controlled reaction and expected to be quantitative until charge conversion,[38] these results suggested that excess polymers prevented the bridging of NPs by the polymer that forms aggregates (**Figure 6.1d**). Assembly under these conditions must then be followed by purification steps to subsequently remove excess free polyelectrolyte.[29]

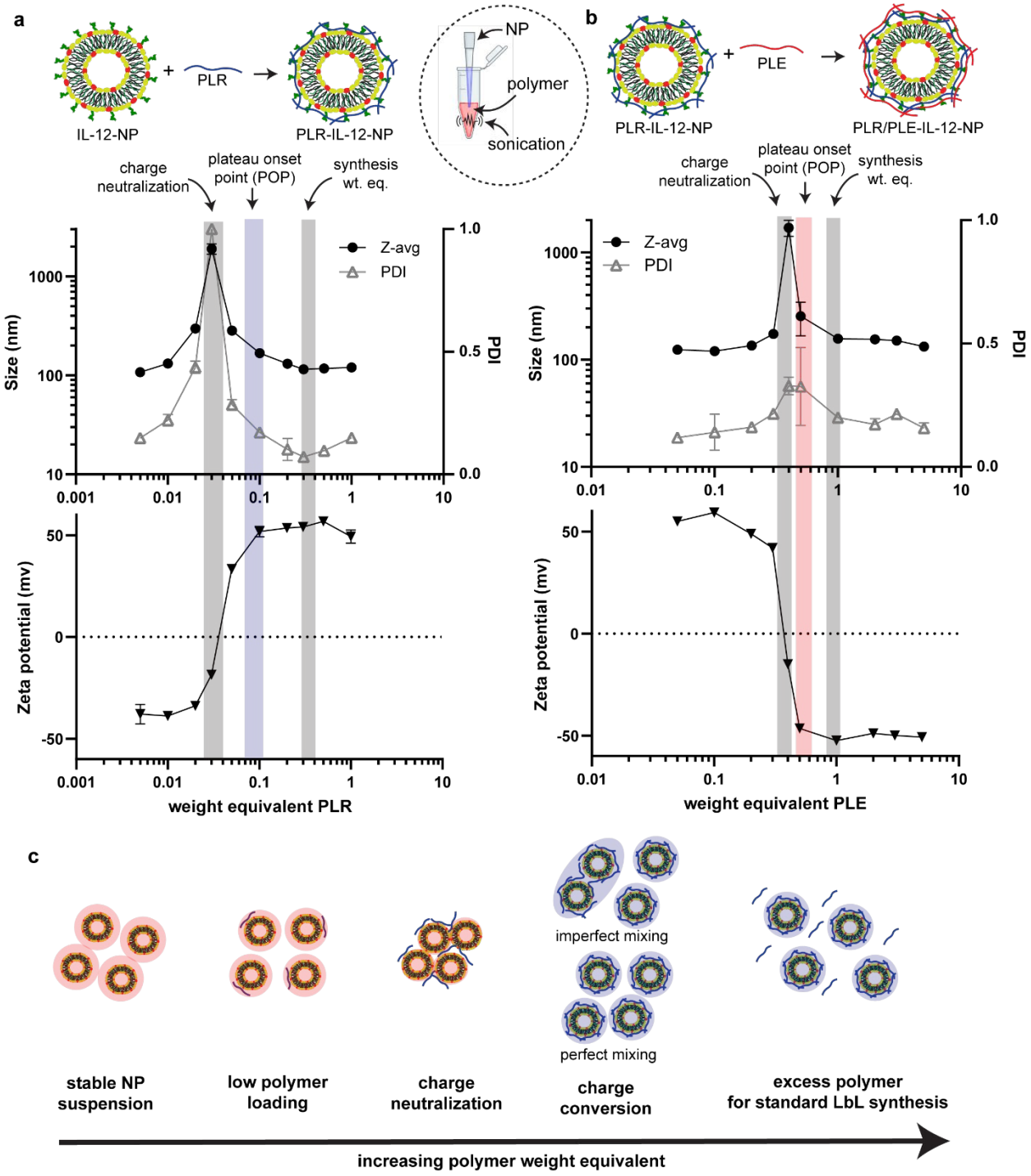

Figure 6.1. Characterization of nanoparticle surface charge conversion upon polyelectrolyte deposition. (a) Schematic for small-scale deposition of PLR onto IL-12 loaded NPs, intensity-weighted particle size (Z-avg), number-averaged (#-avg) size, polydispersity index (PDI), and zeta potential of the resulting polymer-nanoparticle mixtures at increasing PLR weight equivalents to

bare anionic IL-12-NP. **(b)** Schematic for small-scale deposition of PLE onto PLR-IL-12 loaded NPs, Z-avg, #-avg, PDI, and zeta potential of the resulting polymer-nanoparticle mixtures from increasing weight equivalent PLE to PLR-coated IL-12 NPs. **(c)** Schematic representing the different possible resulting assemblies upon increasing polymer weight equivalents.

We next sought to assess whether incubation of NPs with excess polymer increased the amount of polyelectrolyte adsorbed to the NPs. Using conditions identified above that allowed polymer adsorption while maintaining a low polydispersity of the resulting NPs, bare IL-12 NPs or PLR/NPs were added to a solution of fluorescently-tagged PLR (0.3 wt. eq.) or PLE (1 wt. eq.) under sonication to allow polymer adsorption.[27,29] The excess polymer was then removed via tangential flow filtration (TFF). As expected, the production of LbL-NPs via our optimized protocol had the characteristic reversion of surface charge and minor increases in overall size while maintaining overall low PDI (**Figure 6.2a**). Quantification of the amount of polymer bound to the NPs after purification demonstrated that only ~0.1 wt. eq. of PLR and ~0.5-0.6 wt. eq. of PLE were adsorbed (**Figure 6.2b**). These results confirmed that incubation of NPs with polymer wt. eq. beyond the zeta potential POP (**Figure 6.1b-c)** does not increase the amount of polymer incorporated into the LbL films.

To better understand the limitations of performing LbL-NP assembly at the POP amount of polymer-to-NP wt. eq., we performed small, low-concentration (~50 µL at 0.5 mg/mL) and larger-scale (~1 mL at 5 mg/mL, LS) polymer adsorption experiments and compared them to the standard optimized protocol. The increase in NP production scale did not cause significant differences in the resulting NP size after PLR deposition using excess (0.3 wt.eq.) polymers (**Figure 6.2c**). However, when we attempted to perform layering with the POP of PLR (0.1 wt.eq.), we observed a noticeable increase in NP size. Omitting sonication during the layering led to a further increase in the resulting NP size when layering at POP via the standard approach. Similarly, PLE layering on purified PLR-NPs was found to require excess polymer to prevent NP aggregation during layering (**Figure 6.2d**). Thus, large-scale LbL assembly in static solution even in the presence of sonication could only successfully be performed under conditions of excess polymer, requiring subsequent purification steps.

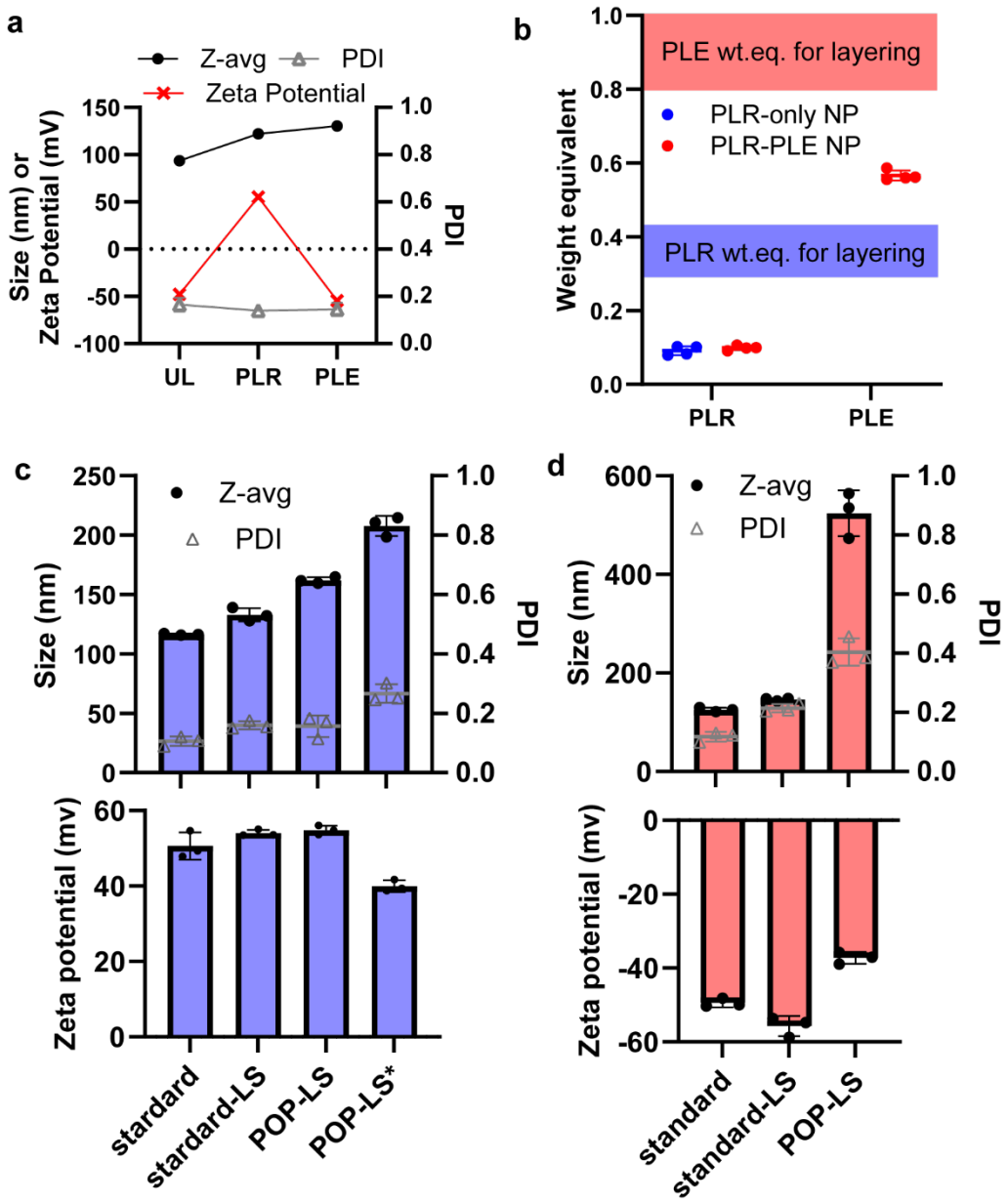

Figure 6.2. Excess polymers prevent NP aggregation during layering via optimized bath sonication protocol. (a) Z-avg size, PDI and zeta potential of IL-12 NPs during LbL assembly. **(b)** Polymer-to-NP wt. eq. retained with the NPs after TFF purification. **(c)** Z-avg size, PDI and zeta potential of the resulting PLR-IL-12-NPs generated via different layering strategies. **(d)** Z-avg size, PDI and zeta potential of the resulting PLR/PLE-IL-12-NPs generated via different layering strategies on TFF purified PLR-IL-12-NPs.

6.3.2 Microfluidics-enabled mixing generates homogeneous LbL-NPs without intermediate purification steps

As polymer wt. eq. beyond POP only increased the number of free polymers in the solution without affecting the LbL film, we wanted to explore if we could assemble LbL-NPs at POP for PLR and PLE without purification steps. To overcome the limitations described above for LbL film assembly on NPs, we explored using microfluidic (MCF) channels for the mixing of polymers with NPs. We used a commercial MCF cartridge with a toroidal mixer.[30,32] This MCF chip platform has been developed for lab and clinical-scale cGMP manufacturing of NPs, making it an ideal candidate for clinical-scale manufacturing of LbL-NPs.[30] For mixing, solutions of either liposomes or LbL polymers were introduced into the two entry flow ports (**Figure 6.3a**). We first evaluated the effect of flow rate through the channels on the adsorption of PLR to anionic IL-12 liposomes, combining PLR and liposomes at the POP. The target was to achieve similarly sized NPs as the standard optimized bath sonication protocol. Increasing the flow rate led to reduced PLR-NP Z-avg size and PDI (**Figure 6.3b**) while maintaining charge conversion (**Figure 6.3c**) demonstrating improved sample homogeneity without disturbing polymer adsorption. Importantly, at flow rates of >3 mL/min, PLR-NPs reached our targets of the standard optimized protocol expected for layered, non-aggregated particles.

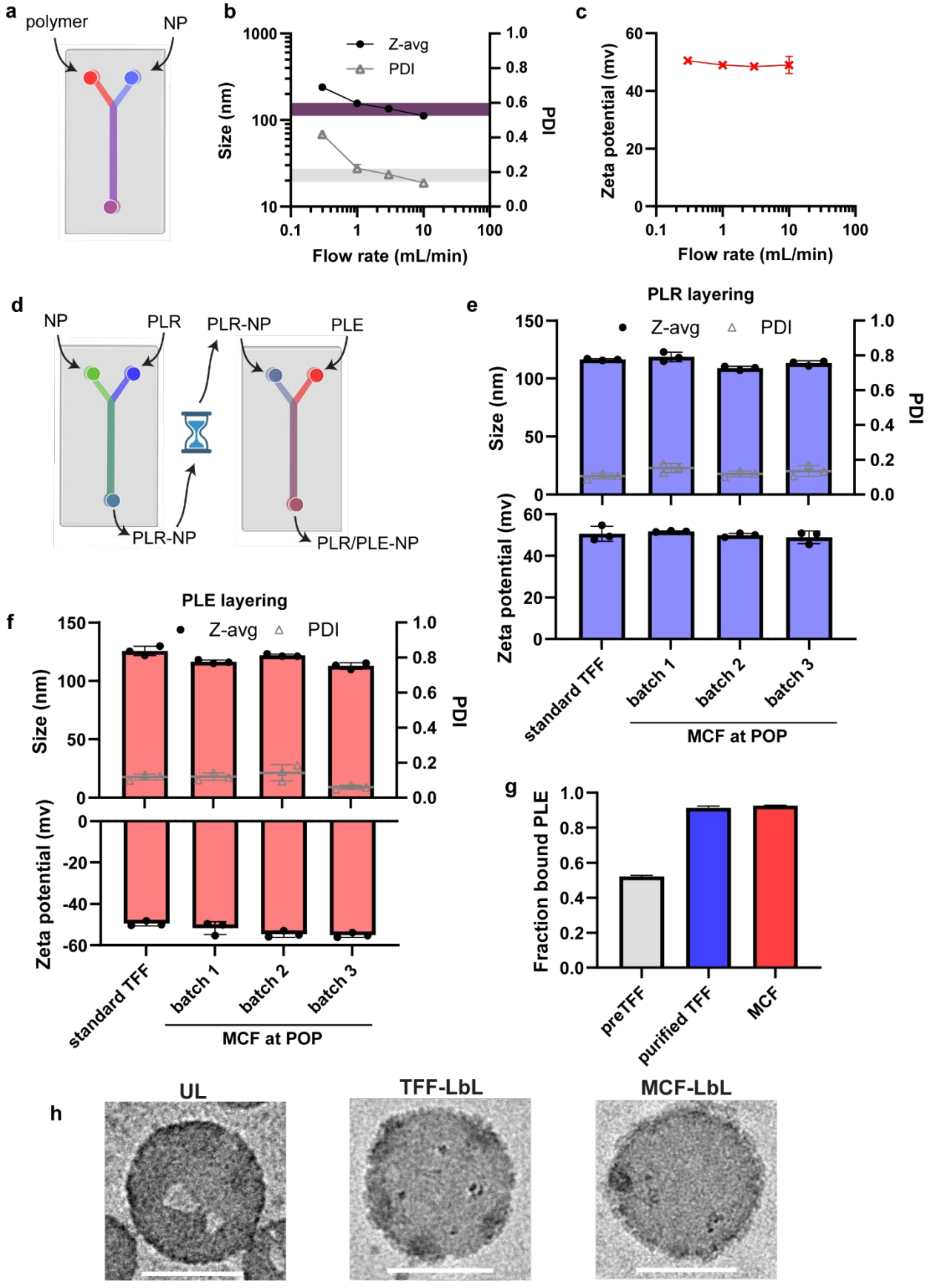
a
polymer
NP
b
Z-avg
PDI
Size (nm)
PDI
Flow rate (mL/min)
c
Zeta potential (mv)
Flow rate (mL/min)
d
NP
PLR
PLR-NP
PLE
PLR-NP
PLR/PLE-NP
e
PLR layering
Z-avg
PDI
Size (nm)
PDI
Zeta potential (mv)
standard TFF
batch 1
batch 2
batch 3
MCF at POP
f
PLE layering
Z-avg
PDI
Size (nm)
PDI
Zeta potential (mv)
standard TFF
batch 1
batch 2
batch 3
MCF at POP
g
Fraction bound PLE
preTFF
purified TFF
MCF
h
UL
TFF-LbL
MCF-LbL

Figure 6.3. Microfluidic fluid mixing chips enable homogeneous LbL-NP assembly without the need of purification steps. (a) Schematic for polymer deposition onto NPs via microfluidics chip. **(b)** Z-avg size and PDI, of NPs layered with POP PLR using a microfluidics chip with increasing channel fluid flow rates (both polymer and NP channels had equal flow rates). Shaded regions indicate target NP measurements from optimal layering conditions for the current NP formulation. **(c)** Zeta potential measurements of particle mixtures from **b**. **(d)** Schematic for LbL-NP assembly using titrated polymer-to-NP wt. eq. without the need of purification steps. **(e)** Z-avg size, PDI, and zeta potential of the resulting PLR-IL-12-NPs generated using titrated PLR-to-NP wt.eq. via MCF compared to target NP measurements. **(f)** Z-avg size, PDI, and zeta potential of the resulting PLE/PLR-IL-12-NPs generated using titrated PLR-to-NP wt.eq. then titrated PLE-to-NP wt. eq. via MCF compared to target NP measurements. **(g)** Fraction of fluorescently labeled PLE polymer associated with NPs after optimized TFF-based layering before and after TFF purification compared to titrated polymer layering using MCF. **(h)** Negative stain transmission electron microscopy (TEM) of unlayered (UL) IL-12 NPs or PLE/PLR-IL-12-NPs assembled via either the optimized TFF-based protocol or the titrated polymer-to-NP wt. eq. MCF protocol.

Based on these promising findings, we devised a two-stage microfluidic mixing process designed to allow two rounds of polyelectrolyte adsorption at POP, in order to generate LbL-NPs without purification steps. IL-12-liposomes and PLR were combined in a first-stage MCF mixer followed by an incubation step to ensure polymer adsorption and perform quality tests. The output of the first stage and a PLE was used as the input in a second-stage mixer (**Figure 6.3d**). When we performed POP PLR deposition onto IL-12-NPs at increased scales (>1 mL) using MCF, we could readily achieve the target PLR-NP sizes of the standard batch sonication production protocol across multiple batches (**Figure 6.3e**). Similarly, depositing PLE at its POP onto MCF-generated PLR-IL-12 NPs could yield PLR/PLE IL-12 NPs at equal or smaller sizes than the standard batch sonication protocol with reproducibility across batches (**Figure 6.3f**). To validate that all polymers were adsorbed on NPs using the MCF protocol, we used fluorescently tagged PLE polymers to assemble PLE/PLR IL-12 NPs using both the standard optimized TFF-based protocol and the new MCF LbL-NPs. We separated out any free polymers in the LbL-NPs using centrifugal filters and, as expected from the POP, found that only ~50% of PLE was bound to TFF-LbL-NPs prior to purification due to the excess polymers used during assembly with 1 wt. eq. with PLE. On the

other hand, both purified TFF-LbL-NPs and MCF LbL-NPs both had >95% of PLE bound to NPs (**Figure 6.3g**), confirming the lack of free polymers. Analysis of sample morphology via negative stain transmission electron microscopy (TEM) confirmed that both TFF-based and the MCF-based PLE/PLR-IL-12 NPs had a polymer film on the NP based on the reduced staining around the liposome (**Figure 6.3h**). Further, we did not find signs of significant polyplex formation in either LbL-NP formulation on the TEM micrographs.

The experiments above carried out layering in deionized water, but LbL assembly is also sometimes carried out in the presence of salts to create LbL films with thicker layers.[27] We thus tested whether LbL-NPs could be generated in the presence of salt-containing buffers. We first examined varying PLR:liposome mass ratios to find the POP of PLR required for LbL assembly in 25 mM HEPES and 20 mM sodium chloride (NaCl), a buffer composition previously found optimal for loading of siRNA into LbL films.[27] Around 0.15 wt. eq. of PLR was required to reach the plateau point (**Figure E1a-b**). We next compared the size and zeta potential of LbL-NP synthesized from small-scale tests under bath sonication to increased bath sonication and TFF to that of MCF LbL-NPs. Similar to IL-12-LbL-NPs, we found that assembly with MCF enabled more homogenous particle formulations (**Figure E1c-e**), confirming the benefit of NP layering via MCF mixing and the generalizability of this strategy for LbL-NP formulations.

6.3.3 MCF LbL-NPs maintain desired particle properties in vitro and maintain IL-12-LbL-NP efficacy in vivo in a metastatic ovarian cancer mice model

PLE/PLR nanolayers assembled on IL-12 liposomes have two functions: First, the PLE layer promotes the targeting of the particles to ovarian cancer cells, and second, prevention of NP endocytosis following binding to the cancer cells, leading to high retention of the LbL-NPs on the cancer cell membrane. To determine whether PLE/PLR-IL-12-NPs generated via MCF assembly had the expected cell-targeting properties, we dosed a murine metastatic ovarian cancer cell line, OV2944-HM1 (HM-1) with fluorescent NPs prepared by the traditional bath sonication and TFF process or MCF assembly, and quantified NP association with the cells after 4 or 24 hours. As expected, MCF LbL-NPs and TFF-based LbL-NPs had significantly increased HM-1 cell association compared to unlayered (UL) NPs (**Figure 6.4a**). Moreover, MCF-LbL-NPs had equal or better HM-1 association compared to TFF LbL NPs, confirming that MCF layering maintained and potentially improved the desired high ovarian cancer cell affinity. However, the most critical

characteristic of PLE/PLR LbL-NPs is its cell-membrane retention which enables for high intratumoral extracellular residence time of cytokines such as IL-12. Thus, we evaluated the subcellular localization of NPs 24 hours after dosing via confocal microscopy. While UL particles were all endocytosed (**Figure 6.4b**), both TFF-LbL NPs (**Figure 6.4c**) and MCF-LbL NPs (**Figure 6.4d**) presented with NPs on the cancer cell membrane, confirming that PLE/PLR-IL-12-NPs retained their cell surface retention properties when prepared via MCF mixing.

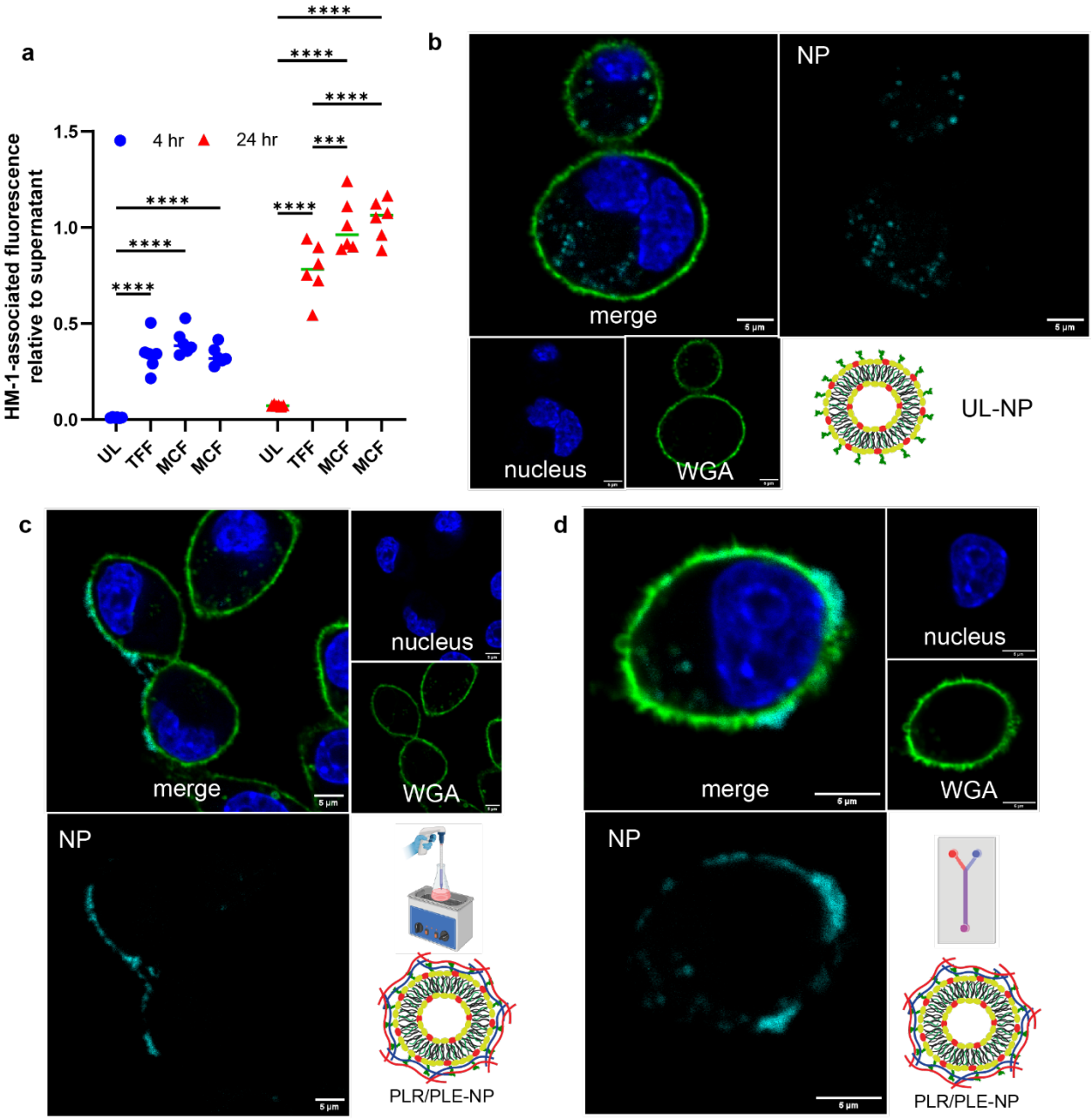

Figure 6.4. MCF-LbL-NPs maintain the desired *in vitro* characteristics of PLE/PLR LbL-NPs. (a) Fluorescence ratio of NPs associated with HM-1 cells relative to NPs remaining in the supernatant at 4 and 24 hours after dosing. **(b)** Representative confocal microscopy of HM-1 cells dosed with UL NPs for 24 hours. **(c)** Representative confocal microscopy of HM-1 cells dosed with TFF-based LbL-NPs for 24 hours. **(d)** Representative confocal microscopy of HM-1 cells dosed with MCF-based LbL-NPs for 24 hours.

Having validated that LbL-NP assembly via MCF maintained the desired cancer cell association properties, we next wanted to validate that the loaded IL-12 maintained a similar bioactivity to that of TFF-based IL-12 NPs. We dosed HEK-Blue IL-12 reporter cell lines with either free IL-12 or IL-12 bound to PLE/PLR-IL-12-NPs generated via the standard TFF-based protocol or MCF. The IL-12 on MCF-LbL maintained its activity like that of TFF-LbL (**Figure 6.5a-b**). We then sought to evaluate the particle performance *in vivo* in mice bearing peritoneally disseminated metastatic HM-1 tumors. We used the same dosing paradigm shown previously to extend survival in this mice model with IL-12 loaded PLE/PLR-LbL-NPs (**Figure 6.5c**) (CITE). Both TFF-based and MCF-based LbL-NPs were found to have better control of tumor growth based on whole-mouse tumor bioluminescence readings (**Figure 6.5d**), **si**gnificantly extending survival of mice compared to either free IL-12 or UL IL-12 NPs (**Figure 6.5e**).

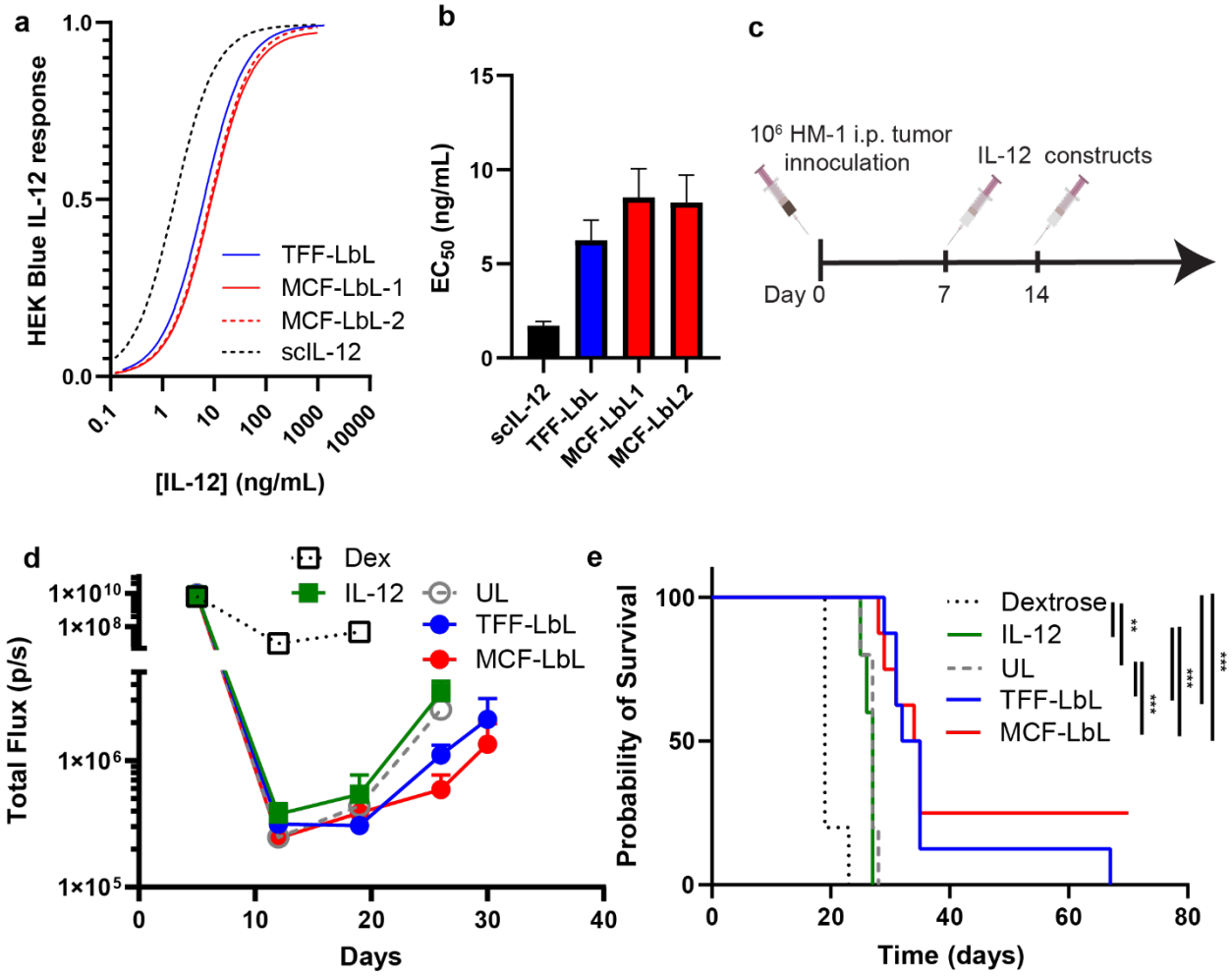

Figure 6.5. MCF-LbL-NPs maintain the bioactivity of IL-12 *in vitro* and its *in vivo* effectiveness in a metastatic mice model of ovarian cancer. (a) HEK-Blue IL-12 reporter cell line response curves for free IL-12 or IL-12 loaded onto LbL-NPs generated via either TFF-based or MCF-based LbL assembly. **(b)** Calculated EC_{50} of curves in **(a)**. **(c)** In vivo treatment scheme of metastatic ovarian cancer. **(d)** Whole animal bioluminescence reading via IVIS of luciferase expressing tumors cells from mice treated as in **(c)**. **(e)** Survival curves of mice treated as in **(c)**.

6.4 Conclusion

Layer-by-layer assembly is a promising technique to modulate the surface properties of NPs for the development of therapeutic drug carriers. Here we demonstrated that microfluidic mixing is highly effective for combining polyelectrolytes and NPs, achieving LbL assembly under conditions amenable to scalable, continuous synthesis for clinical-scale manufacturing. This was facilitated by the finding that MCF mixing enables LbL assembly to occur polymer-to-NP weight

equivalents devoid of excess polymer, allowing for the production LbL-NPs without time-consuming purification steps and loss of NP yields. We validated that these process modifications do not alter the properties of LbL-NPs *in vitro* and *in vivo* based on the known properties of IL-12 loaded PLE/PLR-IL-12-NPs. Taken together, this work provides a simple method to assemble LbL-NPs at various scales and at increased throughput. This approach should facilitate both clinical development of LbL-NPs as well as ease the production of libraries of LbL-NPs which can be implemented to screen for desired traits.

6.5 References

1. Park, H., Otte, A. & Park, K. Evolution of drug delivery systems: From 1950 to 2020 and beyond. *Journal of Controlled Release* **342**, 53–65 (2022).

2. Yusuf, A., Almotairy, A. R. Z., Henidi, H., Alshehri, O. Y. & Aldughaim, M. S. Nanoparticles as Drug Delivery Systems: A Review of the Implication of Nanoparticles' Physicochemical Properties on Responses in Biological Systems. *Polymers (Basel)* **15**, 1596 (2023).

3. Mitchell, M. J. *et al.* Engineering precision nanoparticles for drug delivery. *Nat Rev Drug Discov* **20**, 101–124 (2021).

4. Hammond, P. T. Form and Function in Multilayer Assembly: New Applications at the Nanoscale. *Advanced Materials* **16**, 1271–1293 (2004).

5. Alkekhia, D., Hammond, P. T. & Shukla, A. Layer-by-Layer Biomaterials for Drug Delivery. *Annu Rev Biomed Eng* **22**, 1–24 (2020).

6. Correa, S. *et al.* Tuning Nanoparticle Interactions with Ovarian Cancer through Layer-by-Layer Modification of Surface Chemistry. *ACS Nano* **14**, 2224–2237 (2020).

7. Zhang, X., Liang, T. & Ma, Q. Layer-by-Layer assembled nano-drug delivery systems for cancer treatment. *Drug Deliv* **28**, 655–669 (2021).

8. Zhao, S. *et al.* The Future of Layer-by-Layer Assembly: A Tribute to *ACS Nano* Associate Editor Helmuth Möhwald. *ACS Nano* **13**, 6151–6169 (2019).

9. Poon, Z., Chang, D., Zhao, X. & Hammond, P. T. Layer-by-Layer Nanoparticles with a pH-Sheddable Layer for in Vivo Targeting of Tumor Hypoxia. *ACS Nano* **5**, 4284–4292 (2011).

10. Poon, Z., Lee, J. B., Morton, S. W. & Hammond, P. T. Controlling in Vivo Stability and Biodistribution in Electrostatically Assembled Nanoparticles for Systemic Delivery. *Nano Lett* **11**, 2096–2103 (2011).

11. Morton, S. W., Poon, Z. & Hammond, P. T. The architecture and biological performance of drug-loaded LbL nanoparticles. *Biomaterials* **34**, 5328–5335 (2013).

12. Dreaden, E. C. *et al.* Bimodal Tumor-Targeting from Microenvironment Responsive Hyaluronan Layer-by-Layer (LbL) Nanoparticles. *ACS Nano* **8**, 8374–8382 (2014).

13. Dang, X. *et al.* Layer-by-layer assembled fluorescent probes in the second near-infrared window for systemic delivery and detection of ovarian cancer. *Proceedings of the National Academy of Sciences* **113**, 5179–5184 (2016).

14. Kong, S. M., Costa, D. F., Jagielska, A., Van Vliet, K. J. & Hammond, P. T. Stiffness of targeted layer-by-layer nanoparticles impacts elimination half-life, tumor accumulation, and tumor penetration. *Proceedings of the National Academy of Sciences* **118**, (2021).

15. Boehnke, N. *et al.* Massively parallel pooled screening reveals genomic determinants of nanoparticle delivery. *Science (1979)* **377**, (2022).

16. Morton, S. W. *et al.* A Nanoparticle-Based Combination Chemotherapy Delivery System for Enhanced Tumor Killing by Dynamic Rewiring of Signaling Pathways. *Sci Signal* **7**, (2014).

17. Morton, S. W. *et al.* Osteotropic Therapy via Targeted Layer-by-Layer Nanoparticles. *Adv Healthc Mater* **3**, 867–875 (2014).

18. Dreaden, E. C. *et al.* Tumor-Targeted Synergistic Blockade of MAPK and PI3K from a Layer-by-Layer Nanoparticle. *Clinical Cancer Research* **21**, 4410–4419 (2015).

19. Dreaden, E. C. *et al.* RNA-Peptide nanoplexes drug DNA damage pathways in high-grade serous ovarian tumors. *Bioeng Transl Med* **3**, 26–36 (2018).

20. Lam, F. C. *et al.* Enhanced efficacy of combined temozolomide and bromodomain inhibitor therapy for gliomas using targeted nanoparticles. *Nat Commun* **9**, 1991 (2018).

21. Mensah, L. B. *et al.* Layer-by-layer nanoparticles for novel delivery of cisplatin and PARP inhibitors for platinum-based drug resistance therapy in ovarian cancer. *Bioeng Transl Med* **4**, (2019).

22. Kong, S. *et al.* Synergistic combination therapy delivered via layer-by-layer nanoparticles induces solid tumor regression of ovarian cancer. *Bioeng Transl Med* **8**, (2023).

23. Gu, L., Deng, Z. J., Roy, S. & Hammond, P. T. A Combination RNAi-Chemotherapy Layer-by-Layer Nanoparticle for Systemic Targeting of KRAS/P53 with Cisplatin to Treat Non–Small Cell Lung Cancer. *Clinical Cancer Research* **23**, 7312–7323 (2017).

24. Deng, Z. J. *et al.* Layer-by-Layer Nanoparticles for Systemic Codelivery of an Anticancer Drug and siRNA for Potential Triple-Negative Breast Cancer Treatment. *ACS Nano* **7**, 9571–9584 (2013).

25. Roh, Y. H. *et al.* Layer-by-Layer Assembled Antisense DNA Microsponge Particles for Efficient Delivery of Cancer Therapeutics. *ACS Nano* **8**, 9767–9780 (2014).

26. Choi, K. Y. *et al.* Binary Targeting of siRNA to Hematologic Cancer Cells In Vivo Using Layer-by-Layer Nanoparticles. *Adv Funct Mater* **29**, (2019).

27. Correa, S., Boehnke, N., Deiss-Yehiely, E. & Hammond, P. T. Solution Conditions Tune and Optimize Loading of Therapeutic Polyelectrolytes into Layer-by-Layer Functionalized Liposomes. *ACS Nano* **13**, 5623–5634 (2019).

28. Boehnke, N. *et al.* Theranostic Layer-by-Layer Nanoparticles for Simultaneous Tumor Detection and Gene Silencing. *Angewandte Chemie* **132**, 2798–2805 (2020).

29. Correa, S. *et al.* Highly Scalable, Closed-Loop Synthesis of Drug-Loaded, Layer-by-Layer Nanoparticles. *Adv Funct Mater* **26**, 991–1003 (2016).

30. Liu, Y., Yang, G., Hui, Y., Ranaweera, S. & Zhao, C. Microfluidic Nanoparticles for Drug Delivery. *Small* **18**, (2022).

31. Precision NanoSystems. Technologies and solutions for advancing RNA, small-molecule and protein nanomedicine. *Biopharma Dealmakers* https://www.nature.com/articles/d43747-020-01108-x (2020).

32. Webb, C. *et al.* Using microfluidics for scalable manufacturing of nanomedicines from bench to GMP: A case study using protein-loaded liposomes. *Int J Pharm* **582**, 119266 (2020).

33. Precision NanoSystems. Accelerating the Development and Scale-Up of mRNA Vaccines. *Precision NanoSystems Articles* https://www.precisionnanosystems.com/resources-and-community/knowledge-center/articles/detail/accelerating-the-development-and-scale-up-of-mrna-vaccines (2022).

34. Feldman, R. A. *et al.* mRNA vaccines against H10N8 and H7N9 influenza viruses of pandemic potential are immunogenic and well tolerated in healthy adults in phase 1 randomized clinical trials. *Vaccine* **37**, 3326–3334 (2019).

35. Barberio, A. E. *et al.* Cancer Cell Coating Nanoparticles for Optimal Tumor-Specific Cytokine Delivery. *ACS Nano* **14**, 11238–11253 (2020).

36. Barberio, A. E. *et al.* <scp>Layer-by-layer</scp> interleukin-12 nanoparticles drive a safe and effective response in ovarian tumors. *Bioeng Transl Med* (2022) doi:10.1002/btm2.10453.

37. Lieschke, G. J., Rao, P. K., Gately, M. K. & Mulligan, R. C. Bioactive murine and human interleukin-12 fusion proteins which retain antitumor activity in vivo. *Nat Biotechnol* **15**, 35–40 (1997).

38. Kleimann, J., Gehin-Delval, C., Auweter, H. & Borkovec, M. Super-Stoichiometric Charge Neutralization in Particle−Polyelectrolyte Systems. *Langmuir* **21**, 3688–3698 (2005).

CHAPTER 7

Polymer avidity on polyelectrolyte-coated nanoparticles regulates cancer cell binding and uptake kinetics

7.1 Introduction

Nanoparticles (NPs) are promising tools to modulate the pharmacology of a drug and improve its therapeutic window.[1,2] While NPs passively accumulate in certain diseased tissues, targeted delivery systems can significantly augment NP localization to desired tissues, minimizing off-target toxicities.[3] Among various methods to develop targeted NP delivery systems, the layer-by-layer (LbL) assembly technique is a simple and versatile approach to engineer nanostructures with controlled composition and functionality.[4,5] This technique involves the sequential adsorption of oppositely charged polymers onto NP surfaces, allowing for the assembly of LbL-NPs with tailored surface chemistries. We have successfully employed LbL-NPs to target various tumor tissues *in vivo*.[6–9]

The LbL assembly process is highly influenced by the conditions of the solution in which it is performed.[10,11] Parameters such as pH and ionic strength affect the structure, stability, and functionality of the resulting polyelectrolyte film.[12,13] Modulation of pH alters the degree of ionization of charged residues which can regulate the polymer conformation and amount of adsorbed polymer.[12] Similarly, charge screening due to higher ionic strength alters the polyelectrolyte conformation from a rigid rod to a random coil leading to an increased polymer mass deposition and a rougher surface.[13,14] We have previously optimized these parameters for the loading and delivery of nucleic acids *in vivo* from LbL-NPs.[10] However, the effect of solution conditions in other applications of LbL-NPs is unknown. Moreover, polymer molecular weight (MW) can influence the adsorbed polymer conformation and control the stability of polymer-substrate linkage but has not been well explored in LbL-NPs.[11,14]

We have found that liposomal NPs coated with a bilayer of poly-L-arginine (PLR) and poly-L-glutamate (PLE) are highly effective at delivering a potent cytokine – interleukin-12 (IL-12) - to cancer cell surfaces.[15,16] Unlike most NPs, PLE-coated LbL-NPs undergo limited endocytosis, allowing for prolonged extracellular NP presentation. This prolonged extracellular NP presentation enabled lipid-IL-12 conjugate release within the tumor microenvironment, improving therapeutic responses.

Here we sought to evaluate the role of solution conditions and polymer size in regulating IL-12 delivery from PLE-coated LbL-NPs to further augment the delivery of IL-12 from PLE-coated LbL-NPs. We show that LbL film assembly at increased ionic strength can directly inhibit IL-12 bioavailability and prevent serum-mediated lipid exchange from LbL-NPs, reducing IL-12 effectiveness *in vivo*. However, we find that by increasing the polymer size of PLR and PLE, we can maintain lipid release from LbL-NPs while increasing NP affinity toward cancer cells and improving cell surface retention of IL-12 NPs. When evaluated *in vivo*, PLE-IL-12-NPs with LbL films composed of large polymers significantly improved therapeutic responses.

7.2 Methods

7.2.1 Materials

1,2-distearoyl-sn-glycero-3-phosphocholine (DSPC), 1,2-dioleoyl-sn-glycero-3-phosphoethanolamine-N-[4-(p-maleimidophenyl)butyramide] (sodium salt) (18:1 MPB-PE), 1-palmitoyl-2-oleoyl-sn-glycero-3-phospho-(1'-rac-glycerol) (sodium salt) (POPG), 1,2-dioleoyl-sn-glycero-3-phosphoethanolamine-N-dibenzocyclooctyl (DOPE-DBCO), and cholesterol were purchased from Avanti Polar Lipids. All poly-L-arginine (PLR) and poly-L-glutamic acid (PLE) with were purchased from Alamanda Polymers except PLR_{700} which was purchased from Sigma (PLR_{700} is an approximation of the average repeat units of the polymer based on the batch used). BDP 650/665 azide (Lumiprobe) and BDP 630/650 azide (Lumiprobe) were conjugated to DOPE-DBCO in chloroform to generate fluorescently labeled lipids. Successful conjugation was validated via thin-layer chromatography which indicated <1% free dye. Deionized water was of ultrapure grade obtained through a Milli-Q water system (EMD Millipore).

7.2.2 Recombinant single-chain IL-12 production

Single-chain IL-12 sequence[17] was synthesized as a genomic block (Integrated DNA Technologies) and cloned into gWIZ expression vector (Genlantis). Plasmids were transiently transfected into Expi293 cells (ThermoFisher Scientific). After 5 days, cell culture supernatants were collected and protein was purified in an ÄKTA pure chromatography system using HiTrap HP Niquel sepharose affinity column, followed by size exclusion using Superdex 200 Increase 10/300 GL column (GE Healthcare Life Sciences). Endotoxin levels in purified protein was

measured using Endosafe Nexgen-PTS system (Charles River) and assured to be <5 EU/mg protein.

7.2.3 Liposome synthesis

A lipid solution was prepared by mixing (all mole %) 65% DSPC (25 mg/mL), 24% cholesterol (25 mg/mL), 6% POPG (25 mg/mL) and 5% 18:1 MPB-PE (5 mg/L) then formed into a thin film using a rotary evaporator (Buchi). Lipid films were allowed to further dry overnight in a desiccator, then were hydrated at 0.5-1 mg/mL using deionized water and sonicated for 3-5 minutes at 65 °C then extruded (Avestin Liposofast LF-50) once at 65 °C through a 100 nm membrane (Cytiva Nuclepore) then 3X through 50 nm membranes (Cytiva Nuclepore) . Extruded liposomes were added to an ice bath.

For covalent linkage of scIL-12 to Mal-liposomes, the solution pH of MPB-PE liposomes was adjusted to pH 5 with hydrochloric acid prior to lipid film hydration, and following membrane extrusion, liposomes at 0.33 mg/mL were adjusted to pH 7.0 with 10 mM HEPES prior followed by addition of scIL-12 containing a terminal cysteine residue at a molar ratio of 25:1 of MPB-PE lipid to protein for at least 12 hours at 4 °C in a rotating mixed. Any remaining maleimides were quenched with a 100-fold molar excess of L-cysteine (Sigma) for 1.5 hrs on ice.

For fluorescence labeling of liposomes, 0.2 mol% of DSPC content was replaced by either DOPE-650/665 or DOPE-630/650. IL-12 concentrations were measured via enzyme-linked immunoassay (ELISA) (Peprotech). Lipid content was quantified by dissociating the NPs in 90% DMSO and determining the NP fluorescence in a plate reader based on a standard curve of the sample prior to extruding (all measurements were done in 90% DMSO).

7.2.4 Layer-by-Layer (LbL) film deposition onto NPs

Assembly of polyelectrolyte layers was performed by adding unlayered particles to a diH_2O solution with 0.3-0.4 weight equivalents (wt.eq.) of PLR relative to lipid in a glass vial under sonication and incubating on ice for at least 30 min. Excess PLR polymer was purified by TFF through a 100 kDa mPES membrane (Repligen) pre-treated with a 10 mg/mL solution of free PLR. For the terminal PLE layer, purified particles coated with PLR were added to a diH_2O solution with PLE in a glass vial under sonication at 1 wt.eq. of polymer to lipid. LbL particles were then purified by TFF on a separate 100 kDa mPES membrane (Repligen) to remove any excess PLE.

7.2.5 Characterization of particle preparations

Dynamic light scattering (DLS) and zeta potential measurements were made on a Zetasizer Nano ZSP (Malvern). Nanoparticle micrographs were acquired using Transmission Electron Microscopy (TEM) on a JEOL 2100F microscope (200 kV) with a magnification range of 10,000-60,000X. All images were recorded on a Gatan 2kx2k UltraScan CCD camera. Negative-stain sample preparation was performed by adding 10 μL of NPs on a 200 meshes copper grid coated with a continuous carbon film and allowing for sample adsorption for 60 seconds. Excess solution was then removed by touching the grid with a kimwipe. The grid was then quickly washed by adding 10 μL of negative staining solution, phosphotungstic acid (PTA), 1% aqueous solution then removing excess by touching the grid with a kimwipe. Then, the grid was mounted on a JEOL single tilt holder equipped in the TEM column for image capture.

7.2.6 LbL-NP salt stress test

LbL-NPs were diluted in 15 mM HEPES (pH 7.3) to 0.1 mg/mL in a 1.5 mL disposable cuvette (Fisherbrand). A 2 M NaCl stock solution was then used to increase the ionic strength of the solution. Samples were allowed to incubate for 10-15 min prior to measuring particle size via DLS. After DLS readings, the concentration of NaCL was increased and the process was repeated until particles had coalesced (> 1 μm in diameter).

7.2.7 Fluorescent labeling of polymers

PLE at 10 mg/mL was labeled by reacting with 5 molar equivalents of sulfo-cyanine3 NHS ester (Lumibrobe) in PBS adjusted to pH ~8.5 with 0.1 M sodium bicarbonate. Excess dye was removed via extensive 0.9wt% NaCldialysis followed by extensive diH_2O dialysis using a 3 kDa regenerated cellulose membrane (Repligen) and the purified PLE-cy3 was lyophilized until use.

7.2.8 Analysis of LbL film stability and lipid release

PLR/PLE films were assembled onto Mal-UL NPs as described in *Layer-by-Layer (LbL) film deposition onto NPs,* but the PLE solution was doped with 50% PLE-cy3. Particles were incubated in a buffer solution containing 15 mM HEPES (pH 7.3), 150 mM sodium chloride (NaCl), 1% pen-strep, and 10% fetal bovine serum at 0.1 mg/mL in a shaker at 37 °C. At defined intervals,

aliquots were extracted from the incubation solution and free polymers were separated from the NP. Samples were spun on a 300 kDa centrifugal filter (VivaSpin500, Sartorius) at 10x*g* for 15 min and the permeate PLE or lipid fluorescence was compared to the fluorescence of the initial sample. Particles were validated to lack free polymers by centrifuging in diH_2O. Fluorescence was measured on 96 well plates using a plate reader (Tecan Infinite 200).

7.2.9 Cell Culture

OV2944-HM-1 cells were acquired through Riken BRC and were cultured in α-MEM. HEK-Blue IL-12 (InvivoGen) cells were cultured and used for IL-12 bioactivity assessment according to the manufacturer's instructions. Cell media was also supplemented with 10% FBS and penicillin/streptomycin with cells incubated in a 5% carbon dioxide humidified atmosphere at 37 °C. All cell lines were murine pathogen tested and confirmed mycoplasma negative by Lonza MycoAlert™ Mycoplasma Detection Kit.

7.2.10 In vitro cellular association

HM-1 cells were plated on a tissue-culture 96-well plate at a density of 50K cells per well. The next day, wells were dosed with NPs and left for the target incubation time indicated. For assessment of NP-associated fluorescence in a fluorescence plate reader, a dose of 0.05 mg/mL was used and before cell washing with PBS, the supernatant was removed from the well and diluted 10X with DMSO. Cells were then washed three times with PBS and disrupted with DMSO. Fluorescence of NPs associated with cells was then normalized to supernatant fluorescence. The relative fluorescence of each formulation was then compared to an unlayered liposome control containing the same fluorophore. For assessment of IL-12 on the surface of cancer cells, cells were washed 4 hours after dosing NPs with PBS and then PE anti-IL-12 monoclonal (BioLegend) or Alexa Fluor® 700 anti-IL-12 (BioLegend) were incubated with cells for 1 hr in cell media. After incubation with antibody, cells were washed with PBS and the fluorescence of NP and of IL-12 Ab were measured on a plate reader. To determine IL-12 presentation efficiency, the ratio of IL-12 Ab to NP fluorescence for each formulation was then determined and normalized to that of $PLE_{100}PLR_{50}$ LbL-NPs. To quantify IL-12 half-life, the cells were left in cell media for 24 or 48 hours after washing out unbound NPs prior to anti-IL12 Ab incubation. The total IL-12 fluorescence was then used to determine a half-life.

For analysis via flow cytometry, NPs were dosed at the indicated concentrations and allowed to incubate with cells at 37°C. Cells were washed with PBS then detached from the plates using 0.25% trypsin and stained with DAPI (15 min incubation) for viability assessment and fixed with 2% paraformaldehyde (30 min incubation) until analysis by flow cytometry using an LSR Fortessa (BD Biosciences).

7.2.11 In vitro confocal imaging

For confocal imaging, 8-well chambered coverglasses (Nunc Lab-Tek II, Thermo Scientific) were coated with rat tail collagen type I (Sigma-Aldrich) per the manufacturer's instructions. HM-1 cells were plated into the wells at a density of 10K/well and left to adhere overnight prior to NP treatment. After the desired incubation time with NPs, cells were washed 3x with PBS. After washing, cells were fixed in 4% paraformaldehyde for 15 minutes then washed (3x with PBS) and stained with wheat germ agglutinin (WGA) conjugated to Alexa Fluor488 (Invitrogen) and Hoechst 33342 (Thermo Scientific) following manufacturer's instructions. For extracelluar IL-12 visualization, cells were stained with PE-anti-IL-12 monoclonal antibody (BioLegend) for 1 hr in 10% goat serum and then washed 3x with PBS. Images were analyzed using ImageJ. Chamber slides were imaged on an Olympus FV1200 Laser Scanning Confocal Microscope.

7.2.12 Animals

All animal work was conducted under the approval of the Massachusetts Institute of Technology Division of Comparative Medicine IACUC in accordance with federal, state, and local guidelines. B6C3F1 mice were purchased from Jackson Laboratories. Female mice were used between 8-12 weeks of age unless otherwise noted.

7.2.13 Pharmacokinetic and biodistribution in metastatic ovarian cancer model

B6C3F1 mice were inoculated with firefly luciferase and mCherry-expressing OV2944-HM1 (HM-1-mCherry-luc) cells through intraperitoneal (i.p.) injection of 10^6 cells in PBS. Two weeks after tumor inoculation, mice were injected with IL-12 NPs containing fluorescently labeled lipid (DOPE-630/650, 0.2 mol%). After 4 hrs, mice were euthanized, ascites cells were harvested via peritoneal lavage, and organs were removed and placed in PBS under ice. Organs were then transferred to a 1 mg/mL D-luciferin solution in PBS and incubated for 5 minutes then placed in

an IVIS to determine each organ's BLI and NP fluorescence. Data were analyzed using Living Image software. Background fluorescence measurements were made for each organ based on signals from mice treated with dextrose. For correlation analysis, the weight-normalized bioluminescence flux (p/s/g) and radiant efficiency ([p/s] / [μW/cm²]/g) for each organ were analyzed on Graphpad Prism 10 for their correlation via the Pearson's correlation coefficient.

7.2.14 Efficacy studies with metastatic ovarian cancer model

B6C3F1 mice were inoculated intraperitoneally with 10^6 cells of HM-1-luc in PBS. One week after inoculation, treatment was initiated as indicated on each figure. All treatments included the same IL-12 dose. Bioluminescence was measured on an IVIS 10 minutes after i.p. injection of 3 μg of D-luciferin sodium salt (GoldBio) for 30 days after tumor inoculation or as needed to track tumor burden.

7.2.15 Statistical Analysis

GraphPad PRISM 10 was used to perform statistical analyses. Comparisons between two groups was performed via unpaired t-tests. For multiple groups or multiple variable analysis, one-way, or two-way ANOVAs were used with Tukey's posthoc correction for time-based analysis or Sidak posthoc for other ANOVA analysis.

7.3 Results and Discussion

7.3.1 Polymer conformation of LbL film assembled in deionized water is required for effective delivery of IL-12 from LbL-NPs

In our prior work delivering IL-12 from PLE-NPs, the LbL films were assembled in deionized water (DI) employing PLR with 50 repeat units (PLR_{50}) and PLE with 100 repeat units (PLE_{100}).[15,16] However, the assembly of LbL films on NPs in solutions buffered with HEPES (25 mM, pH 7.3) and mild ionic strength (20 mM sodium chloride, NaCl) has been shown to increase the amount of adsorbed polymer and is expected to increase film thickness.[10] We compared the effect of adsorbing PLR and PLE in either DI or the buffered solution (termed hNa) onto liposomes with IL-12 covalently linked to phospholipid headgroups of the lipid bilayer (**Figure 7.1a**). The final LbL-NP size and zeta potential were similar among the formulations with a slight size increase when assembled in hNa (**Figure F1a-b**). However, particles assembled in hNa exhibited

a thicker LbL film when imaged via negative stain transmission electron microscopy (TEM, **Figure 7.1b-c**). To evaluate film and NP colloidal stability, we devised an assay in which LbL-NPs are exposed to increasing concentrations of NaCl (**Figure F1c**). At a critical concentration of NaCl, the film destabilizes, and particles begin to coalesce at a rate dependent on their steric colloidal stability. LbL NPs assembled in hNa had increased film stability and reduced aggregation upon film destabilization compared to assembly in DI (**Figure 7.1d**), consistent with a rougher film providing greater steric stabilization.

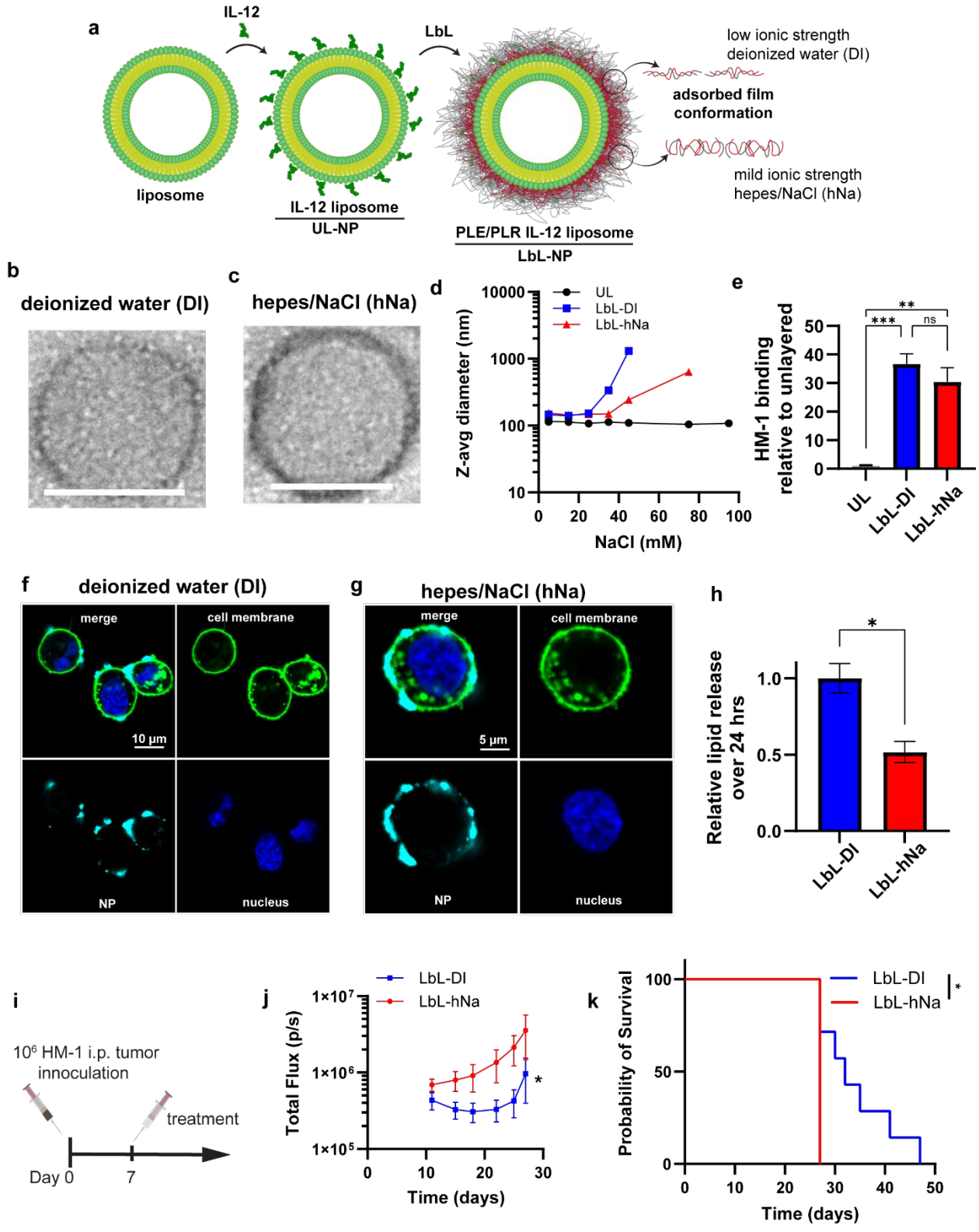
a
IL-12
LbL
low ionic strength
deionized water (DI)
adsorbed film
conformation
mild ionic strength
hepes/NaCl (hNa)
liposome
IL-12 liposome
UL-NP
PLE/PLR IL-12 liposome
LbL-NP
b
deionized water (DI)
c
hepes/NaCl (hNa)
d
UL
LbL-DI
LbL-hNa
Z-avg diameter (nm)
NaCl (mM)
e
HM-1 binding
relative to unlayered
ns
UL
LbL-DI
LbL-hNa
f
deionized water (DI)
merge
cell membrane
10 μm
NP
nucleus
g
hepes/NaCl (hNa)
5 μm
h
Relative lipid release
over 24 hrs
i
10⁶ HM-1 i.p. tumor
innoculation
treatment
Day 0
7
j
Total Flux (p/s)
Time (days)
k
Probability of Survival
Time (days)

Figure 7.1. Assembly of LbL film under mild ionic strength generates thicker layers, but reduces IL-12 bioavailability and limits lipid release. (a) Schematic of LbL film conformation on IL-12 LbL-NPs due to assembly in higher ionic strength buffer. Negative stain TEM of IL-12 LbL-NPs assembled either in DI (b) or hNa (c). Scale bars represent 100 nm. (d) Assessment of LbL-NP film stability through exposure of NPs to increasing concentrations of sodium chloride (NaCl). (e) Fluorescently labeled NPs were dosed to HM-1 cells *in vitro*. Four hours after dosing, cells were washed and the NP fluorescence associated with cells was measured on a fluorescence plate reader. Shown are the normalized fluorescence readings relative to an unlayered negatively charged liposome. (f-g) Fluorescently labeled NPs were dosed to HM-1 cells in vitro. Four hours after dosing, cells were washed, fixed, and then stained with wheat germ agglutinin (cell membrane stain) and Hoechst 33342 (nucleus stain), and then visualized via confocal microscopy. Shown are representative confocal microscopy images of HM-1 cells incubated for 4 hours with LbL-NP assembled in DI (f) or hNa (g). (h) Quantification of lipid release from LbL-hNa relative to LbL-DI after 24 hours incubation in serum-containing media. (i-k) B6C3F1 mice (n = 7/group) inoculated with 10^6 HM-1-luc tumor cells on day 0 were treated on days 7 with 20 μg of IL-12 conjugated to LbL-NPs assembled in either DI or hNa. Shown are the experimental timeline **(i),** in vivo IVIS whole-animal i.p. BLI readings **(**mean ± s.e.m., **j)**, and overall survival **(k)**. Statistical comparisons between survival curves were performed using a log-rank (Mantel–Cox) test.

To determine if these thicker films could affect cancer cell binding, we incubated LbL-NPs assembled in either DI or hNa for 4 hrs with a highly metastatic ovarian cancer cell line – OV2944-HM-1 (HM-1). Assembly in either DI or hNa did not affect the LbL-NP affinity towards cancer cells (**Figure 7.1d)** and both formulations showed strong cell membrane retention properties of PLE-coated NPs (**Figure 7.1f-g).** While the thicker films did not affect cellular interactions, we theorized that it could hinder IL-12 accessibility and prevent the ability of lipid release from the NPs which we have found to be crucial for the therapeutic efficacy of IL-12-LbL-NPs. Consistent with a thicker LbL-film promoting steric hindrance of IL-12 recognition by IL-12 receptors, particles assembled in hNa had reduced IL-12 bioactivity compared to films assembled in DI when evaluated on a reporter cell line (**Figure F1c**). Indeed, LbL-hNa particles showed similar bioactivity as tetralayer LbL-DI NPs. We next incubated particles assembled in either DI or hNa in serum-containing media for 24 hrs then determined the total lipid released by separating serum-

bound lipids from NPs on a centrifugal filter. LbL-NPs assembled in hNa could reduce the amount of lipid released by over 50% compared to DI-assembled films (**Figure 7.1h**).

Given the potential reduced therapeutic efficacy of hNa LbL-NPs, we inoculated mice with peritoneally disseminated HM-1 tumors and then treated the mice with a single dose of IL-12-LbL-NPs with either DI or hNa films (**Figure 7.1i**). Tumor bioluminescence readings showed that mice treated with DI-assembled LbL-NPs had greater tumor control (**Figure 7.1j**), which ultimately lead to significantly improved survival (**Figure 7.1k**).

7.3.2 High MW polyelectrolytes increase LbL-NPs film stability without affecting lipid release or IL-12 bioavailability

Having discovered that the thicker films assembled in hNa hindered the therapeutic efficacy of IL-12 delivered from PLE-LbL-NPs, we theorized that we could instead increase film stability by increasing the polymer size while assembling in DI (**Figure 7.2a**). The thinner DI-assembled films could facilitate lipid release and maintain full IL-12 bioactivity. As large polymers can bridge and crosslink two particles[18], we first wanted to ensure it was feasible to assemble LbL-NPs using high molecular weight (HMW) polymers (PLR_{700}/PLE_{800}) and compared it to our standard low molecular weight (LMW) film ($PLR_{50}PLE_{100}$). Layering with long polyamino acids did not lead to significant changes in particle size (**Figure 7.2b**) or zeta potential (**Figure 7.2c**). Surprisingly, when the film stability was assessed by our salt stress experiment, PLR_{700}/PLE_{800} did not show signs of aggregation even at substantially higher NaCl concentrations (**Figure 7.2d**), suggesting that the higher MW polymer chains can increase film and particle stability. To directly evaluate the film stability, we fluorescently tagged the PLE chains on the LbL-NPs and then exposed them to a physiological solution containing serum proteins. While PLR_{50}/PLE_{100} show a ~60-70% burst release of PLE but the burst release of PLE from PLR_{700}/PLE_{800} was reduced almost 2-fold (**Figure 7.2e**). At longer time points, however, the total fraction of PLE released was equivalent for both formulations.

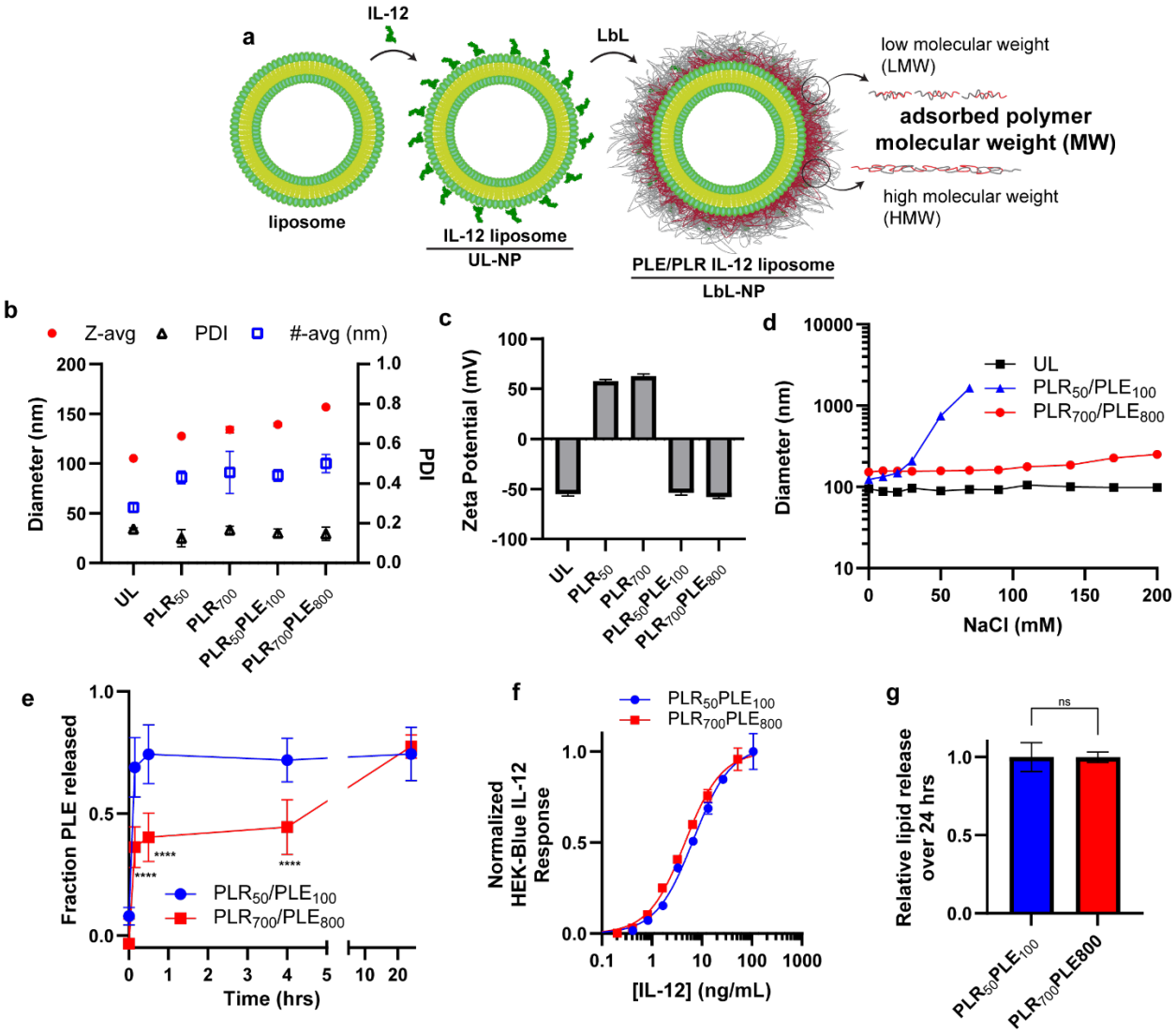

Figure 7.2. High MW polyelectrolytes stabilize LbL-NP but maintain IL-12 bioactivity and lipid release properties (a) Schematic IL-12 LbL-NPs with films composed of low or high molecular weight (MW) polymers. (b) Dynamic light scattering size and polydispersity measurements of LbL-NPs composed of low or high molecular weight (MW) polymers. (c) Apparent surface zeta potential measurements of LbL-NPs composed of low or high molecular weight (MW) polymers. (d) Assessment of LbL film and NP stability via a salt stress test. (e) Release of PLE from LbL-NPs in 10% serum. (f) HEK-Blue IL-12 response. (g) Relative lipid release in 10% serum from LbL-NPs assembled in deionized water with low molecular weight polymers or high molecular weight.

Importantly, PLR_{700}/PLE_{800} LbL-NPs did not affect IL-12 bioactivity (**Figure 7.2f**). Moreover, when we quantified the total lipid release after incubating the particles for 24 hrs in serum-containing media, there was no difference between the formulations (**Figure 7.2g**). These results suggested that we could increase LbL-NP film and NP stability by increasing the size of the adsorbed polymer MW while maintaining the desired physical properties of the LbL-NPs for IL-12 delivery.

7.3.3 High MW PLR and PLE increase LbL-NPs association with cancer cells while high MW PLE increases the efficiency of cell membrane presentation of NPs

To understand the effects of polymer size on the biological interactions with cancer cells, we generated a library of PLR/PLE LbL-NPs composed of a combinatorial assembly of four PLR sizes (PLR_{50}, PLR_{100}, PLR_{200}, PLR_{700}) and three PLE sizes (PLE_{100}, PLE_{200}, and PLE_{800}). Analysis of particle size showed similar particle diameters and low polydispersity (polydispersity index < 0.2) albeit the use of PLE_{800} could increase the hydrodynamic size by ~10-20 nm (**Figure F2a**). No major differences in zeta potential could be observed (**Figure F2b**) nor did any of the films affect IL-12 bioactivity (**Figure F3c**), confirming that the DI-assembled films did not result in thicker polymer assemblies. Incubation of these PLR/PLE LbL-NPs formulations with HM-1 cells revealed that high MW PLR and medium MW PLE yielded the highest NP association (**Figure 7.3a**). However, effective IL-12 delivery requires not only NP association but also prevention of NP endocytosis to prolong the extracellular presentation of the IL-12. Thus, after incubating NPs with LbL-NPs for 4 hours, cells were washed and incubated with a fluorescently tagged monoclonal antibody against IL-12 to bind to NPs on the cell membrane of cancer cells (**Figure 7.3b**). The fluorescence ratio of the IL-12 antibody to total NP fluorescence was then used to determine the extracellular presentation efficiency of the formulations. As expected, while negligible amounts of IL-12 staining were observed for UL NPs, our standard LMW $PLR_{50}PLE_{100}$ significantly improved the extracellular presentation of IL-12 (**Figure 7.3c**). Consistent with the role of PLE in promoting the retention of LbL-NPs on the cancer cell surfaces, we found that PLE_{800} could increase the surface presentation of NPs by ~50% regardless of the PLR size (**Figure 7.3d**).

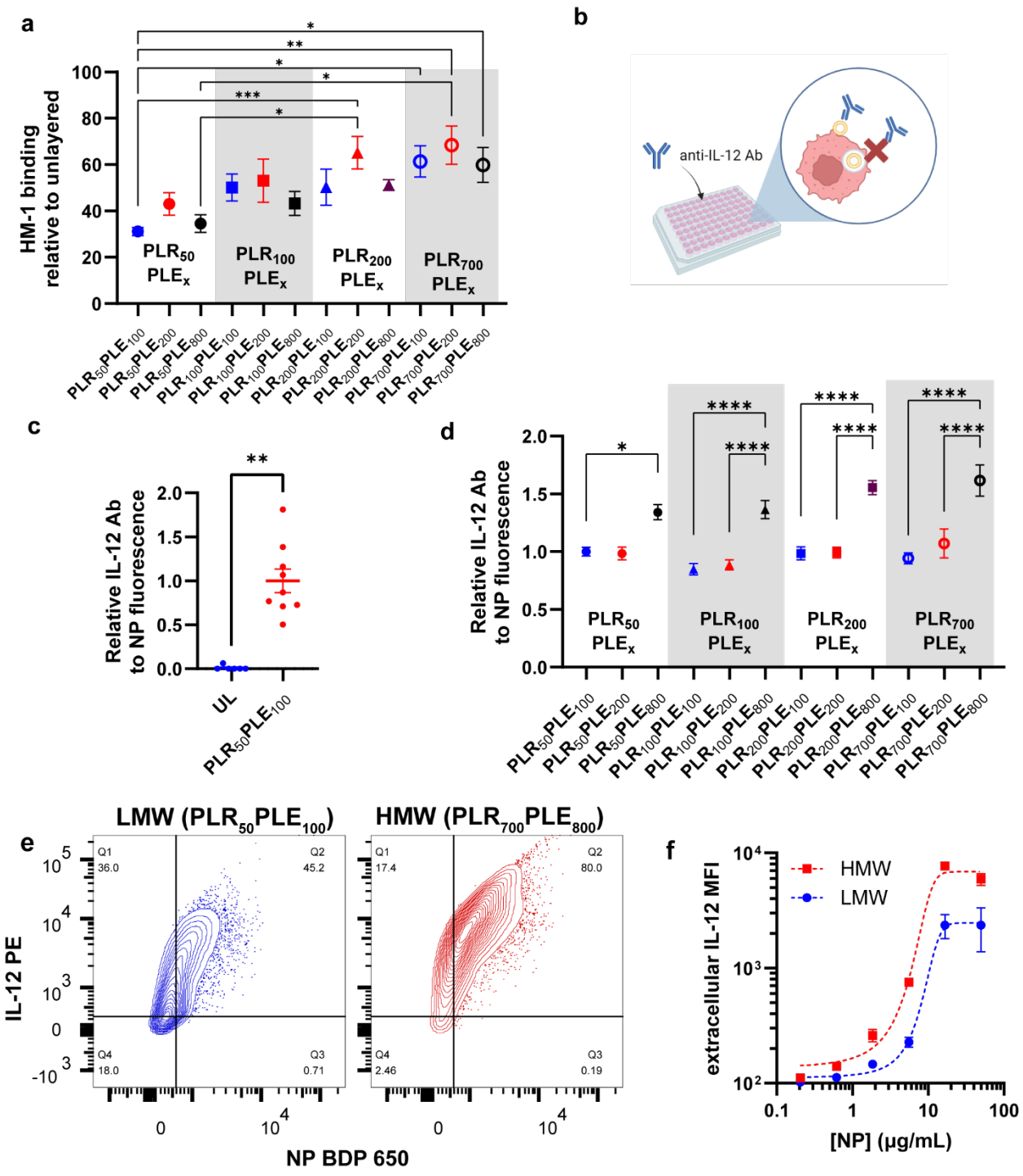

Figure 7.3. High MW polyelectrolytes increase cancer cell binding and increased PLE MW augments efficiency of the surface presentation of LbL-NPs. (a-d) Fluorescently labeled NPs were dosed to HM-1 cells *in vitro*. Four hours after dosing, cells were washed, and stained with anti-IL-12 monoclonal antibody. After IL-12 Ab binding, cells were again washed and the NP and IL-12 fluorescence associated with cells was measured on a fluorescence plate reader. Shown are

the normalized fluorescence readings relative to an unlayered negatively charged liposome (a), schematic for staining extracellular presented IL-12 NPs (b), the ratio of IL-12 to NP fluorescence of UL and $PLR_{50}PLE_{100}$ NPs normalized to $PLR_{50}PLE_{100}$, and the ratio of IL-12 to NP fluorescence for the library of polyelectrolyte MWs normalized to $PLR_{50}PLE_{100}$. (e-f) Fluorescently labeled NPs were dosed to HM-1 cells *in vitro*. Four hours after dosing, cells were washed, suspended, stained with an anti-IL-12 monoclonal antibody, re-washed and fixed. Shown are representative flow plots of IL-12 fluorescence and NP fluorescence of HM-1 cells dosed with 15 μg/mL of $PLR_{50}PLE_{100}$ (LMW) or $PLR_{700}PLE_{800}$ (HMW) (e), and quantitation of extracellular IL-12 median fluorescence intensity (MFI) of HM-1 cells dosed with LMW and HMW LbL-NPs across various NP concentrations (f).

To further compare the NP binding and IL-12 presentation efficiency of PLR/PLE LbL-NPs composed of either LMW ($PLR_{50}PLE_{100}$) to the HMW ($PLR_{700}PLE_{800}$), we dosed various concentrations of NPs to HM-1 cells and then stained for extracellular IL-12 and analyzed NP and IL-12 fluorescence via flow cytometry. As expected, HMW LbL-NPs increased both NP association and total IL-12 presented (**Figure 7.3e**). This effect increased the total IL-12 presented in the cell surface by 2-4 fold for all NP concentrations (**Figure 7.3f**), confirming that the use of HMW polymers can improve cancer cell binding and extracellular presentation of IL-12.

7.3.4 High MW polymers increase the half-life of LbL-NPs on cancer cell surfaces

In addition to inhibiting initial NP endocytosis upon binding to cancer cells, PLE-NPs are efficiently retained at the cell surface.[6] We hypothesized that the polymer size might also affect the long-term retention of IL-12 LbL-NPs on cancer cell membranes. To measure the cell membrane half-life of LbL-NPs, HM-1 cells were exposed to NPs for 4 hours to associate with cancer cells. Afterward, the NP-bound cells were washed, and fresh cell culture medium was added. The cells were then incubated with fluorescent anti-IL-12 antibodies at 0, 24, or 48 hours after the removal of unbound NPs. The total IL-12 antibody staining at each time point was used to calculate the half-life. Increasing both PLR and PLE sizes increased the surface half-life of IL-12 (**Figure 7.4a**), with HMW polymers yielding an almost 3-fold increase in IL-12 half-life compared to LMW LbL-NPs (**Figure 7.4b**). Analysis of HM-1 cells dosed with either LMW or

HMW LbL-NPs for 48 hrs and then visualized via confocal microscopy showed a clear increase in total IL-12 presented extracellularly (**Figure 7.4c)**.

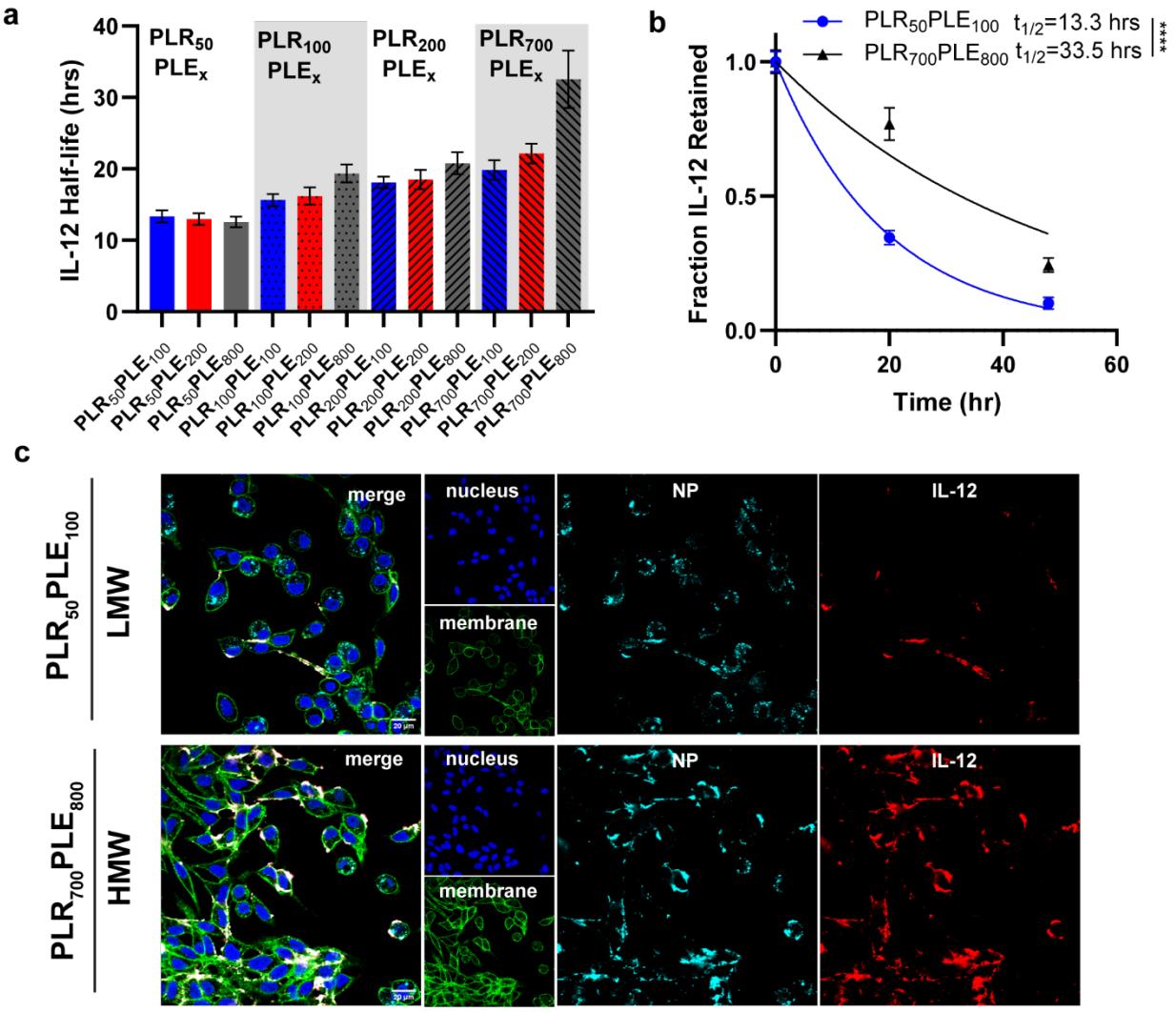

Figure 7.4. HMW polyelectrolyte LbL films increase the half-life of IL-12 on cancer cell membranes. (a-b) Fluorescently labeled NPs were dosed to HM-1 cells *in vitro*. Four hours after dosing, cells were washed, and fresh cell culture media was added. After 0, 24 or 48 hrs after removing unbound NPs, cells were stained with anti-IL-12 monoclonal antibody, washed, and total IL-12 fluorescence associated with cells was evaluated on a fluorescence plate reader to determine an IL-12 fluorescence half-life. Shown are the derived IL-12 half-life for the panel of PLR and PLE MW films (a) and the decay curves comparing the LWM ($PLR_{50}PLE_{100}$) to the HMW ($PLR_{700}PLE_{800}$) film. (c) Fluorescently labeled NPs were dosed to HM-1 cells in vitro. Two days (48 hrs) after dosing, cells were washed, fixed, and then stained with wheat germ agglutinin (cell

membrane stain), Hoechst 33342 (nucleus stain), and anti-IL-12 antibody. Cells were then visualized via confocal microscopy. Shown are representative confocal microscopy images of HM-1 cells treated with LMW or HMW LbL-NPs.

7.3.5 HMW-LbL-NPs increase association with tumor tissues in metastatic ovarian cancer model

Having discovered that the polymer size could significantly augment *in vitro* NP association and IL-12 extracellular presentation on cancer cells, we next sought to evaluate its effectiveness in targeting cancer tissue *in vivo*. Mice were inoculated with peritoneally disseminated HM-1 cells engineered to express mCherry and luciferase to track tumor cells *in vivo*. Two weeks after inoculation, animals were treated intraperitoneally (i.p.) with free IL-12, UL-IL-12 NPs, or LbL-IL-12-NPs assembled with either LMW or HMW polymers (**Figure F3a**). The cellular fraction from ascites was harvested and processed for flow cytometry whereas organs were extracted to quantity total NP fluorescence and tumor bioluminescence intensity (BLI) *ex vivo* using an In Vivo Imaging System (IVIS).

Even though cells in the ascites were primarily immune cells (~70% $CD45^+$) and there was only a minor portion of cancer cells (~1% $CD45^-mCherry^+$, **Figure F3b**), the LbL coating was able to selectively increase NP uptake by cancer cells (**Figure 7.5a**), and not immune cells (**Figure 7.5b**). Moreover, HMW LbL-NPs increased total NP fluorescence on cancer cells ~2-fold compared to LMW LbL-NPs. Assessment of the percentage of NP-positive immune cells and cancer cells confirmed the selectivity of LbL-NPs towards cancer cells with HMW-LbL NPs achieving ~95% NP-positive cancer cells compared to ~75% and ~25% for LMW and UL NPs, respectively (**Figure 7.5c**). Staining with anti-IL-12 antibodies showed that only LbL-NPs could present IL-12 on the surface of cancer cells, with HMW-LbL NPs showing a stronger IL-12 signal (**Figure 7.5d-e**). A small (~10%) fraction of immune cells was also found to have IL-12 presented on their surface which could enable sustained IL-12 activation of immune cells in the ascites.

As expected, *ex vivo* NP fluorescence signal showed that both LbL-NPs strongly associated with tissues with the most metastatic tumor burden (i.e., the omentum and urogenital tract, UGT, **Figure 7.5f**). However, HMW-LbL-NPs significantly outperformed LMW-LbL NPs, as the optimized formulation achieved a 10-fold and 3-fold increase in association with the omentum and

UGT compared to UL whereas LMW-LbL NPs increased association 3-fold and 2-fold, respectively. To confirm that LbL-NPs achieved systemic targeting of disseminated tumor burden, we evaluated the correlation between every tissue's NP signal and BLI. Only mice treated with LbL-NPs had strong (r~0.8) and significant ($p<0.05$) correlation between NP and BLI (**Figure 7.5g-h**). Thus, HMW-LbL-NPs could increase NP accumulation in disseminated cancer tissues while maintaining or improving the targeting properties of LbL-NPs compared to LMW-LbL-NPs.

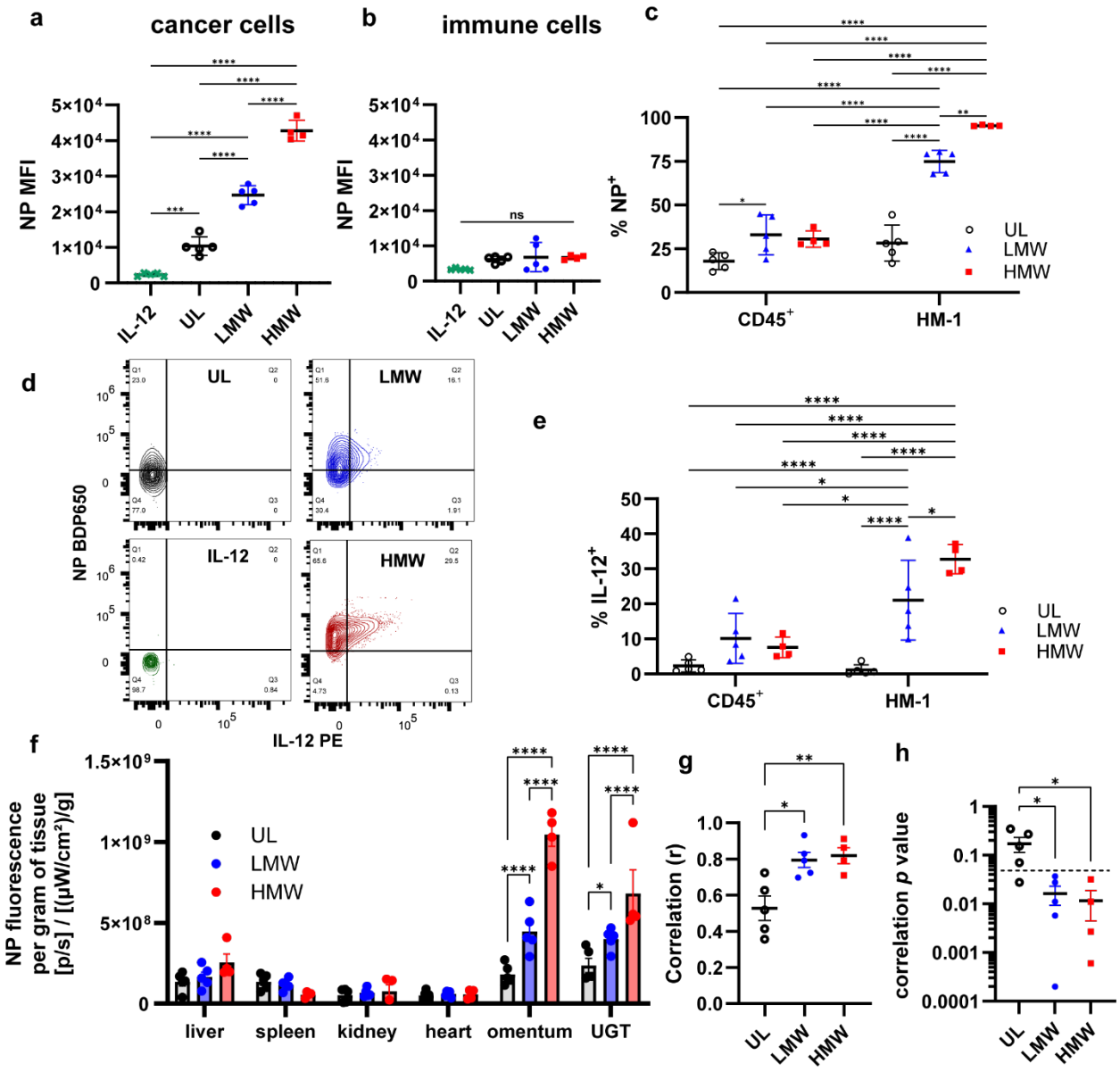

Figure 7.5. HMW polyelectrolyte LbL films increase cancerous tissue NP targeting and increase total IL-12 presentation. (a-h) B6C3F1 mice (n=4-5/group) inoculated with 10^6 HM-1-mCherrry-luc tumor cells on day 0 were administered fluorescently-tagged NPs carrying 20 μg IL-

12 (or an equivalent dose of free IL-12) on day 14. Four hours after dosing, animals were sacrificed, ascites was collected and processed for flow cytometry whereas tissues were analyzed ex-vivo via IVIS. Shown are the median fluorescence intensity (MFI) of NP signal in cancer cells ($CD45^-mCherry^+$, mean ± s.d., a) and immune cells ($CD45^+$, mean ± s.d., b), the percentage of immune cells and cancer cells that were NP-positive (mean ± s.d., c), representative flow cytometry plot of NP and extracellular IL-12 fluorescence of tumor cells (d), the percentage of immune cells and cancer cells that were IL-12-positive (mean ± s.d., e), the weight-normalized tissue NP fluorescence (mean ± s.e.m., **f**), Pearson's correlation coefficient between weight-normalized tissue NP fluorescence and BLI 4 hours after dosing (g), and the significance of the correlation estimates (h).

7.3.6 HMW-LbL-NPs improve the therapeutic efficacy of LbL-NPs in a metastatic model of ovarian cancer

To access the therapeutic impact of the optimized LbL film from HMW-LbL-NPs, we inoculated the i.p. space of mice with HM-1 cells expressing luciferase (HM-1-luc). After 7 and 14 days, mice were treated with 20 μg of IL-12 as a free cytokine or in NP formulations (**Figure 7.6a**). We evaluated UL-NPs, LMW-LbL-NPs ($PLR_{50}PLE_{100}$), HMW-LbL-NPs ($PLR_{700}PLE_{800}$), and a medium MW LbL-NP formulation which had matched *in vitro* HM-1 association but without increased IL-12 presentation efficiency ($PLR_{200}PLE_{200}$, see **Figure 7.3**). Moreover, we tested the efficacy of a single 20 μg dose of HMW-LbL-NPs administered on day 7. All IL-12 treatments yielded drastic reductions in tumor BLI (**Figure 7.6b**). However, only LbL-NP formulations showed reduced BLI readings compared to free IL-12. A single shot of HMW-LbL-NPs had similar performance as two-dose regimens of other LbL-NPs. When given the two-dose regimen of HMW-LbL-NPs, the tumor was controlled for over 26 days whereas all other treatments had rebounded by the same time.

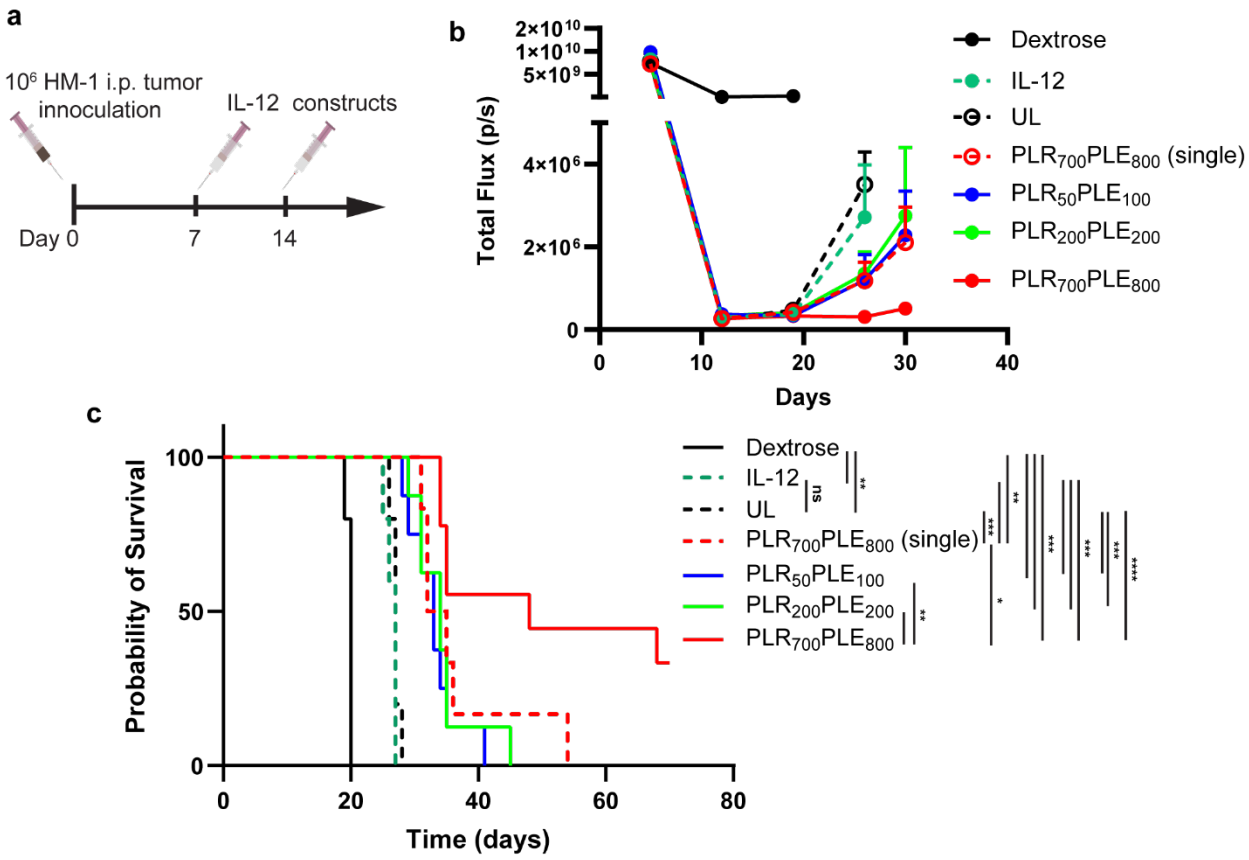

Figure 7.6. HMW polyelectrolytes increase LbL-NP treatment efficacy in a metastatic model of ovarian cancer B6C3F1 mice (n = 10/group) inoculated with 10^6 HM-1-luc tumor cells on day 0 were treated on days 7 and 14 with 20 µg of IL-12 as a free cytokine or conjugated to LbL-NPs. Shown are the experimental timeline **(a),** *in vivo* IVIS whole-animal i.p. BLI readings **(**mean ± s.e.m., **b)**, and overall survival **(c)**.

While mice treated with dextrose survived for only 20 days, IL-12 or UL-NP administration extended survival for one week to ~27 days (**Figure 7.6c**). All LbL-NP treatments could significantly improve survival for at least one more week to ~34 days. This extension in survival could be achieved with a single dose administration of HMW-LbL-NPs. On the other hand, two doses of HMW-LbL-NPs extended the median survival to 47 days, significantly outperforming all other treatment groups and leading to the only treatment with long-term survivors (~30% alive on day 70). Notably, $PLR_{700}PLE_{800}$ LbL-NPs significantly outperformed $PLR_{200}PLE_{200}$ NPs consistent with the required improved surface presentation of IL-12 and not only increasing cellular association.

7.4 Conclusion

The surface chemistry of NPs modulates its interactions with biological systems. Assembly of LbL films on the surface of NP enables control over these interactions.[6] While the effects of solution conditions and polymer length are well described in the literature for 2-D LbL films[19,20], little has been done to explore their properties in LbL-NPs.

Here we show that LbL films achieved by the adsorption of polymers in the presence of buffered solutions with mild ionic strength are more stable. However, the resulting increased film thickness diminished the effectiveness of IL-12 delivery from LbL-NPs due to reduced IL-12 bioavailability and lipid release. On the other hand, longer polymer chains during film assembly in DI increase film and NP stability without hindering IL-12 bioavailability and lipid release from LbL-NPs. Employing the HMW-LbL-NPs improved *in vitro* and *in vivo* tumor accumulation and IL-12 presentation from LbL-NPs compared to LMW polymer films. These enhanced properties allowed for a significant boost in the therapeutic efficacy of HMW-LbL-NPs over LMW-LbL-NPs. Taken together, this work presents novel insights into how LbL film assemblies of the same chemistry may be used to modulate their interaction with biological systems.

7.5 References

1. Manzari, M. T., Shamay, Y., Kiguchi, H., Rosen, N., Scaltriti, M. & Heller, D. A. Targeted drug delivery strategies for precision medicines. *Nat Rev Mater* **6,** 351–370 (2021).

2. Gavas, S., Quazi, S. & Karpiński, T. M. Nanoparticles for Cancer Therapy: Current Progress and Challenges. *Nanoscale Res Lett* **16,** 173 (2021).

3. Ahmad, A., Khan, F., Mishra, R. K. & Khan, R. Precision Cancer Nanotherapy: Evolving Role of Multifunctional Nanoparticles for Cancer Active Targeting. *J Med Chem* **62,** 10475–10496 (2019).

4. Zhang, X., Liang, T. & Ma, Q. Layer-by-Layer assembled nano-drug delivery systems for cancer treatment. *Drug Deliv* **28,** 655–669 (2021).

5. Correa, S., Dreaden, E. C., Gu, L. & Hammond, P. T. Engineering nanolayered particles for modular drug delivery. *Journal of Controlled Release* **240,** 364–386 (2016).

6. Correa, S., Boehnke, N., Barberio, A. E., Deiss-Yehiely, E., Shi, A., Oberlton, B., Smith, S. G., Zervantonakis, I., Dreaden, E. C. & Hammond, P. T. Tuning Nanoparticle Interactions with Ovarian Cancer through Layer-by-Layer Modification of Surface Chemistry. *ACS Nano* **14,** 2224–2237 (2020).

7. Deng, Z. J., Morton, S. W., Ben-Akiva, E., Dreaden, E. C., Shopsowitz, K. E. & Hammond, P. T. Layer-by-Layer Nanoparticles for Systemic Codelivery of an Anticancer Drug and siRNA for Potential Triple-Negative Breast Cancer Treatment. *ACS Nano* **7,** 9571–9584 (2013).

8. Choi, K. Y., Correa, S., Min, J., Li, J., Roy, S., Laccetti, K. H., Dreaden, E., Kong, S., Heo, R., Roh, Y. H., Lawson, E. C., Palmer, P. A. & Hammond, P. T. Binary Targeting of siRNA to Hematologic Cancer Cells In Vivo Using Layer-by-Layer Nanoparticles. *Adv Funct Mater* **29,** (2019).

9. Pickering, A. J., Lamson, N. G., Marand, M. H., Hwang, W., Straehla, J. P. & Hammond, P. T. Layer-by-Layer Polymer Functionalization Improves Nanoparticle Penetration and Glioblastoma Targeting in the Brain. *ACS Nano* (2023). doi:10.1021/acsnano.3c09273

10. Correa, S., Boehnke, N., Deiss-Yehiely, E. & Hammond, P. T. Solution Conditions Tune and Optimize Loading of Therapeutic Polyelectrolytes into Layer-by-Layer Functionalized Liposomes. *ACS Nano* **13,** 5623–5634 (2019).

11. Yuan, W., Weng, G.-M., Lipton, J., Li, C. M., Van Tassel, P. R. & Taylor, A. D. Weak polyelectrolyte-based multilayers via layer-by-layer assembly: Approaches, properties, and applications. *Adv Colloid Interface Sci* **282,** 102200 (2020).

12. Ferreira, M. & Rubner, M. F. Molecular-Level Processing of Conjugated Polymers. 1. Layer-by-Layer Manipulation of Conjugated Polyions. *Macromolecules* **28,** 7107–7114 (1995).

13. Clark, S. L., Montague, M. F. & Hammond, P. T. Ionic Effects of Sodium Chloride on the Templated Deposition of Polyelectrolytes Using Layer-by-Layer Ionic Assembly. *Macromolecules* **30,** 7237–7244 (1997).

14. Stoll, S. in *Colloidal Biomolecules, Biomaterials and Biomedical Applications* (ed. Elaissari, A.) **116,** 211–252 (CRC Press, 2004).

15. Barberio, A. E., Smith, S. G., Correa, S., Nguyen, C., Nhan, B., Melo, M., Tokatlian, T., Suh, H., Irvine, D. J. & Hammond, P. T. Cancer Cell Coating Nanoparticles for Optimal Tumor-Specific Cytokine Delivery. *ACS Nano* **14,** 11238–11253 (2020).

16. Barberio, A. E., Smith, S. G., Pires, I. S., Iyer, S., Reinhardt, F., Melo, M. B., Suh, H., Weinberg, R. A., Irvine, D. J. & Hammond, P. T. <scp>Layer-by-layer</scp> interleukin-12 nanoparticles drive a safe and effective response in ovarian tumors. *Bioeng Transl Med* (2022). doi:10.1002/btm2.10453

17. Lieschke, G. J., Rao, P. K., Gately, M. K. & Mulligan, R. C. Bioactive murine and human interleukin-12 fusion proteins which retain antitumor activity in vivo. *Nat Biotechnol* **15,** 35–40 (1997).

18. Schneider, G. & Decher, G. Functional Core/Shell Nanoparticles via Layer-by-Layer Assembly. Investigation of the Experimental Parameters for Controlling Particle Aggregation and for Enhancing Dispersion Stability. *Langmuir* **24,** 1778–1789 (2008).

19. Petrila, L.-M., Bucatariu, F., Mihai, M. & Teodosiu, C. Polyelectrolyte Multilayers: An Overview on Fabrication, Properties, and Biomedical and Environmental Applications. *Materials* **14,** 4152 (2021).

20. Das, B. P. & Tsianou, M. From polyelectrolyte complexes to polyelectrolyte multilayers: Electrostatic assembly, nanostructure, dynamics, and functional properties. *Adv Colloid Interface Sci* **244,** 71–89 (2017).

CHAPTER 8
Chemically crosslinked layer-by-layer nanoparticles for enzyme-triggered release

8.1 Introduction

Engineered nanoparticles (NP) are promising drug delivery vehicles for disease treatment and diagnosis.[1] Nanomaterials could help overcome many issues with conventional systemic drug therapy such as biodistribution, bioavailability, pharmacokinetics, and cellular uptake. In doing so, NPs have the potential to make treatments more effective and less toxic which has been extensively demonstrated in preclinical models.[2] However, the number of clinically approved nanomedicines has been drastically below projections.[1,2] The lack of clinical success of nanomedicines has been partially attributed to the reliance on passive tissue accumulation of NP.[1,3] Thus, there has been extensive efforts to design nanoparticles with more rational design by inclusion of active targeting and stimuli-responsive materials.[1,3,4] Active targeting enables increased accumulation at target tissues whereas stimuli-responsive materials promote site-specific drug exposure.[3]

One promising approach to promote NP targeting to select tissues has been through altering its surface chemistry via the layer-by-layer (LbL) technique.[5,6] This surface modification has minimal effect on NP size, shape, and rigidity allowing for facile design of optimal drug carriers.[7–9] However, there has been limited strategies that demonstrate stimuli-responsive LbL-NPs. We have previously designed LbL-NPs with stimuli-responsive properties based on the swelling properties of LbL films at different pH, or via the release of polyethylene glycol (PEG) groups due to pH changes or enzymatic cleavage.[10–12] However, these approaches may still lead to nonspecific effects due to polymer detachment from LbL-NPs independent of the stimuli trigger. Further, while we have seen differences in the loading of nucleic acids on LbL-NP films upon changes in buffer ionic strength during layering, the effects of layering solution ionic strength on LbL-NP colloidal stability and film architecture still needs to be evaluated.[7]

In this work, we designed a LbL-NP structure in which we vary the film architecture on the NP surface by altering the layering buffer ionic strength and chemically crosslink the outer-layer polyelectrolytes using enzyme-cleavable peptides to generate a single network of polymers on the NP surface. To generate surface-crosslinked LbL-NPs (scLbL-NPs), we absorbed peptides

with N- and C-terminus azide groups onto LbL-NPs which could create interconnections between alkyne-grafted PLE polymers via copper(I)-catalyzed alkyne-azide cycloaddition (CuAAC). By varying the net charge on the peptide used for adsorption onto LbL-NPs, we find that low net charges induce the least disturbance on the LbL-NP stability. Surprisingly, even zwitterionic peptides were found to absorb onto LbL-NPs. Polymer deposition in the presence of salts yielded LbL-NPs which had increased stability in the presence of physiological saline levels compared to DI-assembled polymer LbL-NPs. Similarly, addition of chemical crosslinks increased colloidal stability of LbL-NPs at physiological saline levels, yielding LbL-NPs stable even at 500 mM NaCl.

When delivered to a target tissue, enzyme-mediated cleavage of the peptides enables site-specific polymer detachment. We generated LbL-NPs with a polyelectrolyte bilayer composed of poly-L-arginine (PLR) and poly-L-glutamate (PLE) which has previously been shown to target cancer cells and promote NP accumulation on the cell membrane.[6,13–15] We performed layering of polymers under both low ionic strength (deionized water, DI-LbL) and mild ionic strength (20 mM sodium chloride, 25 mM HEPES, salt-LbL) to alter the polymer film architecture on the NP surface prior to the addition of chemical crosslinks.

8.2 Methods

8.2.1 Materials

1,2-distearoyl-sn-glycero-3-phosphocholine (DSPC), 1,2-dioleoyl-sn-glycero-3-phosphoethanolamine-N-[4-(p-maleimidophenyl)butyramide] (sodium salt) (18:1 MPB-PE), 1-palmitoyl-2-oleoyl-sn-glycero-3-phospho-(1'-rac-glycerol) (sodium salt) (POPG), and cholesterol were purchased from Avanti Polar Lipids. PLR_{50}, PLE_{100}, and PLE_{100} with 10% alkyne modification were purchased from Alamanda Polymers.

8.2.2 Recombinant single-chain IL-12 production

Single-chain IL-12 sequence[20] was synthesized as a genomic block (Integrated DNA Technologies) and cloned into gWIZ expression vector (Genlantis). Plasmids were transiently transfected into Expi293 cells (ThermoFisher Scientific). After 5 days, cell culture supernatants were collected and protein was purified in an ÄKTA pure chromatography system using HiTrap HP Niquel sepharose affinity column, followed by size exclusion using Superdex 200 Increase 10/300 GL column (GE Healthcare Life Sciences). Endotoxin levels in purified protein was

measured using Endosafe Nexgen-PTS system (Charles River) and assured to be <5 EU/mg protein.

8.2.3 Liposome synthesis

A lipid solution was prepared by mixing (all mole %) 65% DSPC (25 mg/mL), 24% cholesterol (25 mg/mL), 6% POPG (25 mg/mL) and 5% 18:1 MPB-PE (5 mg/L) then formed into a thin film using a rotary evaporator (Buchi). Lipid films were allowed to further dry overnight in a desiccator, then were hydrated at 0.5-1 mg/mL using deionized water and sonicated for 3-5 minutes at 65 °C then extruded (Avestin Liposofast LF-50) once at 65 °C through a 100 nm membrane (Cytiva Nuclepore) then 3X through 50 nm membranes (Cytiva Nuclepore) . Extruded liposomes were added to an ice bath.

For covalent linkage of scIL-12 to Mal-liposomes, the solution pH of MPB-PE liposomes was adjusted to pH 5 with hydrochloric acid prior to lipid film hydration, and following membrane extrusion, liposomes at 0.33 mg/mL were adjusted to pH 7.0 with 10 mM HEPES prior followed by addition of scIL-12 containing a terminal cysteine residue at a molar ratio of 25:1 of MPB-PE lipid to protein for at least 12 hours at 4 °C in a rotating mixed. Any remaining maleimides were quenched with a 100-fold molar excess of L-cysteine (Sigma) for 1.5 hrs on ice. Particles without IL-12 were generated with the same composition and processing, but no IL-12 was added during overnight incubation in 10 mM HEPES (pH 7.0). Lipid concentration was determined with the Stewart Assay[21] and IL-12 content was determined via ELISA (Peprotech). Unaltered or LbL-NPs were dissociated in 1% triton-X100 for IL-12 ELISA quantification.

8.2.4 Layer-by-Layer (LbL) film deposition onto NPs

Assembly of DI-LbL layers was performed by adding unlayered particles to a diH_2O solution with 0.3-0.4 weight equivalents (wt.eq.) of PLR relative to lipid in a glass vial under sonication and incubating on ice for at least 30 min. Excess PLR polymer was purified by TFF through a 100 kDa mPES membrane (Repligen) pre-treated with a 10 mg/mL solution of free PLR. For the terminal PLE layer, purified particles coated with PLR were added to a diH_2O solution with PLE in a glass vial under sonication at 1 wt.eq. of polymer to lipid. LbL particles were then purified by TFF on a separate 100 kDa mPES membrane (Repligen) to remove any excess PLE. For assembly of salt-LbL layers, polymer solutions were made in 50 mM HEPES (pH 7.4) with 40 mM NaCl at wt. eq.

of 0.5 for PLR and 2 for PLE. Polymers were mixed with 1:1 volume of NPs then purified via TFF using diH_2O as the replacement buffer.

8.2.5 Characterization of particle preparations

Dynamic light scattering (DLS) and zeta potential measurements were made on a Zetasizer Nano ZSP (Malvern). Nanoparticle micrographs were acquired using Transmission Electron Microscopy (TEM) on a JEOL 2100F microscope (200 kV) with a magnification range of 10,000-60,000X. All images were recorded on a Gatan 2kx2k UltraScan CCD camera. Negative-stain sample preparation was performed by adding 10 μL of NPs on a 200 meshes copper grid coated with a continuous carbon film and allowing for sample adsorption for 60 seconds. Excess solution was then removed by touching the grid with a kimwipe. The grid was then quickly washed by adding 10 μL of negative staining solution, phosphotungstic acid (PTA), 1% aqueous solution then removing excess by touching the grid with a kimwipe. Then, the grid was mounted on a JEOL single tilt holder equipped in the TEM column for image capture.

8.2.6 Peptide synthesis

The peptides +1, +2, and +3 peptides of sequence K(N_3)GGPVGLIGGK(N_3), K(N_3)GGPVGLIGRK(N_3), and K(N_3)RGPVGLIGRK(N_3), respectively, were made with a C-terminus amid in the Koch Institute Biopolymer and Proteomics core using the Intavis Model MultiPep multiple peptide synthesizer and purified via reverse phase high-pressure liquid chromatography. The zwitterionic peptide had the sequence K(N_3)GGPVGLIGGK(N_3)G, with a C-terminus carboxylic acid. Large-scale peptide production was also done via solid-state peptide synthesis for the +1 peptide.

8.2.7 Peptide adsorption

Nanoparticles were mixed with peptide solution under sonication in either deionized water or in the 50 mM HEPES (pH 7.3) and 40 mM NaCl. Samples were left to incubate for 10 min prior to DLS characterization.

8.2.8 LbL crosslinking

To perform the copper-catalyzed click chemistry reaction, particles were mixed with 1 mM copper sulfate, 2 mM tris(benzyltriazolylmethyl)amine (THPTA), and 20 mM sodium ascorbate. Samples were left at 25 °C for 5 hrs then left overnight at 4 °C. To quench the reaction, 0.5mM of ethylenediaminetetraacetic acid (EDTA) was added. For IL-12 scLbL-NPs, particles were then purified via TFF on 100 kDa mPES membrane (Repligen) using DI as replacement buffer.

8.2.9 LbL-NP salt stress test

LbL-NPs were diluted in 15 mM HEPES (pH 7.3) to 0.1 mg/mL in a 1.5 mL disposable cuvette (Fisherbrand). A 2 M NaCl stock solution was then used to increase the ionic strength of the solution. Samples were allowed to incubate for 15 min prior to measuring particle size via DLS. After DLS readings, the concentration of NaCL was increased and the process was repeated until particles had coalesced (> 1 μm in diameter).

8.2.10 Cell Culture

HEK-Blue IL-12 (InvivoGen) cells were cultured and used for IL-12 bioactivity assessment according to the manufacturer's instructions. Cell media was also supplemented with 10% FBS and penicillin/streptomycin with cells incubated in a 5% carbon dioxide humidified atmosphere at 37 °C. All cell lines were murine pathogen tested and confirmed mycoplasma negative by Lonza MycoAlert™ Mycoplasma Detection Kit.

8.2.11 MMP-9 cleavage

To cleave peptides crosslinked on purified scLbL-NPs, samples were mixed with 12.5 nM of preactivated human MMP-9 (Sigma) and incubated at 37 °C for 5 hrs. The bioactivity of IL-12 on the scLbL-NPs was measured on samples after incubation with or without MMP-9 to determine the effect of MMP-9.

8.2.12 Statistical Analysis

GraphPad PRISM 10 was used to perform statistical analyses. Comparisons between two groups was performed via unpaired t-tests. For multiple groups or multiple variable analysis, one-way, or

two-way ANOVAs were used with Tukey's posthoc correction for time-based analysis or Sidak posthoc for other ANOVA analysis.

8.3 Results and Discussion

8.3.1 Polyelectrolyte adsorption in water or in presence of mild ionic strength yield layer-by-layer nanoparticles with varied film architecture.

To chemically crosslink the film on LbL-NPs, we used a PLE polymer in which 10% of the glutamate residues were replaced by an alkyne group. A bilayer film composed of PLR and the alkyne-grafted PLE was assembled onto negatively charged unlayered (UL) liposomes. The film conformation was altered by layering in deionized water (DI) or mild ionic strength and buffering capacity (salt, **Figure 8.1a**). We have previously shown that under salt conditions, the LbL film is thicker and more stable. As expected, assembly under both conditions yielded LbL-NPs with similar size and low polydispersity (**Figure 8.1b-c**). The presence of a thicker LbL film was apparent when particles were imaged via negative-stain transmission electron microscopy (NS-TEM, **Figure 8.1d**).

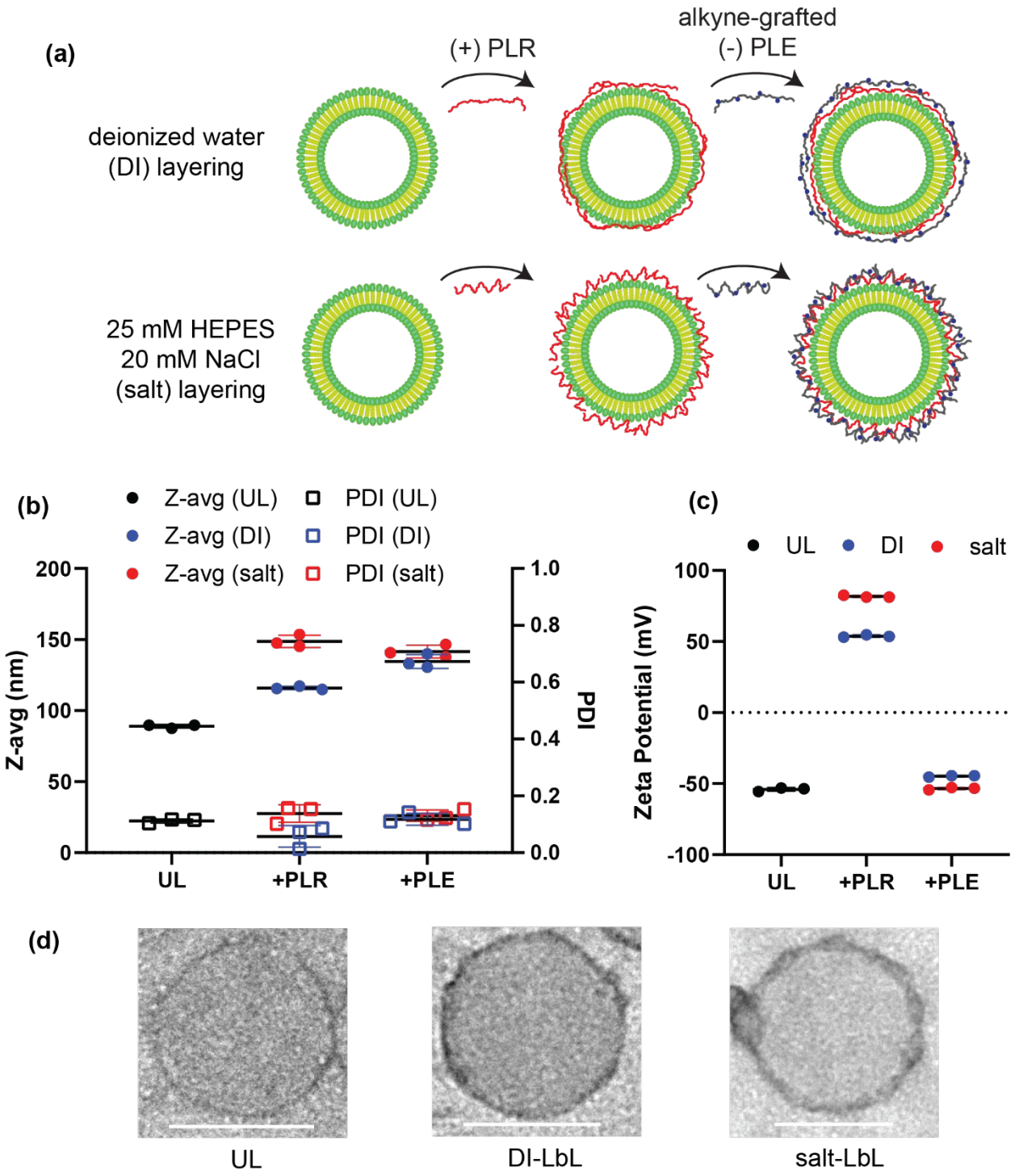

Figure 8.1. Solution conditions during LbL assembly control film thickness. (a) Diagram of LbL assembly either in deionized water (DI) or in the presence of a mild ionic strength solution (salt). (b) Particle hydrodynamic size (Z-avg) and polydispersity index (PDI) during LbL assembly. (c) Zeta potential of particles during LbL assembly. (d) Negative stain transmission electron microscopy of unlayered (UL), DI-LbL, or salt-LbL NPs.

8.3.2 Peptide charge regulates maximum loading capacity onto LbL-NPs.

To achieve the chemical crosslinks between alkyne-grafted PLE polymers, we employed a bi-functionalized peptide containing azide groups at the N- and C-terminus. In between the azide groups, a matrix metalloprotease IX (MMP-9) cleavable peptide sequence (PVGLIG)[16] was added owing to the high expression of this enzyme in many cancerous tissues.[17] We generated a library of peptides with varying charges by altering the number of added arginine residues (**Figure 8.2a**). When adsorbed onto the surface of the DI-LbL NPs in DI (**Figure 8.2b**), high peptide loadings increased the zeta potential consistent with the expected added positive charges to the LbL film (**Figure 8.2c**). At the high peptide loadings, it was possible to destabilize the NPs as indicated by an increase in the particle size. Moreover, using peptides with increased charge densities led to changes in the zeta potential and particle destabilization at lower peptide loadings. Surprisingly, even the zwitterionic peptide increased the zeta potential suggesting that this peptide could also adsorb onto the LbL-NPs. The zwitterionic peptide was found to have a greater destabilizing effect than even +1 peptide since at the 2^0 μmol peptide to mg lipid ratio it caused particle destabilization whereas the +1 peptide did not. When adsorbed under salt conditions onto salt-LbL NPs (**Figure 8.2d**), most peptides did not cause significant effects on either the zeta potential nor the particle size suggesting an increased peptide adsorption capacity of these thicker films (**Figure 8.2e**). The lack of change in zeta potential is consistent with the measurement reflecting the adsorbed polyelectrolyte film Donnan potential and not the surface potential when performed on a thicker film at higher ionic strength.[18,19] Indeed, high loadings of multivalent peptides increased particle size confirming the interaction of peptides with the salt-LbL-NPs.

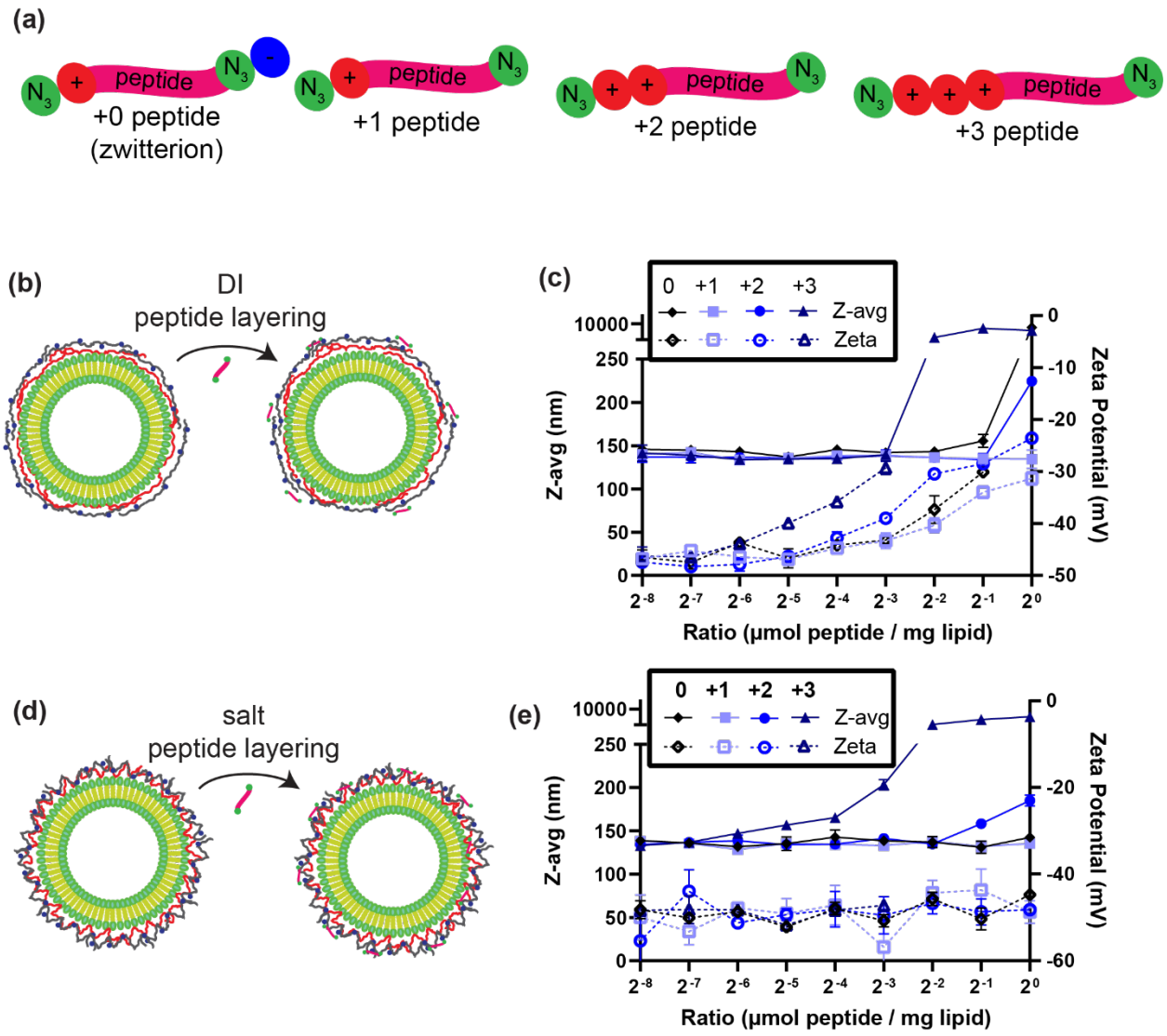

Figure 8.2. Stable peptide loading onto DI-LbL and salt-LbL NPs depends on film conformation and peptide charge. (a) Schematic of peptides used in adsorption studies. (b) Diagram of peptide adsorption under DI conditions onto DI-LbL NPs. (c) Hydrodynamic size and zeta potential of DI-LbL NPs after peptide adsorption. (d) Diagram of peptide adsorption under salt conditions onto salt-LbL NPs. (e) Hydrodynamic size and zeta potential of salt-LbL NPs after peptide adsorption.

8.3.3 Peptide crosslinking confers increased LbL film stability

Having found that peptides could adsorb on the LbL-NPs, we next sought to evaluate if they could be used to crosslink the PLE polymers on the NP surface. Given that higher molecular weight PLE polymers stabilize the LbL film and the NP stability at higher ionic strength, we theorized that we could use a salt stability stress test (**Figure 8.3a**) to evaluate for successful cross-linking. As found previously, salt-LbL NPs showed improved stability compared to DI-LbL NPs under this assay (**Figure 8.3b**). We first characterized the stability of DI-LbL NPs with varying amounts of peptides absorbed on the surface. Consistent with multivalent peptides facilitating bridging interactions, their adsorption reduced the particle stability in the salt-stress test (**Figure 8.3c**).

We next performed the crosslinking reaction by exposing the LbL-NPs with varying amounts of peptides adsorbed on the surface to the reagents required to initiate the copper-catalyzed click chemistry reaction between alkyne and azides (**Figure 8.3d**). Particles were incubated overnight to generate surface-crosslinked LbL-NPs (sc-LbL-NPs) before quenching the reaction by adding 0.5 mM of EDTA. Except for high (>2^{-3} μmol peptide to mg lipid) onto the salt-LbL NPs, all conditions tested yielded monodisperse particles that retained their size (<200 nm, **Figure 8.3e**). Importantly, for both salt-LbL or DI-LbL NPs, peptide crosslinking could significantly improve the stability of the LbL-NPs. At peptide loadings above 2^{-4} it was possible to observe particles that did not crash (>1000 nm in size) during the full-time course of the experiment which we ended at supraphysiological ionic strength (400 mM NaCl). These particles instead showed indications of film swelling given their increase in size. However, only a few conditions yielded scLbL-NPs that were stable to these high ionic strength conditions after allowing them to equilibrate overnight (**Figure 8.3e blue curves**). It was also possible to note that sc-salt-LbL-NPs had a more efficient use of the peptides as lower peptide-to-lipid ratios were required to yield a discernable difference in particle stability. For example, +0 peptide required 2^{-3} ratio to yield a sc-DI-LbL-NP that behaved differently from uncrosslinked particles, whereas only 2^{-6} peptide crosslinked on salt-LbL NPs could already show increased stability. This observation could be due to the higher interpenetration of polymers when assembled in higher ionic strength facilitating polymer-to-polymer crosslinks.

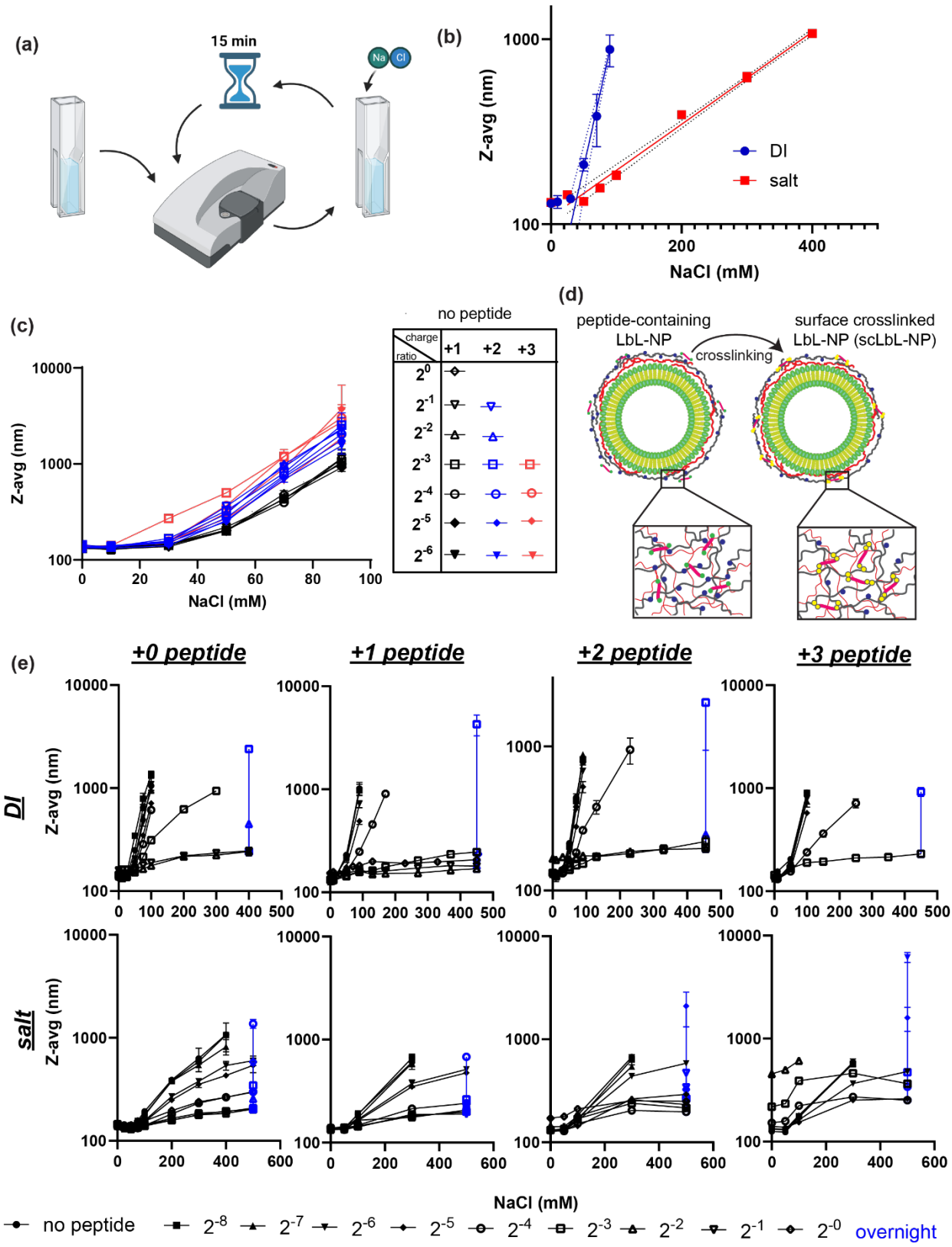
(a)
15 min
Na
Cl
(b)
Z-avg (nm)
NaCl (mM)
DI
salt
(c)
Z-avg (nm)
NaCl (mM)
no peptide
charge ratio
+1
+2
+3
(d)
peptide-containing LbL-NP
crosslinking
surface crosslinked LbL-NP (scLbL-NP)
(e)
+0 peptide
+1 peptide
+2 peptide
+3 peptide
DI
salt
Z-avg (nm)
NaCl (mM)
no peptide
overnight

Figure 8.3. The generation of chemical crosslinks on LbL-NPs yields greater film stability. (a) Diagram of salt stress test. (b) Z-avg size of DI-LbL and salt-LbL at various concentrations of NaCl during the salt stress test. (c) Salt stress test of DI-LbL with various peptide loadings. (d) Diagram of crosslinking polymers on the surface of LbL-NPs. (e) Salt stress curves from various scLbL-NPs assembled in either DI or salt conditions with varying amounts of peptides adsorbed on the surface.

8.3.4 Crosslinking of LbL film assembled on IL-12 loaded NPs regulates surface exposure of IL-12

PLR/PLE LbL-NPs are effective at delivering cytokines to the tumor microenvironment. We thus decided to employ this crosslinking strategy on liposomes with IL-12 conjugated to their surfaces (**Figure 8.4a**). To first validate that we could generate IL-12-scLbL-NPs, we adsorbed and crosslinked +1 peptide at ratios of 2^{-4}, 2^{-3}, and 2^{-1} to IL-12-LbL-NPs with films assembled in either DI or salt. The +1 peptide was selected given its ability to effectively crosslink and stabilize scLbL-NPs without significantly affecting LbL-NP properties. Similar to particles devoid of IL-12, crosslinking showed a peptide-dependent effect on LbL film stability for both DI (**Figure 8.4b**) and salt (**Figure 8.4c**). However, it was apparent that the the crosslinking was not as effective at preventing particle coalescence given the large increased in size, potentially due to the surface-bound IL-12 interfering with complete film coverage.

We next evaluated the surface availability of IL-12 by dosing the NPs to a reporter cell line engineered to contain IL-12 receptors and response to IL-12 signaling. Crosslinking could significantly reduce the amount of available IL-12 from the surface of IL-12-scLbL-NPs assembled in either DI (**Figure 8.4d**) or salt (**Figure 8.4e**). Consistent with our prior experiments, salt-LbL-NPs could inhibit IL-12 bioavailability from the surface of NPs due to their thicker film (**Figure 8.4f**). Moreover, we found that IL-12-scLbL-NPs appeared to show a maximum reduction in IL-12 availability at 2^{-4} to 2^{-2} ratio suggesting that overloading of peptides may saturate alkyne residues and prevent efficient crosslinking (**Figure 8.4g**).

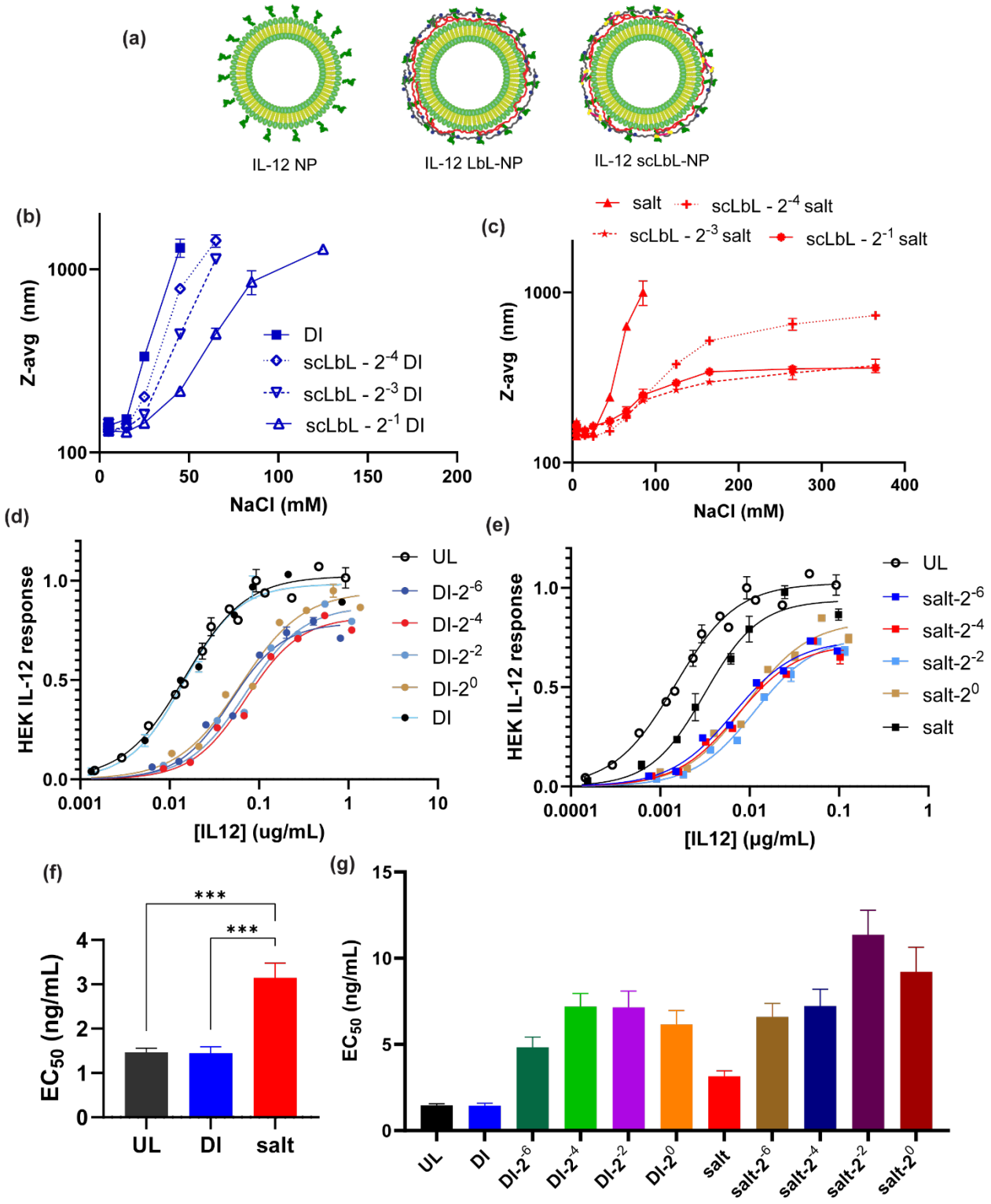

Figure 8.4. Increased film stability of scLbL-NP inhibit IL-12 recognition from the NP surface. (a) Schematic for IL-12-NPs, LbL-NPs, and IL-12-scLbL-NPs. Salt stability stress test in DI assembled (b) and salt-assembled (c) IL-12 scLbL-NPs. HEK-Blue IL-12 response curves from

DI-assembled (d) and salt-assembled (e) IL-12 scLbL-NPs. (f) Calculated IL-12 EC_{50} form UL NPs compared to DI and salt-assembled LbL-NPs. (g) Calculated IL-12 EC_{50} from all scLbL-NPs tested.

8.3.5 Enzyme exposure recovers IL-12 bioactivity from scLbL-NPs

We next sough to evaluate if exposure to the MMP-9 enzyme could recover some of the lost IL-12 bioavailability by shedding of the LbL-film (**Figure 8.5a**). We exposed the IL-12-scLbL-NPs to MMP-9 for five hours and then evaluated the resulting bioactivity on the reporter cell line. Both IL-12 scLbL-NPs assembled in DI or in salt showed recovery of IL-12 bioavailability (**Figure 8.5b-e**).

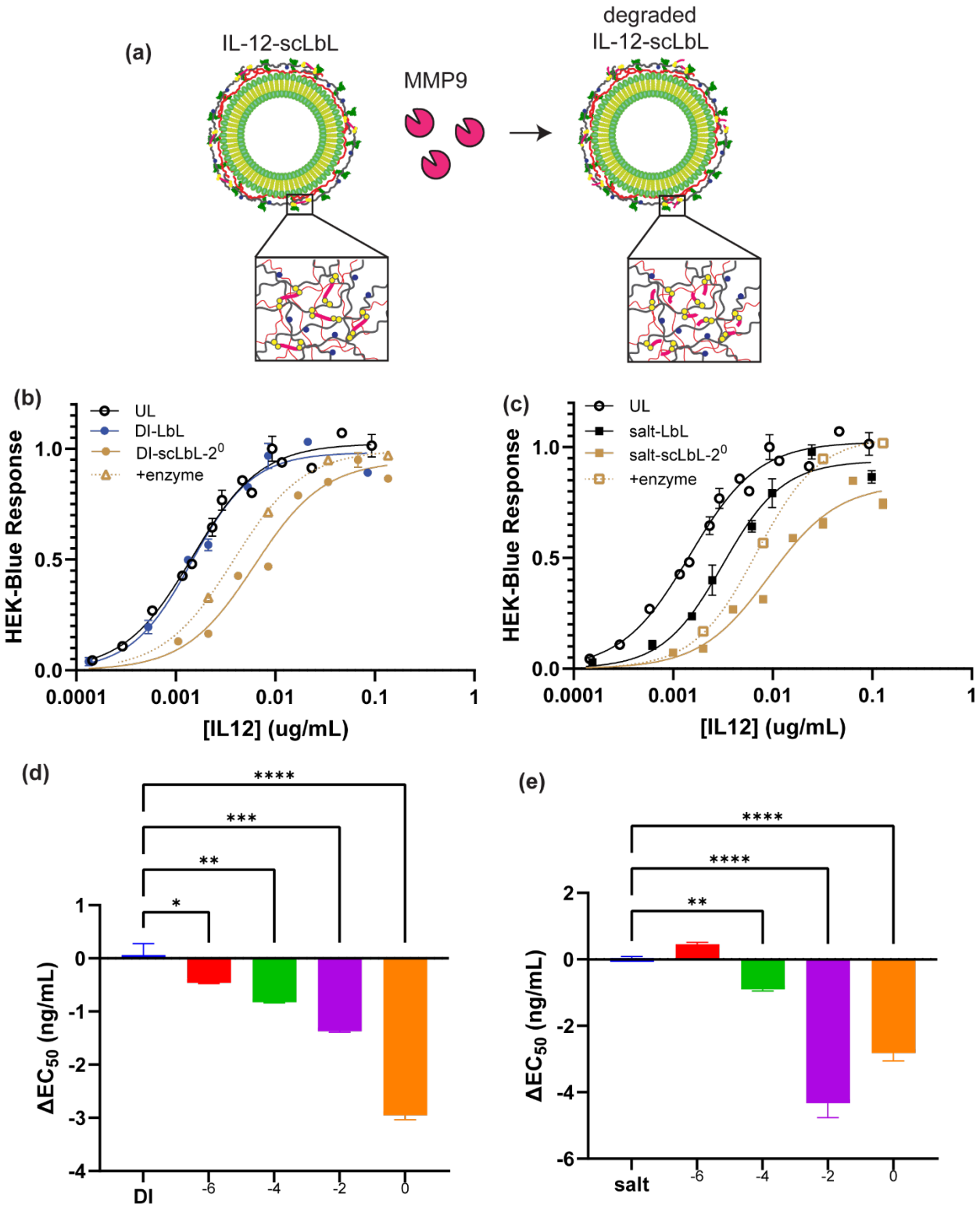

Figure 8.5. Exposure of IL-12 scLbL-NPs to MMP-9 recovers IL-12 bioactivity. (a) Diagram of MMP-9 effect on IL-12 scLbL-NPs. (b) HEK-Blue IL-12 curves of DI-scLbL-NP incubated

with or without MMP-9 enzyme. (e) HEK-Blue IL-12 curves of salt-scLbL-NP incubated with or without MMP-9 enzyme. (d) The change in EC_{50} of DI-assembled IL-12 scLbL-NPs incubated with or without MMP-9. (f) The change in EC_{50} of salt-assembled IL-12 scLbL-NPs incubated with or without MMP-9.

8.4 Conclusion

Here we show that crosslinking the polyelectrolytes on the surface of LbL-NPs significantly increases film stability allowing particles to remain in supraphysiological levels of ionic strength without coalescence. Moreover, using NP with IL-12 conjugated to its surface, we find that crosslinked LbL-NPs can prevent IL-12 recognition by IL12 receptors on reporter cell lines. This inhibition of IL-12 bioavailability was reversible by exposing scLbL-NPs to MMP-9 which could effectively cleave the peptides mediating the crosslinks.

Future work is needed to better disassemble scLbL-NPs upon exposure to a stimuli in the tumor microenvironment as the current scLbL-NPs were not able to fully recover IL-12 bioactivity.

8.5 References

1. Mitchell, M. J. *et al.* Engineering precision nanoparticles for drug delivery. *Nat Rev Drug Discov* **20**, 101–124 (2021).

2. Mitragotri, S. *et al.* Drug Delivery Research for the Future: Expanding the Nano Horizons and Beyond. *Journal of Controlled Release* **246**, 183–184 (2017).

3. Uthaman, S., Huh, K. M. & Park, I.-K. Tumor microenvironment-responsive nanoparticles for cancer theragnostic applications. *Biomater Res* **22**, 22 (2018).

4. Pham, S. H., Choi, Y. & Choi, J. Stimuli-Responsive Nanomaterials for Application in Antitumor Therapy and Drug Delivery. *Pharmaceutics* **12**, 630 (2020).

5. Alkekhia, D., Hammond, P. T. & Shukla, A. Layer-by-Layer Biomaterials for Drug Delivery. *Annu Rev Biomed Eng* **22**, 1–24 (2020).

6. Correa, S. *et al.* Tuning Nanoparticle Interactions with Ovarian Cancer through Layer-by-Layer Modification of Surface Chemistry. *ACS Nano* **14**, 2224–2237 (2020).

7. Correa, S., Boehnke, N., Deiss-Yehiely, E. & Hammond, P. T. Solution Conditions Tune and Optimize Loading of Therapeutic Polyelectrolytes into Layer-by-Layer Functionalized Liposomes. *ACS Nano* **13**, 5623–5634 (2019).

8. Boehnke, N. *et al.* Massively parallel pooled screening reveals genomic determinants of nanoparticle delivery. *Science (1979)* **377**, (2022).

9. Kong, S. M., Costa, D. F., Jagielska, A., Van Vliet, K. J. & Hammond, P. T. Stiffness of targeted layer-by-layer nanoparticles impacts elimination half-life, tumor accumulation, and tumor penetration. *Proceedings of the National Academy of Sciences* **118**, (2021).

10. Dreaden, E. C. *et al.* Bimodal Tumor-Targeting from Microenvironment Responsive Hyaluronan Layer-by-Layer (LbL) Nanoparticles. *ACS Nano* **8**, 8374–8382 (2014).

11. Poon, Z., Chang, D., Zhao, X. & Hammond, P. T. Layer-by-Layer Nanoparticles with a pH-Sheddable Layer for in Vivo Targeting of Tumor Hypoxia. *ACS Nano* **5**, 4284–4292 (2011).

12. Boehnke, N. *et al.* Theranostic Layer-by-Layer Nanoparticles for Simultaneous Tumor Detection and Gene Silencing. *Angewandte Chemie* **132**, 2798–2805 (2020).

13. Tošić, I. *et al.* Lipidome-based Targeting of STAT3-driven Breast Cancer Cells Using Poly- <scp>l</scp> -glutamic Acid–coated Layer-by-Layer Nanoparticles. *Mol Cancer Ther* **20**, 726–738 (2021).

14. Barberio, A. E. *et al.* Cancer Cell Coating Nanoparticles for Optimal Tumor-Specific Cytokine Delivery. *ACS Nano* **14**, 11238–11253 (2020).

15. Barberio, A. E. *et al.* <scp>Layer-by-layer</scp> interleukin-12 nanoparticles drive a safe and effective response in ovarian tumors. *Bioeng Transl Med* **8**, (2023).

16. Chau, Y., Tan, F. E. & Langer, R. Synthesis and Characterization of Dextran−Peptide−Methotrexate Conjugates for Tumor Targeting via Mediation by Matrix Metalloproteinase II and Matrix Metalloproteinase IX. *Bioconjug Chem* **15**, 931–941 (2004).

17. Li, M., Zhao, G., Su, W.-K. & Shuai, Q. Enzyme-Responsive Nanoparticles for Anti-tumor Drug Delivery. *Front Chem* **8**, (2020).

18. Ohshima, H. *Theory of Colloid and Interfacial Electric Phenomena*. vol. 12 (Elsevier, 2006).

19. Lowry, G. V. *et al.* Guidance to improve the scientific value of zeta-potential measurements in nanoEHS. *Environ Sci Nano* **3**, 953–965 (2016).

20. Lieschke, G. J., Rao, P. K., Gately, M. K. & Mulligan, R. C. Bioactive murine and human interleukin-12 fusion proteins which retain antitumor activity in vivo. *Nat Biotechnol* **15**, 35–40 (1997).

21. Stewart, J. C. M. Colorimetric determination of phospholipids with ammonium ferrothiocyanate. *Anal Biochem* **104**, 10–14 (1980).

CHAPTER 9

Surface avidity of anionic poly(amino acids) enables targeted nanoparticle delivery to cancer-associated amino acid transporters

9.1 Introduction

Nanoparticles (NPs) are promising vehicles for drug delivery in part due to their ability to modulate drug bioavailability and pharmacokinetics.[1,2] A key benefit of nanotherapeutics is its ability to accumulate at sites of disease through either passive or active targeting mechanisms.[1,3,4] Passive NP accumulation occurs due to biological factors such as the reticuloendothelial system (RES) phagocytic capacity or tissue microvasculature alterations. NP properties such as particle shape, charge, and surface properties modulate passive uptake by altering RES uptake or preventing the adsorption of serum proteins. On the other hand, active NP uptake is attributed to the presentation of ligands that promote receptor-specific uptake of the nanocarrier, often in the form of surface-conjugated antibodies.

We have identified that surface modification of nanoparticles via the layer-by-layer (LbL) technique with carboxylated polyamino acid (i.e. polyglutamate and polyaspartate) enabled NP binding to cancer cells with high affinity and specificity.[5,6] Unlike other LbL-NPs with high cancer cell affinity, such as hyaluronic acid (HA)-coated particles that target CD44 receptors and promote rapid receptor-mediated endocytosis, there are no known targets for these anionic polyamino acids. One potential mechanism of particle binding is through non-specific hydrogen bonding interactions of the carboxylic acids and glycoproteins on the surface of cancer cells. However, while only differing by a single carbon on the sidechain, poly-L-glutamate (PLE) coating promoted prolonged surface retention of NPs whereas a poly-L-aspartate (PLD) coating yielded a gradual internalization of NPs. Such specificity suggests that in addition to the high hydrogen-bonding potential of these coatings, the interactions of PLE and PLD with cancer cells may have distinct interaction partners that alter uptake pathways.

Here we discovered the binding targets of PLE and PLD LbL-NPs. Through a combination of experimental approaches, data analytics, and artificial intelligence protein interaction modeling, we demonstrate that LbL film assembly allows for high avidity presentation of amino acid side chains that interact with amino acid transporters overexpressed in cancer tissues. Further, we show how PLE cell membrane retention is enhanced by surface receptor cluster formation. Lastly, we

find that we can use gene expression of amino acid transporters to predict efficient LbL-NP uptake and how PLD NPs interact with differing amino acid transporters than PLE.

9.2 Methods

9.2.1 Materials

1,2-distearoyl-sn-glycero-3-phosphocholine (DSPC), 1,2-dioleoyl-sn-glycero-3-phosphoethanolamine-N-[4-(p-maleimidophenyl)butyramide] (sodium salt) (18:1 MPB-PE), 1-palmitoyl-2-oleoyl-sn-glycero-3-phospho-(1'-rac-glycerol) (sodium salt) (POPG), 1,2-dioleoyl-sn-glycero-3-phosphoethanolamine-N-dibenzocyclooctyl (DOPE-DBCO), and cholesterol were purchased from Avanti Polar Lipids. Poly-L-arginine (PLR) with a molecular weight (MW) of 9.6 kDa and poly-L-glutamic acid (PLE) with a MWs of 15 kDa (PLE_{100}) or 120 kDa (PLE_{800}) were purchased from Alamanda Polymers. BDP TMR azide (Lumiprobe) and BDP 630/650 azide (Lumiprobe) were conjugated to DOPE-DBCO in chloroform to generate fluorescently labeled lipids. Successful conjugation was validated via thin-layer chromatography which indicated <1% free dye. Fluorescently-labeled carboxylated polystyrene particles were purchased from ThermoFisher. V9302 and TFB-TBOA, were purchased from MedChemExpress and L-γ-Glutamyl-p-nitroanilide (GPNA) was purchased from Sigma. Anti-CD44 antibody (IM7, functional grade), and anti-GLUT-1 antibody were purchased from Invitrogen. For anti-SLC1A5, two clones directed at extracellular epitopes were purchased - AB_2806719 from Invitrogen and AB_2878679 from Proteintech. An intracellular epitope directed anti-SLC1A5 (AB_2756720) was purchased from Alomone Labs. Deionized water was of the ultrapure grade obtained through a Milli-Q water system (EMD Millipore).

9.2.2 Recombinant single-chain IL-12 production

Single-chain IL-12 sequence[7] was synthesized as a genomic block (Integrated DNA Technologies) and cloned into gWIZ expression vector (Genlantis). Plasmids were transiently transfected into Expi293 cells (ThermoFisher Scientific). After 5 days, cell culture supernatants were collected and protein was purified in an ÄKTA pure chromatography system using HiTrap HP Niquel sepharose affinity column, followed by size exclusion using Superdex 200 Increase 10/300 GL column (GE Healthcare Life Sciences). Endotoxin levels in purified protein was measured using Endosafe Nexgen-PTS system (Charles River) and assured to be <5 EU/mg protein.

9.2.3 Liposome synthesis

A lipid solution was prepared by mixing (all mole %) 70% DSPC (25 mg/mL), 24% cholesterol (25 mg/mL), and 6% POPG (25 mg/mL) and then formed into a thin film using a rotary evaporator (Buchi). Lipid films were allowed to further dry overnight in a desiccator, then were hydrated at 0.5-1 mg/mL using deionized water and sonicated for 3-5 minutes at 65 °C then extruded (Avestin Liposofast LF-50) once at 65 °C through a 100 nm membrane (Cytiva Nuclepore) then 3X through 50 nm membranes (Cytiva Nuclepore). Extruded liposomes were added to an ice bath. Lipid stocks were stored at -20 °C in amber vials in chloroform. For fluorescence labeling of liposomes, 0.2 mol% of DSPC content was replaced by either DOPE-TMR or DOPE-630/650. Lipid concentration content was determined based on the fluorescence of the pre-extruded lipid sample of known concentration.

9.2.4 IL-12 Liposome synthesis

For covalent linkage of scIL-12 to liposomes, 5 mol% of DSPC was replaced with 5% of 18:1 MPB-PE (5 mg/L) and dried in the same method as standard liposomes. For lipid film hydration, the solution pH of MPB-PE liposomes was adjusted to pH 5 with hydrochloric acid to prevent maleimide hydrolysis. Following membrane extrusion, liposomes at 0.33 mg/mL were adjusted to pH 7.0 with 10 mM HEPES followed by the addition of scIL-12 containing a terminal cysteine residue at a molar ratio of 25:1 of MPB-PE lipid to protein for at least 12 hours at 4 °C in a rotating mixer. Any remaining maleimides were quenched with a 100-fold molar excess of L-cysteine (Sigma) for 1.5 hrs on ice. Unlayered IL-12 liposomes were then purified via tangential flow filtration using a 100 kDa (mPES, Repligen) hollow fiber membrane for 7 diafiltration volumes.

For fluorescence labeling of liposomes, 0.2 mol% of DSPC content was replaced by either DOPE-TMR or DOPE-630/650. IL-12 concentrations were measured via enzyme-linked immunoassay (ELISA) (Peprotech) and lipid content was determined based on the fluorescence of the pre-extruded lipid sample of known concentration.

9.2.4 Layer-by-layer (LbL) film deposition onto nanoparticles

Assembly of polyelectrolyte layers was performed by adding unlayered particles to a diH_2O solution with 0.3-0.4 weight equivalents (wt.eq.) of PLR relative to lipid in a glass vial under

sonication and incubating on ice for at least 30 min. Excess PLR polymer was purified by TFF through a 100 kDa mPES membrane (Repligen) pre-treated with a 10 mg/mL solution of free PLR. For the terminal PLE layer, purified particles coated with PLR were added to a diH_2O solution with PLE in a glass vial under sonication at 1 wt.eq. of polymer to lipid. LbL particles were then purified by TFF on a separate 100 kDa mPES membrane (Repligen) to remove any excess PLE.

For high throughput LbL assembly onto carboxylated polystyrene particles or assembly of varied outer-layer chemistries of IL-12 liposomes, LbL assembly was performed through a microfluidics-based method. Briefly, polymer wt.eq. were titrated to core particles based on the amount of polymer required for the onset of the plateau point of zeta potential. Then the particle solution and titrated amount of polymer were mixed using a microfluidics cartridge (Precision Nanosystems).

9.2.5 Characterization of particle preparations

Dynamic light scattering (DLS) and zeta potential measurements were made on a Zetasizer Nano ZSP (Malvern).

9.2.6 Grafted PLE-liposome assembly

To generate liposomes with grafted PLE polymers, PLE_{100} with a C-terminus azide (PLE-N3) was purchased from Alamanda Polymers. A lipid solution in chloroform with 69.8 mol% DSPC, 30 mol% cholesterol, 0.2 mol% DOPE-630/650 was allowed to dry overnight in a desiccator then suspended at 10 mg/mL in 10% MEGA-10. A separate solution with 10 mg/mL of DOPE-DBCO in 10% MEGA-10 was made and mixed with 2 molar excess of PLE-N3 and allowed to react overnight at 25 °C to generate DOPE-PLE. The two samples were mixed to generate a lipid solution containing 0.5 mol% of the DOPE-PLE and then liposome assembly was induced by diluting the sample with phosphate-buffered saline (10 mM, pH 7.4) to 0.01% MEGA-10. Samples were concentrated and purified from detergent via TFF in a 100 kDa mPES membrane.

9.2.7 Fluorescent labeling of PLE polymers

PLE_{100} or PLE_{800} at 10 mg/mL was labeled by reacting with 5 molar equivalents of sulfo-cyanine3 NHS ester (Lumibrobe) in PBS adjusted to pH ~8.5 with 0.1 M sodium bicarbonate. Excess dye was removed via extensive 0.9 wt% NaCl dialysis followed by extensive diH2O dialysis using a

3 kDa regenerated cellulose membrane (Repligen) and the purified PLE-cy3 was lyophilized until use. For assembly of LbL films with fluorescently tagged PLE, the PLE layering solution was doped with 33% of PLE-cy3.

9.2.8 Cell Culture

OV2944-HM-1 cells were acquired through Riken BRC and were cultured in α-MEM supplemented with 10% FBS and 1% penicillin/streptomycin. Glioma stem cells and associated RNA sequencing data were provided by the Pollard and Carragher Laboratories at the University of Edinburgh.[8] Glioma cells were cultured in DMEM/HAMS-F12 supplemented with N2, B27, 10% glucose, 1% pen/strep, MEM nonessential amino acids, EGF (10 ng/mL) and FGF (10 ng/mL). Culture vessels were coated with Cultrex Laminin (R&D Systems) for 3 h at 10 μg/mL before use. Laminin was added to cell culture media at a concentration of 2 μg/mL. Media was replaced twice weekly and passaged every 5–7 days at a ratio between 1:4 and 1:6 using Accutase (Sigma). Cells were incubated in a 5% carbon dioxide humidified atmosphere at 37 °C. All cell lines were murine pathogen tested and confirmed mycoplasma negative by Lonza MycoAlert™ Mycoplasma Detection Kit.

9.2.9 In vitro cellular association

HM-1 cells were plated on a tissue-culture 96-well plate at a density of 50K cells per well. The next day, wells were dosed with NPs and left for the target incubation time. For assessment of NP-associated fluorescence in a fluorescence plate reader, the supernatant was removed from the well and diluted 10X with DMSO. Cells were then washed three times with PBS and disrupted with DMSO. The fluorescence of the NPs associated with cells was then normalized to supernatant fluorescence. The relative fluorescence of each formulation was then compared to an unlayered liposome control containing the same fluorophore.

For analysis via flow cytometry, NPs were dosed at the indicated concentrations and allowed to incubate with cells at 37°C. Cells were washed with PBS then detached from the plates using 0.25% trypsin and stained with DAPI (15 min incubation) for viability assessment and fixed with 2% paraformaldehyde (30 min incubation) until analysis by flow cytometry using an LSR Fortessa (BD Biosciences). The EC_{50} of NP binding was determined based on a dose-response curve fit (Hill equation) of the percentage of NP-positive cells for each NP concentration. To

determine the number of glutamate residues in each particle, the wt.eq. of PLE polymers required to achieve the plateau of the zeta potential measurements was used combined with the particle size. For liposomes, an average lipid molecular weight of 800 Da was assumed and the total lipid per liposomes was estimated abased on the surface area of a unilamellar liposome with a lipid headgroup size of 0.71 nm^2. For polystyrene particles, their mass was estimated based on a sphere volume with a polystyrene density of 1 g/cm^3.

9.2.10 siRNA depletion

Knockdown of siRNAs was performed by plating HM-1 cells at 5k cells/well in a 96-well plate. The next day, cells were dosed with anti-SLC1A5 siRNA (ON-TARGETplus siRNA mouse Slc1a5, Horizon Discovery) or scramble siRNA (ON-TARGETplus Non-targeting Control Pool, Horizon Discovery) at 200 nM using Lipofectamine RNAiMAX (ThermoFihser) in Opti-MEM (ThermoFisher) medium according to manufacturer instructions. Four days after siRNA dosing, cells were washed with fresh HM-1 media and dosed with 10 μg/mL or NPs for 30 minutes prior to cell processing for flow cytometry.

9.2.11 NanoPrism dataset analysis

We rank-ordered cells based on their weighted average NP-cell association from cells incubated with NPs for 24 hrs. This metric is indicative of NP association with a cancer cell.[9] The median gene expression of the top 100 and bottom 100 cells of the list was then calculated to derive a fold change in median gene expression. For each NP formulation evaluated, this fold change in gene expression was then used to perform gene set enrichment analysis (GSEA) with the Hallmark Gene Sets[10] with WebGestalt 2019.[11]

To mitigate NP core effects from the LbL coating, we assessed the fold change in gene expression relative to the unlayered (UL) nanoparticle core. The lists of upregulated genes for each LbL-NP formulation were then used to determine a list of genes that were upregulated on both PLE NP formulations, but not on HA or PAA-coated NPs.

9.2.12 Confocal Microscopy

For confocal imaging, 8-well chambered coverglasses (Nunc Lab-Tek II, Thermo Scientific) were coated with rat tail collagen type I (Sigma-Aldrich) per the manufacturer's instructions. HM-1

cells were plated into the wells at a density of 10K/well and left to adhere overnight prior to NP treatment. After the desired incubation time with NPs, cells were washed 3x with PBS. After washing, cells were fixed in 4% paraformaldehyde for 15 minutes then washed (3x with PBS) and stained. For cell membrane staining, wheat germ agglutinin (WGA) conjugated to Alexa Fluor488 (Invitrogen) was used. For cell membrane receptor staining, cells were permeabilized for 10 min with 0.1% saponin (Sigma), washed (3x PBS), and then incubated with primary antibodies directed at intracellular epitopes of SLC1A5 or GLUT-1 in 0.5% BSA for at least 3 hrs at 25 °C. Cells were then washed (3x PBS) and stained with secondary anti-rabbit IgG conjugated to Alexa Fluor488 (Invitrogen) for 30 minutes (for anti-CD44 staining, anti-rat IgG AlexaFluor488 was used). Hoechst 33342 (Thermo Scientific) nuclear staining was included in all preparations following manufacturer's instructions. Images were analyzed using ImageJ. Slides were imaged on an Olympus FV1200 Laser Scanning Confocal Microscope.

Confocal images of HM-1 cells at a 60x magnification were analyzed on ImageJ using the Correlation Threshold function to determine the correlation between receptor staining and NP fluorescence.

For evaluation of the percentage of NP signal colocalized on the surface of HM-1 cells, an RO1 on the cell was used and the same function was applied to determine the Mander's Coefficient between the NP signal and the wheat germ agglutinin cell membrane stain.

9.2.13 Glioblastoma cell line NP association screen

Glioblastoma cells were seeded on 96-well plates at a density of 15k cells per well in 100 µL of the appropriate culture media and allowed to adhere overnight. Fluorescent LbL-NPs and UL-NPs generated as described previously were dosed at 5 µg/mL.[6] After 24 hrs of incubation, cells were washed three times with PBS and detached with 25 µL of trypsin-EDTA or Accutase. 200 µL of FACS buffer (PBS with 1% bovine serum albumin and 1 mM EDTA) with 1 µg/mL propidium iodide (Thermo Fisher) was used to quench the dissociation, and cells were pipetted vigorously to achieve a single-cell suspension. Cells were transferred to a new 96-well plate without any laminin or PLL coating, and samples were analyzed using a BD LSR II Flow Cytometer.

9.2.14 Public data set analysis

The gene expression of SLC1A5 in tumor, metastatic, and normal ovarian tissues was obtained from TMNplot.[12] The gene expression of SLC1A5 and SLC1A3 from human ovarian cancer cell lines and the primary non-cancerous tissues were obtained from the Human Protein Atlas.[13,14] The fold change in gene expression of SLC1A5 in human cancers compared to normal tissues was derived from Gene Expression Profiling Interactive Analysis (GEPIA).[15]

9.2.15 AlphaFold 3 Artificial Intelligence Modeling

The AlphaFold Server running AlphaFold 3 was used to predict the interaction of four residue-long polyamino acids with the human protein sequences of amino acid transporters. Four sodium ions were included in the model to ensure amino acid transporters had the required amount of sodium ions. The highest-ranking model predicted for each job in which the polyaminoacid was docket to the outward-facing binding pocket was used. The highest overall ranking prediction was used if none of the five predictions yielded attachment to the binding pockets. Each amino acid transporter pair was modeled five times and the output inter-chain ipTM between the polyaminoacid and the transporter was extracted.

9.2.16 Statistical Analysis

GraphPad PRISM 10 was used to perform statistical analyses. Comparisons between two groups was performed via unpaired t-tests. For multiple groups or multiple variable analysis, one-way, or two-way ANOVAs were used with Tukey's posthoc correction for time-based analysis or Sidak posthoc for other ANOVA analysis.

9.3 Results

9.3.1 Mode of surface polyelectrolyte presentation and avidity regulates binding affinity

We first sought to characterize if the LbL film was required to yield the high-affinity binding of carboxylated polyamino acids to cancer cells. We compared the cell-associated NP fluorescence after incubation of the ovarian cancer cell line OV2944-HM1 (HM-1) with either unmodified liposomes or liposomes that contained PLE in either an LbL film or grafted onto phospholipids of the liposome bilayer (**Figure 9.1a**). While the PLE-LbL increased NP binding ~10-fold, grafted PLE polymers reduced binding by a similar magnitude, suggesting that the mode of polyamino

acid presentation from the NP surface was critical for cellular interactions (**Figure 9.1b**). We next evaluated the cancer cell affinity of two PLE polymers with varying degrees of polymerization (PLE_{100} or PLE_{800}) to that of the PLE_{100} polymers assembled on a LbL-NP. While increasing the polymer chain length PLE_{100} to PLE_{800} residues increased EC_{50} ~9-fold, comparing PLE100 to PLE100 on a LbL-NP increased the affinity 50000-fold (**Figure 9.1c**). Comparing the estimated number of glutamate (E) residues per particle to the observed cellular affinity yielded a clear log-log relationship indicating that the high surface avidity of glutamate residues from the LbL film drove the high-affinity interactions (**Figure 9.1d**).

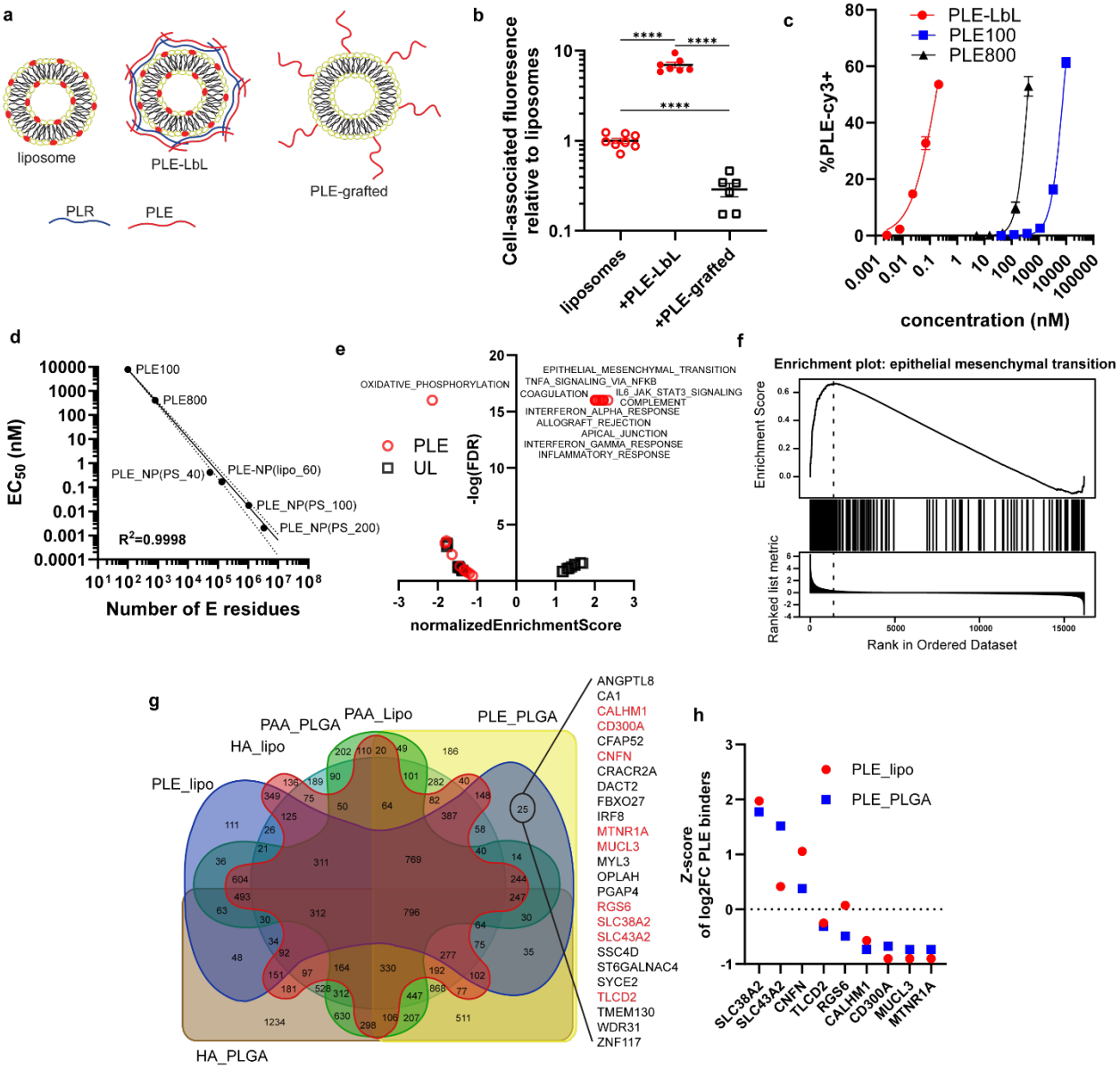

Figure 9.1. LbL film enables high-affinity binding to cancer cells. (a) Diagram of different surface modifications with PLE. (b) Fluorescently labeled NPs were dosed to HM-1 cells *in vitro*. Four hours after dosing, cells were washed and NP fluorescence associated with cells was measured on a fluorescence plate reader. Shown are the normalized fluorescence readings relative to an unlayered negatively charged liposome. (c) PLE labeled with a fluorescence tag was dosed to HM-1 cells either in the LbL-film on an NP (PLE100 was used to assemble film on NP) or as free polymers at a degree of polymerization of 100 or 800. Cells were washed and suspended to read via flow cytometry for the percentage of PLE+ cells. Shown are the results of the experiment with varying PLE concentrations. Curve represents dose-response fit. PLE-NP concentration indicates the number of PLE-coated NPs. (d) Relationship between estimated number of glutamate (E) residues per particle and the derived EC_{50} from the experiment in (c) and EC_{50} of NP+ cells dosed with PLE-coated carboxylate-modified polystyrene (PS) NPs of varying diameters (40 nm, 100 nm, and 200 nm). (e-f) Data from NanoPrism was used to rank cell lines based on their uptake of NPs, the median gene expression of the top 100 cell lines was compared to the median expression of the bottom 100 cell lines to derive the fold chance in gene expression for each formulation that was then used to perform gene-set enrichment analysis (GSEA) against the hallmark gene sets. Shown are the volcano plot for liposomal PLE-NP and UL-NP with the top 20 Hallmark gene sets hits (e), GSEA enrichment plot of liposomal PLE-NP against the epithelial-to-mesenchymal transition (EMT) Hallmark gene set. (g-h) The fold change in gene expression for PLE, HA, and PAA LbL coated NPs made with either liposomal or polylactic-co-glycolic acid (PLGA) cores were normalized to their unlayered cores to derive gene expression signatures that corresponded to high LbL-film binding, but low binding towards the unlayered cores. Upregulated genes were compared to find genes specific towards PLE-coated NPs of either liposomal or PLGA cores. Shown are venn diagram of genes upregulated on cells high for LbL-NP binding relative to UL-NPs for the indicated NP formulations (g) and calculated Z-score of extracellular cell membrane genes shared between PLE_LIPO and PLE_PLGA NPs (h).

To understand what cellular changes promote the binding of avidity glutamate residues on the surface of cancer cells, we next mined the nanoPRISM dataset which screened for the interaction of various NPs with or without LbL assembly with 488 pooled human cancer cell lines.[9] For each NP formulation, we quantified the fold change in median gene expression of the top 100

cell lines interacting with that NP to the bottom 100 cell lines. This rank-ordered gene set was then used to perform Gene Set Enrichment Analysis (GSEA) against the Hallmark gene sets. While unlayered (UL) liposomes showed no major hits, PLE-coated liposomes yielded many significant gene set hits, mostly related to inflammatory responses (**Figure 9.1e**). Oxidative phosphorylation was negatively enriched suggesting higher uptake by highly proliferative cells. Moreover, cells with high PLE-liposome association had a genetic signature indicative of epithelial-to-mesenchymal (EMT) transition indicating a strong potential of PLE coating to target highly metastatic cancers (**Figure 9.1f**). Consistent with prior experiments, STAT3 signaling was a significant hit for increasing the uptake of PLE-liposomes.[16] While indicative of overall PLE-liposome uptake, these genetic signatures were not specific as similar hits were observed for liposomes coated with hyaluronic acid (HA) which can target CD44 overexpression in cancer cells (**Figure G1a**). However, non-specific carboxylated polymers such as polyacrylic acid (PAA) did not present with strong gene signature hits, confirming the unique targeting ability of only certain polymeric coatings (**Figure G1b**).

Similar gene set hits were obtained for PLE-coated poly(lactic-co-glycolic acid) (PLGA) NPs (**Figure G1c**) to that of PLE-liposomes, but some could be attributed to the PLGA core (**Figure G1d**). Thus, to minimize core effects, we quantified a relative fold-change in gene expression which could remove gene signature hits from the unlayered NP while maintaining ones for the LbL coating (**Figure G1e**). To search for potential specific cellular alterations that drive PLE-NP binding, we then used the relative fold change in gene expression over UL NPs to determine upregulated genes that were shared for PLE-PLGA and PLE-liposomes but not upregulated in cells with high uptake of PAA or HA-coated NPs. Only 25 genes met this criterion of which we focused on the 9 transmembrane proteins which could interact with the extracellular environment to mediate NP uptake (**Figure 9.1g**). Of these 9 hits, the highest upregulated gene was SLC38A2, an amino acid transporter that regulates net glutamine uptake in cancer cells (**Figure 9.1h**). [17,18] The accumulation of intracellular amino acids through SLC38A2 drives the transport of other key amino acids through obligatory exchange transporters such as SLC1A5 and SLC7A5, commonly overexpressed in cancer cells.[17–19] Consistent with a greater amino acid uptake activity, a second selectively upregulated gene for high PLE-NP binding cells was another net importer of amino acids - SLC43A2.[20] These results indicated that cells with higher amino acid

demand preferentially bound to PLE-NPs suggesting a role of the polymer amino acid constituency in mediating cellular targeting.

9.3.2 The association of poly-L-glutamate (PLE) coated LbL-NPs is blocked by glutamine transport inhibitors

Cancer cells often become dependent on certain amino acids such as glutamine or aspartate.[21–24] To sustain the intracellular amino acid pool requirement, cancer cells modulate a network of over 60 highly redundant transmembrane proteins that mediate cellular amino acid transport.[25] Based on our analysis of the NanoPrism dataset, we theorized that the polyamino acid composition of PLE-NPs confers the targeting ability of these LbL-NPs through interactions with amino acid transporters overexpressed on cancer cells. Thus, we sought to evaluate if amino acid uptake inhibitors could prevent PLE-NP binding to cancer cells. Before NP dosing, HM-1 cells were pretreated with various concentrations of glutamine uptake inhibitors - L-γ-Glutamyl-p-nitroanilide (GPNA) and V9302 – or glutamate uptake inhibitors - TFB-TBOA. To evaluate the specific effect of the increased uptake due to PLE coating, the data was normalized to the uptake of UL-NPs. While the potent glutamate uptake inhibitor TFB-TBOA did not affect PLE-NP binding even at concentrations 1000x higher than its reporter IC_{50} (~10-100 nM), both glutamine uptake inhibitors could prevent PLE-NP binding at concentrations above their IC_{50} (**Figure 9.2a**). To confirm the specificity of glutamine transporter blockers on PLE-NPs, we repeated the experiments with HA, PAA, or dextran-sulfate (DXS) coated NPs. GPNA (**Figure 9.2b**) and V9302 (**Figure 9.2c**) had a dose-dependent blocking of only PLE-NPs binding but not other LbL-coated NPs.

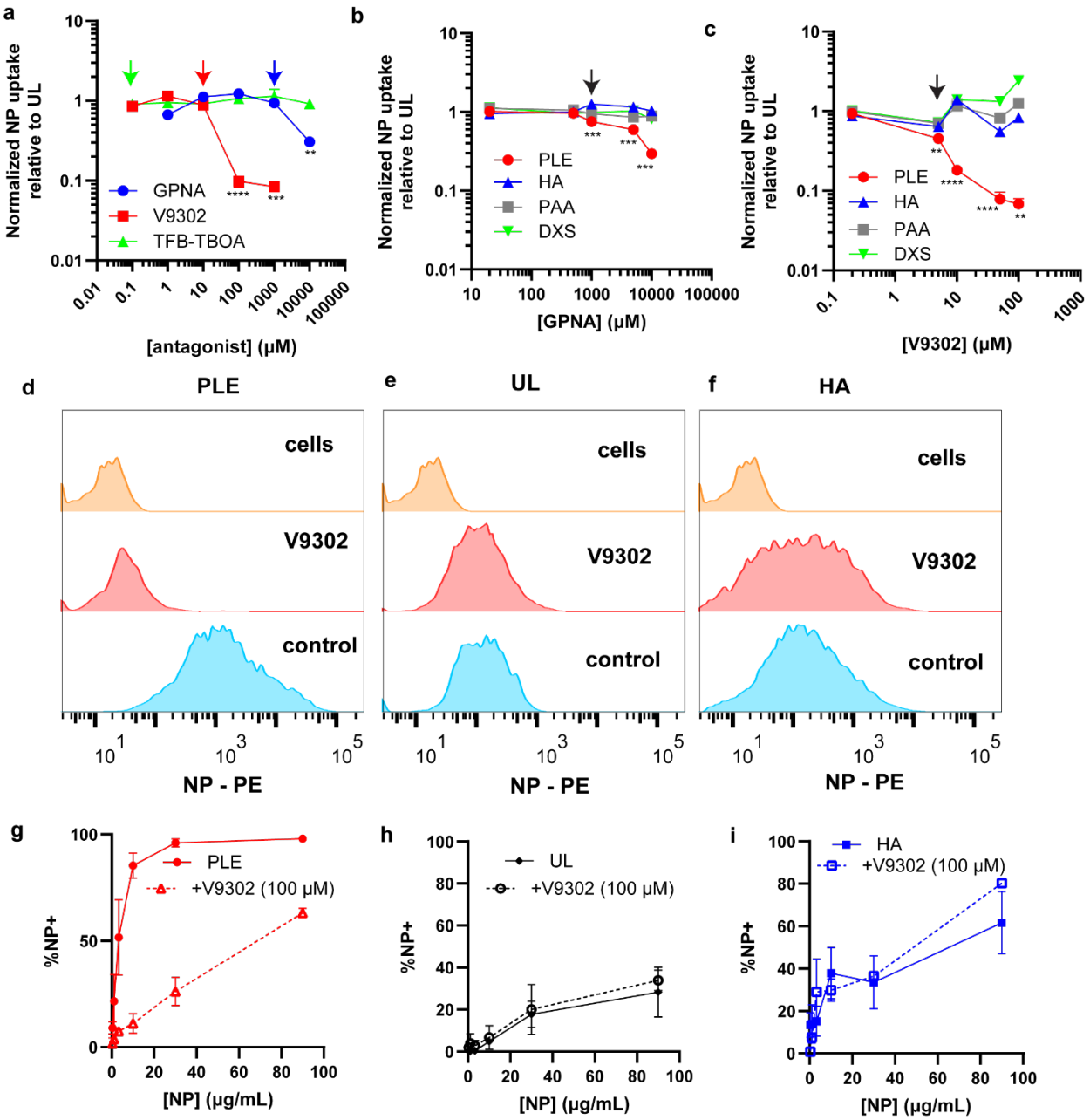

Figure 9.2. Association of PLE-coated NPs is blocked with glutamine transport inhibitors. (a-c) HM-1 cells were plated in 96 wells at a density of 50k cells/well and left to adhere overnight. Cells were then treated with varying concentrations of amino acid transport inhibitors for 15 minutes before NP dosing at 50 μg/mL (a) or 25 μg/mL (b-c) per well. Four (a) or two (b-c) hours after NP dosing, wells were washed twice with PBS and total NP fluorescence associated with cells and remaining in supernatant was measured in a fluorescence plate reader to determine total NP uptake. Shown are the normalized NP uptake of PLE-coated NPs relative to UL at different

inhibitor concentrations of GPNA, TFB-TBOA and V9302 (a), the normalized NP uptake of various outer layer LbL-coated NPs relative to UL at different inhibitor concentrations of GPNA (b), and the normalized NP utpake of various outer layer LbL-coated NPs relative to UL at different inhibitor concentrations of V9302 (c). Arrows indicate IC_{50} for inhibitors derived from literature. (d-i) HM-1 cells were plated in 96 well plates at 50 k cells/well and left to adhere overnight. Cells were then treated with 100 μM of V9302 for 15 minutes prior to NP dosing at varying concentrations. Two hours after NP treatment, cells were washed with PBS, and suspended for flow cytometry analysis of NP uptake. Shown are representative NP fluorescence histograms of HM-1 cells dosed with 30 μg/mL of PLE-NPs (d), UL-NPs (e), or HA-NPs (f) with or without 100 μM of V9302 compared to untreated cells, and the percentage of NP-positive cells in PLE-NP treated (g), UL-treated (h), or HA-NP treated (i) HM-1s with or without 100 μM of V9302 across a range of NP concentrations.

To further evaluate the effect of transport blockage NP uptake, we preincubated HM-1 cells with a dose of V9302 shown previously to block more than 90% of glutamine uptake (100 μM[26]) and then dosed with varying concentrations of either PLE-coated, UL, or HA-coated NPs and then quantified the percentage of NP-positive HM-1 cells. While V9302 could significantly inhibit PLE binding across all concentrations of NPs, there was no effect of the inhibitor on the association with either UL or HA-coated NPs (**Figure 9.2d-i**). These results confirmed the role of amino acid transporters in regulating PLE-NP binding.

9.3.3 Availability of SLC1A5 glutamine transporter modulates PLE-LbL NP binding to cancer cells

Both GPNA and V9302 can block glutamine import by acting on various glutamine transporters known to be overexpressed on cancer cells including SLC38A2 and SLC1A5.[26,27] While we had identified SLC38A2 expression as a specific driver of PLE-NP uptake (**Figure 9.1h**), we theorized that its expression drove an increased activity of SLC1A5 since SLC38A2 has limited activity in most cancer cells grown in amino acid-rich media.[28] Indeed, the inclusion of a system A specific amino acid transporter inhibitor, α-(methylamino)isobutyric acid (MeAIB), did not affect PLE-NP uptake (**Figure G2**). Moreover, glutamate is known to be transported by SLC1A5 which is overexpressed in most cancer types, suggesting that PLE-NPs may specifically target SLC1A5.[29–

[32] To selectively block SLC1A5, we dosed HM-1 cells with antibodies directed against the transporter before dosing with either PLE-NP, UL-NPs, or HA-NPs. As a cell membrane receptor control Ab, we also evaluated the effect of an anti-CD44 Ab. Only anti-SLC1A5 and not anti-CD44 Abs could dramatically reduce PLE-NP association (**Figure 9.3a-d**). However, blockage of SLC1A5 with Abs did not affect UL or HA-NPs association, confirming the specificity of PLE-NP binding to the glutamine transporter (**Figure 9.3a-d**).

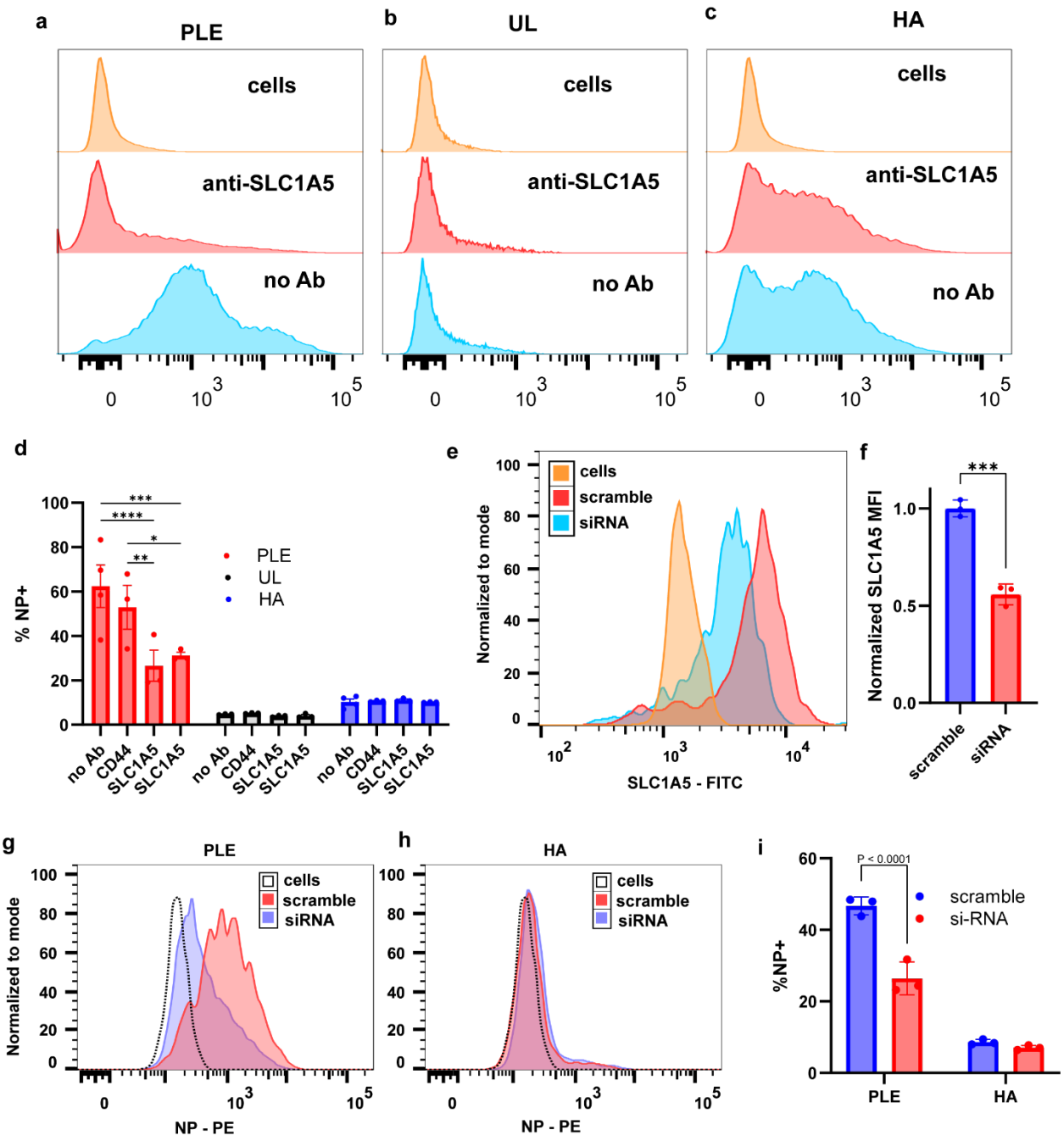

Figure 9.3. Modulation of SLC1A5 availability regulates PLE-NP binding. (a-d) HM-1 cells were plated in 96 well plates at 50 k cells/well and left to adhere overnight. Cells were then treated with antibodies (Abs) against either CD44 or two extracellular epitopes of SLC1A5 for 1 hr. After Ab treatment, cells were dosed with 10 µg/mL of NPs for 15 minutes, washed with PBS, and suspended for flow cytometry analysis of NP uptake. Shown are representative histogram plots of NP fluorescence for cells treated with PLE-NPs (a), UL-NPs (b), and HA-NPs (c) in the presence

of anti-SLC1A5 antibody or control treatments, and the percentage of NP+ cells with or without Abs for PLE, UL and HA NPs. (e-i) HM-1 cells were plated in 96 well plates at 5 k cells/well and left to adhere overnight. The next day, cells were treated with either anti-SLC1A5 siRNA or scramble siRNA at 200 nM for 96 hrs. Cells were then washed with fresh complete media and dosed with 10 μg/mL of NPs for 30 min. After NP incubation, cells were washed with PBS, and suspended for flow cytometry analysis of NP uptake. Shown are representative flow cytometry of total anti-SLC1A5 Ab staining in cells treated with either scramble of anti-SLC1A5 siRNA (e), quantitation of median fluorescence intensity (MFI) of total anti-SLC1A5 staining (f), representative flow cytometry histograms of NP fluorescence of HM-1 cells with partial SLC1A5 knockdown for PLE-NP (g) and HA-NP (h) treatments, and the percentage of NP positive cells with partial SLC1A5 RNA knockdown treated with PLE-NP or HA-NP (i).

To confirm the specificity of PLE-NP binding to SLC1A5, we performed a transient knockdown of SLC1A5 gene expression via siRNAs to partially reduce total SLC1A5 levels in HM-1 cells (**Figure 9.3e-f**). Dosing of PLE-coated HA-coated LbL-NPs to these HM-1 cells with reduced SLC1A5 protein levels showed a significant reduction in uptake of PLE-NPs without affecting HA-NP binding (**Figure 9.3g-i**). Thus, the LbL coating on PLE-NPs is capable of directly binding to SLC1A5.

9.3.4 Clustering of SLC1A5 on the cell surface prolongs surface retention of PLE-NPs

Having discovered a direct binding target of PLE-NPs, we theorized that the SLC1A5 interaction could contribute to the high cell surface retention of PLE-NPs. We have previously successfully used this property of PLE-NPs to deliver interleukin-12 (IL-12) to the tumor extracellular microenvironment. We thus generated fluorescently labeled IL-12-NPs with or without PLE-coating and dosed them to HM-1 cells. After particle incubation, we visualize their interaction with SLC1A5 via confocal microscopy. While unlayered (UL) NPs were rapidly endocytosed with no signs of interaction with SLC1A5, PLE-coated NPs formed clusters on the cell surface of HM-1 cells that showed strong staining towards SLC1A5 (**Figure 9.4a**). The correlation of NPs with cell surface receptors was specific towards SLC1A5 as neither CD44 nor GLUT-1 colocalized with PLE-NPs (**Figure 9.4a, Figure G2a**). Quantification of signal correlation between NP signal and receptor staining showed a clear effect of PLE-coating in promoting NPs attachment to SLC1A5, but not GLUT-1 or CD44 (**Figure 9.4b**). We confirmed this correlation was specific to PLE NPs as other LbL-NP coatings did not show a signal correlation even when the NPs were found on the surface of cancer cells (**Figure 9.4c, Figure G2b**). PLD NPs had a small level of correlation when on the cell surface, but that appeared to be lost potentially due to NP internalization, suggesting that a polyaspartate coating may have similar interactions to PLE-NPs

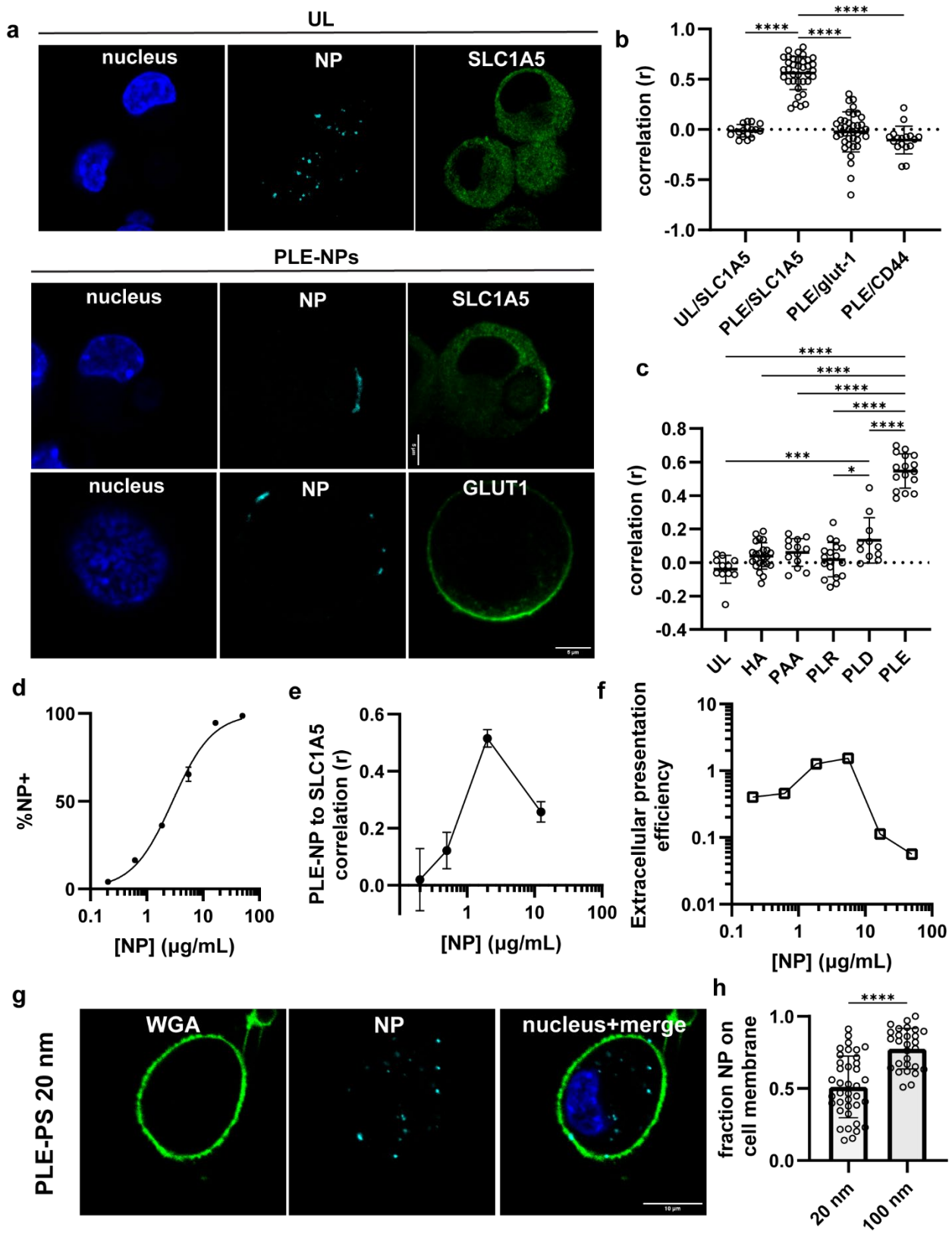
a
UL
nucleus
NP
SLC1A5
PLE-NPs
nucleus
NP
SLC1A5
nucleus
NP
GLUT1
b
correlation (r)
UL/SLC1A5
PLE/SLC1A5
PLE/glut-1
PLE/CD44
c
correlation (r)
UL
HA
PAA
PLR
PLD
PLE
d
%NP+
[NP] (µg/mL)
e
PLE-NP to SLC1A5 correlation (r)
[NP] (µg/mL)
f
Extracellular presentation efficiency
[NP] (µg/mL)
g
PLE-PS 20 nm
WGA
NP
nucleus+merge
h
fraction NP on cell membrane
20 nm
100 nm

Figure 9.4. PLE-NPs colocalize with SLC1A5 transporters on the cell surface. (a-c) HM-1 cells were plated in 8-well glass chamber slides at 10 k cells/well and left to adhere overnight. Cells were dosed with 1.5 μg/mL of NPs for 2 hrs. After NP treatment, cells were washed with PBS, fixed with PFA, and then rapidly permeabilized with saponin. Cells were then treated with primary antibodies for 3 hours followed by secondary antibody for 30 minutes. Shown are high magnification images of HM-1 cells treated with UL-NPs stained against SLC1A5 and HM-1 cells treated with PLE-NPs stained against either SLC1A5 or GLUT-1 transporters (a), correlation analysis between NP signal and cell membrane transporter stain (b), and correlation analysis between varied NP formulations and SLC1A5 staining (c). (d) HM-1 cells were plated in 96-well plates at 50 k cells/well and allowed to adhere overnight. Cells were then dosed with varying concentration of PLE-IL12 NPs. Four hours after dosing, cells were processed for flow cytometry. Shown are the percentage of NP-positive cells for each concentration of NP dosed. (e) The same process as (a-c) was followed but various concentrations of LbL-NPs were tested. Shown are the correlation between NP signal and SLC1A5 stain. (f) The same protocol of (d) was followed but prior to cell fixing, cells were incubated with anti-IL-12 antibody for 1 hr at 4 °C and washed. Shown is the extracellular IL-12 presentation efficiency (ratio between extracellular IL-12 stain to total NP uptake at 24 hrs compared to the same ratio at 4 hrs after dosing). (g-h) HM-1 cells were plated in 8-well glass chamber slides at 10 k cells/well and left to adhere overnight. Cells were dosed with 1 μg/mL of NPs for 4 hrs. After NP treatment, cells were washed with PBS, fixed with PFA, and then stained with Hoechst 33342 and wheat germ agglutinin (WGA) and visualized on a confocal microscope. Shown are representative HM-1 cells dosed with 20 nm PLE-PS particles (g) and the quantification of the fraction of NP pixels colocalized with cell membrane pixels (h).

While SLC1A5 itself has a low internalization rate (half-life 20-60 hrs[33,34]) which could aid in the surface retention of PLE-NPs, we theorized that the cell surface SLC1A5-NP clusters could contribute to the high cell surface retention property of PLE-NPs similar to certain galectin lattice structures.[35] To evaluate the effect of clustering, we dosed increasing concentrations of NPs to HM-1 cells and either imaged cells via confocal microscopy or quantified NP uptake via flow cytometry. Below the NP EC_{50}, we could observe a clear increase in the correlation between PLE-NPs and SLC1A5 signal (**Figure 9.3d-e**), suggesting an increase in cluster size or clustering efficiency. However, NP doses above the EC_{50} reduced SLC1A5 clustering without affecting the

total fraction of NP binding to the cell surface (**Figure 9.3d-e, Figure G3a-b**), likely due to the saturation of SLC1A5 receptors on the cell surface (i.e., lack of multiple receptors for a single particle to bind to). To determine if the reduced clustering would affect the rate of NP internalization, we compared the extracellular IL-12 staining signal to the total NP signal from flow cytometry at 4 and 24 hrs after dosing with NPs. At or below the EC_{50}, NPs were effectively presented on the cell surface with ~50% of the IL-12 signal remaining extracellularly at 24 hrs at low doses, consistent with a ~20 hr half-life[34] of SCL1A5 (**Figure 9.3f**). Strikingly, there was little to no NP uptake near the EC_{50} as the ratio of external IL-12 to total NP remained constant (value ~1). On the other hand, doses above the EC_{50} were readily internalized, suggesting that the lack of receptor clustering may facilitate NP internalization.

While surface retention of PLE-NPs is desirable for the delivery of drugs targeting the extracellular space, certain drug delivery applications may benefit from rapid NP internalization. Consistent with clustering-induced surface retention of PLE-NPs, we have previously shown that the addition of a co-polymer of PLE with polyethylene glycol (PEG) to the LbL film prevented surface retention of NPs in cancer cells.[6] PEG may act to sterically inhibit cluster formation at the cell surface and potentially allows for other interactions at the cell surface. To avoid employing PEG on PLE-NPs to promote internalization, we theorized that the faster internalization kinetics of small NP may avoid cluster assembly.[36] Moreover, as SLC1A5 has been previously shown to colocalize with caveolin-1, small PLE-NPs may readily fit into caveola pits for rapid internalization.[37,38] We thus coated carboxylated polystyrene NPs of either 20 nm or 100 nm in diameter with a PLE LbL film. As found previously[5], 100 nm PLE-NPs accumulated on the cell surface (**Figure G4**). However, when we dosed HM-1 cells with 20 nm PLE-NPs, we could readily observe internalized PLE-NPs within 4 hours after dosing (**Figure 9.4g).** Quantification of total NP localization with the cell membrane confirmed that small PLE-NPs had higher internalization than larger NPs (**Figure 9.4h**).

9.3.5 PLE-NP association correlates with SLC1A5 expression

To further verify the interaction and selectivity of PLE towards SLC1A5, we turned to computation modeling via AlphaFold 3.[39] We provided the human protein sequences of either SLC1A5 or SLC38A2 combined with small (n = 4) polymers of glutamine (PLQ), glutamate (PLE), or a control amino acid with low SLC1A5 interaction – phenylalanine (PLF).[40] Given the ability of

Alpha Fold 3 to include ions and the requirement of sodium by these transporters, they were included in the model.[41,42] Model prediction was evaluated five times, and the chain-pair interface predicted template modeling (ipTM) score was extracted from the top-ranked prediction. The ipTM score is used to rank a specific interface between two chains, with values above 0.8 representing confident high-quality predictions, values above 0.6 suggesting potential interactions, and below 0.3 as non-interacting.[39,43] Both PLQ and PLE were found inside the binding pocket of SLC1A5 with ipTM scores indicative of binding (~0.6, **Figure 9.5a, Figure G5a**). Unlike PLE, PLQ often resulted in the highest-ranking prediction binding to SLC1A5 on the inward-facing side (**Figure G5a)**, but these were not included in the analysis. On the other hand, PLF had significantly reduced ipTM scores and was found outside any known pocket (**Figure G5b**). Unfortunately, AlphaFold is unable to account for pH effects as it does not predict the pKa or charged states of titratable residues.[44] Given that glutamate binding to SLC1A5 is favored at acidic pH, our results likely underestimated the interactions between PLE and SCL1A5.[29] pH sensitivity analysis of the outward-open SLC1A5 crystal structure (6MP6) shows that a critical aspartate residue ($Asp464^{45}$) in the binding pocket is protonated at acid (pH=6.0), which explains its higher affinity towards glutamate (**Figure G5c**).[46] Performing the same analysis on SLC38A2 with PLQ and PLE showed that PLQ could interact favorably (ipTM>0.6) with the binding pocket, whereas PLE had significantly lower ipTM scores and did not bind to a known pocket of SLC38A2 (**Figure 9.5b, Figure G5d)** which agreed with the lack of the SLC38A2 inhibitor on PLE-NP binding (**Figure G2**).

SLC1A5 is overexpressed in human cancers and acts as a biomarker for poor prognosis.[17,32,47–49] Moreover, in line with PLE-NPs binding with cells an inflammatory gene expressing signature (**Figure 9.1e**), tumor samples with high SLC1A5 show similar inflammatory GSEA Hallmark gene set enrichments.[48] Thus we theorized that SLC1A5 expression could be predictive of PLE-NP binding. We previously screened a library of LbL-NPs including PLE-NPs on various human ovarian cancer cell lines and primary non-cancerous tissues.[5] To confirm SLC1A5 overexpression in human ovarian cancer, we analyzed bulk RNA sequencing data of human ovarian cancer tissue from public data sets. Indeed, there was a clear increase in SLC1A5 in ovarian cancer tumors compared to normal tissue which was further increased in metastatic ovarian cancer samples (**Figure 9.5c**). To determine if these genetic markers could predict binding to PLE-NPs we correlated the expression levels of SLC1A5 in the human ovarian cancer cell lines

to their preference towards PLE-NPs over other NPs (PLE-NP Z-score). Except for one cell line (OVCAR4), we observed a strong relationship between PLE-NP binding and its SLC1A5 expression level (**Figure 9.5d**). This was a surprising result as these transporters may be restricted intracellularly until certain environmental contexts induce surface trafficking and the redundancy of glutamine transporters.[50–54] Further, a hypoxia-induced isoform of SLC1A5 is a known mitochondrial transporter restricted to the intracellular space.[55] Indeed, the outlier OVCAR4 has a hypoxia-like gene signature based on analysis of the expression level of hypoxia-induced genes (**Figure G6**).

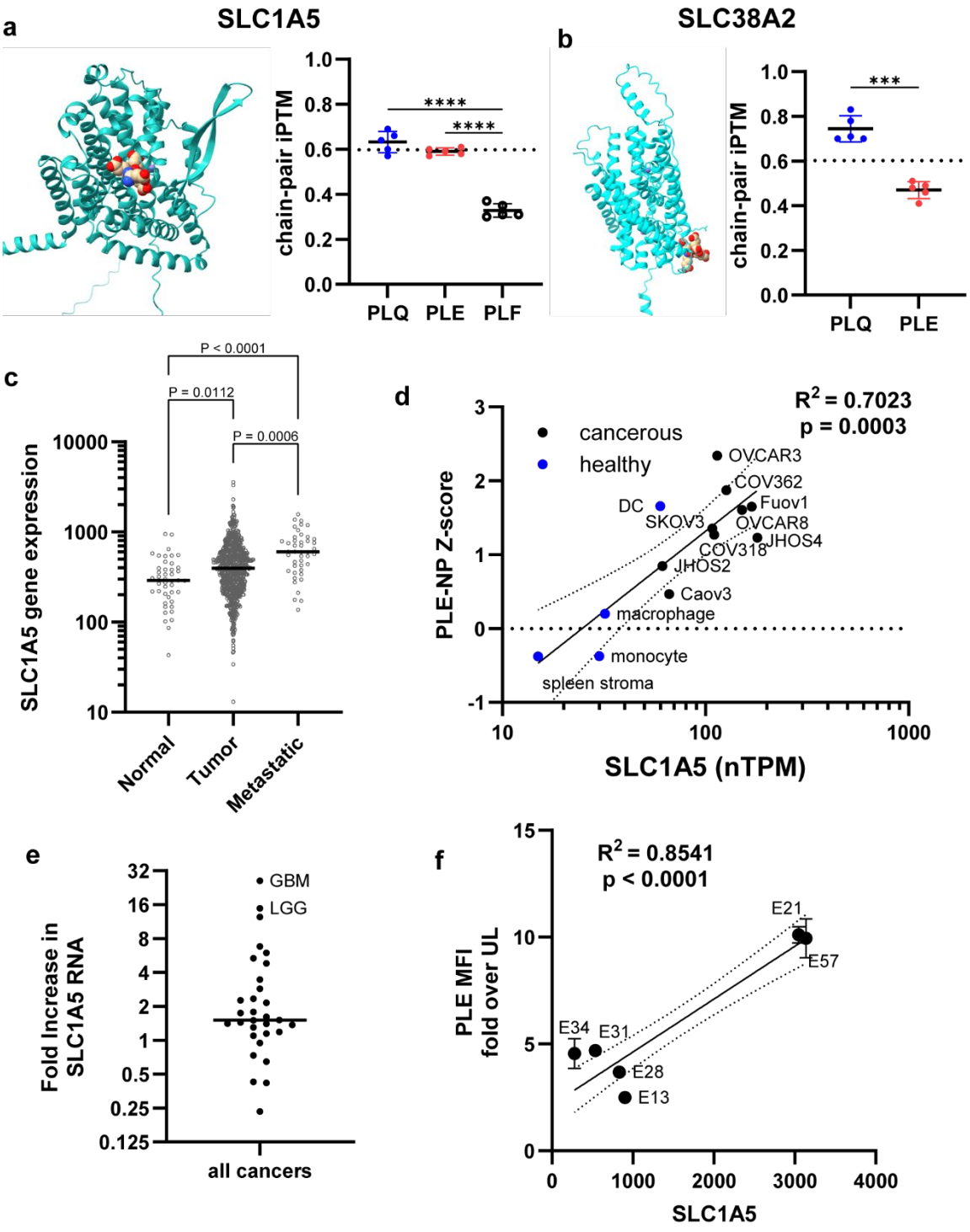

Figure 9.5. AlphaFold artificial intelligence model predicts PLE binding to SLC1A5 and its expression correlated with PLE-NP association. (a) Representative AlphaFold 3 model structure of SLC1A5 and PLE and the calculated chain-pair ipTM scores between SLC1A5 with PLQ, PLE and PLF. (b) Representative AlphaFold 3 model structure of SLC38A2 and PLE and

the calculated chain-pair ipTM scores between SLC38A2 with PLQ and PLE. (c) SLC1A5 expression from human samples from normal, tumor, or metastatic tissue (data from TMNplot) showing increased SLC1A5 expression in cancerous and metastatic tissues. (d) Analysis of PLE-NP Z-scores from NP screen against various human ovarian cancer cell lines and primary healthy tissues as a function of SLC1A5 RNA expression (RNA expression of human cell lines derived from Protein Atlas). R^2 from linear fit and p-value from non-zero slope test. Dashed lines represent 95% confidence interval of curve fit. (e) Fold increase in SLC1A5 RNA expression between tumor and healthy samples across various cancer types and highlighting high fold-changes in brain-derived cancers (data from GEPIA). (f) Fold increase in PLE-NP association relative to UL NPs in a library of glioblastoma cells lines against SLC1A5 gene expression. R^2 from linear fit and p-value from non-zero slope test. Dashed lines represent 95% confidence interval of curve fit.

In addition to ovarian cancer cells, we previously showed that PLE-NPs are highly selective towards glioblastoma *in vitro* and *in vivo*.[6] Consistent with these experimental observations, brain tumors are one of the cancers with the highest fold change in SLC1A5 gene expression compared to healthy tissue (**Figure 9.5e**).[48] Thus, we sought to validate the effect of high SLC1A5 expression on PLE-NP binding using glioblastoma cell lines. We dosed six glioblastoma cell lines with PLE or UL liposomes and quantified total NP fluorescence via flow cytometry. There was a clear relationship between the enhancement in NP uptake due to PLE coating and the expression levels of SLC1A5 in the tested glioblastoma cell lines (**Figure 9.5f**).

9.3.6 Poly-L-aspartate coating enables affinity towards anionic amino acid transporters

Having established a binding target for PLE, we next sought to find a mechanism for the differences between PLE and PLD-coated NPs. The partial association of PLD and SLC1A5 seen via confocal microscopy (**Figure 9.4c**) indicated that PLD may bind to similar amino acid transporters overexpressed in cancer cells. Indeed, analysis of PLE and PLD NP uptake from cell line screening data showed a clear correlation between the two NPs suggesting that similar cell line traits promoted their uptake (**Figure 9.6a-b**). Thus, we tested if the glutamine uptake inhibitor V9302 could also inhibit PLD-NP binding to HM-1 cells. We found that, like PLE, PLD binding was inhibited by V9302 in a dose-dependent manner (**Figure 9.6c**). However, when we evaluated the effect of the anionic amino acid transport inhibitor (TFB-TBOA), it could block PLD NP

binding but did not affect PLE NP binding (**Figure 9.6d**). Thus, unlike PLE, PLD coating maintains binding to anionic amino acid transporters, potentially due to PLE's larger side chain residue.

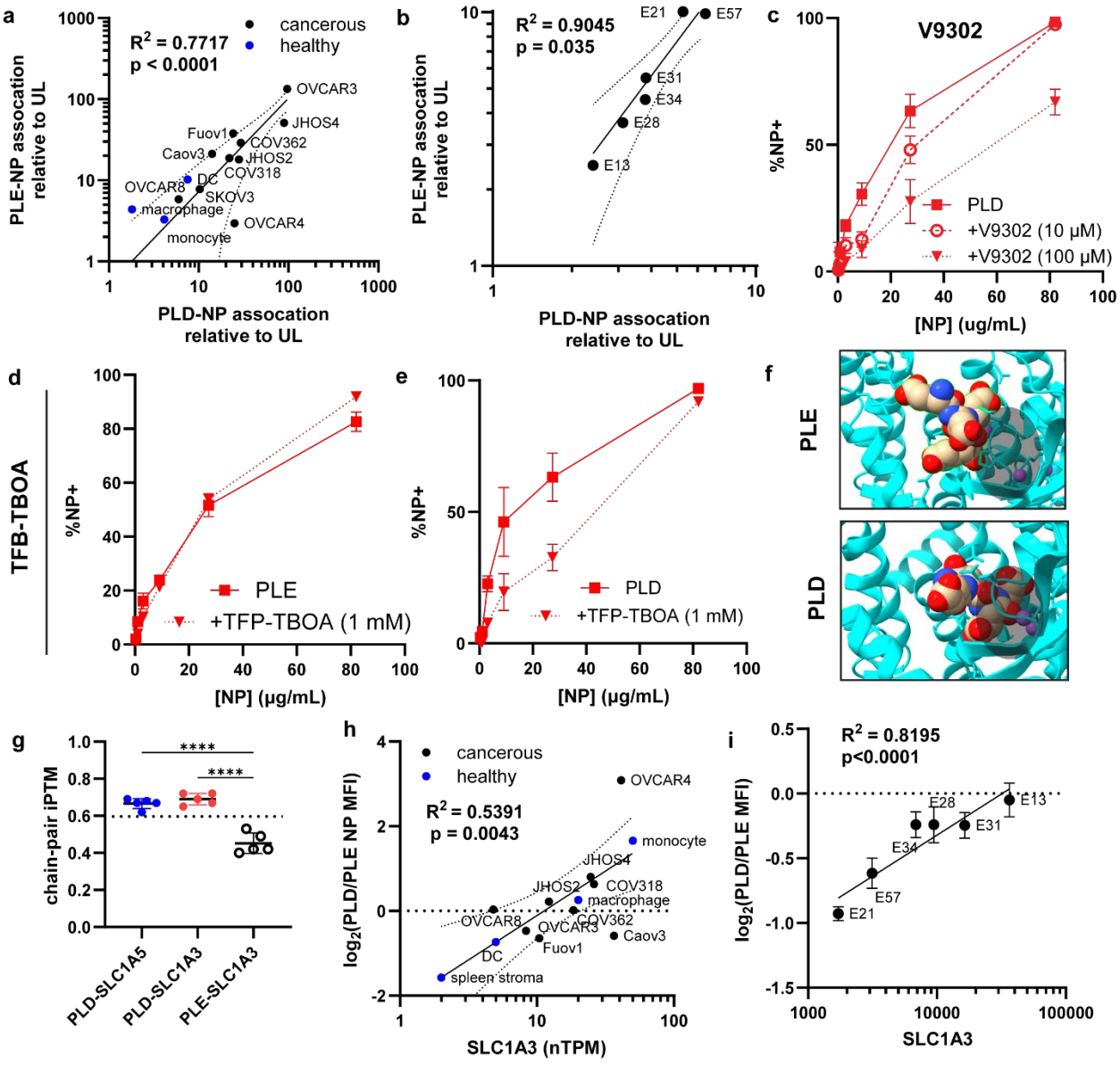

Figure 9.6. PLD-coated NPs associate both glutamine transporters and anionic amino acid transporters. (a) Log-log plots of fold increase in PLE and PLD coated LbL-NPs relative to UL NPs in a library of ovarian cancer cells lines and primary healthy cells. R^2 from linear fit and p-value from non-zero slope test. Dashed lines represent 95% confidence interval of the curve fit.

(b) same as (a) but on the library of glioblastoma cell lines. (c-e) HM-1 cells were plated in 96 well plates at 50 k cells/well and left to adhere overnight. Cells were then treated with either V9302 or TFB-TBOA for 15 minutes before NP dosing at varying concentrations. Two hours after NP treatment, cells were washed with PBS, and suspended for flow cytometry analysis of NP uptake. Shown are the percentage of NP-positive cells in PLD-treated HM-1s with 10 μM of V9302, 100 μM of V9302 or without V9302 (c), and the percentage of NP-positive cells in PLE-NP treated (d), or PLD-NP treated (e) HM-1s with or without 1 mM of TFB-TBOA. (f) Representative AlphaFold 3 model structure of SLC1A3 and PLE and SLC1A3 with PLD focused on the binding pocket indicated by the dark shading. (g) AlphaFold 3 calculated chain-pair ipTM scores between SLC1A5 with PLD, SLC1A3 with PLD, and SLC1A3 with PLE. (h-i) The NP median fluorescence intensity (MFI) of PLD-NP treated cells was normalized to the MFI of PLE-treated cells and plotted against SLC1A3 expression of the cel line. Shown are the plots of the NP screen against ovarian cancer cells and primary healthy tissue (h) and on glioblastoma cells lines (i). R^2 from linear fit and p-value from non-zero slope test. Dashed lines represent 95% confidence interval of the curve fit.

Of the various anionic amino acid transporters, SLC1A3 has been implicated as a major contributor to cancer progression and is overexpressed in many solid tumors.[56–59] We used the human sequence of SLC1A3 to evaluate PLD and PLE binding to this transporter via AlphaFold 3. As SLC1A3 also requires sodium ions for transport activity, these were included in the model.[60] Consistent with our expectation of PLE's side chain size hindering binding, AlphaFold predictions showed that PLE could bind near the pocket, but did not fit inside (**Figure 9.6f**). On the other hand, PLD was predicted to bind inside the pocket. Indeed, quantification of chain-pair ipTM scores showed that PLD had favorable binding to both SLC1A5 and SLC1A3, but PLE had a significantly lower score towards SLC1A3 (**Figure 9.6g**).

We next decided to explore if the expression of SLC1A3 could predict the binding of PLD over PLE NPs. There was a clear correlation between the preference for PLD over PLE NPs from our cell line screening data sets and their SLC1A3 expression levels (**Figure 9.6h-i**). As hypoxia induces SLC1A3 expression[61], consistent with the hypoxic-like state of OVCAR4, these cells had a high SLC1A3 expression and a high preference for PLD-NPs over PLE. These effects were also observed on primary non-cancerous cell lines since macrophages and monocytes which had similar

levels of SLC1A5 showed similar PLE-NP binding, but the higher SLC1A3 expression in monocytes showed higher PLD uptake. Importantly, the ability of PLD NPs to bind to SLC1A3 explains the increased rate of PLD over PLE endocytosis since anionic amino acid transporters have a much shorter surface half-life (<1 hr[62,63]) compared to SLC1A5 (20-60 hrs[33,34]). Further, consistent with prior reports of caveolin-mediated PLD-NP trafficking, the uptake of anionic amino acid transporters mediated through caveolin.[62,64]

9.4 Discussion

Targeted NPs widen the therapeutic window of drugs and enable effective bioimaging approaches. Modulation of surface chemistry via the LbL technique is a successful strategy to afford NPs with targeting motifs. While anionic polyamino acid LbL coatings have shown successful *in vivo* targeting of cancerous tissues and allowed for control over NP internalization rates, their targets have remained unknown. Here we report that anionic LbL polyamino acid coatings confer targeting of amino acid transporters overexpressed in cancerous tissues. PLE coating showed a strong specificity towards a glutamine transporter SLC1A5 whereas PLD interacted with SLC1A5 and SLC1A3, an anionic amino acid transporter.

We demonstrate that the high affinity of LbL-NPs to cancer cells was directly correlated with the avidity of amino acid presentation enabled by the LbL technique and that cancer cells with higher expression of net amino acid importers associate with more PLE-NPs. We validated the association of PLE with SLC1A5 via small molecule transport inhibitors, antibody blocking, and genetic silencing. Moreover, we confirm PLE binding to the pockets of SLC1A5 using the artificial intelligence model of AlphaFold 3 which predicts their direct interaction. We also discovered that PLE-NP binding to SLC1A5 induces cell membrane cluster formation, hindering NP internalization. PLD-coated particles, however, not only attach to glutamine transporters but also to anionic amino acid transporters such as SLC1A3, which helps explain their faster internalization compared to PLE-NPs. Analysis of LbL-NP screens with cell lines demonstrates that SLC1A5 expression correlated with PLE-NP uptake and that the preference for PLD-NPs was related to the expression of SLC1A3.

Prior work has aimed at developing polymers to target SLC1A5, by grafting glutamine residues to the polymer.[65,66] However, as we show here, through the LbL coating we can achieve dramatically higher affinity towards cancer tissues. Interestingly, glutamate has been used as a

control compared to glutamine with little discussion on the potential glutamate-SLC1A5 interaction.[65,66] Glutamate attachment via the side chain carboxylic acid has also been employed but such an approach led to no interaction with SLC1A5 and unclear binding partners, likely due to the presentation of the amino and carboxyl groups present on all amino acids.[67,68] Grafting of glutamine residues onto branched polyethylenimine (PEI) for polyplexes has also been used.[69] However, glutamine residues are more likely to interact with other glutamine transporters such as SLC38A2 (**Figure 9.5b**). Moreover, unlike PLE-LbL-NPs, these particles were readily internalized, suggesting alternative interactions of the NP such as those from its positive charge.

Taken together the data presented here provides the first demonstration that high avidity presentation of anionic amino acids from LbL-NPs enables targeting to overexpressed amino acid transporters. These insights may guide future applications of these LbL-NPs as well as allow for future rational design of next-generation polymeric coatings

9.5 References

1. Manzari, M. T., Shamay, Y., Kiguchi, H., Rosen, N., Scaltriti, M. & Heller, D. A. Targeted drug delivery strategies for precision medicines. *Nat Rev Mater* **6,** 351–370 (2021).

2. Cabral, H., Li, J., Miyata, K. & Kataoka, K. Controlling the biodistribution and clearance of nanomedicines. *Nature Reviews Bioengineering* **2,** 214–232 (2023).

3. Ahmad, A., Khan, F., Mishra, R. K. & Khan, R. Precision Cancer Nanotherapy: Evolving Role of Multifunctional Nanoparticles for Cancer Active Targeting. *J Med Chem* **62,** 10475–10496 (2019).

4. Durymanov, M., Kamaletdinova, T., Lehmann, S. E. & Reineke, J. Exploiting passive nanomedicine accumulation at sites of enhanced vascular permeability for non-cancerous applications. *Journal of Controlled Release* **261,** 10–22 (2017).

5. Correa, S., Boehnke, N., Barberio, A. E., Deiss-Yehiely, E., Shi, A., Oberlton, B., Smith, S. G., Zervantonakis, I., Dreaden, E. C. & Hammond, P. T. Tuning Nanoparticle Interactions with Ovarian Cancer through Layer-by-Layer Modification of Surface Chemistry. *ACS Nano* **14,** 2224–2237 (2020).

6. Pickering, A. J., Lamson, N. G., Marand, M. H., Hwang, W., Straehla, J. P. & Hammond, P. T. Layer-by-Layer Polymer Functionalization Improves Nanoparticle Penetration and Glioblastoma Targeting in the Brain. *ACS Nano* (2023). doi:10.1021/acsnano.3c09273

7. Lieschke, G. J., Rao, P. K., Gately, M. K. & Mulligan, R. C. Bioactive murine and human interleukin-12 fusion proteins which retain antitumor activity in vivo. *Nat Biotechnol* **15,** 35–40 (1997).

8. Pollard, S. M., Yoshikawa, K., Clarke, I. D., Danovi, D., Stricker, S., Russell, R., Bayani, J., Head, R., Lee, M., Bernstein, M., Squire, J. A., Smith, A. & Dirks, P. Glioma Stem Cell Lines Expanded in Adherent Culture Have Tumor-Specific Phenotypes and Are Suitable for Chemical and Genetic Screens. *Cell Stem Cell* **4,** 568–580 (2009).

9. Boehnke, N., Straehla, J. P., Safford, H. C., Kocak, M., Rees, M. G., Ronan, M., Rosenberg, D., Adelmann, C. H., Chivukula, R. R., Nabar, N., Berger, A. G., Lamson, N. G., Cheah, J. H., Li, H., Roth, J. A., Koehler, A. N. & Hammond, P. T. Massively parallel pooled screening reveals genomic determinants of nanoparticle delivery. *Science (1979)* **377,** (2022).

10. Liberzon, A., Birger, C., Thorvaldsdóttir, H., Ghandi, M., Mesirov, J. P. & Tamayo, P. The Molecular Signatures Database Hallmark Gene Set Collection. *Cell Syst* **1,** 417–425 (2015).

11. Liao, Y., Wang, J., Jaehnig, E. J., Shi, Z. & Zhang, B. WebGestalt 2019: gene set analysis toolkit with revamped UIs and APIs. *Nucleic Acids Res* **47,** W199–W205 (2019).

12. Bartha, Á. & Győrffy, B. TNMplot.com: A Web Tool for the Comparison of Gene Expression in Normal, Tumor and Metastatic Tissues. *Int J Mol Sci* **22,** 2622 (2021).

13. The Human Protein Atlas. (2024). at <proteinatlas.org>

14. Jin, H., Zhang, C., Zwahlen, M., von Feilitzen, K., Karlsson, M., Shi, M., Yuan, M., Song, X., Li, X., Yang, H., Turkez, H., Fagerberg, L., Uhlén, M. & Mardinoglu, A. Systematic transcriptional analysis of human cell lines for gene expression landscape and tumor representation. *Nat Commun* **14,** 5417 (2023).

15. Tang, Z., Li, C., Kang, B., Gao, G., Li, C. & Zhang, Z. GEPIA: a web server for cancer and normal gene expression profiling and interactive analyses. *Nucleic Acids Res* **45,** W98–W102 (2017).

16. Tošić, I., Heppler, L. N., Egusquiaguirre, S. P., Boehnke, N., Correa, S., Costa, D. F., Moore, E. A. G., Pal, S., Richardson, D. S., Ivanov, A. R., Haas-Kogan, D. A., Nomura, D. K., Hammond, P. T. & Frank, D. A. Lipidome-based Targeting of STAT3-driven Breast Cancer Cells Using Poly- <scp>l</scp> -glutamic Acid–coated Layer-by-Layer Nanoparticles. *Mol Cancer Ther* **20,** 726–738 (2021).

17. Huang, M., Chang, J., Lin, W., Cheng, Y., Li, F., Suen, C., Hwang, M., Chang, C. & Mou, K. Y. SLC38A2 Overexpression Induces a Cancer-like Metabolic Profile and Cooperates with SLC1A5 in Pan-cancer Prognosis. *Chem Asian J* **15,** 3861–3872 (2020).

18. Bröer, A., Rahimi, F. & Bröer, S. Deletion of Amino Acid Transporter ASCT2 (SLC1A5) Reveals an Essential Role for Transporters SNAT1 (SLC38A1) and SNAT2 (SLC38A2) to Sustain Glutaminolysis in Cancer Cells. *Journal of Biological Chemistry* **291,** 13194–13205 (2016).

19. Menchini, R. J. & Chaudhry, F. A. Multifaceted regulation of the system A transporter Slc38a2 suggests nanoscale regulation of amino acid metabolism and cellular signaling. *Neuropharmacology* **161,** 107789 (2019).

20. Guetg, A., Mariotta, L., Bock, L., Herzog, B., Fingerhut, R., Camargo, S. M. R. & Verrey, F. Essential amino acid transporter Lat4 (*Slc43a2*) is required for mouse development. *J Physiol* **593,** 1273–1289 (2015).

21. Li, X., Peng, X., Li, Y., Wei, S., He, G., Liu, J., Li, X., Yang, S., Li, D., Lin, W., Fang, J., Yang, L. & Li, H. Glutamine addiction in tumor cell: oncogene regulation and clinical treatment. *Cell Communication and Signaling* **22,** 12 (2024).

22. Jin, J., Byun, J.-K., Choi, Y.-K. & Park, K.-G. Targeting glutamine metabolism as a therapeutic strategy for cancer. *Exp Mol Med* **55,** 706–715 (2023).

23. Bhutia, Y. D., Babu, E., Ramachandran, S. & Ganapathy, V. Amino Acid Transporters in Cancer and Their Relevance to "Glutamine Addiction": Novel Targets for the Design of a New Class of Anticancer Drugs. *Cancer Res* **75,** 1782–1788 (2015).

24. Helenius, I. T., Madala, H. R. & Yeh, J.-R. J. An Asp to Strike Out Cancer? Therapeutic Possibilities Arising from Aspartate's Emerging Roles in Cell Proliferation and Survival. *Biomolecules* **11,** 1666 (2021).

25. Gauthier-Coles, G., Vennitti, J., Zhang, Z., Comb, W. C., Xing, S., Javed, K., Bröer, A. & Bröer, S. Quantitative modelling of amino acid transport and homeostasis in mammalian cells. *Nat Commun* **12,** 5282 (2021).

26. Schulte, M. L., Fu, A., Zhao, P., Li, J., Geng, L., Smith, S. T., Kondo, J., Coffey, R. J., Johnson, M. O., Rathmell, J. C., Sharick, J. T., Skala, M. C., Smith, J. A., Berlin, J., Washington, M. K., Nickels, M. L. & Manning, H. C. Pharmacological blockade of ASCT2-dependent glutamine transport leads to antitumor efficacy in preclinical models. *Nat Med* **24,** 194–202 (2018).

27. Bröer, A., Fairweather, S. & Bröer, S. Disruption of Amino Acid Homeostasis by Novel ASCT2 Inhibitors Involves Multiple Targets. *Front Pharmacol* **9,** (2018).

28. Gauthier-Coles, G., Bröer, A., McLeod, M. D., George, A. J., Hannan, R. D. & Bröer, S. Identification and characterization of a novel SNAT2 (SLC38A2) inhibitor reveals synergy with glucose transport inhibition in cancer cells. *Front Pharmacol* **13,** (2022).

29. Scalise, M., Mazza, T., Pappacoda, G., Pochini, L., Cosco, J., Rovella, F. & Indiveri, C. The Human SLC1A5 Neutral Amino Acid Transporter Catalyzes a pH-Dependent Glutamate/Glutamine Antiport, as Well. *Front Cell Dev Biol* **8,** (2020).

30. Oppedisano, F., Pochini, L., Galluccio, M. & Indiveri, C. The glutamine/amino acid transporter (ASCT2) reconstituted in liposomes: Transport mechanism, regulation by ATP and characterization of the glutamine/glutamate antiport. *Biochimica et Biophysica Acta (BBA) - Biomembranes* **1768,** 291–298 (2007).

31. Utsunomiya-Tate, N., Endou, H. & Kanai, Y. Cloning and Functional Characterization of a System ASC-like Na+-dependent Neutral Amino Acid Transporter. *Journal of Biological Chemistry* **271,** 14883–14890 (1996).

32. Ni, J., Dai, W., Liu, C., Ling, Y. & Mou, H. A pan-cancer analysis of SLC1A5 in human cancers. *Heliyon* **9,** e17598 (2023).

33. Console, L., Scalise, M., Tarmakova, Z., Coe, I. R. & Indiveri, C. N-linked Glycosylation of human SLC1A5 (ASCT2) transporter is critical for trafficking to membrane. *Biochimica et Biophysica Acta (BBA) - Molecular Cell Research* **1853,** 1636–1645 (2015).

34. Xiao, H. & Wu, R. Quantitative investigation of human cell surface N-glycoprotein dynamics. *Chem Sci* **8,** 268–277 (2017).

35. Nabi, I. R., Shankar, J. & Dennis, J. W. The galectin lattice at a glance. *J Cell Sci* **128,** 2213–2219 (2015).

36. Doiron, A. L., Clark, B. & Rinker, K. D. Endothelial nanoparticle binding kinetics are matrix and size dependent. *Biotechnol Bioeng* **108,** 2988–2998 (2011).

37. Wang, Z., Tiruppathi, C., Minshall, R. D. & Malik, A. B. Size and Dynamics of Caveolae Studied Using Nanoparticles in Living Endothelial Cells. *ACS Nano* **3,** 4110–4116 (2009).

38. Esaki, N., Ohkawa, Y., Hashimoto, N., Tsuda, Y., Ohmi, Y., Bhuiyan, R. H., Kotani, N., Honke, K., Enomoto, A., Takahashi, M., Furukawa, K. & Furukawa, K. <scp>ASC</scp> amino acid transporter 2, defined by enzyme-mediated activation of radical sources, enhances malignancy of GD2-positive small-cell lung cancer. *Cancer Sci* **109,** 141–153 (2018).

39. Abramson, J., Adler, J., Dunger, J., Evans, R., Green, T., Pritzel, A., Ronneberger, O., Willmore, L., Ballard, A. J., Bambrick, J., Bodenstein, S. W., Evans, D. A., Hung, C.-C., O'Neill, M., Reiman, D., Tunyasuvunakool, K., Wu, Z., Žemgulytė, A., Arvaniti, E., Beattie, C., Bertolli, O., Bridgland, A., Cherepanov, A., Congreve, M., Cowen-Rivers, A. I., Cowie, A., Figurnov, M., Fuchs, F. B., Gladman, H., Jain, R., Khan, Y. A., Low, C. M. R., Perlin, K., Potapenko, A., Savy, P., Singh, S., Stecula, A., Thillaisundaram, A., Tong, C., Yakneen, S., Zhong, E. D., Zielinski, M., Žídek, A., Bapst, V., Kohli, P., Jaderberg, M., Hassabis, D. & Jumper, J. M. Accurate structure prediction of biomolecular interactions with AlphaFold 3. *Nature* (2024). doi:10.1038/s41586-024-07487-w

40. Pingitore, P., Pochini, L., Scalise, M., Galluccio, M., Hedfalk, K. & Indiveri, C. Large scale production of the active human ASCT2 (SLC1A5) transporter in Pichia pastoris — functional and kinetic asymmetry revealed in proteoliposomes. *Biochimica et Biophysica Acta (BBA) - Biomembranes* **1828,** 2238–2246 (2013).

41. Mazza, T., Scalise, M., Pappacoda, G., Pochini, L. & Indiveri, C. The involvement of sodium in the function of the human amino acid transporter ASCT2. *FEBS Lett* **595,** 3030–3041 (2021).

42. Zhang, Z., Albers, T., Fiumera, H. L., Gameiro, A. & Grewer, C. A Conserved Na+ Binding Site of the Sodium-coupled Neutral Amino Acid Transporter 2 (SNAT2). *Journal of Biological Chemistry* **284,** 25314–25323 (2009).

43. Weeratunga, S., Gormal, R. S., Liu, M., Eldershaw, D., Livingstone, E. K., Malapaka, A., Wallis, T. P., Bademosi, A. T., Jiang, A., Healy, M. D., Meunier, F. A. & Collins, B. M. Interrogation and validation of the interactome of neuronal Munc18-interacting Mint proteins with AlphaFold2. *Journal of Biological Chemistry* **300,** 105541 (2024).

44. Laurents, D. V. AlphaFold 2 and NMR Spectroscopy: Partners to Understand Protein Structure, Dynamics and Function. *Front Mol Biosci* **9,** (2022).

45. Yu, X., Plotnikova, O., Bonin, P. D., Subashi, T. A., McLellan, T. J., Dumlao, D., Che, Y., Dong, Y. Y., Carpenter, E. P., West, G. M., Qiu, X., Culp, J. S. & Han, S. Cryo-EM structures of the human glutamine transporter SLC1A5 (ASCT2) in the outward-facing conformation. *Elife* **8,** (2019).

46. Schmitz, M., Schultze, A., Vanags, R., Voigt, K., Di Ventura, B. & Öztürk, M. A. patcHwork: a user-friendly pH sensitivity analysis web server for protein sequences and structures. *Nucleic Acids Res* **50,** W560–W567 (2022).

47. Sheraj, I., Guray, N. T. & Banerjee, S. A pan-cancer transcriptomic study showing tumor specific alterations in central metabolism. *Sci Rep* **11,** 13637 (2021).

48. Chen, P., Jiang, Y., Liang, J., Cai, J., Zhuo, Y., Fan, H., Yuan, R., Cheng, S. & Zhang, Y. SLC1A5 is a novel biomarker associated with ferroptosis and the tumor microenvironment: a pancancer analysis. *Aging* (2023). doi:10.18632/aging.204911

49. Zhang, H., Cui, K., Yao, S., Yin, Y., Liu, D. & Huang, Z. Comprehensive molecular and clinical characterization of SLC1A5 in human cancers. *Pathol Res Pract* **224,** 153525 (2021).

50. Gegelashvili, M., Rodriguez-Kern, A., Pirozhkova, I., Zhang, J., Sung, L. & Gegelashvili, G. High-affinity glutamate transporter GLAST/EAAT1 regulates cell surface expression of glutamine/neutral amino acid transporter ASCT2 in human fetal astrocytes. *Neurochem Int* **48,** 611–615 (2006).

51. Ling, R., Bridges, C. C., Sugawara, M., Fujita, T., Leibach, F. H., Prasad, P. D. & Ganapathy, V. Involvement of transporter recruitment as well as gene expression in the substrate-induced adaptive regulation of amino acid transport system A. *Biochimica et Biophysica Acta (BBA) - Biomembranes* **1512,** 15–21 (2001).

52. Gegelashvili, M., Rodriguez-Kern, A., Pirozhkova, I., Zhang, J., Sung, L. & Gegelashvili, G. High-affinity glutamate transporter GLAST/EAAT1 regulates cell surface expression of glutamine/neutral amino acid transporter ASCT2 in human fetal astrocytes. *Neurochem Int* **48,** 611–615 (2006).

53. Avissar, N. E., Sax, H. C. & Toia, L. In Human Entrocytes, GLN Transport and ASCT2 Surface Expression Induced by Short-Term EGF are MAPK, PI3K, and Rho-Dependent. *Dig Dis Sci* **53,** 2113–2125 (2008).

54. Yang, Z., Follett, J., Kerr, M. C., Clairfeuille, T., Chandra, M., Collins, B. M. & Teasdale, R. D. Sorting nexin 27 (SNX27) regulates the trafficking and activity of the glutamine transporter ASCT2. *Journal of Biological Chemistry* **293,** 6802–6811 (2018).

55. Yoo, H. C., Park, S. J., Nam, M., Kang, J., Kim, K., Yeo, J. H., Kim, J.-K., Heo, Y., Lee, H. S., Lee, M. Y., Lee, C. W., Kang, J. S., Kim, Y.-H., Lee, J., Choi, J., Hwang, G.-S., Bang, S. & Han, J. M. A Variant of SLC1A5 Is a Mitochondrial Glutamine Transporter for Metabolic Reprogramming in Cancer Cells. *Cell Metab* **31,** 267-283.e12 (2020).

56. Bertero, T., Oldham, W. M., Grasset, E. M., Bourget, I., Boulter, E., Pisano, S., Hofman, P., Bellvert, F., Meneguzzi, G., Bulavin, D. V., Estrach, S., Feral, C. C., Chan, S. Y., Bozec, A. & Gaggioli, C. Tumor-Stroma Mechanics Coordinate Amino Acid Availability to Sustain Tumor Growth and Malignancy. *Cell Metab* **29,** 124-140.e10 (2019).

57. Xu, L., Chen, J., Jia, L., Chen, X., Awaleh Moumin, F. & Cai, J. SLC1A3 promotes gastric cancer progression via the PI3K/AKT signalling pathway. *J Cell Mol Med* **24,** 14392–14404 (2020).

58. Sun, J., Nagel, R., Zaal, E. A., Ugalde, A. P., Han, R., Proost, N., Song, J., Pataskar, A., Burylo, A., Fu, H., Poelarends, G. J., van de Ven, M., van Tellingen, O., Berkers, C. R. &

Agami, R. <scp>SLC</scp> 1A3 contributes to L-asparaginase resistance in solid tumors. *EMBO J* **38,** (2019).

59. Tajan, M., Hock, A. K., Blagih, J., Robertson, N. A., Labuschagne, C. F., Kruiswijk, F., Humpton, T. J., Adams, P. D. & Vousden, K. H. A Role for p53 in the Adaptation to Glutamine Starvation through the Expression of SLC1A3. *Cell Metab* **28,** 721-736.e6 (2018).

60. Bastug, T., Heinzelmann, G., Kuyucak, S., Salim, M., Vandenberg, R. J. & Ryan, R. M. Position of the Third Na+ Site in the Aspartate Transporter GltPh and the Human Glutamate Transporter, EAAT1. *PLoS One* **7,** e33058 (2012).

61. Hu, H., Takano, N., Xiang, L., Gilkes, D. M., Luo, W. & Semenza, G. L. Hypoxia-inducible factors enhance glutamate signaling in cancer cells. *Oncotarget* **5,** 8853–8868 (2014).

62. González, M. I., Krizman-Genda, E. & Robinson, M. B. Caveolin-1 Regulates the Delivery and Endocytosis of the Glutamate Transporter, Excitatory Amino Acid Carrier 1. *Journal of Biological Chemistry* **282,** 29855–29865 (2007).

63. Michaluk, P., Heller, J. P. & Rusakov, D. A. Rapid recycling of glutamate transporters on the astroglial surface. *Elife* **10,** (2021).

64. Krycer, J. R., Fazakerley, D. J., Cater, R. J., C. Thomas, K., Naghiloo, S., Burchfield, J. G., Humphrey, S. J., Vandenberg, R. J., Ryan, R. M. & James, D. E. The amino acid transporter, <scp>SLC</scp> 1A3, is plasma membrane-localised in adipocytes and its activity is insensitive to insulin. *FEBS Lett* **591,** 322–330 (2017).

65. Yamada, N., Honda, Y., Takemoto, H., Nomoto, T., Matsui, M., Tomoda, K., Konno, M., Ishii, H., Mori, M. & Nishiyama, N. Engineering Tumour Cell-Binding Synthetic Polymers with Sensing Dense Transporters Associated with Aberrant Glutamine Metabolism. *Sci Rep* **7,** 6077 (2017).

66. Honda, Y., Nomoto, T., Takemoto, H., Matsui, M., Taniwaki, K., Guo, H., Miura, Y. & Nishiyama, N. Systemically Applicable Glutamine-Functionalized Polymer Exerting Multivalent Interaction with Tumors Overexpressing ASCT2. *ACS Appl Bio Mater* **4,** 7402–7407 (2021).

67. Leiske, M. N., Mazrad, Zihnil. A. I., Zelcak, A., Wahi, K., Davis, T. P., McCarroll, J. A., Holst, J. & Kempe, K. Zwitterionic Amino Acid-Derived Polyacrylates as Smart Materials Exhibiting Cellular Specificity and Therapeutic Activity. *Biomacromolecules* **23,** 2374–2387 (2022).

68. Leiske, M. N., De Geest, B. G. & Hoogenboom, R. Impact of the polymer backbone chemistry on interactions of amino-acid-derived zwitterionic polymers with cells. *Bioact Mater* **24,** 524–534 (2023).

69. Wu, J., Li, Z., Yang, Z., Guo, L., Zhang, Y., Deng, H., Wang, C. & Feng, M. A Glutamine-Rich Carrier Efficiently Delivers Anti-CD47 siRNA Driven by a "Glutamine Trap" To Inhibit Lung Cancer Cell Growth. *Mol Pharm* **15,** 3032–3045 (2018).

CHAPTER 10
Thesis Summary and Future Directions

10.1. Thesis Summary

The ultimate goal of this thesis was to engineer layer-by-layer nanoparticles (LbL-NPs) for the delivery of the potent immunostimulant IL-12 and to explore scalable production methods for NP-based drug delivery vehicles. We have advanced LbL-NPs' application in cancer immunotherapy and scalable production in the following directions:

On the scale-up side, we developed a scalable approach to generate lipidic adjuvant nanoparticles which has enabled Phase 1 clinical trials. With a similar approach, we discovered methods to control the shape and size of lipid-based nanocarriers. Lastly, we created a simple approach to rapidly and assemble LbL coatings on NPs at clinically relevant scales.

On the LbL-NP side, we discovered the mechanism of IL-12 delivery from LbL-NPs gaining key insights on how the LbL film and the liposomal NPs behave in physiological environments. Moreover, we discovered how the polymer conformation on the NP surface can regulate the exposure of the underlying lipids and conjugate cytokines which can hinder the delivery of IL-12. On the other hand, increasing film stability through higher molecular weight polymers yields LbL-NPs with increased cancer cell association and improved LbL-NP properties. Lastly, we discover the targets on cancer cells of anionic polyamino acid coatings on LbL-NPs.

10.2. Future Directions

Based on the advancements made, future work could focus on optimizing CND formulations and further exploring LbL-NPs for cytokine delivery. CNDs are promising drug delivery vehicles especially when combined with the LbL-NP coating. Thus, using LbL-CNDs as a platform for delivering lipid-conjugated therapeutics (such as small molecules or proteins) could yield meaningful improvements over current strategies. For example, one could use CNDs with surface conjugated IL-12 and coated with high molecular weight poly-L-arginine (PLR) and poly-L-glutamate for increased tumor penetration and association in disseminated ovarian cancer. Moreover, combining the IL-12 LbL-NPs with current standard-of-care chemotherapy regimens may yield improvements compared to the single treatment modalities. Future work may also explore the optimization of lipid composition to control the rate of IL-12 lipid conjugate release

from the LbL-NPs. Lastly, the known targets of PLE and PLD also allow for a more rational selection of cancer types that could yield efficient targeting from these coatings. Moreover, targeting these amino acid transporters could have benefits for the delivery of drugs inhibiting amino acid metabolism in cancer cells.

Appendix A

Table A1: RP-HPLC conditions and gradient.

Column	Jupiter C4		Accucore C8	
Column Temperature	40 °C		40 °C	
ELSD Temperature	40 °C		40 °C	
Aqueous Phase (A)	0.1% TFA Water		0.1 M TEAA Water	
Organic Phase (B)	0.1% TFA Acetonitrile		0.1 M TEAA 2-propanol	
Flow Rate	1 ml/min			
Gradient	Time	%B	Time	%B
	0	30	0	5
	5	30	5	5
	13	45	10	40
	17	45	15	40
	20	70	20	55
	27	85	30	55
	31	85	32.5	65
	41	95	36	65
	46	95	40	85
	47	30	45	85
	51	30	50	90
			70	95
			75	95
			75.05	5
			80	5

Table A2: Staggered dilution steps for QS-21 SMNP assembly.

Dilution Step	Dilution Factor Relative to Starting Material	Equilibration Time (min)
1	10X	10
2	25X	45
3	30X	20
4	35X	20
5	40X	10
6	45X	10
7	50X	10
8	60X	10
9	75X	10
10	85X	10
11	100X	10

Table A3: Critical Quality Attributes (CQAs) of SMNPs.

Appearance	Colorless to whitish, clear to slightly opalescent suspension
QS-21:cholesterol:DPPC:MPLA mass ratio	10 : 2 ± 0.3 : 1 ± 0.3 : 1 ± 0.3
Particle size (Z_{avg})	40 – 80 nm
Polydispersity index (PDI)	≤ 0.25
Residual MEGA-10	≤ 1 μg/mL
Particle morphology	Cage-like as characterized via negative stain TEM

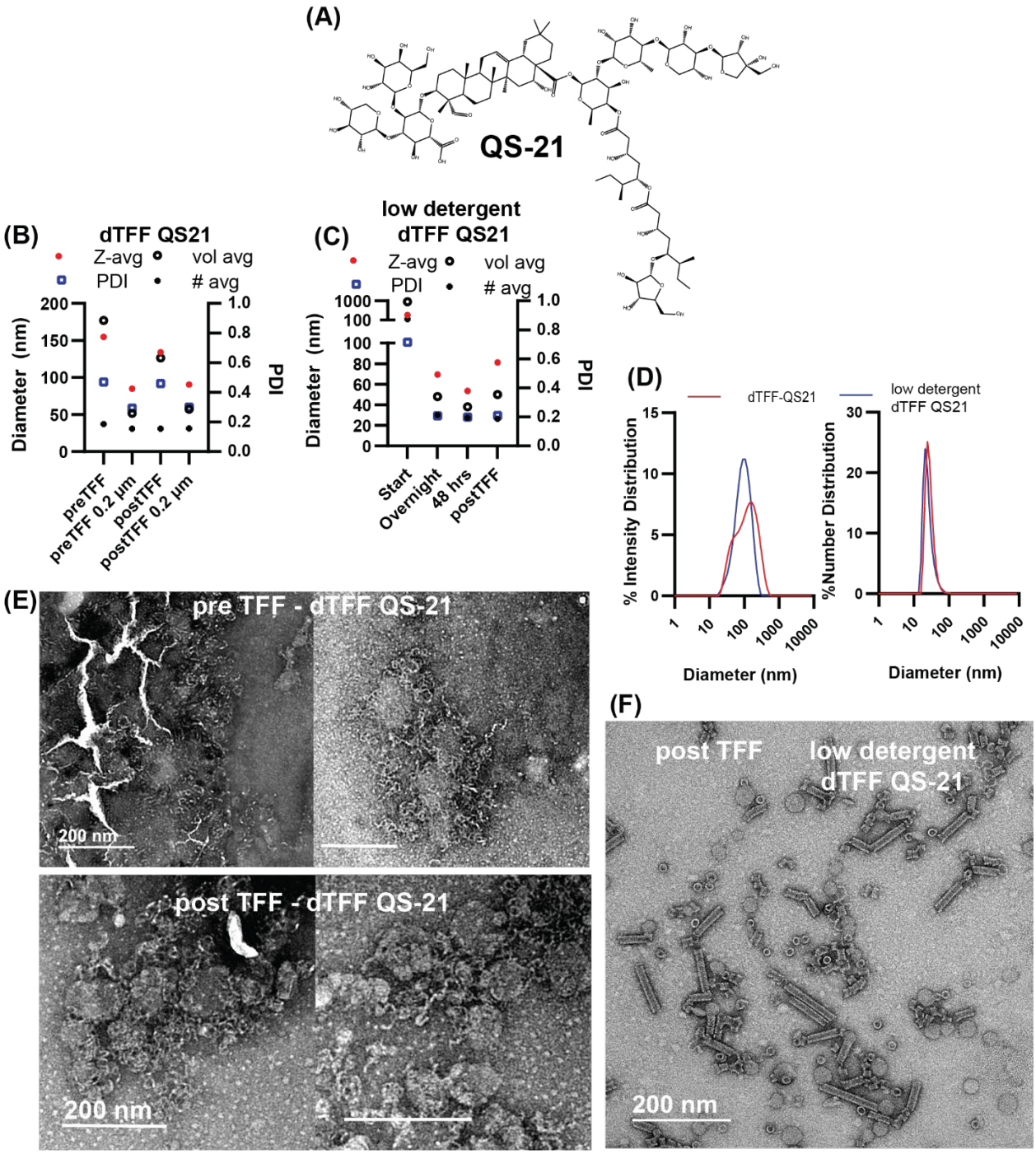

Figure A1: Protocols for generation of Quil-A based SMNPs fail to form ISCOMs when saponin is substituted for QS-21. (A) Chemical structure of the major isomer of QS-21. (B, C) DLS Z-avg, vol-avg, number-avg and PDI for attempts using dTFF (B) and low detergent dTFF (C) – error bars omitted for clarity. (D) DLS intensity-based and number-based distribution for standard dTFF and low detergent dTFF. (E) TEM micrographs of samples for standard dTFF

before (top) and after (bottom) TFF process. (F) TEM micrographs of final product from low detergent dTFF.

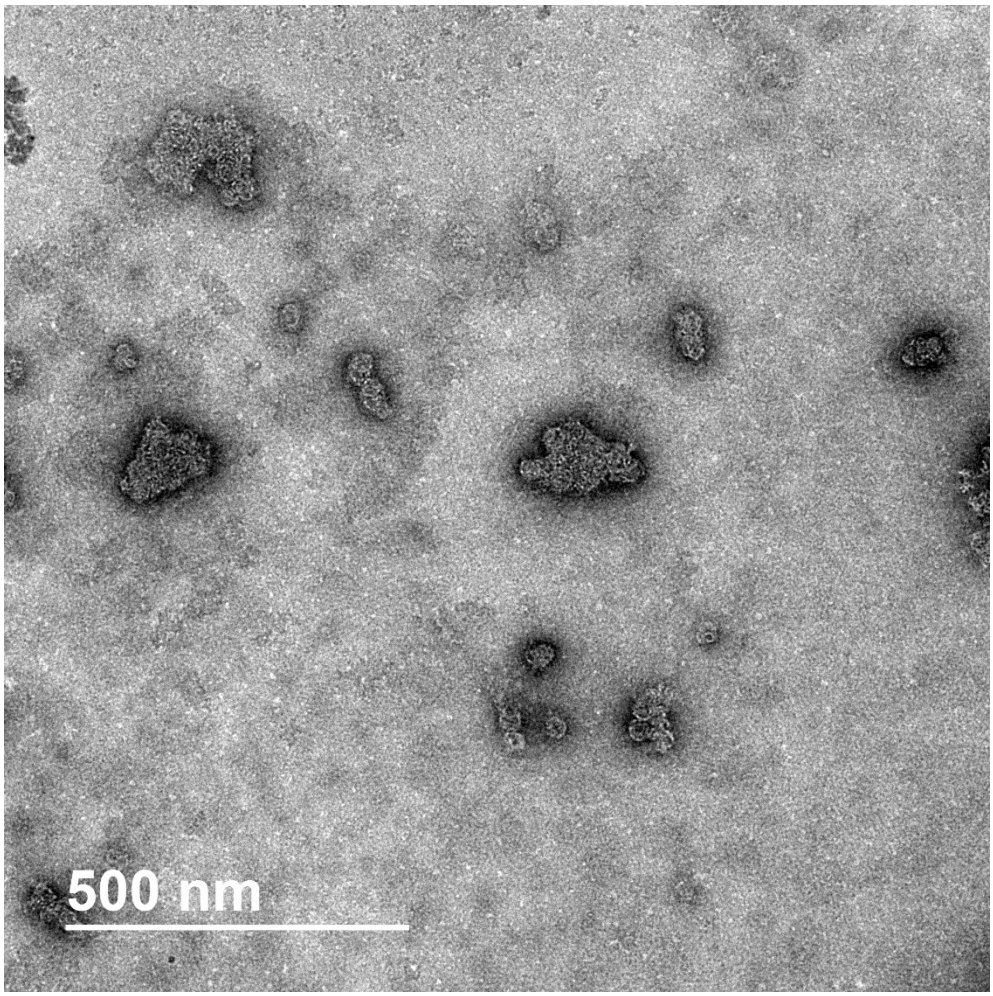

Figure A2: Rapid dilution of lipid/QS-21/MEGA-10 mixture enables formation of large aggregates. TEM micrograph of sample rapidly diluted to below CMC.

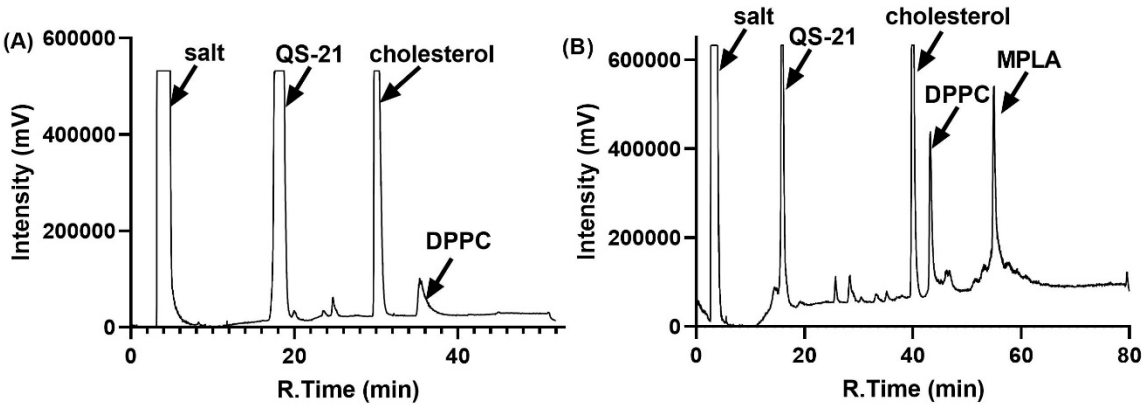

Figure A3: Reverse-phase (RP) high-pressure liquid chromatography (HPLC) coupled with a evaporative light scattering detector enables quantification of each component in QS-21 SMNPs. (A) Representative chromatogram of QS-21 SMNP particles separated on a Jupiter C4 column with acetonitrile gradient ranging from 30 to 95%. (B) Representative chromatogram of QS-21 SMNP particles separated on a Accucore C8 column with ispopropanol gradient ranging from 5 to 95%.

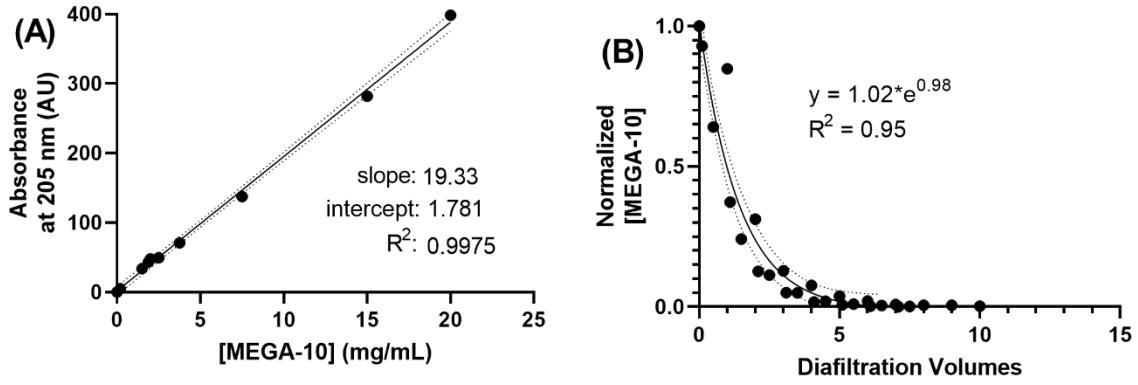

Figure A4: TFF with 100 kDa membranes is an effective method for removal of MEGA-10 from QS-21 SMNPs. (A) Standard curve generated based on MEGA-10 absorbance at 205 nm. (B) Concentration of MEGA-10 in permeate from three independent batches of QS-21 SMNPs. Dashed lines indicate 95% confidence interval from fitted curves.

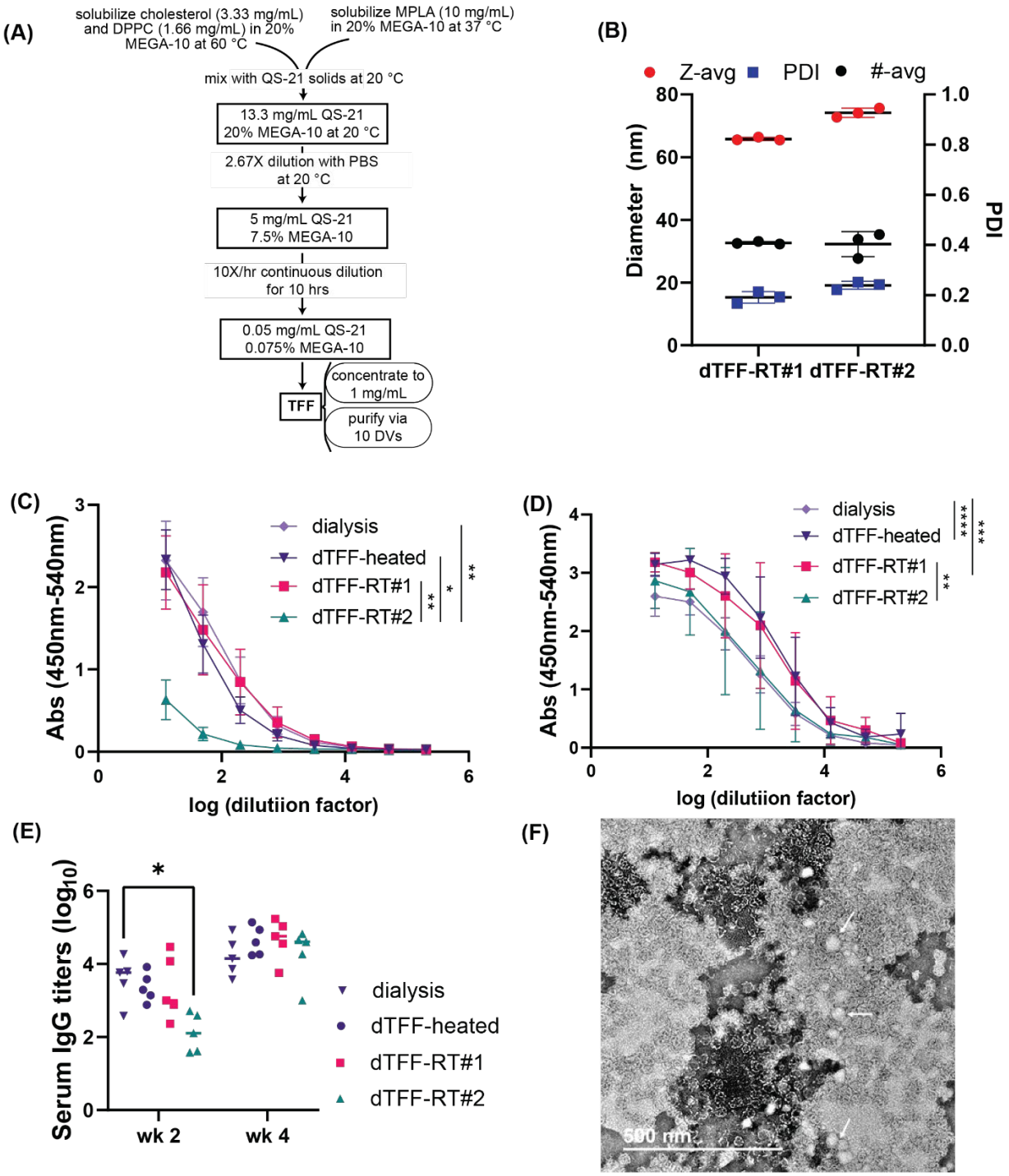

Figure A5: Room temperature (RT) QS-21 SMNPs can lead inhomogeneous preparations. (A) Diagram for QS-21 SMNP synthesis at room temperature (RT) through continuous dilution. (B) DLS Z-avg, and PDI for RT QS-21 SMNP samples from two independent batches. Serum IgG titer curves at week two (C) and week four (D) for particles generated via dialysis, dTFF with heating of QS-21 and two independent batches of dTFF SMNPs with QS-21 at room temperature

for mice immunized with 2 μg of N332-GT2 trimer and 5 μg of SMNP. (E) Summary of serum IgG titers at week 2 and 4 from (C) and (D). (F) TEM micrograph showing SMNPs generated at RT with presence of lipidic vesicles. White arrows indicate lipid nanoparticles.

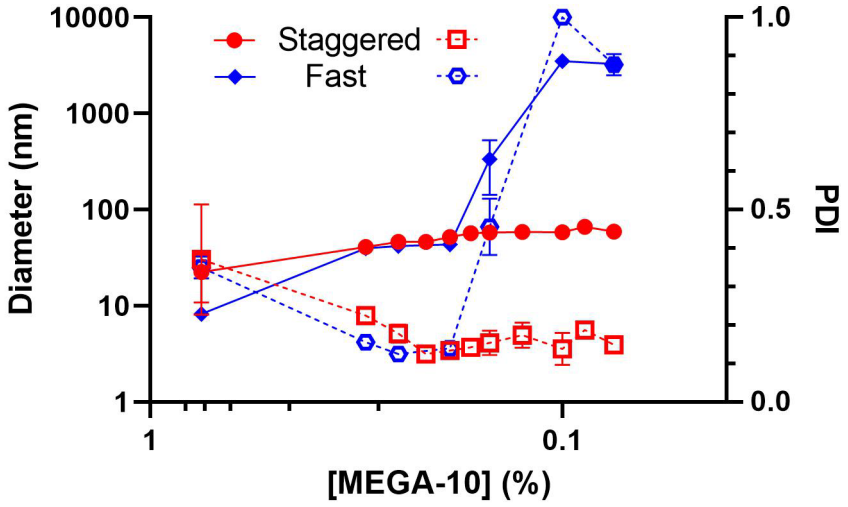

Figure A6: Staggered dilution enables proper assembly of QS-21 ISCOMs devoid of MPLA. A sample with 7.5% MEGA-10 and 5 mg/mL of QS-21-ISCOM components (QS-21, cholesterol and DPPC at a 5:1:1 mass ratio) was either rapidly diluted to final MEGA-10 concentrations or diluted via the staggered protocol of **Table S2.** DLS intensity-weighted size (Z-avg) and PDI were measured after overnight incubation for the fast diluted samples or after the appropriate incubation time for the staggered dilution protocol.

Appendix B

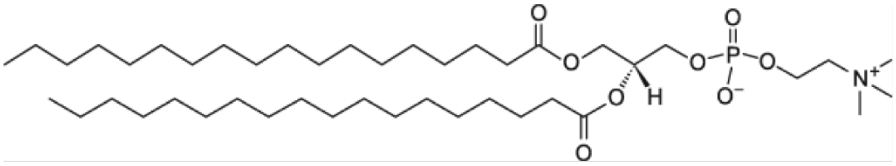

1,2-distearoyl-sn-glycero-3-phosphocholine (**DPSC**)

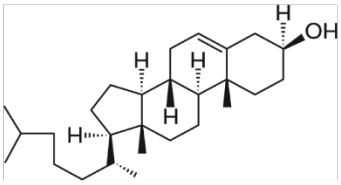

cholesterol

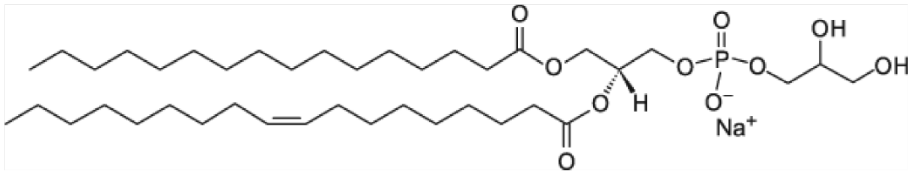

1-palmitoyl-2-oleoyl-sn-glycero-3-phospho-(1'-rac-glycerol) (sodium salt) (**POPG**)

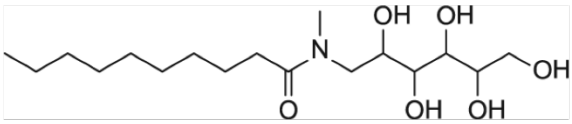

N-decanoyl-N-methylglucamine (**MEGA-10**)

Figure B1. The chemical structure of components used to generate liposomes from dilution.

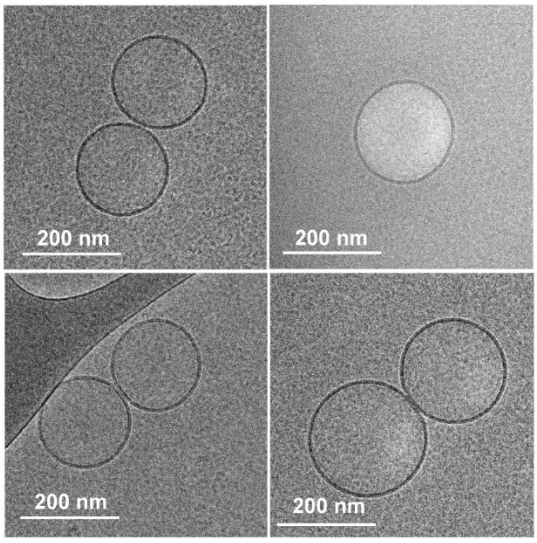

Figure B2. Representative cryo-TEM micrographs of 200 nm liposomes formed in region iii.

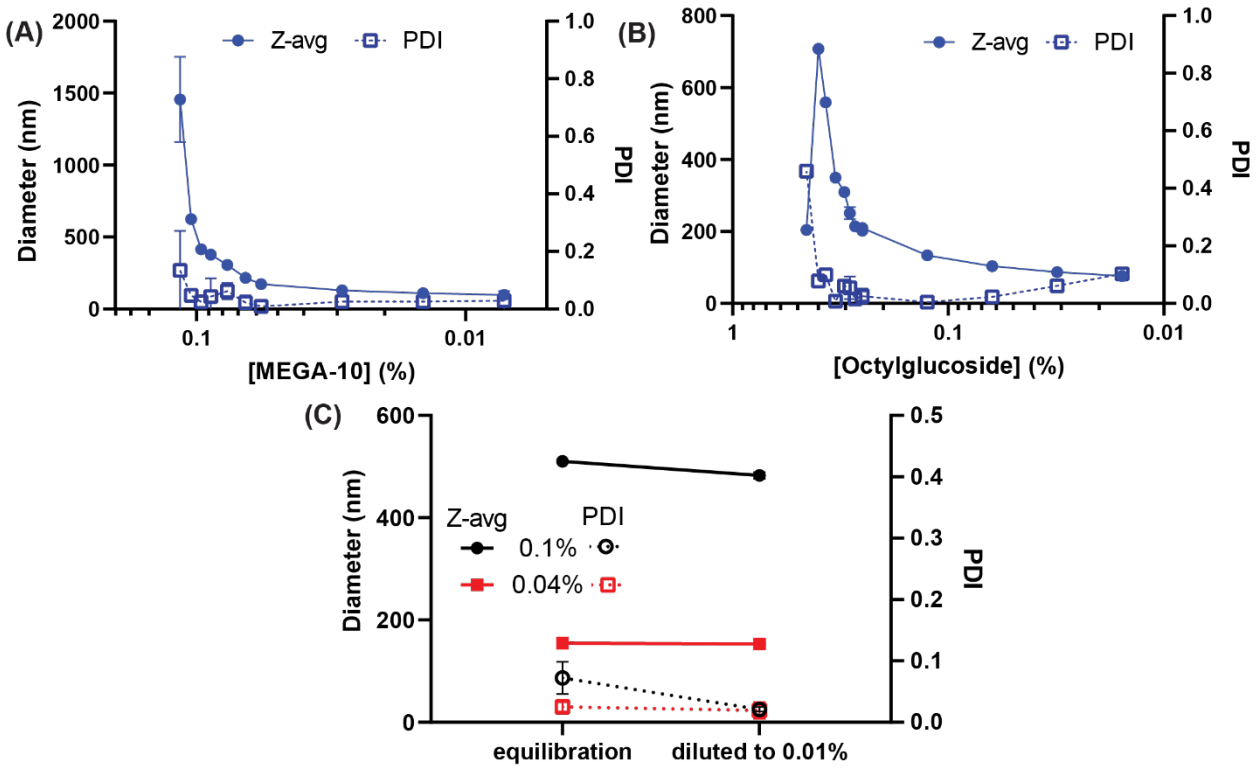

Figure B3. Detergent concentration after dilution controls the equilibrium size of liposomes. **(A)** DLS intensity-weighted size (Z-avg) and PDI after overnight incubation of a 10 mg/mL of 6:3:1 molar mixture of DSPC:cholesterol:POPG in 10% MEGA-10 diluted to various final detergent

concentrations. **(B)** DLS intensity-weighted size (Z-avg) and PDI after overnight incubation of a 20 mg/mL of 6:3:1 molar mixture of DSPC:cholesterol:POPG in 10% octylglucoside diluted to various final detergent concentrations. **(C)** Effect of dilution samples equilibrated at 0.1% or 0.04% MEGA-10 overnight to 0.01% MEGA-10 on particle size (Z-avg) and PDI; samples were allowed to equilibrate at 0.01% overnight.

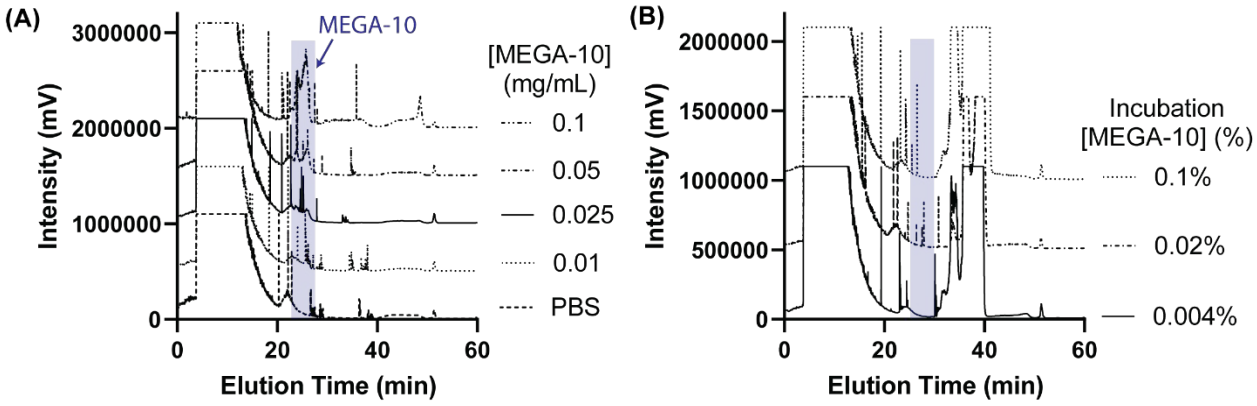

Figure B4. TFF of assembled lipid vesicles enables efficient removal of MEGA-10. **(A)** ELSD chromatogram of MEGA-10 at increasing concentrations. **(B)** ELSD of final purified particles incubated at either 0.1%, 0.02%, or 0.004% MEGA-10. Shaded regions indicate MEGA-10 elution times.

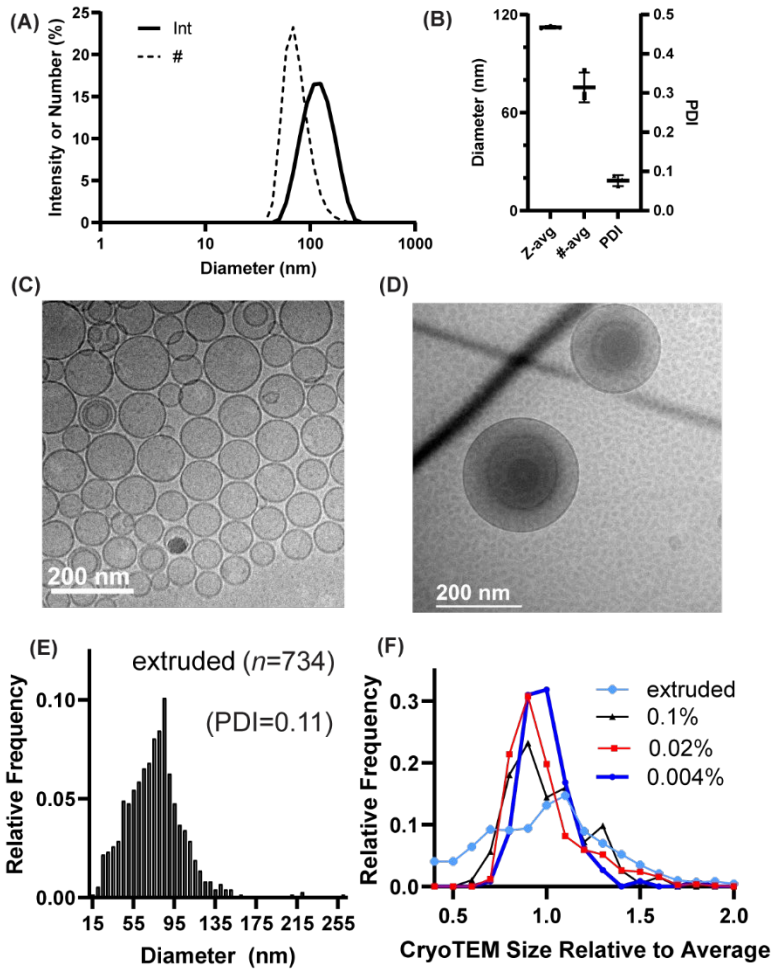

Figure B5. Characteristics of liposomes generated from lipid film hydration followed by extrusion with a 50 nm pore sized membrane. **(A)** DLS intensity-based and number-based size distribution. **(B)** Z-avg, number-average, and PDI. **(C)** Representative cryoTEM micrograph from liposomes generated via thin film hydration followed by extrusion on a 50 nm pore-sized membrane. **(D)** CryoTEM micrograph of extruded liposomes showing large (>50 nm) vesicles. **(E)** CryoTEM micrograph analysis of particle size from the extruded sample. Parenthesis indicates the total number of particles quantified and PDI based on the measured particle sizes from cryoTEM. **(F)** Normalized histograms of samples generated from detergent dilution into 0.1%, 0.02%, and 0.004% MEGA-10 then purified via TFF compared to liposomes generated via thin-film hydration followed by extrusion through 50 nm pore membrane.

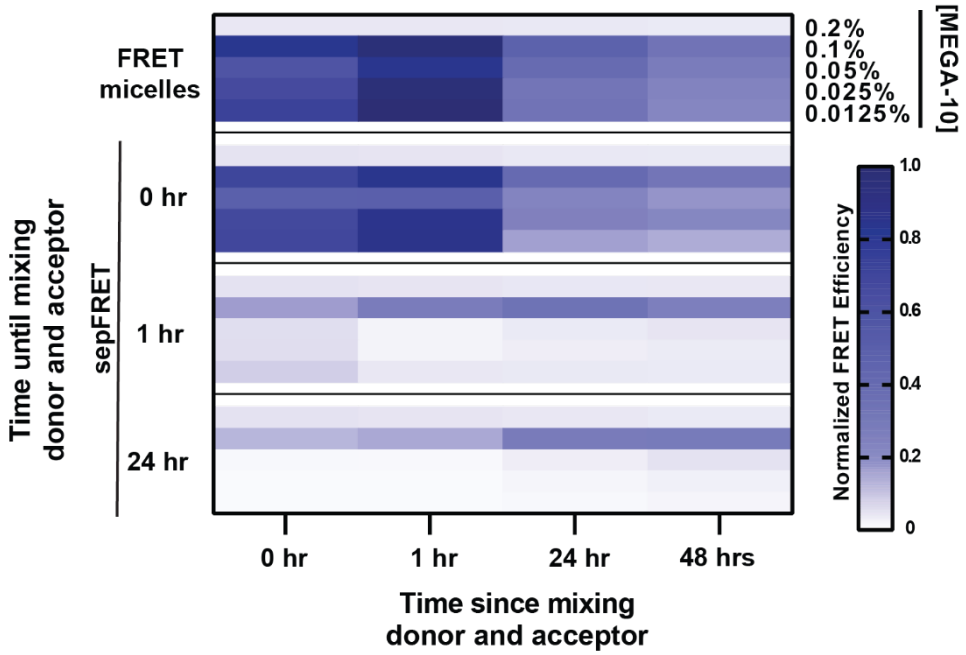

Figure B6. Analysis of lipid exchange via FRET reveals that assembled liposomes in region iv are stable whereas particles in region iii have high rates of lipid exchange even after no change in particle size. Normalized FRET efficiency from samples containing 1mol% of dye diluted with PBS to various concentrations of MEGA-10 and mixed after set incubation periods.

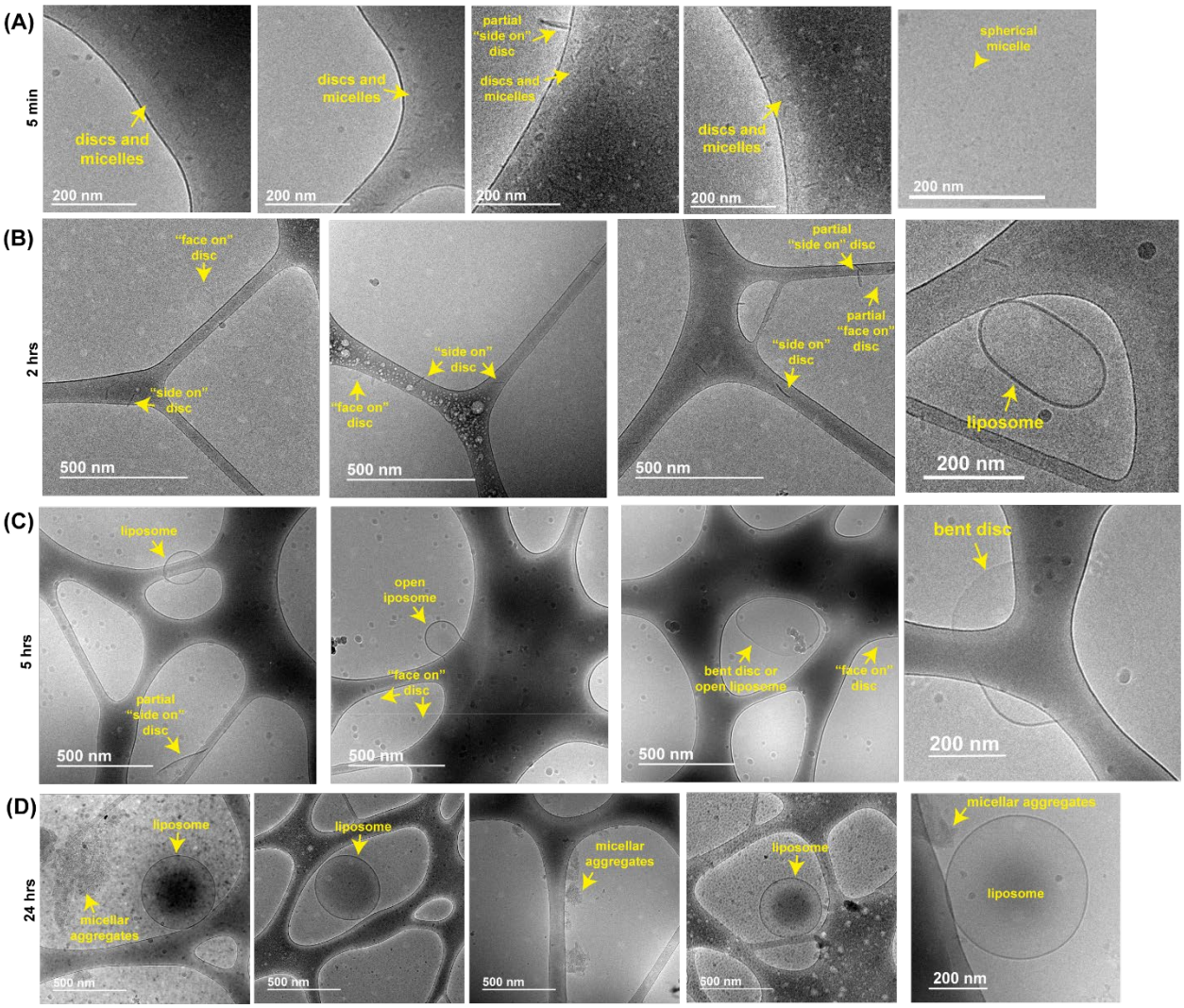

Figure B7. Assessment of liposome assembly via cryo-TEM. **(A-D)** Cryo-TEM micrographs of 10 mg/mL 6:3:1 DSPC:Chol:POPG sample in 10% MEGA-10 rapidly diluted to 0.1% MEGA-10 with 10 mM HEPES 150 mM NaCl and frozen 5 minutes, 2 hours, 5 hours and 24 hours after dilution, respectively.

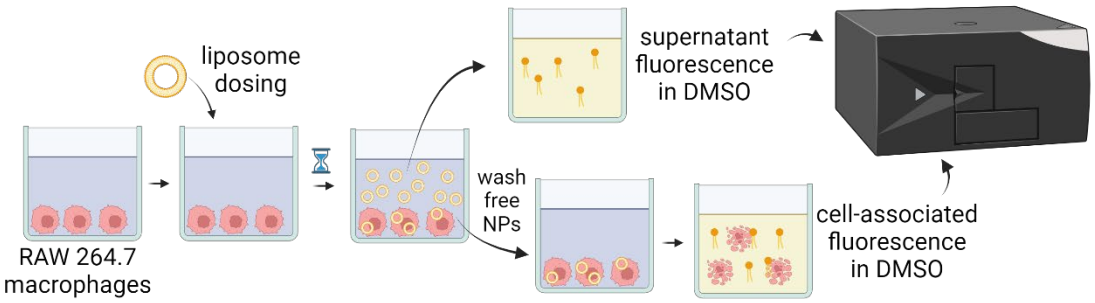

Figure B8. Diagram of the experimental protocol to determine the percentage of liposome fluorescence associated with macrophages.

Appendix C

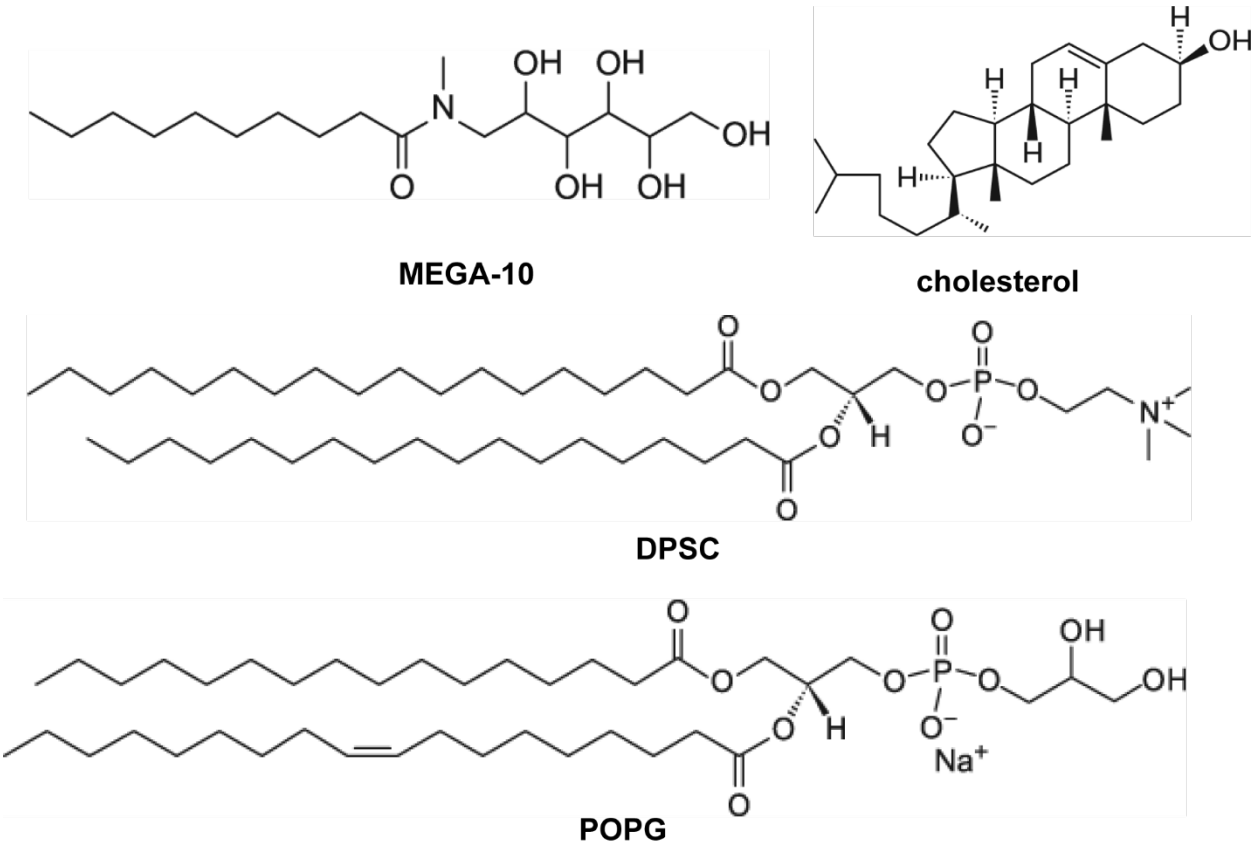

Figure C1. Chemical structure of components used for particle self-assembly.

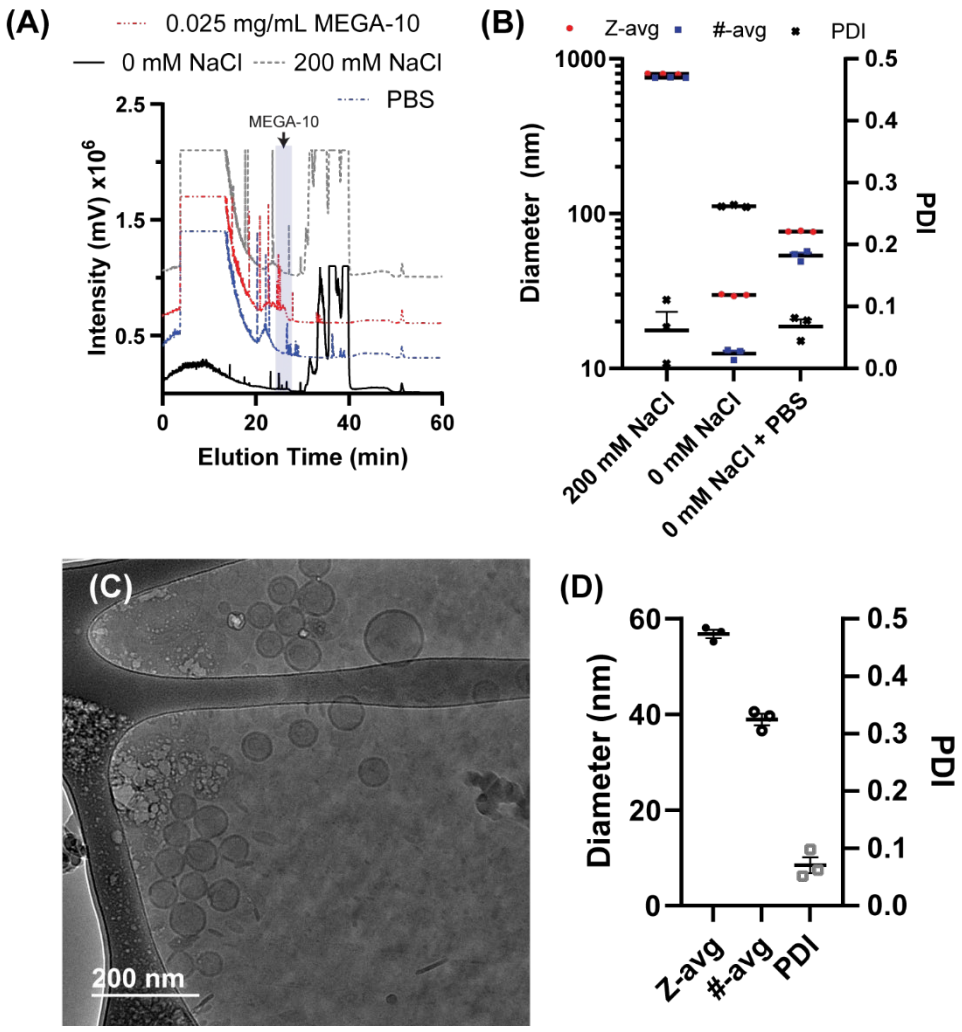

Figure C2. Characterization of lisCNDs and high POPG composition diluted with PBS. (A) Representative chromatograms from high-pressure liquid chromatography (HPLC) coupled with an evaporative light scattering detector (ELSD) for PBS only, 0.025 mg/mL sample in PBS, and samples allowed to be assembled at 0.1% MEGA-10 in 0 mM NaCl or 200 mM NaCl buffers then purified via TFF. **(B)** Z-avg, #-avg and PDI of purified samples allowed to assemble at 0.1% MEGA-10 in 200 mM NaCl, 0 mM NaCl, or 0 mM NaCl then exposed to 1X PBS after purification. **(C)** CryoTEM micrographs of purified samples from dilution of lipid/detergent micelles using 0 mM NaCl, but then added 1X PBS. **(D)** Size and PDI of lipid/detergent micelles

with 3:3:4 molar ratios of DSPC:cholesterol:POPG diluted to 0.05% MEGA-10 then purified via TFF. Error bars represent SEM.

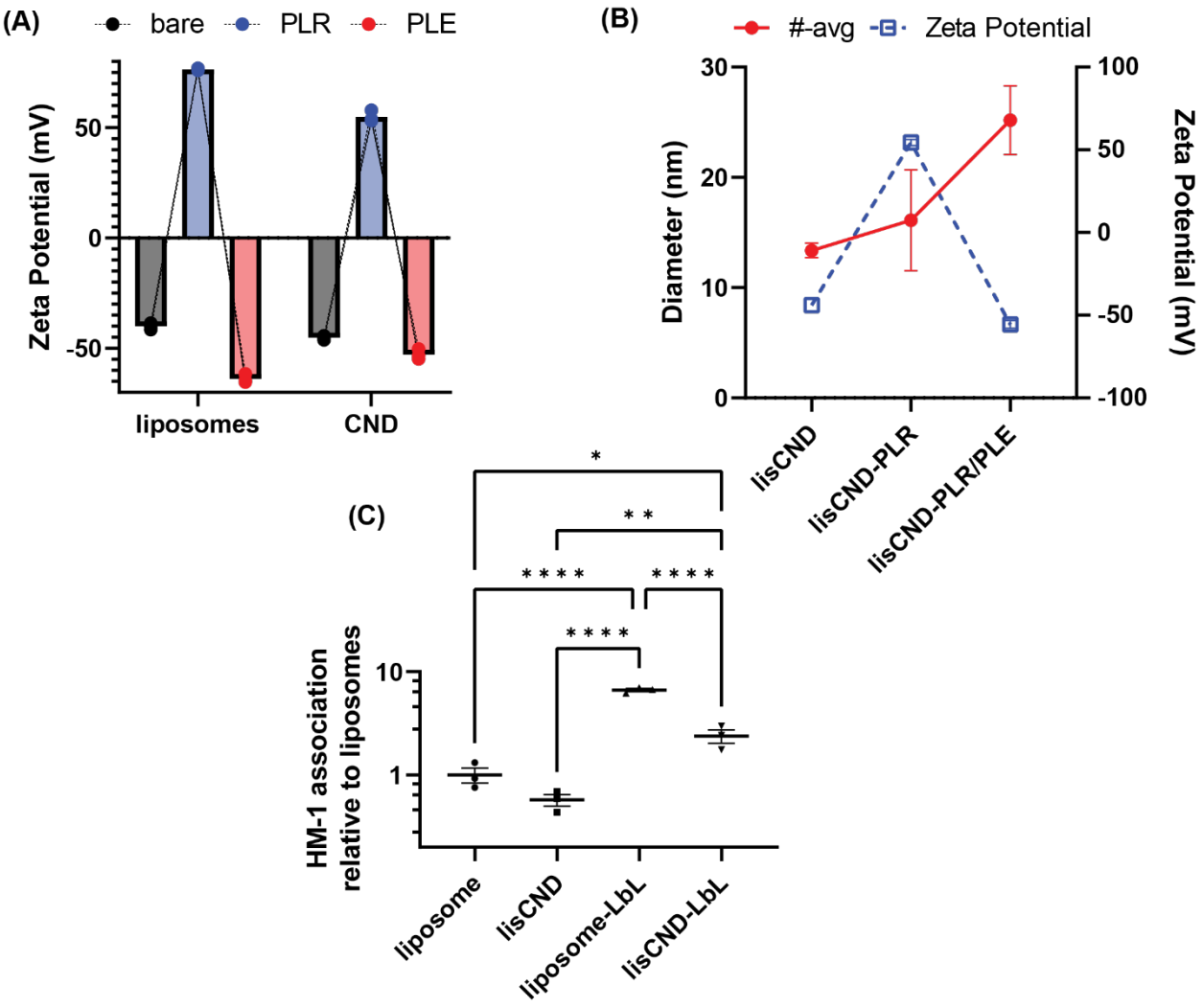

Figure C3. Characteristics of LbL-CNDs and LbL-lisCNDs. (A) Zeta potential of liposomes and CNDs upon layering with PLR and PLE. **(B)** Size and zeta potential of lisCNDs upon layering with PLR and PLE. **(C)** In vitro HM-1 association of NPs relative to liposomes 24 hrs after dosing cells. Error bars represent SEM. Statistical comparisons in C was performed using one-way analysis of variance (ANOVA) with Tukey's multiple-comparisons test. Asterisks denote p-values: ****$p < 0.0001$, ***$p < 0.001$, **$p < 0.01$, *$p < 0.05$.

Appendix D

Table D1: Lipid composition of nanoparticles and summary characteristics.

Lipid or trait	Nickel-headgroup	Maleimide-headgroup
DSPC; 1,2-distearoyl-sn-glycero-3-phosphocholine	65 mol%	65 mol%
Cholesterol	23.9 mol%	23.9 mol%
POPG; 1-palmitoyl-2-oleoyl-sn-glycero-3-phospho-(1'-rac-glycerol) (sodium salt)	6.1 mol%	6.1 mol%
18:1 DGS-NTA(Ni); 1,2-dioleoyl-sn-glycero-3-[(N-(5-amino-1-carboxypentyl)iminodiacetic acid)succinyl] (nickel salt)	5 mol%	0 mol%
18:1 MPB-PE; 1,2-dioleoyl-sn-glycero-3-phosphoethanolamine-N-[4-(p-maleimidophenyl)butyramide] (sodium salt)	0 mol%	5 mol%
Diameter (Z-avg) unlayered (UL)	86.3 nm	87.7 nm
Diameter (#-avg) unlayered (UL)	60.2 nm	57.8 nm
PDI unlayered (UL)	0.08	0.14
Zeta potential unlayered (UL)	-58 mV	-63 mV
Diameter (Z-avg) PLR-PLE (LbL)	121.3 nm	122.5 nm
Diameter (#-avg) PLR-PLE (LbL)	84.7 nm	81.2 nm
Zeta potential PLR-PLE (LbL)	-63 mV	-63 mV
PDI PLR-PLE (LbL)	0.11	0.13

Table D2: Lipid composition of SAT NPs.

Lipid	SAT NPs (mol%)
DSPC; 1,2-distearoyl-sn-glycero-3-phosphocholine	65%
Cholesterol	23.9%
DSPG; 1,2-distearoyl-sn-glycero-3-phospho-(1'-rac-glycerol) (sodium salt)	6.1%
16:0 MPB-PE; 1,2-dipalmitoyl-sn-glycero-3-phosphoethanolamine-N-[4-(p-maleimidophenyl)butyramide] (sodium salt)	5%

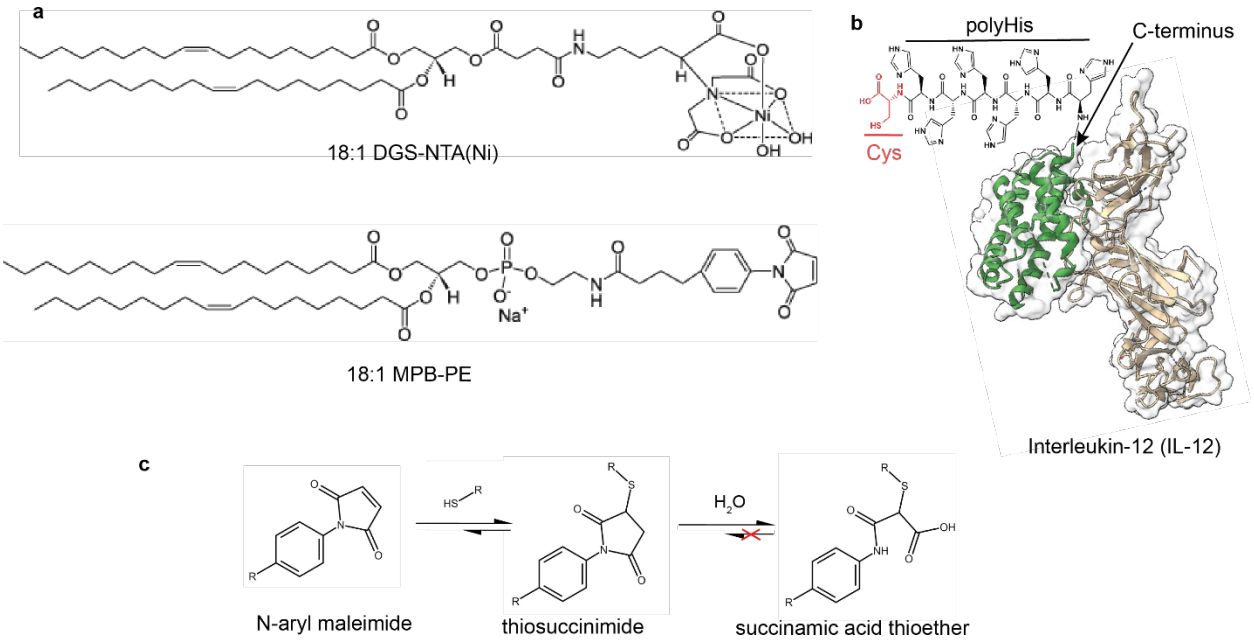

Figure D1. Headgroup-modified lipids for IL-12 conjugation. a, Chemical structure of headgroup-modified lipids with either chelated nickel or N-aryl maleimide. N-aryl maleimide was employed to prevent potential thiosuccinimide retro-Michael addition and subsequent thiol-exchange, as this headgroup favors thiosuccinimide hydrolysis into sTable Duccinamic acid thioethers. **b**, IL-12 crystal structure derived from PDB 1F45 showing C-terminus used to engineered terminal poly-histidine (polyHis) tag and terminal cysteine. **c,** Reaction pathway for irreversible maleimide-based conjugation with thiols.

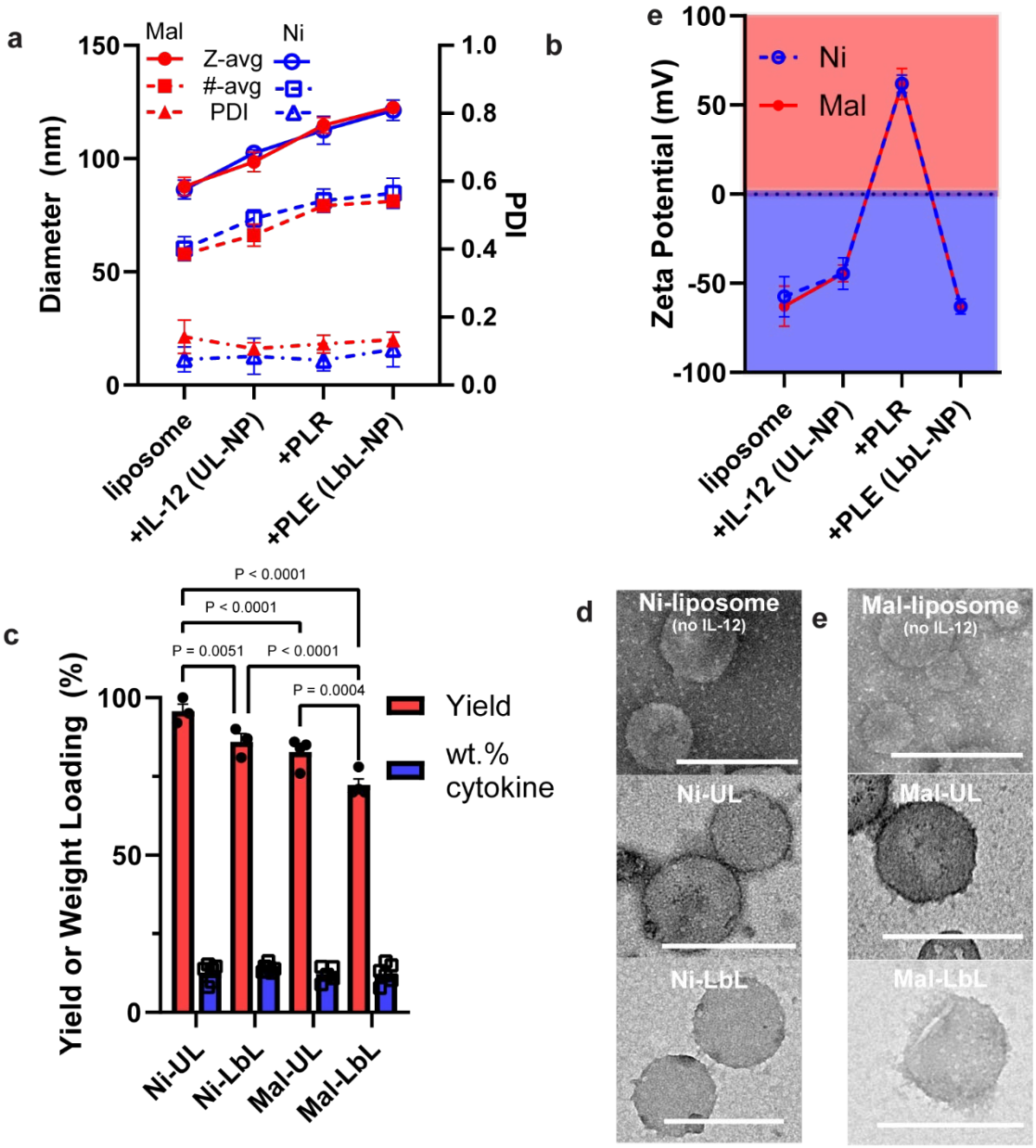

Figure D2. Synthesis of LbL-NPs conjugated with IL-12 via either maleimide-cysteine reaction or nickel-histidine interaction yield similar particle biophysical properties. a, Intensity-weighted hydrodynamic size (Z-avg), number average size (#-avg), and polydispersity index (PDI) of NPs during synthesis as measured via dynamic light scattering (mean ± s.d.). **b,** Zeta potential of NPs during synthesis as measured via electrophoretic mobility in deionized water (mean ± s.d.). **c,** Yield and weight loading of IL-12 for unlayered and layered particles with nickel-histidine linker (Ni-UL and Ni-LbL) and unlayered and layered particles with a maleimide-cysteine bond (Mal-UL and Mal-LbL) (mean ± s.e.m.). **d-e,** Negative-stain (NS) transmission electron microscopy (TEM) with phosphotungstic acid of particles during synthesis with nickel-containing lipids (**d**) and maleimide-containing lipids (**e**) - scale bars represent 200 nm. Unlayered (UL) NPs without IL-12 presented the typical low-contrast micrographs of liposomes. When conjugated with IL-12, however, a dark rim around the liposomes could be observed which became diffuse after LbL deposition, suggesting successful IL-12 conjugation and LbL coating. Data are presented as

mean values ± error with $n = 3$ independent batches of NPs. Statistical comparisons in **c** were performed using two-way analysis of variance (ANOVA) with Tukey's multiple-comparisons test.

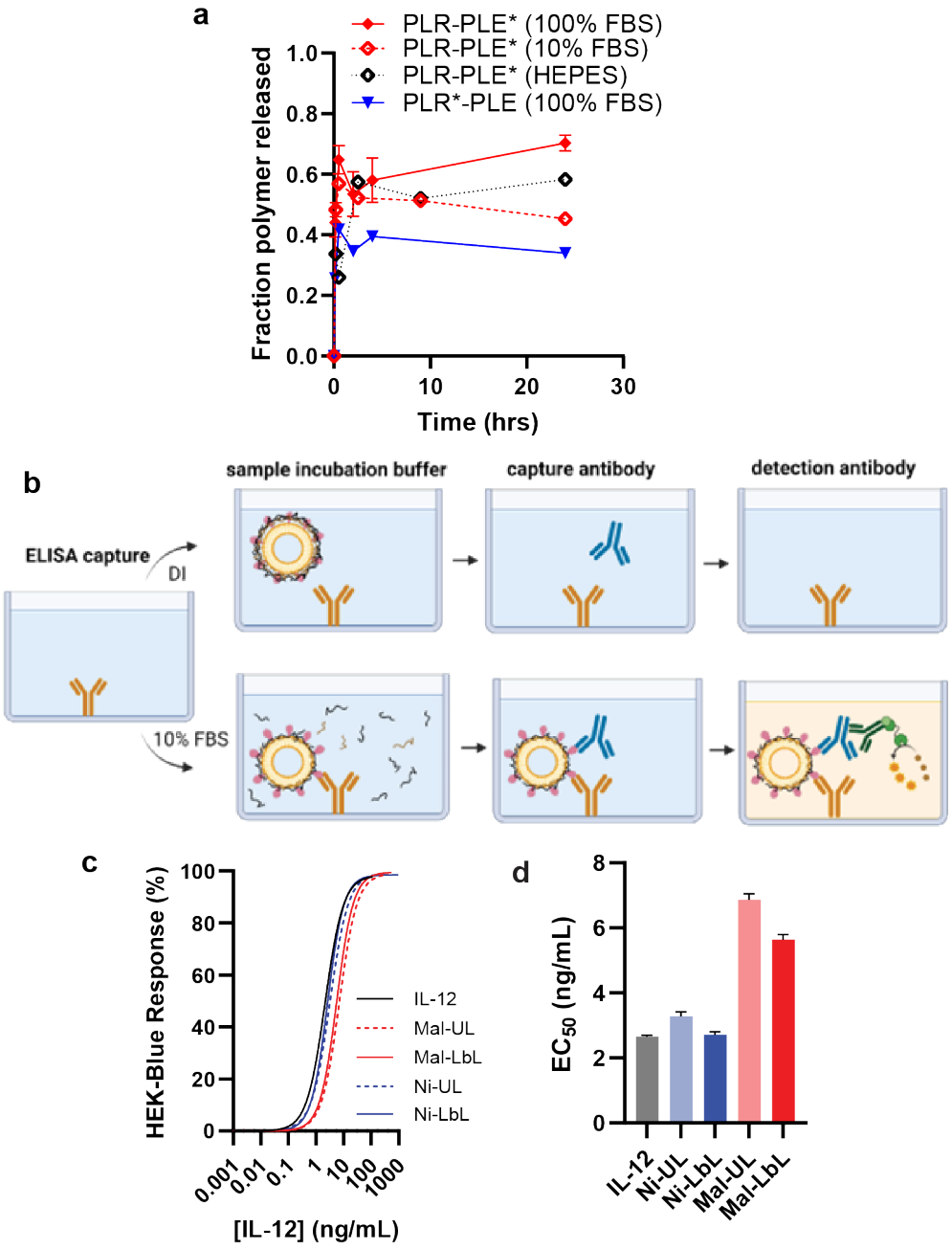

Figure D3. Polyelectrolyte film is partially released in buffers with physiological ionic strength and does not block IL-12 availability in LbL-NPs. A, Measurement of PLE or PLR release from LbL film on NPs incubated at 37 °C in 15 mM HEPES 150 mM NaCl (HEPES), 10%, or 100% FBS (mean ± s.e.m). **b,** Schematic for monoclonal antibody capture of NP-bound IL-12 and detection in varying buffer conditions. **c,** HEK-Blue IL-12 reporter cell line response to IL-12 in various formats (n>100 points per curve from 7 independent particle batches). (**d**) Calculated IL-12 EC_{50} from HEK-Blue IL12 response curves (mean ± s.e.m).

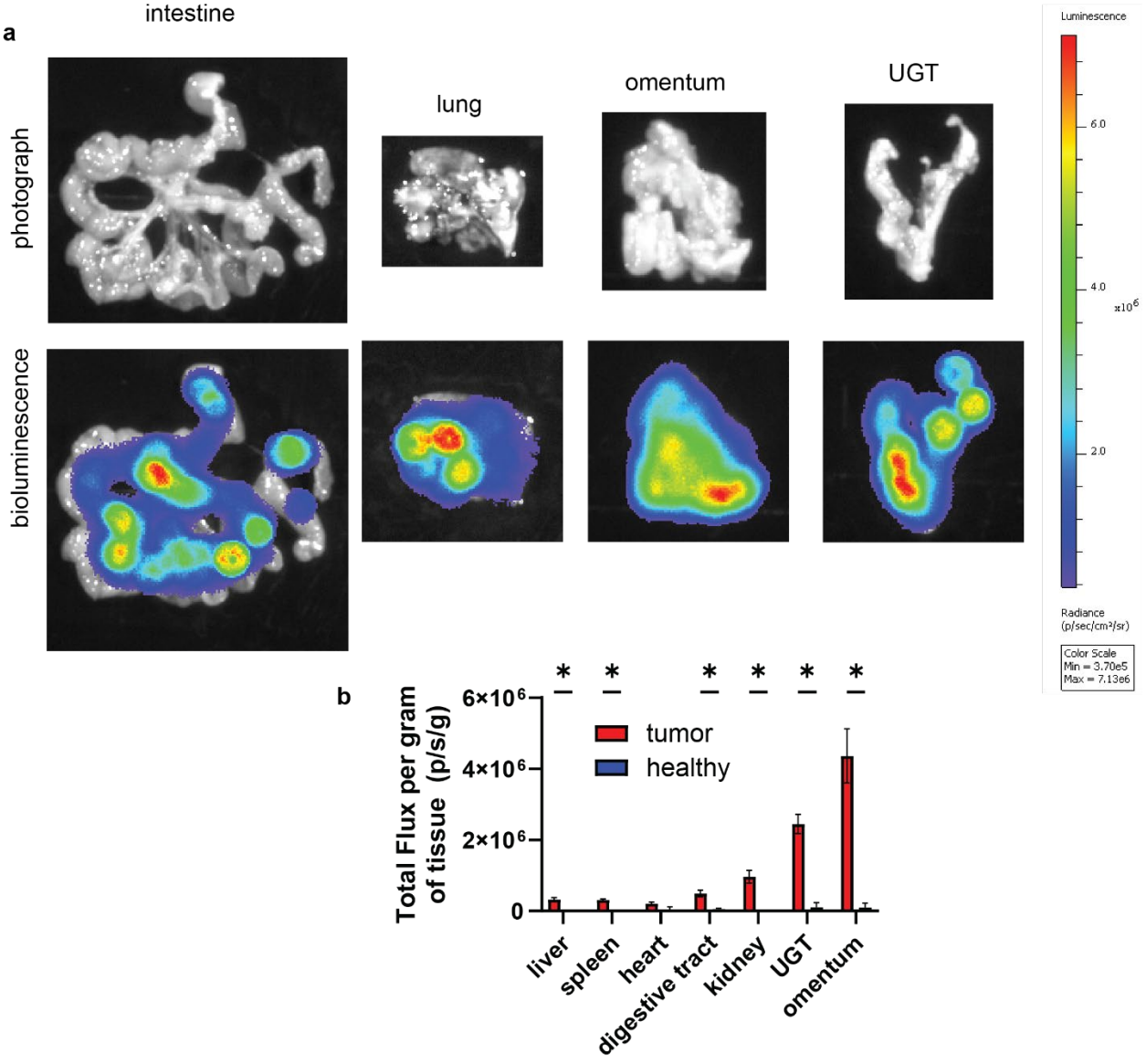

Figure D4. Characterization of metastatic ovarian cancer model - OV2944-HM1. **a-b,** B6C3F1 mice were inoculated with 10^6 HM-1-luc tumor cells i.p. on day 0 (n = 40) or left as naïve healthy animals (n = 10). Shown are representative, intestine, lung, omentum and UGT ex-vivo IVIS BLI images (**a**) and quantitation of BLI signal in healthy organs compared to organs two weeks after tumor inoculation (mean ± s.e.m, **b**). Statistical comparisons in **b** were performed using the nonparametric Mean-Whitney test with correction for multiple comparisons based on a false discovery rate of 1% (q=0.0136).

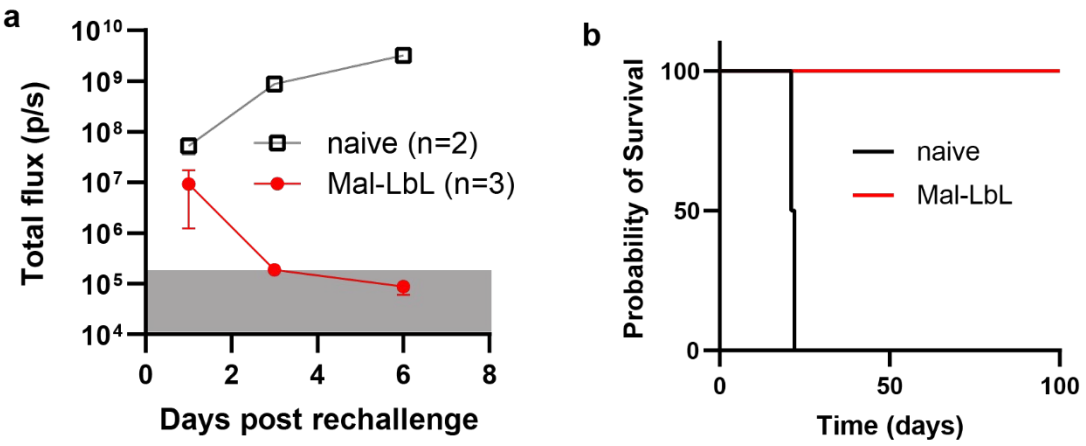

Figure D5. Mice with complete remission of metastatic ovarian cancer demonstrate strong immune memory induction upon i.p. luc-HM-1 rechallenge. a-b, B6C3F1 mice (n = 10/group) inoculated with 10^6 HM-1-luc tumor cells on day 0 were treated on days 7 and 14 with 20 µg of IL-12 as a free cytokine or conjugated to NPs. On day 100, surviving Mal-LbL mine (n = 3) or naïve (n = 2) were injected with $3x10^5$ luc-HM-1 cells i.p. Shown are in vivo IVIS whole-animal i.p. BLI readings (mean ± s.e.m., **b**), and overall survival (**c**).

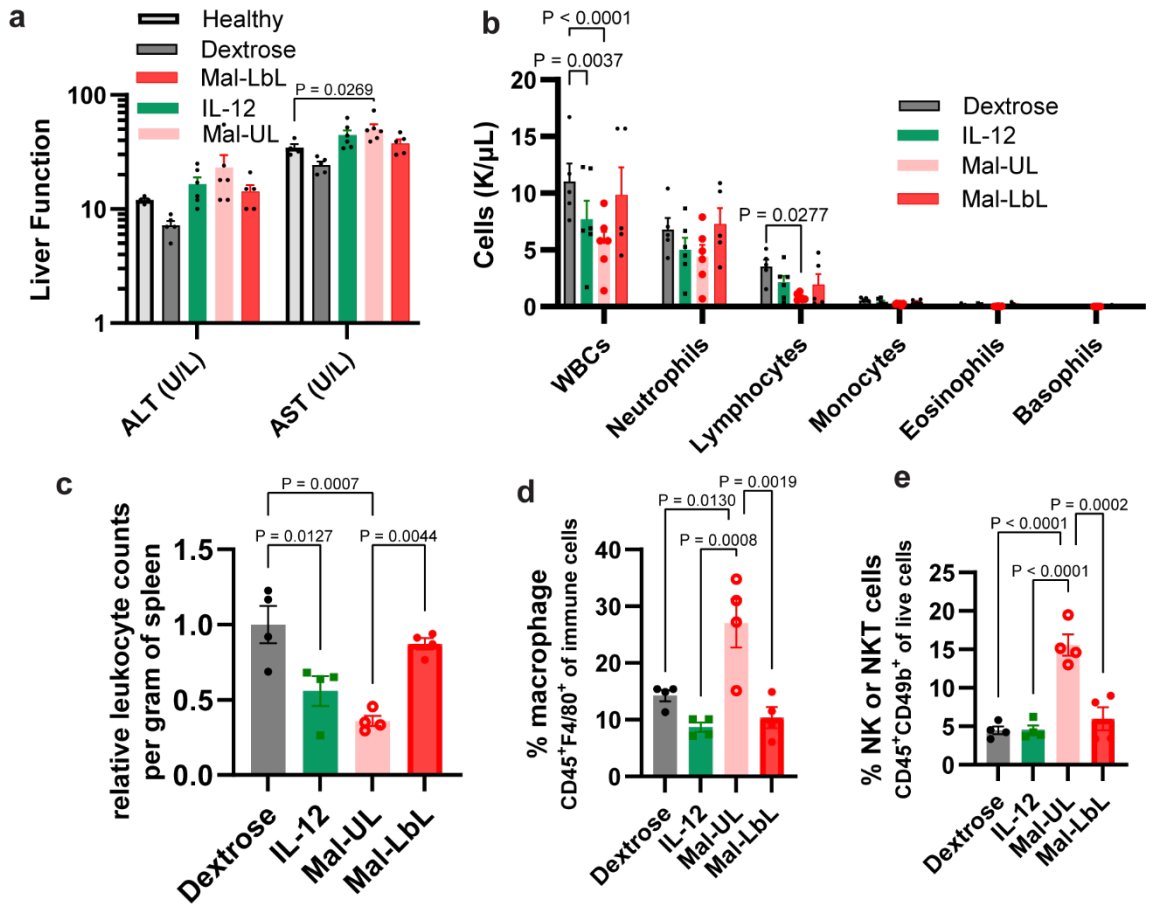

Figure D6. Intraperitoneal dosing of 20 µg of Mal-LbL NPs does not cause systemic toxicity. a-e, B6C3F1 mice inoculated with 10^6 HM-1 tumor cells on day 0 were treated on days 10 with 20 µg of IL-12 as a free cytokine or conjugated to Mal NPs (UL and LbL). Two days after dosing blood (n = 6/group) and spleens (n = 4/group) were harvested and sent for a complete blood panel or processed for flow cytometry analysis, respectively. Shown are serum levels of liver damage markers (alanine transaminase – ALT - and aspartate aminotransferase - AST) compared to healthy mice controls (n = 4, **a**), complete blood count panel (**b**), quantitation of live leukocyte ($CD45^+$) counts in spleen (**c**), and percentage of macrophage (**d**) and NK (**e**) cell in splenocytes. Statistical comparisons performed using two-way (**a,b**) or one-way (**c,d,e**) analysis of variance (ANOVA) with Tukey's multiple-comparisons (liver enzyme measurement was compared to healthy controls).

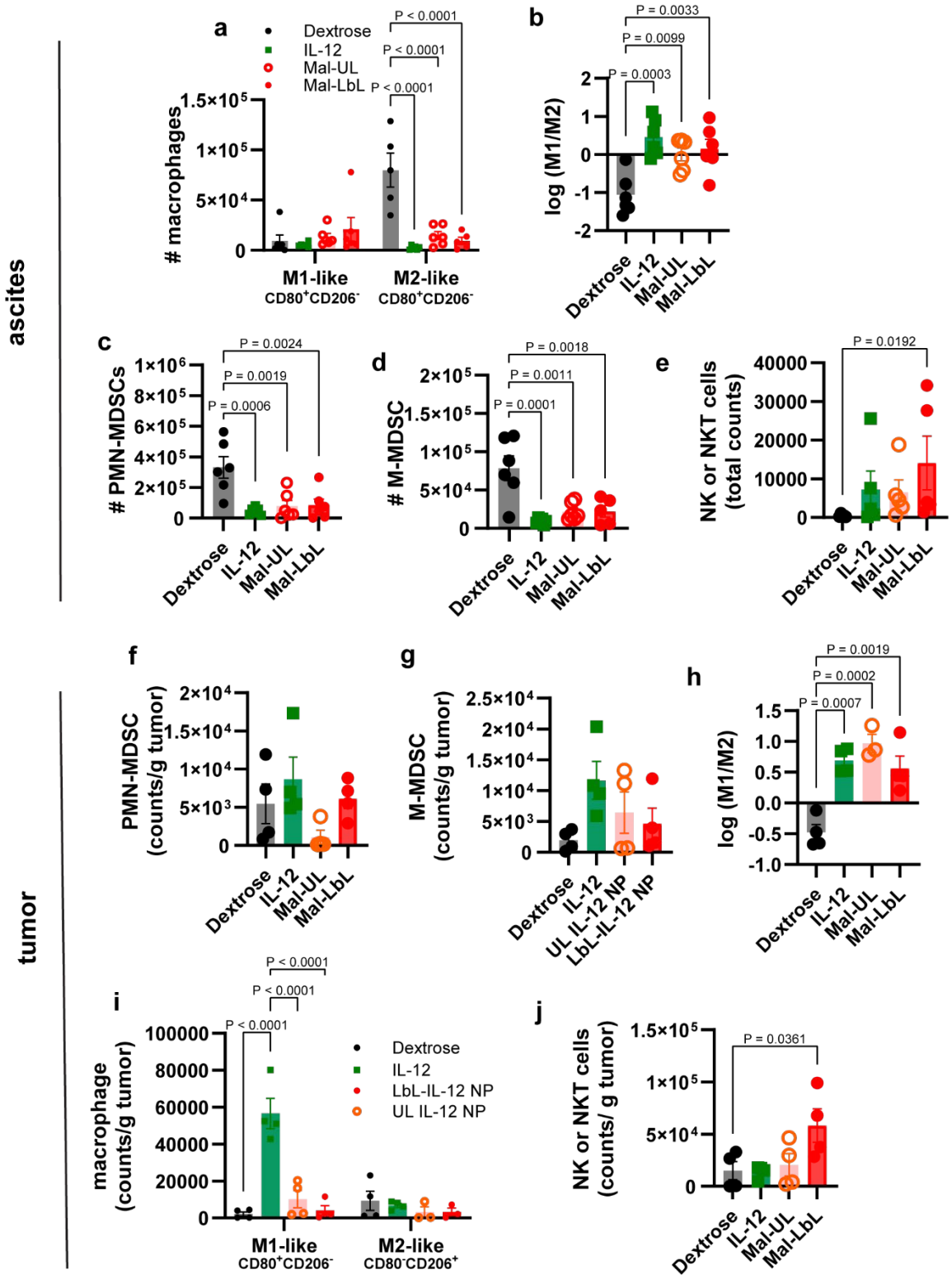

Figure D7. Immune phenotyping of cells in ascites fluid and tumor tissues. a-j, B6C3F1 mice inoculated with 10^6 HM-1 tumor cells on day 0 were treated on days 10 with 20 µg of IL-12 as a free cytokine or conjugated to Mal NPs (UL and LbL). Two days after dosing ascites (n = 6/group) and i.p. tumor nodules (primarly omentum tissue, n =

4/group) were harvested and processed for flow cytometry analysis. Shown are total counts of M1-like and M2-like macrophages **(a)**, logarithmic of M1-like to M2-like macrophages ratio (**b**), and total counts of PMN-MDSC (**c**), M-MDSC (**d**), and NK cells (**e**) in ascites fluid. Also shown are total counts of PMN-MDSC (**f**) and M-MDSC (**g**), logarithmic of M1-like to M2-like macrophages ratio (**h**), and total counts of M1-like and M2-like macrophages (**i**), and NK cells (**j**) in tumor nodules. Statistical comparisons were performed using two-way (**a,i**) or one-way (**b,c,d,e,h,j**) analysis of variance (ANOVA) with Tukey's multiple comparisons (liver enzyme measurement was compared to healthy controls).

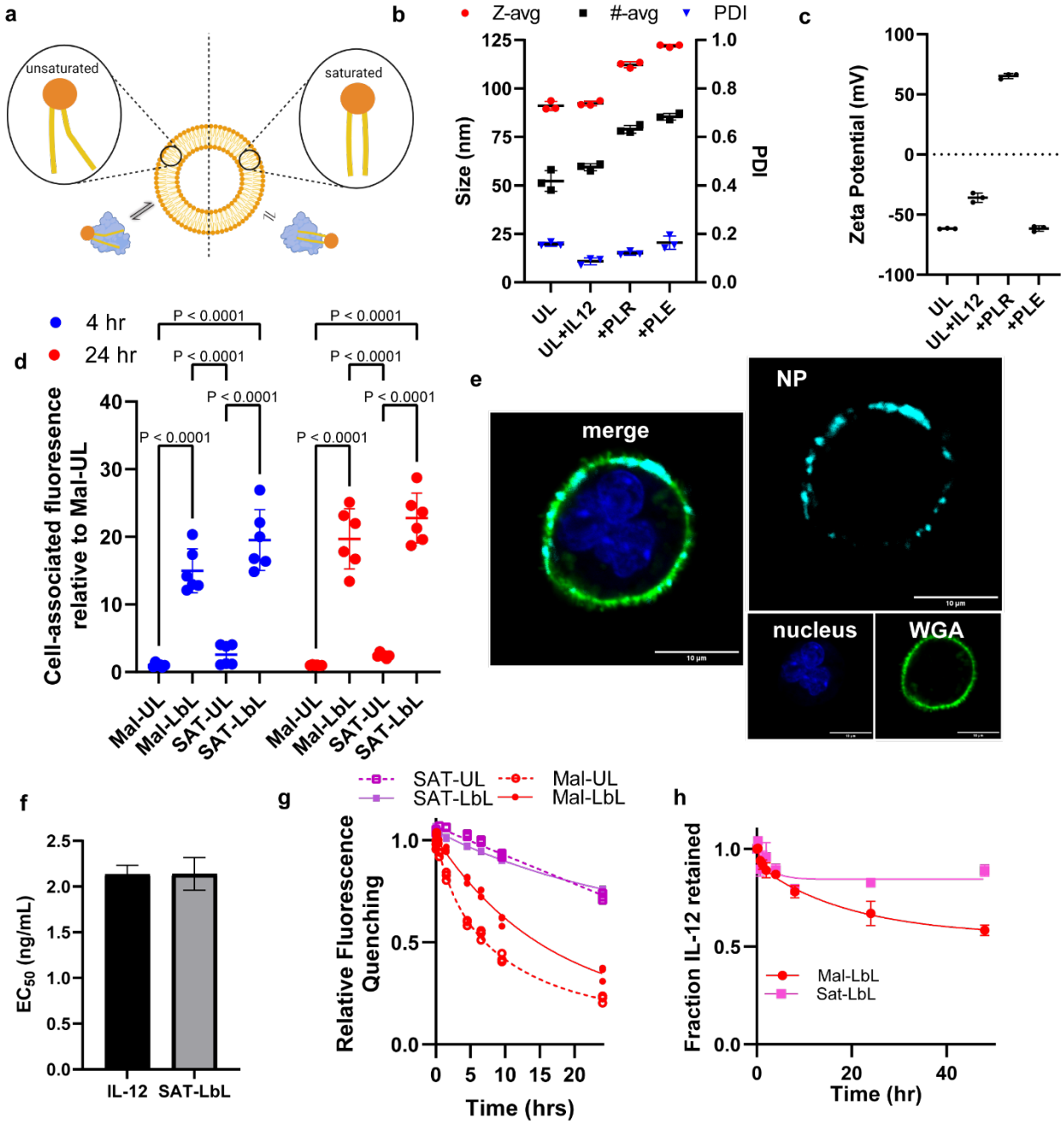

Figure D8. Characterization of Mal IL-12 NPs composed of saturated (SAT) lipids. a, Illustration of liposome bilayer composition effect on lipid exchange rate with serum proteins. **b,** Intensity-weighted hydrodynamic size (Z-avg), number average size (#-avg), and PDI of NPs during synthesis as measured via DLS (mean ± s.d.). **c,** Zeta potential of NPs during synthesis as measured via electrophoretic mobility in deionized water (mean ± s.d.). **d,** Association of NP fluorescence with HM1 cells *in vitro* relative to unlayered NPs after 4 and 24 hours of incubation (mean ± s.d.). **e,** Representative confocal microscopy images of HM-1 cells dosed with SAT-LbL for 4 hours. **f,** Calculated IL-12 EC_{50} of IL-12 compared to SAT-LbL NPs from HEK-Blue IL-12 assay (mean ± s.e.m.). **g,** Assessment of de-quenching from fluorophore detachment from unsat and SAT NPs when incubated with 100% FBS at 37 °C – curves represent the best fit of a two-phase decay model. **h,** Quantification of IL-12 retention with Mal-LbL or SAT-LbL upon incubation with 100% FBS (mean ± s.e.m.) – curves represent the best fit of a two-phase decay model. Statistical comparisons performed in **d** using two-way analysis of variance (ANOVA) with Tukey's multiple-comparisons. Data are representative of at least two independent experiments.

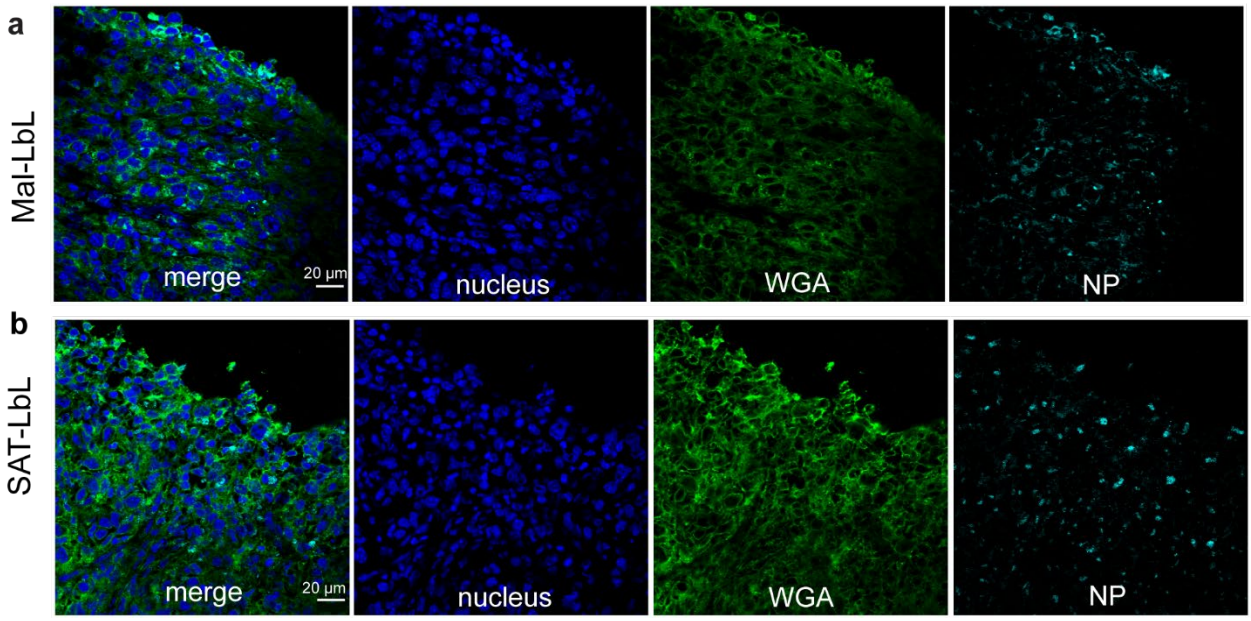

Figure D9. Confocal microscopy analysis of histological cryosections of omentum tumor nodules demonstrates both Mal-LbL and SAT-LbL penetrate tumor tissue. a-b, B6C3F1 mice were inoculated with 10^6 HM-1-luc tumor cells on day 0 were administered fluorescently-tagged Mal-LbL of SAT-LbL NPs carrying 20 μg IL-12 on day 14. One day after dosing, animals were sacrificed, and the omentum containing tumor nodules was frozen in optimal cutting temperature (OCT) compound then frozen sectioned and stained for confocal microscopy analysis. Shown are representative confocal images of omental tumor nodules from Mal-LbL (**a**) and SAT-LbL (**b**) treated animals.

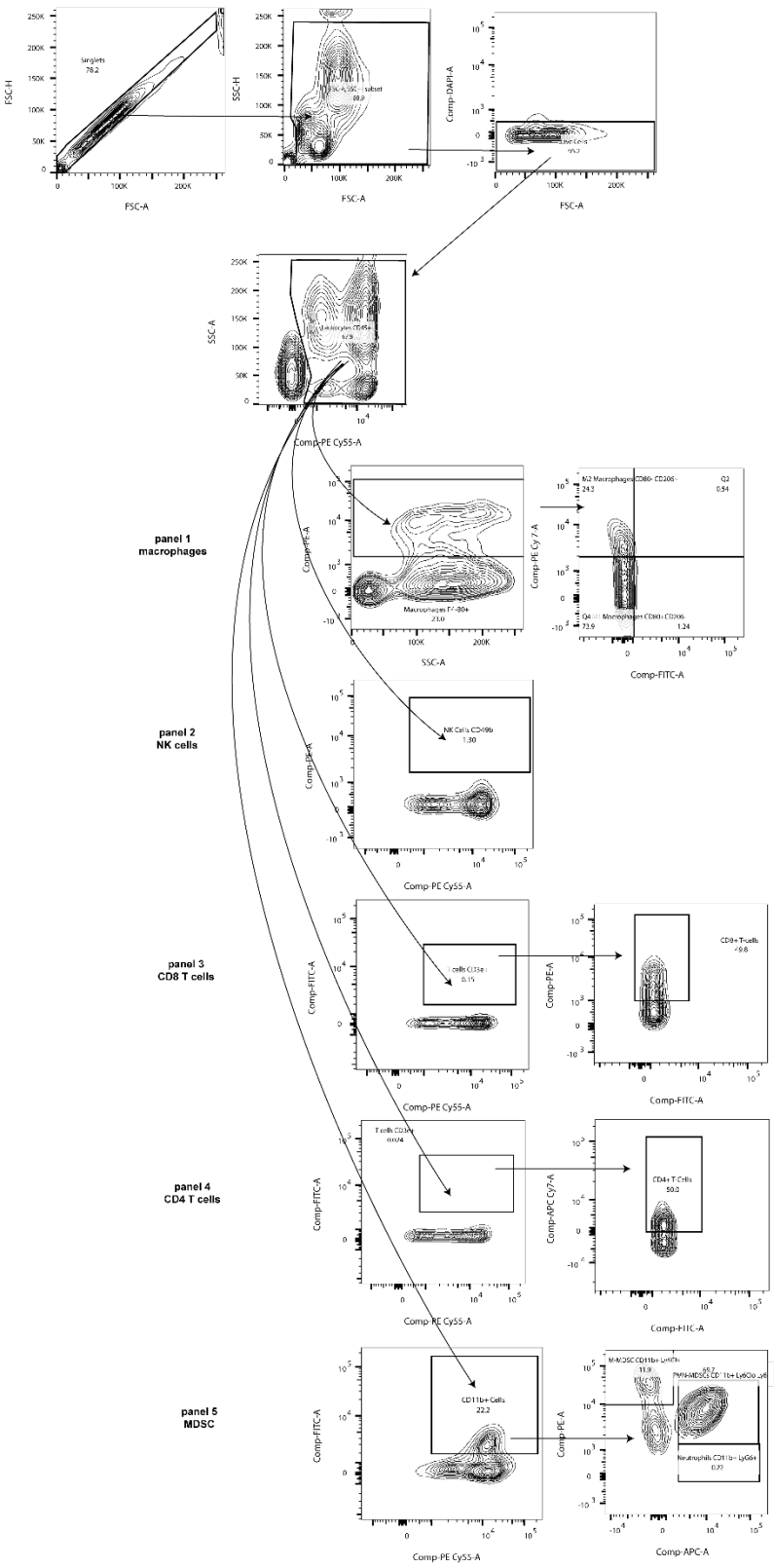

Figure D10. Flow cytometry cell gating strategy.

Appendix E

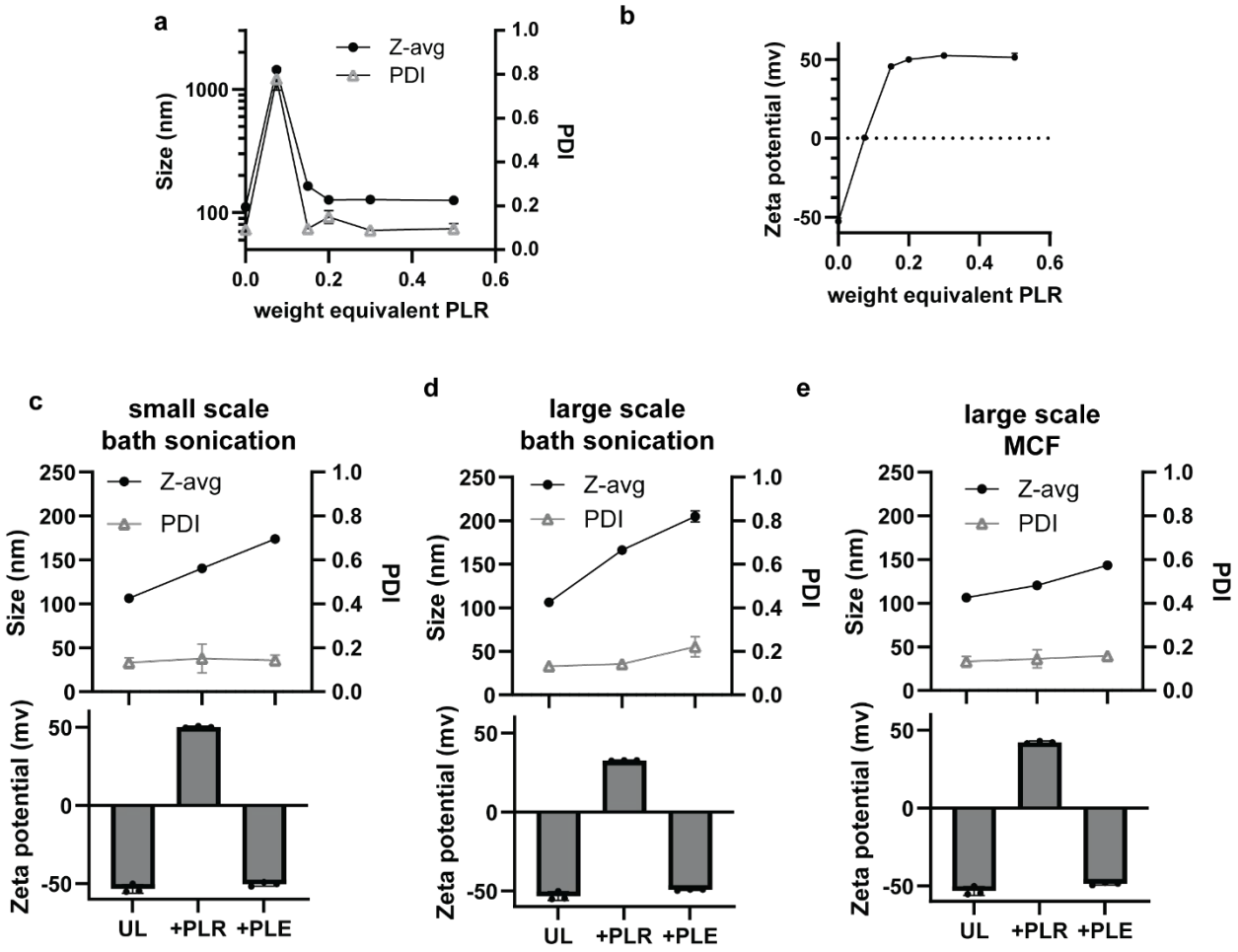

Figure E1. Microfluidic fluid mixing chips enable homogeneous LbL-NP assembly in optimized buffer solutions. (a) Z-avg size and PDI of NPs layered with increasing PLR-to-NP wt. eq. in 25 mM HEPES and 20 mM NaCl. **(b)** Zeta potential of NPs layered with increasing PLR-to-NP wt. eq. in 25 mM HEPES and 20 mM NaCl. **(c)** Z-avg size, PDI, and zeta potential of NPs layered with PLR and PLE using small-scale bath sonication mixing of polymers and NPs. **(d)** Schematic, Z-avg size, PDI, and zeta potential of NPs layered with PLR and PLE using large-scale bath sonication mixing of polymers and NPs. **(e)** Schematic, Z-avg size, PDI, and zeta potential of NPs layered with PLR and PLE using MCF mixing of polymers and NPs.

Appendix F

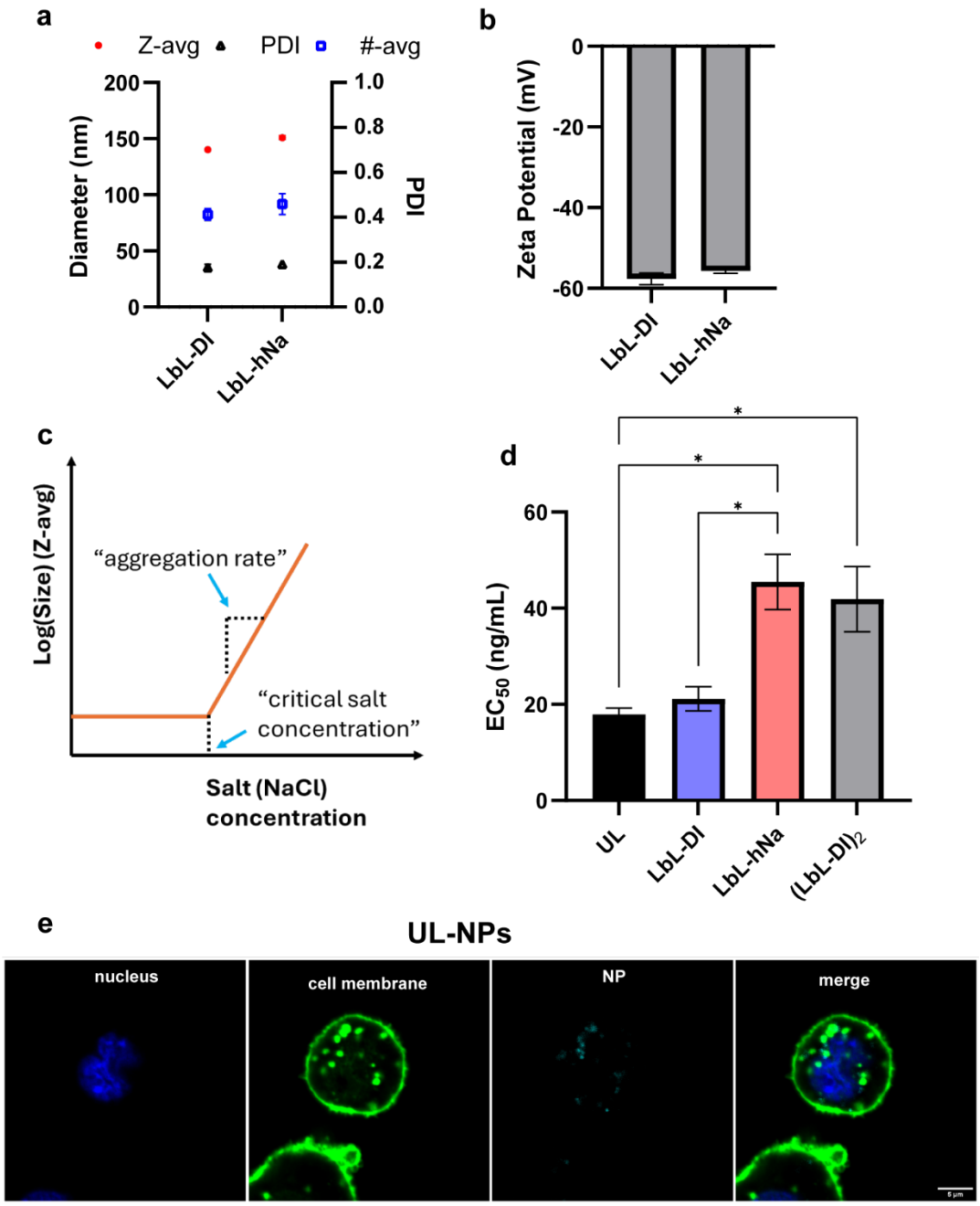

Figure F1. Biophysical characterization of LbL-NP library assembled in DI or hNa. (a) Dynamic light scattering size and polydispersity index (PDI) measurements of LbL-NPs assembled either in deionized water (D) or in the presence of mild ionic strength (hNa). (b) Apparent surface zeta potential measurements of LbL-NPs assembled either in DI or hNa. (c) Diagram of salt stability assay. (d) HEK-Blue IL-12 derived EC_{50} of IL-12 in NP preparations. (e) Representative confocal microscopy image of HM-1 cells incubated with UL-NPs for 4 hrs.

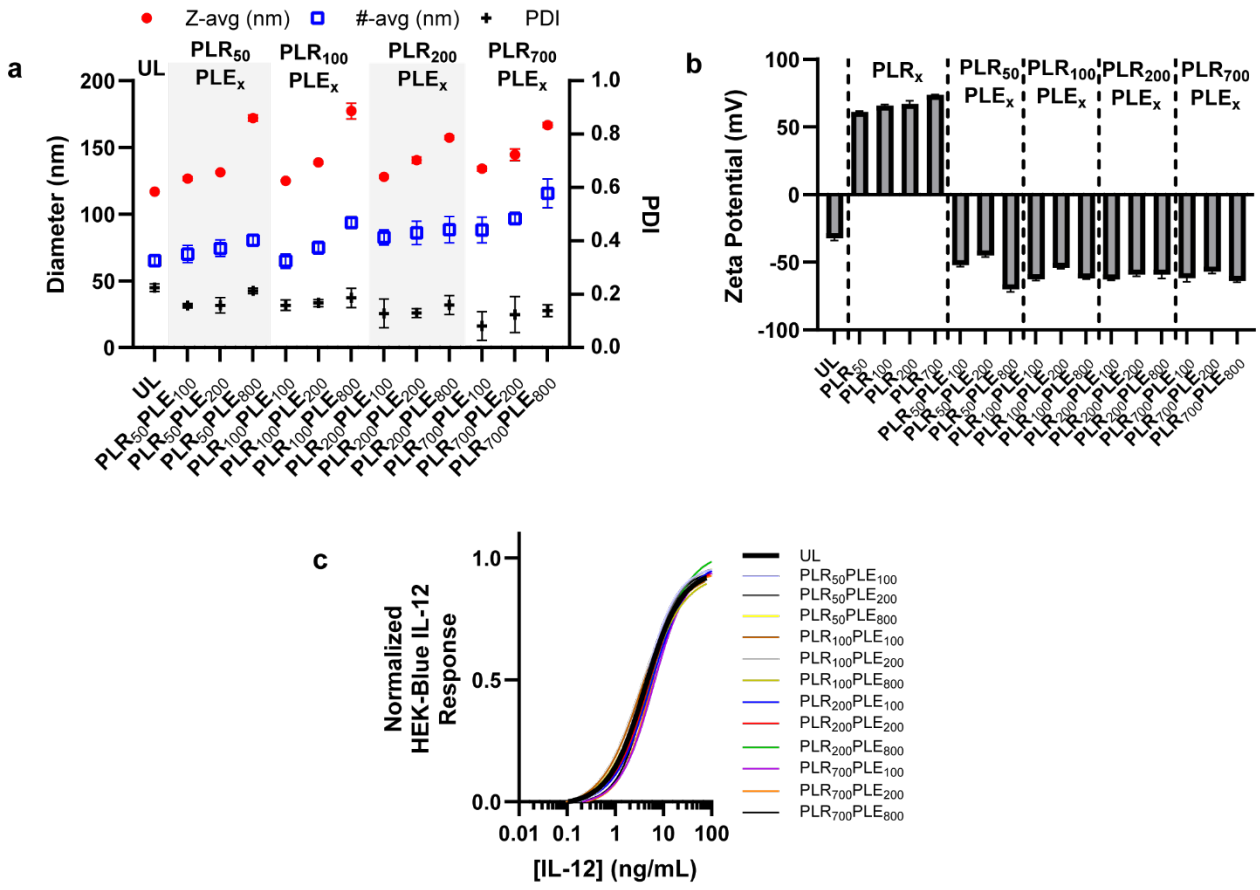

Figure F2. Biophysical characterization of LbL-NP library composed of various polymer MWs. (a) Dynamic light scattering size and polydispersity measurements of LbL-NPs composed of various molecular weight (MW) polymers. (b) Apparent surface zeta potential measurements of LbL-NPs composed of low or high molecular weight (MW) polymers. (c) HEK-Blue IL-12 of panel of MWs.

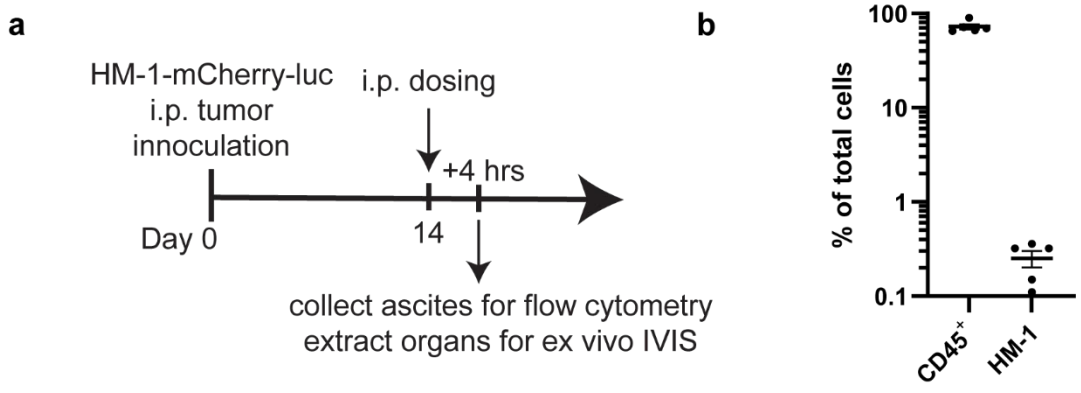

Figure F3. Biodistribution study. (a) Treatment timeline of mice bearing HM-1-mCherry-luc tumors for biodistribution study. (b) Assessment of cellular fraction immune cells and tumor cells of ascites in HM-1 mice.

Appendix G

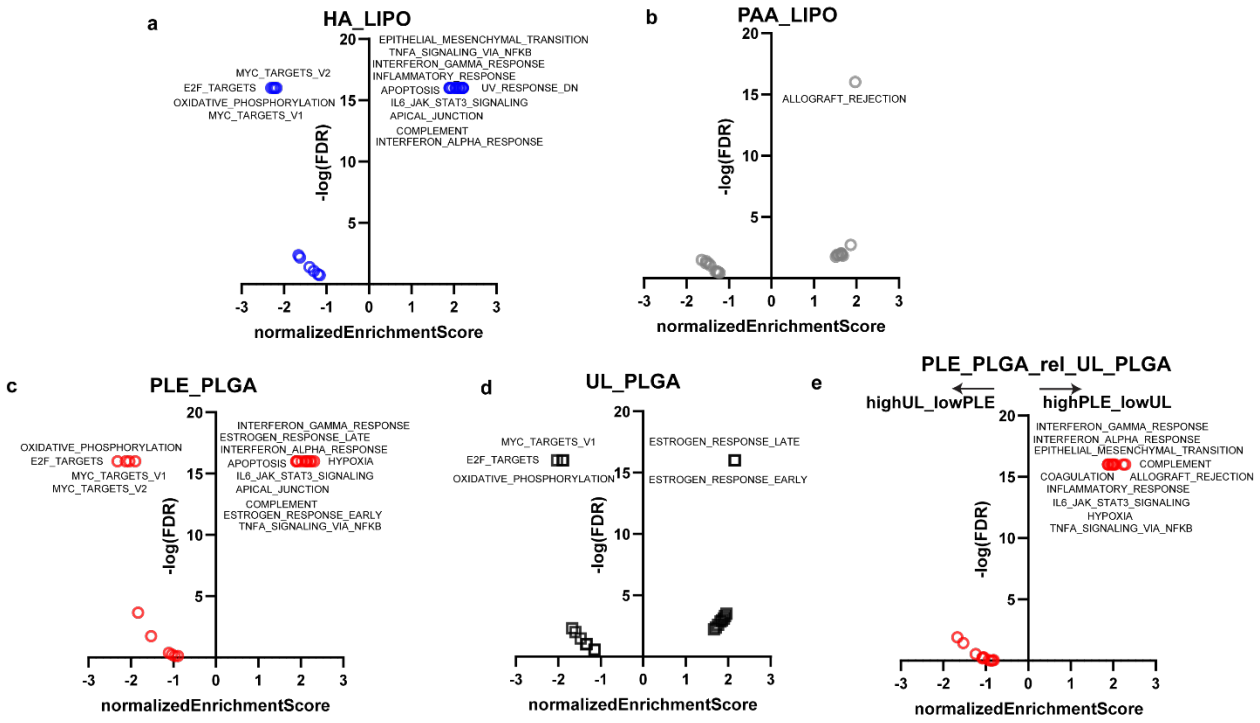

Figure G1. GSEA analysis of LbL-NP uptake. (a-d) Data from NanoPrism was used to rank cell lines based on their uptake of NPs, the median gene expression of the top 100 cell lines was compared to the median expression of the bottom 100 cell lines to derive the fold chance in gene expression for each formulation that was then used to perform gene-set enrichment analysis (GSEA) against the hallmark gene sets. Shown are the volcano plot for liposomal HA-NP (a), liposomal PAA-NP (b), PLE-coated PLGA NPs (c), and unlayered PLGA NPs (d) with the top 20 Hallmark gene sets hist. (e) The fold change in gene expression for PLE-coated PLGA NPs were normalized to UL PLGA NPs derive gene expression signatures that corresponded to high LbL-film binding, but low binding towards the unlayered cores. Shown are the volcano plot of PLE coated PLGA-NPs after normalization to UL PLGA NPs.

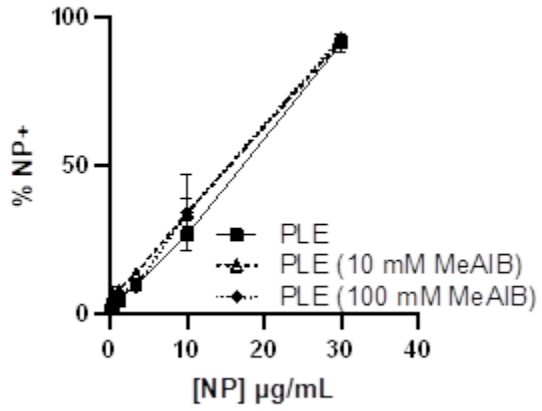

Figure G2. System A amino acid transport inhibitor MeAIB does not impair PLE-NP binding. HM-1 cells were plated in 96 well plates at 50 k cells/well and left to adhere overnight. Cells were then treated with 10 or 100 mM of MeAIB for 15 minutes prior to NP dosing at varying concentrations. Two hours after NP treatment, cells were washed with PBS, and suspended for flow cytometry analysis of NP uptake. Shown are the percentage of NP+ cells at each concentration of NP dosed.

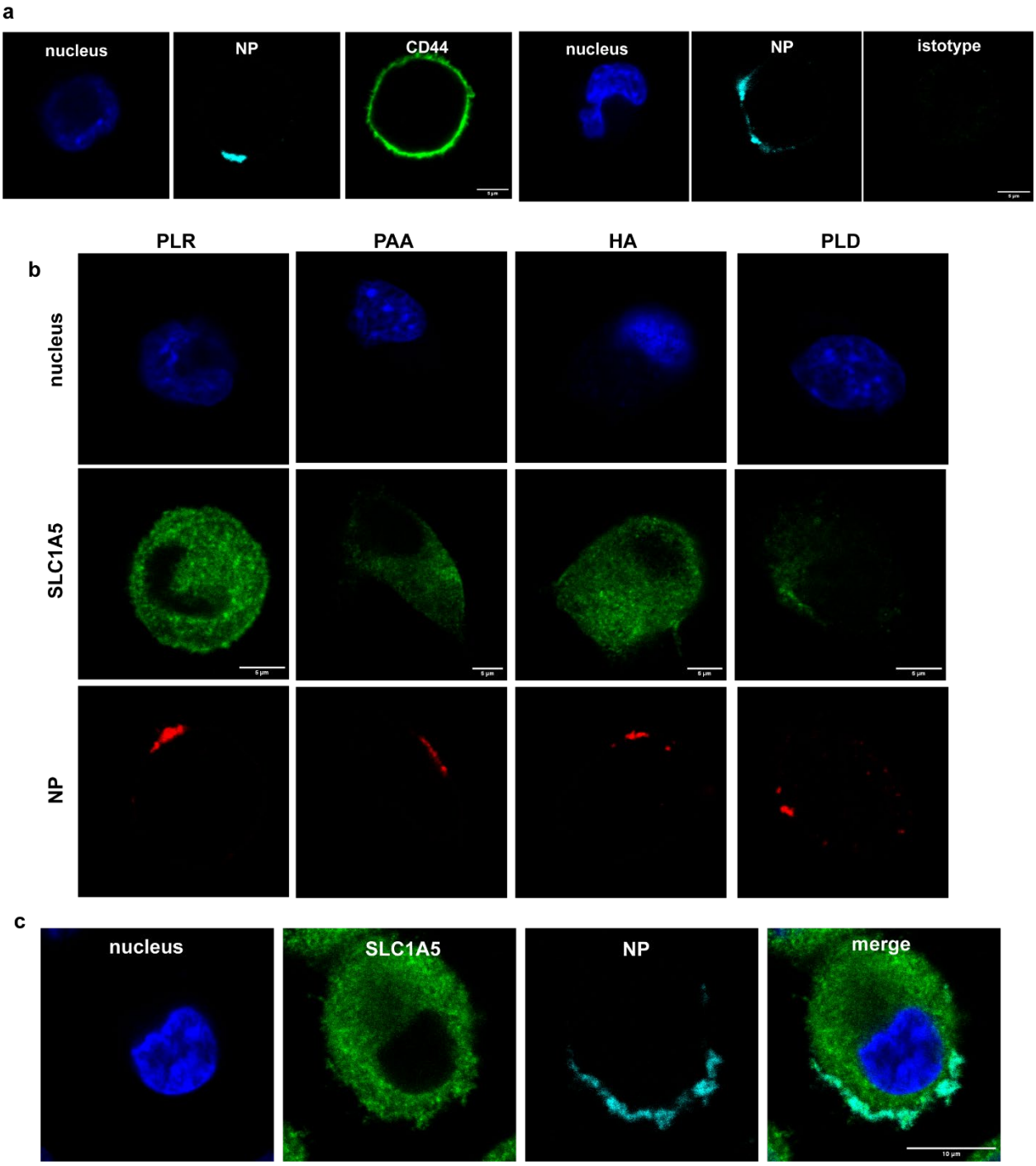

Figure G3. PLE coating is required for high colocalization of SLC1A5 with LbL-NPs. (a-b) HM-1 cells were plated in 8-well glass chamber slides at 10 k cells/well and left to adhere overnight. Cells were dosed with 1.5 µg/mL of NPs for 2 hrs. After NP treatment, cells were washed with PBS, fixed with PFA, and then rapidly permeabilized with saponin. Cells were then treated with primary antibodies for 2 hours followed by secondary antibodies for 30 minutes.

Shown are HM-1 cells treated with PLE-NPs and stained with an anti-CD44 Ab or isotype control (a), and HM-1 cells treated with various outer layer LbL-NPs and stained with anti-SLC1A5 Abs (b). (c) The same protocol was followed as (a-b) but cells were treated with 13.5 μg/mL of PLE-NPs.

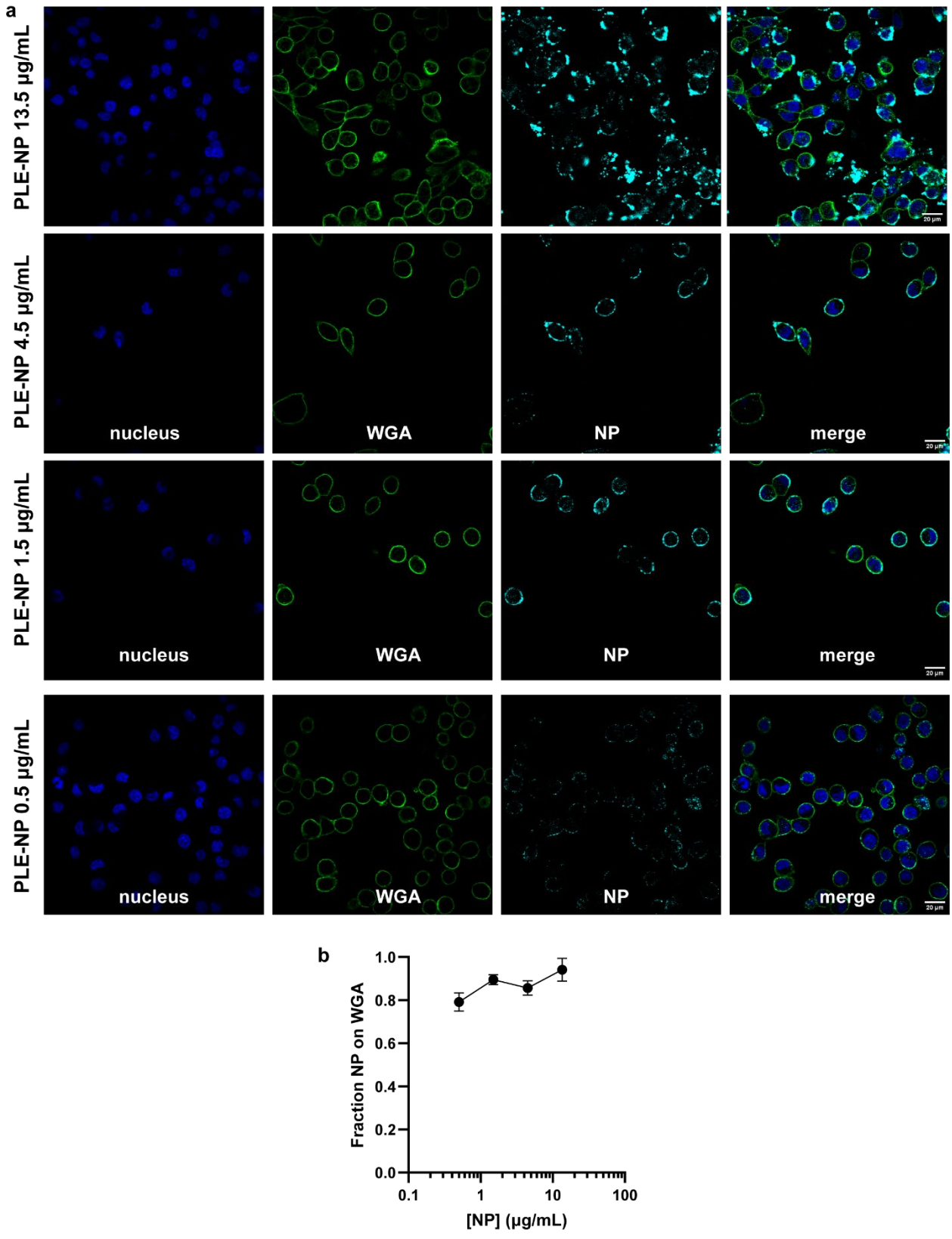
a
PLE-NP 13.5 µg/mL
PLE-NP 4.5 µg/mL
PLE-NP 1.5 µg/mL
PLE-NP 0.5 µg/mL
nucleus
WGA
NP
merge
20 µm
b
Fraction NP on WGA
1.0
0.8
0.6
0.4
0.2
0.0
0.1
1
10
100
[NP] (µg/mL)

Figure G4. PLE-NPs associate primarily on the cell membrane. (a-b) HM-1 cells were plated in 8-well glass chamber slides at 10 k cells/well and left to adhere overnight. Cells were dosed with varying concentrations of NPs for 4 hrs. After NP treatment, cells were washed with PBS, fixed with PFA, and then stained with Hoechst 33342 and wheat germ agglutinin (WGA) and visualized on a confocal microscope. Shown are representative confocal images of HM-1 cells treated with various concentrations of PLE-NPs (a) and quantification of the fraction of NP pixel colocalized with cell membrane pixels (b).

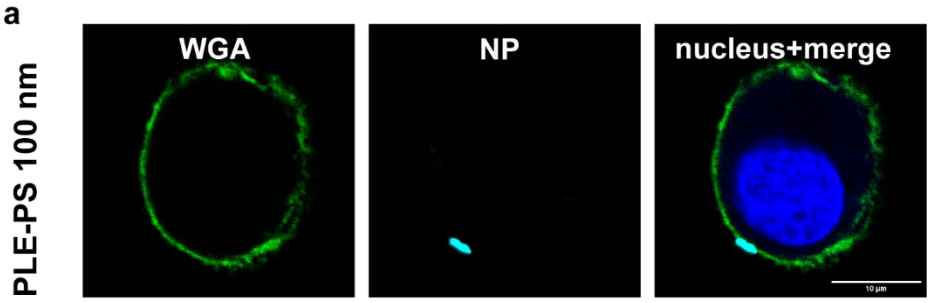

Figure G5. 100 nm polystyrene PLE-NPs are retained at the cell membrane. HM-1 cells were plated in 8-well glass chamber slides at 10 k cells/well and left to adhere overnight. Cells were dosed with 1 µg/mL of NPs for 4 hrs. After NP treatment, cells were washed with PBS, fixed with PFA, and then stained with Hoechst 33342 and wheat germ agglutinin (WGA) and visualized on a confocal microscope. Shown is a representative HM-1 cell dosed with 100 nm PLE-PS particles.

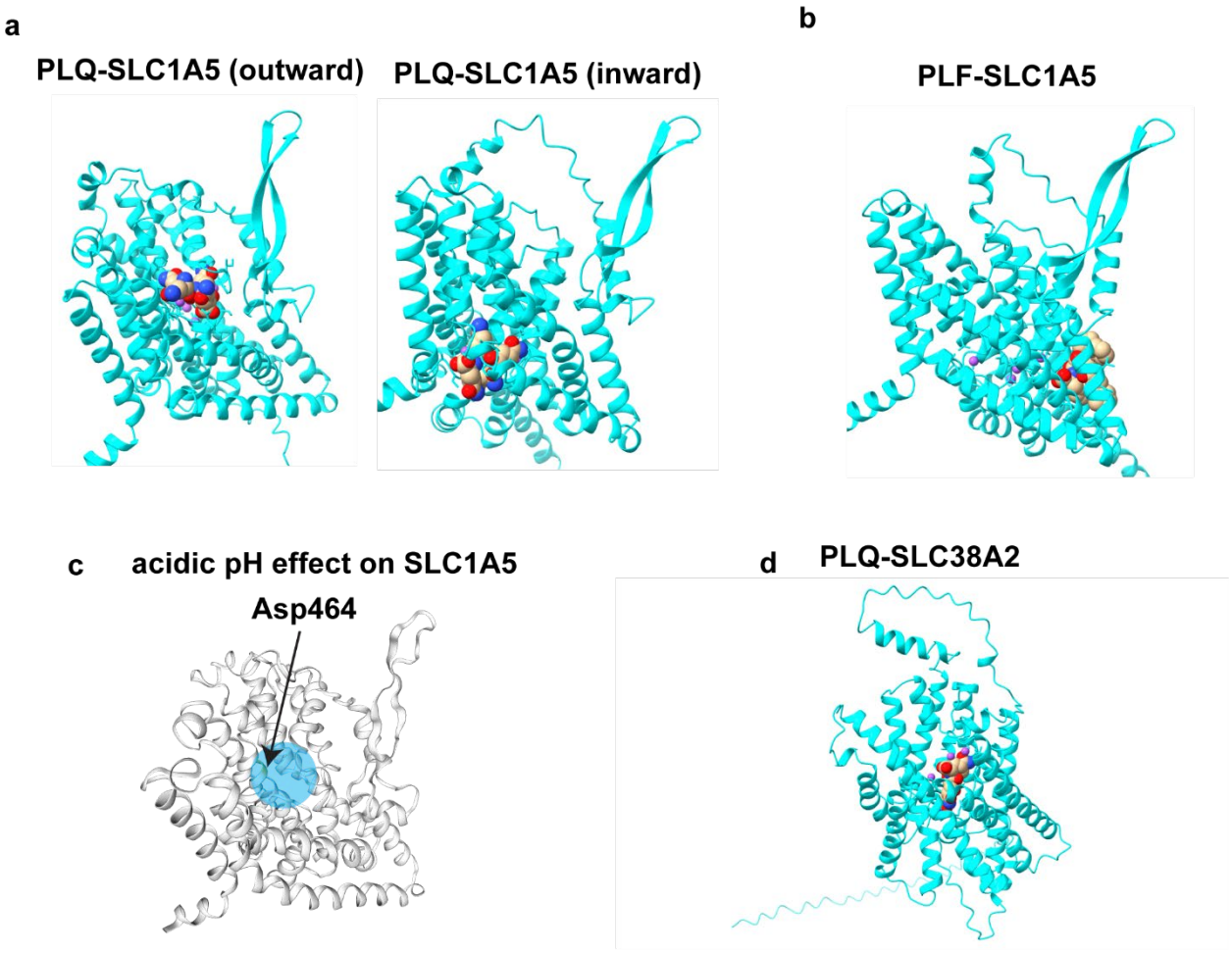

Figure G6. Modeling predictions. (a) Representative AlphaFold 3 model structure of SLC1A5 and PLQ bound to the outward or inward orientation of SLC1A5. (b) Representative AlphaFold 3 model structure of SLC1A5 and PLF binding to a transmembrane region. (c) patcHwork prediction of change in ionization states of amino acids in SLC1A5 from pH of 7.4 to pH of 6.0. (d) Representative AlphaFold 3 model structure of SLC38A2 and PLQ.

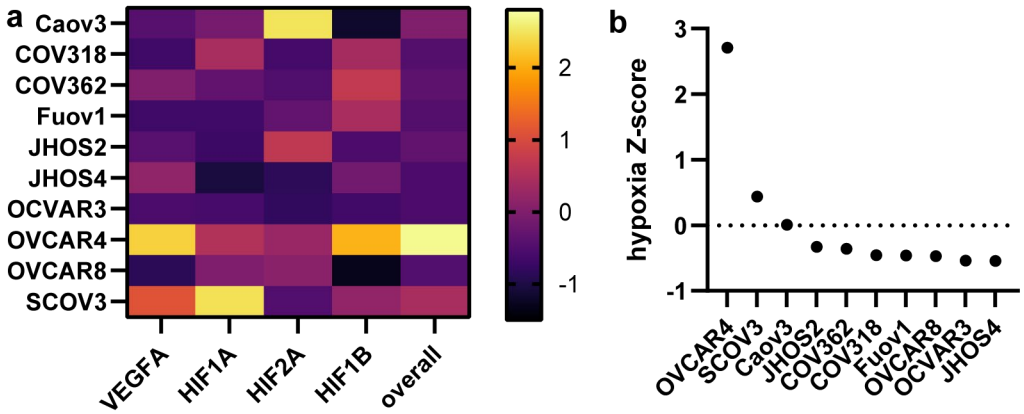

Figure G7. Analysis of hypoxia-related gene expression in ovarian cancer cell lines. (a) Heat map of Z-score for each gene across the cell lines and the "overall" hypoxia metric determined by the product of gene expression for each gene. (b) Z-score of the overall hypoxia expression levels. Expression levels extracted from the ProteinAtlas.